ACOUSTIC ABSORPTION AND THE UNSTEADY FLOW ASSOCIATED WITH CIRCULAR APERTURES IN A GAS TURBINE ENVIRONMENT

Jochen Rupp

A doctoral Thesis

Submitted in partial fulfilment of requirements for the award of Doctor of Philosophy of Loughborough University

May 2013

Abstract

This work is concerned with the fluid dynamic processes and the associated loss of acoustic energy produced by circular apertures within noise absorbing perforated walls. Although applicable to a wide range of engineering applications particular emphasis in this work is placed on the use of such features within a gas turbine combustion system. The primary aim for noise absorbers in gas turbine combustion systems is the elimination of thermo-acoustic instabilities, which are characterised by rapidly rising pressure amplitudes which are potentially damaging to the combustion system components. By increasing the amount of acoustic energy being absorbed the occurrence of thermo-acoustic instabilities can be avoided.

The fundamental acoustic characteristics relating to linear acoustic absorption are presented. It is shown that changes in orifice geometry, in terms of gas turbine combustion system representative length-to-diameter ratios, result in changes in the measured Rayleigh Conductivity. Furthermore in the linear regime the maximum possible acoustic energy absorption for a given cooling mass flow budget of a conventional combustor wall will be identified. An investigation into current Rayleigh Conductivity and aperture impedance (1D) modelling techniques are assessed and the ranges of validity for these modelling techniques will be identified. Moreover possible improvements to the modelling techniques are discussed. Within a gas turbine system absorption can also occur in the non-linear operating regime. Hence the influence of the orifice geometry upon the optimum non-linear acoustic absorption is also investigated. Furthermore the performance of non-linear acoustic absorption modelling techniques is evaluated against the conducted measurements. As the amplitudes within the combustion system increase the acoustic absorption will transition from the linear to the non-linear regime. This is important for the design of absorbers or cooling geometries for gas turbine combustion systems as the propensity for hot gas ingestion increases. Hence the relevant parameters and phenomena are investigated during the transition process from linear to non-linear acoustic absorption.

The unsteady velocity field during linear and non-linear acoustic absorption is captured using particle image velocimetry. A novel analysis technique is developed

which enables the identification of the unsteady flow field associated with the acoustic absorption. In this way an investigation into the relevant mechanisms within the unsteady flow fields to describe the acoustic absorption behaviour of the investigated orifice plates is conducted. This methodology will also help in the development and optimisation of future damping systems and provide validation for more sophisticated 3D numerical modelling methods.

Finally a set of design tools developed during this work will be discussed which enable a comprehensive preliminary design of non-resonant and resonant acoustic absorbers with multiple perforated liners within a gas turbine combustion system. The tool set is applied to assess the impact of the gas turbine combustion system space envelope, complex swirling flow fields and the propensity to hot gas ingestion in the preliminary design stages.

Keywords: Acoustic Absorption, Rayleigh Conductivity, Impedance, Gas Turbine Engine, Combustion System, Passive Damping, Thermo-Acoustic Instability, Particle Image Velocimetry, Proper Orthogonal Decomposition.

Acknowledgement

This thesis has been conducted on a part-time basis at Loughborough University whilst I am employed by Rolls-Royce. First of all I would like to thank Lesley Hawkins and Ken Young at Rolls-Royce for giving me the opportunity of conducting this research at Loughborough University. Special thanks goes to John Moran who in addition to supporting my application to undertake the research also took the role of my industrial mentor providing invaluable advice and guidance throughout this work. A big thank you goes to Michael Spooner and Michael Whiteman of the Combustion and Casings Engineering Department at Rolls-Royce for their support throughout my thesis by ensuring I could spend sufficient time away from Rolls-Royce during my studies at Loughborough University. Without the support from Rolls-Royce this thesis would not have been possible and this is much appreciated. The support from Rolls-Royce Deutschland, in particular Sermed Sadig, Miklós Gerendás and Waldemar Lazik is gratefully acknowledged.

I would like to thank every member of the Rolls-Royce University Technology Centre at Loughborough University. They provided a great working atmosphere in which colleagues became friends. A special mention is required for my supervisor Jon Carrotte for his never ending advice, support, guidance, patience and encouragement throughout this work. I hope I will get many opportunities in the future to show Jon that my golf handicap has still not improved. Many thanks to Adrian Spencer for his invaluable support as well as the support provided to me by Jim McGuirk. I would like to thank Duncan Walker and Ashley Barker for their continuous encouragement throughout my research both inside and outside the tearoom. The help from Tim Bradley and Vivek Savarianandan during the non-resonating liner experiments is also gratefully acknowledged. I want to thank the technicians for the excellent work on the experimental test facility, drilling a large amount of holes whenever required.

This thesis is dedicated to my wife Maria and my parents, Rudolf and Elfriede who are always there for me, with patience and encouragement without which this work would not have been achieved.

Table of Contents

List of Figures

Nomenclature

Parameter	Description
A	Surface area
A_D	Geometric aperture area
A_d	Effective aperture area
$a_k(t)$	POD analysis temporal coefficient
B	Stagnation enthalpy
B_C	Stagnation enthalpy within damper cavity (i.e. between damping and metering skin)
C	Circumference
C_L	Centreline
C_D	Discharge coefficient
c	Speed of sound
c_s	Spring stiffness constant
D	Geometric diameter
d	Diameter of orifice vena contracta
$\dot{E}$	Kinetic energy flux
E_{kin}	Kinetic energy
f	Frequency
F	Force
H	Combustor height
K_D	Orifice Rayleigh Conductivity
k	Wave number
L_D	Axial length of damper
L	Orifice length
L_{eff}	Orifice effective length
L_{corr}	Orifice length correction
L_0	Slug length of unsteady jet flow

M	Mach number
m	Mass
$\dot{m}$	Mass flow
N	Amount of apertures or amount of samples
P	Total pressure
p	Static pressure
P_a	Aperture pitch
Q	Volume flux
Q	Resonance parameter
R	Radius
Rv_C	Vortex core radius
R_{VR}	Vortex ring radius
R_C	Reflection coefficient
R_Z	Resistance
Re	Reynolds number
r	Radial coordinate
S	Separation between liners, damper backing cavity depth
St	Strouhal number $St = \omega R/\overline{U}_D$
St_d	Strouhal number $St = \omega R/\overline{U}_d$
St_j	Jet Strouhal number $St = \omega R/\overline{U}_J$
T	Time period of one acoustic cycle
t	Time
Δt	Inter-frame time between two laser pulses
U	Velocity
U_j	Mean jet velocity
U_D	Mean velocity in plane of aperture
U_{blow}	Mean blowing velocity
U_{bulk}	Area averaged mean flow velocity
U_d	Mean velocity at end of vena contracta
u_D	Unsteady velocity in plane of the aperture

u_d	Unsteady velocity at end of vena contracta
u_v	Vortex ring velocity
u_c	Unsteady velocity within damper cavity (i.e. between damping and metering skin)
V	Volume
u, v, w	Velocity components in Cartesian coordinates
W_D	Damper width
x	Axial coordinate
X_Z	Reactance
x, y, z	Cartesian coordinates
Z	impedance
z	Normalised impedance $z = Z/\rho c$

Greek Symbols

Parameter	**Description**
γ	Ratio of specific heats
Γ	Inertia
Γ_C	Circulation
δ	Admittance
Δ	Acoustic absorption coefficient
ε_x	Error in the measurement of parameter *x*
ζ_L	Fluid dynamic loss coefficient
ζ_{vis}	Loss coefficient due to unsteady boundary layer
η	Liner compliance
λ	Wave length
μ	Dynamic viscosity
ν	Kinematic viscosity
Π	Energy flux
Π_L	Acoustic energy loss
Π_P	Acoustic energy loss normalised with incident pressure amplitude

Π_{norm}	Acoustic energy loss normalised with incident pressure amplitude and mean mass flow across the apertures
ρ	Density
σ	Porosity
σ_ω	Circulation amplitude per unit length
σ_x	Standard deviation of parameter *x*
$\phi_k(x)$	POD analysis spatial mode
ω	Angular frequency
$\vec{\omega}$	Vorticity
ω_N	Normalised vorticity $\omega_N = \vec{\omega}\overline{U}_{blow}/D$

Subscripts

Parameter	**Description**
D	Parameter is derived in the plane of the aperture
d	Parameter is derived at end of vena contracta
ds	Downstream
i	Incident acoustic wave
in	Inflow
n	Normalised parameter
out	Outflow
pk	0 to peak amplitude
QS	Quasi-steady
r	Reflected acoustic wave
rms	Root mean square amplitude
tot	Total
us	Upstream
+	Acoustic wave travelling downstream
-	Acoustic wave travelling upstream

Superscripts

Parameter	Description
+	Acoustic wave travelling downstream
-	Acoustic wave travelling upstream
QS	Quasi-steady

Mathematical symbols

Parameter	Description
a‘	Time varying parameter a
$\overline{a}$	Time averaged parameter a
$\langle a \rangle$	Ensemble average of parameter a
a^*	Complex conjugate parameter a
$\hat{a}$	Fourier transformed amplitude of parameter a
$\lvert\hat{a}\rvert$	Magnitude of Fourier transformed amplitude a

Abbreviations

Parameter	Description
CCD	Charged Coupled Device
CFD	Computational Fluid Dynamics
DNS	Direct Numerical Simulation
FFT	Fast Fourier Transformation
FOV	Field Of View
LES	Large Eddy Simulation
Nd:YLF	Neodym Yttrium Lithium Fluoride
OPR	Overall Pressure Ratio
PIV	Particle Image Velocimetry
POD	Proper Orthogonal Decomposition
RANS	Reynolds-Averaged Navier-Stokes
RQL	Rich Quench Lean

1 Introduction

This thesis is concerned with the fluid dynamic processes and the associated loss of acoustic energy produced by circular apertures within noise absorbing perforated walls. Therefore the work is applicable to a wide variety of engineering applications, although in the current work particular emphasis is placed on the use of such features within a gas turbine combustion system. The primary aim in this application is the elimination of thermo-acoustic instabilities by increasing the amount of acoustic energy absorbed. In this way any coupling between the acoustic pressure oscillations and unsteady heat release is suppressed.

1.1 Gas Turbine Combustion Systems

Figure 1.1 shows a schematic of a state of the art turbofan gas turbine engine as it is used in the civil aviation industry. Within the combustion system of a gas turbine the chemical energy of the fuel is converted into thermal energy, i.e. heat release. The generated heat release is expanded in the downstream turbine which is driving the compressor and the fan upstream of the combustor. Any thermal energy which is not used by the engine to compress the air upstream of the combustor is then used within the jet nozzle to generate thrust (e.g. Rolls-Royce (2005)).

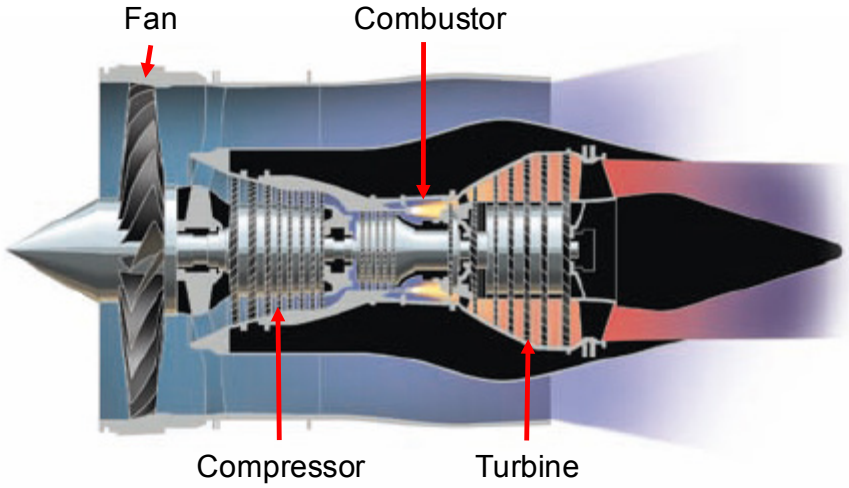

Figure 1.1: Schematic of Turbofan jet engine, from Rolls-Royce (2005)

Current civil turbofan aero-engines are powered using conventional rich-quench-lean (RQL) combustion systems. A schematic of such a full annular combustion chamber is

shown in Figure 1.2. A more detailed summary of gas turbine combustion chambers can be found, for example, in Lefebvre and Ballal (2010). The air delivered by the compressor typically enters the combustion system through an annular pre-diffuser. Downstream of the pre-diffuser the air is split into various streams with the majority of the air being fed around the combustor to the primary and secondary ports, the combustor wall cooling system and the turbine blade cooling system. In addition a small amount of air enters the combustion chamber via the swirlers of the fuel injector. Thus the flame is swirl stabilised within the primary zone of the combustion chamber, where the fuel is atomised, vaporised and mixed with the various air streams prior to combustion. The aim is to generate adequate residence time and turbulence levels to generate the required mixing of fuel and air for flame stabilisation.

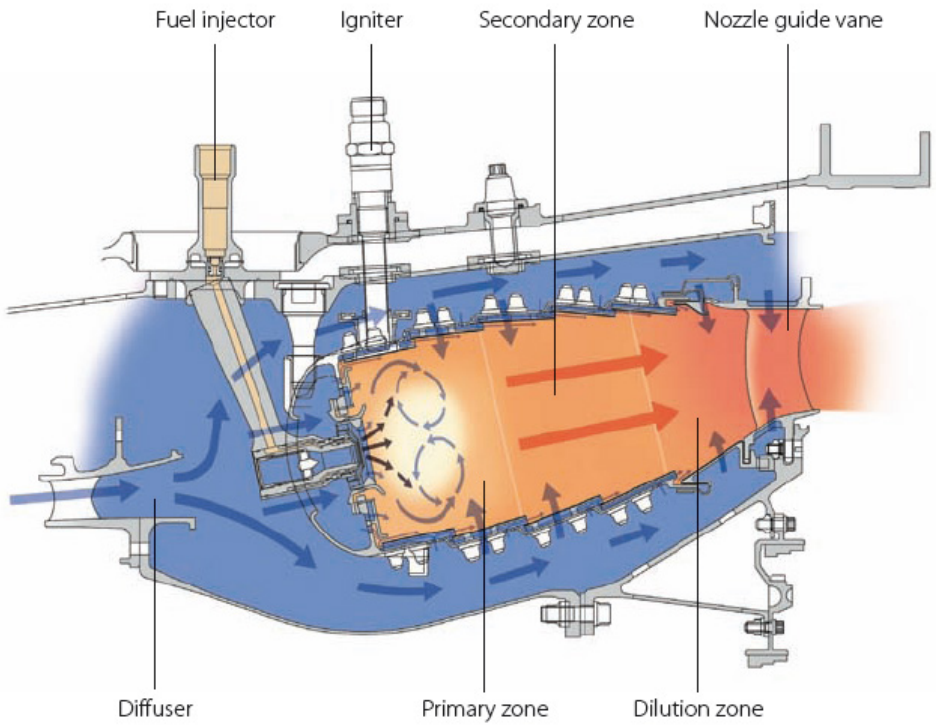

Figure 1.2: Schematic of conventional gas turbine combustion system (Rolls-Royce (2005))

The primary and secondary ports are designed to control pollutant emissions by feeding an optimised amount of air into the combustor. Within the dilution zone the temperature of the hot gas inside the combustor is further reduced by feeding a further 20-40% of the air into the dilution ports (Lefebvre and Ballal (2010)). The aim of this

zone is to generate an adequate temperature exit profile which is suitable for the nozzle guide vane of the high pressure turbine at the exit of the combustor. This is important for the turbine life and its cooling requirement. Moreover, the radial and overall temperature profiles at the combustor exit have a significant impact upon the efficiency of the turbine downstream of the combustor.

1.1.1 Environmental Aspects of Gas Turbine Combustion Systems

Pollutant emissions emitted by aviation affect the local air quality near the airports as well as the upper troposphere and lower stratosphere (8-12 km altitude) for civil aviation. The pollutant emissions at altitude can cause chemical reactions which lead to ozone (O_3) production and cloud formation. A measure of the affects of the pollutant emissions on the climate is indicated by the radiative forcing (RF) parameter as described by Prather et. al. (1999). The radiative forcing index is based on the balance between radiative heating effects produced by the sun and terrestrial cooling effects. Any man made emissions in the atmosphere will change this balance and therefore produce positive radiative forcing (i.e. heating of the atmosphere) or negative radiative forcing (i.e. cooling of the atmosphere) which will ultimately lead to climate change. The main emissions emitted by gas turbine combustion systems burning a hydrocarbon fuel are (Figure 1.3):

- Carbon monoxide (CO) and carbon dioxide (CO_2)
- Nitric oxides (NO) and nitrogen dioxide (NO_2), which are grouped together under the term NO_X
- Unburned hydrocarbons (UHC)
- soot
- Water vapour (H_2O)

The sulphur (S) indicated in Figure 1.3 is controlled via the sulphur content within the fuel. The major direct emissions which will be affected by the combustion processes are CO_2 and NO_X emissions. Carbon dioxide is a greenhouse gas which will lead to positive radiative forcing. Moreover CO_2 is absorbed by the oceans and leads to an increased ocean acidification. NO_X at cruise altitude (8-13km) is leading to chemical reactions

where methane (CH_4) is reduced and ozone (O_3) is increased. Ultimately this also leads to a positive change in radiative forcing (Prather et. al. (1999), ICAO (2010)).

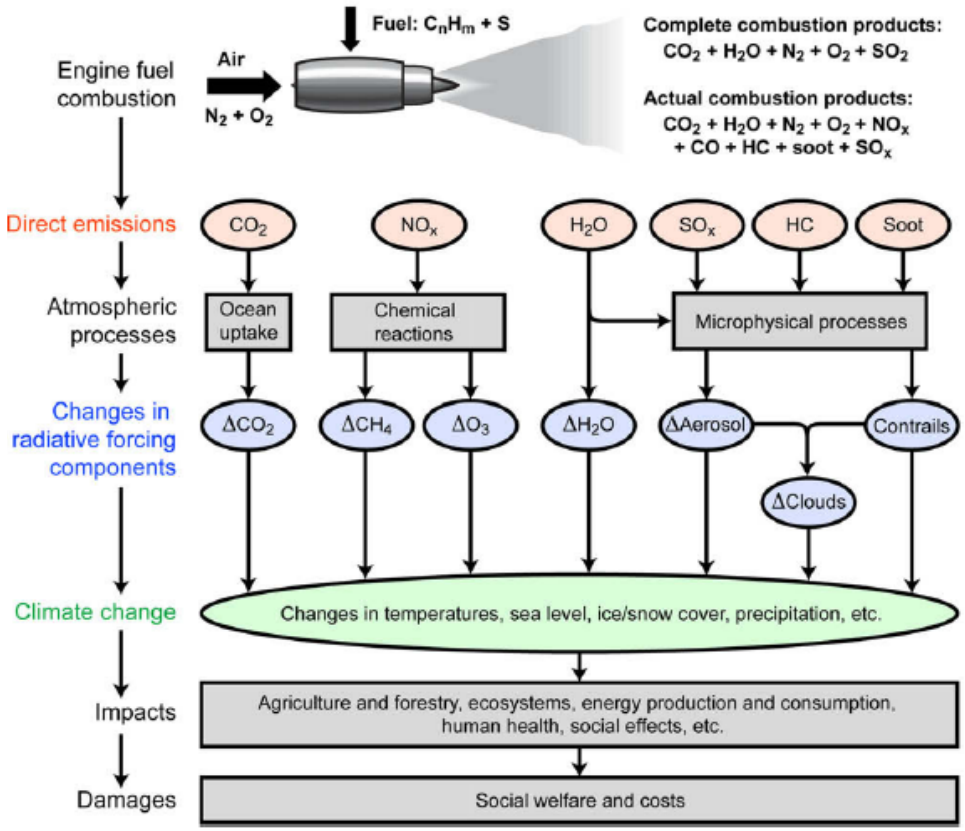

Figure 1.3: Schematic of aviation emissions and their effects on climate change from Lee et. al. (2009)

Currently the impact on CO_2 emissions emitted by aviation is 2% of the world total CO_2 emissions (Prather et. al. (1999), ICAO (2010)). However current predictions show that the world wide air traffic is anticipated to grow by 4-5% per year (ACARE (2011)). Therefore CO_2 emissions will increase if the technology of the used aircraft and engine is not improved. The Advisory Council for Aeronautics Research in Europe (ACARE (2001)) set a target to reduce CO_2 emissions from aircraft by 50% in the year 2020. For aero-engine manufacturers this means future aero-engines will have reduced fuel burn and therefore reduced CO2 emissions in the year 2020 by 15-20% (Rolls-Royce (2010)) as indicated in Figure 1.4. The remaining 20-25% is due to more efficient aircraft and 5-10% is due to improved air traffic management.

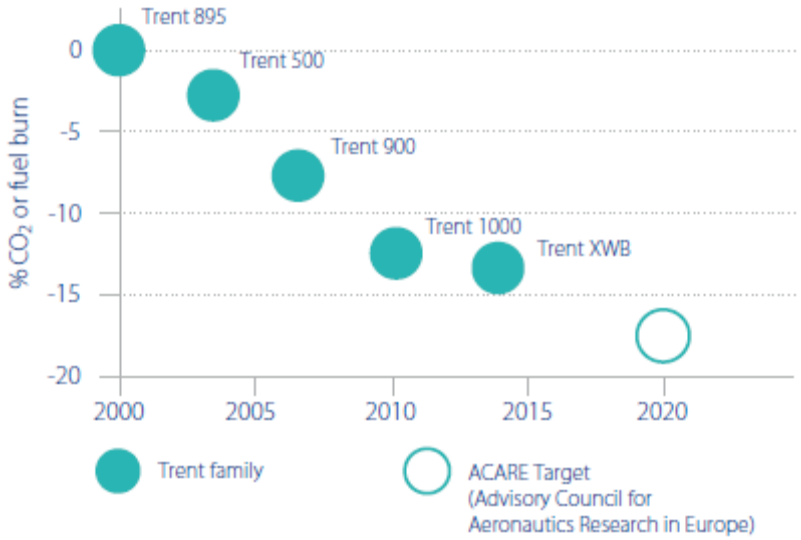

Figure 1.4: CO_2 reduction of Rolls-Royce aero-engines, from Rolls-Royce (2010)

The ACARE 2020 target for NO_X emissions reductions were set to 80%. On an engine level this means a NO_X reduction in the order of 60% as shown in Figure 1.5. In this case the NO_X reduction is shown relative to a baseline NO_X standard given by the Committee on Aviation Environmental Protection (CAEP) in 2004. More recently ACARE Vision 2050 (ACARE (2011)) has proposed the CO_2 and NO_X emissions targets for the year 2050. In this report a 75% reduction in CO_2 and a 90% reduction in NO_X emissions is set. Current aero-engine combustion systems have combustion efficiencies higher than 99.9% at take-off and cruise conditions (Lewis et. al. (1999), Rolls-Royce (2005), Lefebvre and Ballal (2010)). The CO_2 emissions are directly linked to the necessary fuel burn, as it is a product of complete combustion. Therefore CO_2 can only be reduced if less fuel is needed for the transport of goods and passengers within an aircraft. Thus the CO_2 emissions are a product of aero-engine efficiency, air frame efficiency and air traffic management.

Improvements in aero-engine efficiency can be achieved by improving the efficiency of the components of the engine, i.e. turbomachinery efficiency, leakage reduction, cooling reductions, etc. Moreover improvements in thermal efficiency can be used to reduce the amount of fuel used, and thus reduce the amount of CO_2 produced, for the generation of the necessary thrust of the engine. The improvement in thermal efficiency is achieved by increasing the overall pressure ratio (OPR) of the engine. Unfortunately this means the combustor inlet temperatures increase, which in turn generates higher combustion temperatures and thus higher turbine inlet temperatures. Lefebvre and

Ballal (2010) as well as Lewis et. al. (1999) show that NO_X emissions increase with increasing temperature. Another driver for NO_X is the residence time within the combustor (Lefebvre and Ballal (2010)). Thus improvements in thermal efficiency of the gas turbine also lead to increasing NO_X emissions. Hence different combustion concepts are necessary to achieve both requirements: reduced CO_2 and reduced NO_X emissions.

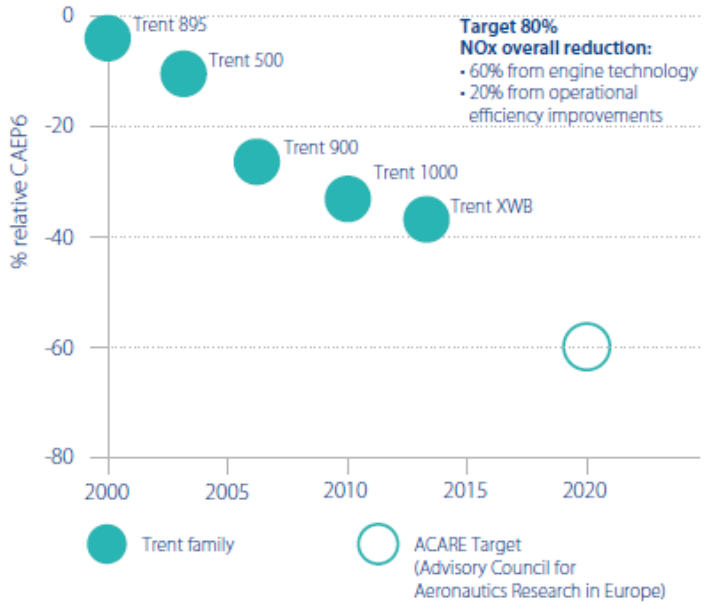

Figure 1.5: NO_X reduction of Rolls-Royce aero-engines, from Rolls-Royce (2010)

Current combustion technology utilises RQL concepts to control the NO_X emissions generated in the combustion chamber. As already mentioned nitrogen oxide emissions are generated at high combustion temperatures which occur near stoichiometric equivalence ratios (~1). Hence a rapid quenching is needed from rich equivalence ratios in the primary zone to lean equivalence ratios in the dilution zone leading to reduced NO_X generation as indicated in Figure 1.6. However due to high temperatures in the primary zone dissociation processes can lead to large amounts of carbon monoxide (CO). Hence if the mixture is cooled too quickly then the CO would not react any further which leads to low combustion efficiency and large amounts of toxic CO emissions.

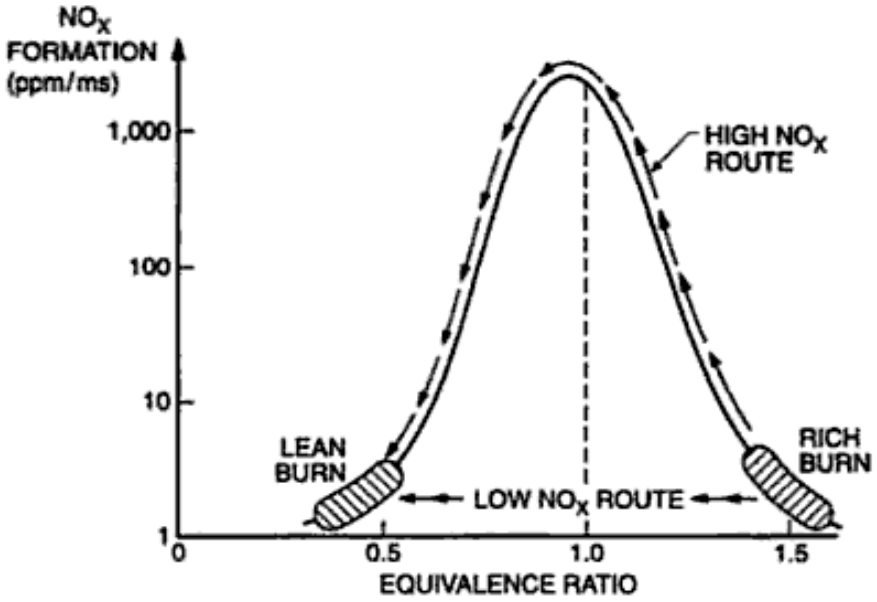

Figure 1.6: NO_X formation in RQL Combustors, from Lefebvre and Ballal (2010)

The drive to low emissions in the future is forcing a change in combustor technology for aero gas turbines from rich burn to lean burn combustors. In this case the NO_X-increase due to the change from rich (i.e. equivalence ratio larger than one) to lean (i.e. equivalence ratio smaller than one) air fuel ratio will be avoided and the combustion process will be undertaken at entirely lean equivalence ratios (equivalence ratios smaller one in Figure 1.6). Lean premixed prevapourised gas turbine combustors have been used for industrial machines to achieve the stringent NO_X emission targets for land based gas turbines. Many examples of industrial lean burn combustors can be found in Huang and Yang (2009). Initial lean burn combustor design for flight engines were so called double annular combustion systems (Figure 1.7) as shown for example in Dodds (2002), similar combustion systems can also be found in Lewis et. al. (1999). The combustor consists of a fuel rich pilot stage (which is always operational) and a lean mains fuel injector which is optimised for low NO_X emissions at high power engine operation. More recently Dodds (2005) and Klinger et. al. (2008) show a staged lean burn combustion system where the pilot and mains fuel injectors are combined into one injector (Figure 1.8). It can be seen that the fuel injectors are much larger than for the rich burn example. This is caused by the increasing amount of air that is required to enter the combustor through the fuel injector for lean combustion, which must be achieved without increasing the combustor pressure drop. For lean burn applications approximately 70% of the air within the combustor enters through the swirlers within

the fuel injector, whereas only 10-20% of the air enters the RQL combustor through the fuel spray nozzle. Thus no further mixing ports are necessary as this would drive the combustor towards its weak extinction limits. The only additional air which enters the combustor is that necessary for wall cooling. The pilot injector is used to provide the necessary stability and light up characteristic during low power operation whereas the lean mains burner is predominantly fuelled at medium to high power engine condition (Lazik et. al. (2008)) to achieve reduced NO_X emissions.

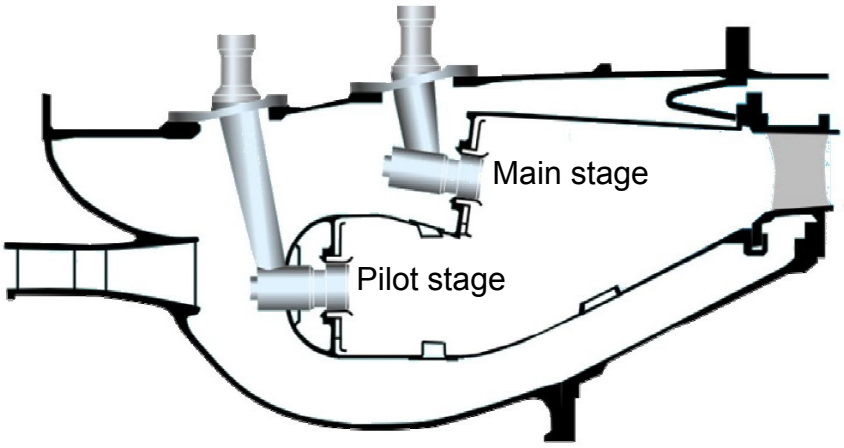

Figure 1.7: Schematic of double annular combustor, similar to Dodds (2002)

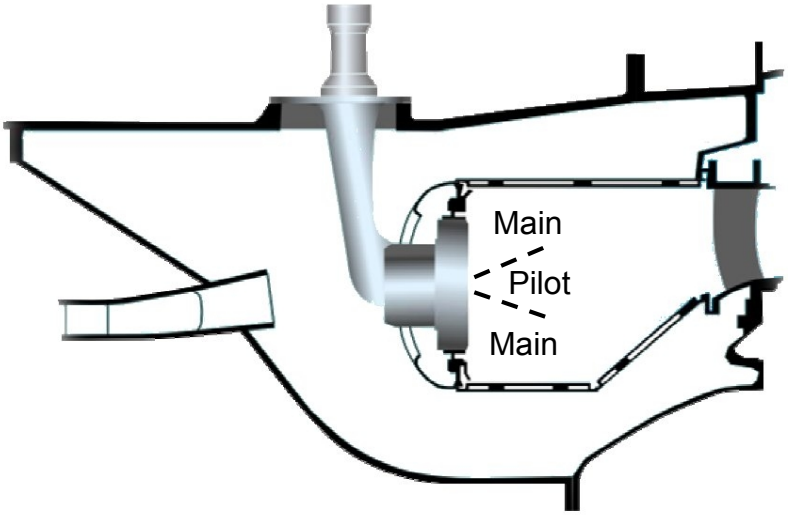

Figure 1.8: Schematic of staged lean burn combustion system, similar to Dodds (2005) and Klinger et. al. (2008)

Lean burn combustion technology has been used on industrial gas turbines over many years. Based on the experience of operating lean burn combustion systems on industrial engines many challenges have arisen for engineers (Lefebvre and Ballal (2010)), e.g.

flash back, margin to lean blowout, adequate combustion efficiency during operating envelope, homogeneous air fuel ratio at the fuel injector to achieve low emissions, sufficiently low pressure loss across the combustion system, etc. For aero-engines there is also a further challenge which is altitude relight. However, one of the major challenges for lean burn combustion is the avoidance of thermo-acoustic instabilities, based on the experience from lean burn combustors operating within industrial gas turbines. Thermo-acoustic instabilities cause large acoustic pressure oscillations within the combustor leading to reduced life and possible structural damage. The avoidance of this instability by increasing the acoustic energy absorption of the combustion system is the main focus of this thesis.

1.2 Thermo-Acoustic Instability

Thermo-acoustic instabilities, also known as combustion instabilities, can occur in any engineering application where heat is added within a confined volume, such as for example boilers, furnaces (Putnam (1971)), rocket engines (Hart and McClure (1965), Yang and Anderson (1995), Culick (2006)), gas turbine combustors (Scarinci and Halpin (2000), Dowling and Stow (2003), Eckstein (2004), Kaufmann et. al. (2008)), ramjets and afterburners (Rogers and Marble (1956), Bonnell et. al. (1971), Langhorne (1988)). Each of those combustion systems is characterised by various acoustic resonance frequencies due to their geometry. The added heat release rate can couple with the acoustics of the combustion system geometry, thereby supplying energy to the acoustic pressure oscillation. This leads to rapidly rising pressure amplitudes within the combustion chamber due to the large amount of energy being released. The high pressure amplitudes limit the component life, or in the worst cases, cause structural damage to the combustion chamber.

In the literature early references to this phenomenon can be found in conjunction with the singing flame by Higgins (1802), who experimented with hydrogen flames within a vertical tube generating an audible sound at the fundamental frequency of the tube. A similar observation was made in conjunction with the well-known Rijke tube. Rijke (1859) discovered that a loud tone was audible by putting a heated mesh into the lower half of a glass tube where both ends of the tube were open to atmosphere. Observations

stated that it was dependent on the position of the heat source if a loud tone was audible or not. Rayleigh (1896) investigated these phenomena and came to the conclusion that the added heat release from the mesh is increasing the pressure amplitude associated with the acoustic resonance mode of the tube. Moreover the heat source has to be placed so that the added heat release is in phase with the pressure oscillation for the audible tone to occur. This is the basis of the Rayleigh Criterion for which a simple mathematical description can be written as (e.g. Lieuwen(1999)):

$$\int_V \int_T Q'(x,t) \cdot p'(x,t)\, dt dV \geq acoustic\ losses \tag{1.1}$$

If unsteady heat release *Q'* is added in phase with the fluctuations in pressure *p'* then the pressure amplitude can potentially increase, whereas if the heat release is added out of phase with the pressure oscillations then the amplitudes will decay within one time period *T*. However, for acoustic pressure amplitudes to grow in magnitude, the product of unsteady heat release and pressure oscillations has to be larger than the acoustic losses within the combustion system. This criterion has been used by many authors to investigate and predict the stability of combustion systems (e.g. Chu (1965), Lieuwen (1999), Lawn (2000), Dowling and Hubbard (2000), etc.).

In the context of thermo-acoustic instabilities within gas turbine combustion systems the added heat release by the flame can couple with the acoustics of the combustion chamber geometry. For example unsteady heat release results in the propagation of acoustic waves, which can alter the pressure drop across the fuel injector which in turn causes the velocity field of the fuel injector to oscillate. This can lead to fluctuations in stoichiometry so that the interaction of the pressure wave with the fuel injector flow field leads to further unsteady heat release. This simplified feedback mechanism can thereby lead to self-excitation as shown schematically in Figure 1.9. However the initial mechanism which is causing the self-excited combustion instability can be much more complex. More detailed feedback mechanisms can be found in Paschereit e. al. (1999), Candel (2002) or Sattelmayer (2003). Turbulence and large scale coherent structures within the fuel injector flow field (Coats (1996), Poinsot et. al. (1987)), local equivalence ratio oscillations and spatial heat release distribution (Lieuwen and Zinn (1998), Kato et. al. (2005)) as well as propagating entropy waves within the combustion

system (Eckstein et. al. (2004), Eckstein (2004)) can cause the onset of thermo-acoustic instabilities. In general lean burn combustion is more prone to thermo-acoustic instabilities. One of the reasons for this behaviour is that the changes in rate of combustion due to oscillations in fuel air ratio is larger for lean combustion than for rich combustion, especially near the lean blow out regime (e.g. Dowling (2003) or Huang and Yang (2009)).

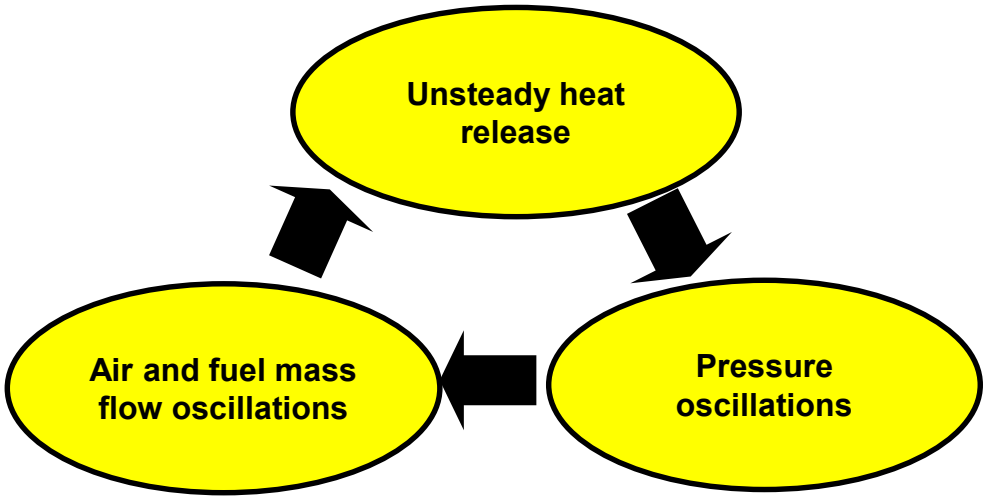

Figure 1.9: Thermo-acoustic feedback cycle as in Lieuwen (1999)

The challenge for gas turbine combustion engineers is to develop a lean burn combustion system design which is not susceptible to thermo-acoustic instabilities. Ideally the instability needs to be avoided at source, i.e. the design of the fuel injector suppresses the onset of thermo-acoustic instabilities. Steele et. al. (2000), for example, reduced the onset of thermo-acoustic oscillations by influencing the residence time of the air and fuel mixture within the premixing ducts. Further examples of fuel injector design to effectively avoid combustion instability can be found in Huang and Yang (2009). However, currently only limited design rules exist to develop a combustion system fulfilling all the requirements for an aero-engine combustor (Lefebvre and Ballal (2010)) which then exhibits no susceptibility to thermo-acoustic instabilities over the operating envelope of the engine. In recent years numerical and experimental studies have been undertaken to understand the thermo-acoustic characteristic of lean burn fuel injectors which includes, for example, measurements of flame transfer functions (Paschereit et. al. (2002), Schuermans et. al. (2010)). The flame transfer function treats the burner and the flame as a black box and relates the heat release oscillations to the

input pressure oscillation onto the fuel injectors. If the transfer function is measured in an acoustic resonance free system, it can be transferred into acoustic models of full engine combustion system geometry. Hence the stability of the gas turbine combustion system can then be analysed. With this in mind the described mechanisms can be investigated and the stability of the gas turbine combustion system can be assessed. However, as already mentioned, currently there are only limited design rules which can be used to influence the transfer function of a fuel injector so that there is no risk of thermo-acoustic instability throughout the operating envelope of an aero-gas turbine engine. Hence additional forms of the suppression of thermo-acoustic instability are under development.

One method of control is to influence the phase of the heat release relative to the pressure oscillation using fuel staging. As already explained in an earlier section staged lean burn combustion systems can have multiple fuel lines. Therefore the fuel split between the various injectors can be adjusted so that pressure amplitudes due to thermo-acoustic instabilities are minimised (Steele et. al. (2000), Scarinci and Halpin (2000), Mongia et. al. (2003)). This can be achieved by radially and circumferentially staging the fuel within a fully annular combustion system. The circumferential fuel variation is also known as asymmetric fuelling. However, due to the changes in combustion temperatures across the combustor it is possible that stringent NO_X emissions cannot be met using this strategy. Moreover the changes in fuel staging and asymmetric fuelling can have adverse effects on the temperature profile at combustor exit. This can then lead to reduced turbomachinery efficiency and a reduced life of the turbine components.

A further option to change the phase relationship between unsteady heat release and the acoustic pressure oscillation is active control. For example, a dynamic pressure sensor within the combustion chamber can be used to monitor the acoustic pressure oscillations. If the pressure amplitudes rise an actuator in the fuel supply line can be used to oscillate the fuel at the same frequency so that the heat release and pressure oscillations are out of phase with each other. Many researchers have worked in this field to develop algorithms for active instability control systems, e.g. Schuermans (2003), Riley et. al.(2003), Dowling and Morgans (2005), Illingworth and Morgans (2010). All of this work has shown that it is possible to suppress thermo-acoustic instability by

controlling the fuel supply. However, most of the work was aimed at stationary gas turbines operating with gaseous fuels, with the weight and size of the fuel actuators meaning it is currently not practical for aero-gas turbines. Moreover the challenge remains to design reliable liquid fuel actuator valves which operate in the range of several hundred Hertz with a specified accuracy on the fuel modulation amplitudes within the harsh gas turbine combustion system environment. Moran et. al. (2001) shows the application of active control on an afterburner of a RB199 full scale military turbofan aero engine. The tests were conducted on the ground with the active control being aimed at the low frequency combustion instability known as reheat buzz with frequencies well below 300 Hz. The system demonstrated a significant reduction in pressure amplitude and showed the potential for active control applications in the future. Furthermore Umeh et. al. (2007) studied the use of active control for a gas turbine aero engine. To overcome the challenge of operating an actuator valve at more than 500 Hz, the control algorithm was aimed at low frequencies corresponding to half of the combustion instability frequency. It could be shown that the thermo-acoustic instability frequency could be successfully reduced by this technique.

All the discussed methods in this section so far have focussed on influencing the product of the unsteady heat release and the unsteady pressure fluctuation, i.e. the amount of energy driving the instability. However this work is aimed at the absorption of the energy, i.e. the optimisation of acoustic losses within a gas turbine combustor. If the energy absorbed can exceed the amount of energy driving the instability the thermo-acoustic oscillation can be avoided. In general this is known as the passive control of combustion instabilities and is presented in the next section.

1.3 Passive Control of Thermo-Acoustic Instabilities

Thermo-acoustic instabilities can be passively controlled by increasing the absorption (i.e. damping) of the acoustic waves within the combustion chamber. Hence, the aim of this approach is to enhance the acoustic energy absorption within the combustion system geometry to a level whereby the acoustic pressure amplitudes can be reduced or, more desirably, the onset of the combustion instability suppressed. The suppression of the combustion instability is possible if all the generated acoustic energy is absorbed

before the reflected pressure waves can interact with the fuel injector flow field and other features of the combustion system. In this case the simplified feedback cycle in Figure 1.9 can be broken leading to suppression of thermo-acoustic instability. A modern combustion system contains a variety of components that can potentially provide some acoustic damping (Figure 1.10). These include, for example, combustor ports, cooling rings or effusion cooled liners.

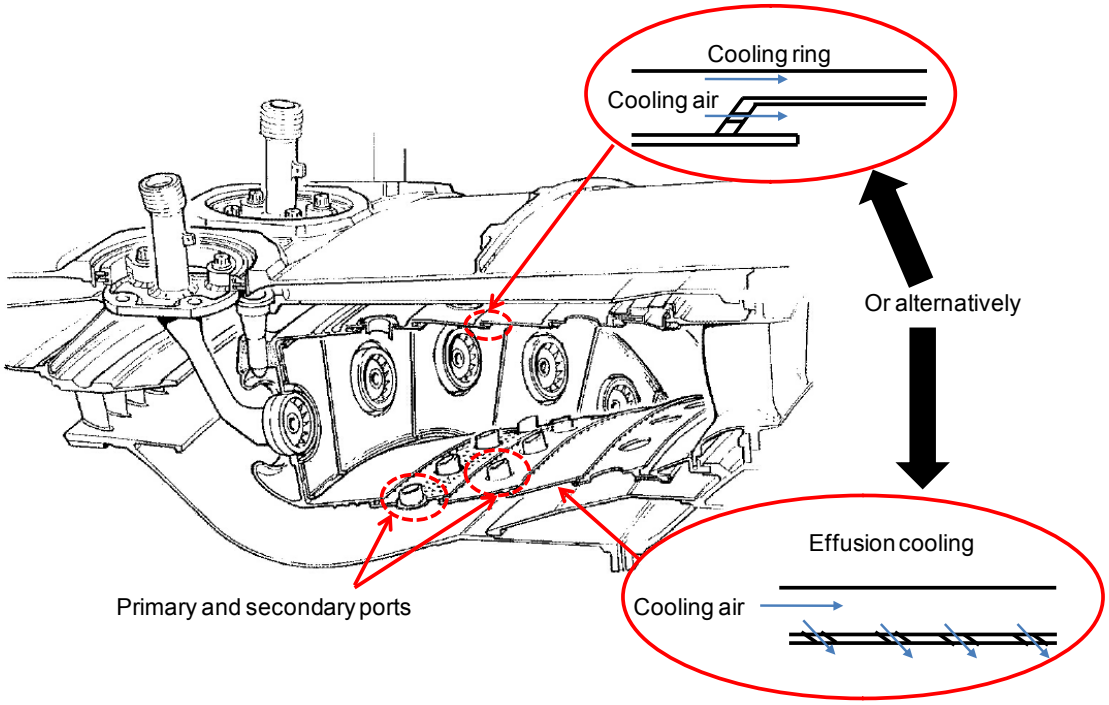

Figure 1.10: Schematics of common combustor apertures which interact with acoustic pressure waves

In general the amount of damping provided by the various combustor apertures is assumed to be small, hence the amount of damping is often assumed to be negligible. Thus additional passive damping devices must be incorporated within the system whose primary purpose is to absorb acoustic energy. The most common devices used are Helmholtz resonators and perforated liners.

1.3.1 Helmholtz Resonators

1.3.1.1 The Harmonic Oscillator

A Helmholtz resonator, as shown on the left hand side in Figure 1.11 and described for example in Rayleigh (1896) or Kinsler et. al. (1999), consists of a neck with length L and cross-sectional area A. One side of the neck is connected to a volume V and the

other side is open to an incident oscillating pressure amplitude onto the neck. The Helmholtz resonator is an harmonic oscillator which can be described in its simplest form as a mass-spring-damper system (right hand side in Figure 1.11). Thus the damped forced harmonic oscillator can be described using the following differential equation (Kinsler et. al. (1999):

$$m\frac{d^2x}{dt^2} + R_Z\frac{dx}{dt} + c_s x = F(t) = F\exp(i\omega t) \tag{1.2}$$

This equation describes the balance of forces surrounding the mass element in Figure 1.11), where the parameter x denotes the displacement of the mass. Hence the first term of the left hand side describes the inertial force due to the acceleration of the mass, the force due to the resistance R_Z within the damper element is given in the second term on the left hand side and the force due to the spring element is represented in the last term on the left hand side of equation (1.2). The system is forced by a harmonic force which is equivalent to a pressure oscillation incident onto the neck of the resonator

$$F(t) = A\,\hat{p}\exp(i\omega t), \tag{1.3}$$

where the pressure amplitude is represented by the parameter $\hat{p}$. If the wavelength λ is much larger than the neck length L ($\lambda >> L$) the air within the neck can be described as a single column of air representing the mass m (e.g. Kinsler et. al. (1999)):

$$m = \rho A L_{eff} \tag{1.4}$$

As the equation shows the mass is the product of the density ρ, the neck cross-sectional area A and the effective length L_{eff}. The effective acoustic neck L_{eff} represents the geometric length L of the neck and an additional acoustic length correction. Acoustic radiation effects at the neck outlet acts as an additional mass to the neck and are accounted for by this additional length correction. The end corrections can be estimated for flanged and unflanged terminations as in Kinsler et. al. (1999):

Flanged termination $L_{eff} = L + 2\cdot 0.85\,R$, (1.5)

Unflanged termination: $L_{eff} = L + (0.85 + 0.6)R$, (1.6)

where R denotes the radius of the neck. In practice these length corrections are often estimated from experimental data for a given resonator neck geometry.

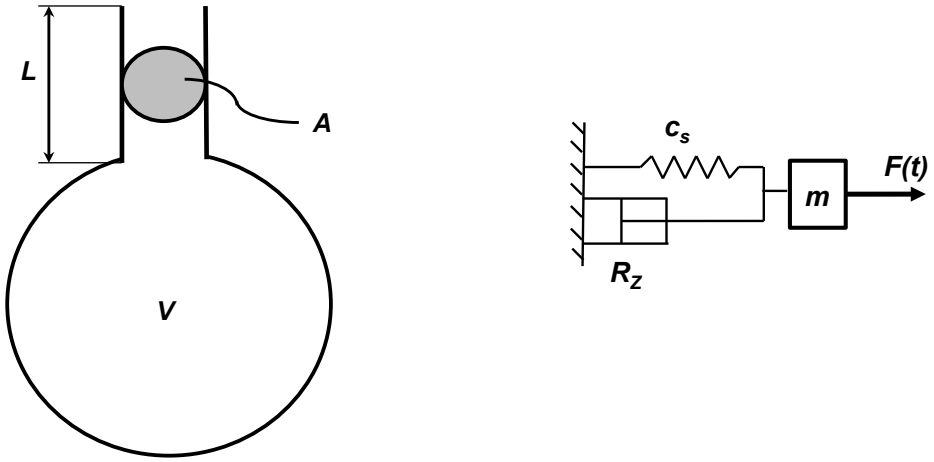

Figure 1.11: Schematic of a Helmholtz resonator and its equivalent harmonic oscillator (Kinsler et. al. (1999))

The pressure oscillation within the volume V is assumed to be uniform, in other words the acoustic pressure amplitude at a given time t is constant throughout the volume. Moreover the volume V of the resonator represents the spring c_S element in the harmonic oscillator system (third term on the left hand side in equation (1.2)). A force is required to move the mass against the stiffness of the spring which is the product of the stiffness and its displacement x:

$$F = c_s \cdot x \tag{1.7}$$

For the resonator the stiffness can be estimated by investigating the change of its volume due to the displacement of the column of air within the neck. In other words it can be assumed that the air within the neck acts like a piston which changes the volume by the amount of its displacement and the neck cross-sectional area. If the piston is pushing into the volume the change in volume can be defined as $dV = -Ax$. As the volume changes so does the density of the air within the volume:

$$\frac{d\rho}{\rho} = -\frac{dV}{V} = \frac{Ax}{V}, \tag{1.8}$$

therefore the pressure within the resonator volume has to rise, which can be estimated assuming an isentropic compression:

$$p = \rho c^2 \frac{d\rho}{\rho} = \rho c^2 \frac{A}{V} x . \tag{1.9}$$

Parameter c refers to the speed of sound in this expression. The force which is required to achieve the neck displacement is the force due to the incidental pressure amplitude as described in (1.3). Thus substituting equation (1.3) into (1.9) and comparing it to equation (1.7) results in a spring stiffness c_S of

$$c_s = \rho c^2 \frac{A^2}{V}. \tag{1.10}$$

An important parameter is the impedance Z of the Helmholtz resonator which describes the relationship between unsteady pressure amplitude incident onto the resonator neck and unsteady velocity amplitude of the column of air within the neck. This parameter can be derived using equation (1.2) together with equations (1.3), (1.4) and (1.10):

$$\rho A L_{eff} \frac{du'}{dt} + R_Z u' + \rho c^2 \frac{A^2}{V} \int u' \, dt = \hat{p} \, A \exp(i\omega t). \tag{1.11}$$

Note the circumflex above the pressure parameter indicates the amplitude of the acoustic pressure oscillation. Moreover, in this case the displacement of the mass within the neck has been expressed as the oscillating velocity which is defined as $u' = \hat{u} \exp(i\omega t)$. Thus substituting the expression for the oscillating velocity into equation (1.11) leads to the impedance of the Helmholtz resonator

$$Z = \frac{\hat{p}}{\hat{u}} = R_Z + iX_Z = \frac{R_Z}{A} + i\left(\rho\omega L_{eff} - \frac{\rho A c^2}{\omega V}\right), \tag{1.12}$$

where $i = \sqrt{-1}$. It can be seen that the impedance of the resonator is split into two parts: the resistance R_Z and the reactance of the resonator X_Z. The resistance term influences the amount of acoustic energy being absorbed. The reactance term of the Helmholtz resonator is equal to zero for the Helmholtz resonator when forced at its resonant frequency

$$X_Z = \rho\omega L_{eff} - \frac{\rho A c^2}{\omega V} = 0\,. \tag{1.13}$$

Thus the well known definition of the resonant frequency of the Helmholtz resonator (e.g. Rayleigh (1896), Ingard (1953), Kinsler et. al. (1999)) is:

$$\omega_{res} = 2\pi f_{res} = c\sqrt{\frac{A}{VL_{eff}}} \tag{1.14}$$

1.3.1.2 Acoustic Damping Mechanism

During the resonance condition for the Helmholtz resonator large pressure amplitudes occur within the resonator volume. This pressure oscillation is 90° out of phase with the incident pressure amplitude leading to a harmonic velocity oscillation of the air column within the neck being also 90° out of phase with the incident pressure. An unsteady jet flow is developed, due to the high unsteady pressure difference across the resonator neck which leads to the shedding of vortex rings at the outlet of the neck (Zinn (1970), Ingard (1953)). Thus the acoustic energy is transferred into the kinetic energy of vortex rings shed off the resonator neck. More recently Tam and Kurbatskii (2000) as well as Tam et. al. (2001) used a direct numerical simulation (DNS) method to investigate the flow field of a Helmholtz resonator with a slit shaped resonator neck during acoustic absorption. This also confirmed that vortex ring structures shed off the edge of the resonator neck are responsible for the loss of acoustic energy. Moreover Tam et. al. (2010) have used the DNS method on a resonant liner with rectangular apertures. The flow field of this study also revealed vortex ring structures responsible for the acoustic energy absorption. It was mentioned that the shape of the aperture had a significant effect upon the dissipation of acoustic energy. This agrees with the outcome of the work conducted by Disselhorst and van Wijngaarden (1980) and later on Atig et. al. (2004), who studied the influence of vortex rings forming at the end of resonating pipes at high sound pressure amplitudes. It was concluded that the acoustic losses were strongly dependent on the duct exit geometry and its influence on the vortex ring formation processes.

In addition to the flow effects external to the neck there is a further mechanism of acoustic energy dissipation which is represented by the viscous losses due to the

boundary layer within the neck (Keller and Zauner (1995) or Bellucci et. al. (2004)). Zinn (1970) as well as Hersh and Rogers (1976) mention that the viscous losses due to the boundary layer within the neck remain constant with pressure amplitude but the losses due to the momentum transfer into vortex rings are pressure amplitude dependent and dominate the acoustic energy absorption at high pressure amplitudes. Hence the viscosity effects could reduce the acoustic absorption as it reduces the unsteady velocity amplitudes within the neck and thus the transfer of acoustic energy into vortex rings. All the described acoustic energy absorption effects, i.e. flow structures external to the neck and boundary layers within the neck, are accounted by the resistance parameter R_R in equations (1.2) or (1.12).

If the pressure waves are exciting the resonator away from its resonance frequency than the pressure fluctuation in the volume is reduced, relative to the resonance condition, as less power is transferred from the incidental wave into the resonator volume. This leads to small velocity oscillations and therefore to reduced acoustic energy loss due to the reduced kinetic energy transfer. Hence the acoustic absorption of such a device is only adequate over a narrow frequency band close to the resonance frequency. Therefore the device has to be carefully tuned onto the damping frequency.

1.3.1.3 Non-Linear Absorption of Helmholtz Resonators

In general the amount of acoustic energy absorption can be described using an absorption coefficient. This parameter relates the acoustic energy loss relative to the incident acoustic energy onto the absorbing device. For a linear acoustic absorber the absorption coefficient remains constant, i.e. the amount of acoustic absorption is a linear function of the incident acoustic energy. However, the acoustic absorption characteristic of a Helmholtz resonator is known to be non-linear. This means that the acoustic absorption is a function of the incident acoustic pressure amplitude. In other words the amount of acoustic energy loss generated by the resonator is not increasing or decreasing at the same rate as the incident acoustic energy. The reason for this behaviour is the non-linear relationship between the incident pressure amplitude and the neck velocity amplitude. Ingard and Ising (1967) conducted hot-wire anemometer measurements at the exit of orifice geometries subjected to various levels of acoustic pressure amplitudes. It can be seen that for increasing pressure amplitude the orifice

velocity amplitude was a non-linear function of incident pressure amplitude: $p' \sim u'^2$. Moreover it was also noticed that the velocity amplitudes showed the occurrence of harmonics at large acoustic pressure amplitude forcing.

Due to this non-linear behaviour the acoustic loss generated by the Helmholtz resonator decreases with increasing incident pressure amplitude (Zinn (1970)). For a linear acoustic absorber the amount of acoustic energy loss generated is linearly related to the incident pressure wave, i. e. $p' \sim u'$ (Hersh and Rogers (1976), Ingard and Ising (1967)). Hence for a linear absorber the relative amount of acoustic energy absorbed to the incident energy is constant.

1.3.1.4 Application to Gas Turbine Combustors

Due to their large acoustic energy absorption Helmholtz resonators have been used in many engineering applications to reduce the amount of acoustic noise. Putnam (1971) discussed an application of a resonator to a combustion chamber of an aircraft heater and it was mentioned that the pressure oscillations in the tubular combustor could be completely suppressed. Laudien et. al. (1995) describes the use of Helmholtz resonators to successfully reduce the pressure amplitudes within rocket engine combustors. Bellucci et. al. (2004) and (2005) have shown that the pressure amplitude within an industrial gas turbine combustor can be greatly reduced by using Helmholtz resonators. Moreover Gysling et. al. (2000) significantly reduced the pressure amplitudes within a three sector test rig of a full annular industrial gas turbine combustor. Further applications of Helmholtz resonators on a can-annular combustion system of an industrial gas turbine have been reported by Krebs et. al. (2005). It was shown that the operating envelope of the gas turbine could be increased due to the application of Helmholtz resonators to the combustor. Scarinci (2005) successfully damped low frequency pressure oscillations on an aero-derivative industrial gas turbine using Helmholtz resonators.

One of the challenges of applying a Helmholtz resonator to a gas turbine combustor is to adequately cool the device. Moreover, due to the large velocity oscillations within the resonator neck, hot gas from the combustion chamber can be ingested into the resonator volume (Barker and Carrotte (2006)). Therefore cooling air has been used to

continuously flush the resonator cavity as shown in Keller and Zauner (1995). The same technique has been applied in Bellucci et. al. (2004) and (2005) or Krebs et. al. (2005).

Within gas turbine combustion systems the resonators have to be carefully placed. First of all the resonators can only generate acoustic damping if they are placed where an oscillating pressure occurs. This is especially important if the resonator is placed within a combustion system generating acoustic standing waves. In this case regions of the combustion system are exposed to the maximum acoustic pressure oscillation, i.e. anti-nodes, and locations at which no pressure oscillations occur, i.e. nodes. Thus maximum absorption is achieved if the resonator is located at a pressure anti-node. If the resonator is placed on an acoustic node no acoustic absorption can be generated. Hence knowledge of the acoustic mode shape within the combustion system is crucial. Moreover the resonator itself can significantly influence the mode shape within an acoustic system. Thus pressure nodes can occur within a combustion system at the resonator position. Hence at least a second resonator is needed, placed half a wave length away, to be able to damp the acoustic pressure wave. However, due to the interactions of the resonators with the acoustic waves various other acoustic resonance modes can occur as shown in Stow and Dowling (2003). Laudien et. al. (1995) also reported that the distance between the various resonator locations was important to stabilise the acoustic system within a rocket engine combustor.

Garrison et. al. (1972) investigated the design of Helmholtz resonators for the application in afterburners. In this case multiple resonators were used to damp the pressure oscillations occurring in a jet engine afterburner. A perforated plate was used as shown in Figure 1.12. The volume is enclosed by the perforated plate and the backing cavity. Each aperture with cross-sectional area S_n is equivalent to one separate Helmholtz resonator. Therefore each aperture within the perforated liner represents a resonator neck, with an associated neck length equal to the plate thickness. The volume of each resonator is defined by the area within one aperture pitch P_a and the corresponding backing cavity depth S. If the incident wave is normal to the perforated liner and the amplitude of the incident wave is not changing along the perforated liner, then no walls within the backing cavity are necessary (as there is no phase difference between the pressure amplitudes in the several volumes). Nevertheless the volumes can

be separated, for example with a honeycomb panel, to avoid the onset of any mode shapes within the backing cavity volume.

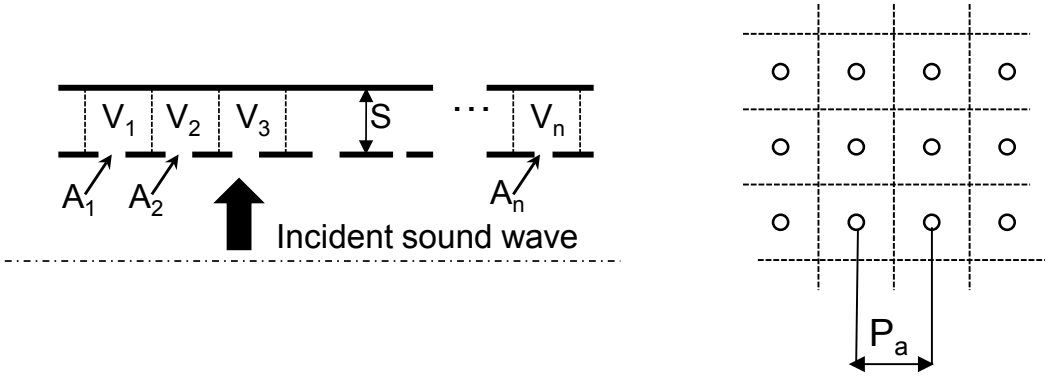

Figure 1.12: Helmholtz resonator application for jet engine afterburners as used in Garrison et. al. (1972)

Resonator arrays as shown in Figure 1.12 can be also used in jet engine intakes and exhausts. In these cases the resonator necks can be exposed to high velocity cross-flows which interact with the acoustic absorption of a resonator. Ko (1972) has investigated the absorption of a liner with multiple resonators under two different duct flow regimes: uniform flow and shear flow. The mean flow Mach number was varied between 0 and 0.6. It is shown that the boundary layer thickness has an influence on the sound attenuation but this is specific to the Mach number, the flow direction and the acoustic mode within the duct. Cummings (1987) investigated the performance of a resonator under fully developed turbulent pipe flow for internal combustion engine exhaust silencers.

1.3.1.5 Review of Acoustic Studies of Helmholtz Resonators

Helmholtz resonators can come in a variety of configurations. The geometrical dependencies of a Helmholtz resonator have been investigated analytically, numerically and experimentally by many authors. Ingard (1953) has investigated resonators with circular and rectangular necks connected to circular and rectangular volumes. The focus of the work was to produce design tools for the various geometries to achieve optimum sound absorption and to estimate their resonance frequencies. Moreover Selamet and Lee (2003) investigated resonators with their necks extended into the volume which can be very useful if design space is limited as, for example, in jet engines. Chanaud (1994) has developed models to predict the resonance frequencies with various neck cross-

sectional areas, e.g. cylindrical, rectangular and cross-shaped. Tang (2005) has also shown that the sound absorption of a Helmholtz resonator can be improved if the neck of the resonator is tapered. Moreover a model was developed which predicts the resonance frequency of a Helmholtz resonator with a tapered neck.

Unfortunately, Helmholtz resonators only provide absorption over a relatively narrow frequency range, i.e. within a narrow band around its resonance frequency, and this often conflicts with the requirement for adequate acoustic damping throughout the operating range of the gas turbine. To overcome this issue a range of resonators can be connected to the combustion system geometry tuned to various frequencies as mentioned in Richards et. al. (2003). This has also been demonstrated for silencer systems (e.g. Seo and Kim (2005)). This technique could also be applied to jet engine intakes and exhaust ducts or afterburners. Garrison et. al. (1972) investigated resonator geometries in series as shown in Figure 1.13 for their application in jet engine afterburners. In this case the two resonator frequencies are closely tuned to each other using the volume sizes or the length, diameter and porosity of the perforations. Therefore the interaction between the two devices enables large acoustic absorption over a wider frequency band.

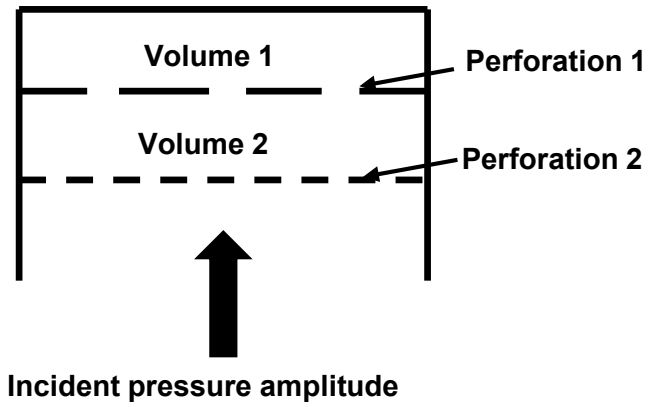

Figure 1.13: Helmholtz resonators in series similar to Garrison et. al. (1972), or Bothien et. al. (2012)

Similar concepts have been investigated by Bothien et. al. (2012) within industrial gas turbine combustors. Moreover Hafsteinsson et. al. (2010) showed resonators in series as a method to suppress fan noise in the intake of a jet engine. Furthermore Xu et. al. (2010) has developed theoretical models to describe the same concept.

To overcome the narrow frequency band characteristic Zhao and Morgans (2009) have used active control in conjunction with a Helmholtz resonator. In this study the resonator neck area was controlled with an active control system to successfully suppress the instability of a Rijke tube. A further example of actively tuning a resonator was also conducted by Zhao et. al. (2009). In this case the back plate of a resonator volume was vibrated by a control system to actively increase the acoustic absorption of the resonator over a wider frequency bandwidth. Another option of tuning a resonator onto the frequency of a combustion system would be to actively change the volume of the resonator (e.g. De Bedout et. al. (1997)).

1.3.2 Multi-Aperture Perforated Screens with Mean Flow

1.3.2.1 Absorption Mechanism of Circular Holes with Bias Flow

Including orifices and ports in combustion chambers can suppress thermo-acoustic oscillations as described in Putnam (1971). The amount of apertures needed to significantly reduce the pulsations was evaluated experimentally which is indicated by the quote in Putnam (1971):

"*To stop pulsation, drill one hole in front of the furnace; if that doesn't work, drill two holes!"*

Initial investigations of the acoustic energy transmission through jet nozzles, e.g. Bechert et. al. (1977), showed that the loss of acoustic energy was dependent on the mean bias flow through the nozzle. Bechert (1980) found that the acoustic energy absorption at low frequency is a function of the mean Mach number through the jet nozzle. Howe (1979a) also investigated the absorption of sound due to the flow through a jet nozzle (Figure 1.14) analytically for low Mach numbers by using a vortex sheet model and described the mechanism with which acoustic energy is absorbed within the jet flow. A flow with mean jet velocity U_j passing through the orifice develops a vorticity sheet downstream of the jet nozzle. This vorticity sheet lies in the region of shear between the core nozzle flow and the surrounding air, with the vortex sheet origin being at the edge of the nozzle. An incident acoustic pressure wave p_i travels towards the jet nozzle and at the nozzle part of the acoustic energy will be reflected back upstream (p_r), part of the acoustic energy gets transmitted through the nozzle whilst

some of the acoustic energy is absorbed. Basically the incident pressure oscillation alters the pressure drop across the jet nozzle which generates a pulsatile jet flow. Thus the velocity amplitude in the exit of the jet nozzle enhances the shedding of vorticity in the free shear layer on the edges of the nozzle. The mean flow convects the vorticity away from the orifice rim and the generated vorticity subsequently is transformed into heat further downstream via viscous dissipation processes. Therefore acoustic energy is transferred into kinetic energy associated with the vorticity structures in the shear layer of the unsteady jet flow.

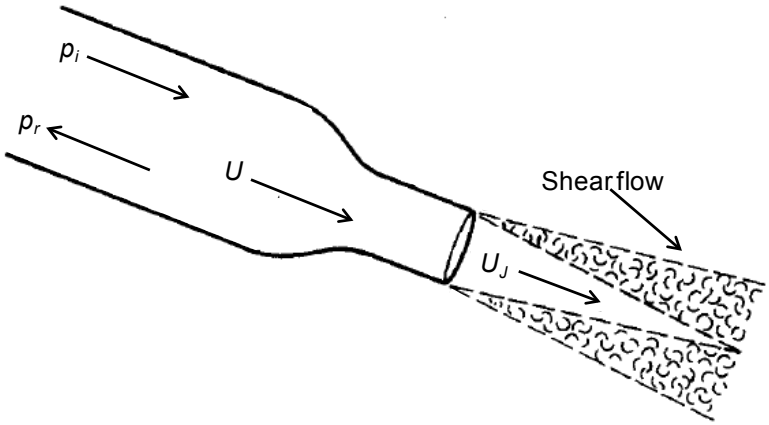

Figure 1.14: Schematic of a jet nozzle from Howe (1979a)

Howe (1979b) applied a similar theory to develop an analytical model to predict the acoustic losses associated with a circular orifice subjected to an unsteady pressure drop with mean flow. In this case Howe (1979b) assumed that the orifice plate is infinitesimal thin, the jet flow is irrotational and vorticity is similarly shed in a thin cylindrical shear layer starting from the edge of the aperture. However, the mechanism related to the acoustic absorption basically remained the same. One outcome of this work was the development of an analytical expression to describe the Rayleigh Conductivity for an orifice. The Rayleigh conductivity KD relates the unsteady volume flow $\hat{Q}$ through an orifice to the unsteady pressure drop across the orifice $\Delta\hat{p} = \hat{p}_{us} - \hat{p}_{ds}$.

$$K_D = -\frac{i\omega\rho\hat{Q}}{\hat{p}_{us} - \hat{p}_{ds}} = D\left(\Gamma(St) - i\delta(St)\right) \tag{1.15}$$

In this case ω represents the angular frequency of the oscillation, D represents the orifice diameter and the indices *us* and *ds* denote the pressure just upstream and downstream of the orifice. The parameter Γ is a measure of the inertia within the orifice flow field and the variable δ represents the acoustic admittance of the orifice. The admittance is a measure of the ability of the orifice velocity flow field to oscillate. Moreover the amount of acoustic energy being absorbed is proportional to the acoustic admittance (Howe (1979b), Luong et. al. (2005)). Hence increases in admittance result in an increasing amount of acoustic absorption.

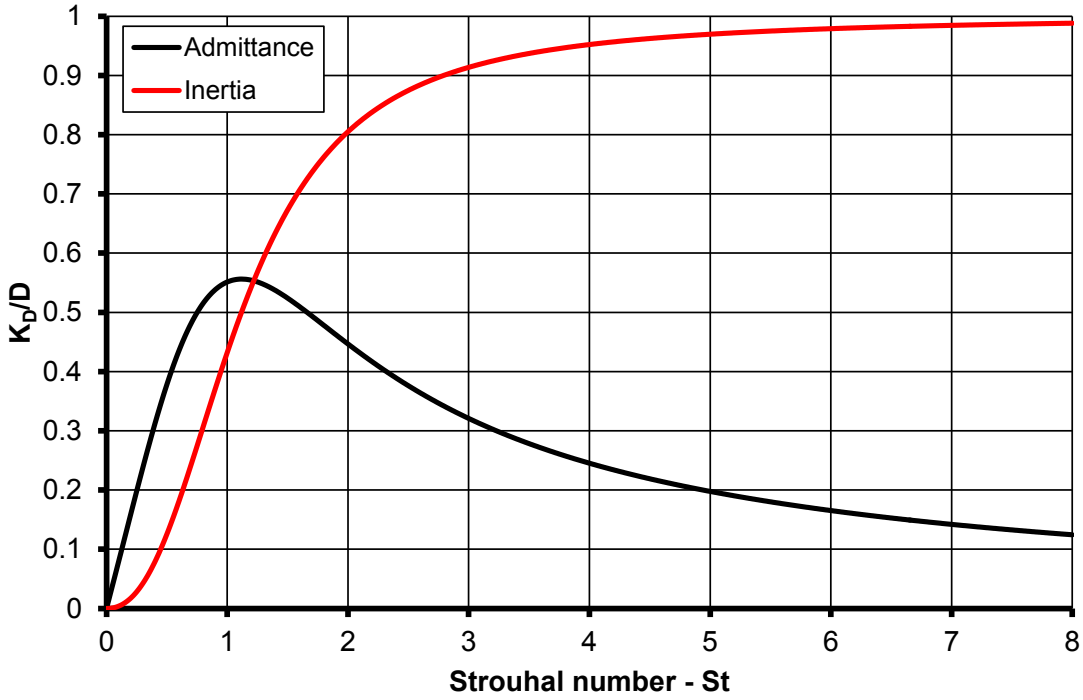

Figure 1.15: Rayleigh Conductivity as in Howe (1979b)

For the assumptions made the solution of the model derived by Howe (1979b) showed that the Conductivity is only dependent on the Strouhal number (Figure 1.15):

$$St = \frac{2\pi f R}{\overline{U}_D} = \frac{\omega R}{\overline{U}_D} \tag{1.16}$$

and is defined using the angular frequency of the pressure oscillation ω, the aperture radius R and the mean velocity in the plane of the aperture $\overline{U}_D$.

It can be seen that the ability to absorb acoustic energy (δ) steadily increases with Strouhal number in the range $0 < St < 1$. After that the ability to absorb acoustic energy

steadily decreases to an asymptotic value. As described by Howe (1979b) the variation of admittance (δ), and hence absorption, with Strouhal number is due to the length scales associated with the vorticity produced by the incident acoustic waves around the rim of the aperture. At large Strouhal numbers the shed vorticity will have a small influence on the fluctuating orifice flow. This is because small length scales mean the induced velocities from individual vortex rings cancel. However, at low Strouhal numbers the large length scales mean the vorticity of one sign can stretch far downstream and will impact on the flow through the orifice.

The inertia (Γ) is negligible at low Strouhal numbers as the time scales are large for the oscillating velocity field to react to the pressure oscillation. Hence at Strouhal numbers close to zero the velocity field in the aperture is in phase with the incident pressure wave. With increasing Strouhal number the mass of the fluid within the aperture becomes more significant and the influence of inertia on the fluctuating velocity amplitude within the orifice increases. Thus the phase between the incident pressure fluctuation and the velocity oscillation within the aperture increases towards the high Strouhal number limit ($\Gamma \to 1,\ \delta \to 0$). In this case the phase difference between the incident pressure and the velocity is 90 degrees.

The broadband characteristic of the absorption is mainly due the inclusion of mean flow through the aperture of the nozzle and its generation of a vorticity sheet. Acoustic waves over a wide frequency band can interact with the vorticity structures so giving rise to the broadband characteristic.

1.3.2.2 Perforated Walls with Bias Flow and Linear Acoustic Absorption

The acoustic absorption of a perforated wall with bias flow remains in the linear acoustic absorption regime as long as the unsteady velocity amplitude within the aperture is smaller than the mean flow velocity through the orifice ($p' \sim u'$ for $u' << \overline{U}$). In this case the acoustic admittance and inertia of the orifice flow is independent of the incident excitation pressure amplitude. Moreover the acoustic absorption coefficient remains constant with increasing pressure amplitude as the acoustic energy loss is increasing in proportion to the incident acoustic energy. In general, as mentioned in the previous section, Helmholtz resonators have very little (or no) flow across the neck of

the resonator. Hence the neck velocity amplitude is larger or similar to the mean velocity through the neck ($p' \sim u'^2$ for $u' \geq \overline{U}$). Therefore the absorption is within the non-linear absorption regime. Hence the admittance and inertia are a function of incident pressure amplitude and the acoustic absorption coefficient changes with increasing incident pressure amplitude.

Many investigations into the absorption of perforated liners either within the linear absorption regime (e.g. Hughes and Dowling (1990), Jing and Sun (1999), Eldredge and Dowling (2003), Lahiri et. al. (2011), etc) or in the non-linear absorption regime (e.g. Salikuddin and Brown (1990), Salikuddin et. al. (1994) or Cummings (1986), etc) have been described. Only a few researchers have investigated the transition from linear to non-linear absorption (Ingard and Ising (1967), Melling (1973), Betts (2000) Bellucci et. al. (2004b).

As already mentioned the point at which the transition between linear and non-linear absorption occurs is dependent on the velocity amplitude relative to the mean velocity. Therefore the flow field generated by the acoustic pressure amplitude and its dependency on the orifice geometry needs to be further understood. Hence there is a need for detailed flow field studies on the transition from linear to non-linear absorption for gas turbine combustor relevant orifice geometries and absorption regimes over the operating range of a gas turbine combustion system.

1.3.2.3 Application to Gas turbine Combustors

Due to the ability of absorbing adequate amounts of acoustic energy over a broad frequency bandwidth acoustic liners with mean bias flow have also been applied to gas turbine combustors. Scarinci (2005) showed the application of an acoustic liner within an aero-derivative Rolls-Royce Trent 60 industrial gas turbine. Moreover a similar type of damper has been introduced by Lörstad et. al. (2009) in a SIEMENS SGT 800 industrial gas turbine combustor. It has been shown that the pressure amplitudes within the combustion system could be significantly reduced compared to the previous design without the perforated wall. Macquisten et. al. (2006) used a porous liner within a tubular single sector combustion rig with a down-scaled industrial gas turbine burner. The instabilities generated by the burner could be suppressed successfully if the mean

flow across the porous liner was sufficiently low. Perforated liners backed by a resonant cavity have also been used successfully by Tran et. al. (2008) to control the inlet boundary condition of a gas burner. Perforated liners to reduce the noise generated by a jet engine fan have also been used within the intake of jet engines (Dean and Tester (1975), Betts (2000)).

1.3.2.4 Review of Acoustic Experiments on Perforated Liners

Many studies into the bulk absorption characteristics of perforated liners have been undertaken to optimise the absorption of the liner geometry and understand the relevant design parameters. Perforated liners backed by a resonant cavity have been investigated for example by Hughes and Dowling (1990). In this investigation a perforated liner backed by a rigid wall, as shown in Figure 1.12, has been studied with a bias flow across the perforated wall. Note the Helmholtz resonator study introduced in section 1.3.1.4 aimed at the non-linear acoustic absorption regime, where the velocity oscillation is in the order of the mean flow if not larger ($u' \geq \overline{U}$). For the liner backed by a resonant cavity with mean flow, which is the case in this section, the acoustic absorption is investigated in the linear acoustic absorption regime. Thus for the purpose of this study the velocity amplitudes were much smaller than the mean flow velocity, i.e. $u' << \overline{U}$. In this case the bias flow represents the cooling flow through the apertures of a passive damping device applied to a jet engine afterburner. This application is also known as a screech damper. Screech is a high frequency (more than 1 kHz) thermo-acoustic instability which occurs in tubular geometries and is characterised by circumferential or radial pressure waves within the tubular afterburner duct. These pressure waves can be damped by a perforated liner with resonant backing cavity.

The absorption generated by a perforated liner backed with a plane rigid screen is frequency dependent. If the system is in resonance it is possible to absorb all incident acoustic energy for the geometries investigated. Moreover Hughes and Dowling (1990) also developed an analytical model to describe the acoustic absorption of the tested liner. The model was based on the theory developed by Howe (1979b) and showed good agreement with the acoustic measurements. A similar investigation has been undertaken by Dowling and Hughes (1992) where an array of slits was investigated instead of a

circular aperture. Again all the incident sound energy could be absorbed if the perforated liner was backed by a resonant cavity.

Jing and Sun (1999) investigated a similar arrangement as in Hughes and Dowling (1990). It was shown that the acoustic absorption of a perforated liner backed by a resonating cavity can be enhanced by introducing a mean bias flow through the perforation. Moreover, not only was the absorption increased but the frequency band over which increased acoustic absorption occurs was larger. Jing and Sun (1999) extended the theory presented in Howe (1979b) by adding an acoustic length correction to the theory. Comparisons to the measurement showed good agreement. Moreover Jing and Sun (2000) developed a numerical model of the shear layer downstream of the orifice by including more realistic orifice jet profiles measured by Rouse and Abul-Fetouh (1950) for sharp edged apertures. It was intended to model the orifice length effects more realistically for orifice length-to-diameter ratios ranging from 0.4 to 0.6. This model showed significant differences to the modified theory developed by Howe (1979b) and Jing and Sun (1999).

Eldredge and Dowling (2003) applied the length corrected model from Jing and Sun (1999) based on the theory developed by Howe (1979b) to acoustic absorption measurements with a grazing flow across the perforated liner. In this case the perforated liner was backed by a volume which was not in acoustic resonance. The developed model showed good agreement for the investigated geometries with the absorption model which does not take the grazing flow effects into account. Forster and Michel (2003) investigated the absorption of perforated plates with open area ratios from 4 to 20%. It is reported that the absorption of the liners could be increased within a Mach number range associated with the mean flow across the liner. Heuwinkel et. al. (2007) investigated experimentally various liners of different porosity at various mean bias flows and mean grazing flows across the perforated liner. It is shown that more than 50% of the acoustic energy could be absorbed over a wide frequency bandwidth. Observations of the data showed that the absorption was dependent on the bias flow velocities. A further observation was made that the absorption of the liner increased with increasing spacing between the apertures. Furthermore, Lahiri et. al. (2011) developed an experimental database of the acoustic bulk properties relating to

perforated liners including variations on bias flow, liner porosity, liner thickness, grazing flow across the liners as well as the orifice shape. In general the experimental data agreed with the used acoustic absorption model based on the Conductivity developed by Howe (1979b).

In general for acoustic absorbers to work, the pressure drop across the perforated liner has to be sufficiently low. However, for many practical engineering applications and, in particular gas turbine combustion applications, it is likely that the Strouhal number is relatively low (Rupp et. al. (2012)). For example in the case of standard effusion cooling geometries the Strouhal number can be much smaller than 0.1. This is due the pressure drop distribution of impingement effusion cooling geometries with a total wall pressure loss typically of order 3% and the typical instability frequencies being below 1000 Hz for large gas turbine jet engine. Hence any reduction in pressure drop to significantly increase the orifice Strouhal number, and therefore its ability to absorb acoustic energy (Figure 1.15), leads to significant reductions in cooling performance. Moreover reduced wall pressure losses lead to a significant increase in the risk of hot gas ingestion.

Finally the space envelope for a damping device for flight engine gas turbine combustion systems is limited due to weight constraints. Hence the application of an optimised broadband linear absorber remains challenging (Rupp et. al. (2012)). Enhancement of the linear acoustic absorption by using resonant liner applications leads to the application of large length-to-diameter orifice geometries due to the limited volume in the combustor design envelope. Hence efficient damping designs have to be developed which satisfy the damping, cooling and weight requirements for a combustion chamber of a flying jet engine. Therefore accurate modelling techniques describing the gas turbine combustion chamber design envelope are necessary and not fully understood for the investigated geometry and operating conditions within this study.

1.3.2.5 Numerical Flow Field Investigations Related to Acoustic Absorption for Perforated Liners with Bias Flow

Eldredge et. al. (2007) used a Large Eddy Simulation (LES) model to calculate the Rayleigh conductivity and compare the results to those of the analytical model proposed

by Howe (1979b). The analytical conductivity model and the LES calculation compare reasonably well for the low frequency range. However, it is suggested that the analytical model needs to be modified for more sophisticated geometries (e.g. angled holes) and also needs to include the effect of liner thickness. These features can induce shear layers inside the aperture which give rise to more complicated interactions between the acoustic energy and unsteady velocity fields. LES velocity contours are presented which show separated jets introducing shear layers inside the aperture, as well as downstream of it, which will influence the acoustic energy dissipation. More recently Mendez and Eldredge (2009) compared the results derived from an LES study with various analytical absorption models. The LES based data was in good agreement with the more detailed model presented by Jing and Sun (2000) using jet profiles. Hence the profile of the jet is also of importance to accurately predict the acoustic absorption of an orifice plate with varying thickness-to-diameter ratio. Moreover the potential of LES was shown for understanding the fluid dynamic processes related to acoustic absorption. In a similar way Andreini et. al. (2011) used LES to investigate the flow fields of perforated liners. The acoustic absorption calculated by the LES study was compared to the models developed by Howe (1979b) and Jing and Sun (1999) as well as to the test results from Bellucci et. al. (2004b). The models did in general agree within the investigated orifice experiments but also showed differences to the investigated analytical models. Gunasekaran and McGuirk (2011) developed a pressure based CFD methodology to adequately captures the acoustic wave propagation in low Mach number (i.e. essentially incompressible) flows. The predictions were in good agreement with the acoustic absorption data measured by Rupp et. al. (2010b). Moreover the method presented by Gunasekaran and McGuirk (2011) showed the same flow field characteristics in the numerical solutions as highlighted by the PIV measurements from Rupp et. al. (2010b).

Nevertheless the application of CFD to acoustic absorption processes is challenging since this involves large grid sizes and small time steps. This leads to the calculation of single apertures. In RANS (Reynolds Averaged Navier Stokes) CFD modelling techniques the choice of an adequate turbulence model will be important for an accurate prediction of the unsteady flow flied. Moreover, in LES based approaches, the accuracy of the employed sub-grid scale models will have an effect on the accuracy of the

unsteady velocity field prediction. Furthermore there is a lack of measured unsteady velocity field data in the vicinity of circular apertures during acoustic absorption, which is of great importance for the validation of the numerical predictions and the analysis of the found discrepancies between the analytical absorption models and the numerical solutions derived by CFD.

1.4 Objectives

In general this work is aimed on the investigation of the acoustic energy loss associated with passive damping techniques applied to practical engineering geometries with the emphasis of gas turbine aero-engine combustion systems. The use of passive damping techniques was successfully applied to industrial gas turbine combustion systems. Apart from the application to afterburners, this technology has not been applied to aero-engine gas turbine combustors. The challenge to design efficient acoustic absorbers for gas turbine combustors for aero jet engine applications lies within the compromise between combustor wall cooling demands, sufficiently low bias flow velocities for achieving adequate acoustic absorption as well as the challenge of fitting a damper geometry within the limited design space of an aero gas turbine (i.e. to minimise the impact upon the weight of the engine). The air split through a gas turbine aero engine combustor is well defined to satisfy the combustion requirements along with the cooling requirements for the combustor walls and the downstream high pressure turbine. Moreover in lean burn combustion systems a large amount of air has to enter the combustor through the fuel injector to achieve the low emission targets. Furthermore the amount of flow through the damper device incorporated into the combustor wall could affect the cooling efficiency of the wall and even the combustion process near the perforated wall. Thus reduced combustion efficiency and increases in emissions can be expected. Hence the passive damper design can only use a limited amount of air, to stay within the air budgets of the combustion system and the downstream high pressure turbine. All the mentioned aspects have to be assessed throughout the design process of an acoustic damper incorporated into this challenging environment. Hence further improvements to the currently available design tools are necessary.

The main objective of this work is to provide the means by which the acoustic energy loss associated with a conventional gas turbine combustion system can be determined. To be able to fulfil the main objective of this work the acoustic characteristics of the unsteady flow through various apertures typically found in aero engine gas turbine combustors and their operating conditions need to be investigated. In this case length-to-diameter ratios between 0.5 and 10 can be typically found for various combustion system features. Acoustic measurements of various porosities have been conducted in the past (as discussed in the previous sections) but are often concerned with relatively thin apertures with small length-to-diameter ratio and do not fully extend over the operating conditions and geometries found within practical engineering geometries. Moreover the previously mentioned studies of acoustic dampers are often limited to the linear acoustic absorption regime. During the occurrence of thermo-acoustic instabilities it is possible that large pressure amplitudes within the combustor are generated. Hence not only the linear acoustic abruption regime will be investigated but also the non-linear acoustic absorption regime. Furthermore many linear acoustic absorption theories aimed on predicting the acoustic energy loss of apertures are based on the assumption of infinitesimal thin apertures with cylindrical shear layers. Hence the performance of these modelling techniques need to be assessed over the geometry range and operating range of gas turbine combustors. A further objective is the optimisation of the investigated geometries to enhance the acoustic absorption within a combustion system. Only limited studies have investigated the influence of the shape of the aperture upon the linear and non-linear acoustic absorption. Hence better understanding of the aperture geometry influence is necessary, not only to increase the acoustic absorption available but also to improve current modelling technologies and extend them to those geometries.

Many studies in the reviewed literature where concerned with the optimisation of passive damping systems. However the majority of these cases where aimed on determining the global acoustic properties of the system, i.e. the acoustic absorption of the device. Little work has been undertaken to investigate the fluid dynamic processes leading to acoustic absorption associated with circular apertures. Some of the work, which has been conducted numerically, has shown that the flow field is of great

importance for the loss of acoustic energy. This is further illustrated by the observed changes in acoustic absorption characteristics as the mean flow passing through the orifice is varied. Hence to understand the acoustic absorption characteristics and the orifice shape influences further it is necessary to investigate the unsteady fluid dynamic processes leading to the loss of acoustic energy. Current linear and non-linear acoustic modelling tools are simulating the unsteady velocity field interaction with the incident pressure field. A more detailed measurement of the relevant fluid dynamic processes is necessary to improve the accuracy of the current modelling tools. Therefore a methodology shall be developed which identifies the relevant fluid dynamic processes associated with the acoustic energy absorption of circular apertures. The aim for this work is to assess the unsteady flow field experimentally. However the data can then be used as validation data for future CFD applications in follow on work.

As already mentioned acoustic dampers applied to gas turbine combustors operate within a challenging environment where complex swirling flow fields are used to efficiently atomise and mix the air and fuel prior to combustion. These complex flow fields have the potential to interact with the unsteady flow field of the circular apertures within the acoustic damper. The acoustic absorption characteristics described in the literature are mostly based on simple acoustic ducts, with and without cross-flow arrangements, and in the absence of more complex swirling flow fields. Thus an investigation of the influence of such complex flow fields interacting with the acoustic damper performance needs to be assessed. This will then deliver an understanding if simplified test rigs to assess the acoustic absorption performance are sufficient.

Finally the gained knowledge from the previously described tasks should be used to improve the current design tools for acoustic absorbers. This should include an improvement in the accuracy of the acoustic absorption prediction for various gas turbine representative orifice geometries with length-to-diameter ratios of 0.5 to 10.

As the acoustic damping geometry in this work will have a cooling flow through the aperture the focus on the modelling technique will be on the linear acoustic absorption. This would be sufficient for an accurate stability assessment of a full annular combustor as initially the amplitudes would remain small. If the combustion system is unstable the pressure amplitudes will grow and the acoustic absorption transitions into the non-linear

regime. In this case hot gas can be ingested into the damper cavity which causes the combustor wall to overheat. Hence the design tool should include the assessment of the risk of hot gas ingestion to occur and identify the shortfalls in the non-linear acoustic absorption modelling tools.

2 Fundamentals of Unsteady Flow through a Circular Orifice

This section outlines the fundamental fluid dynamic and acoustic processes for unsteady jet flow through circular orifices. Initially a brief introduction to jet flows is given for steady state conditions followed by the concept of vorticity and its link with the unsteady flow characteristics of round jets. The acoustic governing equations are also introduced along with the fundamental assumptions associated with the acoustic modelling techniques for circular apertures.

2.1 Steady State Flows through Circular Orifice Plates

On the left hand side of Figure 2.1 a schematic of an orifice located within a steady (i.e. time independent) total pressure field (P_1 and P_2) is shown. Fluid is flowing through the orifice and a jet develops downstream of the aperture (right hand side of Figure 2.1).

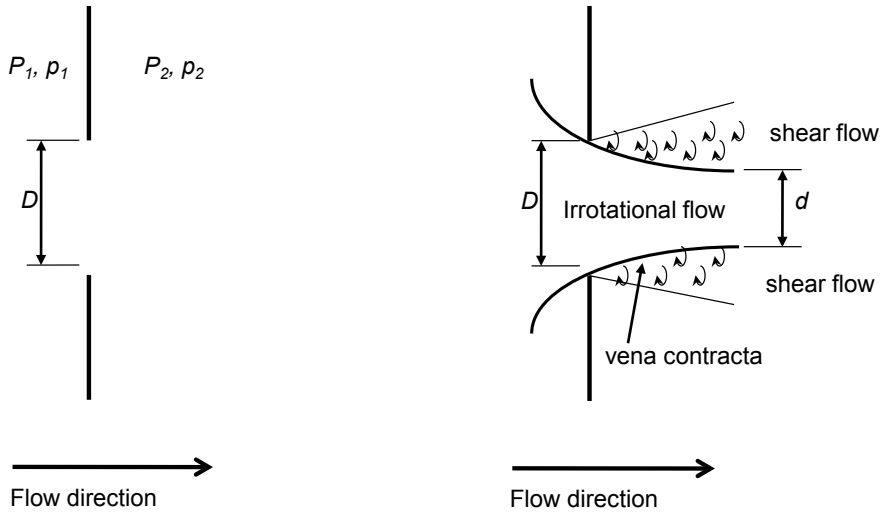

Figure 2.1: Schematic of flow through a circular orifice

The flow regions of the jet can be divided into

- An inviscid core flow in the centre of the jet (which is also irrotational)
- A viscous region which corresponds to the shear layer surrounding the inviscid core of the jet.

In general inviscid flow can be described by continuity of mass (Oertel and Boehle (2002))

$$\frac{\partial \rho}{\partial t} + \vec{u}\nabla\rho + \rho\nabla\vec{u} = 0 \ , \tag{2.1}$$

and momentum

$$\rho\frac{\partial \vec{u}}{\partial t} + \rho\,\vec{u}\nabla\vec{u} + \nabla p = 0 \ . \tag{2.2}$$

In this case we assume the flow is incompressible ($\rho = const$) as the Mach number of the flow is small *(M << 1)*. Moreover the flow is assumed to be steady ($\partial/\partial t = 0$). Therefore the momentum equation can be integrated along a stream line through the orifice (Douglas et. al. (2005)) which leads to the Bernoulli equation (neglecting gravitational effects):

$$p + \frac{1}{2}\rho u^2 = p + q = const \ . \tag{2.3}$$

The sum of static (p) and dynamic (q) pressures is known as the total pressure P. According to the Bernoulli equation the total pressure is constant along a streamline within an inviscid fluid flow. In the case of the steady orifice flow of Figure 2.1 the velocity of the flow through the orifice can now be defined. Using the Bernoulli equation for incompressible flow it is possible to define the velocity of the jet core flow through the orifice:

$$P_1 = p_2 + \frac{1}{2}\rho U_d^2 \Rightarrow U_d = \sqrt{\frac{2}{\rho}(P_1 - p_2)} = \sqrt{\left(\frac{2}{\rho}\Delta p\right)} . \tag{2.4}$$

Due to the curvature of the streamlines on the inflow side of the aperture a vena contracta is formed (right hand side in Figure 2.1). At the end of the vena contracta the streamlines are parallel and its flow area is smaller than the geometric area of the orifice, i.e. $d<D$. Moreover a shear layer along the surface of the vena contracta is generated. Along this surface a rotational shear flow is formed in which viscous forces are present and turbulence is generated in the form of vortices and eddies. The generated vortices within the shear layer dissipate the kinetic energy of the jet.

Due to the occurrence of the vena contracta the actual flow area of the orifice is smaller than the geometric area (A_D). Hence the mass flow through the orifice is dependent on the area of the vena contracta. This area is referred to as the effective area (A_d) of the orifice such that:

$$\dot{m} = \rho A_d U_d = \rho A_D C_D U_d \quad \text{where } C_D = \frac{A_d}{A_D} = \frac{\pi d^2}{\pi D^2} . \tag{2.5}$$

Therefore the effective area of an orifice can be calculated if the discharge coefficient (C_D) is known. Lichtarowicz et. al. (1965) shows that the discharge coefficient of a sharp edged infinitesimal thin orifice is dependent on the Reynolds number. The Reynolds number relates inertial forces to viscous forces and is defined as (e.g. Batchelor (2000)):

$$Re = \frac{\rho U_d D}{\mu} . \tag{2.6}$$

The viscous forces are represented by the dynamic viscosity μ. In general the Reynolds number is used to assess if the flow through a system is of laminar or turbulent nature. For small Reynolds number the flow is dominated by viscous interactions in the laminar flow regime. At high Reynolds numbers inertial forces dominate and this is associated with the turbulent flow regime. Thus the laminar or turbulent flow regime will have an effect upon the shear layers in the jet flow so that the vena contracta (and ultimately the discharge coefficient) will also be affected. However, not only does the Reynolds number influence the discharge coefficient, but it can also be affected by the geometry of the aperture. Lichtarowicz et. al. (1965) have investigated discharge coefficients of orifice length-to-diameter ratios of *L/D* in the range 0.5 - 10. It is shown that for a given *L/D* ratio the discharge coefficient of the investigated geometries remains constant for Reynolds numbers higher than 5000. It is worth noting that the data from Lichtarowicz et. al. (1965) indicates varying discharge coefficients for changing aperture length-to-diameter ratios for Reynolds numbers greater than 5000, i.e. the Reynolds number independent range (Figure 2.2).

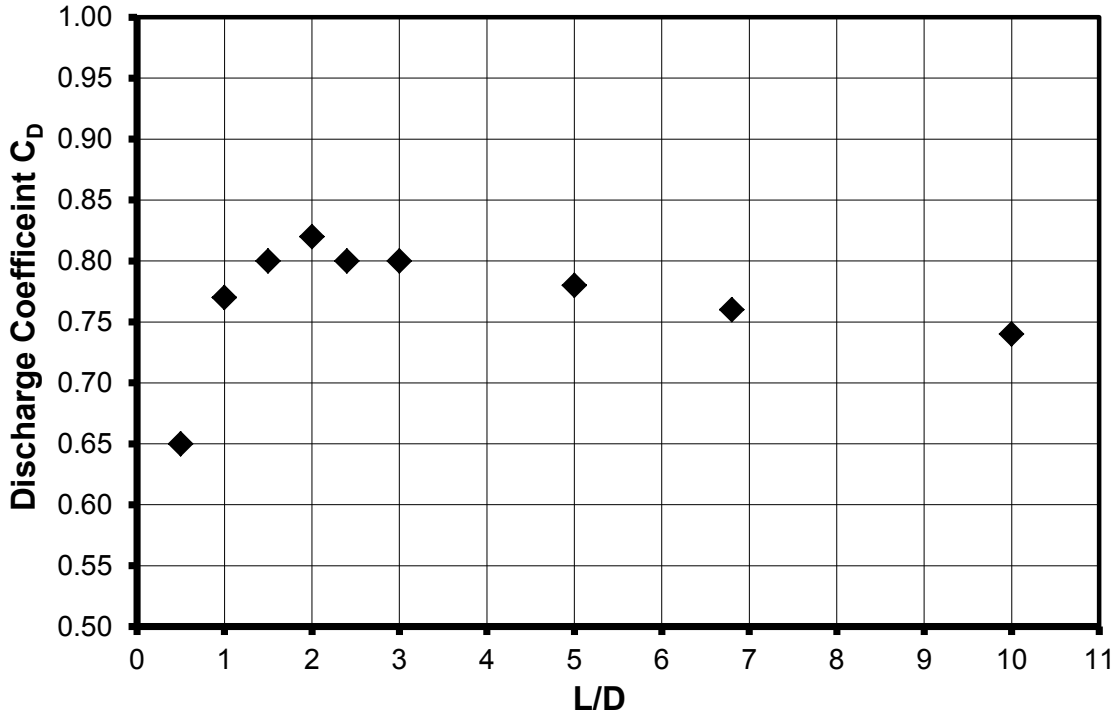

Figure 2.2: Discharge coefficient for orifice with length-to-diameter ratio *L/D* 0.5 to 10 from Lichtarowicz et. al. (1965)

It can be seen that the discharge coefficient increases in the range of *L/D* 0.5 to 2, but then drops steadily at greater values of length-to-diameter ratio. This behavior is caused by the flow characteristics through the orifice. For thin orifice plates the flow is contracting as shown on the left hand side in Figure 2.3. However if the thickness or the length of the orifice is increased the flow starts to attach to the wall inside the orifice at $L/D \approx 2$ as shown on the right hand side in Figure 2.3. Due to the attaching flow inside the orifice the effective area of the orifice increases resulting in a larger discharge coefficient. Increasing the length of the orifice further will result in the development of a boundary layer within the aperture. In this case the discharge coefficient is a superposition of (i) the ratio of effective to geometric area and (ii) the losses due to friction associated with the orifice boundary layer. Hence the measured discharge coefficient reduces for $L/D > 2$.

Further influences on the orifice discharge coefficient are the orifice shape itself (e.g.; chamfered inlets or outlets, angled apertures, etc) or if the orifice is subjected to a cross-flow, e.g. Hay and Spencer (1992), Hay et. al. (1994), Gritsch et. al. (1998), Rowbury et. al. (2001), etc.

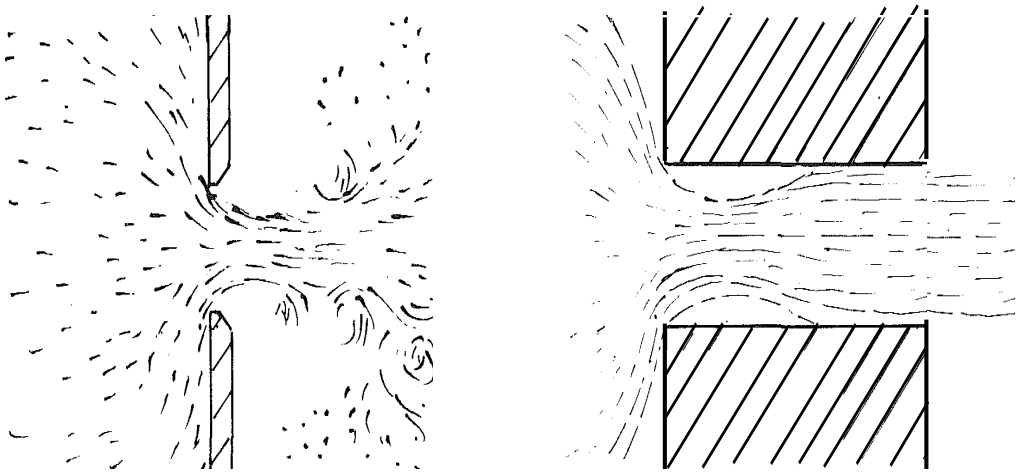

Orifice with $L/D < 2$ Orifice with $L/D \geq 2$

Figure 2.3: Schematic of the flow field through a short ($L/D < 2$) and long orifice ($L/D \geq 2$), from Hay and Spencer (1992)

2.2 Naturally Occurring Phenomena in Unsteady Circular Jet Flow

As discussed in the previous section, flow exhausting from a circular aperture or nozzle consists of regions characterised by inviscid flow and shear layers. The flow separates off the edge of a nozzle and generates a free shear layer downstream of the orifice. Viscous effects generate vorticity in the shear layer. In general these effects are unsteady and inherently the reason for unsteady instability phenomena associated with round jets. The vorticity $\vec{\omega}(\vec{x},t)$ can be used to describe the rotational flow field as defined for example in Saffman (1992) in Cartesian coordinates:

$$\vec{\omega}(\vec{x},t) \equiv curl\,\vec{u} = \begin{pmatrix} \dfrac{\partial w}{\partial y} - \dfrac{\partial v}{\partial z} \\ \dfrac{\partial u}{\partial z} - \dfrac{\partial w}{\partial x} \\ \dfrac{\partial v}{\partial x} - \dfrac{\partial u}{\partial y} \end{pmatrix} . \tag{2.7}$$

Note the potential flow region of the jet is inviscid and therefore the vorticity in this region is $\vec{\omega}(\vec{x},t) = 0$, i.e. the flow is irrotational. Another important parameter to characterise the rotational flow field is the circulation (Saffman (1992)):

$$\Gamma_C = \oint_C \vec{u}\, d\vec{s} = \int_A \vec{\omega} \cdot \vec{n}\, dA \ . \tag{2.8}$$

The circulation is defined as a line integral of the velocity $\vec{u}$ around a curve C surrounding a rotational flow element. Using Stoke's theorem the vorticity can also be expressed as the sum of the vorticity $\vec{\omega}$ through the area A enclosed by the curve C, where $\vec{n}$ is the normal vector on surface A.

The interaction of the vorticity within the free shear layer of the jet can cause the development of coherent structures and ultimately lead to flow instabilities. Michalke (1972) shows a flow visualisation of the vorticity structures in the free shear layer of a round jet which agrees well with the schematic and description shown in Yule (1978) (Figure 2.4). The schematic shows the growth of a flow instability in the shear layer of a jet flow characterised by laminar and turbulent flow regimes. Initially, near the exit nozzle of the jet, natural instabilities in the laminar shear layer produce regions of vorticity in the form of small scale vortex ring structures. These structures travel downstream in the shear layer of the jet and interaction with surrounding vortex ring structures can cause the vortex rings to merge, thereby forming a large scale vortex ring structure or a vortex puff as described in Crow and Champagne (1971). This phenomenon is known as self-excited jet instability or the "*preferred mode"* of a jet (Hussain and Zaman (1981)) where the large scale structures occur periodically on a characteristic time-scale associated with the jet flow, which is defined by the Strouhal number. The Strouhal number is defined as the frequency f of the occurrence of the structures, the nozzle diameter D and the mean jet velocity U_d:

$$St_j = \frac{fD}{U_d}. \tag{2.9}$$

According to Crow and Champagne (1971) the self-excited roll up of vortical structures within the shear layer occurs at jet Strouhal numbers of $St_j = 0.3$. The ring structures interact with the shear layer of the jet and entrain air from the stagnant fluid outside the jet flow as well as from the potential core within the jet flow (Figure 2.4). The vortex rings develop instability waves within the vorticity field of the shear layer and the interaction of the generated vortices results in the break-up of the large scale structure within the turbulent flow region. Within the turbulent field large scale eddies are still present but these structures are not circumferentially coherent unlike vortex rings (Yule

(1978)). The structures then decay to smaller scales until they fully dissipate in the turbulent field.

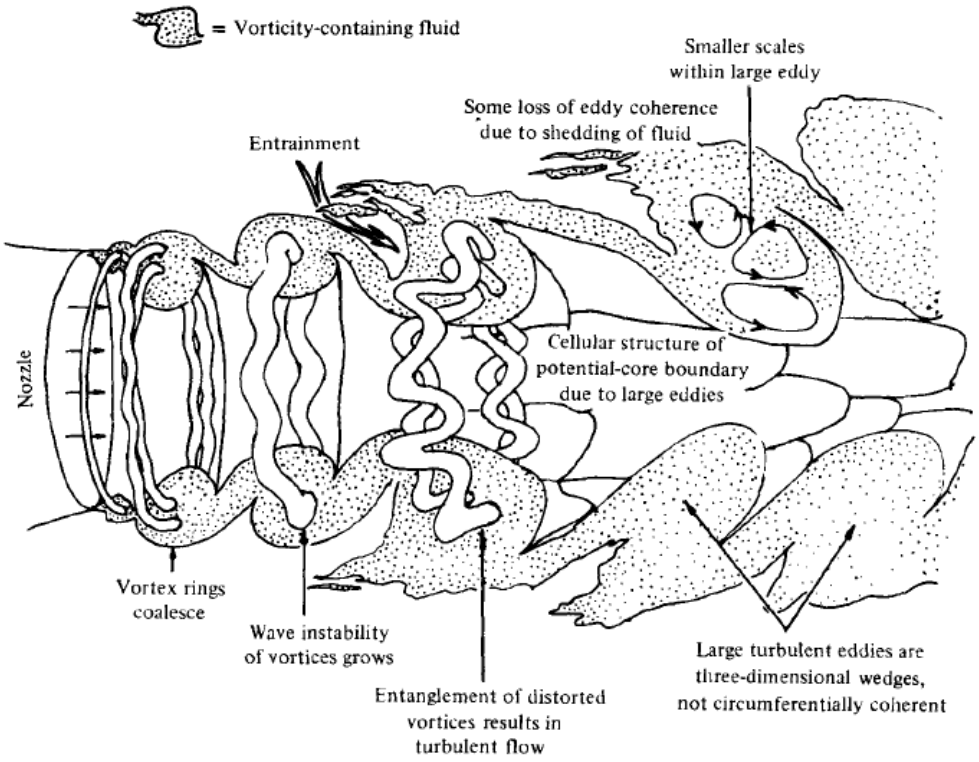

Figure 2.4: Free shear layer instability in a transitional jet downstream of a jet nozzle, from Yule (1978)

2.3 Forced Unsteady Phenomena in Circular Jet Flow

Over the years many authors have investigated the instabilities associated with jets flows and their sensitivity to acoustic forcing (Brown (1935), Crow and Champagne (1971), Heavens (1980), etc). The forcing of the jet can be conducted with an acoustic pressure amplitude altering the static pressure upstream or downstream of a jet nozzle periodically. The result of the pressure amplitude forcing is an unsteady velocity amplitude. For the low amplitude forcing the velocity amplitudes are much lower than the mean jet velocity (i.e. $\hat{u}/\overline{U} << 1$). In contrast unsteady velocity amplitudes larger than the mean velocity are indicative of a high amplitude forcing regime (i.e. $\hat{u}/\overline{U} \geq 1$). However the size of the unsteady velocity amplitude is not only dependent on the static pressure amplitude, it is also dependent on the time scale of the applied forcing.

If the time scale of the pressure oscillation is large, forces associated with the inertia of the jet flow (due to the acceleration of the mass of the jet) are negligible compared to the forces of the unsteady static pressure variation. Hence this regime can be described as the quasi-steady jet flow regime where the inertial forces associated with the jet are negligible. In this regime large perturbation pressure amplitudes will lead to large velocity oscillations and vice versa. Alternatively, if the time scale of the pressure oscillations is small, forces associated with the inertia of the jet flow, are significant compared to the forces of the unsteady static pressure variation. Thus in this regime large pressure oscillations will lead to reduced velocity oscillations due to the influence of the inertial forces.

2.3.1 Low Amplitude Forcing

Brown (1935) investigated large scale structures within acoustically forced jet flows using flow visualization. It was observed that the occurrence of large scale vortices was more pronounced if the jet was forced at certain frequencies. Acoustic forcing of the jet at those Strouhal numbers also leads to the largest perturbation of the jet centreline velocity. Hussain and Zaman (1980) investigated the coherent structures by forcing the jet on its "*preferred mode*" ($St_j = 0.3$) and measured the velocity oscillations in the jet flow using a hot wire anemometer. The flow visualisation conducted by Heavens (1980) also showed large scale coherent vortices. Heavens (1980) noticed that the structures travel with a velocity of 0.5 U_d. More recently Schram and Riethmueller (2002) used particle image velocimetry (PIV) to investigate the acoustically forced flow field of a round jet. In this case the pairing and merging of subsequent vortices was of particular interest and it was shown that the entrainment is locally enhanced due to the vortex pairing in the excited flow field.

2.3.2 High Amplitude Forcing (Vortex Rings)

Another unsteady phenomenon relevant to pulsatile jet flows is the roll up and generation of axisymmetric vortex rings which pinch off the edge of the jet nozzle. This phenomenon occurs if the jet flow is forced in such a way that reverse flow occurs during one time period of excitation, e.g. synthetic jets (Jabbal et. al. (2006)) or non-linear acoustic absorption (Ingard and Labate (1950)). Another possibility of generating

a vortex ring is by an impulsive flow injection using a piston (Didden (1979)). The latter is used to show a flow visualization from Didden (1979) in Figure 2.5 to discuss the formation of a vortex ring.

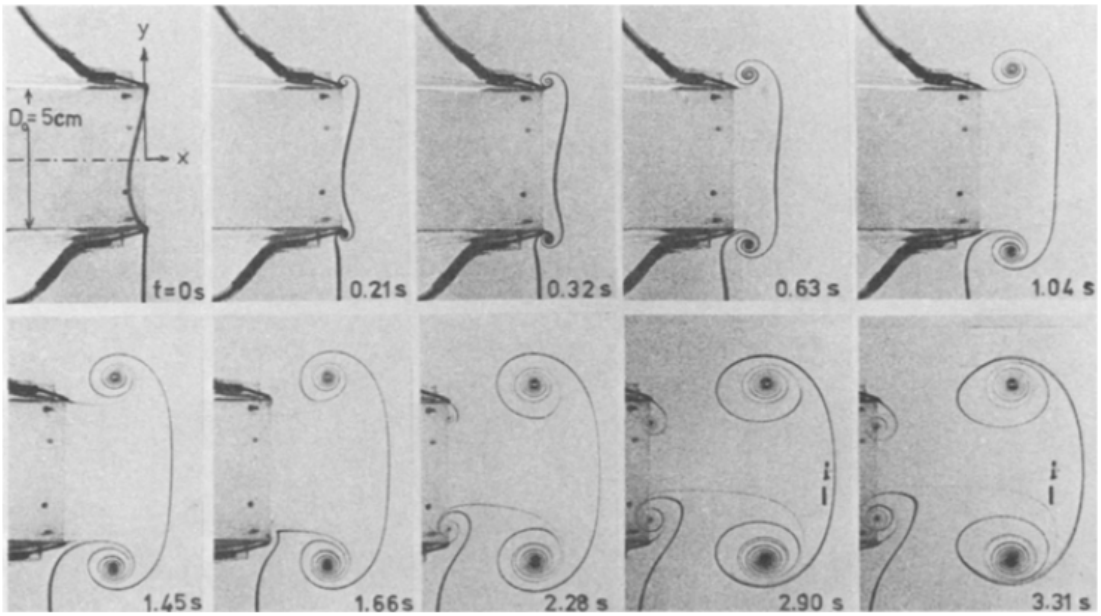

Figure 2.5: Formation of a vortex ring from Didden (1979)

A piston was used to eject water through a nozzle into a water tank. Dye was injected at the edge of the nozzle to visualize the formation of the vortex ring. The piston was accelerated within the initial 0.3s. Afterwards the fluid was pushed through the nozzle at a constant flow speed. At 1.6s the piston reached the end position and the jet velocity dropped to zero. It can be seen that during the ejection period the shear layer rolls up at the edge of the jet nozzle. Due to rotation of the vortex sheet, fluid from the potential velocity field of the jet is entrained, and this increases the size of the ring vortex further. Moreover the rotational flow field induces a velocity field which causes the vortex ring to pinch off from the rim of the jet nozzle just before the end of the piston stroke. From then on the vortex ring propels itself away from the nozzle edge while some of the vorticity containing shear layer generates an opposite rotation on the inside of the nozzle edge (1.66s onwards).

Figure 2.6 shows a simplified example of a vortex ring (e.g. (Maxworthy (1977)) where y represents the axial coordinate, x represents the radial coordinate, ϕ the azimuthal coordinate. As a first approximation the vortex ring is assumed to be

axisymmetric, hence the flow field is constant along the azimuthal coordinate. Moreover the vortex core itself is described by the cylindrical coordinate system *(y', Φ, x')*. The vorticity is concentrated within the core of the vortex ring. Thus the core of a vortex ring is dominated by rotational flow. The core of an ideal vortex is also referred to as a forced vortex (e.g. Douglas et. al. (2005)) which is characterised by a constant angular velocity. A second region of the vortex flow field is the free vortex which surrounds the forced vortex core. This region is irrotational and thus some text books describe it as the potential vortex (Douglas et. al. (2005)). However in the case of vortex rings which occur in engineering flow fields the differentiation is not as simple. Many researchers have investigated methodologies to identify the size of the vortex core radius R_C (e.g. Jeong and Hussain (1995), Schram and Riethmueller (2001), Graftieaux et. al. (2001), Kolar (2007), etc). Vortex rings are classified according to their nondimensional size R_{VC}/R_{VR} (e.g. Batchelor (2000)) where the parameter R_{VR} denotes the radius of the vortex ring. The radius of the vortex ring is defined as the distance of the centre of the vortex core (*y'*-axis) to the centre of the vortex ring on the *y*-axis (see Figure 2.6). Semi-empirical expressions for the kinetic energy and velocity of the vortex rings are available for thin vortex rings ($R_{VC}/R_{VR} << 1$) as shown for example in Sullivan et. al. (2008) or Saffman (1992):

$$\text{Kinetic energy } E_K = \frac{1}{2}\rho\,\Gamma_C^2\,R_{VR}\left(\ln\frac{8R_{VR}}{R_{VC}} - \alpha\right) \tag{2.10}$$

$$\text{Velocity of ring vortex } U_V = \frac{\Gamma_C}{4\pi R_{VR}}\left(\ln\frac{8R_{VR}}{R_{VC}} - \beta\right), \text{ where } \beta = \alpha - 1. \tag{2.11}$$

The parameter β and the core radius R_{VC} were chosen according to Saffman (1970): $\beta = 0.558$, $R_{VC} = \sqrt{4\nu T}$ where T was the duration of the piston stroke which generated the vortex ring and ν represents the kinematic viscosity. Sullivan et. al. (2008) used those expressions with reasonable agreement compared to their experimental data.

As indicated in the schematic of Figure 2.6 the vorticity distribution does not necessarily drop to zero outside the vortex core. Maxworthy (1977) defined the core of the vortex ring at the maximum velocity $|\vec{u}| = \sqrt{u^2 + v^2}$ using the maximum measured

velocity along the core radius using Laser Doppler Velocimetry. In this case only 50% of the total vorticity ($\omega_\phi = \partial u/\partial y - \partial v/\partial x$) was within the core of the vortex ring.

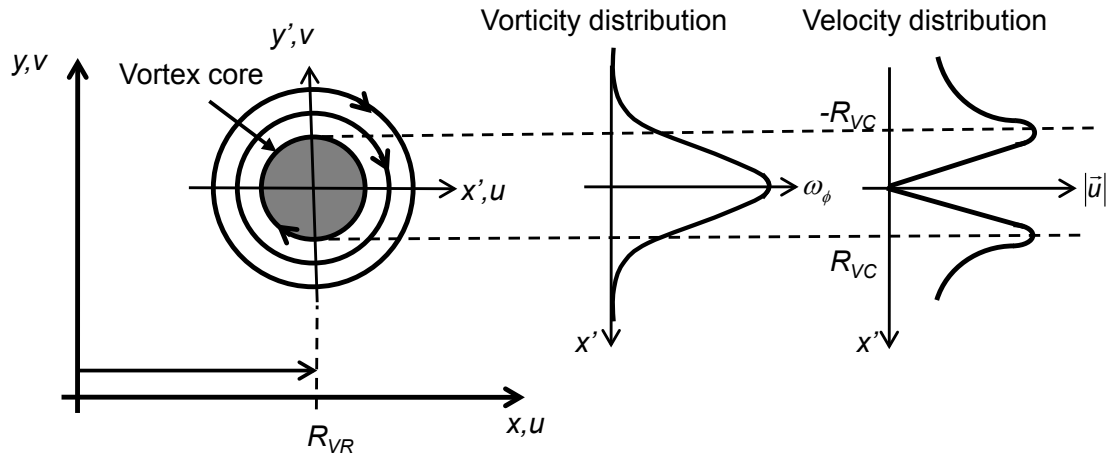

Figure 2.6: Schematic of vortex ring

Gharib et. al. (1998) measured the circulation of vortex rings using particle image velocimetry during the formation of vortex rings. The vortex rings were formed using a piston pushing fluid in a water tank similar to Didden (1979). A parameter quantifying the energy put into the vortex ring is its formation number which was defined in Gharib et. al. (1998) as

$$\frac{L_0}{D} = \frac{\overline{U}_P t}{D}. \tag{2.12}$$

The formation number relates the piston stroke length L_0 to the orifice diameter D. Moreover the stroke length can also be expressed by the mean piston velocity $\overline{U}_P$ multiplied by the time duration t for the piston stroke. Gharib et. al. (1998) found that the circulation in the core of the vortex ring increases for formation numbers up to $L_0/D \approx 4$. Thereafter the total circulation of the vortex ring increased but the core circulation remained constant. This leads to secondary flow features downstream of the vortex rings such as wakes and secondary vortex rings which account for the general increase in circulation. Similar observations were made by Jabbal et. al. (2006).

Hence the flow field of a vortex ring generated by an acoustic wave in the non-linear absorption regime will be strongly dependent on the pressure amplitude. Thus the onset of secondary flow fields or the transition from laminar to turbulent vortex rings, as

described by Glezer (1988), could be important for the amount of non-linear acoustic absorption attainable (i.e. where the unsteady flow field is generated by an acoustic pressure oscillation rather than a moving piston).

2.4 Fundamentals of Acoustics

This section will give a brief overview into the propagation of one dimensional plane acoustic waves. In this work only linear acoustic oscillations are considered. This means that the acoustic pressure amplitude p' is much smaller than the ambient pressure $\overline{p}$ within the fluid, i.e. $p' << \overline{p}$. The fluctuating pressure and velocity can be described as (Dowling and Stow (2003)):

$$p(x,t) = \overline{p} + p'(x,t) \text{ and } u(x,t) = \overline{u} + u'(x,t). \tag{2.13}$$

The acoustic oscillation is treated as a harmonic oscillation so that the fluctuating pressure and velocity are defined as:

$$p'(x,t) = \hat{p}(x)exp(i\omega t) \text{ and } u'(x,t) = \hat{u}(x)exp(i\omega t). \tag{2.14}$$

The parameters $\hat{p}$ and $\hat{v}$ denote the time independent pressure and velocity amplitudes. For an acoustic plane wave these quantities are only dependent on the axial location. Furthermore the exponential function is the harmonic variation of the unsteady pressure and velocity in time (t). The parameter ω represents the angular frequency of the oscillation.

2.4.1 The Acoustic Wave Equation

The propagation of plane waves in an isothermal duct can be derived using a mass conservation and an inviscid momentum balance for an ideal gas in a control volume as introduced earlier in equations (2.1) and (2.2). Initially only acoustic oscillations in the absence of mean flow are considered, i.e. $\overline{U} = 0$. Substituting equations (2.13) into the mass and momentum equations (2.1) and (2.2) and linearising the equations leads to the unsteady form of the linear mass and momentum equations in the axial direction (e.g. Schuermans (2003) or Dowling and Stow (2003)):

$$\frac{\partial \rho'}{\partial t} + \bar{\rho}\frac{\partial u'}{\partial x} = 0 \text{ and} \tag{2.15}$$

$$\bar{\rho}\frac{\partial u'}{\partial t} + \frac{\partial p'}{\partial x} = 0. \tag{2.16}$$

Differentiating equation (2.15) with respect to time and differentiating equation (2.16) with respect to the axial coordinate x, and using the isentropic expression for pressure and density $p'/\bar{p} = \gamma\, \rho'/\bar{\rho} \Leftrightarrow \rho' = 1/c^2\, p'$ leads to the well-known acoustic wave equation (e.g. Dowling and Stow (2003) or Schuermans (2003)):

$$\frac{1}{c^2}\frac{\partial^2 p'}{\partial t^2} - \frac{\partial^2 p'}{\partial x^2} = 0. \tag{2.17}$$

In the case where a uniform mean flow is present it can be shown that the wave equation can take a similar form by using a coordinate transformation (as for example shown in Schuermans (2003)). Therefore the convective acoustic wave equation can be defined as (e.g. Schuermans (2003), Dowling and Stow (2003)):

$$\frac{1}{c^2}\left(\frac{\partial}{\partial t} + \bar{u}\frac{\partial}{\partial x}\right)^2 p' - \frac{\partial^2 p'}{\partial x^2} = \frac{1}{c^2}\frac{D^2 p'}{Dt^2} - \frac{\partial^2 p'}{\partial x^2} = 0. \tag{2.18}$$

2.4.2 Plane Acoustic Waves

For plane acoustic waves in a 1D duct the exact solution of the wave equation can be defined as (e.g. Dowling and Stow (2003)):

$$p'(x,t) = f(t - x/c) + g(t + x/c) \tag{2.19}$$

and the acoustic velocity perturbation is described as

$$u'(x,t) = \frac{1}{\bar{\rho}c}\left(f(t - x/c) - g(t + x/c)\right). \tag{2.20}$$

The parameters f and g are also known as Riemann invariants. In general equation (2.19) describes the acoustic pressure oscillation at every position x along a duct (Figure 2.7) as the superposition of two acoustic waves, one wave travelling in the positive axial direction (f) and the other travelling in the negative axial direction (g).

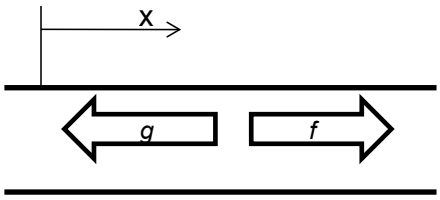

Figure 2.7: Example of plane acoustic waves in a 1D duct

In this work the Fourier transformed versions for the expressions of acoustic pressure and velocity are used:

$$\hat{p}(x)\exp(i\omega t) = \hat{p}_+ \exp(i\omega t - ik_+ x) + \hat{p}_- \exp(i\omega t + ik_- x) \text{ and.} \tag{2.21}$$

$$\hat{u}(x)\exp(i\omega t) = \frac{1}{\overline{\rho c}}\left(\hat{p}_+ \exp(i\omega t - ik_+ x) - \hat{p}_- \exp(i\omega t + ik_- x)\right) \tag{2.22}$$

The circumflex denotes that the parameters are complex amplitudes and the variables k_+ and k_- represent the wave numbers for acoustic waves travelling with (+) and against (-) the mean flow direction. Thus the wave numbers are defined as

$$k_\pm = \frac{\omega}{c(1 \pm M)}. \tag{2.23}$$

In this case M denotes the mean flow Mach number within the duct. If the complex amplitudes of the downstream and upstream travelling waves are known the acoustic pressure and the velocity oscillation at any axial position x can be determined.

A useful acoustic parameter to describe various acoustic elements or boundary conditions is the specific acoustic impedance which relates the acoustic pressure amplitude to the acoustic velocity oscillation (Kinsler et. al. (2000) or Beranek (1954))):

$$Z = \frac{\hat{p}}{\hat{u}}. \tag{2.24}$$

A more convenient way to describe the impedance is to use the acoustic volume velocity using the cross-sectional area of a duct A (Kinsler et. al. (2000)):

$$Z = \frac{\hat{p}}{\hat{u}A}. \tag{2.25}$$

2.4.3 Acoustic Energy Flux

The acoustic intensity for plane waves in a duct with mean flow can be defined as (e.g. Morfey (1971)):

$$I = \langle p'u' \rangle + \frac{1}{\rho c} M \langle p'^2 \rangle + M \langle p'u' \rangle + \frac{1}{\rho c} M^2 \langle p'^2 \rangle . \tag{2.26}$$

Integrating the intensity across the duct area leads to the flux of acoustic energy as defined in (Blokhintsev (1946), Heuwinkel et. al. (2007)):

$$\Pi_+ = \frac{|\hat{p}_+|^2}{2\rho c} A (1+M)^2 \text{ and} \tag{2.27}$$

$$\Pi_- = \frac{|\hat{p}_-|^2}{2\rho c} A (1-M)^2 . \tag{2.28}$$

The parameter A represents the cross-sectional area of the tube and M denotes the mean Mach number of the flow in the tube. Note in this work the Mach number was much smaller than one. Hence the Mach number terms in (2.26) to (2.28) have negligible influence.

2.4.4 Acoustic Absorption Coefficient

The acoustic absorption of a test specimen exposed to plane acoustic waves upstream and downstream of the test section (Figure 2.8) can be characterised by the acoustic absorption coefficient.

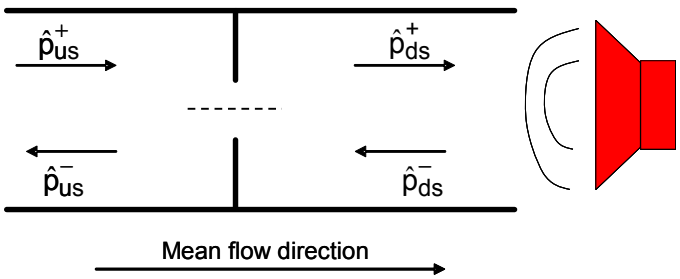

Figure 2.8: Example of plane waves upstream and downstream of a test specimen

In this case the test specimen consists of a circular orifice disc through which a mean flow passes. Hence the absorption coefficient can be calculated using the stagnation enthalpy as defined in Eldredge and Dowling (2003):

$$B' = p' \cdot (1 \pm M). \tag{2.29}$$

Thus the absorption coefficient is defined as the difference between the incident and reflected enthalpy relative to the incident enthalpy, i.e. Eldredge and Dowling (2003):

$$\Delta = \frac{\left|\hat{B}_{ds}^{-}\right|^2 + \left|\hat{B}_{us}^{+}\right|^2 - \left|\hat{B}_{ds}^{+}\right|^2 - \left|\hat{B}_{us}^{-}\right|^2}{\left|\hat{B}_{ds}^{-}\right|^2 + \left|\hat{B}_{us}^{+}\right|^2} = 1 - \frac{\left|\hat{B}_{ds}^{+}\right|^2 + \left|\hat{B}_{us}^{-}\right|^2}{\left|\hat{B}_{ds}^{-}\right|^2 + \left|\hat{B}_{us}^{+}\right|^2}. \tag{2.30}$$

2.5 Aero-Acoustic Considerations

In this section the principles of acoustic oscillations and the governing equations of the underlying fluid dynamics are described. In this way the basis of modelling unsteady flows and their acoustic absorption, associated with circular apertures, is introduced.

2.5.1 The Rayleigh Conductivity

The Rayleigh Conductivity of an orifice as shown in Figure 2.9 is defined as:

$$K_D = -\frac{i\omega\rho\,\hat{Q}}{\hat{p}_{us} - \hat{p}_{ds}} = -\frac{i\omega\rho A\hat{u}_D}{\Delta\hat{p}}. \tag{2.31}$$

Thus the Rayleigh Conductivity relates the unsteady volume flux $(\hat{Q})$ across the aperture to the unsteady pressure drop $(\Delta\hat{p})$ across the orifice. Moreover the Conductivity is therefore inversely proportional to the volume velocity based impedance, i.e. $K_D \sim 1/Z$.

The Rayleigh Conductivity is an unknown quantity, i.e. the unsteady volume flux through an aperture is not known for a given pressure oscillation across the orifice. Hence Howe (1979b) developed an analytical model to describe the Rayleigh Conductivity of an orifice arrangement with bias flow as shown in Figure 2.9. The model was based on an axis-symmetric jet flow with the origin of the (r,θ,x)-coordinate system in the plane of the aperture. Howe (1979b) assumed that the Reynolds number is large so that the unsteady flow is not dependent on Reynolds number effects. Moreover the Mach number of the jet flow through the aperture was

assumed to be low to enable the flow to be treated as incompressible. A harmonic pressure oscillation p'_{us} upstream of the orifice drives an unsteady flow through the orifice. Howe (1979b) assumed that the orifice is infinitesimally thin and the jet flow through the orifice is irrotational. To avoid singularities at the edge of the aperture, due to the inviscid jet flow, it is assumed that vorticity is shed at the edge of the aperture rim as this is known from the Kutta-condition (from inviscid flow over aerofoils). The vorticity is a succession of vortices with infinitesimally small cores which generate a cylindrical sheet downstream of the orifice at $x > 0$ and $r = R$.

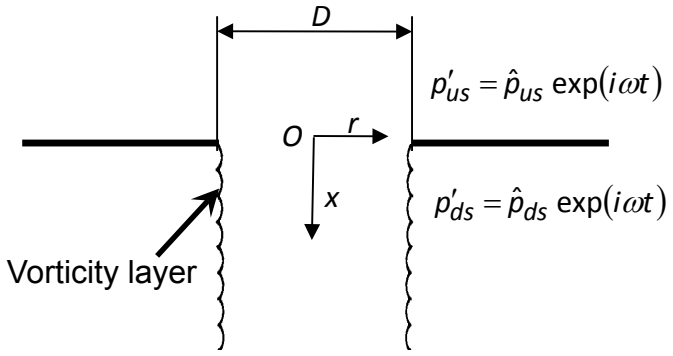

Figure 2.9 Schematic of unsteady orifice flow field, as in Howe (1979b)

The pressure and velocity perturbation is described with the use of the stagnation enthalpy *B:*

$$B = \frac{p}{\rho} + \frac{1}{2}\vec{v}^2 = \hat{B}\exp(i\omega t). \tag{2.32}$$

Howe (1979b) then used the divergence of the momentum equation of the unsteady jet flow with a thin vorticity sheet at the edge of the aperture as:

$$\nabla^2 B = -div(\vec{\omega}\times\vec{v}). \tag{2.33}$$

In this case the vorticity vector is defined as $\vec{\omega} = \overline{\vec{\omega}} + \vec{\omega}'$. Howe (1979b) has investigated the right hand side of this equation in more detail and defined the linearised version of the cross product as:

$$\vec{\omega}\times\vec{v} = \overline{\vec{\omega}}\times\vec{v}' + \vec{\omega}'\times\overline{U} + \overline{\vec{\omega}}\times\overline{U} \quad . \tag{2.34}$$

A further assumption was that the radial length scale of the shed vorticity is much smaller than the shear layer thickness. Hence the radial component of $\vec{v}'$ can be

neglected and therefore only the second term within equation (2.34) is important to calculate the effect of the shed vorticity. This was previously utilized to predict the behaviour of a jet flow exiting from a nozzle (Howe (1979a)). Thus equation (2.33) reduces to:

$$\nabla^2 B = -div\left(\vec{\omega}' \times \overline{U}\right). \tag{2.35}$$

Moreover it was assumed that the vortex rings generated by the vorticity oscillation $\vec{\omega}'$ are travelling with constant axial velocity $\overline{U}$. Hence on the basis of the described assumptions the vorticity fluctuation due to the incident pressure oscillation can be defined as:

$$\vec{\omega}' = \sigma_\omega \, \vec{e}_\theta \, H(x)\, \delta(r-R) \exp\left(-i\omega t - i\omega x/U\right). \tag{2.36}$$

The Heaviside function *H(x)* ensures that vorticity is only shed downstream of the orifice ($x \geq 0$). Moreover the Dirac delta function satisfies the assumption that vorticity is only shed within an infinitesimal thin cylindrical shear layer of radius *R*. The parameter σ represents the amplitude of the shed vorticity per unit length. Differentiating the vorticity and substituting it into equation (2.35) whilst assuming an axisymmetric flow field leads to:

$$\frac{1}{r}\frac{\partial}{\partial r}\left(r\frac{\partial B}{\partial r}\right) + \frac{\partial^2 B}{\partial x^2} = -\left(\frac{\sigma_\omega U R}{r}\right) H(x)\delta'(r-R)\exp\left(i\frac{\omega}{U}x\right). \tag{2.37}$$

The equation was solved analytically as shown in Howe (1979b) by deriving a solution for the circulation amplitude of the shed vorticity. Howe (1979b) then used the solution of the inhomogeneous Poisson equation to derive an expression for the Rayleigh Conductivity:

$$K_R = -\frac{i\omega\rho A \hat{u}_D}{\hat{p}_{us} - \hat{p}_{ds}} = 2R\left(\Gamma(St) - i\delta(St)\right). \tag{2.38}$$

The parameters Γ and δ (Figure 1.8) are solely dependent on the Strouhal number. In this case I_1 and K_1 are modified Bessel functions and the definition of the inertia and the admittance follows from the solution of equation (2.37):

$$\Gamma = \frac{I_1(St)^2\left(1+\frac{1}{St}\right)+\frac{4}{\pi^2}exp(2St)cosh(St)K_1(St)^2\left(cosh(St)-\frac{sinh(St)}{St}\right)}{I_1(St)^2+\frac{4}{\pi^2}exp(2St)cosh^2(St)K_1(St)^2}, \tag{2.39}$$

$$\delta = \frac{\frac{2}{\pi\, St}I_1(St)K_1(St)exp(2St)}{I_1(St)^2+\frac{4}{\pi^2}exp(2St)cosh^2(St)K_1(St)^2}. \tag{2.40}$$

Furthermore the Strouhal number was defined based on the orifice radius R and the angular frequency ω as

$$St = \frac{2\pi f\, R}{\overline{U}} = \frac{\omega R}{\overline{U}}. \tag{2.41}$$

According to Howe (1979b), the mean velocity parameter $\overline{U}$ represents the vortex sheet velocity, which was estimated to $\overline{U} = 0.5\,\overline{U}_d$. Moreover the asymptotic analysis in Howe (1979b) suggests that the contraction ratio between the area of the vena contracta and the area of the aperture was also calculated to be 0.5. Thus for the purpose of this work the mean bias flow velocity in the plane of the aperture $\overline{U}_D$ will be used as an assumption for the mean vortex sheet velocity. Hence the Strouhal number definition in equation (1.16).

The acoustic energy dissipated due to the unsteady pressure oscillation across the orifice can be defined as in Luong et. al. (2005):

$$\Pi_L = \frac{1}{T}\int_0^T Re\left(\hat{Q}\,exp(i\omega t)\right)Re\left(\Delta\hat{p}\,exp(i\omega t)\right)dt \ . \tag{2.42}$$

This represents the flux of acoustic energy through the orifice assuming incompressible orifice flow (i.e. M <<1). Using the Rayleigh Conductivity model form Howe (1979b) an averaged loss of acoustic energy (Luong et. al. (2005)) can be defined, which is dependent on the admittance (δ), the unsteady pressure amplitude ($\Delta\hat{p}$), the radius of the orifice (R), the density (ρ) and the frequency (ω):

$$\Pi_L = \left|\Delta\hat{p}\right|^2 \frac{R\delta}{\rho\omega} \ . \tag{2.43}$$

Over the years various modifications to the Rayleigh Conductivity model defined by Howe (1979b) have been undertaken. Wendoloski (1998) solved the divergence of the momentum equation as defined in (2.37) taking the effects of the open area ratio, or porosity, between the upstream channel and the orifice into account.

Moreover a numerical solution was used by Jing and Sun (2000) to extend the shed vorticity amplitudes, as defined by Howe (1979b), to an orifice plate with finite thickness. Therefore the expression of the unsteady vorticity as defined in (2.36) was modified to:

$$\vec{\omega}' = \sigma_\omega \ \vec{e}_\theta \ \delta(n_s)\exp(-i\omega t - i\omega s/U). \tag{2.44}$$

In this case the shear layer was defined using a jet profile as in Rouse and Abul-Fetouh (1950) instead of the assumption of a cylindrical shear layer. Hence the shed vorticity oscillation is dependent on the vortex stream line s and the coordinate normal to the vortex stream line n_s. However the data in Rouse and Abul-Fetouh (1950) was measured for infinitesimal thin orifice plates at various contraction ratios between the orifice and a feed tube. Thus, strictly speaking, the profiles are only valid for infinitesimal thin L/D ratios. Therefore the assumption in this case is that the jet profiles do not change for the range of investigated L/D ratios in Jing and Sun (2000). The divergence of the resulting inhomogeneous Poisson equation could not be solved analytically. Hence a boundary element method was used to solve the equation numerically. The Conductivity derived by Jing and Sun (2000) is shown in Figure 2.10. This figure is taken from Jing and Sun (2000) and the parameters have been adopted to suit the nomenclature of this work. It was not part of this work to compute the equations derived by Jing and Sun (2000). It can be seen that the conductivity varies with aperture length-to-diameter ratio L/D. The solution with length-to-diameter ratio of 0.0 is identical to the Conductivity model from Howe (1979b). The model was used and compared to some experimental data from impedance measurements for perforated liners. It can be seen in Jing and Sun (2000) that the model agreed with the trends in the experimental data. It was also mentioned that the developed model was not valid if

reattachment of the flow field within the orifice occurs, i.e. $L/D \sim 2$. A description of this model can also be found in Lee et. al. (2007) who extended the theory to include orifice interaction effects between apertures in perforated liners.

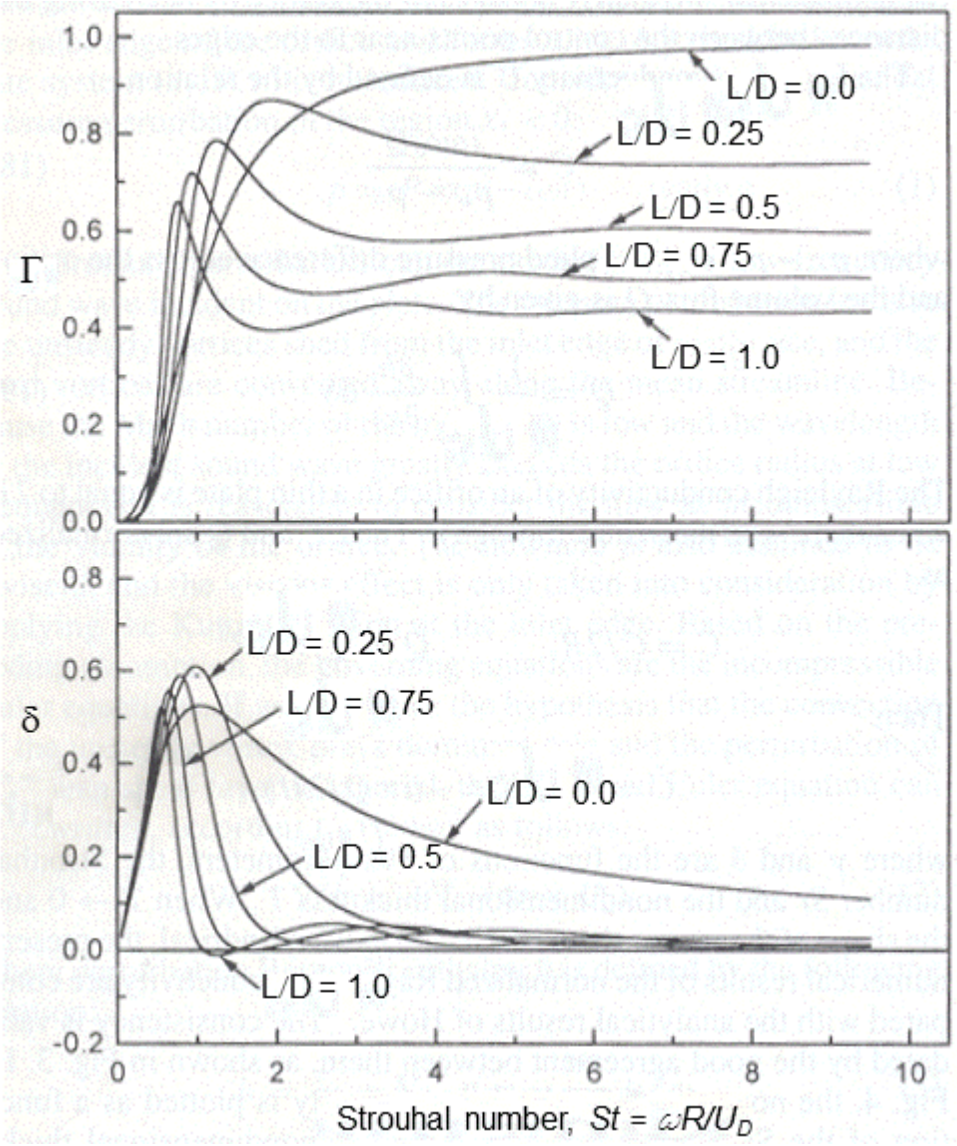

Figure 2.10: Rayleigh Conductivity from Jing and Sun (2000)

2.5.2 Modifications to the Rayleigh Conductivity Model

Of more significance to this work is the work of Jing and Sun (1999), who introduced a length correction to the Rayleigh conductivity as defined by Howe (1979b). In this way more practical engineering applications could be investigated. In this case the normalised acoustic impedance for an orifice was used:

$$z = \frac{\hat{p}}{\rho c \hat{u}}. \tag{2.45}$$

Using the Rayleigh Conductivity model from Howe (1979b) and substituting for the unsteady velocity in the normalized acoustic impedance leads to the expression for the normalized acoustic impedance of an orifice as described in Jing and Sun (1999):

$$z = \frac{\hat{p}_{ds} - \hat{p}_{us}}{\hat{u}_D} = \frac{\pi \omega R}{2c}\left(\frac{\delta}{\delta^2 + \Gamma^2} - i\frac{\Gamma}{\delta^2 + \Gamma^2}\right). \tag{2.46}$$

Note that the wave number k is defined as $k = \omega/c$. Jing and Sun (1999) compared the derived normalized specific impedance of the orifice with the impedance for a tube without mean flow. The impedance of the tube was taken from Beranek (1954) for the condition $R > 0.01/\sqrt{f}$ (which is also valid for every orifice investigated in this work):

$$z_T = \frac{\sqrt{2\nu\omega}}{c}\frac{L}{R} - i\frac{\omega L}{c}. \tag{2.47}$$

In this case the resistance of the orifice is caused by the viscosity of the boundary layer within the tube. Hence the use of the kinematic viscosity ν. The frequency is expressed using the parameter ω and the thickness or length of the tube is described by the parameter L. The reactance of the impedance $(\omega L/c)$ is due to the mass of the fluid within the tube. Note the length of the orifice within the reactance term can also include an acoustic length correction. Jing and Sun (1999) neglected the resistance part of the impedance as the length-to-diameter ratio was small and therefore the viscous effects negligible. Using this methodology the normalised impedance for the orifice, based on the Rayleigh Conductivity by Howe (1979b), was extended with the inertia part due to the increased mass within an orifice of physical length (Jing and Sun (1999)):

$$z_{tot} = \frac{\pi \omega R}{2c}\left(\frac{\delta}{\delta^2 + \Gamma^2} - i\frac{\Gamma}{\delta^2 + \Gamma^2}\right) - i\frac{\omega}{c}L. \tag{2.48}$$

Jing and Sun (1999) compared this expression to their measurements of perforated liners within an impedance tube for apertures with length-to-diameter ratios up to L/D = 0.65. The experiments showed good agreement with the measured data. Moreover many

other authors used the modified Rayleigh Conductivity model with acoustic absorption models for perforated liners, e.g. Eldredge and Dowling (2003).

2.5.3 Non-Linear Absorption Modelling

Over the years many authors have associated the non-linear acoustic damping mechanism of an unsteady orifice flow field with large scale vortex ring structures (Ingard and Labate (1950), Zinn (1970), Whiffen and Ahuja (1983),Tam et. al. (2001), Jing and Sun (2002), Lebedeva et. al. (2005), etc.). To illustrate this Figure 2.11 shows an orifice which is surrounded by an harmonic acoustic pressure field upstream (p'_{us}) and downstream (p'_{ds}) of the orifice. In this case there is no mean flow entering and exiting the aperture. The acoustic pressure oscillation causes an unsteady velocity perturbation u' in the orifice. Subsequently the pulsatile velocity generates a vortex sheet at the edge of the orifice. In the absence of a mean flow field the velocity oscillation changes direction during one time period of an acoustic cycle. In other words the flow is reversing during one half of the acoustic cycle.

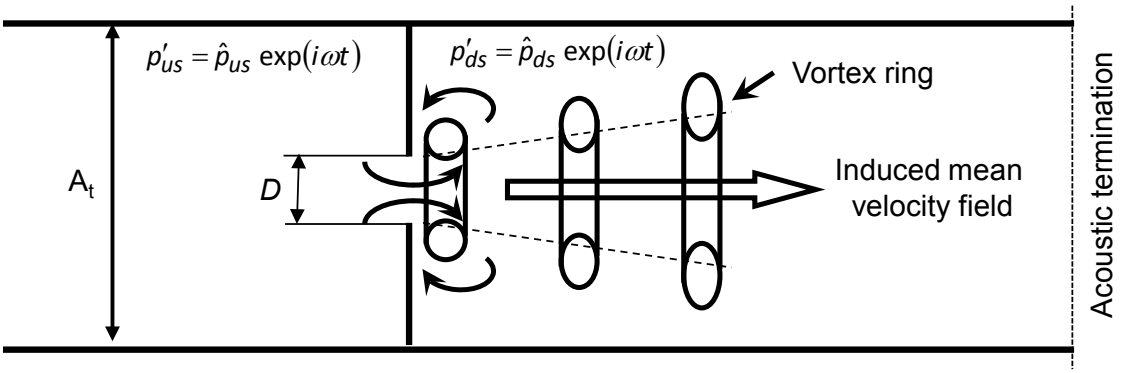

Figure 2.11: Schematic of large scale structures associated with non-linear absorption

As a consequence of the fluid motion large scale flow structures are generated as the vorticity sheet rolls up into a vortex ring at the edge of the aperture. Subsequently the vortex rings pinch off at the rim of the aperture. Due to the rotation of the vortex a velocity field is induced in the centre of the vortex ring which propels the vortex ring away from the orifice. In this way acoustic energy is transferred into the kinetic energy of the large scale vortex ring structures which subsequently dissipate into turbulence and heat further away from the orifice exit. Note that with no mean flow present vortex rings occur on either side of the orifice. Over the years many authors developed

modelling techniques for the non-linear relationship between the pressure oscillation and the velocity oscillation, e.g. Ingard (1970), Zinn (1970), Cummings and Eversman (1983), Cummings (1986), Keller and Zauner (1995), Bellucci et. al. (2004), etc. A summary of the developed methods is given here to highlight some of the assumptions and challenges for the developed models. Moreover added mean flow across the aperture can cause the absorption mechanism to transition between the linear and non-linear absorption regime dependent on the ratio of unsteady velocity amplitude to mean velocity. This complexity is also included within the modelling techniques introduced in this section.

A momentum balance, as shown in the steady case for incompressible flow (Ingard (1970), Cummings (1986), Bellucci et. al. (2004)) can be used to describe the non-linear acoustic behaviour of an orifice within a duct:

$$p_{ds} - p_{us} = -\frac{1}{2}\rho U_D |U_D| \zeta_L - \rho \zeta_{vis} U_D - \rho\, l_{eff} \dot{U}_D \,. \tag{2.49}$$

Note that in this case the velocity U_D in the plane of the aperture is used. Hence the occurrence of a loss coefficient ζ_L compared to, for example, the Bernoulli equation (2.3) in section (2.1) which was defined using the velocity at the end of the vena contracta. According to Ingard (1970) the loss coefficient can be described based on the discharge coefficient:

$$\zeta_L = \frac{1}{C_D^2}, \tag{2.50}$$

whereas Cummings (1986) also includes the porosity of the orifice (ratio between open area and total area of the orifice plate):

$$\zeta_L = \frac{1 - \sigma^2 C_D^2}{C_D^2}. \tag{2.51}$$

Alternatively Bellucci et. al. (2004) uses a high Reynolds number loss coefficient dependent on flow direction and area contraction upstream and downstream of the orifice as defined in Batchelor (2007). The second term on the right hand side takes viscous losses (ζ_{vis}), due to the boundary layer within the orifice, into account (Bellucci

et. al. (2004)). Inertia effects due to the mass of the fluid within the orifice are accounted for by the last term on the right hand side, which includes the physical length and the length corrected parts of the orifice (Ingard (1970), Cummings (1986) and Bellucci et. al. (2004). Substituting the mean and harmonic velocity and pressure oscillations according to equations (2.13) and (2.14) into the momentum equation (2.49) leads to:

$$p'_{ds} - p'_{us} = -\Phi - \rho\zeta_{vis}U'_D - \rho\, l_{eff}\dot{U}'_D\,. \tag{2.52}$$

Note the viscous component due to the mean flow is negligible. The non-linear pressure loss term Φ in the momentum equation (2.52) is then defined as (Bellucci et. al. (2004)):

$$\Phi = \frac{1}{2}\rho\zeta_L\left(\left(\overline{U}_D + U'_D\right)\left|\overline{U}_D + U'_D\right| - \overline{U}_D\left|\overline{U}_D\right|\right). \tag{2.53}$$

Keller and Zauner (1995) derived a solution for the pressure loss term, including the presence of mean flow through the aperture, using a Fourier expansion of the non-linear velocity term $u'_D|u'_D|$. Only using the fundamental harmonics of the Fourier expansion lead to the pressure loss term defined by Bellucci et. al. (2004) in the frequency domain:

$$\hat{\Phi} = \rho\zeta_L g\left(\frac{\overline{U}_D}{|\hat{u}_D|}\right)|\hat{u}_D|\hat{u}_D\,. \tag{2.54}$$

The assumption of using the fundamental harmonics of the Fourier expansion is valid based on the experiments and analytical investigations in Ingard (1970) showing a significant reduction in velocity amplitudes for harmonics larger than the fundamental frequency.

The function $g\left(\overline{U}_D/|\hat{u}_D|\right)$ is defined as in Keller and Zauner (1995) or Bellucci et. al. (2004):

$$g\left(\frac{\overline{U}_D}{|\hat{u}_D|}\right)=\begin{cases}\dfrac{2}{\pi}\left[\dfrac{\overline{U}_D}{|\hat{u}_D|}\arcsin\left(\dfrac{\overline{U}_D}{|\hat{u}_D|}\right)+\dfrac{\sqrt{1-\left(\dfrac{\overline{U}_D}{|\hat{u}_D|}\right)^2}}{3}\left(2+\left(\dfrac{\overline{U}_D}{|\hat{u}_D|}\right)^2\right)\right] & \text{if } \dfrac{\overline{U}_D}{|\hat{u}_D|}<1 \\ \dfrac{\overline{U}_D}{|\hat{u}_D|} & \text{if } \dfrac{\overline{U}_D}{|\hat{u}_D|}>1\end{cases}. \tag{2.55}$$

This function is the basis for the transition from linear to non-linear absorption within the model. In other words, if $\overline{U}_D/\left|\hat{U}_D\right|<1$ then the relationship between the pressure and velocity amplitude is non-linear. If the velocity ratio $\overline{U}_D/\left|\hat{U}_D\right|>1$ the solution of the equation leads to the linear pressure loss term:

$$\hat{\Phi}=\rho\varsigma_L g\left(\frac{\overline{U}_D}{|\hat{u}_D|}\right)|\hat{u}_D|\hat{u}_D=\rho\varsigma_L\frac{\overline{U}_D}{|\hat{u}_D|}|\hat{u}_D|\hat{u}_D=\rho\varsigma_L\overline{U}_D\hat{u}_D. \tag{2.56}$$

The momentum equation can also be expressed in the frequency domain (Bellucci et. al. (2004)):

$$i\omega\rho\, l_{eff}\hat{u}_D+\hat{p}_{ds}-\hat{p}_{us}+\rho\left(\zeta_{vis}\hat{u}_D\right)+\hat{\Phi}=0. \tag{2.57}$$

Finally the viscosity term is defined according to Bellucci et. al. (2004):

$$\left(\zeta_{vis}\hat{U}_D\right)=(1+i)\frac{L}{D}\sqrt{2\nu\omega}\left(1+\frac{\gamma-1}{\sqrt{\mathrm{Pr}}}\right)\hat{u}_D. \tag{2.58}$$

It can be seen that the viscosity is not only affecting the resistance part of the inertia but also the reactance part. In other words viscous effects within the aperture boundary layer introduce an additional phase shift between excitation pressure amplitude and the aperture flow field velocity amplitude.

2.5.3.1 Downstream Acoustic Boundary Conditions

The downstream pressure amplitude $\hat{p}_{ds}$ is dependent on the acoustic geometry. If this pressure amplitude is known then the momentum equation can be solved iteratively to calculate the velocity amplitude within the orifice. Various boundary conditions can be used for the acoustic termination indicated in Figure 2.11:

i) Anechoic boundary condition

In the case of an anechoic termination the downstream pressure amplitude can be defined using the characteristic impedance (ρc) as in Ingard (1970):

$$\hat{p}_{ds} = \left(\frac{\pi D^2}{4 A_t} \right) \rho c \, \hat{u}_D \,. \tag{2.59}$$

ii) Plenum boundary condition

If the downstream termination consists of a plenum then the downstream pressure amplitude would be equal to zero: $\hat{p}_{ds} = 0$.

iii) Helmholtz resonator

For the orifice being attached to a resonating volume, as for example in a Helmholtz resonator, the pressure amplitude in the cavity can be calculated by using a mass balance within the resonator volume (e.g. Bellucci et. al. (2004)):

$$\frac{\partial m'}{\partial t} = V \frac{\partial \rho'}{\partial t} = - \rho U_D' A_D \,. \tag{2.60}$$

Assuming an isentropic compression and expansion due to the oscillating mass flow and transferring the equation into the frequency domain leads to the expression for the pressure amplitude within the resonator volume:

$$\hat{p}_{ds} = i \frac{\rho c^2}{\omega V} \hat{u}_D A_D \,. \tag{2.61}$$

2.5.3.2 Acoustic Energy Loss Calculation

The expressions for the downstream pressure amplitudes together with the momentum equation can be used to solve for the velocity perturbation within the orifice. Loss of acoustic energy is associated with the flux of the energy within the orifice itself (Bellucci et. al. (2004)):

$$\Pi_L = \frac{1}{2} \mathrm{Re}\left(\hat{u}_D^* \hat{p}_{us} \right) A_O \,. \tag{2.62}$$

The fluid dynamic loss mechanism ζ_L as well as the length correction l_{eff} are not necessarily known a priori and are often derived empirically. However, these parameters have a significant effect on the unsteady velocity amplitudes and hence upon the loss of acoustic energy. Keller and Zauner (1995) showed in their investigations that the loss coefficients changed by a large amount if there was a mean flow through the resonator. Moreover their experiments showed that an improvement of the loss coefficient due to rounded edges of the investigated resonator neck lead to an increase in measured absorption. Hence the behaviour of fluid dynamic processes such as vortex rings will have a large effect upon the parameters used to predict the non-linear absorption characteristic correctly.

3 Experimental Facilities and Methods

In general the objective was to undertake a series of measurements to further understand the fundamental absorption characteristic of isolated orifice plates representative of apertures typically found in gas turbine combustors. Therefore an isothermal acoustic test facility has been used at ambient pressure and temperature. The test facility was adapted in various ways to allow the study of fundamental acoustic absorption characteristics as well as more gas turbine combustion system representative geometry in a cost effective manner. Thus simple acoustic test configurations were used to study the fundamental acoustic absorption characteristics while measuring the unsteady flow field surrounding the apertures. Thereafter more complex acoustic test configurations have been used to investigate the damping characteristic of perforated liners which are directly applicable to gas turbine combustors. In this case the findings and modelling techniques developed during the fundamental single aperture measurements were then applied to explore the optimisation of passive dampers suitable for gas turbine combustion systems. The objectives of the various experimental facilities used are summarised in Table 3.1. Each experiment was conducted under isothermal atmospheric conditions at ambient pressure and temperature in the test facility shown in Figure 3.1. The facility is arranged on three floors: the upper floor is used as a plenum, the middle floor contains the test cell (where the test section is located) and the fan room and the lower floor is used as another plenum. Each plenum has a volume of approximately 50 m^3 and acts as an open acoustic boundary condition for the acoustic test sections. The air flow rate and flow direction through the rest rig can be controlled with a centrifugal fan and suitable ducting. Either the air is drawn out of the lower plenum or air is blown into the lower plenum. The air flow direction in Figure 3.1 is indicated with blue arrows. A 120 mm diameter circular duct connects the lower plenum with the test cell where the duct terminates with a flange arrangement. The flange is used as an interface to the various test sections investigated during this work. Square test sections have been connected to the test facility via the discussed flanged interface. Hence an interface duct was manufactured for each test section with a smooth transition piece from the round inlet duct to the rectangular test section to minimise acoustic

losses and excessive acoustic reflections which would reduce the amount of acoustic energy transferred into the test section.

Test Sections	Objectives
Fundamental acoustic absorption and Rayleigh Conductivity measurements	• Acoustic absorption coefficient measurement • Acoustic energy loss measurement • Unsteady flow field measurement to investigate interactions between the unsteady flow field and the linear and non-linear acoustic absorption characteristic. • Develop validation data to assess the performance of analytical acoustic absorption models for gas turbine combustion system relevant aperture geometries over wide range of Strouhal numbers.
Multi-aperture perforated liner test section	• Measure the acoustic absorption of perforated liners suitable to gas turbine combustion system design envelope. • Validate analytical absorption models for multi aperture and multi skin acoustic dampers.
Single sector combustion system test section	• Measure the acoustic absorption characteristic under the influence of a complex fuel injector flow field. • Validate analytical absorption models. • Investigate gas turbine combustion system design envelope.

Table 3.1: Overview of test sections used for the investigation of fundamental absorption characteristics

To generate plane acoustic waves two JBL AL6115 600 W loudspeakers were used attached to the inlet duct in the lower plenum. The loudspeakers are driven by a Chevin Research A3000 amplifier system. A reference to the acoustic driver system and the test facility can be found in Barker et. al. (2005). The excitation frequency from the loudspeakers for the conducted experiments ranges from 10 Hz to 1000 Hz and the pressure amplitudes can vary between 115 dB- 145 dB for the test sections investigated in this work.

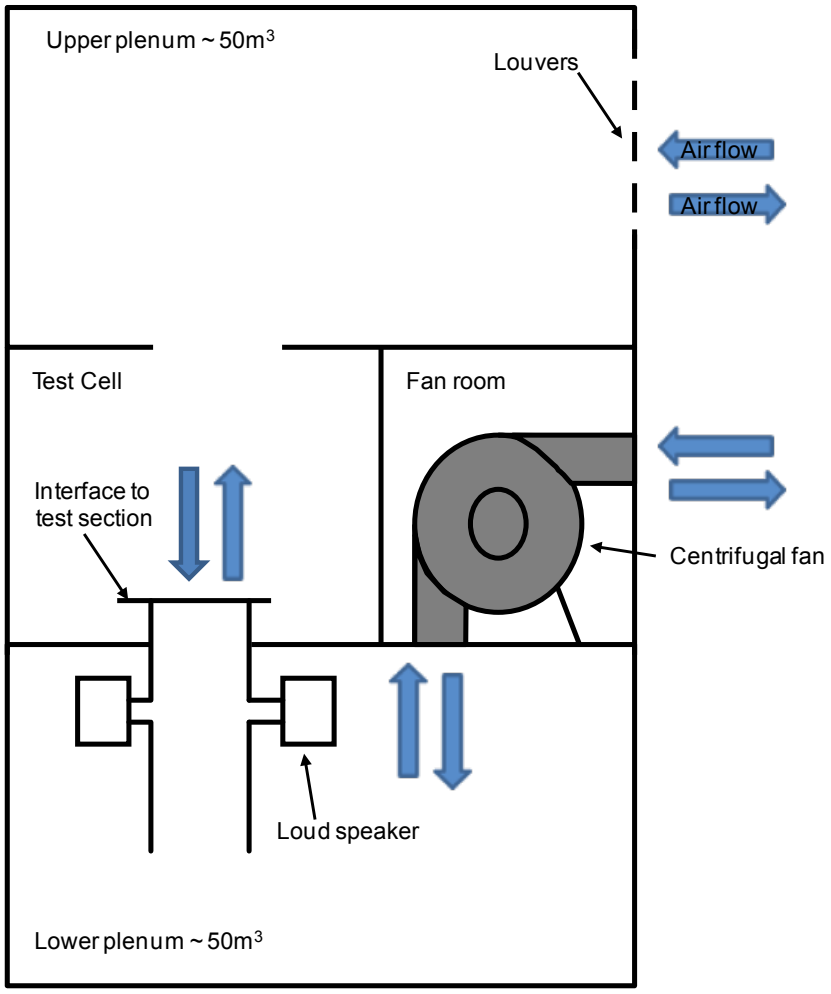

Figure 3.1: Schematic of the aero-acoustic test facility, not to scale

3.1 Scaling from Gas Turbine Engines to Experimental Test Rig Geometry

Before the developed test sections are discussed the relevant scaling from engine applications to small scale isothermal experiments will be discussed. Scaling is important so that the data measured in the ambient labscale environment is transferrable between engine and test rig. Modern gas turbine aero-engine combustion systems typically operate at approximately 40 bar combustor inlet pressure and 900 K inlet temperature (take-off conditions). Note that the combustion temperatures downstream of the liner are higher than 900 K, however for the performance of the perforated liner the cooling air temperature passing through the apertures is the relevant quantity. In comparison, the isothermal test facility operates at 1 bar and 290 K temperature. Hence the relevant non-dimensional scaling parameters used in this investigation have to be

identified to relate the atmospheric test results back to the full scale engine operating conditions.

As already discussed the acoustic absorption due to perforated liners is mainly dependent on the Strouhal number as defined by Howe (1979b). Hence:

$$St_{Engine} = \frac{\omega R}{\overline{U}_D} = St_{Rig} \tag{3.1}$$

Another important parameter for the scaling of passive damper geometry is the ratio of incident pressure amplitude to mean pressure difference across the perforated liner, i.e.:

$$\hat{P}^n_{Engine} = \frac{\hat{p}_{pk}}{\Delta\overline{p}} = \hat{P}^n_{Rig} \,. \tag{3.2}$$

The pressure amplitude in this case was chosen as the *0-peak* amplitude. As will be subsequently shown this parameter has a direct influence on determining if the liner is within the linear or non-linear regime.

Furthermore the Mach number which relates the velocity through the apertures to the speed of sound was kept constant between the test rig and the engine:

$$\overline{M}_{Engine} = \frac{\overline{U}_d}{c} = \overline{M}_{Rig} \,. \tag{3.3}$$

The Mach number is linked to the mean pressure drop across the apertures. Moreover the pressure drop across a gas turbine wall remains constant across the operating envelope of the engine. Therefore the pressure drop (*dp/p*) within the atmospheric test rig has to be the same to operate at the same Mach number through the apertures. The pressure drop is defined as the mean pressure drop across the aperture related to the upstream pressure:

$$\left(\frac{\Delta\overline{p}}{\overline{p}}\right)_{Engine} = \frac{\overline{p}_{us} - \overline{p}_{ds}}{\overline{p}_{us}} = \left(\frac{\Delta\overline{p}}{\overline{p}}\right)_{Rig} \,. \tag{3.4}$$

For convenience in this work the mean pressure drop across the apertures will be referred to as *dp/p*.

The impact of the Reynolds number on the scaling of the acoustic absorption test configuration is of second order. This is valid as long as the Reynolds number is sufficiently high above any transitional flow effects. Hence although the Reynolds number could not be conserved for the measurements conducted in this work, it was ensured that the Reynolds number was above any transitional effects.

As already discussed the aim was to assess combustion system relevant aperture geometry. Therefore cooling ring, effusion tiles, primary port and single skin effusion geometries need to be assessed. Table 3.2 shows an overview of the relevant geometries on conventional and modern gas turbine combustors. The Strouhal numbers have been estimated using combustor inlet pressures of 40 bar and 900 K inlet temperature. The frequency depends on the size of the full annular combustion systems and hence a range from 400 to 900 Hz was considered.

Orifice Type	***D* in mm**	***L/D***	**Strouhal number *St***	**Reynolds number *Re***	**Mean pressure drop *dp/p***
Cooling ring	0.7…1	6…8	0.01…0.03	34000…50000	3%
Single effusion skin	0.7…1	>10	0.01…0.03	34000…50000	3%
Effusion tile	0.7…1	2…7	0.02…0.18	6000…29000	0.1 – 1%
Ports	10…20	~0.5	0.14…0.65	490000…990000	3%

Table 3.2: Combustor orifice geometries relevant to gas turbine engines

Combustor background noise levels have been estimated to be of order 150 dB at 40 bar pressure. Therefore the pressure amplitude scaling of equation (3.2) leads to 118 dB pressure amplitude at ambient pressure for the relevant pressure drop across the aperture. The pressure amplitude in dB is defined as:

$$dB = 20 \cdot log\,10\left(\frac{\hat{p}_{rms}}{2 \cdot 10^{-5}}\right). \tag{3.5}$$

Note that the amplitude used for the decibel scale is the root mean square amplitude which can be calculated using the peak amplitude:

$$\hat{p}_{rms} = \frac{\hat{p}_{pk}}{\sqrt{2}}. \tag{3.6}$$

However pressure amplitudes due to a thermo-acoustic instability at 40 bar can rise to 190 dB, which is in the order of the combustor pressure drop at 40 bar combustor inlet pressure. For the investigated orifice geometries the mean pressure drop ranges from 0 to 3%. Hence the scaled max amplitude for the isothermal condition ranges from 131 to 160 dB at ambient pressure. The maximum available pressure amplitude within the test facility on the square duct dimensions is 145 dB. Hence the pressure amplitude excitation range was set between 115 and 145 dB, and it is acknowledged that the very high limit cycle amplitudes cannot be simulated.

For the experiments conducted the test sections were designed to ensure constant Strouhal and Mach numbers between the test rig and the engine geometry. Moreover to remain within the relevant absorption regime (i.e. linear or non-linear) the pressure amplitudes were scaled relative to the aperture pressure drop to ensure similarity with the engine pressure amplitude forcing. Therefore the diameter, excitation frequency and excitation amplitudes were scaled according to the introduced non-dimensional parameters.

3.2 Fundamental Investigation of the Acoustic Absorption by Circular Apertures

This section will describe the test facilities which have been used to conduct the fundamental acoustic absorption investigations. Initially a single aperture test rig has been used to measure the acoustic absorption whilst particle image velocimetry (PIV) has been conducted. Thereafter the facility has been modified to increase the Strouhal number range over which the Rayleigh Conductivity of the apertures could be measured.

3.2.1 Acoustic Absorption Measurements and PIV Investigations

The objective for the experiments in this section was to provide sufficient optical access and accurate acoustic measurements to develop a methodology for the flow field characterisation relevant to linear and non-linear acoustic absorption of circular orifice plates. Therefore the unsteady flow field was measured during acoustic excitation using a high speed particle image velocimetry (PIV) system. To avoid refraction in the optical measurement technique a rectangular duct with a 120 mm by 120 mm cross-section was

chosen. Moreover the test rig walls were made out of Perspex, again to allow optical access, with a wall thickness of 20 mm to avoid structural vibration effects due to the acoustic forcing. Furthermore the duct was also supported at regular intervals to keep the structural resonance frequencies well above the acoustic excitation frequencies. The area of the duct was sufficient to generate pressure amplitudes up to 145 dB which was necessary for the non-linear absorption measurements at elevated mean pressure drops across the orifice.

The experiments have been conducted at ambient conditions and a schematic of the test section is shown in Figure 3.2. Descriptions of the same test facility can also be found in Rupp et. al. (2010) and Rupp et. al. (2010b). Note that the blue arrows represent air flow and the red arrows plane acoustic waves. The test rig inlet was in the upper plenum and the mean flow exit was located in the lower plenum. Thus the acoustic boundary conditions for the test rig were open boundary conditions (i.e. with pressure amplitude equal to zero). In this case air was drawn from the upper plenum through the test section and exhausted via the lower plenum. The test section consists of a flange to which suitable orifice plates could be attached. These plates were of varying thickness (L) and contained orifices of varying diameter (D). It is worth noting that in these experiments the orifice behaviour is investigated without interaction effects from neighbouring apertures. Thus the test specimens represent a single aperture within a perforated liner where the aperture pitch (P) is large enough to ensure no interaction between the apertures. Moreover no cross flow effects upon the acoustic behaviour of the aperture are investigated within these experiments.

The design of the flange arrangement for the orifice plate was optimised for optical access and is shown in detail in Figure 3.3. The orifice was clamped between the upstream and downstream duct. To avoid unwanted interference from vibration or leakage, the ducts were clamped together on four corners of the test rig using L-shaped fixtures. Therefore obstacles for the optical measurement technique due to standard flange arrangements could be avoided. Hence the laser sheet could be aligned across the orifice centreline and the high speed camera could be focused immediately upstream and downstream of the orifice enabling a clear view through the Perspex wall to obtain a field of view (FOV) as indicated in Figure 3.3.

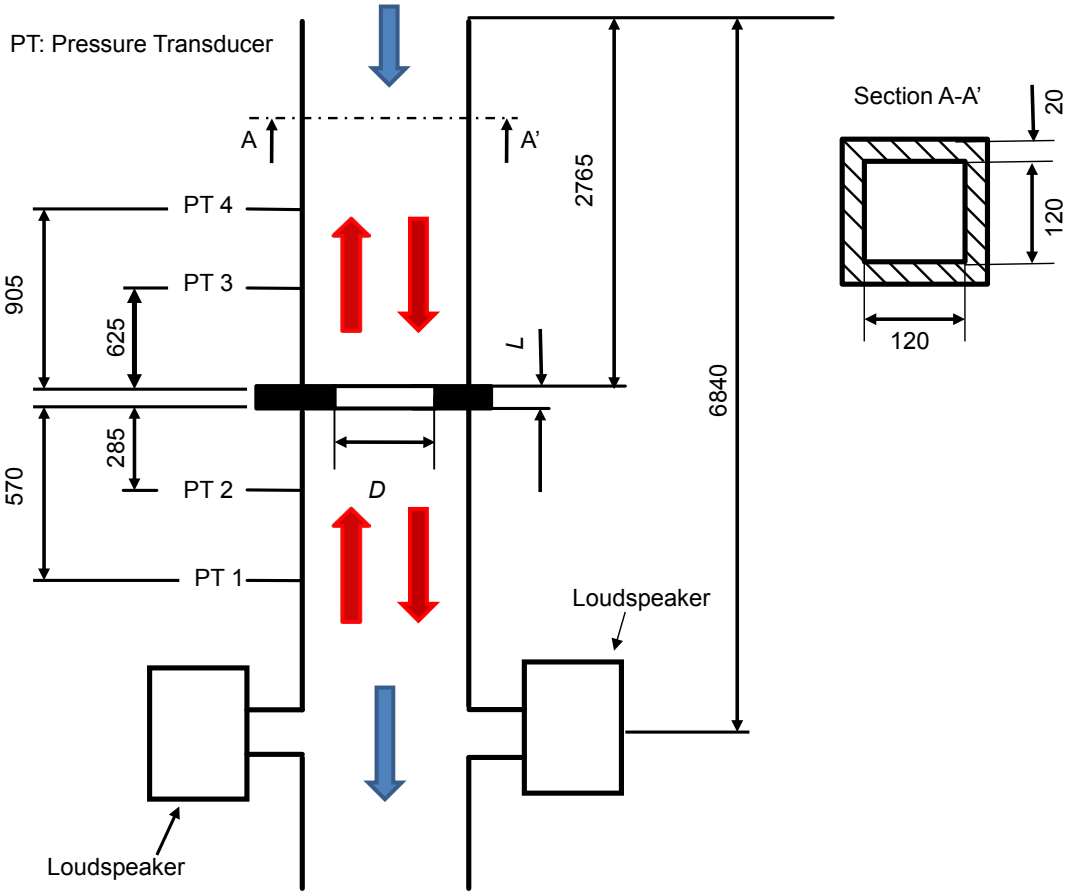

Figure 3.2: Test rig dimensions and dynamic pressure transducer positions (PT), dimensions in mm not to scale

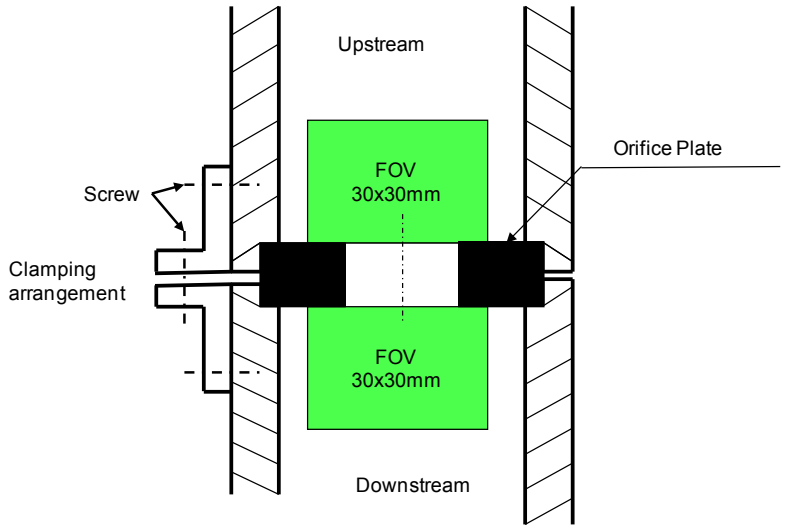

Figure 3.3: Schematic of optical access for PIV measurement, cut through the centreline of the orifice plate

The air flow was controlled by the centrifugal fan and the experiments have been conducted over a range of steady mean pressure drops (*dp/p*) across the orifice of 0 to

3%. The pressure drop between the inlet plenum and a pressure tapping downstream of the orifice plate was obtained using a Furnace FC0510 micro-manometer.

The loudspeakers generated plane acoustic waves (red arrows in Figure 3.2). This assumption of axial plane wave propagation within the test rig is valid as long as the excitation frequency is below the cut-on frequency of radial or circumferential acoustic resonance modes. In this case the distance between the duct walls is 120 mm. For radial modes to be sustained their wave length must be twice the width of the test rig, i.e. 240 mm (a half wave radial mode could then be sustained if the cut-on frequency of this wave would be excited). This can be estimated using the following equation:

$$f_{rad}^{cut} = \frac{\sqrt{\gamma RT}}{\lambda} = \frac{c}{2L_D} = \frac{340m/s}{0.24m} = 1416.7Hz$$

Higher order modes are generated in the near field of the loudspeakers. However, if the excitation frequencies remain below 1400 Hz the radial modes will be highly damped and will have no influence within the acoustic test section starting two meters upstream of the loudspeakers. Thus only plane acoustic waves can be considered.

The excitation frequency for the linear and non-linear acoustic absorption measurements was chosen to satisfy two requirements:

- Constant unsteady pressure drop across the aperture,
- Low excitation frequency for an adequate temporal resolution for the PIV measurement technique.

As equation (2.43) shows the acoustic energy absorbed by a circular orifice is dependent on its admittance and the unsteady pressure amplitudes upstream and downstream of the orifice. Furthermore the admittance of a circular orifice is solely dependent on the Strouhal number through the orifice (Howe (1979b). Therefore the unsteady pressure amplitudes on either side of the aperture are important if various orifice plates are compared with each other. The pressure amplitude downstream of the orifice is always the maximum pressure amplitude ($\hat{p}_{-} = \hat{p}_{max}$) for all orifice geometries due to the area change from duct to aperture. However the acoustic pressure amplitude immediately upstream of the aperture is dependent on the excitation frequency and the length of the

upstream duct. Therefore the upstream duct length was chosen so that a half wave resonant mode or a full wave resonant mode (including the relevant length correction) was present. Therefore a pressure node was located just upstream of the orifice ($\hat{p}_+ = 0$) for all orifice geometries and excitation pressure amplitudes on this test rig which were chosen as 62.5 and 125 Hz (see Figure 3.4).

The sampling frequency of the high speed PIV system is 1100 Hz. Hence the excitation frequency for the conducted measurements (62.5 and 125 Hz) was adequate to ensure a good temporal resolution, i.e. 18 instantaneous velocity fields per acoustic cycle for 62.5 Hz excitation and 9 instantaneous velocity fields per acoustic cycle for 125 Hz excitation.

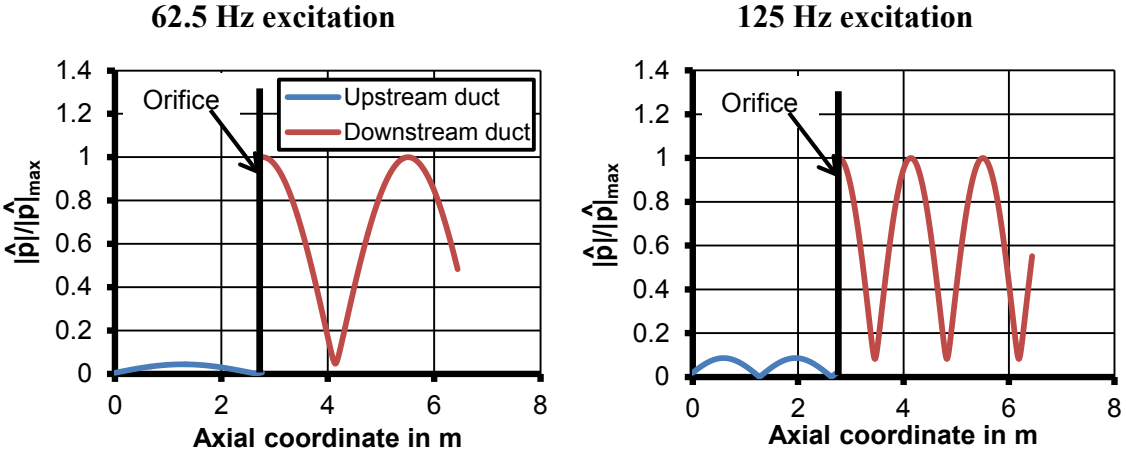

Figure 3.4: Amplitude mode shape for upstream and downstream duct

The test specimens chosen for the isothermal test rig have been scaled according to the Strouhal number ranges identified for the combustion system geometry in Table 3.2. Hence the orifice diameters have been selected as defined in Table A.1. The associated Strouhal and Reynolds number ranges for the chosen diameters are shown in Table 3.3 to simulate the combustor orifice geometries at 62.5 Hz and 125 Hz for the chosen mean pressure drop range from 0 to 3%. However the Reynolds number of the combustor ports could not be simulated due to test rig geometry and mass flow restrictions, but, as already discussed the Reynolds number has a negligible influence on the acoustic absorption for the range of conditions tested. However, tests will be conducted were the Strouhal number is kept constant and the Reynolds number increased to prove the insensitivity of acoustic absorption with Reynolds number for the conditions tested.

D in mm	Strouhal number range	Reynolds number range
9.1	0.04…0.2	7800…43000
12.7	0.05…0.55	10000…57000

Table 3.3: Combustor orifice geometries relevant to gas turbine engines for acoustic absorption experiments

The test rig was used to measure the acoustic energy loss associated with a circular aperture. This loss was then intended to be correlated with the kinetic energy within the unsteady flow field to identify the flow field structures associated with the acoustic absorption. In this case the plane acoustic waves (red arrows in Figure 3.2) travelled upstream (i.e. against the mean flow) towards the orifice. At the orifice one portion of the acoustic energy is reflected, some energy is transmitted whilst the remaining energy part is absorbed. On the upstream side the transmitted acoustic energy generates plane waves which travel towards the open boundary condition, were they fully reflect within the frequency range of interest and then travel back towards the orifice. Therefore the acoustic energy has to be measured on both sides of the aperture to identify the acoustic energy loss due to the aperture flow field. Thus two pairs of Kulite dynamic pressure transducers, located upstream and downstream of the orifice plate, were used to obtain the acoustic absorption (PT1-PT4 in Figure 3.2). The positions of these transducers were optimised for the chosen acoustic forcing frequencies. Hence none of the transducers were located on an acoustic pressure node (p'=0). The transducers were calibrated as discussed in section 4.1.1. The decomposition of the acoustic waves within the duct was conducted using the two-microphone-method which is described in section 4.1.2.

3.2.2 Rayleigh Conductivity Measurements

The primary objective for this experimental configuration was to accurately measure the Rayleigh Conductivity of various orifice geometries relevant to gas turbine combustion chambers. This requires an accurate measurement of the pressure amplitudes immediately upstream and downstream of the orifice. Moreover the performance of Rayleigh Conductivity models, e.g. the Rayleigh Conductivity model as described in Howe (1979b), can be assessed. In general this is an experiment which could have been conducted on the test facility mentioned in the previous section.

However the aim of this experiment was to measure the Rayleigh Conductivity over a wide Strouhal number range rather than at specific frequencies. This would lead to reduced accuracy using the two-microphone method (described in section 4.1.2) over a wide frequency band (e.g. 20 to 1000 Hz). Hence a multi-microphone method (described in section 4.1.3) would have to be applied to accurately measure the pressure amplitudes on the upstream and downstream side of the orifice. This would generate a significant cost as the amount of dynamic pressure transducers would be doubled.

A more cost effective approach was to modify the test configuration as shown in Figure 3.5. In this case the fan was used to blow air through the test rig as indicated by the blue arrows. The duct geometry upstream of the orifice was unchanged but for this setup the test rig was terminated immediately downstream of the orifice test specimen. Therefore the sound was able to radiate into the surrounding plenum. Thus it can be assumed that the pressure oscillation immediately downstream of the aperture is zero for the range of excitation frequencies investigated. In the upstream duct a multi-microphone method was used to accurately measure the pressure and velocity amplitudes in the plane immediately upstream of the orifice. A similar setup is described in Howe (1979b) and used for the derivation of the analytical Rayleigh Conductivity model. Hence the measurements undertaken within the linear acoustic absorption regime can be used to assess the performance of the model developed by Howe (1979b). However the Rayleigh Conductivity was also measured within the non-linear acoustic absorption regime.

For this setup the acoustic energy loss cannot be directly measured as the transmitted energy into the plenum was not captured. However the acoustic loss generated by the apertures can be inferred using the measured admittance and pressure amplitudes on the upstream side of the orifice using equation (2.43).

The air flow through the test rig was chosen so that the pressure drop (dp/p) across the orifice was set to 0.5%. The pressure downstream of the test specimen was ambient and the upstream pressure was measured using a static pressure tapping within the duct prior to the orifice. Moreover the frequency was varied in increments of 20 Hz from 20 to 1000 Hz. These conditions correspond to a Strouhal number range of 0.02-1.6. At the maximum frequency of 1000 Hz it is still valid to assume plane axial waves within the

rectangular test section. As already discussed radial modes are expected to cut on at approximately 1400 Hz. The pressure amplitude for the tests within the linear absorption regime was set to 130 dB for the plane wave incident onto the test specimen, for the non-linear acoustic absorption regime the pressure amplitude being increased to 145 dB.

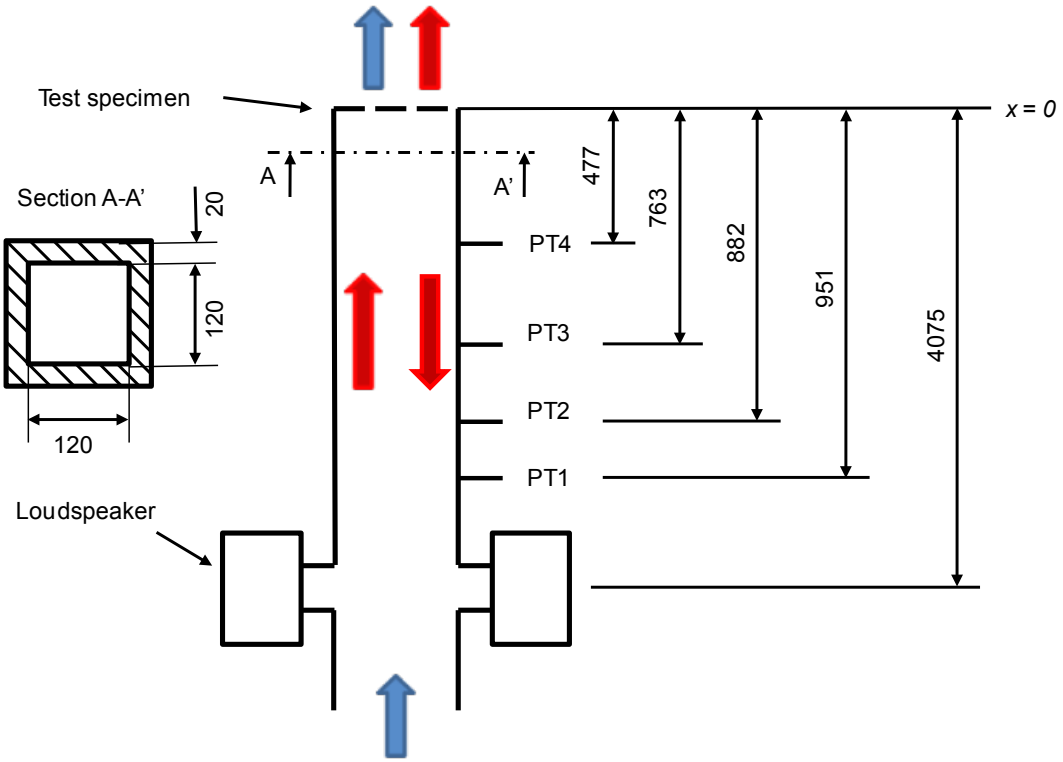

Figure 3.5: Schematic of the test facility for Rayleigh Conductivity measurements, dimensions in mm not to scale

To derive the Rayleigh Conductivity the impedance was measured just upstream of the orifice (x = 0 Figure 3.5). During the commissioning phase of the experimental facility the effects of the acoustic radiation upon the impedance measurements have been assessed. The aim was to ensure the radiation of acoustic energy does not affect the resistance measurements, since the radiation and inertia effects will be contained in the reactance of the impedance. However the influence of radiation upon these measurements is small and is discussed further in chapter 5.4.

Using this approach various test specimens have been investigated that are relevant to the gas turbine combustion system design envelope. The investigated geometries are defined in appendix A.2.

3.3 Experiments on Combustion System Representative Acoustic Damper Geometries

In this section test facilities used for the experimental assessment of gas turbine representative acoustic dampers are introduced. This included

- a facility in which a multi-aperture perforated liner could be incorporated, the size of which was broadly representative of that found for a single sector of a full annular combustion system,
- a facility which simulated a single sector of a combustion system including the fuel injector and associated flow field.

3.3.1 Experiments of Combustion System Representative Acoustic Liners (No Influence of the Fuel Injector Flow Field)

The objective for this test rig was to validate design tools and acoustic absorption models for perforated liners applicable to gas turbine aero combustion systems. Isothermal tests were conducted at ambient pressure and temperature on the test configuration described in Figure 3.6. The test rig consists of a 115 mm by 130 mm rectangular cross-section. This cross-section was representative of a sector of an annular combustor. The damper cross-sectional area (40.3 mm by 115 mm) is slightly smaller than the duct area. This was necessary to achieve combustion system representative porosities at the relevant pressure drop to remain within the cooling envelope of a modern gas turbine combustor.

Air is drawn through the passive damper (blue arrows Figure 3.6) which consists of a metering skin, a volume representative of that available within the combustion system space envelope and a damping skin. The pressure drop across the test section was set to 3% which is representative of a gas turbine combustor wall. The detailed geometry of the test section is described in appendix A.3.

Two loudspeakers are used to generate a plane wave travelling towards the test section (red arrows in Figure 3.6). In this case the reflection coefficient was measured. Although a small amount of acoustic energy can be transmitted through the passive damper assembly, as a first assumption this transmitted wave is neglected. To ensure this assumption is valid the metering skin described in Table A.4 was designed with a

small porosity and long apertures with *L/D* ratio of 16.67. This ensures that the unsteady velocity amplitude in the metering skin apertures remains small and the acoustic behaviour of the metering skin is similar to a rigid wall. Hence the difference between the incident and reflected wave is assumed to be the acoustic energy loss, which was subsequently used for the validation of the acoustic models.

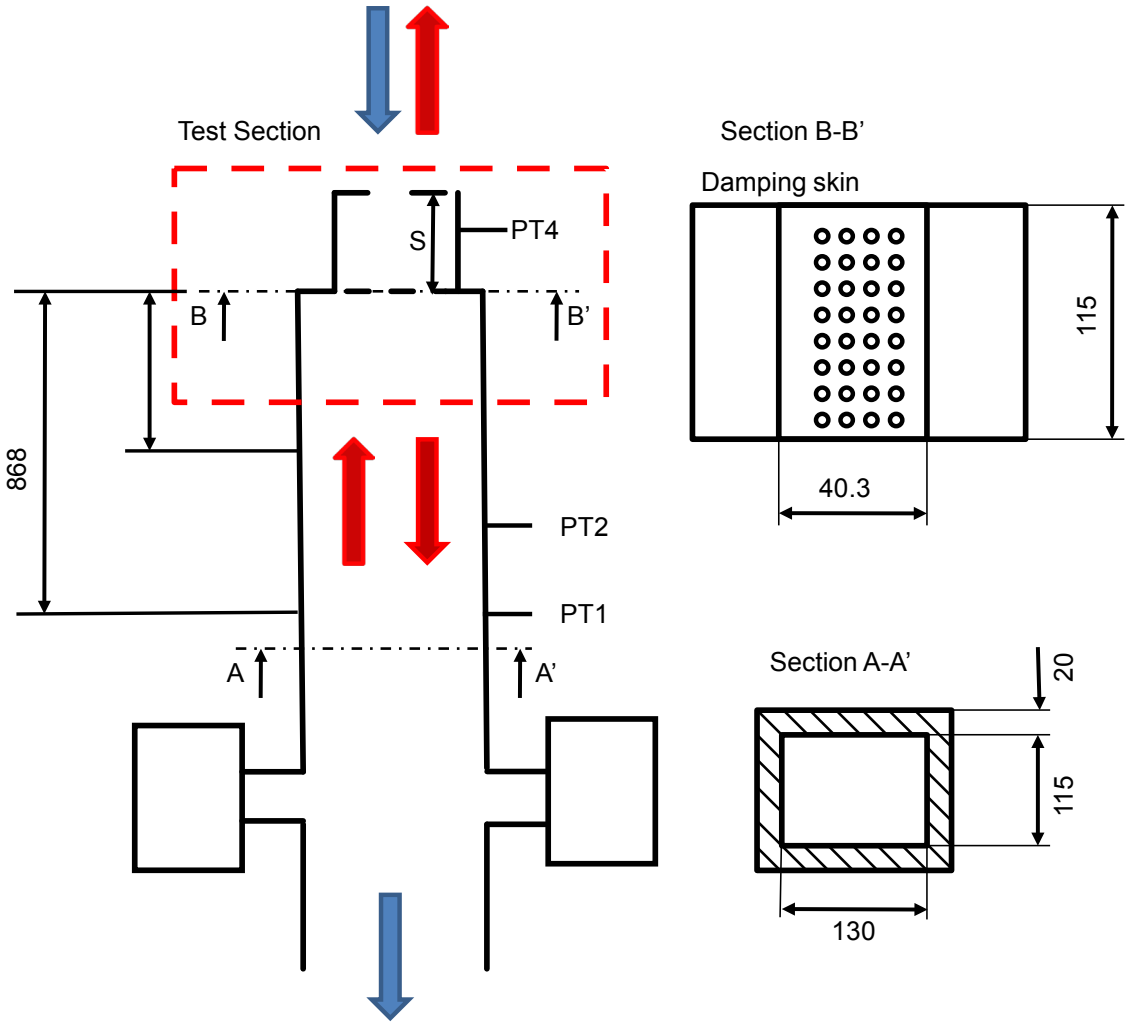

Figure 3.6: Schematic of resonating linear damper test facility, dimensions not to scale

The excitation amplitude was of order 135 dB and was therefore mainly in the linear acoustic absorption regime. The excitation frequencies were 300 to 450 Hz based on the described Strouhal number and pressure amplitude scaling (section 3.1).

Kulite dynamic pressure transducers were mounted on the test rig as shown in Figure 3.6. Hence the acoustic energy fluxes of the plane waves could be measured using a multi-microphone method for transducer positions shown. Furthermore a Kulite

transducer was located within the damper cavity. This transducer was used to assess the unsteady pressure drop across the damping skin and investigate the resonance frequency of the volume.

3.3.2 Experiments on Acoustic Dampers Exposed to Fuel Injector Flow Field

This experimental facility was developed to assess passive damping systems exposed to complex fuel injector flow fields. Therefore a test section representative of a single sector of a full annular gas turbine combustion system including the fuel injector flow field was developed. The main objectives of this test section were:

- to investigate the space envelope needed for an efficient passive damper,
- to investigate the effects of a complex fuel injector flow field, relevant to gas turbine combustion systems, impinging on the damper surface,
- to further validate the used acoustic absorption modelling techniques.

The experimental configuration mounted onto the ambient isothermal aero acoustic facility is shown in Figure 3.7 and is broadly representative of a single sector of a (simplified) fully annular lean burn combustion system. The following description of the test rig can also be found in Rupp et. al. (2012). A square cross-section of 120 mm by 120 mm duct is used with a gas turbine combustion system representative fuel injector mounted on to the upstream end of a square acrylic duct. The damper section consists of a width W_D and length L_D. An aperture of size $W_D \cdot L_D$ on one wall of the duct, immediately downstream of the fuel injector, enables various passive damper assemblies to be inserted. This simulates the presence of a passive damper in the outer (or inner) wall of a flame tube. The parameter S represents the separation between the damping and the metering skin.

Atmospheric air is drawn through the fuel injector and damper assembly (as indicated by the blue arrows in Figure 3.7), whilst holes and slots within the injector mounting plate also simulate the presence of a starter film passing over the damper surface. The presence of the fuel injector and starter films etc are thought to generate a reasonable isothermal representation of the complex flow field to which the passive damper would

be exposed within an engine environment. Having passed through the test section this flow then continues down the duct before issuing into a plenum. Typical operating conditions correspond to a 3% pressure drop *(dp/p)* across the fuel injector and damper.

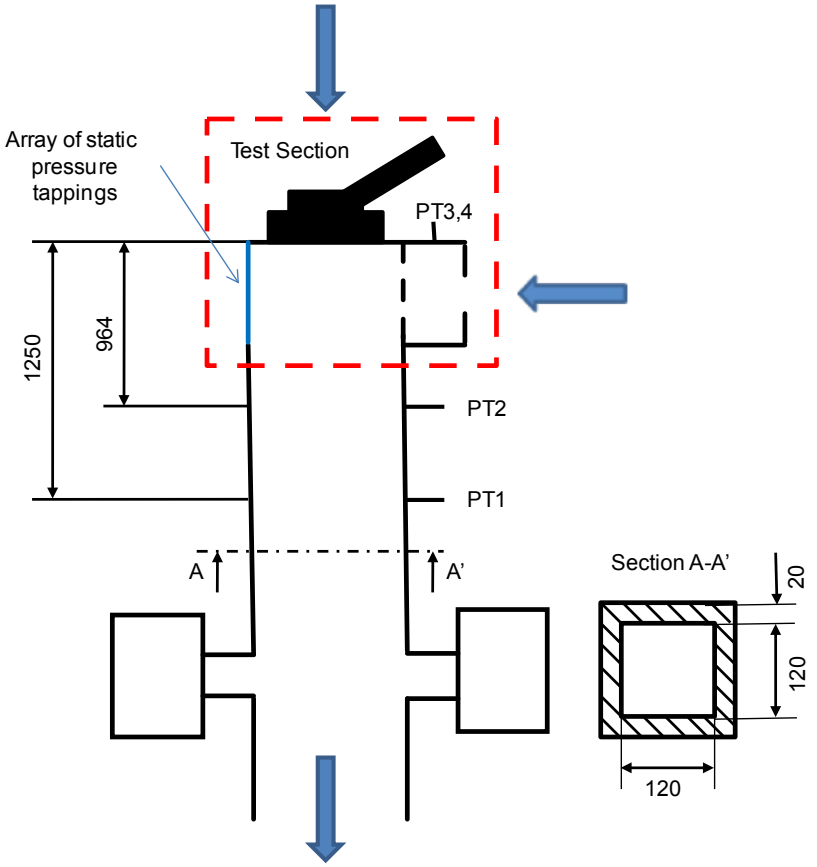

Figure 3.7: Schematic of non-resonating linear damper test facility, dimensions in mm, not to scale

The damper as shown in Figure 3.8 consists of two skins or liners and its design highlights some of the conflicting requirements associated with operating a porous liner in a gas turbine combustion environment. The relatively high pressure drop across the flame tube liner indicates potentially high velocities through any orifices (and hence low Strouhal numbers). To increase the Strouhal number to a point where, as indicated by Howe (1979b), some acoustic absorption will take place would require orifices of relatively large diameter. However, this would result in an unacceptably high flow rate for the combustion system. Consequently the passive damper consists of two skins in which the outermost liner is the metering skin. As its name suggests this meters or controls the flow through the damper and hence most of the mean pressure drop occurs across this skin. In this case the metering skin pressure drop is set to ~2.7% *dp/p*. Hence

the remaining pressure drop across the damping skin is set to ~0.3% *dp/p*. A large number of small diameter holes can be used to obtain appreciable acoustic absorption. However, it should be acknowledged there is a compromise between the amount of bias flow available, the need to keep the liner cool and the amount of acoustic absorption that can be achieved. The porosities and definition of the damping and metering skin are defined in appendix A.3.

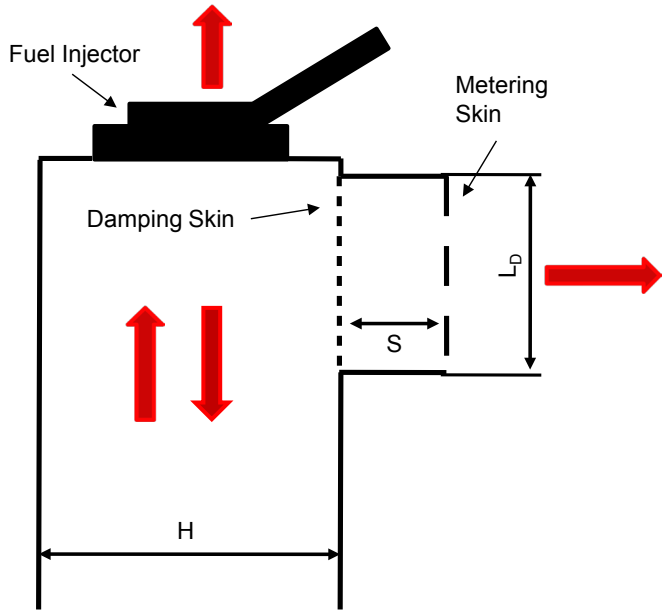

Figure 3.8: Schematic of non-resonating damper test section, not to scale

The acoustic test conditions were chosen to be representative of those conditions likely to be of interest at engine conditions (when appropriately scaled). In this case the diameters of the aperture remains of the same size as for the engine. Hence acoustic frequencies were in the range of 250 Hz to 350 Hz using engine Strouhal number scaling (equation (3.1)). Therefore the acoustic forcing frequencies are well below the cut-on frequency associated with any higher order duct modes (~1400 Hz). The excitation amplitudes were set to 135 dB. This was based on the amplitude scaling applied for the experiments relative to gas turbine combustors (section 3.1).

The complex flow field along the damping skin generated by the fuel injector and the starter film was assessed using an array of static pressure tappings on the opposite side of the damping skin as indicated in Figure 3.7. In this case an array of 3 by 4 static pressure tappings was used along the width and the length of the damper connected to a set of Furnace FCO 330 pressure transducers.

Not only is the flow field more complex for this test section but the acoustic system is also more complex. Two Kulite dynamic pressure transducers were used to measure the acoustic waves within the flow duct using the two-microphone method. The positions of the pressure transducers have been optimised for the frequency range of interest (PT1 and PT2 in Figure 3.7). Moreover two more Kulite transducers have been used to assess the pressure amplitudes in the cavity between the metering and damping skins (PT3 and PT4 in Figure 3.7). However, due to space constraints this was only possible for those tests with larger spacing between the liners ($S/H \geq 0.3$). As Figure 3.8 indicates the incident plane acoustic wave (red arrows represent plane acoustic waves) onto the test section is partly reflected back, part of the wave is transmitted through the fuel injector, part of the wave is transmitted through the damper and finally some of the acoustic energy will be absorbed. Only a qualitative assessment can be conducted, which is based on the change in reflection coefficient due to the change in liner separation S_D. However in later chapters of this work a methodology is developed which allows the discrimination of the acoustic loss from the transmission of acoustic energy through the injector.

4 Instrumentation and Data Reduction

In this chapter the experimental methods and data reduction techniques will be discussed along with an assessment of the experimental accuracies. Initially the acoustic instrumentation and associated analysis methods will be introduced, followed by the particle image velocimetry methods used to capture the unsteady flow field.

4.1 Acoustic Measurements

The acoustic measurements have been conducted using four miniature high sensitivity Kulite XCS-093 dynamic pressure transducers. Within this work the sensors will be referred to as Kulite transducers. A National Instruments LabView data acquisition system was used as described in Barker et. al. (2005). The acquisition system is outlined in Figure 4.1. The supply voltage of 10Vdc is supplied by a SCXI- 1520 strain gauge module. Furthermore the Kulite signal output was conditioned by a SCXI-1143 module. The temperature within the test rig was measured using a K-Type thermocouple connected to the SCXI-1112 module which was also within the SCXI-1000 chassis. Finally the data was acquired using a PC equipped with a National Instruments LabView PCI-6052E data acquisition card with a 16 bit range for the discretisation of the analogue signal.

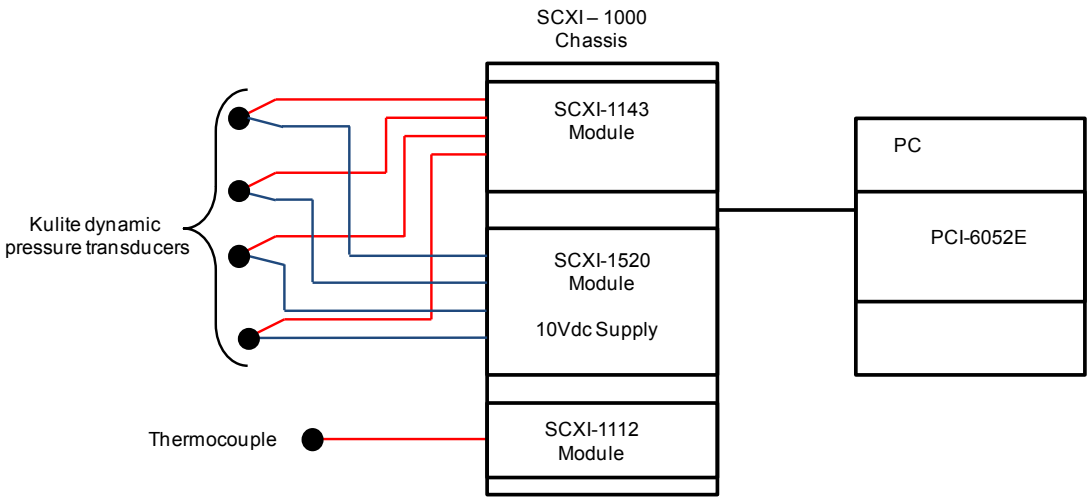

Figure 4.1: Dynamic data acquisition setup, from Barker et. al. (2005)

The sampling frequency of the data acquisition system was set up to 40 kHz. Moreover the pressure signal was sampled using eight blocks of 2^{15} samples, resulting in a time window of 0.8192 s per data block. Each of the time histories has been Fourier transformed using the Fast Fourier Transformation method with a Hamming window.

Thereafter an ensemble average over the eight time histories has been conducted on the Fourier transformed amplitudes:

$$\hat{p}_i(f) = \frac{1}{N}\sum_{n=1}^{N}\hat{p}_{i,n} \,. \tag{4.1}$$

In this case the subscript *i* represents the Kulite transducer number (i.e. *i= 1, 2, 3, 4*) and *n* is the time history number (i.e. *n = 1,2,...,8*). Moreover the parameter *N* represents the total amount of time histories *N = 8*.

The auto power spectra of each transducer signal can then be calculated using the averaged Fourier transformed pressure amplitudes (Lynn (1989))

$$\hat{S}_{ii}(f) = \hat{p}_i(f)\hat{p}_i^*(f) \,. \tag{4.2}$$

Furthermore, one of the signals (Kulite 1) is chosen as a reference to which the other signals can be compared. For example the cross-power spectrum relative to the reference signal (Kulite 1)

$$\hat{S}_{1i}(f) = \hat{p}_1(f)\hat{p}_i^*(f), \tag{4.3}$$

can be calculated, using subscript *i* to denote the transducer number. Finally the frequency response functions have been calculated using the auto- and cross-power spectra (Lynn (1989)):

$$\hat{H}_{1i}(f) = \frac{\hat{S}_{1i}(f)}{\hat{S}_{11}(f)}, i = 2,3,4 \,. \tag{4.4}$$

Hence the measured complex amplitude of each transducer relative to the reference transducer could be calculated:

$$\hat{p}_1(f) = \sqrt{2\hat{S}_{11}(f)} \text{ and} \tag{4.5}$$

$$\hat{p}_i(f) = \sqrt{2\hat{S}_{11}(f)}\hat{H}_{1i}(f) \ . \tag{4.6}$$

This relates each amplitude measurement in magnitude and phase relative to the reference transducer which is needed for the two-microphone and multi-microphone method introduced in sections 4.1.3 and 4.1.4.

4.1.1 Dynamic Pressure Transducer Calibration

For the static calibration of the Kulite dynamic pressure sensors a cylindrical vessel was used. All four transducers have been connected to the vessel. Moreover two calibrated reference pressure transducers (Furnace Controls differential pressure transducer Model 332 with an accuracy of 0.5% and a Furnace FC0510 Micro-Manometer with an accuracy of 0.1%) were also connected to the same vessel. The static pressure inside the vessel was set using a pump connected to the volume which pressurised and evacuated the volume over the range -5000 Pa to +5000 Pa. In this way the static pressure and the output voltage from the Kulite transducers was measured. Figure 4.2 shows an example of a static calibration curve representative for all four dynamic pressure transducers. It can be seen that over the range tested the transducer follows a linear curve with the same slope for negative as well as positive static pressure. The slopes of the curves are then used to convert the voltage to pressure signals within the data acquisition system. This static calibration has been conducted at regular intervals and the sensitivities always remained within 1%.

The dynamic pressure transducers have also been calibrated in terms of their fluctuating magnitude and phase relationship relative to each other. This is particularly important for the analysis using the two-microphone and the multi-microphone method. Therefore the dynamic calibration of the Kulite transducers has been conducted using the acoustic test rig shown in Figure 4.3, which is basically an open ended duct with loudspeakers attached. Four Kulite transducers have been mounted at the same axial position within the duct of cross-section 120 by 120 mm. On each side of the duct a dynamic pressure transducer is centrally mounted as shown on view B-B' in Figure 4.3. Both sides of the test rig were open to atmosphere. Two loudspeakers, as described in the previous sections, have been used to generate plane acoustic waves (red arrows in Figure 4.3). The plane acoustic waves only change their amplitude in the axial direction.

Hence all four dynamic pressure transducers should measure the same pressure amplitude with the same phase as they are mounted at the same axial plane.

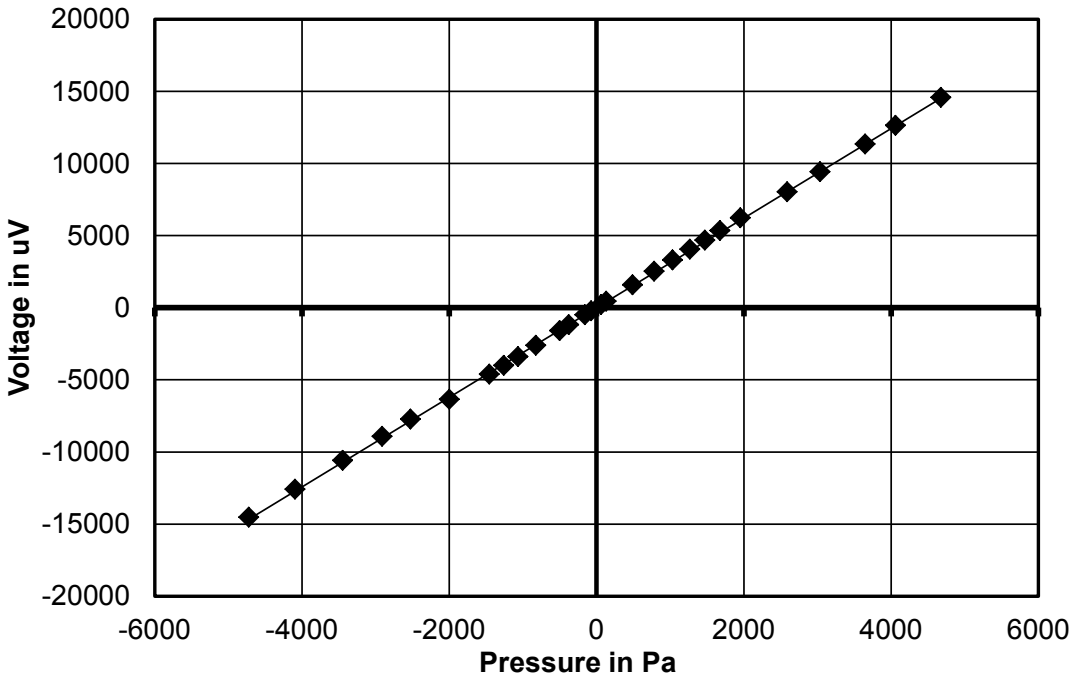

Figure 4.2: Example of static calibration curve

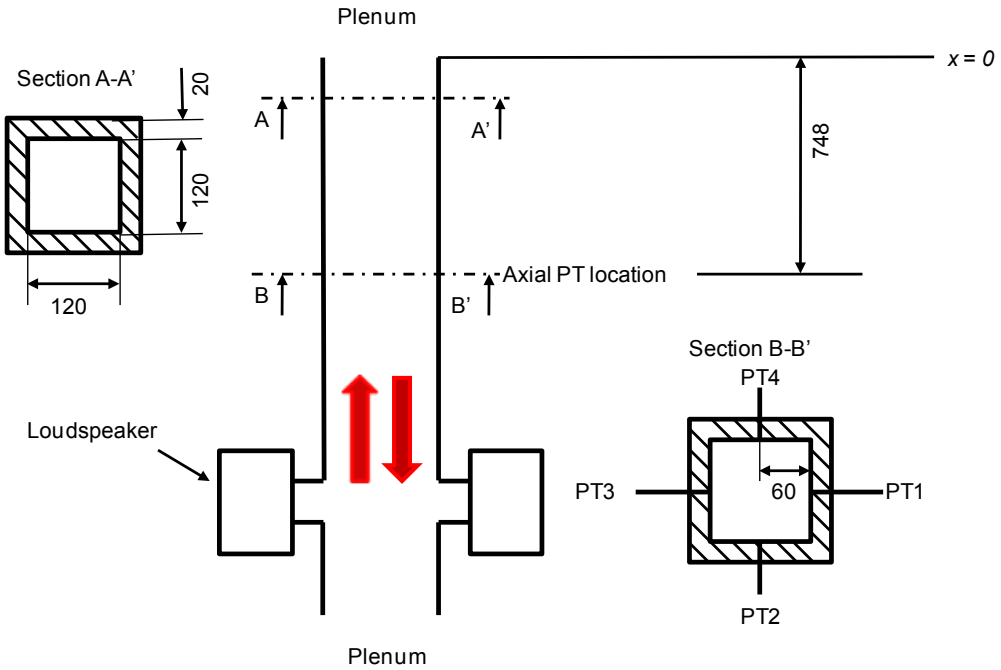

Figure 4.3: Test rig for dynamic Kulite calibration

The dynamic calibration has been conducted over a relevant frequency range (from 62 to 1000 Hz). The pressure signals have been acquired and the relative complex amplitudes of the transducers have been calculated as described in section (4.1).

The relative variation in magnitude between the four transducers was investigated using the average magnitude

$$|\overline{p}| = \frac{\sum_{i=1}^{4} |\hat{p}_i|}{4} \tag{4.7}$$

of the four transducers and the standard deviation of each transducer(Montgomery and Runger (1994)):

$$\sigma_{\hat{p}} = \sqrt{\frac{\sum_{i=1}^{4} \left(|\hat{p}_i| - |\overline{p}|\right)^2}{4-1}} \,. \tag{4.8}$$

Thus deviation of the magnitude of each transducer relative to the average signal could be calculated:

$$\varepsilon_{\hat{p}i} = \frac{\sigma_{\hat{p}}}{|\overline{p}|} \,. \tag{4.9}$$

This deviation is shown in Figure 4.4. It can be seen that the variation in magnitude, relative to the average, is below 1% for frequencies which are not in the vicinity of a pressure node, i.e. pressure amplitude is equal to zero. In the vicinity of a pressure node this error is larger due to the significant reduction in signal to noise ratio. However, this is due to the mode shapes of the calibration rig and can be neglected as the transducers are not normally placed in the vicinity of such pressure nodes.

The phase difference relative to Kulite 1 is shown in Figure 4.5. It can be seen that there is a negligible phase difference between Kulite 1 and Kulite 2. However, there is a linear increase in phase difference with excitation frequency for Kulites 3 and 4 relative to Kulite 1. This is related to a constant time delay associated with the multiplexer data acquisition card. The card does not sample all four channels simultaneously and a constant time delay is applied between the sampling of the channels. This leads to an increase in sampling time relative to the channel number, i.e. channel 2 will have the smallest phase difference and channel 4 has the largest. This phase change is constant and therefore a phase correction within the data reduction routine can be applied using a constant time delay based on the slope of the phase with respect to the frequency.

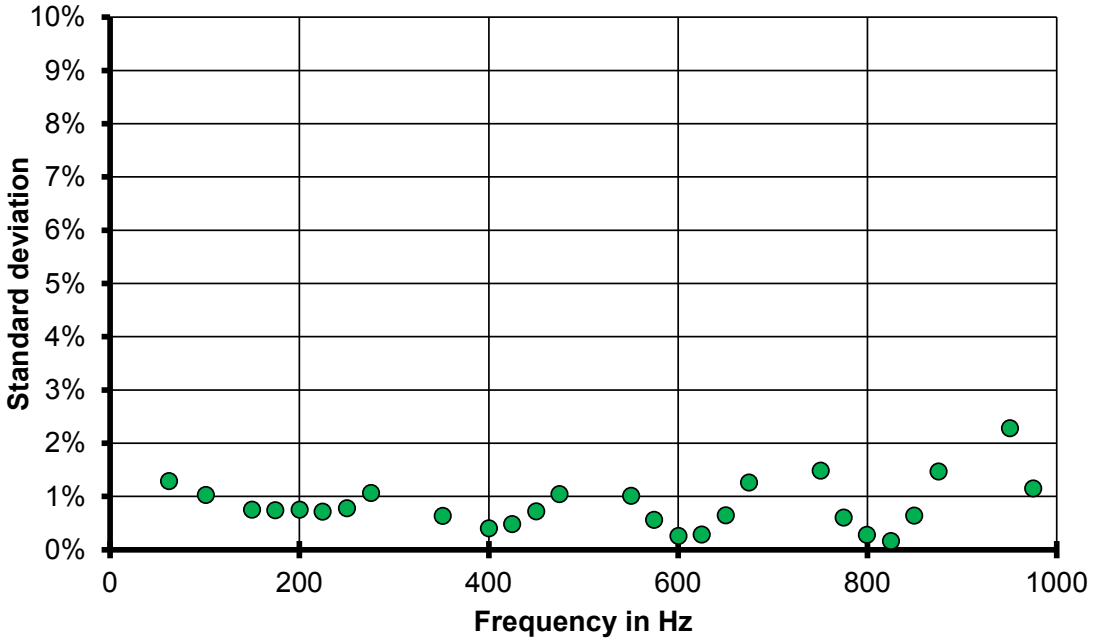

Figure 4.4: Deviation of measured amplitude from mean amplitude for all four Kulites

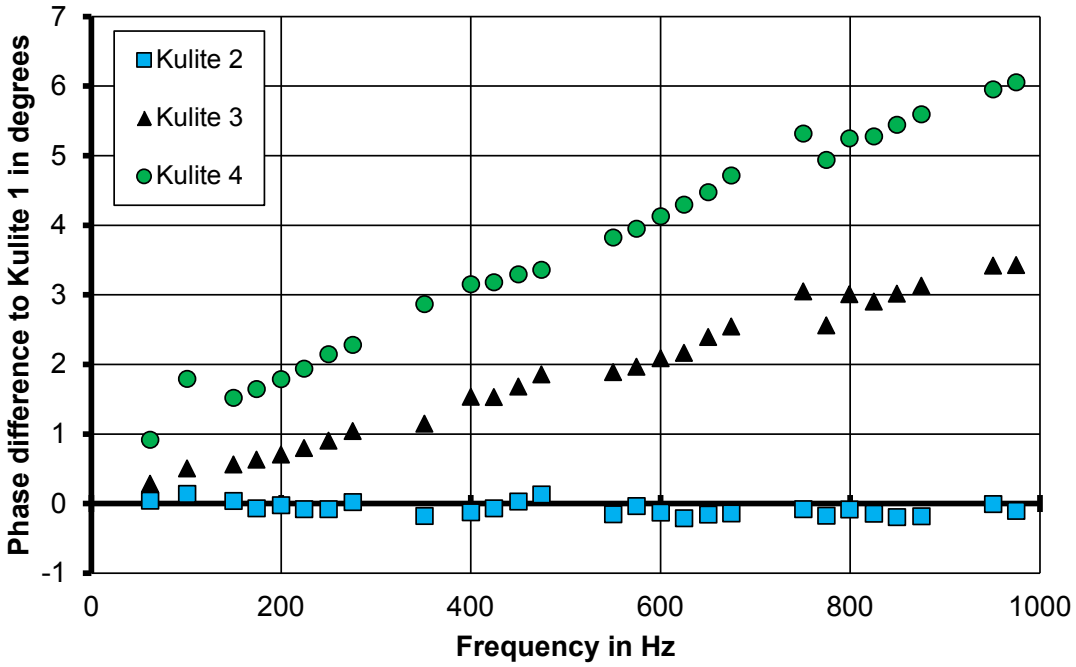

Figure 4.5: Phase difference relative to Kulite 1

Figure 4.6 shows the corrected phase using the gradient of the phase difference shown in Figure 4.5. Note outliers which do not follow the linear curve are also caused by the vicinity of a pressure node for the measurement and can therefore be neglected. The phase correction leads to phase differences between the Kulite channels of -0.3° to 0.3° which are acceptable for the measurements.

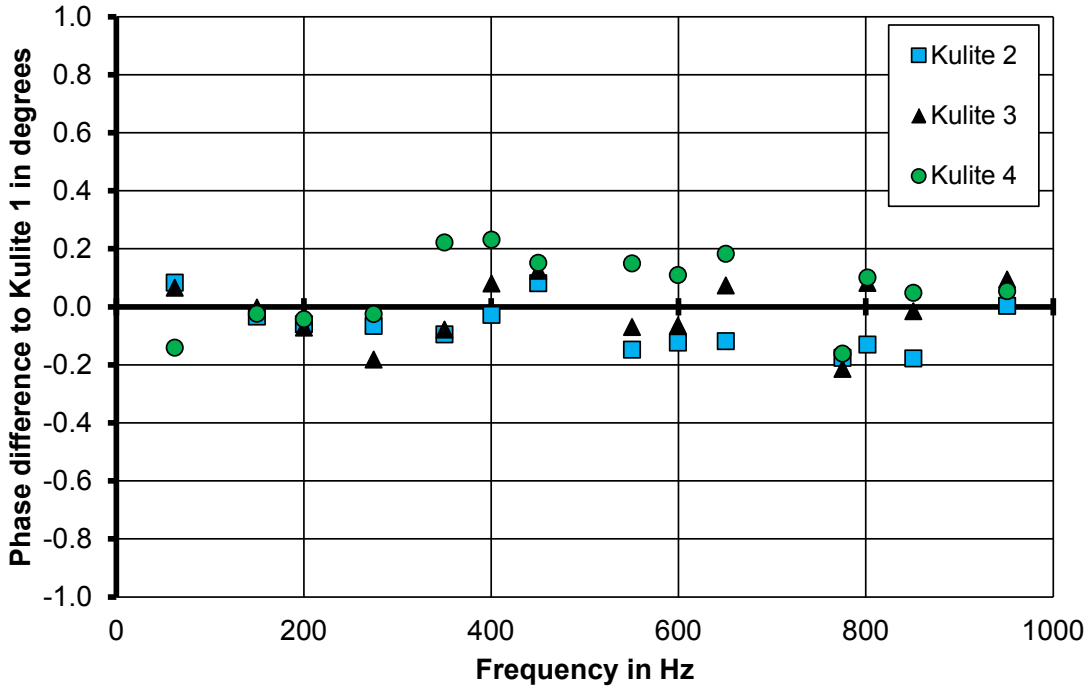

Figure 4.6: Phase correction after calibration relative to Kulite 1

4.1.2 Two Microphone Method

Figure 4.7 shows a schematic which is used to describe the two microphone method in this section. A plane wave is generated by a loudspeaker and travels towards a test specimen. This is referenced to as the incident wave which has a pressure amplitude $\hat{p}_i$. At the test specimen, which could also be an acoustic boundary condition such as a closed or open end, a portion of the incident wave energy is reflected ($\hat{p}_r$). Hence the acoustic pressure $\hat{p}(x)$ at any point within the duct is a superposition of the incident and reflected pressure wave:

$$\hat{p}(x)\exp(i\omega t) = \hat{p}_i \exp(i\omega t - ik_+ x) + \hat{p}_r \exp(i\omega t + ik_- x). \tag{4.10}$$

As discussed in the previous chapter this is also the solution of the wave equation for plane, one dimensional acoustic waves. Seybert and Ross (1977) proposed a decomposition of the upstream and downstream travelling wave components if two microphones at two positions x along the duct are used:

$$\hat{p}_1(x_1) = \hat{p}_i \exp(-ik_+ x_1) + \hat{p}_r \exp(ik_- x_1), \tag{4.11}$$

$$\hat{p}_2(x_2) = \hat{p}_i \, exp(-ik_+ x_2) + \hat{p}_r \, exp(ik_- x_2). \tag{4.12}$$

Thus the linear equation system can be solved for the two unknown wave amplitudes $\hat{p}_i$ and $\hat{p}_r$. This is known as the two-microphone method as investigated by various authors, e.g. Johnston and Schmidt (1978), Seybert and Soenarko (1981), Boden and Abom (1986), Abom and Boden (1988).

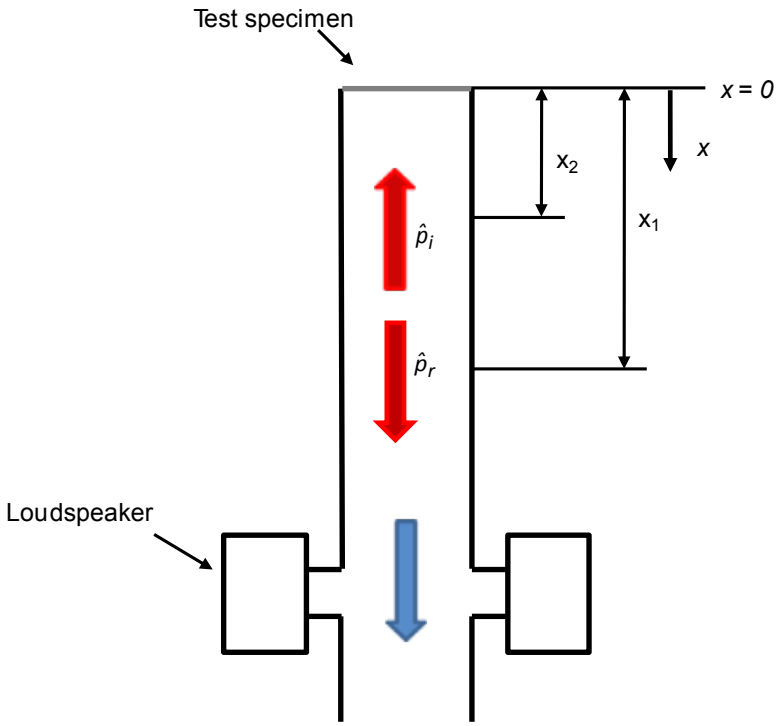

Figure 4.7: Schematic of plane waves for two microphone method, similar to Seybert and Ross (1977)

However in this work, the mean flow velocity travels against the incident pressure wave which differs from the scenario described by Seybert and Ross (1977). Hence the definition for the two-microphone method was modified accordingly and the location of the origin of the axial coordinate, as well as its direction relative to the mean flow, has been defined accordingly. Therefore the two-microphone method was defined as:

$$\hat{p}_1(x_1) = \hat{p}_i \, exp(ik_- x_1) + \hat{p}_r \, exp(-ik_+ x_1), \tag{4.13}$$

$$\hat{p}_2(x_2) = \hat{p}_i \, exp(ik_- x_2) + \hat{p}_r \, exp(-ik_+ x_2). \tag{4.14}$$

The complex amplitudes are calculated from the time histories as defined in section 4.1. Hence the complex amplitudes of the relevant Kulite transducer, calculated from

equation (4.5) and (4.6), will be used for the measured amplitudes $\hat{p}_1(x_1)$ and $\hat{p}_2(x_2)$. Thereafter the incident and reflected wave amplitude can be calculated:

$$\hat{p}_i = \frac{\hat{p}_1(x_1)\exp(-ik_+x_1) - \hat{p}_2(x_2)\exp(-ik_+x_2)}{\exp\left(i2\frac{\omega}{c}\frac{x_1}{1-M^2}\right) - \exp\left(i2\frac{\omega}{c}\frac{x_2}{1-M^2}\right)}, \tag{4.15}$$

$$\hat{p}_r = \frac{\hat{p}_1(x_1)\exp(-ik_-x_1) - \hat{p}_2(x_2)\exp(-ik_-x_2)}{\exp\left(i2\frac{\omega}{c}\frac{x_1}{1-M^2}\right) - \exp\left(i2\frac{\omega}{c}\frac{x_2}{1-M^2}\right)}. \tag{4.16}$$

In general the accuracy of the two micro-phone method is strongly dependent on the position of the pressure transducers. Seybert and Soenarko (1981) report large errors if the microphone is positioned at a pressure node due to the poor signal to noise ratio. Moreover large errors occur if the microphone spacing is exactly half a wave length. In this case the two equations used for the two microphone method are not linearly independent (Abom and Boden (1988)). Hence spacing of half a wave length was avoided. Error estimations on the two microphone method are discussed in section 4.1.4.

4.1.3 Multi-Microphone Method

The measurement of the Rayleigh Conductivity described in section 3.1.2 was carried out over a wide frequency range. Therefore using the two microphone method at fixed measurement locations would have caused unacceptable errors in the impedance measurement and therefore in the calculation of the Rayleigh Conductivity. This is due to the positioning of the dynamic pressure transducers relative to a pressure node within the duct at certain frequencies. Hence a multi-microphone method was used (e.g. Poinsot et. al. (1986), Paschereit et. al. (2002), Schuermans (2003)).

In this case four dynamic pressure transducers have been used. Therefore the over determined linear equation system $Ax = b$ can be formed:

$$\underbrace{\begin{bmatrix} exp(-ik_+x_1) & exp(ik_-x_1) \\ \vdots & \vdots \\ exp(-ik_+x_4) & exp(ik_-x_4) \end{bmatrix}}_{A} \underbrace{\begin{bmatrix} \hat{p}_i \\ \hat{p}_r \end{bmatrix}}_{x} = \underbrace{\begin{bmatrix} \hat{p}_1(x_1) \\ \vdots \\ \hat{p}_4(x_4) \end{bmatrix}}_{b}. \tag{4.17}$$

A least square fit can be used to solve the over determined system whilst minimising the square of the residual:

$$\|r\|^2 = \|b - Ax\|^2. \tag{4.18}$$

The tolerance on the residual was set to 10^{-6}, which is the default tolerance in the used MATLAB routine. In this case the calculation of the wave amplitudes is less prone to errors as its estimation is dependent on multiple transducer measurement positions.

4.1.4 Error Analysis of Acoustic Measurements

In this section error estimates for the acoustic measurements will be discussed. An analogue input signal to the loudspeakers was generated by a Black Star Jupiter 2010 function generator which was accurate to within 0.1 Hz. The measured excitation frequency, using the described LabView data acquisition system, did indicate the forcing amplitudes within 0.1 Hz during the monitoring of the pressure amplitudes (i.e. in agreement with the function generator). Hence the acoustic forcing frequency was accurate to potentially 0.1 Hz.

However the signal has been acquired and stored with a 40 kHz sampling frequency in eight blocks of 2^{15} samples, as described previously. The acquired data has been Fourier transformed and the absorption coefficient and acoustic losses have been calculated using a MATLAB routine. Due to the discretisation of the signal the FFT frequency resolution, or the frequency bin width, was 1.22 Hz. Hence the error on the frequency was within 0.4 Hz, which is a systematic error in the analysis. The error on the amplitude of the measured signal is dependent on the position of the acoustic frequency relative to the centre of the FFT frequency bin width. Therefore a synthetic signal, similar to the measured pressure signal was used to assess the error due to the FFT analysis. Figure 4.8 shows the four time traces of the generated artificial signals. The amplitudes and phase shifts where chosen to be representative of the measured

pressure signals for the four transducers. Moreover the random noise influence was in the same order of magnitude. It can be seen from Figure 4.9 that the synthetic signals represent the random noise as well as other periodic features within the measured pressure spectra with reasonable similarity.

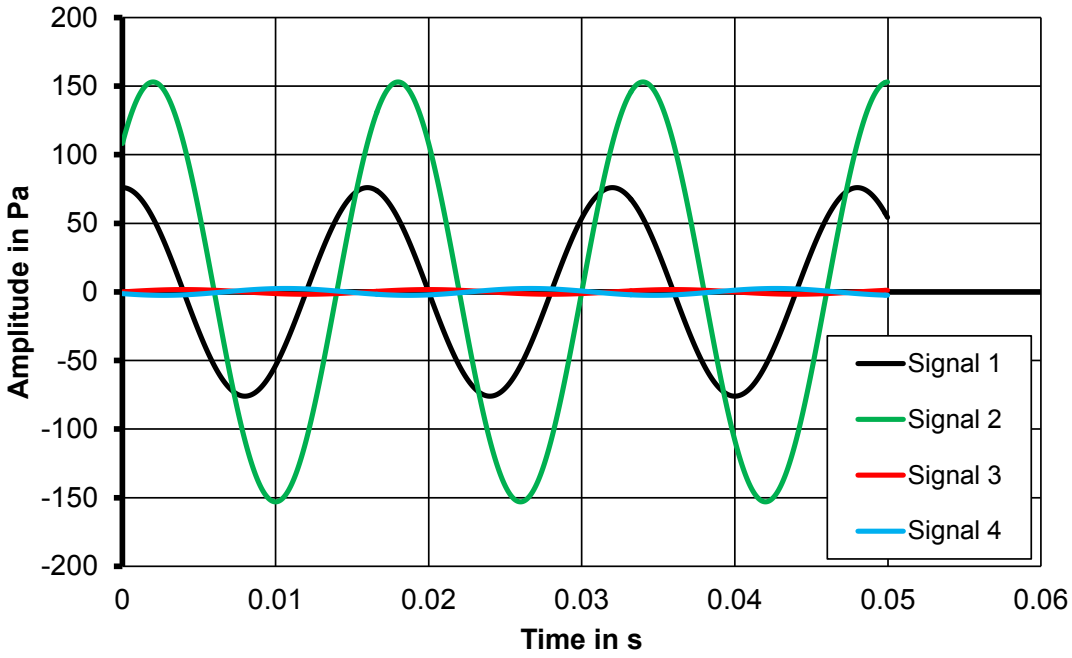

Figure 4.8: Artificial data set to assess discretisation and FFT accuracy

In this case the investigated error on the FFT output was conducted for a 62.5 Hz forcing frequency. All the measured absorption coefficients where within 0.1 Hz of 62.5 Hz and 125 Hz so the actual forcing frequencies for the synthetic test signals are representative of the measured frequencies within the acoustic experiments. The pressure amplitude of the input signal was known, hence the magnitude and phase of the Fourier transformed signals could be assessed. The error on the magnitude was calculated as

$$\varepsilon_{\hat{p},i} = \frac{\left|\hat{p}_{i,FFT} - \hat{p}_{i,S}\right|}{\hat{p}_{i,S}}, \tag{4.19}$$

where $i = 1, 2, 3, 4$ denotes the synthetic signal of each simulated transducer and the subscript s denotes the synthetic signal input, whereas the subscript FFT represents the output of the Fourier transformation. The same can be conducted for the phase difference between the input to the method and the output out of the routine:

$$\varepsilon_{\varphi,i} = \left|\varphi_{i,FFT} - \varphi_{i,S}\right| . \tag{4.20}$$

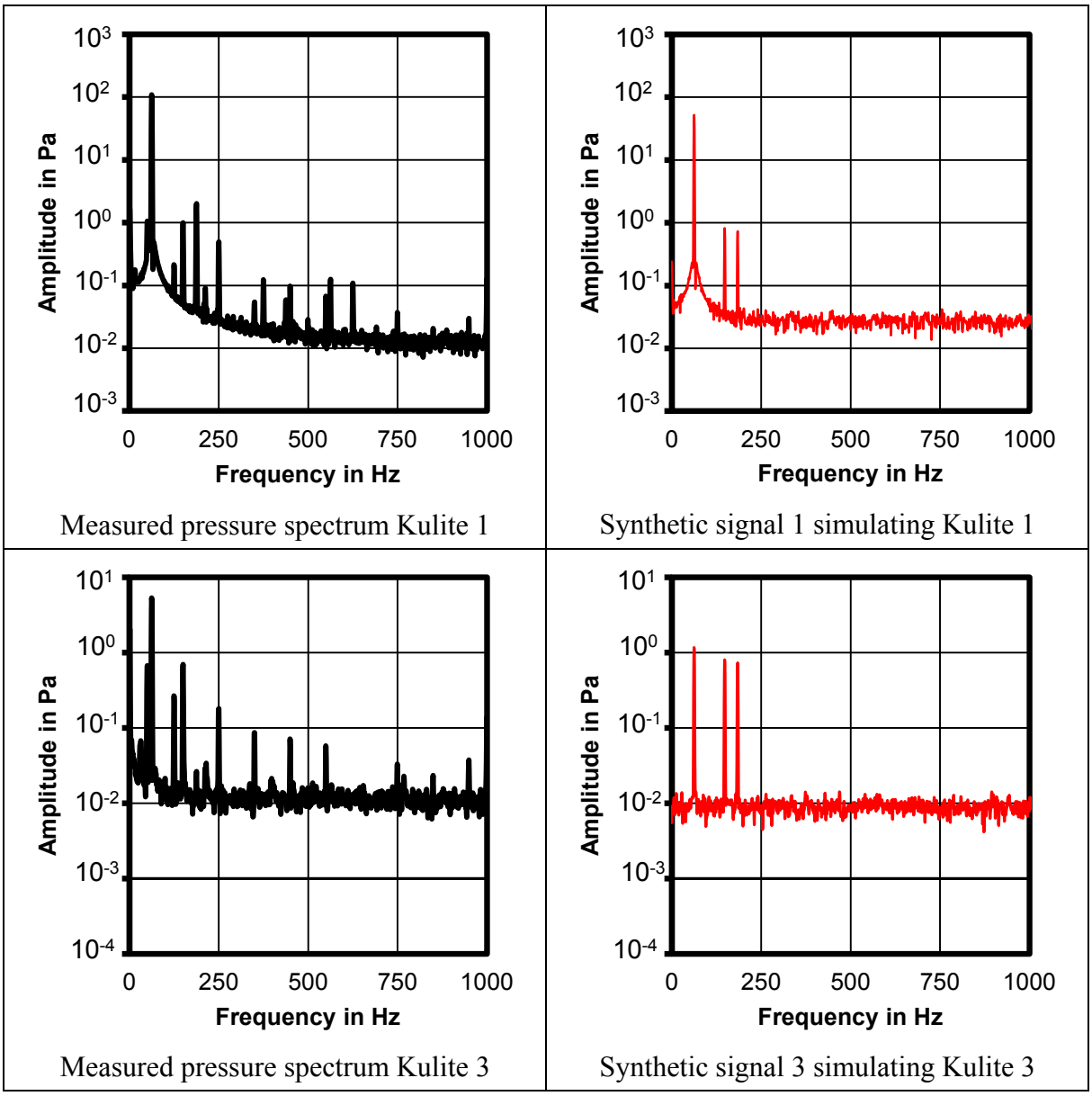

Figure 4.9: Comparison of synthetic signal and measured pressure signals

Thus for the 62.5 Hz excitation frequency the error on the magnitude was 3% and the maximum error on the phase was 0.02°. As already mentioned the deviation on the magnitude is a bias error which leads to magnitudes which are always 3% smaller than the input signal. However the error on the phase of the signal was a random error due to the artificial noise on the test signal. Thus the complex wave amplitudes, $\hat{p}_i$ and $\hat{p}_r$, are affected by the same error in magnitude and a negligible random error in phase. However the absorption coefficient and the conductivity are less affected by the bias

error as these quantities are ratios of wave amplitudes relative to each other (and therefore the bias error reduces). Hence the bias error estimate on the absorption coefficient reduces to 0.5% whilst the bias error on the conductivity measurement is estimated to 0.9%. However another important quantity to validate the PIV methodology is the loss of acoustic energy. This quantity is not normalised and therefore the bias error will have an effect. In this case the systematic error on the acoustic energy loss is estimated to 7%.

Some of the acoustic absorption test cases are conducted at an acoustic excitation frequency of 125Hz. In this case the FFT resolution has been adjusted to 2.44Hz frequency bin size to reduce the initial bias error on the FFT amplitude to the same level as described for the 62.5Hz test cases. For all other measurements within this work the bias error is less important as the calculated quantities are normalised and thus this systematic error cancels out.

In addition to the bias error on the calculated quantities being estimated, the random error on the measured pressure amplitudes was also approximated. The variation of the calculated pressure amplitudes was investigated using the standard deviation between the single events and the calculated mean pressure amplitude of each of the 8 blocks of dynamic data from a representative test point at 62.5 Hz forcing and a mean pressure drop across the orifice of 0.5% *dp/p*:

$$\sigma_{\hat{p}i} = \sqrt{\frac{\sum_{n=1}^{8}\left(\hat{p}_{i,n} - \breve{p}_i\right)^2}{8-1}}\ , \tag{4.21}$$

where the average magnitude of the pressure amplitude is calculated as:

$$\breve{p}_i = \frac{\sum_{n=1}^{8}\hat{p}_{i,n}}{8}. \tag{4.22}$$

Therefore the random error on the pressure amplitude was calculated to

$$\varepsilon_{\hat{p}i,random} = \frac{\sigma}{\breve{p}_i} = 0.3\% . \tag{4.23}$$

With the same procedure the random phase error of each transducer can be estimated as no larger than $\pm 0.16°$. Hence the total random error in the transducer magnitude is of order $\pm 1.3\%$ and the total error in phase is of order $\pm 0.46°$ including the random variation as shown in the dynamic calibration (section 4.1.1).

It is also necessary to investigate the error analysis of the two microphone method. In this case the transducer position has the biggest influence on the size of the error. As can be seen in Seybert and Soenarko (1981) or Boden and Abom (1985) the largest bias errors are present if the pressure transducers are located at the pressure node or anti-node. For the acoustic absorption measurements the error due to the upstream pressure transducers can be neglected in this setup. The acoustic energy transmitted into the upstream duct is two orders of magnitude smaller than the acoustic absorption coefficient. Hence the error influence onto the upstream transducer pair can be neglected.

Therefore the total error estimates for the acoustic quantities within the two microphone method are shown in Table 4.1.

	Pressure amplitude	**Wave amplitude**	**Acoustic loss**	**Absorption coefficient**
Magnitude	3.3%	3.3%	7%	1%
Phase	0.46	0.46		

Table 4.1: Maximum error estimates for quantities calculated with the two microphone method

The absorption coefficient of a datum orifice plate has been repeated several times during the programme and the repeatability of the measurement was within 1%. As the bias errors cancels for these parameters it was assumed that the random error is the only influence on the measurement of the absorption coefficient. Thus the maximum error estimate for the absorption coefficient is $\pm 1\%$.

Placing microphones at locations of pressure nodes and anti-nodes has to be avoided for the two-microphone method due to the occurrence of large errors within the measurement. However for the measurement of the Rayleigh Conductivity in this work a wide frequency range was needed to investigate a wide range of Strouhal numbers. Therefore pressure anti-nodes and nodes cannot be avoided without a great deal of

effort in shifting the microphone positions around for given frequency ranges. A more convenient way to improve the measurement accuracy for this case is the use of a multi-microphone method as described earlier. Thus errors introduced by transducers at pressure nodes or anti-nodes are not as influential for the multi-microphone method. Therefore it can be assumed that the worst case scenario of this method is the accuracy of the two-microphone method. Hence the maximum errors for the investigated parameters are as described previously in Table 4.1.

4.2 High Speed PIV Method

The velocity field upstream and downstream of the orifice during acoustic excitation was measured using high speed particle image velocimetry (PIV). This section will give a brief overview of the method and describe the optimisation of the PIV setup. More detailed explanation and description of the capabilities of the PIV method can be found for example in Adrian (1991), Westerweel (1997), Raffel et. al. (2007), Adrian (2005), Hollis (2004), Robinson (2009), etc. A general arrangement of a PIV measurement system is shown in Figure 4.10. The setup consists of a laser, digital CCD (charged coupled device) camera and tracer particles which are seeded into the flow field. The laser fires two distinct pulses at a given time distance Δt which is known as the inter-frame time. A divergent lens is used to generate a light sheet from the small circular laser beam, which illuminates the flow area of interest. Thus the tracer particles within the light sheet are illuminated and the scattered light is recorded by the digital camera. Thereby two images, separated by Δt, are generated and the velocity field can be calculated by measuring the displacement of the particles in the two images and the inter-frame time Δt:

$$\vec{u}(\vec{x},t)=\frac{\Delta\vec{x}(\vec{x},t)}{\Delta t}. \tag{4.24}$$

In this case PIV is a planar measurement technique, hence the velocity is a vector in the Cartesian (x, y)-plane. The quality of the PIV data acquisition process is strongly influenced by the choice of: tracer particles, flow illumination, optical setup for the recording of the images as well as the time synchronisation of the PIV system (e.g. Hollis (2004)). The optimisation of the PIV system parameters has been conducted

based on the procedure outlined in Hollis (2004). The main parameters used for the PIV measurements are summarised in Table 4.2. Particle image velocimetry has been widely applied in the past to measure the unsteady velocity field of various engineering applications. Hence this is a rather well established technique. However, a brief overview of the main components of the PIV measurement technique is discussed in the following paragraphs.

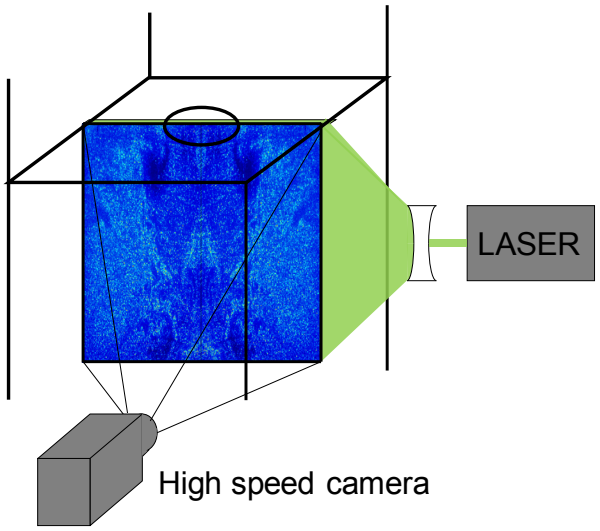

Figure 4.10: Schematic of a PIV setup to measure the flow field downstream of an orifice plate

For the illumination of the flow field a Quantronix Darwin-Duo 527-80-M laser has been used. The laser can generate two pulses of laser light with a repetition rate of 0.1 to 10 kHz. More detailed information about the laser can be found in LaVision (2011). The illuminated flow field was recorded by a LaVision High Speed Star 5 camera containing a CCD array with 1024x1024 pixels. More detailed information about CCD- arrays can be found in Hollis (2004) or Raffel et. al. (2007). A Sigma 105 mm focal length lens was used with a range of f-numbers of $2.8 \leq f^{\#} \leq 22$. The f-number is defined by the ratio of focal length to aperture diameter of the lens. The main objective of the optical setup is to optimise the particle image diameter while ensuring an adequate field of view (FOV), which is the area of interest within the flow field, for the PIV measurement. To optimise the optical setup several parameters must be considered: seeding particle diameter, magnification of the optical setup, the diffraction limited diameter, size of the CCD array, the wavelength of the laser light and the f-number of the lens. Guidance in how to optimise the rather complex system can be found in Hollis

(2004) or Raffel et. al. (2007). In this case the optimisation resulted in a field of view size of 30x30 mm.

Illumination	
Quantronix Darwin Duo 527-80-M	Laser rod consists of Yttrium Lithium Fluoride crystal incorporating Neodym ions (Nd:YLF), wavelength 527nm, 1kHz repetition rate
LaVision laser guiding arm	-10 mm focal length, light sheet thickness approx. 1mm
Camera and optical setup	
LaVision High Speed Star 5	1024x1024 pixel, 17 µm pixel size, 3072 double images, max sampling time 2.793s
Sigma 105 mm focal length lens	f-numbers of $2.8 \leq f^{\#} \leq 22$, field of view (FOV) 30x30 mm
Inter-frame time	6-25µs, depending on mean velocity
Vector field calculation and validation	
Software	LaVision DaVis 7.2
Processing	Initial cell size 64x64, 2 iterations Final cell size 32x32, 3 iterations 50% overlap leading to 64x64 vectors 2^{nd} order correlation
Validation	Remove vectors with Q-ratio < 1.5. Median vector filter >1.3 standard deviation. Replace vectors with 2^{nd}, 3^{rd} or 4^{th} choice vectors. Interpolate if no vector within 4^{th} choice is found. Amount of first choice vectors >95%

Table 4.2: Summary of used PIV system parameters

The sampling frequency of 1100 Hz was chosen to generate an adequate temporal resolution for the chosen acoustic excitation frequencies of 62.5 and 125 Hz. Thus 18 images per acoustic cycle could be recorded for 62.5 Hz excitation and 9 images per acoustic cycle could be captured for 125 Hz acoustic excitation. The inter-frame-time was chosen so that the particle displacement for the two captured frames was optimised

such that the mean particle displacement was within a quarter of the interrogation cell (Kean and Adrian (1990)). Hence the inter-frame time has been changed depending on the mean velocity through the orifice. More detailed discussions of the inter-frame time can be found in Hollis (2004) or Midgley (2005).

The next step is to calculate the velocity from the recorded images. This process is illustrated in Figure 4.11. Frame A and frame B are divided into various interrogation cells. In this case it is approximated that the particles within an interrogation cell move homogeneously. A spatial cross-correlation method is used between the particle pattern of interrogation cells in frame A and frame B with the help of a Fast Fourier Transformation (FFT) method. The outcome of this correlation is a correlation map where the average displacement of the particle pattern within the interrogation cell is indicated by the peak in the correlation map (Figure 4.11). This displacement vector can then be used to calculate the velocity within the interrogation cell using the inter-frame time Δt. A more detailed formulation of the cross-correlation technique can be found for example in Raffel et. al. (2007).

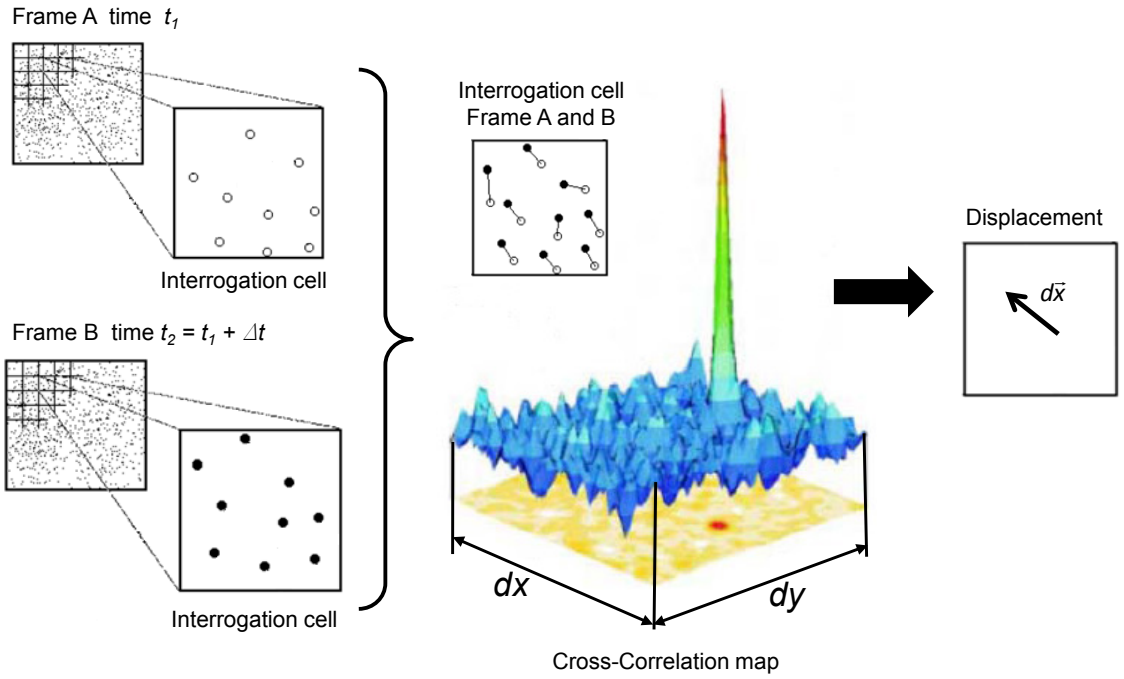

Figure 4.11: Cross-correlation to evaluate particle displacement, from LaVision (2007)

A further improvement in the quality of the vector data is to use adaptive multi pass grids (e.g. Hollis (2004)). In this case the initial cell size was chosen to be 64×64

pixels. During the first two iterations the vector field was calculated using this cell size. Thus a first approximation of the vector field was achieved. During the second iteration the interrogation cells will be shifted according to the previous vector calculation. This ensures a correlation with the same particles which improves the accuracy of the vector data and avoids the loss of particles across the cells. Moreover the information is then used to move the further reduced cells to 32×32 pixels for a further three iterations. Therefore the advantage of this method is that particles within the smaller cells are not lost into surrounding cells for the correlation between the image pairs. Thus the accuracy of the data can be improved (LaVision (2007)).

Finally the quality of the calculated vectors will be checked using various methods such as

- Q-ratios, which takes the ratio of the maximum peaks in the correlation map into account,
- median filters, which investigate the surrounding vectors and
- peak locking parameters, which assess the velocity field on its bias to integer values.

All of these methods have been discussed in detail for example in Westerweel (1994), Hollis (2004), LaVision (2007). Nevertheless a particularly relevant part for all PIV measurements is the adequate choice of seeding particles. This will be discussed in more detailed in the following section.

The described criteria have been used together with the optimisation steps described in Hollis (2004). This lead to 98% first choice vectors within the non-linear absorption measurements at close to zero mean pressure drops across the aperture. The first choice vector percentage was lower in the linear regime as the increased mean jet velocity results in an increased dynamic range in measured velocity between the jet velocity and the acoustic velocity in the surrounding duct. Nevertheless a minimum of 95% of first choice vectors were indicated in DaVis 7.2 for the investigated flow fields.

4.2.1 Tracer Particles

The seeding particles of the flow field have two main functions in the PIV setup: they have to follow the flow accurately and they must scatter enough light to be captured by the camera. Unfortunately these requirements can be in conflict with each other and require careful optimisation. Westerweel (1997) shows that the minimum error in the measurement of the particle displacement occurs for a particle image size of approximately 2 pixels. This optimum pixel diameter can be achieved by the choice of tracer particles together with the optimisation of the optical parameters, while ensuring the particles follow the flow field accurately. The latter is even more challenging for an acoustically forced flow field as the particle has to be able to follow the changes in direction of the flow due to the acoustic excitation. However in this case it should be noted that the acoustic wave does not require resolving, rather it is the pulsatile jet flow that is a result of the acoustic pressure oscillation that must be captured.

The temporal velocity variation of a sphere moving in a fluid at high acceleration but low velocity can be described by the Basset-Boussinesq-Oseen equation (e.g. Schoeneborn (1975), Siegel and Plueddemann (1991), etc). Tondast-Navaei (2005) uses a simplified expression of this equation for the application of seeding particles in an acoustically excited flow field. The assumptions in Tondast-Navaei (2005) were based on:

- the spherical particles do not deform and interact with each other,
- the particle diameter is much smaller than the sound wave length,
- the density of the particle is much greater than the density of the air
- the difference in acceleration between the particles relative to the air is small
- the Reynolds number is small so that Stokes law is valid.

Hence the reduced Bassett-Boussinesq-Oseen equation can be defined as:

$$\frac{4\pi r_p^3}{3}\rho_P \frac{d}{dt} v_P = 6\pi \mu r_p \left(u_F - u_P\right). \tag{4.25}$$

The subscript *F* denotes the working fluid properties, in this case air, and the subscript *P* denotes the particle properties. Tondast-Navaei (2005) rearranged the equation and introduced the relaxation time

$$\tau_P(r_P) = \frac{2}{9}\frac{\rho_P}{\rho_F}\frac{r_p^2}{\nu} \quad . \tag{4.26}$$

In this case the relaxation time is dependent on the density ratio between the air and the seeding particles and the size of the seeding particle. Therefore the larger the particle the larger the relaxation which is a measure of the response of the particle to changes in velocity, i.e. accelerations and decelerations of the flow field. This introduces a phase shift between the particle and the air flow.

$$\varphi = tan^{-1}(\omega\tau_P). \tag{4.27}$$

Using the relaxation time in the differential equation (3.32) leads to the inhomogeneous differential equation:

$$\tau_P \frac{d}{dt} u_P + u_P = u_F . \tag{4.28}$$

In the case described by Tondast-Navaei (2005) this equation was then solved for an acoustic standing wave with the resulting velocity field oscillation

$$u_F = sin\left(\frac{\omega}{c}x\right)cos(\omega t). \tag{4.29}$$

Thus the resulting particle velocity amplitude was defined as:

$$v_p(x,t) = \hat{v}_F\ cos(\varphi)\, sin(\omega t - \varphi) + \hat{v}_F\ sin(\varphi)\ exp\left(-\frac{t}{\tau_P}\right). \tag{4.30}$$

Hence the cosine of the phase angle, Tondast-Navaei (2005) refers to this as "entrainment coefficient", can be used as a measure of how accurate the particle will follow the flow in terms of its amplitude, i.e. for $\varphi \to 0$ the particle velocity will be exactly the same as the velocity of the surrounding air flow. The coefficient was assessed for the available seeding liquid. For these measurements a SAFEX fog generator was used with the particle density being of order $\rho_p = 1000\, kg/m^3$.

Moreover the kinematic viscosity of the air at ambient temperature was set to $\nu = 15.68 \cdot 10^{-6}\ m^2/s$. Figure 4.12 shows the distribution of the entrainment coefficient with particle size. It can be seen that that the particle velocity will accurately follow the flow velocity for particle diameter less than 6 μm.

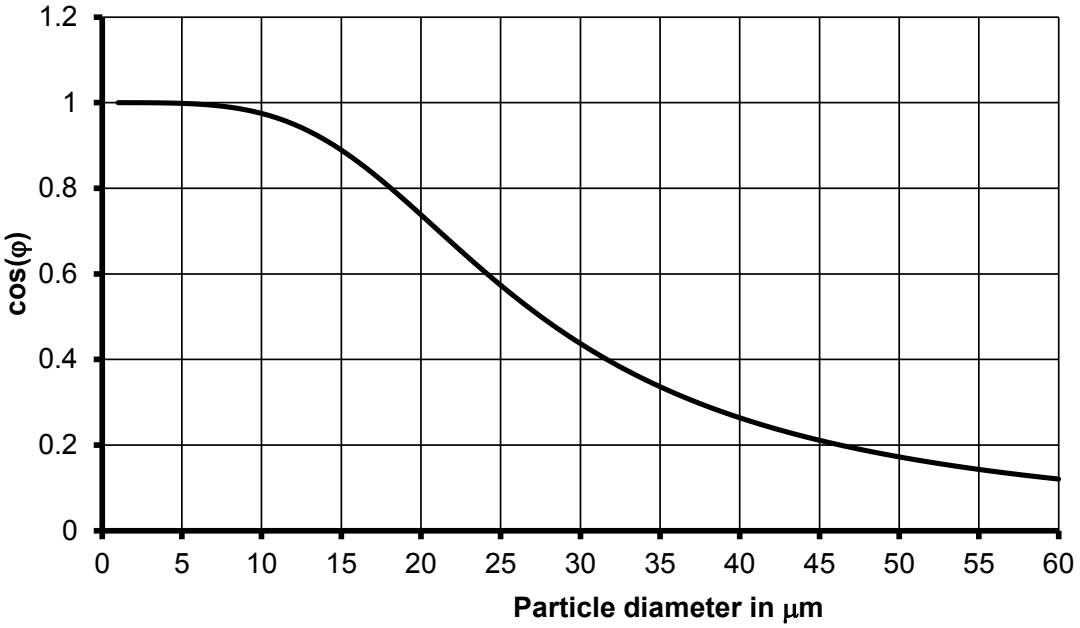

Figure 4.12: Entrainment coefficient relative to particle size

The droplet size of the SAFEX fog generator was measured by Wigley (2008) using a Phase Doppler Anemometer (PDA). The droplet size distribution is shown in Figure 4.13 using a probability density function as a measure of the occurrence of the droplet size within the sample of the PDA measurement. It can be seen that less than 5% of the droplets are greater than 6 μm diameter. Moreover the majority of the droplet diameters are in the order of 3.5 μm. Furthermore the Sauter Mean Diameter was measured to 3.7 μm.

Not only is the size of the seeding particles important but also the amount. As already discussed the PIV method relies on a discretisation of the captured images in several interrogation windows. According to Raffel et. al. (2007), Hollis (2004) or LaVision (2007) the amount of particles within an interrogation cell should be greater than five. In this case the displacement vector detection algorithm for the used software is in the order of more than 95%.

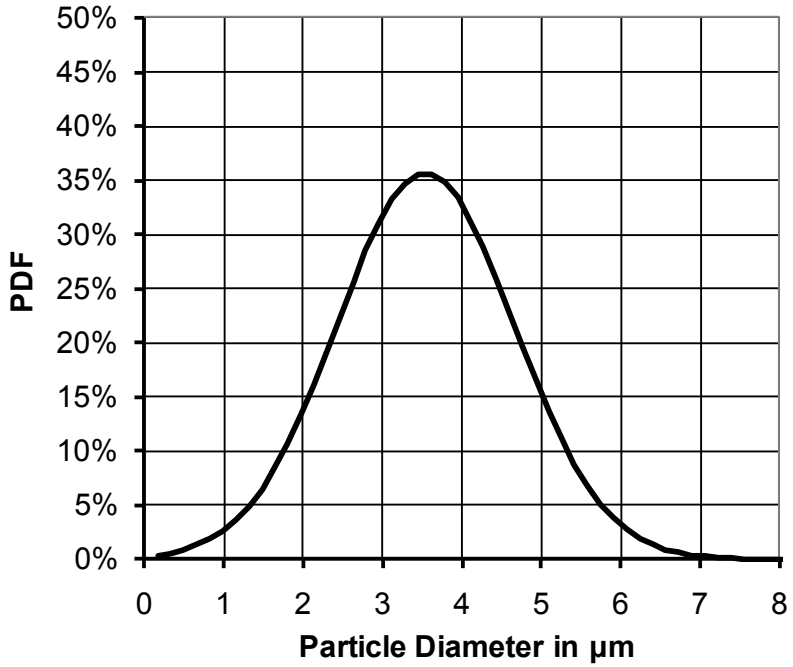

Figure 4.13: Droplet diameter distribution of SAFEX fog seeder

4.2.2 Error Analysis

One of the major influences on the accuracy of the PIV measurement technique is how well the seeding particles are following the flow field. In this case the velocity field is forced with an acoustic pressure oscillation. Hence the particles as discussed earlier had to be chosen so that they are accurately following the fluid velocity field for the given pressure oscillation. A simple way to estimate the error due to the particle slip velocity is shown for example in Adrian (1991):

$$\left|u_p - u_F\right| = \frac{\rho_p d_p^2 \left|\dot{u}_p\right|}{36 \rho_F \nu}. \tag{4.31}$$

In this case the surrounding fluid and the seeding particle is represented by the subscript F and p respectively.

The oscillating velocity field relevant for the particle was estimated to

$$u_p(t) = \hat{u}_p \, sin(\omega t). \tag{4.32}$$

Hence the particle acceleration can be estimated as

$$\left|\dot{u}_p\right| = \omega \hat{u}_p \,. \tag{4.33}$$

Therefore the systematic error in velocity amplitude relative to the fluid velocity amplitude can be estimated

$$\varepsilon_{u,s} = \frac{\left|\hat{u}_p - \hat{u}_F\right|}{\hat{u}_F} \,. \tag{4.34}$$

The calculated errors are summarised for the two forcing frequencies in Table 4.3.

Acoustic forcing frequency in Hz	**Estimated error due to particle slip in %**
62.5	0.8
125	1.6

Table 4.3: PIV error estimate due to particle slip velocities

Another source of error is the random error due to the calculation of the particle displacement within the PIV system analysis algorithm. This error can be estimated to 0.1 pixel (Raffel et. al. (2007)). Thus leading to an accuracy on the oscillating velocity of 0.5 m/s for the shortest inter-frame times of 6μs for the test points at 0.8% *dp/p*. Hence this error can be as high as $\varepsilon_{u,r} = 2.5\%$ for the forced velocity fields within the centre of the jet.

Therefore the total error on the measured velocity amplitudes within the centre of the jet flow can be estimated using (Morris (2001)):

$$\varepsilon_{u,t} = \sqrt{{\varepsilon_{u,s}}^2 + {\varepsilon_{u,r}}^2} = 3\% \,. \tag{4.35}$$

This error can be larger within the shear layer of the jet due to the spatial and temporal resolution of the measurement technique. Further analysis of errors encountered within the PIV measurement of the aero-acoustic flow field is discussed in Chapter 7 and appendix D.

5 Acoustic Absorption Experiments – Linear Acoustic Absorption

Over recent years a great deal of research has been undertaken to measure and model the absorption associated with perforated walls. The current work extends this to orifice geometries typically found in gas turbine combustors and scaled to the relevant operating condition. Acoustic absorption experiments have been undertaken to investigate the relevant absorption mechanisms for these geometries prior to measurements of the associated unsteady flow fields presented later in this work. The current section presents the experimental results associated with the linear acoustic absorption regime. Initially the influence of the mean flow through the aperture, and its influence upon the acoustic absorption, will be investigated. Thereafter the effect of combustion system orifice geometries, in terms of their length to diameter ratio for cylindrical apertures, as well as non-cylindrical orifice shapes, will be considered. Using this data acoustic absorption models and their performance in comparison with the linear acoustic experiments are assessed and are also used to explain some of the experimental results. Finally the amount of linear acoustic absorption available within gas turbine combustion system geometries and operating conditions is discussed.

5.1 Influence of Mean Flow upon Linear Acoustic Absorption

In this case a mean flow through the aperture is applied using the facility described in section 3.1.1. Some example results can be seen in Figure 5.1 similar to those described in Rupp et. al. (2010) and Rupp et. al. (2010b). In this case the acoustic absorption coefficients presented are for orifice plate number 1 (Table A.1) with an aperture diameter of 12.7 mm and an orifice length of 6 mm. The acoustic excitation frequency was 125 Hz and the absorption data is presented as a function of the incident pressure amplitude in dB. Note the dB scale for the data shown in this chapter is based on the peak pressure amplitude not the rms. It is evident that the absorption levels for the test cases with a mean pressure drop across the orifice of 0.5% to 2.9% are independent of the excitation amplitude. Hence this result indicates linear absorption over the range of

values tested. It can also be seen that a decrease in the pressure drop, and hence the mean flow passing through the orifice, results in an increase in absorption coefficient (Rupp et. al. (2010)).

Figure 5.2 shows the measured acoustic absorption coefficient for orifice plate number 3, D = 9.1 mm and L/D = 0.5. In this case the acoustic forcing frequency was chosen to be 62.5 Hz. Again it is observed that the absorption coefficient is independent of the excitation pressure amplitude and thus the absorption mechanism is linear. Moreover the absorption is increasing with reducing pressure drop (as seen in Figure 5.1).

Alternatively the absorption shown results can be presented using the acoustic admittance. The admittance can be calculated from the measured acoustic energy flux incident onto, and reflected by, the orifice plate (equation (2.27) and (2.28)). This can be calculated on either side of the orifice within the experimental facility. Hence the incidental acoustic energy is defined as the energy flux travelling against the flow direction (-) in the downstream duct (*ds*) and the energy flux travelling in the flow direction (+) in the upstream duct (*us*):

$$\Pi_{in} = \Pi_{ds}^{-} + \Pi_{us}^{+} . \tag{5.1}$$

Furthermore the acoustic energy reflected off the orifice plate can be calculated using the acoustic energy flux travelling in the flow direction within the downstream duct and against the flow direction within the upstream side of the test facility:

$$\Pi_{out} = \Pi_{us}^{-} + \Pi_{ds}^{+} . \tag{5.2}$$

The acoustic energy loss is then calculated as the difference of the incidental and reflected acoustic energy:

$$\Pi_{L} = \Pi_{in} - \Pi_{out} . \tag{5.3}$$

According to Howe (1979b) or Luong et. al. (2005) the acoustic energy loss is defined as:

$$\Pi_{L} = \left|\hat{p}_{us} - \hat{p}_{ds}\right|^{2} R \frac{\delta}{\omega \bar{\rho}} . \tag{5.4}$$

In this case the pressure amplitudes are immediately upstream and downstream of the orifice. As already described in Chapter 3.2.1 the pressure amplitude upstream of the orifice is effectively zero, due to a pressure node. Hence the admittance can be calculated using the measured acoustic energy loss and the measured pressure amplitude from the two-microphone method immediately downstream of the orifice:

$$\delta = \frac{\Pi_L \omega \rho}{R \left| \hat{p}_{ds} \right|^2} . \tag{5.5}$$

This has been compared to the admittance defined by Howe (1979b) as shown in equation (2.40). The analytical admittance is only dependent on the Strouhal number. As already described in section 2.5.1 the Strouhal number can be defined using the velocity in the plane of the aperture

$$St = \frac{\omega R}{\overline{U}_D} = \frac{\omega R}{\overline{U}_d C_D} . \tag{5.6}$$

The discharge coefficient for the two orifice plates was measured as 0.73 using the test arrangement described in the appendix B.

In a similar way as in Rupp et. al. (2012) Figure 5.3 shows the admittance derived from the experimental data presented in Figure 5.1 and Figure 5.2 in comparison with the theoretical admittance as described in Howe (1979b). As can be seen the measurements are in excellent agreement with the theory for the investigated Strouhal number range from 0.06 to 0.5. Moreover the admittance is increasing for increasing Strouhal numbers which, in this case, is caused by a reduction in mean velocity across the aperture. Thus the increasing admittance with decreasing mean velocity leads to a larger acoustic energy loss and thus to increasing absorption coefficients as shown in Figure 5.1 and Figure 5.2.

Comparing the two orifice plates leads to the conclusion that plate 1 (Figure 5.1) is generally generating larger acoustic absorption coefficients for the same pressure drop (dp/p = 0.5%) than plate 3 in Figure 5.2. This, to some extent, can be expected as the Strouhal number is increased for plate number 1 in Figure 5.1 due to the larger orifice diameter and higher forcing frequency. Hence as it is indicated in Figure 5.3 the

admittance of the orifice is increasing over the range of Strouhal numbers ($St < 1$) investigated and therefore leads to greater acoustic absorption.

It can be seen from equation (5.4) that the ability to absorb acoustic energy by an orifice is dependent on the unsteady pressure difference, the orifice radius and its admittance (this being a function of Strouhal number). Hence optimising the absorption of a passive damping device or the cooling geometry of a gas turbine combustor can be achieved by (i) maximising the unsteady pressure drop or (ii) the admittance of an orifice geometry. The unsteady pressure drop can be modified using acoustic cavities, (i.e. plenum or resonating cavities surrounding the porosities) whilst the admittance is in general a function of Strouhal number. Hence reducing the mean pressure drop across a perforated liner (and thereby increasing the Strouhal number) increases the admittance and ultimately the acoustic absorption of the damper for Strouhal numbers smaller than one. However, due to cooling reasons within a gas turbine combustion system the mean pressure drop cannot be reduced by large amounts. Thus typical acoustic damper geometries within gas turbine combustors operate at Strouhal numbers below 0.3 (Rupp et. al. (2012)). Furthermore other geometries need to be investigated which affect the admittance of an orifice. In this work the effects of the orifice geometry, in terms of its L/D and its shape, upon the linear admittance are investigated for gas turbine combustion system design applications.

5.2 Reynolds Number Independence

Howe (1979b) assumes in his analysis that the Reynolds number is sufficiently high that the acoustic absorption is independent of the Reynolds number. In this case the Reynolds number is defined as

$$\mathrm{Re} = \frac{\rho U_d D}{\nu} \quad . \tag{5.7}$$

Due to the restrictions on the test facility the experiments could only be conducted over a limited range of Reynolds numbers. However to ensure that the acoustic absorption measurements were independent of Reynolds number tests were conducted using orifice plate geometries 2 and 4 described in Table A.1. The Strouhal number was kept constant and the Reynolds number doubled for the investigated test conditions.

This was achieved by varying the mean flow velocity through the aperture. It can be seen in Figure 5.4 that the admittance remains constant with varying Reynolds number. Hence it can be assumed the measured linear absorption characteristics shown in this section are independent of the mean flow Reynolds number.

5.3 Influence of Orifice Shape on the Linear Acoustic Absorption

As already mentioned in chapter 1.3 conventional as well as modern combustion systems can have a host of orifice geometries for cooling, damping and emissions control purposes. In general the length-to-diameter ratios of apertures within such a system ranges by an order of magnitude (i.e. from one to ten). Hence the acoustic absorption associated with these geometries was also investigated.

Figure 5.5 shows a comparison between two orifice plates of the same diameter 9.1 mm with *L/D* ratios of 0.5 and 2.4 as defined in Table A.1. The mean pressure drop across the orifice was 0.8% which is typically used for double skin impingement effusion cooling geometries. Moreover the forcing frequency was set to 62.5 Hz. The length-to-diameter ratio of 2.4 is representative of combustion system effusion cooling geometries. As can be seen the absorption remained within the linear regime for the investigated excitation pressure amplitudes, i.e. constant absorption coefficients with increasing pressure amplitudes. Moreover there is an increase of approximately 15% in absorption coefficient for the larger *L/D* ratio of 2.4 compared to 0.5. Due to the change in orifice length-to-diameter ratio the Strouhal number for the same pressure drop has changed due to the increase in discharge coefficient (equation (5.6)), i.e. C_D of 0.73 for $L/D = 0.5$ and C_D of 0.84 for *L/D* of 2.4. Thus the Strouhal number for an *L/D* of 2.4 is lower than for *L/D* of 0.5. According to the previous section based on the theory by Howe (1979b), the lower Strouhal number should lead to a reduction in admittance and ultimately in absorption. To the contrary this was not shown by the experiment as absorption coefficients increased with reducing Strouhal numbers. Therefore the change in discharge coefficient seemed to have a beneficial effect upon the absorption of acoustic energy which also suggests that the admittance curve, relative to the Strouhal number, must have changed.

To investigate this behaviour further Figure 5.6 shows a summary of all absorption experiments for *L/D* ratios of 0.5 to 10. In this case the diameters of the orifice plates have remained constant. Furthermore the pressure drop across the orifice plates has been varied from 0.1 to 1 % leading to Strouhal numbers of 0.06 to 0.2 (taking the measured discharge coefficients of the orifice plates into account). First of all it can be seen that the absorption coefficient increases with reducing pressure drop for all orifice plates smaller than *L/D* of 5. For larger orifice plates this has less of an effect. It can be assumed that large *L/D* ratios (*L/D* of five and above) are dominated by inertial forces in the orifice flow field, as the mass of the fluid within the aperture is becoming increasingly larger, and thus the absorption coefficients reduce as unsteady velocities decrease due to the increasing inertial forces. Furthermore boundary layers within the orifices will start to develop for these geometries which will add to the acoustic resistance. This increase in resistance will lead to a reduced admittance due the increased boundary layer viscosity reducing the oscillating velocity field and thus the jet shear layer interaction. Some interesting behaviour though, can be seen for orifice length-to-diameter ratios between 0.5 and 5. The absorption seems to increase for *L/D* ratios from 0.5 to 2, and then decrease for length-to-diameter ratios larger than two. This increase and decrease of absorption coefficient is pressure drop dependent though, as absorption coefficients are dropping for *L/*D > 1 at *dp/p* of 0.3 and below.

In general the shape of the absorption coefficients with changing *L/D* ratio resembles that of the discharge coefficient variation with *L/D* ratio (as shown in Figure 5.7). The discharge coefficients have been measured on the described experimental facility in appendix B. A comparison of the discharge coefficient measurement for the investigated length-to-diameter ratios is compared to discharge coefficients found in the literature, e.g. Lichtarowicz et. al. (1965). The measurement shows the same characteristic as shown in the literature and is in reasonable agreement with the quantitative values. It can be seen that the discharge coefficient initially increases from $0.65 < L/D < 2$ and then gradually decreases. As already discussed in chapter 2.1 this is due to attachment of the flow within the orifice occurring at *L/D* ratios of approximately two. This suggests that the increase in discharge coefficient is also causing an increase in the absorption coefficients. This can also be seen looking into more complicated orifice

shapes as defined in Table A.1. Figure 5.8 shows the linear acoustic absorption measurements for various aperture shapes with respect to its measured discharge coefficients for a mean pressure drop of 0.5%. All orifice lengths were the same (L = 18 mm). Hence it can be assumed as a first approximation that the inertia effects are of similar scale for all the apertures in Figure 5.8. In one case, plate number 12, the conical hole has been tested with two different mean flow directions through the orifice as indicated in Figure 5.9. All the other apertures shown in the figure have been tested with the mean flow direction going from the largest diameter to the smallest diameter, as for the left hand side in Figure 5.9. The experimental data confirms the behaviour seen from the L/D variation as the acoustic absorption coefficient is increasing with increasing discharge coefficient. Hence the highest absorption coefficient was achieved using a Bellmouth shaped inlet and the lowest absorption coefficient is measured for the conical shape in reverse flow direction which provides the lowest measured discharge coefficient.

This apparent effect of the discharge coefficient on the acoustic absorption coefficient suggests that the C_D, not only affects the mean flow field through the orifice but also the unsteady flow field (or more precisely the admittance of the orifice). The edge condition at which vorticity is shed from the rim of the aperture will be affected by changes in the orifice flow as reflected by the change in C_D. Therefore changes in admittance with changing C_D will be investigated in the following section.

5.4 Influence of Orifice Geometry on the Rayleigh Conductivity

The previous section showed the measured absorption coefficient is influenced by the orifice discharge coefficient, but measurements were over a limited Strouhal number range. Moreover the changes in C_D leading to larger acoustic absorption can only be explained if the admittance curves relative to the Strouhal numbers have been changed. Hence an orifice Rayleigh Conductivity experiment has been designed to directly measure orifice admittance and inertia over a wide range of Strouhal numbers and for a range of length-to-diameter ratios (0.14 to 10). Note the shorter orifice plates have been included as the theory presented by Howe (1979b) assumed an infinitesimally thin orifice plate. The pressure drop across the orifice geometries was kept constant to 0.5%.

This was set so that the linear absorption regime was present over a wide range of excitation pressure amplitudes. Experiments with various pressure amplitudes have been undertaken to prove the admittance remained constant and thus the measurement remained in the linear regime. Moreover the excitation frequency was varied between 20 to 1000 Hz to achieve a wide range of Strouhal numbers.

The change in test rig to the facility described in chapter 3.2.2 improved the accuracy of the Rayleigh Conductivity measurements. As was presented in Figure 3.5 the orifice plate was located at the origin of the axial coordinate at $x = 0$. Thus the impedance on the upstream side of the orifice was measured by calculating the pressure amplitude and velocity amplitude immediately upstream of the orifice using the described multi-microphone-method (section 4.1.3):

$$Z(x=0) = \frac{\hat{p}_{ds}(x=0) - \hat{p}_{us}(x=0)}{\hat{u}(x=0)} = \frac{-\hat{p}_{us}(x=0)}{\hat{u}(x=0)} \tag{5.8}$$

Note the downstream pressure amplitude was negligible as the orifice outflow side was open to a large plenum. The Rayleigh Conductivity and the impedance rely on the accurate measurement of the velocity within the orifice. Hence the velocity amplitude within the aperture can be calculated by using the impedance from equation (5.8) and the cross-sectional area of the upstream duct (A_p) along with the orifice plate itself (A_D):

$$Z(x=0) = Z_D = -\frac{\hat{p}_{us}}{\hat{u}_D A_D} = -\frac{\hat{p}_{us}}{\hat{u}_p A_p} \quad . \tag{5.9}$$

In this case multiple apertures have been placed in the test specimen to improve the measurement accuracy. Thus the porosity of the orifice plate has to be considered to be able to reduce the data to a single orifice Conductivity. The porosity is defined as:

$$\sigma = \frac{A_D}{A_p} = \frac{N\,\pi R^2}{A_P} \quad . \tag{5.10}$$

For a single orifice the pressure amplitude upstream of the orifice tends to be close to an anti-node which means that the velocity amplitude is small which can give rise to large errors. However the error can be reduced by increasing the number of orifices within the plate. Hence multiple orifice plates of the same geometry and with gas

turbine combustion system representative pitch-to-diameter ratios (*P/D*) have been optimised to reduce the acoustic wave reflection off the test specimen and thus increase the velocity amplitude in the vicinity of the orifice plate. In this way the measurement accuracy is increased. The specification of the tested aperture geometries can be found in Table A.3.

The Rayleigh Conductivity can then be calculated from the measured quantities as defined by Howe (1979b):

$$K_R = 2R\left(\Gamma - i\delta\right) = -i\omega\rho\pi R^2 \frac{\hat{u}_D}{\hat{p}_{us}} = -i\omega\rho \frac{1}{Z_D}. \tag{5.11}$$

5.4.1 Orifice Conductivity Test Commissioning

Initial commissioning of the test rig has been conducted to estimate the accuracy of the experimental facility. Sun et. al. (2002) used a similar test facility to investigate the effect of grazing flow on the acoustic impedance of an orifice plate. The authors proposed to measure the acoustic reactance at low amplitude and with no mean flow through the apertures to understand how representative the experimental data is compared to reactance data in the literature. The same methodology has been adopted during the commissioning phase of the experiments in this work. For low amplitude acoustic forcing the acoustic reactance is defined as (e.g. Ingard and Ising (1967) or Sun et. al. (2002)):

$$\mathrm{Im}\left(Z_D\right) = \frac{X_Z}{\rho c} = \frac{\omega}{c}\frac{L_{eff}}{\sigma} = \frac{\omega}{c}\frac{\left(L + 1.7R\right)}{\sigma} \tag{5.12}$$

This approach is based on the experimental data shown in Ingard and Ising (1967) in the low amplitude forcing regime without the influence of mean flow. In this case it can be seen that the acoustic reactance of an aperture is constant and the effective length is equal to $L_{eff} = L + 2 \cdot 0.85 \cdot R$.

An example of the measured reactance compared to the theoretical values for the range of frequencies between 50 to 1000 Hz is shown in Figure 5.10. This is an example representative of all the investigated orifice plate geometries. Sun et. al. (2002) compared the gradient of the theoretical curve with the measured data and found a

variation in gradient no worse than 4.1%. For the orifice plates investigated in this work the variation in the gradient of the reactance measurement relative to the literature values was less than 5%. This was used as a criterion to optimise the experiment in terms of the amount of apertures in an orifice plate and the maximum forcing frequency. Thus for longer orifice plates with higher *L/D* ratios the excitation frequency was reduced to a maximum of 600 Hz. Higher frequency would have resulted in larger deviations because the assumption that the orifice is short relative to the acoustic wave length ($\lambda >> L$) is no longer valid.

The impedance (or Rayleigh Conductivity) of an aperture needs to take the acoustic radiation of the orifice flow field into account as well (e.g. Ingard and Ising (1967)). This additional radiation impedance is generated by the aperture flow field analogous to a solid piston representative of the orifice diameter and length. Hence the oscillating orifice flow is also a source of sound radiation. This radiation is split into a resistive and reactive component (e.g. Cummings and Eversman (1983):

$$Z_{rad} \approx \underbrace{\rho c \frac{(k_0 R)^2}{4}}_{resistance} + \underbrace{i\omega\rho L_{eff}}_{reactance} . \tag{5.13}$$

As can be seen from equation (5.13) the reactance is already accounted for in the measurement in terms of the length correction representing the forces due to the fluid acceleration of the orifice flow field. In general the radiation resistance can be neglected as it is very small for the orifice diameters investigated. This is shown in Figure 5.11 for the measured resistance (note in this case the orifice impedance is defined as $Z = \hat{p}/\hat{u}_D$) and the theoretical radiation resistance (equation (5.13)) for the measurement with 0.5% pressure drop and the orifice plate with *L/D* = 0.5. It can be seen that the measured resistance is much larger than the radiation resistance for the majority of the measurement and hence the radiation effects in the resistance term is neglected for the geometries tested.

5.4.2 Orifice Conductivity Test Results

The measured Rayleigh Conductivity for the orifice plate with *L/D* = 0.5 (Plate 20 in Table A.3) is shown in Figure 5.12. It can be seen that the admittance increases from 0

to approximately 0.6 as the Strouhal number increases from 0 to 0.8. The inertia reaches its maximum value of 1.0 at a Strouhal number of 1.3. After the admittance has reached its maximum a steep reduction in admittance for increasing Strouhal number is visible. Furthermore the admittance is negative over a Strouhal number range of 1.4 to 1.8. The change in sign to a negative admittance suggests production of sound instead of absorption.

Figure 5.13 presents a comparison of the measured Rayleigh Conductivity with the theoretical conductivity curves as described by Howe (1979b) (equation (2.39) and (2.40)). The experiment and the theoretical curves are in good agreement up to a Strouhal number value of 0.8. Thereafter the experiment deviates with the theoretical curve with no negative admittance being present in the model. However, over the Strouhal number range of 1.4 to 1.8 it should be noted that a distinct whistling of the jet flow during the experiment was observed. Testud et. al. (2009) noticed jet whistling frequencies for a Strouhal number range of $St_j = fL/\overline{U}_D = 0.2 \ldots 0.4$. The Strouhal number in Testud et. al. (2009) was defined using the length of the aperture. Applying this Strouhal number definition onto the presented data in Figure 5.13 indicates that the negative admittance occurs for $St_j = fL/\overline{U}_D = 0.2 \ldots 0.3$. Hence this is in agreement with the data presented in Testud et. al. (2009). Therefore this could be a plausible explanation for the occurrence of the negative admittance as the whistling is a source of sound energy, and thus more acoustic energy is generated than absorbed leading to a sign change in admittance.

The whistling of the jet is caused by a self-excited oscillation of the fluid due to the dynamic shear layer instability, as discussed in section 2.2 (e.g. Crow and Champagne (1971), Yule (1978), Hussain and Zaman (1981), etc), interacting with the acoustic excitation. In the work presented by Testud et. al. (2009) the measured whistling frequencies occur in the mentioned Strouhal number range of 0.2 to 0.4 based on the length of the aperture. Hence the timescale of the fluid travelling through the aperture, relative to the time scale of the acoustic excitation, is the relevant phenomena for the occurrence of the whistling. Nevertheless other parameters such as the length-to-diameter ratio and the contraction ratio (porosity) of the orifice are also important since they affect the jet shear layer and hence the potential for flow instabilities.

The jet whistling phenomenon is not accounted for in the developed model from Howe (1979b) Furthermore the whistling of the jet could also explain the change of inertia in the experiment relative to the model. As described in section 2.2 large vortex ring structures are generated by shear layer instabilities (e.g. Crow and Champagne (1971)) which affect the unsteady flow field and which can lead to increased inertia within the flow field. A similar change in admittance can also be seen in the measurements of Jing and Sun (2000). Note that changes in the sign of the admittance δ, i.e. imaginary part of the Rayleigh Conductivity, are also visible as changes in sign of the resistance, i.e. real part of the impedance. The data shown in Jing and Sun (2000) for an L/D = 0.6 orifice is changing sign from positive to negative at Strouhal numbers around 1.39, hence this could also be caused by self-excited jet instabilities. Moreover the numerical model from Jing and Sun (2000) which includes jet flow profiles and orifice thickness effects, described in section 2.5, seems to be able to reproduce this phenomenon to some extent.

Although tests have been conducted over a wide range of operating conditions the maximum Strouhal number of interest based on orifice radius and the scaling from engine to test rig is 0.7 (see Table 3.2). The Strouhal number being this large is due to the large diameter port features within a RQL combustor. Possible aero-engine gas turbine passive damper geometries, e.g. Rupp et. a. (2012), are based on Strouhal numbers smaller than 0.3 for combustion instability frequencies below 1000 Hz. In this case a large amount of apertures is needed to distribute the cooling air budget over the combustor wall. Therefore the diameter can be ten times smaller compared to the mentioned RQL port features and hence the Strouhal number is much smaller. Ultimately the behaviour of Strouhal numbers larger than one is not of direct relevance to this work. Nevertheless the Strouhal number scale proposed by Testud et. al. (2009) can be used to ensure the geometries for a passive damping system are sufficiently far away from the potential onset of jet whistling.

The measured admittance for orifice geometries with a range of L/D ratios from 0.14 to 1 are shown in Figure 5.14. In the low Strouhal number regime ($0 < St < 0.5$) the admittance for thin orifice plates ($L/D < 0.5$) is considerably smaller than for L/D larger than 0.5. Moreover the maximum value of admittance occurs at larger Strouhal numbers

for *L/D* ratios smaller than 0.5. For *L/D* ratios larger than 0.5 the maximum admittance values are reduced compared to those for the shorter *L/D* ratios. Moreover the occurrence of the maximum admittance moves to lower Strouhal numbers compared to *L/D* ratios of larger than 0.5.

Figure 5.15 shows the inertia values that are relevant for the previously considered admittance distributions. The inertia starts to increase at lower Strouhal numbers for increased length-to-diameter geometries. This is due to the increased mass within the orifice. Nevertheless the maximum value of inertia reduces for increasing *L/D* ratios. However more detailed investigations of the Rayleigh Conductivity curves indicate why this is the case.

5.4.3 Acoustic Impedance and Rayleigh Conductivity Characteristics

There are two acoustic parameters which can be used to describe the unsteady flow field behaviour of an aperture. Both parameters, the Rayleigh Conductivity and the impedance, are the reciprocal of each other:

$$\frac{K_D}{2R} = (\Gamma - i\delta) \sim \frac{1}{Z_D} = \frac{\hat{u}_D}{\hat{p}} = \frac{R_Z}{R_Z^2 + X_Z^2} - i\frac{X_Z}{R_Z^2 + X_Z^2}. \tag{5.14}$$

As equation (5.14) shows, the admittance (δ) and inertia (Γ) are both a function of resistance and reactance. Therefore the inertia parameter in the Rayleigh Conductivity is not a direct measure of the increased forces necessary to accelerate the fluid mass within the aperture. Nevertheless, as for example equation (5.13) shows, the reactance is a direct measure of the acceleration force increase taking the mass increase and the acceleration time scale into account. This can be seen for the investigated orifice geometries in Figure 5.16. The shown impedance for this as well as any other graph in this thesis is defined as $Z = \hat{p}/\hat{u}_D$. In this case the reactance is normalised with the density and the velocity in the plane of the aperture. This approach is equivalent to normalising the impedance with the product of density, speed of sound and Mach number through the aperture as, for example, used in Lee et. al. (2007). It can be seen that the reactance at a given Strouhal number increases with increasing length-to-diameter ratio. Therefore the mass within the aperture increases due to the increase in aperture length. Thus the increased inertial force due to the acceleration of a larger mass

at the same time scale is increased which ultimately leads to reduced velocity amplitudes.

The Rayleigh Conductivity has the advantage that the admittance value is proportional to the generated acoustic energy loss (equation (5.4)). Hence this parameter can be directly used to compare the ability of an aperture to absorb acoustic energy. However the physical fluid dynamic phenomena causing the admittance distribution are better described using the impedance of the aperture. This will be explained on the example of two different orifice plates with L/D = 0.25 and L/D = 1. Figure 5.17 shows the normalised measured impedances for the example orifice plates. It can be seen that the reactance, and thus the inertial forces due to the acceleration of the increased mass of fluid within the aperture, is larger for the longer orifice with L/D = 1. Furthermore the resistance measured for the longer orifice with L/D = 1 is smaller than for the shorter orifice with L/D = 0.25. The previous chapter showed that orifice geometries with increased discharge coefficients generate higher acoustic absorption coefficient for the investigated low Strouhal numbers. Changes in the steady state discharge coefficient are most likely influencing the resistance of the orifice flow field. Hence the reduced resistance is influenced by the increase in the steady state discharge coefficient from 0.63 for L/D = 0.25 to 0.83 for L/D = 1. The increased resistance for the shorter orifice reduces the velocity oscillation of the aperture relative to the longer orifice within the resistive regime (i.e. resistance > reactance) indicated in Figure 5.17. Therefore the longer orifice (L/D = 1) will generate a larger admittance value in the Rayleigh Conductivity which is representative of the increased velocity oscillation. This can be seen from the admittance curve in Figure 5.14 for Strouhal numbers smaller than 0.6 comparing the apertures with L/D = 0.25 and 1. For Strouhal numbers larger than 0.6 the orifice flow is dominated by the mass effect indicated in the impedance by the larger reactance values than the resistance values (Figure 5.17 reactive regime). Therefore the increased mass of the longer orifice dominates and reduces the velocity oscillation within the aperture due to the increasing phase shift between the pressure and velocity oscillation. This phase shift is caused by the increased time scale to accelerate the larger fluid mass within the aperture. Therefore the admittance of the aperture is reduced

compared to the shorter orifice, as also shown in Figure 5.17, for Strouhal numbers larger than 0.6.

By further increasing the length-to-diameter ratio of the aperture the acoustic reactance increases due to the larger mass within the aperture (Figure 5.16). Therefore the reactive regime in which the acoustic reactance is larger than the acoustic resistance is moved to lower Strouhal numbers (as also indicated in Figure 5.17 where the reactive regime for $L/D = 0.25$ would be at Strouhal numbers larger than two). This leads to reduced velocity oscillations due to the longer time scales required to accelerate the mass within the aperture. Hence the maximum admittance is reduced and moved to smaller Strouhal numbers as shown in Figure 5.18 for increasing L/D ratios.

The shown experimental data indicates that changes in length-to-diameter ratio affect the admittance and the inertia of an orifice due to changes of the discharge coefficient as well as the mass within the orifice. In general the trends in Rayleigh Conductivity with changing length-to-diameter ratio are similar to the work of Jing and Sun (2000) (Figure 2.9). However there is an important difference between the numerical model shown by Jing and Sun (2000) and the experimental data in this work. In the low Strouhal number regime, i.e. $St < 0.2$, the numerical admittance curves shown by Jing and Sun (2000) seem to converge to one curve. In the experimental data of the work presented here an increase in admittance is visible for orifice geometries with increased discharge coefficients. This is in agreement with the absorption measurements in the previous section. Moreover the majority of combustor orifice geometries operate in this Strouhal number regime (Table 3.2). Furthermore the Strouhal numbers of interest for potential passive damper applications to flying gas turbine engine combustors would have to operate at Strouhal numbers of this order (Rupp et. al. (2012)). Hence this range is of great technical interest and is therefore investigated in detail in the following section.

5.5 Quasi-Steady Conductivity

This section investigates the quasi-steady regime and its relevance to acoustic damping. The term quasi-steady is used in this context as it is assumed that the inertia due to the acceleration forces onto the mass of fluid within the orifice has virtually no effect on the oscillating flow field. In other words any transient forces within the flow

field are small relative to the other forces present so the field is purely resistive. As can be seen from Figure 5.15 the inertia term can be neglected up to a Strouhal number of 0.2, for *L/D* ratios up to one. For larger *L/D* ratios up to ten this reduces to Strouhal numbers below 0.1.

The Conductivity within the quasi-steady regime is defined based on equation (5.11) but with $\Gamma = 0$ so that:

$$\delta = \frac{\omega \rho \pi R^2}{2R} \frac{\hat{u}_D}{\hat{p}} \tag{5.15}$$

According to equation (2.3) the incompressible flow through the orifice can be described with the Bernoulli equation. In this case, the steady state variables in equation (2.3) have been replaced with the harmonic unsteady parameters as defined in equations (2.13) and (2.14):

$$\left(\overline{p}_{us} - \overline{p}_{ds}\right) + \left(\hat{p}_{us} - \hat{p}_{ds}\right) = \frac{1}{2} \rho \left(\overline{U}_d + \hat{u}_d\right)^2 \tag{5.16}$$

As already mentioned the downstream pressure amplitude can be assumed to be zero due to the plenum condition downstream of the orifice. Moreover, as the linear absorption regime is considered, equation (5.16) can be linearised and higher order terms can be neglected leading to the quasi-steady linear relationship between pressure and velocity oscillation:

$$\frac{\hat{p}}{2\Delta\overline{p}} = \frac{\hat{u}_d}{\overline{U}_d}. \tag{5.17}$$

Hence the quasi-steady regime describes the pulsatile velocity field relative to the applied pressure oscillation. To calculate the velocity amplitude within the plane of the aperture the continuity of mass has been applied between the end of the vena contracta and the plane of the aperture. Thus equation (5.17) can be rewritten as:

$$\frac{\hat{p}}{2\Delta\overline{p}} = \frac{\hat{u}_d}{\overline{U}_d} = \frac{\hat{u}_D}{\overline{U}_D}. \tag{5.18}$$

Using the mean flow as a description for the mean pressure drop leads to the quasi steady definition of the velocity amplitude in the plane of the aperture:

$$\hat{u}_D = \frac{\hat{p}}{\rho \bar{U}_D} C_D^2 . \tag{5.19}$$

The quasi-steady admittance can be defined by using equation (5.19) in equation (5.15):

$$\delta_{QS} = \frac{\pi}{2} \frac{\omega R}{U_D} C_D^2 = \frac{\pi}{2} St\, C_D^2 . \tag{5.20}$$

It can be seen that this is only dependent on the discharge coefficient and the Strouhal number.

Figure 5.19 shows a comparison between the quasi-steady (QS) calculated admittance compared to the measured admittance. It can be seen that the model agrees very well with the measured admittance within the quasi-steady regime (i.e. which corresponds to low Strouhal numbers). The same comparison is shown in Figure 5.20 for larger length-to-diameter ratios. Figure 5.21 shows the measured admittance and the quasi-steady admittance for length-to-diameter ratios representative of effusion cooling geometries. As shown in Table 3.2 the Strouhal number range is typically between 0.02 to 0.07 so that the majority of these geometries, and associated operating regimes, are located within the quasi-steady regime.

In general the data suggests that the maximum possible admittance for a given Strouhal number is the quasi-steady admittance. The influence of the orifice inertia at higher Strouhal number results in admittance values that are less than the quasi-steady values. Hence the occurrence of the optimum admittance in all the measured Conductivity curves. In other words the maximum unsteady velocity amplitude achievable is within the quasi-steady regime. This behaviour also explains how the discharge coefficient influences the admittance (and thus the acoustic absorption). Increasing discharge coefficients not only indicate larger steady mass flow through the orifice for a given orifice diameter, but it also indicates high unsteady mass flows. The unsteady kinetic energy is a function of unsteady mass flow. Thus for increasing discharge coefficients more acoustic energy can be transferred into unsteady kinetic energy which ultimately dissipates due to the vorticity generated within the shear layers and turbulent viscosity of the unsteady jet. Therefore in this regime the edge of the orifice is not relevant in terms of its influence on the flow structures shed off the rim,

but is relevant as it provides the effective flow area available for the pulsatile mass flow. This explains the absorption coefficient measurements for various length-to-diameter ratios and orifice shapes.

The acoustic absorption of an acoustic damping geometry, or the damping effect of a cooling geometry, can therefore be optimised using an orifice geometry in which its discharge coefficient is maximised. A similar suggestion can be found in conjunction with Helmholtz resonator necks in the work by Keller and Zauner (1995) who stated that improved loss coefficients on resonator neck geometries improve the absorption behaviour of Helmholtz resonators. Hence this possibility will be investigated in the context of linear absorbers in the following section.

5.6 Optimisation of Acoustic Admittance within the Quasi-Steady Linear Absorption regime

As discussed in the previous section the acoustic admittance of an orifice within the quasi-steady regime can be optimised by maximising the discharge coefficient. Hence further orifice plates have been defined in Table A.3 where the inlet edge has been rounded to form a Bellmouth shaped inlet. This has also shown a benefit in the absorption measurements (see Figure 5.8). Hence three orifice length-to-diameter ratios have been investigated using a Bellmouth shape: 0.5, 0.76 and 1.98.

Figure 5.22 shows a comparison between the measured Conductivity of the measured Bellmouth orifice shape with the cylindrical shape for L/D of 0.5. Moreover the quasi-steady prediction of the admittance is also shown in the graph denoted with the acronym QS. It can be seen that the admittance (and hence the acoustic loss) can be increased utilising a larger discharge coefficient. As the orifice is short the Bellmouth inlet is not perfect leading to a discharge coefficient of 0.85. Hence a longer orifice was tested (L/D = 1.98) with a Bellmouth inlet achieving a C_D of approximately one. The measured Conductivity of this orifice is shown in Figure 5.23 and is compared to cylindrical orifice geometries of L/D = 0.5 and 1.98. It can be seen that the admittance is nearly doubled using a Bellmouth shape compared to a cylindrical orifice. This is for a Strouhal number less than 0.1 based on the quasi-steady calculation. Due to the increased mass within the orifice introduced by the Bellmouth shape increased inertial

forces due to the acceleration of a larger fluid mass are expected. This increase in inertia is compared to the cylindrical orifice plates in Figure 5.24. Hence the additional inertia is causing the admittance to deviate from its quasi-steady value at lower Strouhal numbers relative to the cylindrical geometries tested.

However it should be noted as the discharge coefficient increases, so does the mass flow passing through the orifice (for a given orifice diameter). For a combustion system it is important to understand the acoustic absorption per utilised mass flow in comparison to cylindrical orifice geometries with reduced discharge coefficients. Therefore the following section investigates this aspect of damping optimisation with respect to unit mass flow consumption.

5.7 Acoustic Energy Loss Considerations

A gas turbine combustion system has a specified air mass flow distribution which is required to cool the combustor walls, pass sufficient air to the fuel injector and, in conventional rich-quench-lean combustors, to the primary and intermediate ports. Moreover a dedicated amount of air is required by the downstream turbine for cooling requirements associated with the nozzle guide vane and the rotor downstream. Hence the amount of available air for acoustic damping is limited. Thus the combustor damping optimisation, for a given cooling geometry or dedicated acoustic damping geometry, will have a limited air mass flow budget. With this in mind the measured admittances in the previous sections have been used to calculate the acoustic energy loss as defined in equation (5.4). However, to be able to assess the loss per unit mass flow the acoustic loss will be normalised with the incident pressure amplitude and the mean mass flow across the orifice geometry:

$$\Pi_{norm} = \frac{\Pi_L}{\left|\hat{p}_u\right|^2 \overline{\dot{m}}} \tag{5.21}$$

In addition, to compare the data for a given pressure drop the Strouhal number will be defined as:

$$St_d = \frac{\omega R}{\overline{U}_d}. \tag{5.22}$$

The introduced quantities have been used to compare the cylindrical orifice (with *L/D* = 0.5) with the Bellmouth orifice shapes in Figure 5.25. It can be seen that the normalised acoustic loss per unit mass flow measurement for the orifice shapes with *L/D* = 0.5 and 0.76 collapse within the quasi-steady regime (i.e. *St* < 0.3). Moreover the Bellmouth orifice shape with *L/D* of 1.98 is also collapsing within a Strouhal number range smaller than 0.1 (i.e. which corresponds to the quasi-steady regime for this geometry). Hence it can be concluded that the acoustic energy loss per unit mass flow is constant for the investigated orifice shapes for the range of Strouhal numbers typically found within a gas turbine combustion system. The figure also shows that the maximum absorption can only be achieved in the quasi-steady absorption regime. Due to the effects of inertial forces the normalised acoustic loss reduces from the maximum possible absorption for a given mass flow and pressure amplitude for increasing frequencies. Hence the maximum acoustic energy loss limit can be calculated using the expression for the quasi-steady admittance as defined in equation (5.20), with the acoustic loss equation (5.4):

$$\Pi_L^{QS} = \left|\hat{p}_u\right|^2 \frac{R\delta_{QS}}{\omega\rho} = \left|\hat{p}_u\right|^2 \frac{\pi R^2}{2\rho} \frac{C_D^2}{\overline{U}_D} = \frac{\left|\hat{p}_u\right|^2}{4\rho} \frac{\overline{\dot{m}}}{\Delta\overline{p}}. \tag{5.23}$$

Therefore the normalised quasi-steady acoustic energy loss is defined as:

$$\Pi_{norm}^{QS} = \frac{\Pi_L^{QS}}{\left|\hat{p}_u\right|^2 \overline{\dot{m}}} = \frac{1}{4\rho\Delta\overline{p}}. \tag{5.24}$$

Hence the maximum acoustic absorption for a given mass flow and acoustic excitation pressure amplitude is solely dependent on the mean density of the air through the aperture and the mean pressure difference across the orifice.

Figure 5.26 shows a comparison of the normalised acoustic loss for various cylindrical orifice geometries compared with the ideal quasi-steady loss. Within the quasi-steady regime the acoustic loss agrees with the measurement. The quasi-steady regime extends to larger Strouhal numbers for shorter orifice length (e.g. for *L/D* = 0.14 the quasi-steady regime is valid up to a Strouhal number of approximately St_d of 0.6). In

contrast, the quasi steady regime for an orifice geometry of L/D = 1.98 is only valid to approximately St_d of 0.1.

It can be seen that the measured admittance and the quasi-steady calculated admittance agree well for Strouhal numbers up to 0.6 for L/D ratios below 0.5. For larger Strouhal numbers the inertial forces affect the admittance and lead to reduced acoustic energy absorption relative to the quasi-steady theory.

In general the data and the quasi-steady theory enable the calculation of the maximum possible acoustic loss for a given unsteady pressure drop across the liner and a given mean mass flow through the orifice. Moreover the simplicity of the method enables an initial optimisation of acoustic absorbers for gas turbine combustors while defining cooling geometries and other features on a combustion system using perforations. As Figure 5.21 showed the majority of the conventional effusion cooling geometries remain within the quasi-steady regime. Hence length-to-diameter ratios could be optimised to remain within the quasi-steady admittance for a given cooling geometry if the cooling effectiveness allows for the optimisation in hole angle. However the results also show that if the orifice geometry is operating within the quasi-steady regime then there is no advantage in optimising the orifice geometry to try and increase absorption. In other words the increase in admittance does not outweigh the increase in air mass flow consumption. Therefore the acoustic energy loss remains constant for a constant ratio of mean mass flow to mean pressure difference across the orifice.

5.8 Comparison between Linear Acoustic Experiments and Analytical Rayleigh Conductivity Models

As not all of the combustion system orifice geometries operate within the quasi-steady regime, absorption models are necessary to evaluate acoustic absorption for the regimes where inertia cannot be neglected. Hence the Rayleigh Conductivity based models will be compared to the measured Rayleigh Conductivity in this section. The measured data will be compared to the Rayleigh Conductivity defined by Howe (1979b), which will be referred to as the Howe model, and the orifice length modified Rayleigh Conductivity (as defined by Jing and Sun (1999)) which will be referred to as the modified Howe model. The modified Conductivity was defined in equation (2.48) of

section 2.5.2. This length corrected impedance will be used within the Rayleigh Conductivity to compare the measured data with the modified model:

$$\frac{K_R}{2R} = \Gamma_{\mathrm{mod}} - i\delta_{\mathrm{mod}} = -\frac{i\rho\omega\pi R}{2}\frac{\hat{u}_D}{\hat{p}} = -\frac{i\rho\omega\pi R}{2}\frac{1}{z_{tot}\rho c}. \tag{5.25}$$

The modified admittance and inertia parameters are then determined as:

$$\delta_{\mathrm{mod}} = \mathrm{Im}\left(K_R/2R\right) \text{ and} \tag{5.26}$$

$$\Gamma_{\mathrm{mod}} = \mathrm{Re}\left(K_R/2R\right). \tag{5.27}$$

Figure 5.27 shows a comparison between the measured and predicted admittance by the Howe model and the modified Howe model for an orifice length-to-diameter ratio of 0.5. Note for the modified Howe model the geometric length was used without an additional length correction. Moreover the measured discharge coefficient has been applied to estimate the orifice Strouhal numbers. As already discussed the admittance is a function of resistance and reactance (see equation (5.14)). Hence the additional length applied to the reactance of the aperture is also affecting the admittance. It can be seen that the Howe model without length correction is predicting the measured admittance well within a Strouhal number range of zero to one. The drop in measured admittance for Strouhal numbers larger than one has not been reproduced by either of the models. However as already mentioned this is outside the relevant Strouhal number range in this work. The length corrected modified Howe model shows a much reduced admittance relative to the experimental values. This reduction in admittance is caused by the increase in inertia due to the additional orifice length. Figure 5.28 shows the comparison between the measured and calculated orifice inertia for the two different modelling methods. It can be seen that the Howe model without length correction is agreeing very well with the measured data in the Strouhal number range between zero and one. The additional length correction increases the inertia initially in the range from zero to one. As described in section 5.4 this inertia behaviour is due to the increased reactance in the length corrected model which therefore leads to a reduced velocity amplitude within the aperture indicated by the reduced admittance. Hence the inertia prediction by the Howe model seems to be valid for the shown experimental data with aperture *L/D* of 0.5. It can also be seen that the modified model and the initial Howe model converge for the

low Strouhal number range below 0.3. This is due to the diminishing effect of the orifice inertia at low Strouhal numbers.

Figure 5.29 and Figure 5.30 show the measured and predicted admittance and inertia for the orifice geometry that has a smaller *L/D* of 0.25. This also coincides with a reduced discharge coefficient (C_D = 0.63). It can be seen that the Howe model deviates from the experimental data. It is overestimates the admittance compared to the experimental data in the Strouhal number range from zero to one. Moreover the modified Howe model is overestimating the admittance initially but shows an overall reduced admittance relative to the Howe model. Both models do show their optimum admittance at a lower value compared to the measured data. Moreover the optimum admittance is moved to a lower Strouhal number. This behaviour is caused by the significantly increased inertia prediction for both models relative to the experimental data in Figure 5.30. As Figure 5.28 shows the inertia prediction without length correction agrees with the orifice of *L/D* = 0.5. Hence to predict the orifice length of *L/D* = 0.25 correctly the orifice length correction would need to be reduced to correct for the inertia in the Howe model being over predicted. However this would not account for the mismatch in admittance in the low Strouhal number regime of 0 to 0.8. Hence the model cannot be matched to the measured data using the length-correction only. In general this would lead to an overestimation of the acoustic absorption for this geometry. As the inertia is overestimated reducing the length correction would lead to an increase in admittance and thus to an even larger error in absorption. To be able to match the model it would need an increase in discharge coefficient to reduce the admittance in the model, but this contradicts the experimental data and the quasi-steady theory.

Figure 5.31 and Figure 5.32 show the comparison between the Conductivity models and the measured Rayleigh Conductivity for an *L/D* ratio of 1.98. In this case the discharge coefficient has increased compared to the initial comparison of *L/D* = 0.5 (C_D of 0.81 compared to 0.73). It can be seen that the modified model underestimates the admittance in the Strouhal number range from 0 to 0.3. However the modified Howe model agrees much better with the data than the original version. For such an orifice geometry the mass inertia of the aperture flow field is larger than for the initial Howe

model and hence the modified model is predicting the inertia increase due to the larger orifice length more accurately (Figure 5.32). It can therefore be concluded that the length correction implemented in the modified Howe model is necessary for orifice geometries of *L/D* larger than 0.5 for a more accurate prediction of the aperture velocity oscillation. However the discrepancies in the low Strouhal number regime ($St < 0.2$) cannot be compensated with the orifice length correction as the inertia is reproduced correctly. Thus the absorption coefficient would be underestimated in the low Strouhal number regime $St < 0.2$. A further compensation would therefore be necessary in the model which would require an artificial reduction in discharge coefficient.

Finally the Conductivity models are compared to a larger *L/D* of 6.8 in Figure 5.33 and Figure 5.34. In general the modified model agrees much better with the measured data which confirms that this model is more suitable to large length-to-diameter ratios which are dominated by inertia effects.

In general the shown comparison between the used models and the experiments highlights to which geometries the two models can be applied. Based on the experimental data the Howe model is valid for an orifice geometry of *L/D* of 0.5. The modified Howe model though, is valid for orifice geometries of *L/D* larger than 0.5. Moreover one of the weaknesses of these modelling methods is the discrepancies for the admittance predictions and the measured values in the low Strouhal number regimes.

This is further investigated by comparing the predicted acoustic loss to the acoustic loss measured within the acoustic absorption facility (section 5.3). The acoustic loss predicted by the model can be calculated using the following equation:

$$\Pi_p = \frac{\Pi_L}{\left|\hat{p}_{ds}\right|^2} = \frac{R\,\delta_{\mathrm{mod}}}{\rho\omega}. \tag{5.28}$$

In the linear acoustic absorption regime the acoustic loss, relative to the square of the incident pressure amplitude, remains constant. Hence the admittance from the Howe model and the modified Howe model can be used to estimate the acoustic losses within the linear regime which can be compared with the experimental data. Figure 5.35 shows a comparison of the measured and calculated linear acoustic loss from the single orifice absorption coefficient measurements in section 5.1 and the predicted acoustic loss using

the Howe and modified Howe model. The graphs show four different pressure drops for the various *L/D* ratios. Note the error bars for the experimental data have been approximated based on the quasi-steady theory and linear acoustic absorption experiments within the quasi-steady regime.

The Conductivity models agree well for *L/D* = 0.5. However the predicted loss values are significantly less than the measured trends for length-to-diameter ratios from 0.5 to 5. Moreover as already mentioned the modified Howe model agrees better with the experimental data for larger *L/D* ratios than five. In general the discrepancy between the measured and predicted acoustic loss relates back to the used discharge coefficient to estimate the Strouhal number for the Rayleigh Conductivity (equation (5.6)). In this study the measured discharge coefficient was used to estimate the velocity in the plane of the aperture. Hence this assumption is used as a representation of the velocity of the vortices in the orifice shear layer (similar to the approach taken in Hughes and Dowling (1990), Jing and Sun (2000), Eldredge and Dowling (2003) or Luong et. al. (2005)). By increasing the discharge coefficient the velocity in the plane of the aperture increases and the Strouhal number reduces. This causes a reduced admittance for increasing discharge coefficient as both models rely on the curve shown in Figure 1.15. This influence is therefore the reason for the reversed trend in acoustic loss as the absorption reduces with increasing C_D for the model.

Howe (1979b) applied an asymptotic analysis for the Strouhal number tending towards zero onto the derived analytical Rayleigh Conductivity. The outcome of this analysis indicated a contraction ratio of 0.5 between the aperture area and the area of the vena contracta. This was close to the experimental values derived for infinitesimally thin apertures ($C_D \sim 0.6$) and therefore acceptable. However the effect of the used discharge coefficient in the model is significant, as highlighted in Figure 5.36. A comparison between the measured data, the modified Howe model using the measured discharge coefficients and the modified Howe model using a constant C_D of 0.5 is shown. This has a significant effect upon the acoustic loss predicted by the model. The predicted acoustic loss for a reduced discharge coefficient is significantly increased and deviates from the experiment for apertures with *L/D* smaller than two. However the

modified Howe model based on the reduced C_D seems to agree well with the experiments for *L/D* ratios larger than two.

In previous sections, the quasi-steady admittance was introduced (section 5.5 and 5.6), and the developed quasi-steady predictions agreed very well with the measured admittance in the low Strouhal number regime. This suggests that the assumption of using the steady-state discharge coefficient might be valid. Hence the reasons for the mismatch might be related to the asymptotic solutions of the Rayleigh Conductivity as these solutions were used as a baseline to assess the contraction ratio and thus the derivation of the vortex sheet velocity in Howe (1979b). The asymptotic solutions for the Rayleigh Conductivity are defined by Howe (1979b):

$$K_R \approx 2R\left(\frac{1}{3}St^2 - \frac{1}{4}i\pi St\right), \text{ for } St \to 0 \tag{5.29}$$

In the quasi steady regime at small Strouhal numbers the inertia term can be neglected. This is the region where the models converge at low Strouhal numbers (Figure 5.28 to Figure 5.34). Thus the quasi-steady admittance according to this asymptotic solution is defined as

$$\delta_{H,QS} \approx \frac{\pi}{4}St, \text{for } St \to 0\,. \tag{5.30}$$

Comparing the quasi-steady admittance from the Howe model with the quasi-steady admittance derived in equation (5.20) shows that the Howe admittance is by factor two smaller. Hence it can only agree with orifice plates which have a discharge coefficient of C_D = 0.707. In this work apertures with *L/D* of 0.5 are characterised by such a discharge coefficient and hence the model is agreeing well with this geometry. However any other orifice plate geometry, where the $C_D \neq 0.707$, leads to predictions of the absorption which would not match the experimental data. Improved accuracy of predictions could be obtained by changing the discharge coefficient in the Howe model. However this would mean that the discharge coefficients are not related to the actual physical C_D of the associated flow field which is not desirable. A similar observation can be found in Luong et. al. (2005). In this study the Rayleigh Conductivity has been compared to a model developed by Cummings (1986). Cummings (1986) developed an

equation for the non-linear acoustic absorption regime which is similar to the model described in section 2.5.3. Luong et. al. (2005) compared the results of this model for low amplitude, or in other words within the linear regime, with the linear Rayleigh Conductivity based on Howe (1979b). The best agreement between the two models was found for a contraction coefficient (area ratio between aperture and vena contracta) of 0.75 which agrees with the found value in this study for the quasi-steady regime.

The experimental data shown in Figure 5.35 was also used in Figure 5.37 and compared to the acoustic loss prediction in the quasi-steady regime. In this case the quasi steady admittance of equation (5.20) is used to predict the acoustic loss as defined in equation (5.30). The actual measured discharge coefficients have been used to predict the acoustic loss and it can be seen that the prediction agrees with the data very well for all orifice length-to-diameter ratios from 0.5 to 6.8 for mean pressure drops of 1% and 0.8%. Discrepancies between model and experiment are occurring for pressure drops below 0.5% as shown in Figure 5.37 c) and d). In this case the Strouhal number is not within the quasi-steady regime anymore which leads to a reduction in linear acoustic loss due to the influence of increased inertia.

It can be concluded that the aforementioned data suggests (i) limited accuracy of the Howe and modified Howe model for the prediction of acoustic absorption,(ii) use of quasi-steady theory for improved accuracy in the quasi-steady regime but (iii) a desirable solution would be to include inertia effects in a model to predict the acoustic absorption outside the quasi-steady regime. Such a model is described in the following section.

5.9 Linear Absorption Using Unsteady Momentum Equation

An alternative analytical model for the prediction of acoustic absorption was described by Bellucci et. al. (2004) on the basis of the work outlined by Keller and Zauner (1995). This approach is based on a momentum balance across the aperture and is described in detail in section 2.5.3. In this case only the linear version of the model is considered:

$$i\omega\rho L_{eff}\hat{u}_D + \hat{p}_{ds} - \hat{p}_{us} + \rho\left(\zeta_{vis}\hat{u}_D\right) + \rho\varsigma_L\overline{U}_D\hat{u}_D = 0\,. \tag{5.31}$$

The loss coefficient due to viscosity (ς_{vis}) is associated with friction effects due to the boundary layer within the aperture:

$$\zeta_{vis} = (1+i)\frac{L}{D}\sqrt{2\nu\omega}\left(1+\frac{\gamma-1}{\sqrt{\mathrm{Pr}}}\right). \tag{5.32}$$

As can be seen from equation (5.34) the viscosity within the aperture boundary layer not only affects the resistance of the orifice impedance but also increases the reactance of the aperture. The effective length was initially set to the geometric length of the orifice geometries and the downstream pressure is again assumed to be zero.

Defining the loss coefficient as

$$\varsigma_L = \frac{1}{C_D^2} \tag{5.33}$$

ensures that the momentum balance reduces to the quasi-steady admittance as described in equation (5.20). This model should potentially be able to represent the Conductivity of the orifice geometries more reliably as the discharge coefficient can be chosen according to the steady state fluid dynamic properties of the aperture flow field. This leaves only the length correction to be unknown a priori. The following predictions have been undertaken using the measured orifice discharge coefficients and the geometric length of the orifice. Moreover the Conductivity values were obtained by calculating the impedance, as in equation (5.33), and substituting the impedance into (5.11).

Figure 5.38 shows a comparison between the measured and predicted Conductivity using the model developed by Bellucci et. al. (2004). First of all it can be seen that the quasi-steady admittance and the admittance predicted by the Bellucci model are converging in the low Strouhal number range (St < 0.4) as expected. Hence the model captures the pulsatile flow behaviour accurately. In general the admittance predicted by the model agrees very well with the measured data up to a Strouhal number of 0.9. The inertia is also well represented by the model in this Strouhal number range. However, the model cannot represent the Conductivity behaviour at Strouhal numbers larger than 0.9 but as already discussed, this regime is dominated by jet whistling due to shear layer instabilities.

Figure 5.39 shows the prediction using the Bellucci model in comparison with the quasi-steady model and the measured Conductivity data for an L/D ratio of 0.25. The associated reduction in discharge coefficient (C_D = 0.63) causes the admittance to decrease to that of the L/D = 0.5 geometry. As can be seen the model agrees well with the data for Strouhal numbers of 0.9. However as the inertia is underpredicted the model overpredicts the admittance for Strouhal numbers larger than 0.9.

Data is also presented for L/D = 1.98 in Figure 5.40. Again the Bellucci model and the quasi-steady model agree within the quasi-steady regime and follow the measured admittance. However, discrepancies occur around the optimum admittance (St > 0.2) between model and prediction, although the admittance trend is qualitatively represented by the model.

In general it can be seen that the modelling method captures the pulsatile flow in the quasi-steady flow regime very well. Moreover the model does agree with the previously discussed quasi-steady theory which gives further confidence that the input loss coefficient based on the measured mean flow discharge coefficient are representing the unsteady flow field. However as the inertia effects appear to become more important for increasing Strouhal numbers so does the length correction parameter within the model. This parameter is an input and is currently derived based on experimental data. This is discussed in the following section.

5.9.1 Loss Coefficient and Acoustic End Correction Investigation – Linear Absorption Regime

The previous section indicated that the prediction of the acoustic absorption using the linear absorption model proposed by Bellucci et. al. (2004) provides more accurate predictions. In this case the model is reliant on the correct input of a loss coefficient and a length correction. It was shown that the mean flow discharge coefficient and the geometric orifice length are sufficient for an a priori prediction of the unsteady flow field of the aperture during the design process for linear acoustic absorbers. However to improve the accuracy of the model the necessary loss coefficients and acoustic end corrections are further investigated in this section.

To estimate the required input discharge coefficient and loss coefficient to the model for each geometry the input loss coefficient and length correction has been varied until the model matched the experiment. Moreover the length correction and loss coefficient was assumed to be constant with varying frequency. For example the length correction and discharge coefficient can be estimated from the measured impedance. Thus the length correction can be calculated from the measured reactance

$$L_{eff} = \frac{\mathrm{Im}(Z) - \rho\,\mathrm{Im}(\zeta_{vis})}{\omega\rho} \Rightarrow L_{corr} = \frac{L_{eff} - L}{R} \tag{5.34}$$

and the discharge coefficient can be estimated from the resistance

$$\frac{1}{C_D} = \frac{\mathrm{Re}(Z) - \rho\,\mathrm{Re}(\zeta_{vis})}{\rho \bar{U}_d} \,. \tag{5.35}$$

As an example Figure 5.41 shows the variation of length correction and discharge coefficient for the experimental data of an orifice with *L/D* ratio of 0.5 as defined by equations (5.36) and (5.37). Moreover the Rayleigh Conductivity of the orifice is also shown for reference. It can be seen that the effective length of the orifice is constant for a Strouhal number range between 0.4 and 1. In general this is expected for linear absorption. The drop in length correction for Strouhal numbers smaller than 0.4 is caused by the small to negligible inertia in the quasi-steady regime (as indicated in the Conductivity graph). The same can be said about the calculated discharge coefficient from the measured data. As it can be seen the discharge coefficient remains constant for Strouhal between 0.1 and 0.8. Moreover the estimated discharge coefficient agrees with the mean flow discharge coefficient measurement. The graph might also give an explanation for the discrepancies of the model with experiment at Strouhal numbers larger than one. The mentioned flow instabilities seem to affect the unsteady flow field. In this case the one-dimensional modelling parameters are no longer constant which results in an increase of discharge coefficient as well as the length correction within the model. This might highlight the fact that the impact of large scale structures cannot simply be included in the simple analytical models by assuming constant loss coefficients and length correction. However, as Figure 5.41 shows, within the Strouhal number range of interest for a gas turbine combustion system ($St < 1$) it can be assumed that the discharge coefficients and the length corrections remain constant.

Table 5.1 summarises the discharge coefficients and length corrections which produced the best fit to the experimental data. Moreover the measured mean flow discharge coefficients are also shown for the used orifice plates. Initially for orifice geometries with *L/D* smaller than two it can be seen that the mean flow discharge coefficient is sufficient for a good match of the modelling data to the experimental data. This is shown in the comparisons of the measured and predicted Rayleigh Conductivity using discharge coefficient $C_{D,2}$ and the length corrections in Table 5.1 for *L/D* = 0.25, 0.5 and 1.98 in Figure 5.42 to Figure 5.44. It can be seen that the model matches the experimental data very well. Therefore this confirms that the mean flow discharge coefficient can be used in the linear acoustic model for an accurate prediction of aperture C_D with small *L/D*.

L/D	**$C_{D,1}$ from plenum fed steady flow measurement**	**$C_{D,2}$ from best fit of acoustic model**	**L_{corr} from best fit of acoustic model**
0.14	0.62	0.62	0.33
0.25	0.63	0.63	0.61
0.5	0.73	0.73	0.26
0.76	0.79	0.81	0.13
1	0.83	0.83	0.62
1.5	0.81	0.81	0.71
1.98	0.81	0.81	1.06
2.4	0.81	0.81	1.1
3	0.8	0.81	1.35
5	0.8	~0.81	1.8
6.8	0.77	~0.81	2.46
10	0.75	~0.81	3.1

Table 5.1 Measured length corrections and discharge coefficients, cylindrical apertures

However, for *L/D* ratios larger than two the discrepancy between the measured mean flow discharge coefficient $C_{D,1}$ and the matched coefficient $C_{D,2}$ values increases. Moreover it seems as if larger discharge coefficients are required to match the model to

the experimental result. Figure 5.45 shows an example for the measurement and modelling result for *L/D* of 6.8 using $C_{D,2}$ and the length correction form Table 5.1. It seems as if an even larger discharge coefficient is needed to match the data more accurately. As the aperture length increases to geometries with *L/D* larger than two the mean flow field characteristic within the orifice changes. Thus the interaction of the unsteady flow with the orifice internal boundary layer becomes more important. Hence the influence of the viscosity model for larger *L/D* orifice geometries will be assessed in the following section.

5.9.2 Sources of Errors in the Analytical Modelling for Apertures with Large Length-to-Diameter Ratios

The previous section highlighted that the analytical model showed larger discrepancies for the prediction of the admittance for apertures with *L/D* ratios larger than two. Moreover as Table 5.1 showed the input discharge coefficient to the model for the long apertures was required to be larger than the measured discharge coefficient. The reasons for the increasing errors and deviations from the mean flow discharge coefficient could be caused by changes in the flow behaviour through the aperture. This is illustrated in Figure 5.46 for a short aperture with $L/D < 2$ and a long aperture with $L/D > 2$. It can be seen that for the case of a short aperture the inflow into the orifice generates a vena contracta, with the minimum area A_d being at the point where the stream lines passing through the aperture are parallel (see section 2.1). In this way the discharge coefficient is a measure of the area contraction between the aperture A_D and the area of the vena contracta. The viscosity effect within the aperture is negligible due to the short length of the orifice. In this case the mean flow discharge coefficient is agreeing well with the discharge coefficient derived from the acoustic experiment as discussed in section 5.9.1. Based on the comparisons between measurements and modelling in these cases it seems sufficient to model the acoustic resistance with the measured discharge coefficient and the model was successfully applied to orifice geometries from *L/D* of 0.14 to 2 (e.g. Figure 5.42 to Figure 5.44). However for the case of a long aperture ($L/D > 2$) the measured mean flow discharge coefficient is a measure of the losses associated with the inflow into the aperture, the viscous losses inside the orifice and its associated velocity profile as well as the loss generated by the outflow

profile of the aperture. Hence an acoustic modelling method has to be able to reproduce the complex processes with a representative loss coefficient and unsteady viscosity model. In the current model the viscosity is explicitly modelled with an unsteady viscosity expression shown in Bellucci et. al. (2004) which was based on Kirchhoff (1868). A similar expression is also shown in Keller and Zauner (1995). The viscosity term is only accounting for the loss due to the unsteady flow across the boundary layer. Another model which is simulating unsteady laminar Poiseuille flow within the apertures can be found for example by Bellucci et. al. (2004b) but has not been used in this work. However the choice of the most representative friction model, in addition to the accurate prediction of the inflow and outflow profiles and their unsteady behaviour is thought important and most likely the reason for the observed discrepancies.

A brief investigation of the impact of the viscosity and loss coefficients is shown in Figure 5.47 which compares the predicted energy loss by the model with the measured acoustic loss from experiments described in section 3.2.1 and 5.3. Two variations of the model have been applied to the calculation. A first prediction was conducted using $C_{D,2}$ and the length correction from Table 5.1 as an input, also including the viscosity term in the calculation. In this case the loss coefficient is thought to represent the inflow and outflow losses of a reattaching orifice flow field (e.g. $L/D = 2$) without the influence of the boundary layer viscosity, which is therefore modelled by the unsteady viscosity model. The second option was to use the mean flow discharge coefficient $C_{D,1}$ from Table 5.1 without the viscosity terms. Thus the viscous losses due to the unsteady flow are thought to be negligible and the viscous losses are included in the mean flow discharge coefficient. Both options gave the same result as can be seen in Figure 5.47 indicating either method would be an option to model longer apertures. The proposed methods to model long apertures will be further investigated in chapter 8.3.3 where the damping characteristics of multi-aperture liners with large L/D ratios are assessed.

In general for the practical engineering applications considered in this work the model captures the pulsatile flow behaviour well. However this model relies on input parameters such as loss coefficients (based on C_D), length corrections and adequate viscosity models. As a first assumption in the linear acoustic regime with Strouhal numbers smaller than one the loss coefficients and length corrections are assumed to be

constant. In this case no unsteady flow structures such as large scale vortex rings are present in the pulsatile flow field and the structures in the shear layer do not seem to have a particular important role in the sense that they do not affect the jet flow in a positive or negative manner. Unless the excitation frequencies are near self-excited jet flow instabilities (as for L/D = 0.5 geometries Figure 5.38). In this case the model deviates from the measurement. This suggests that flow field structures within the shear layers have an effect upon the Conductivity of the orifice which cannot be represented by the model unless the loss coefficients and the length correction allow for this behaviour. In this case the assumptions for the loss coefficient are too simple to predict shear layer instabilities. This would be the advantage of a vortex sheet model as described in the previous section. For example Bellucci et. al. (2004b) have used the described Rayleigh Conductivity by Howe (1979b) to predict the loss coefficient based on the vortex sheet model. However the discrepancies shown in section 5.8 indicate that this approach would need improvements. The data given by Jing and Sun (2000) indicated that flow instabilities could be captured. Hence improved vortex sheet models with detailed jet trajectories could be used to generate Strouhal number dependent loss coefficients. Moreover advanced CFD techniques (e.g. Mendez and Eldredge (2009) or Gunasekaran and McGuirk (2011)) could be applied to improve the accuracy of the used loss coefficients and aperture internal viscosity models.

5.10 Closure

In this chapter the fundamental acoustic characteristics relating to linear absorption has been discussed. It was shown that changes in orifice geometry, in terms of gas turbine combustion system representative L/D ratios, result in changes in the measured admittance of the Rayleigh Conductivity. The changes in admittance are associated with changes in the steady flow discharge coefficients as well as the increased mass inertia due to the length of the aperture. In fact within the linear quasi-steady regime increases in the orifice discharge coefficients lead to increases in admittance with the maximum admittance being reached for ideal discharge coefficients of one provided by a Bellmouth orifice shape. However, for a fixed geometric area the increasing mean mass flow through the aperture, due to increasing discharge coefficient, means there is no benefit in acoustic loss per unit mass flow. Thus within a combustion system orifice

geometry the linear absorption is governed by a pulsatile flow field which subsequently dissipates due to turbulence. The acoustic energy is therefore transformed into kinetic energy of the unsteady jet flow; with the maximum energy transfer is limited to the quasi-steady regime. Hence the maximum acoustic absorption for a given pressure amplitude and mean mass flow consumption is achieved in the linear quasi-steady regime independent of orifice geometry.

It was shown that the Rayleigh Conductivity model based on the theory described by Howe (1979b) agrees with the measured Rayleigh Conductivity for an orifice of *L/D* of 0.5 up to a Strouhal number of 0.9. This model was derived on the assumption of a thin cylindrical shear layer and infinitesimal thin apertures. Hence the model can only be applied to small *L/D* orifices. Moreover some discrepancies are shown in the quasi-steady (low Strouhal number) regime which showed that the model is only valid for thin apertures with a discharge coefficient of 0.7. This discrepancy might be caused by the assumption of a thin cylindrical shear layer compared to a vorticity profile surrounding the unsteady jet.

The modified Howe model was able to predict the measured Conductivities for orifice geometries with *L/D* values larger than 0.5. However the described increasing admittance, with increasing mean flow discharge coefficient within the quasi-steady regime, could not be reproduced by the modified Howe model. The modified Howe model is a length corrected version of the Howe model and relies on the Rayleigh Conductivity curve for an infinitesimal thin aperture with a thin cylindrical shear layer. This Rayleigh Conductivity is only a function of Strouhal number and thus the mean velocity of the vorticity within the thin shear layer. Hence assuming that this velocity can be estimated by the mean flow discharge coefficient could cause erroneous results within the length modified model.

A model based on a momentum balance by Bellucci et. al. (2004) is capable of reproducing the measured behaviour in the low Strouhal number regime and is the preferred option for practical engineering applications. This model agrees with the quasi-steady theory in the low Strouhal number regime and agrees with the observed changes in admittance with changing aperture *L/D*. However the model is only accurate as long as the aperture unsteady loss coefficient and length correction parameters

remain constant as a first approximation. This is valid as long as there are no large vortex structures generated within the jet flow shear layer as, for example, in the vicinity of natural jet flow instabilities. Nevertheless this approach seems sufficient for gas turbine combustion system geometries investigated in this work as the Strouhal number remains low and therefore far away from natural occurring flow instabilities through the aperture. However for orifice plates with *L/D* larger than two the analytical modelling becomes more challenging. In this case the mean flow discharge coefficients are no longer a sole measure of area contraction, but are also affected by the viscous drag due to the boundary layer within the aperture. Moreover the effect of the unsteady viscosity models is increasing with aperture length. Thus the use of an adequate viscosity model representative of the aperture internal flow field, together with a meaningful inflow and outflow loss coefficient, becomes important.

Figures

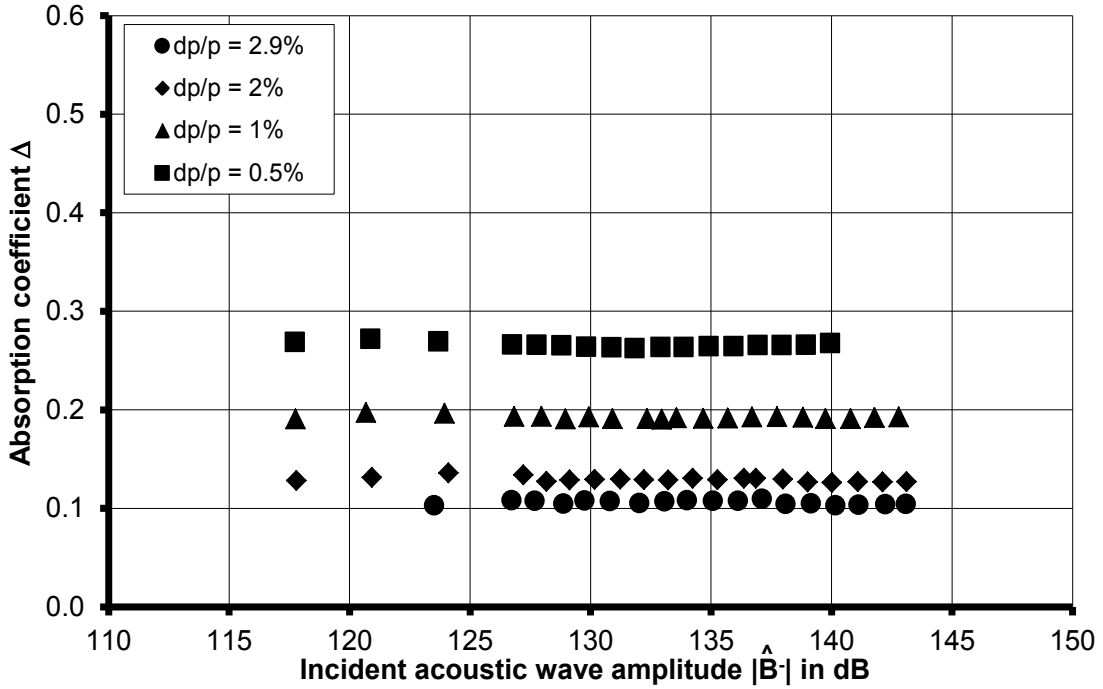

Figure 5.1: Linear acoustic absorption with mean flow, plate number 1, *L/D* = 0.47, *f* = 125Hz

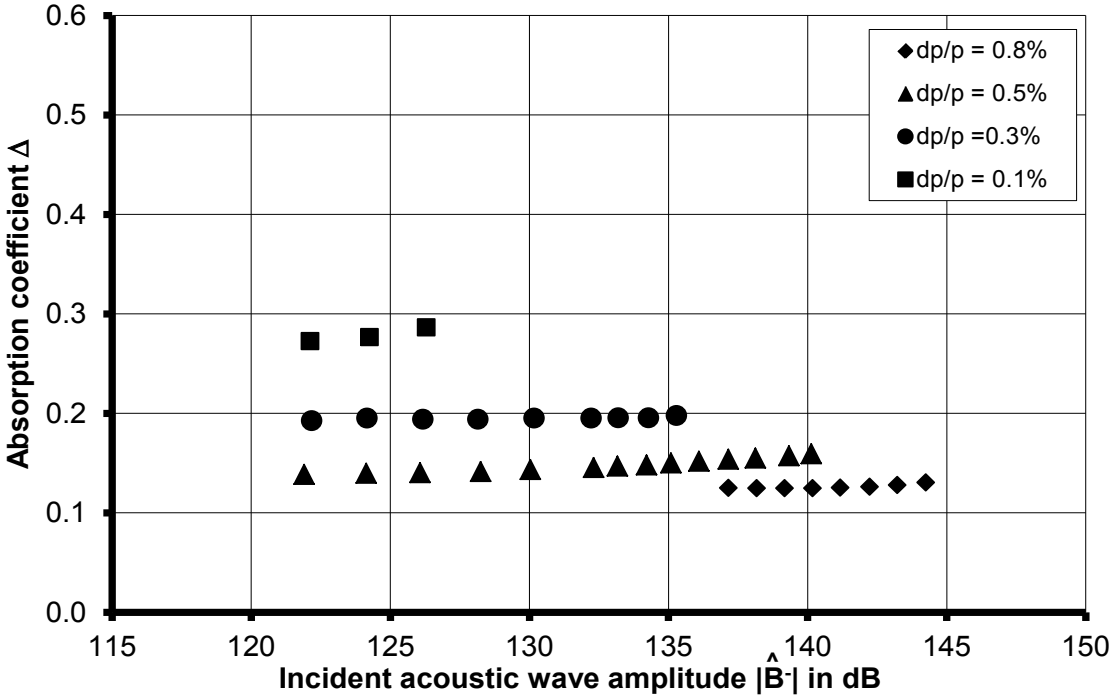

Figure 5.2: Linear acoustic absorption with mean flow plate number 3, *L/D* = 0.5, *f* = 62.5 Hz

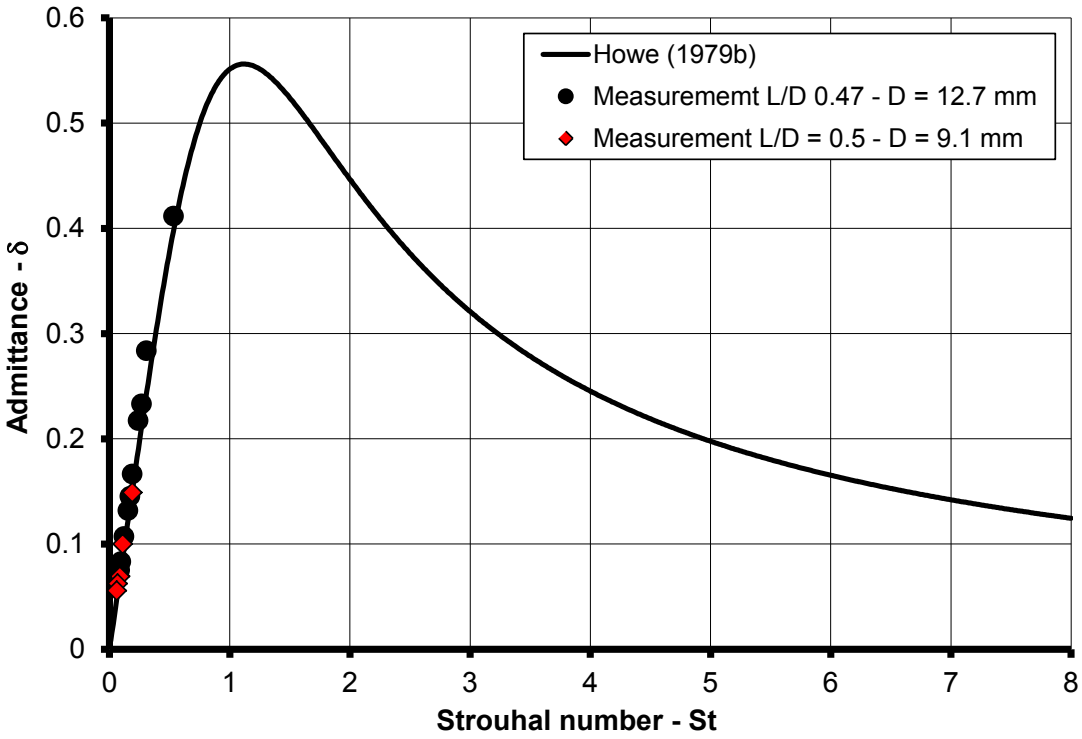

Figure 5.3: Measured admittance and comparison to theory from Howe (1979b), Plate numbers 1 and 3.

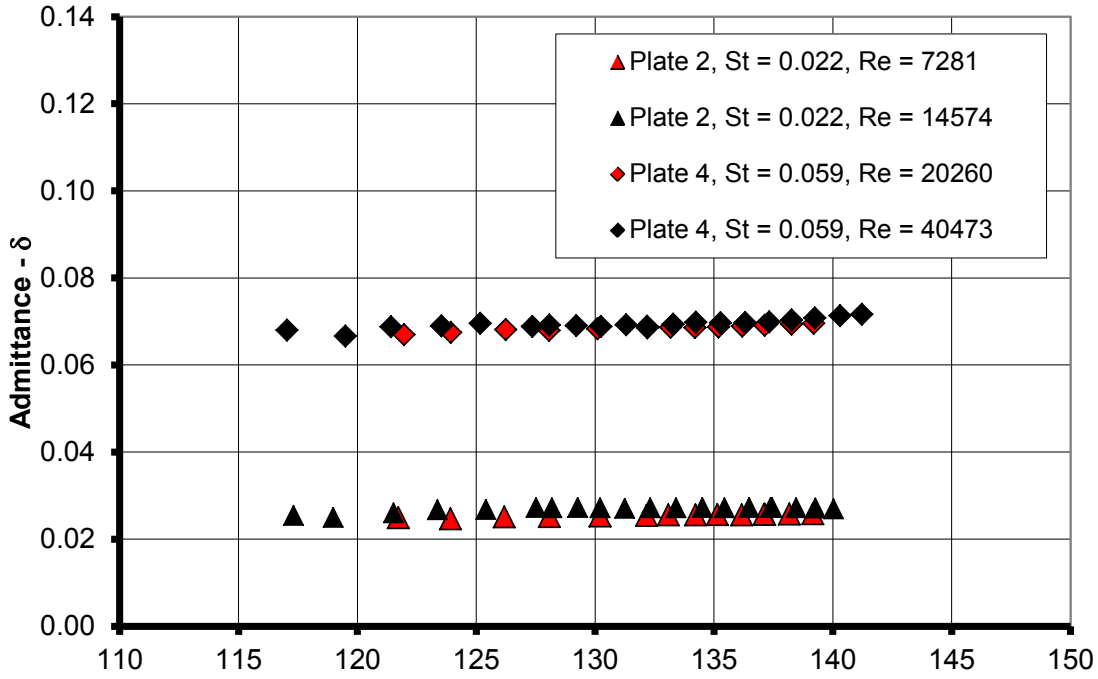

Figure 5.4: Measured admittance at constant Strouhal number and varying Reynolds number for Plate numbers 2 and 4.

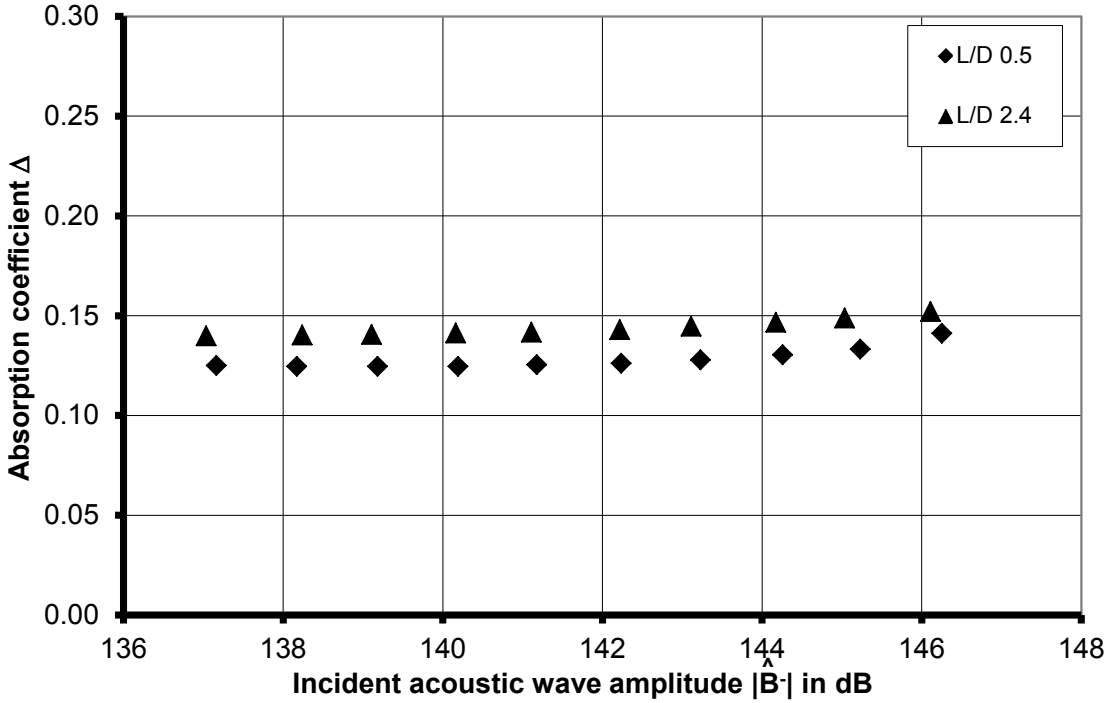

Figure 5.5: Comparison of absorption coefficient. Plate number 3, *L/D* = 0.5 and plate number 7, *L/D* = 2.4. f = 62.5Hz, *dp/p* = 0.8%.

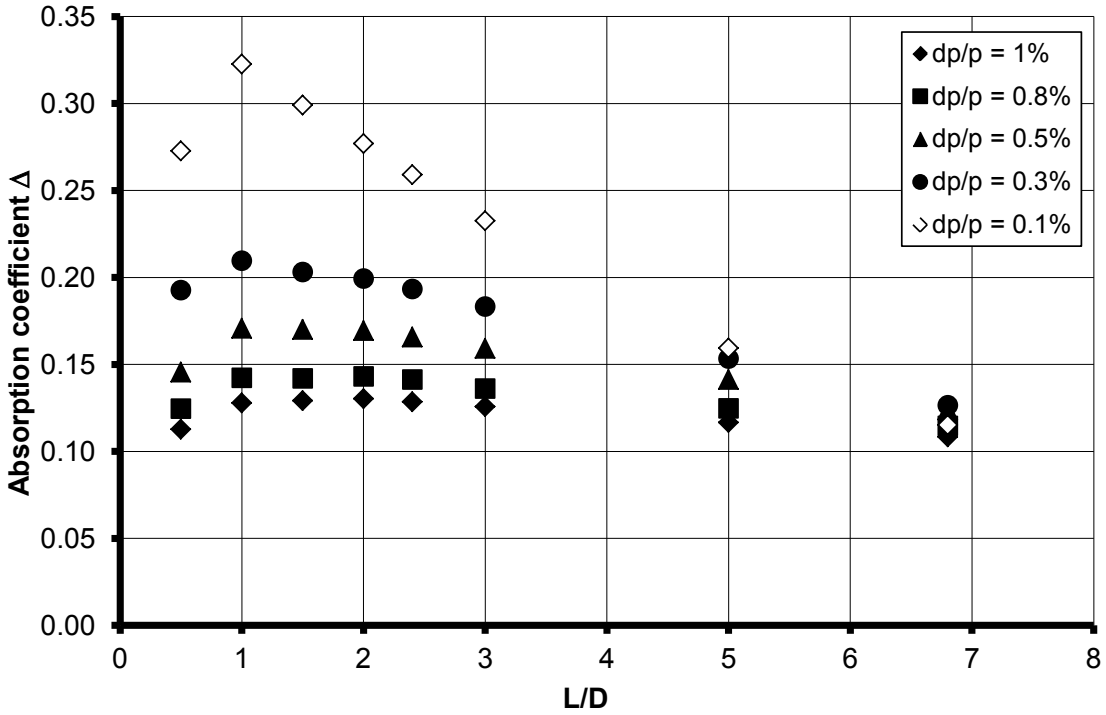

Figure 5.6: Absorption coefficients for various L/D ratios at a range of pressure drops. Plate numbers 3 to 11.

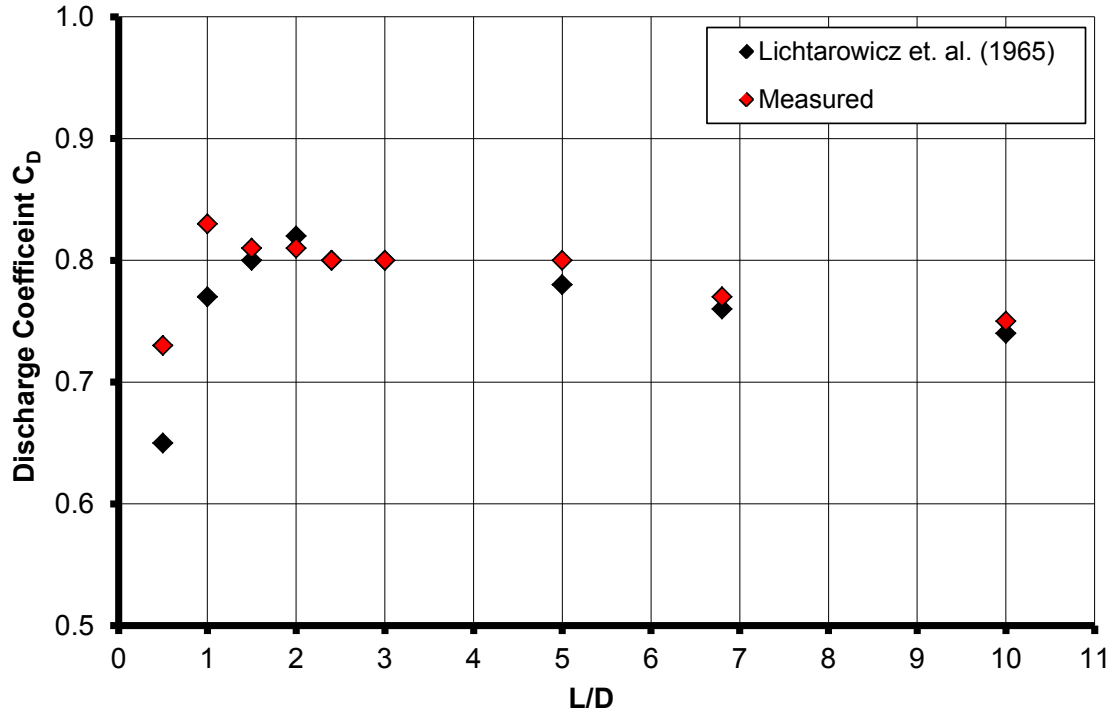

Figure 5.7: Discharge Coefficient measurement for various L/D ratios. Plate numbers 3 to 11

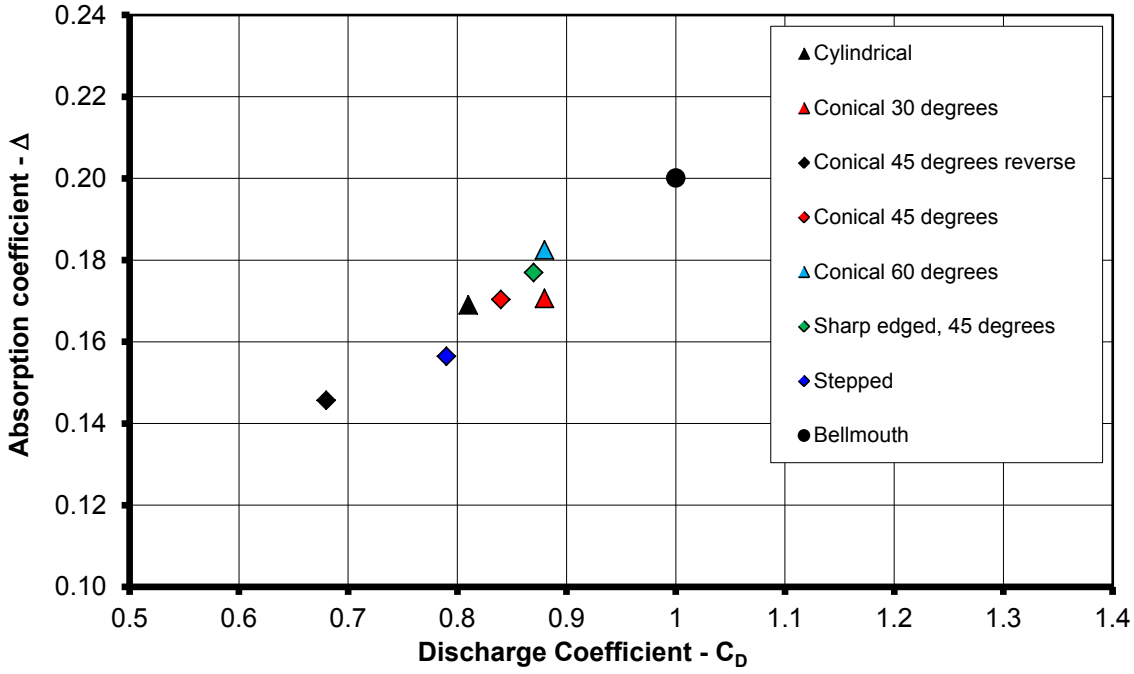

Figure 5.8: Absorption coefficients for various orifice shapes at a pressure drop of *dp/p* = 0.5%.

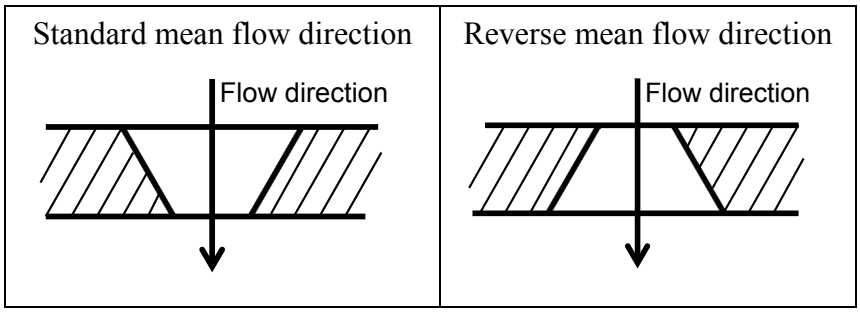

Figure 5.9: Definition of flow direction through shaped orifice

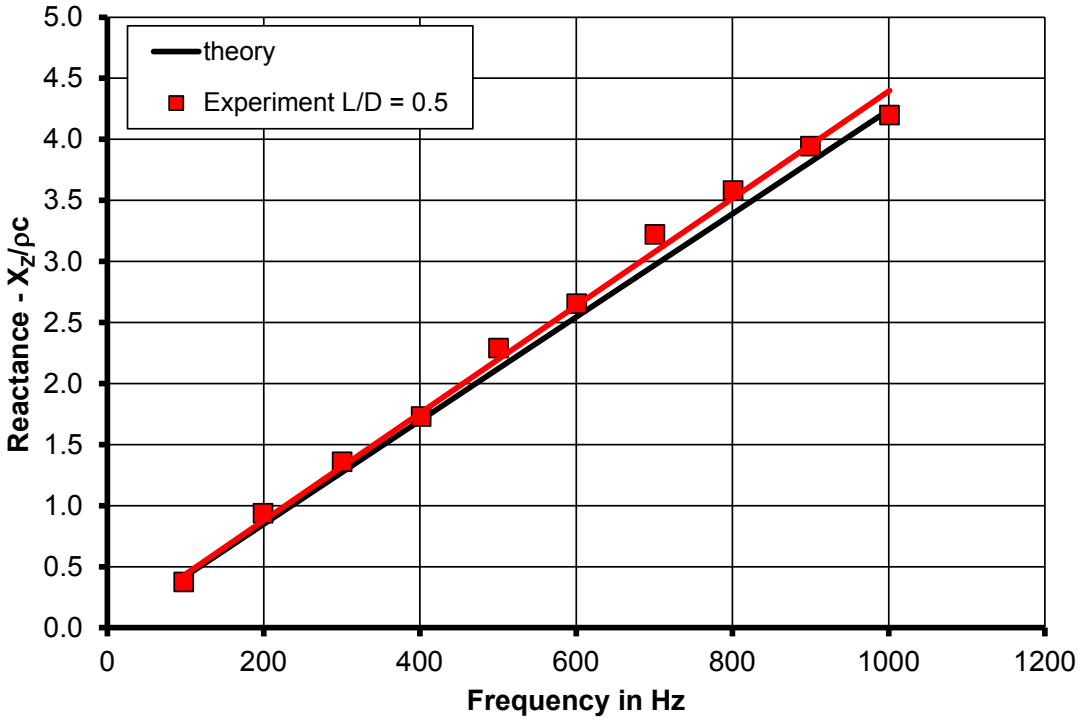

Figure 5.10: Orifice reactance measurement and comparison to theoretical values. Plate number 20, *L/D* = 0.5.

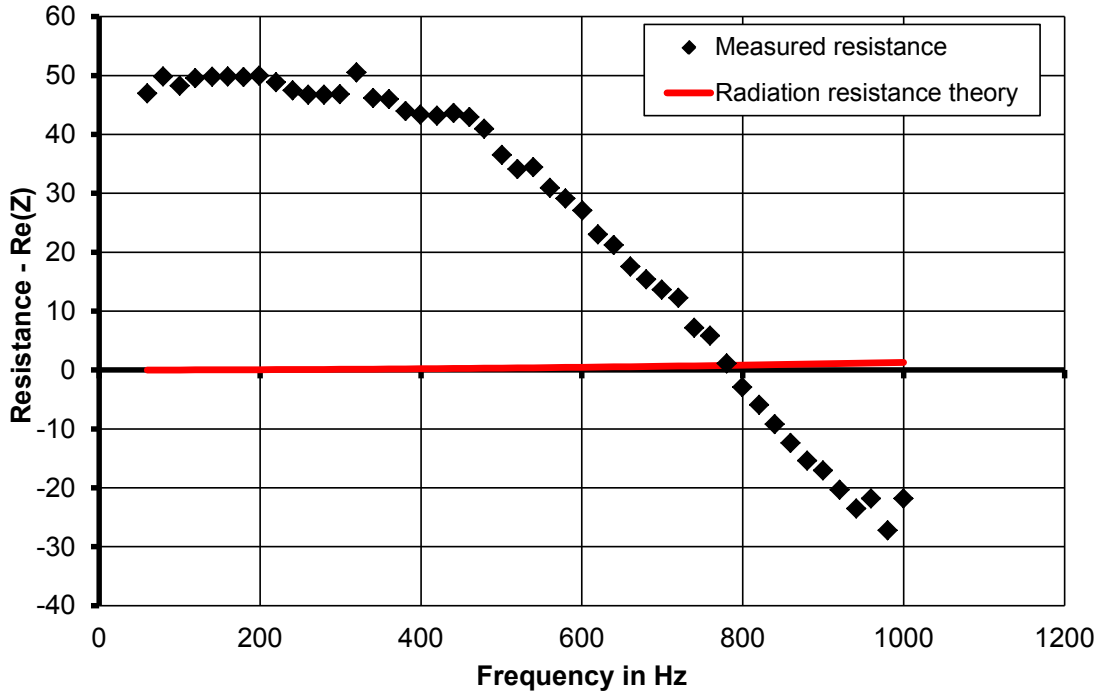

Figure 5.11: Comparison of measured resistance and theoretical radiation resistance. Plate number 20, *L/D* = 0.5.

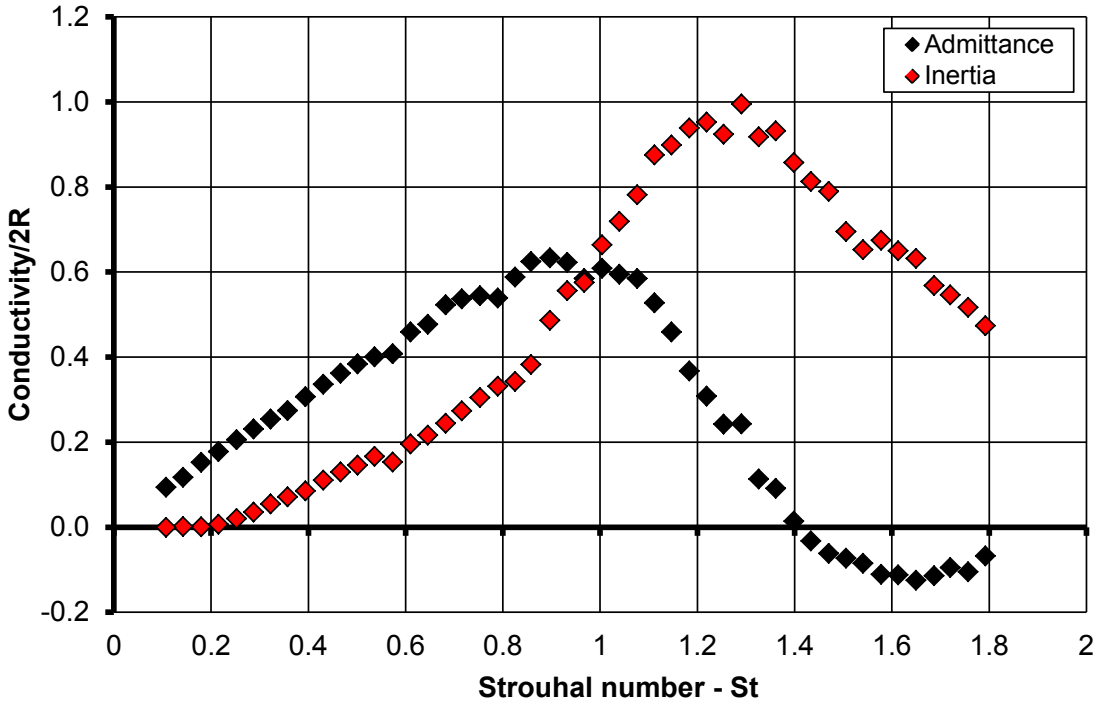

Figure 5.12: Measured Rayleigh Conductivity. Plate number 20, *L/D* = 0.5.

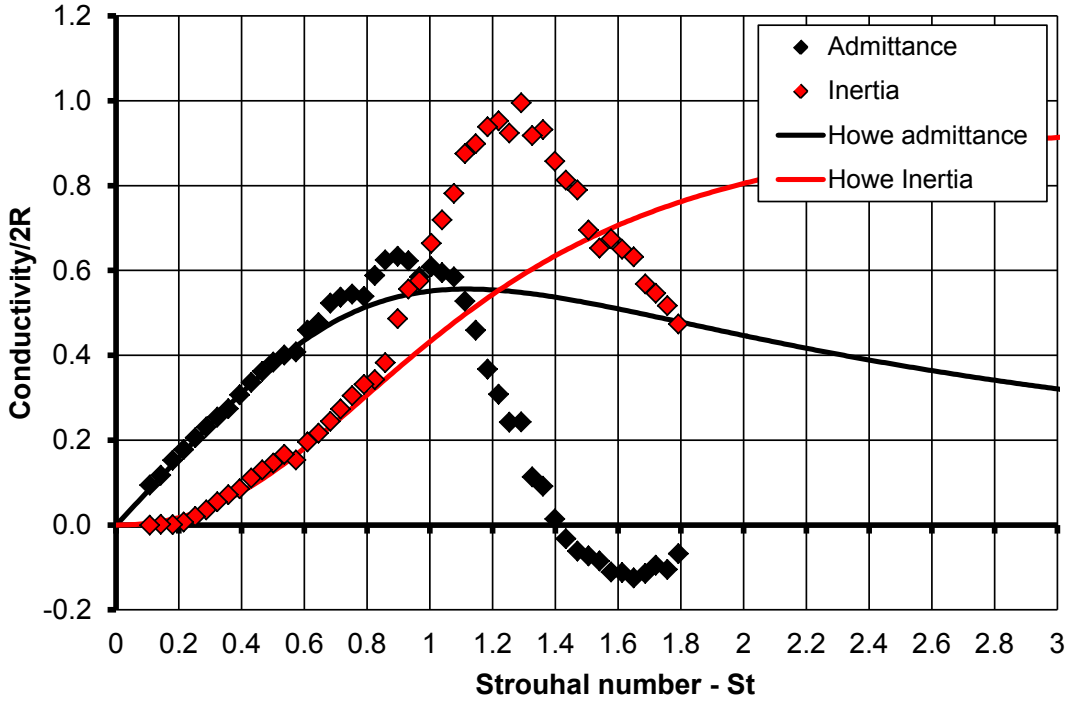

Figure 5.13: Measured Rayleigh Conductivity and comparison to Howe (1979b). Plate number 20, *L/D* = 0.5.

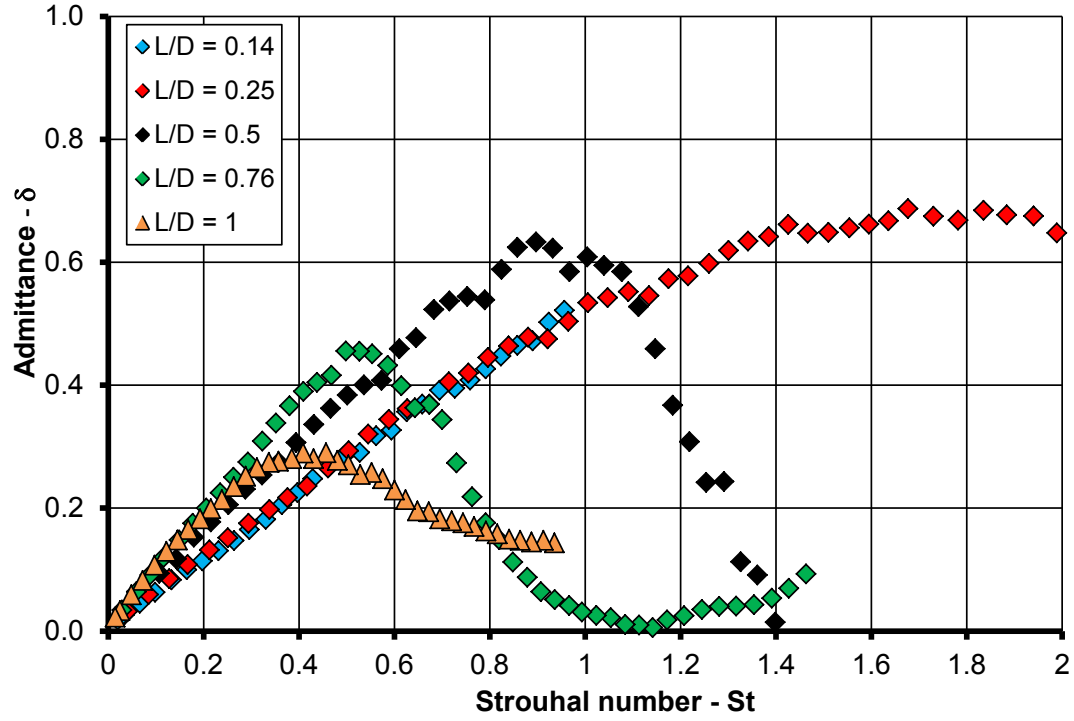

Figure 5.14: Measured admittance for plate numbers 18-22: 0.14 < *L/D* < 1.

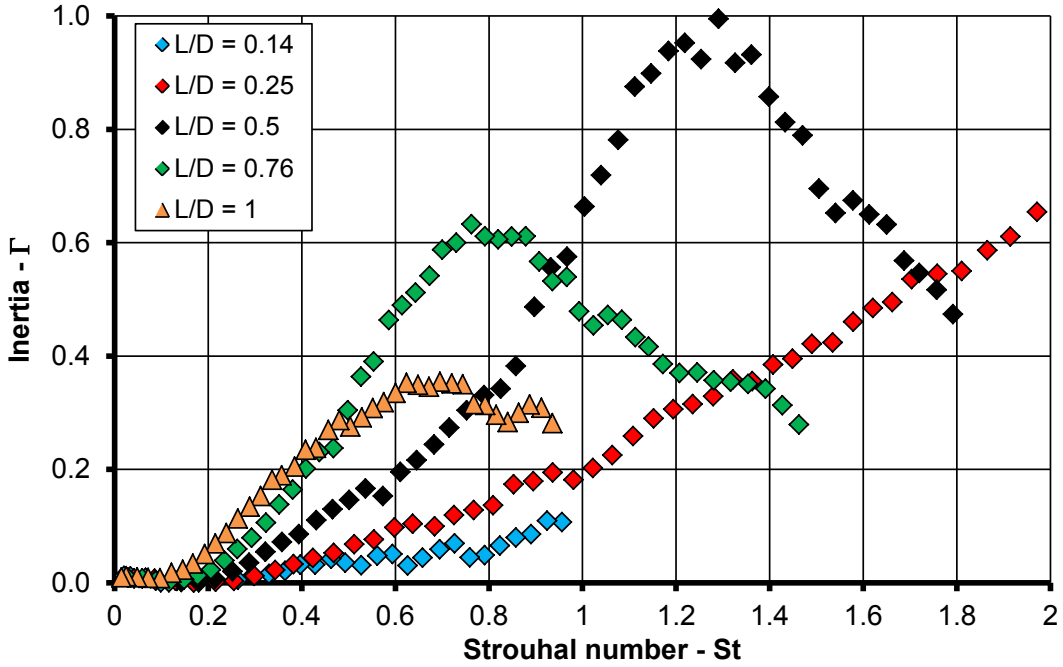

Figure 5.15: Measured inertia for plate numbers 18-22: 0.14 < *L/D* < 1.

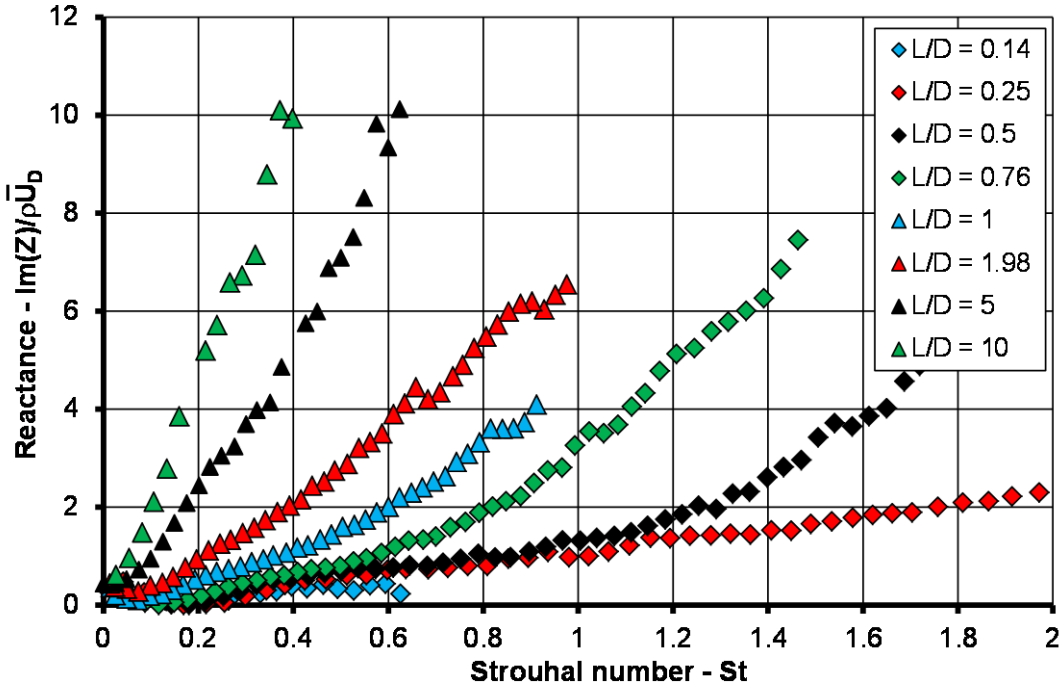

Figure 5.16: Orifice reactance for plate numbers 18-22, 24, 27 and 29.

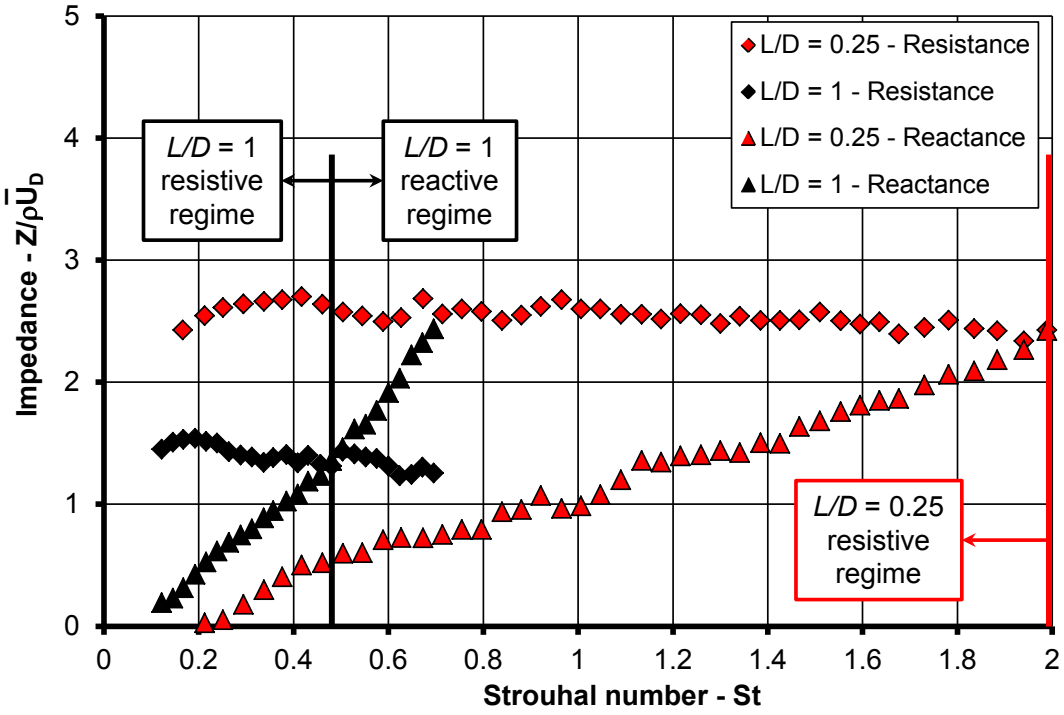

Figure 5.17: Orifice impedance for plate numbers 19 and 22: *L/D* of 0.25 and 1.

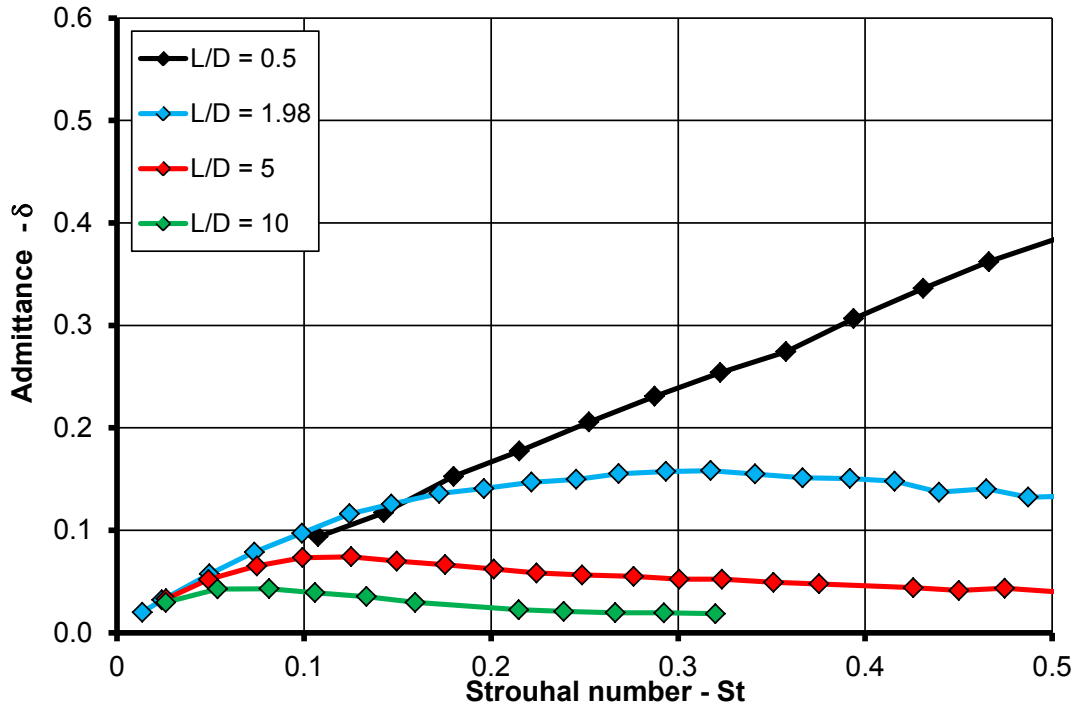

Figure 5.18: Measured admittance for plate number: 20, 24, 27 and 29.

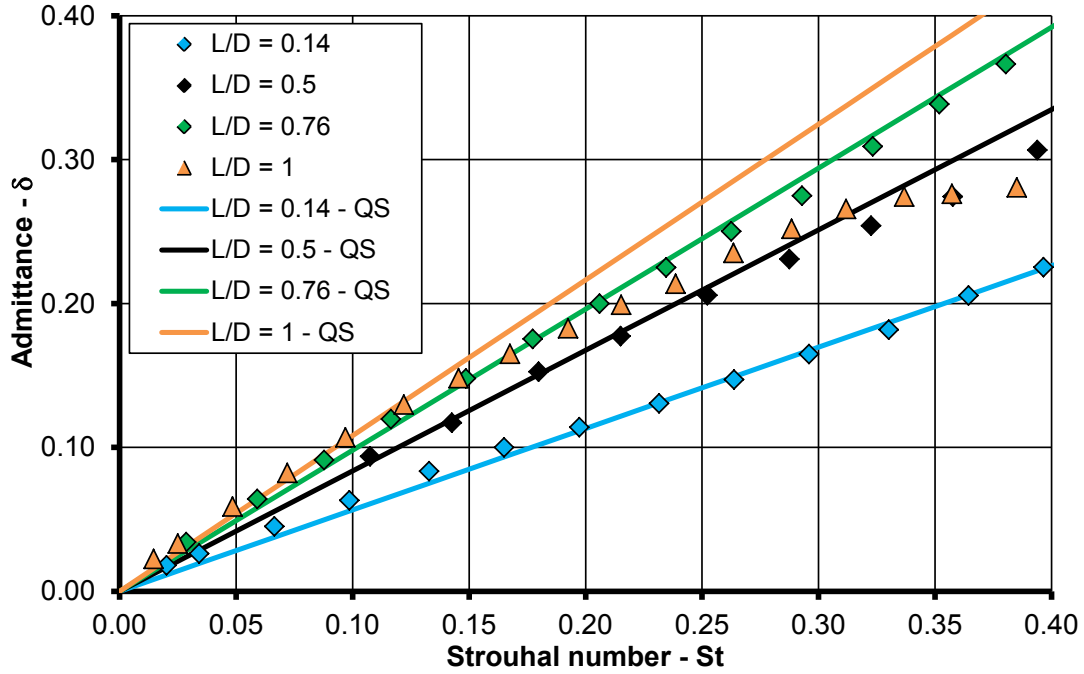

Figure 5.19: Measured admittance compared to calculated quasi-steady (QS) admittance. Orifice plate numbers: 18-22.

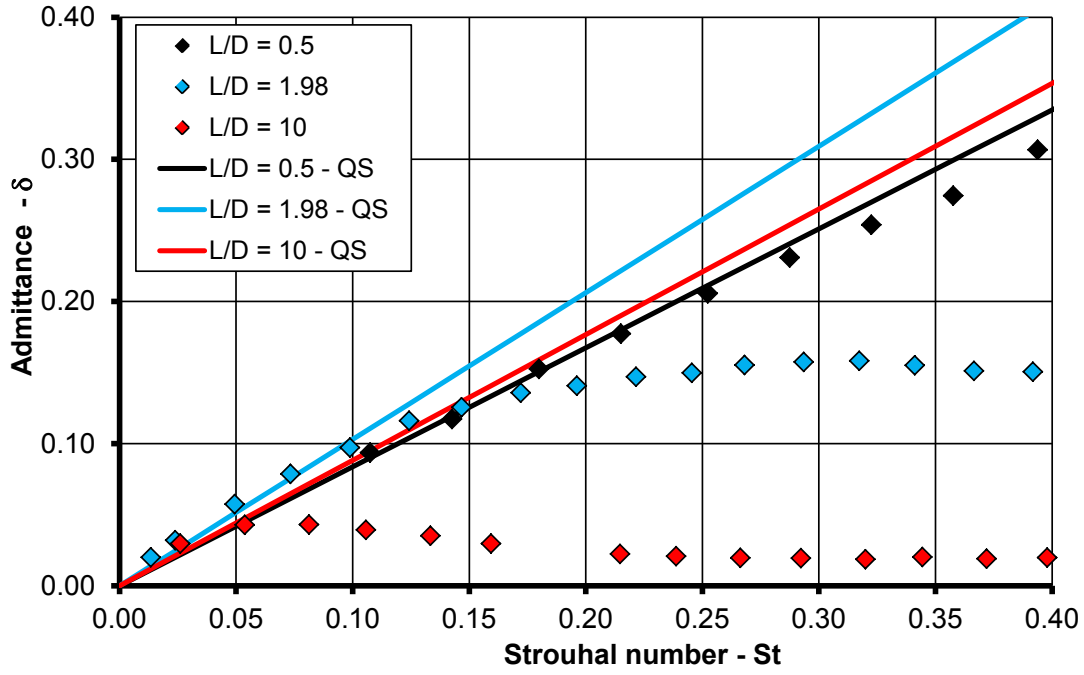

Figure 5.20: Measured admittance compared to calculated quasi-steady (QS) admittance. Orifice plate number: 20, 24 and 29.

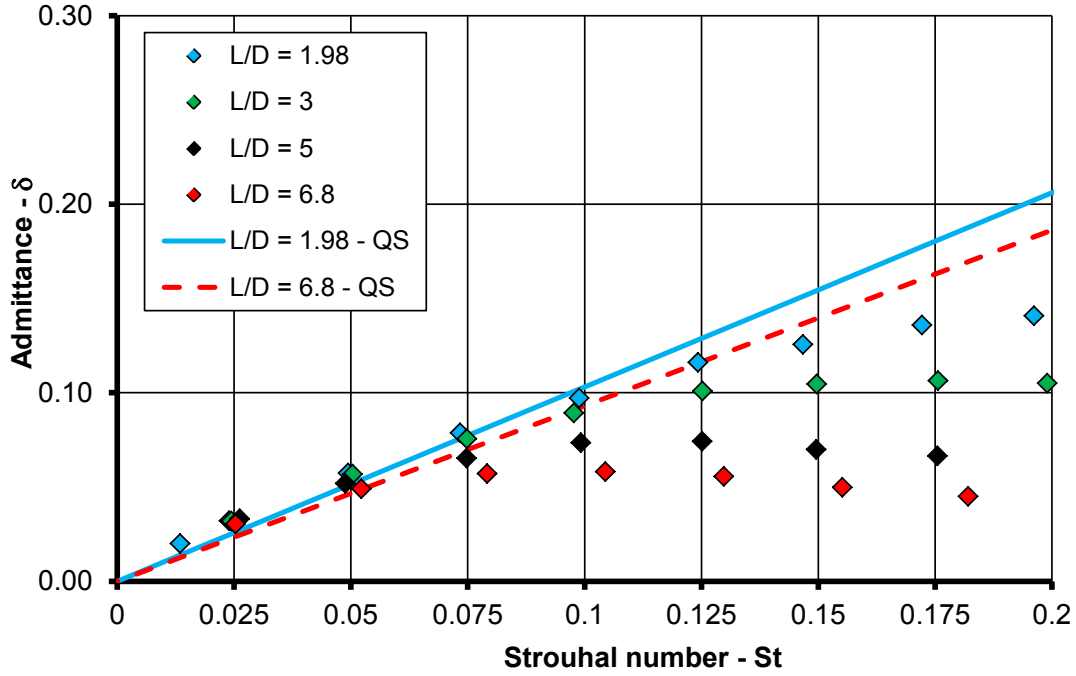

Figure 5.21: Measured admittance compared to calculated quasi-steady (QS) flow resistance. Effusion cooling geometries, orifice plate number: 24, 26-28.

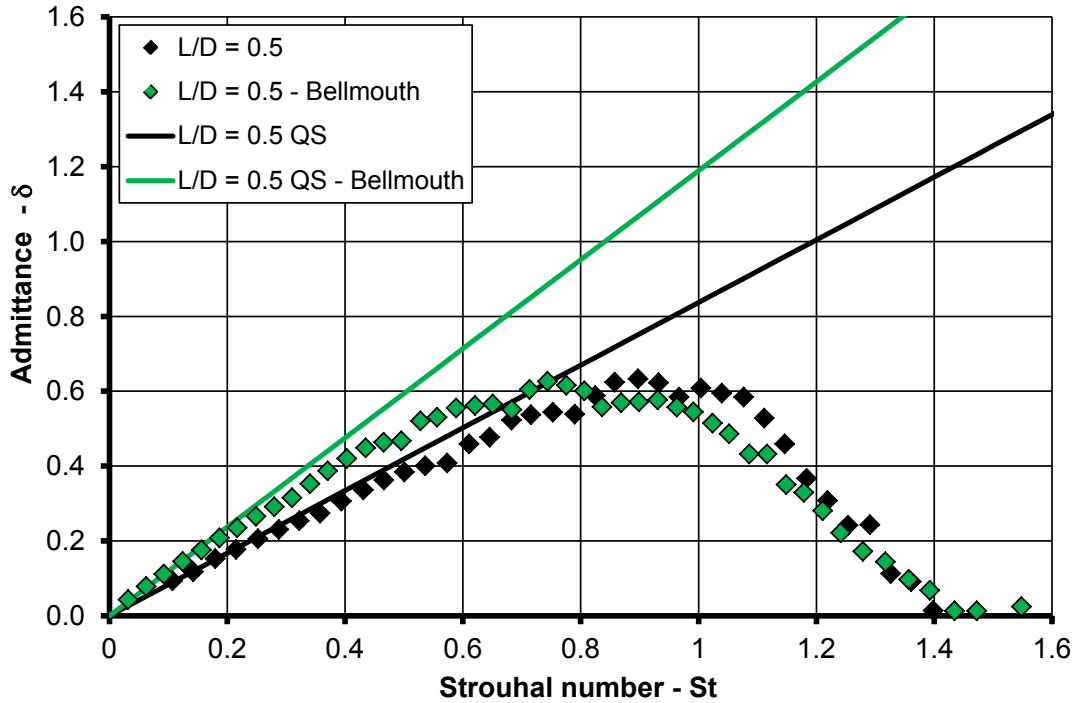

Figure 5.22: Admittance of Bellmouth orifice geometry compared to cylindrical orifice. Plate number 20 and 31.

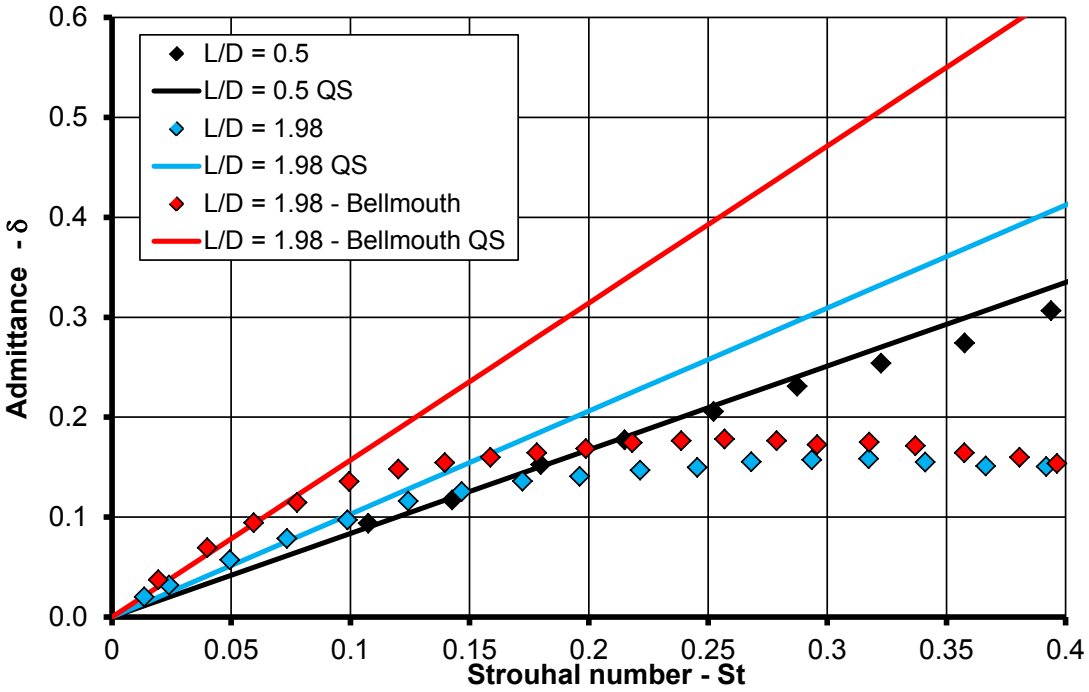

Figure 5.23: Admittance of Bellmouth orifice geometry compared to cylindrical orifice. Plate number 20, 24 and 33.

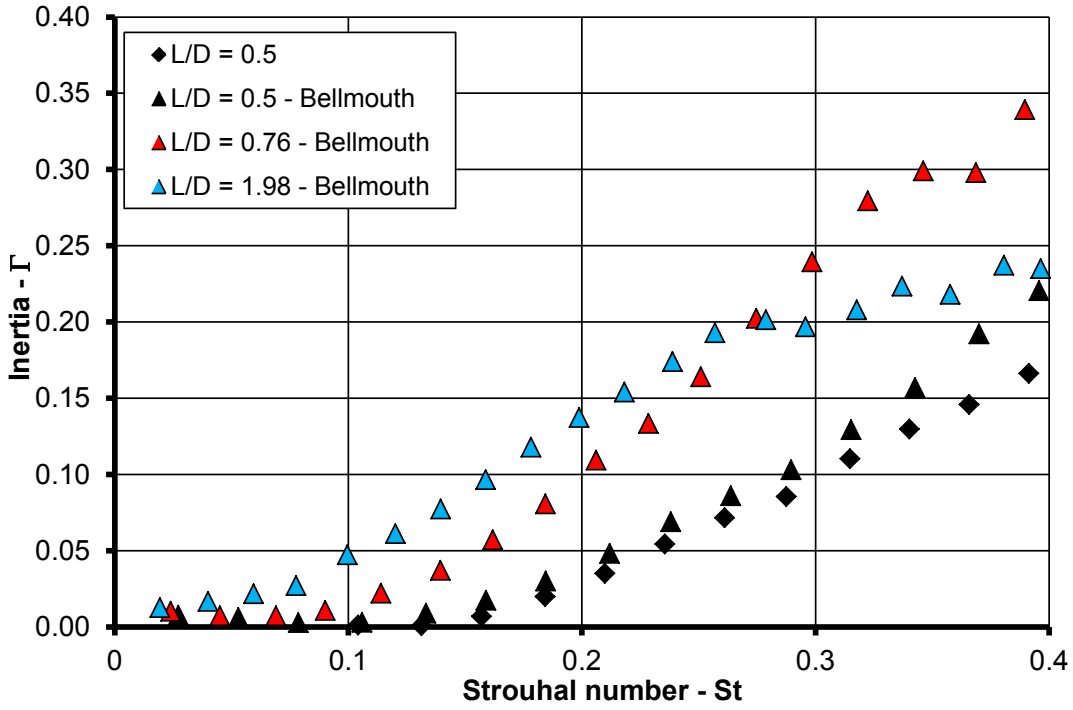

Figure 5.24: Inertia of cylindrical orifice *L/D* = 0.5 and comparison with Bellmouth orifice shape. Plate numbers: 20, 31, 32 and 33.

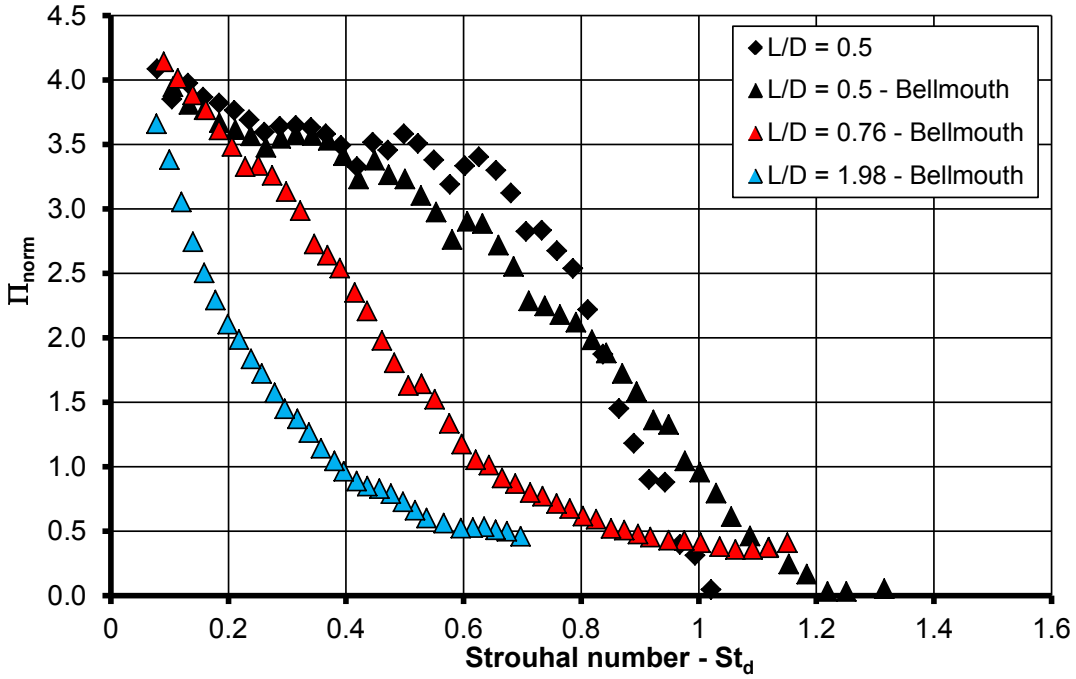

Figure 5.25: Normalised acoustic loss per unit mass flow, cylindrical orifice comparison with Bellmouth orifice shape. Plate numbers: 20, 31, 32 and 33.

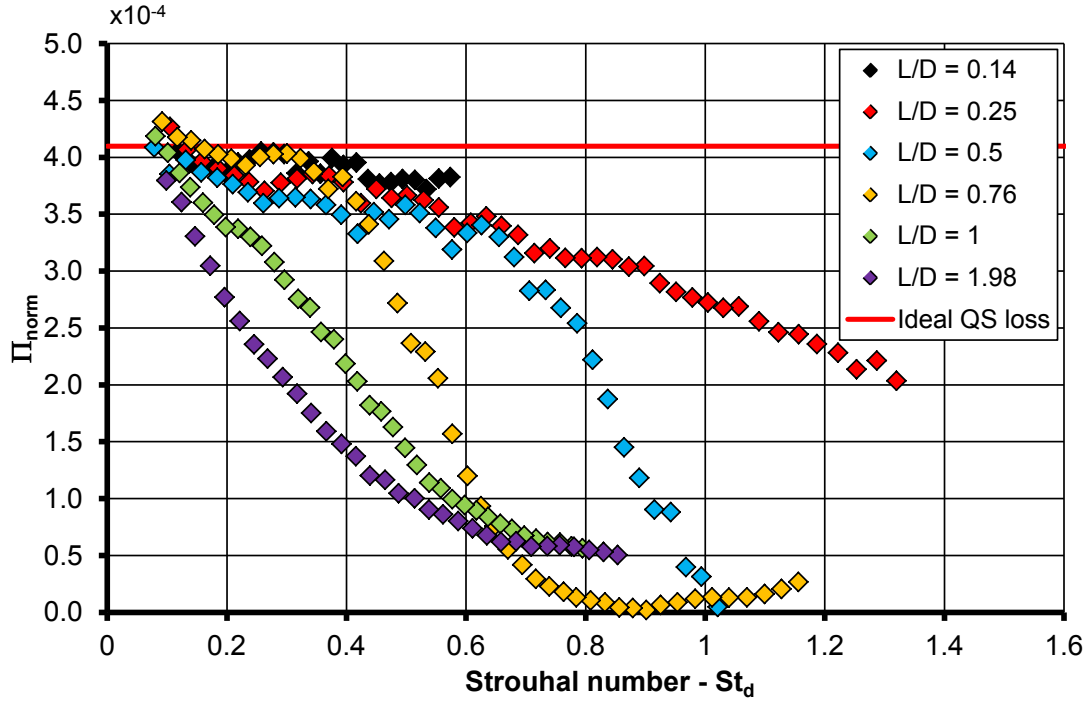

Figure 5.26: Normalised acoustic energy loss per unit mass flow. Plate numbers: 18-22 and 24, 0.14 < *L/D* < 1.98.

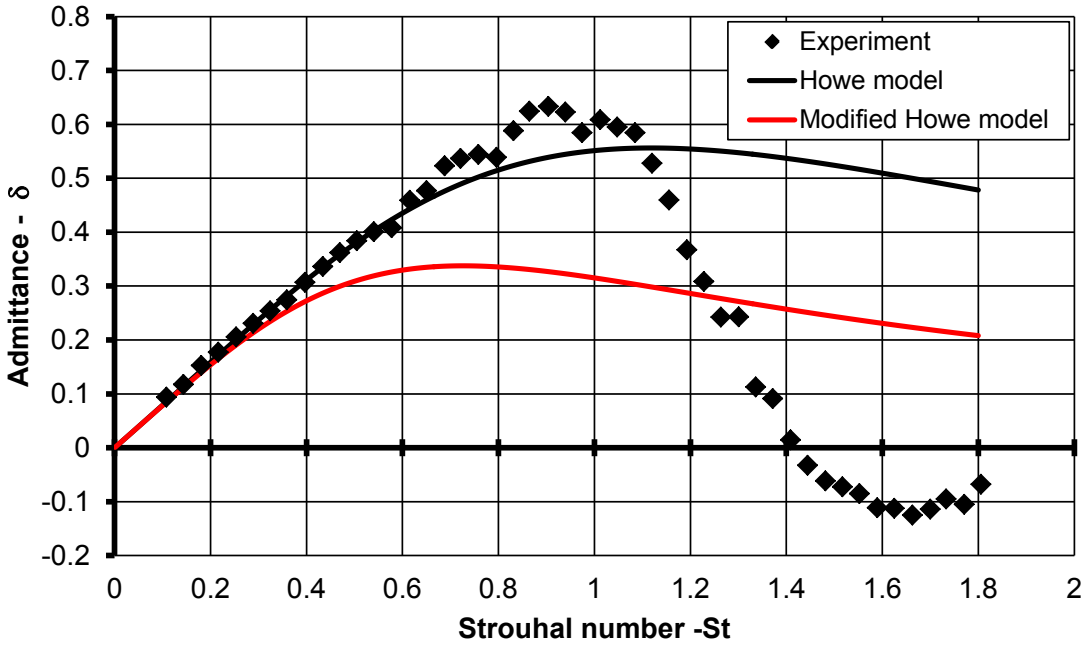

Figure 5.27: Comparison between measured and predicted admittance using Rayleigh Conductivity models. Plate number 20, *L/D* = 0.5

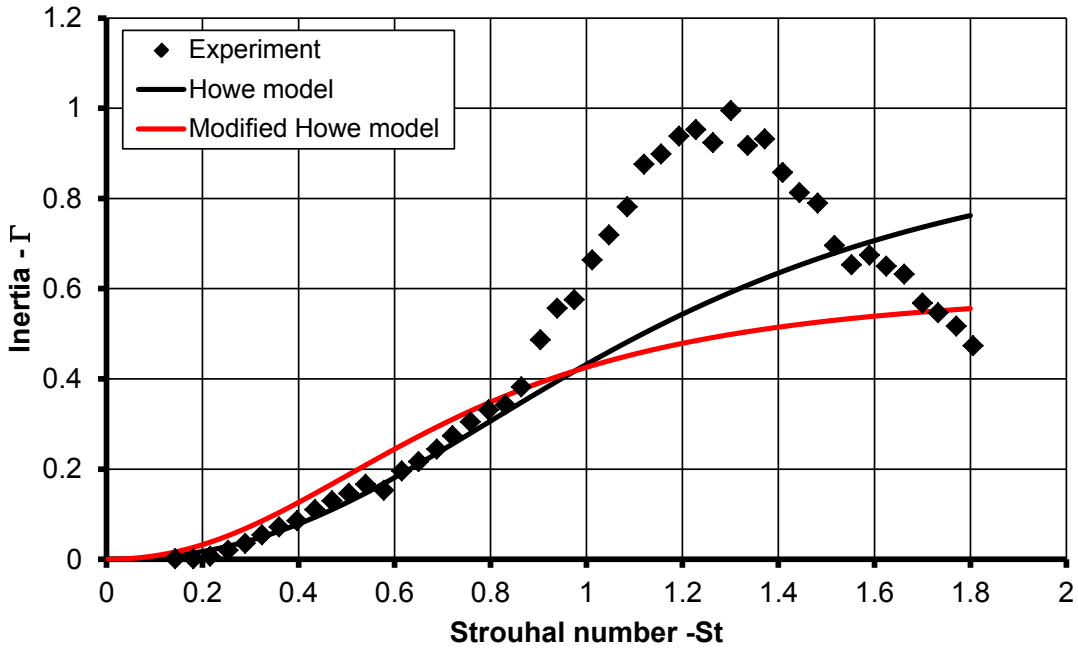

Figure 5.28: Comparison between measured and predicted inertia using Rayleigh Conductivity models. Plate number 20, *L/D* = 0.5.

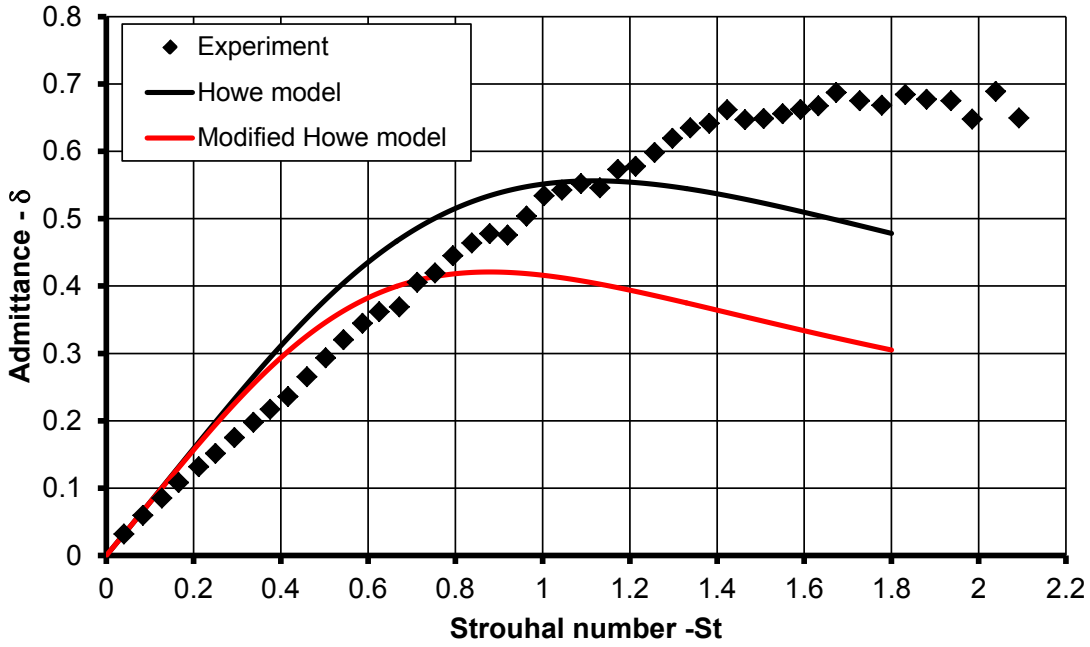

Figure 5.29: Comparison between measured and predicted admittance using Rayleigh Conductivity models. Plate number 19, *L/D* = 0.25.

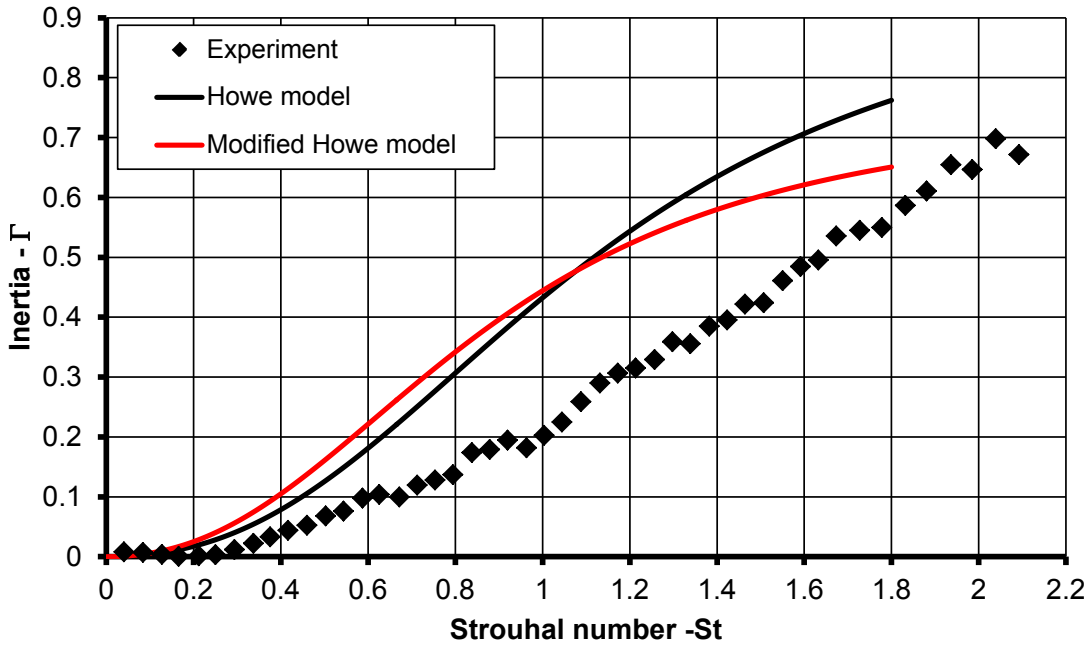

Figure 5.30: Comparison between measured and predicted inertia using Rayleigh Conductivity models. Plate number 19, *L/D* = 0.25.

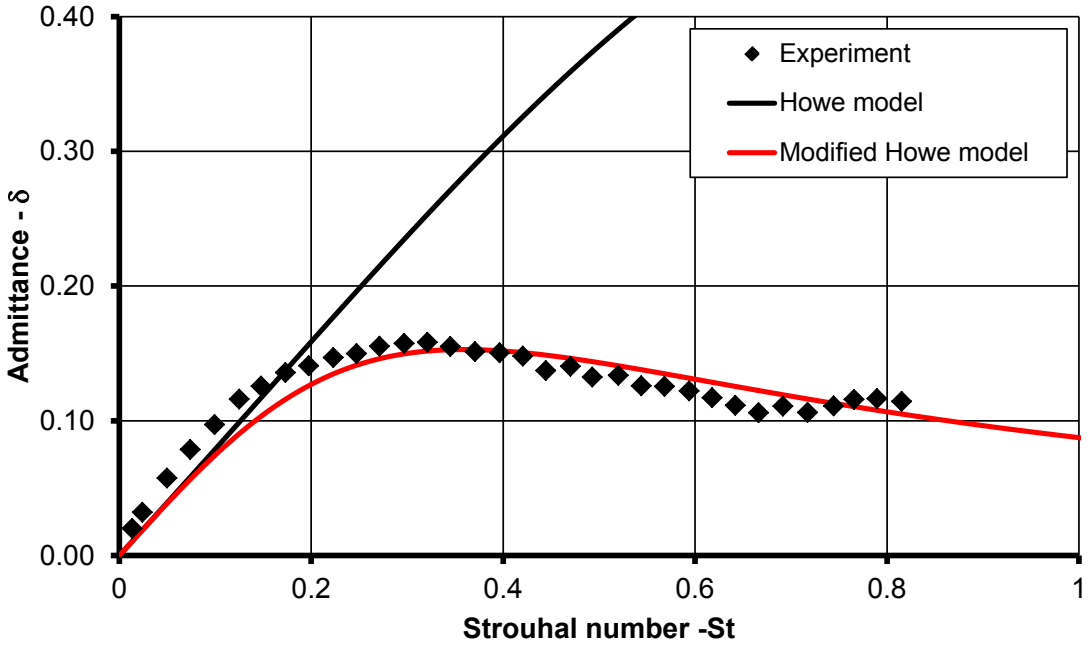

Figure 5.31: Comparison between measured and predicted admittance using Rayleigh Conductivity models. Plate number 24, *L/D* = 1.98.

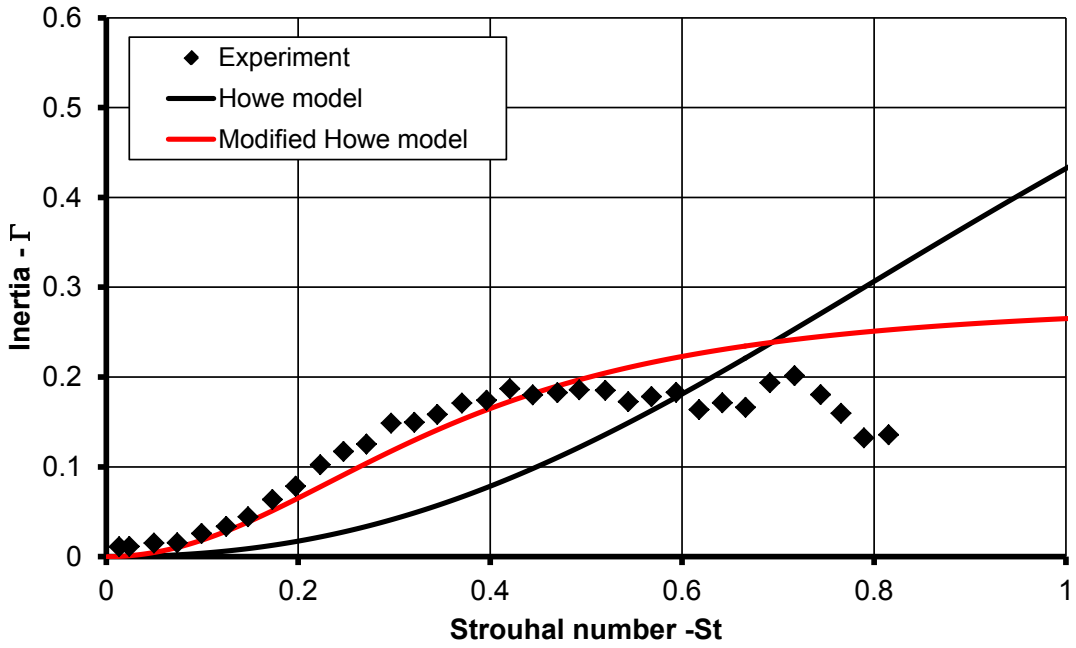

Figure 5.32: Comparison between measured and predicted inertia using Rayleigh Conductivity models. Plate number 24, *L/D* = 1.98.

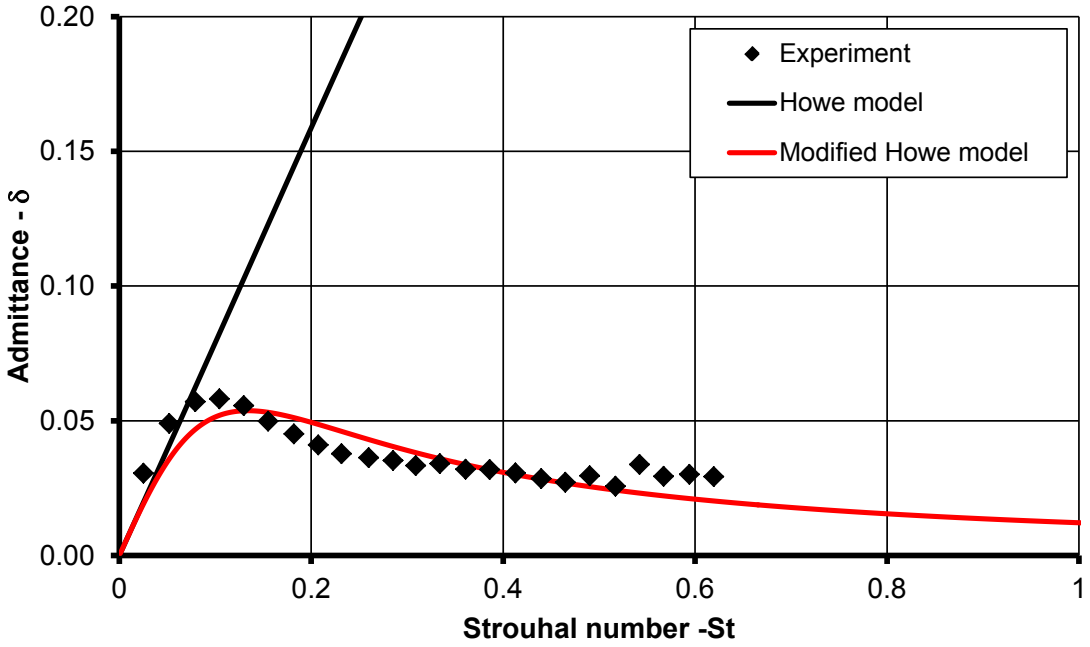

Figure 5.33: Comparison between measured and predicted admittance using Rayleigh Conductivity models. Plate number 28, *L/D* = 6.8.

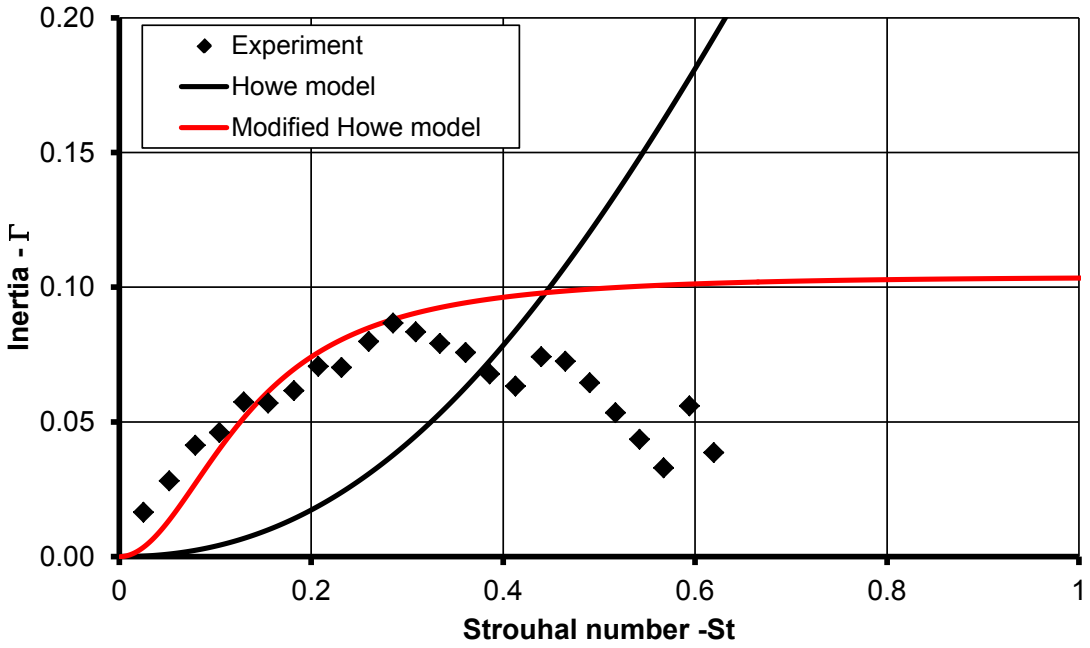

Figure 5.34: Comparison between measured and predicted inertia using Rayleigh Conductivity models. Plate number 28, *L/D* = 6.8.

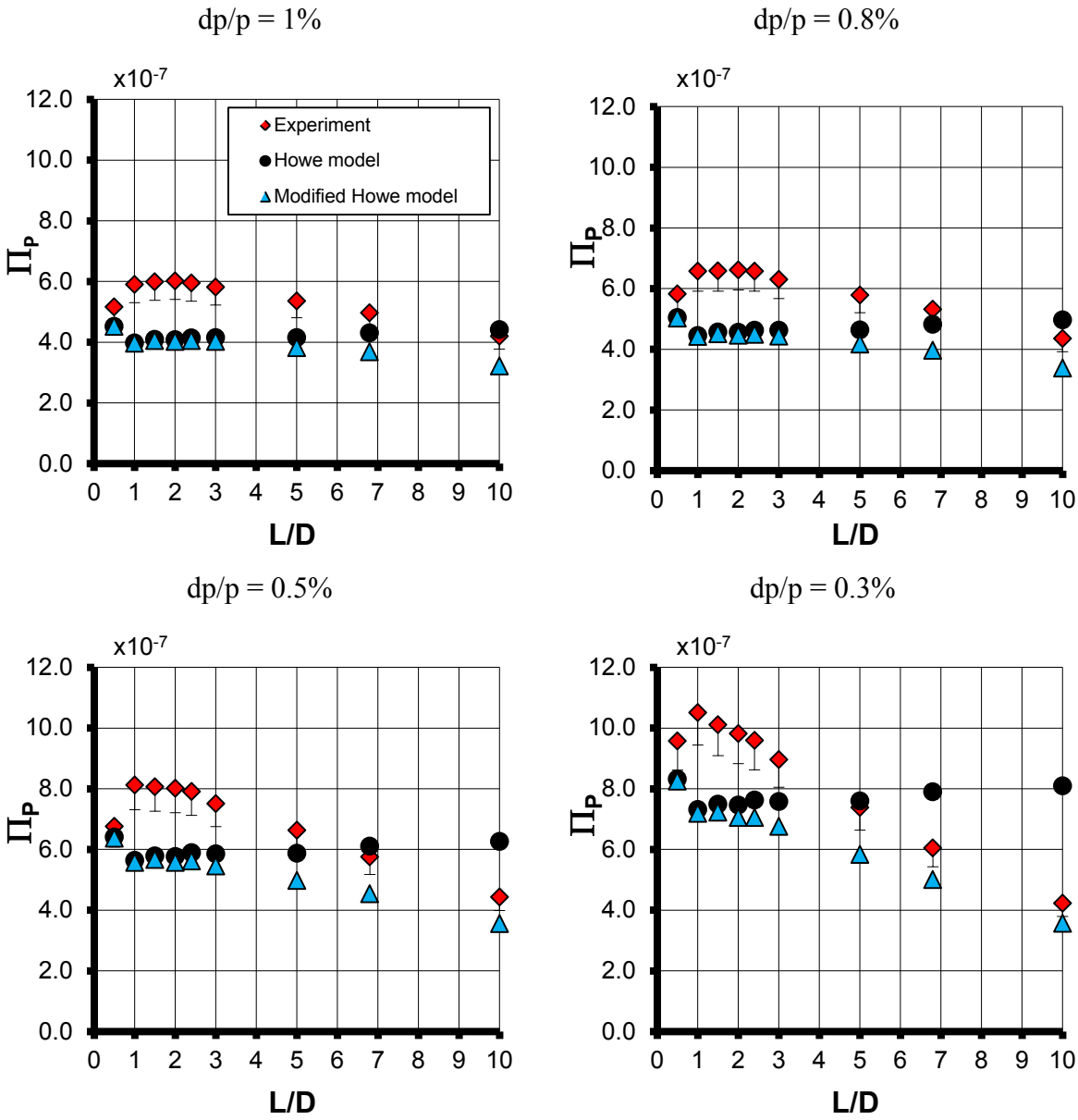

Figure 5.35: Comparison between experiments and Rayleigh Conductivity models from acoustic absorption coefficient measurements. Plate numbers: 3 – 11.

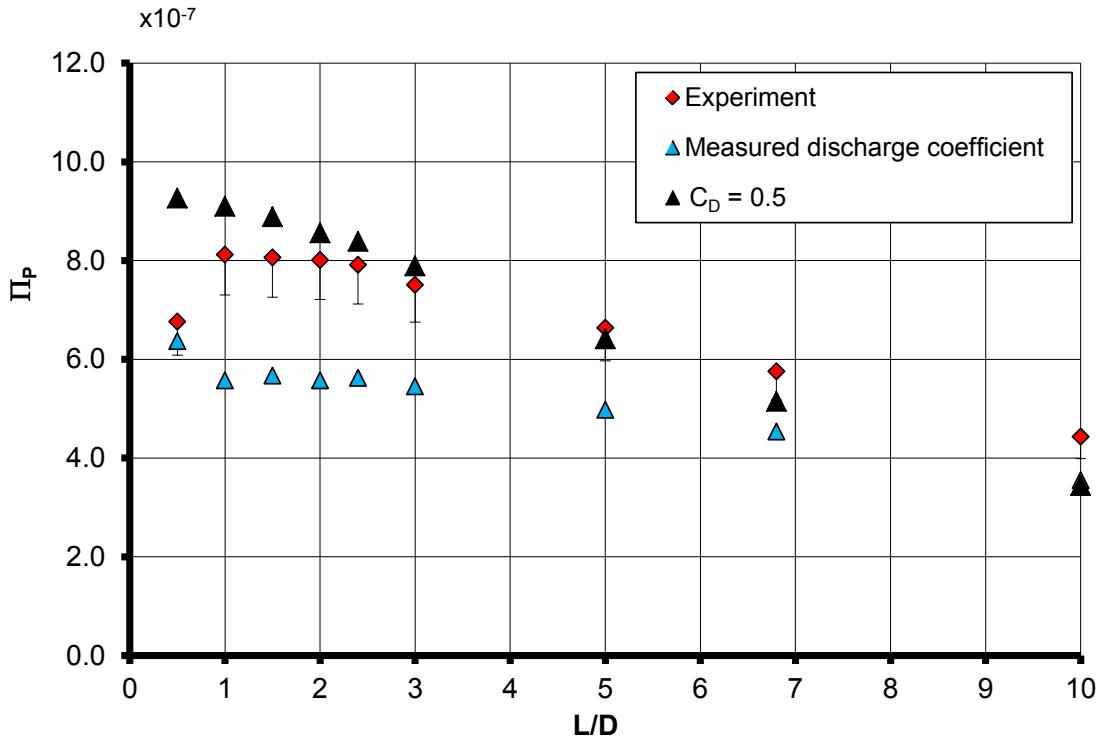

Figure 5.36: Effect of discharge coefficient on the comparison between experiments and the modified Howe model. Plate numbers: 3 – 11, *dp/p* = 0.5%.

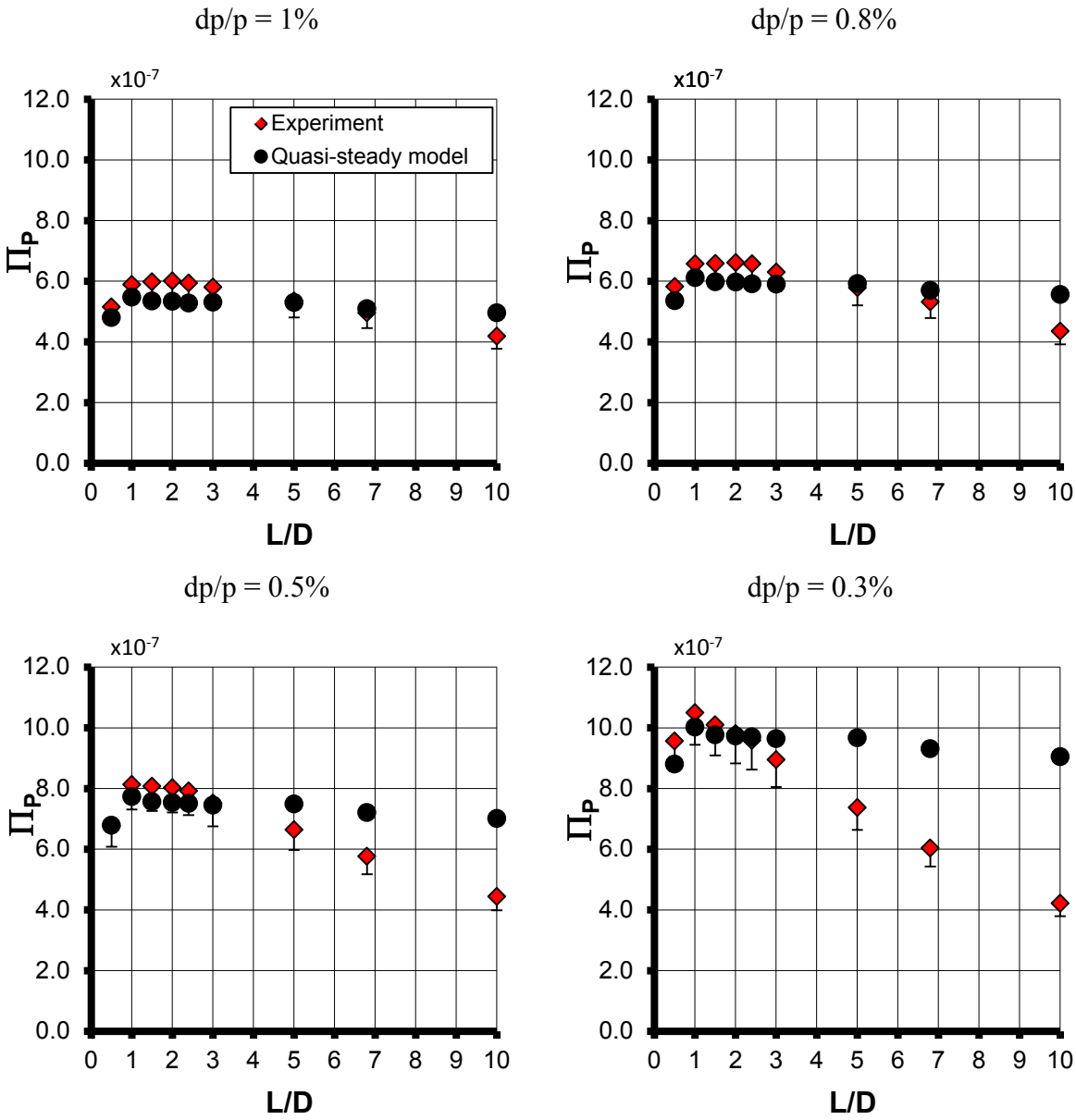

Figure 5.37: Comparison between experiments and quasi-steady admittance model for absorption coefficient experiments. . Plate numbers: 3 – 11.

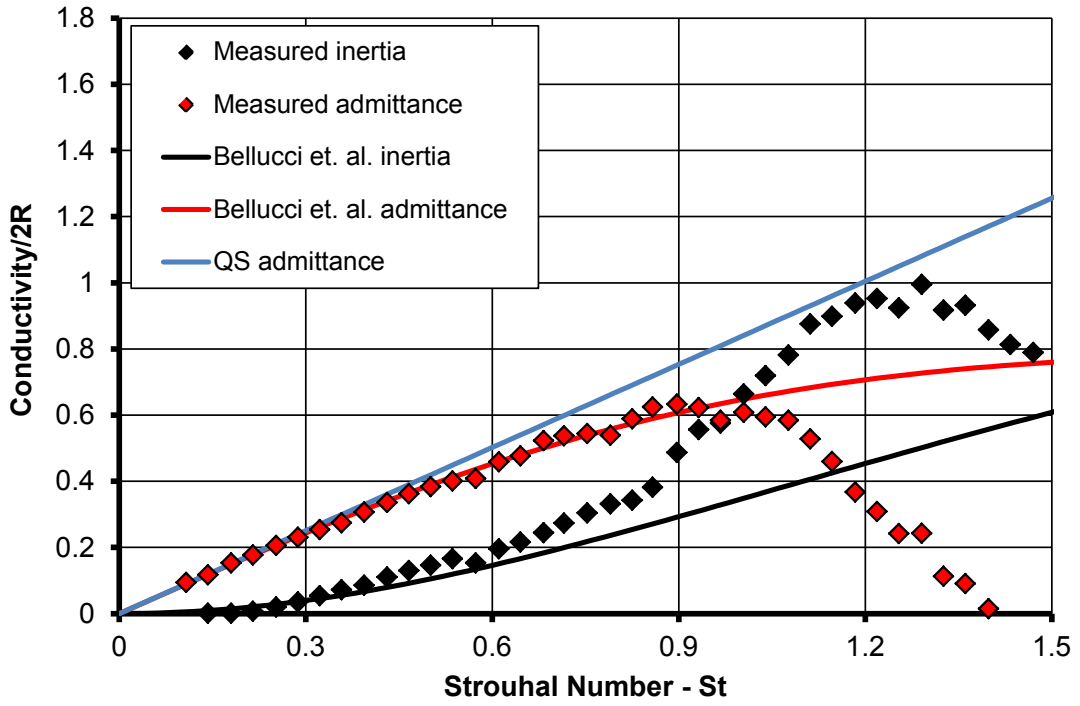

Figure 5.38: Predicted and measured Rayleigh Conductivity using theory based on Bellucci et. al. Plate number 20, *L/D* = 0.5

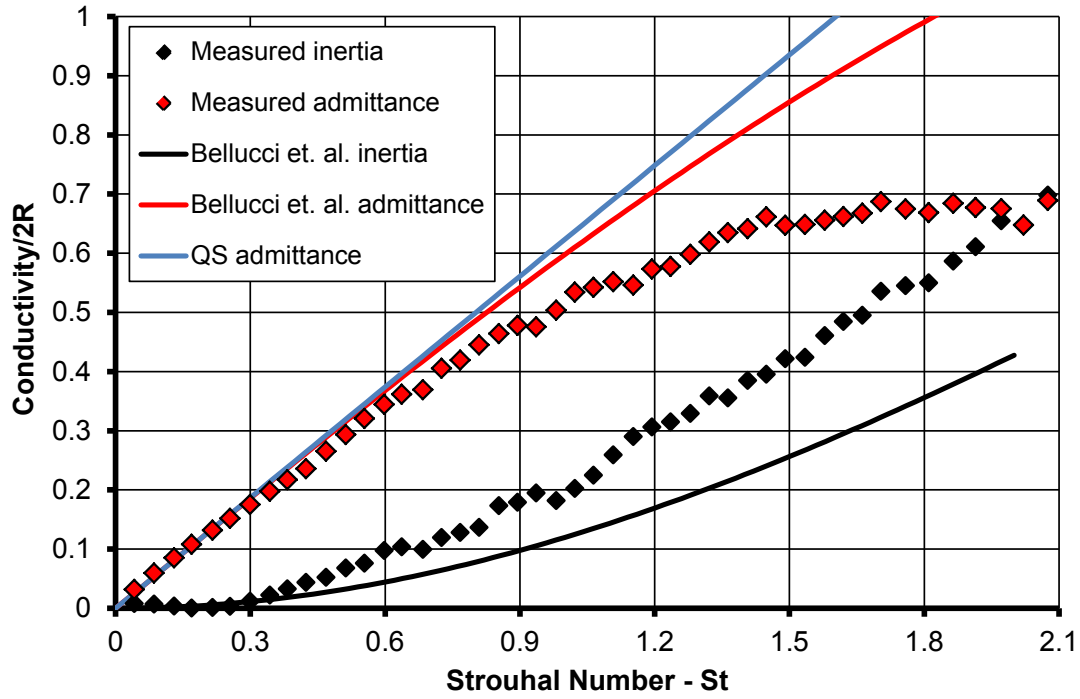

Figure 5.39: Predicted and measured Rayleigh Conductivity using theory based on Bellucci et. al. Plate number 19, *L/D* = 0.25.

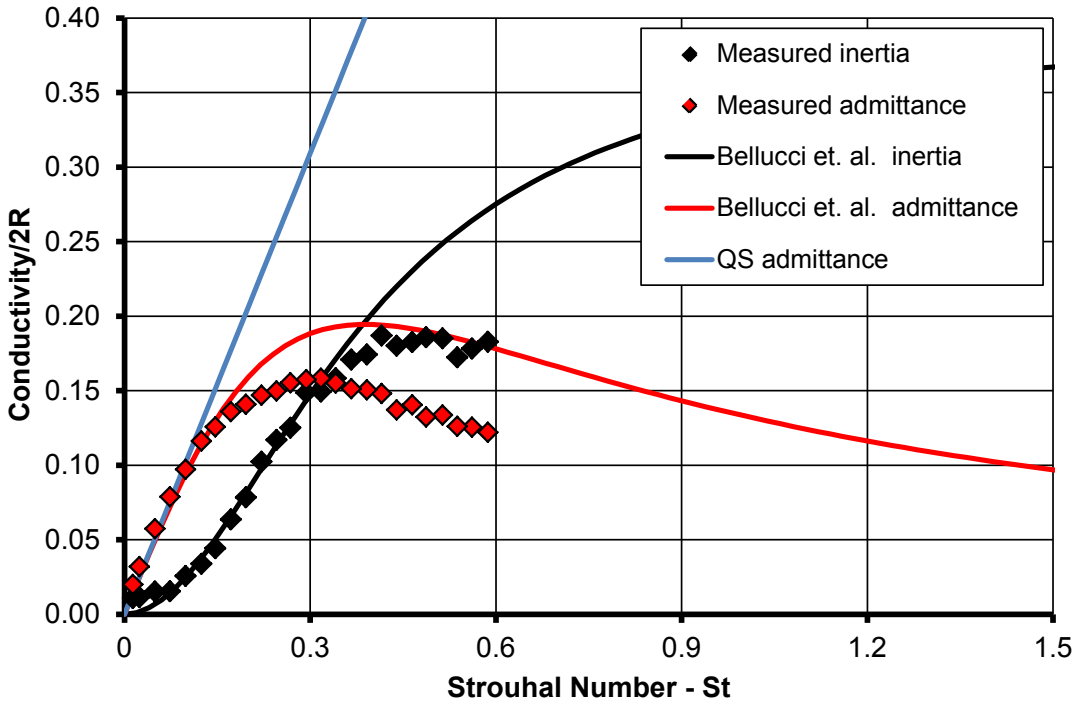

Figure 5.40: Predicted and measured Rayleigh Conductivity using theory based on Bellucci et. al. Plate number 24, *L/D* = 1.98

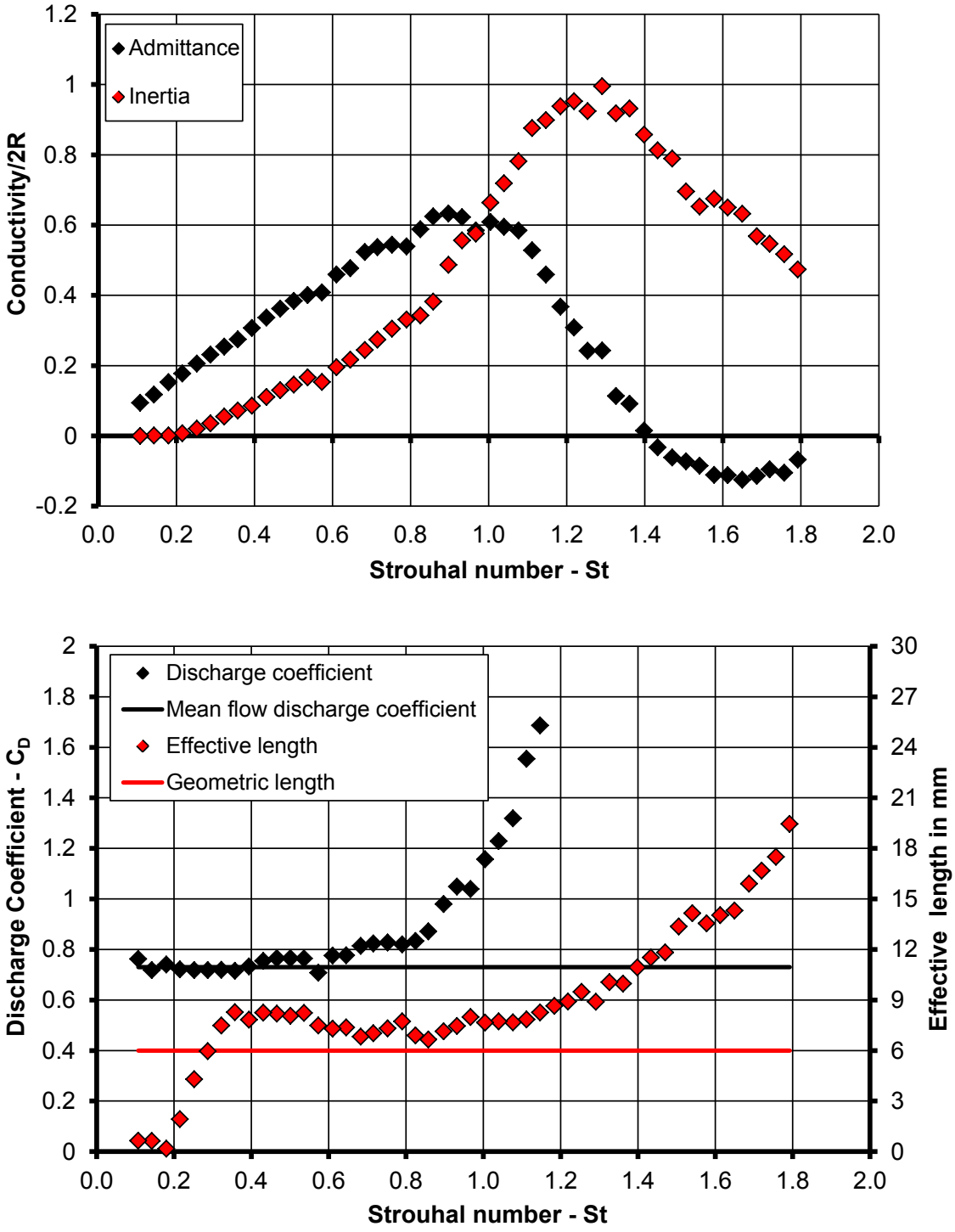

Figure 5.41: Experimental estimation of discharge coefficient and acoustic length correction, Plate number 20, *L/D* = 0.5.

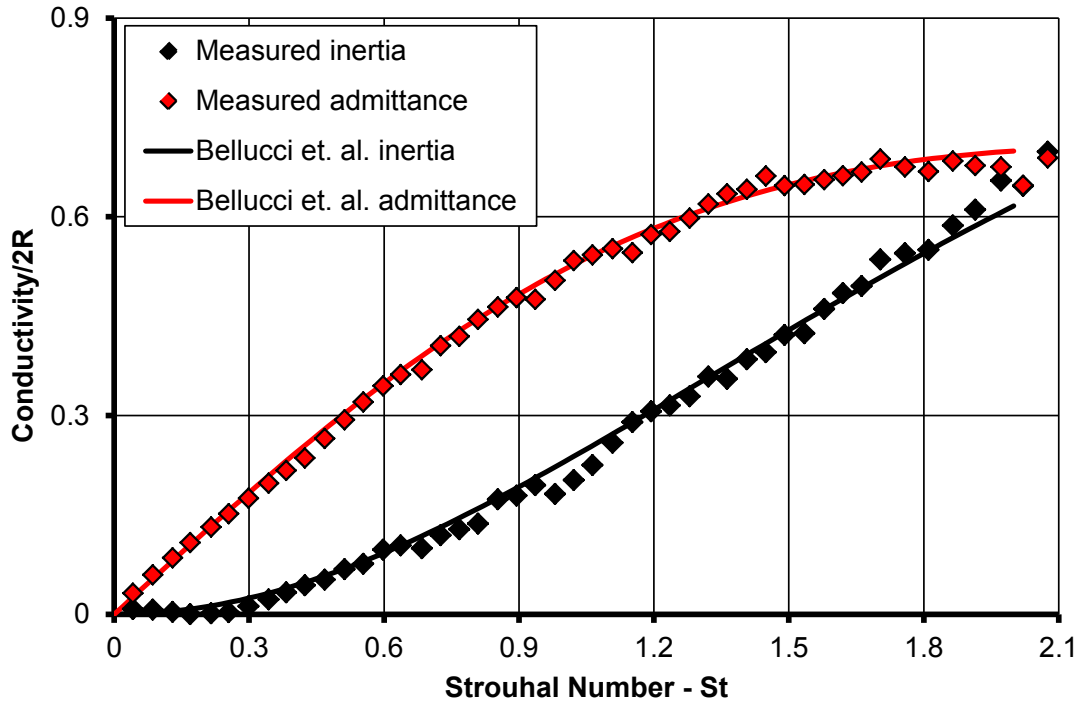

Figure 5.42: Comparison of Bellucci et. al. model using calculated discharge coefficient and length correction with experimental data. Plate number 19, *L/D* = 0.25.

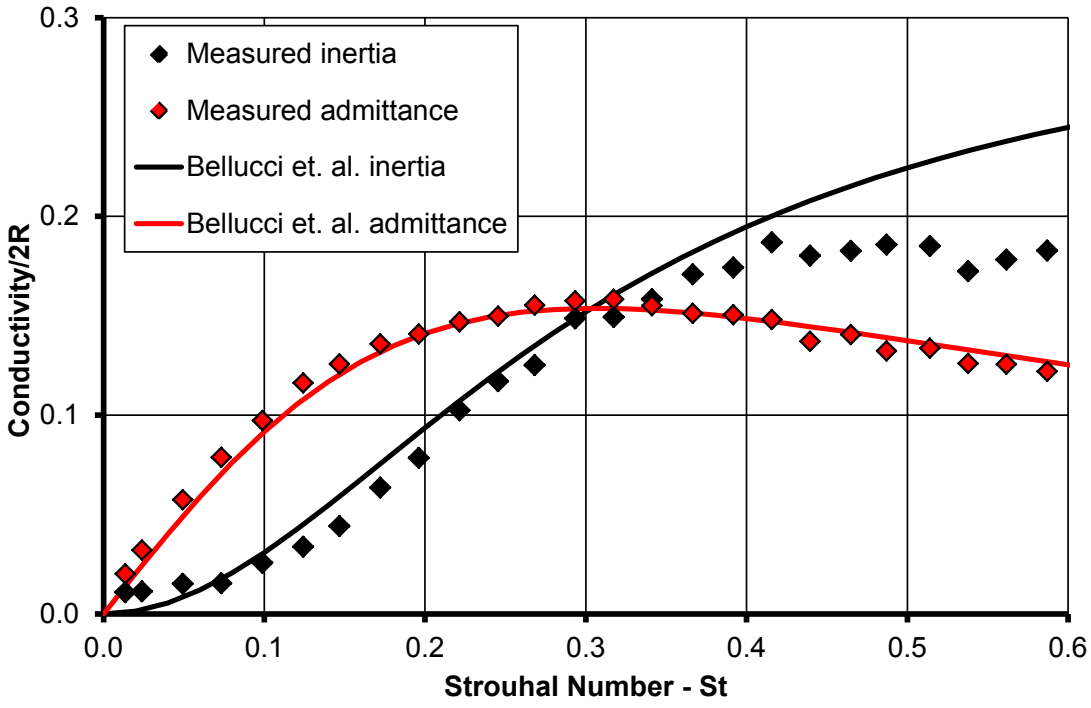

Figure 5.43: Comparison of Bellucci et. al. model using calculated discharge coefficient and length correction with experimental data. Plate number 24, L/D = 1.98.

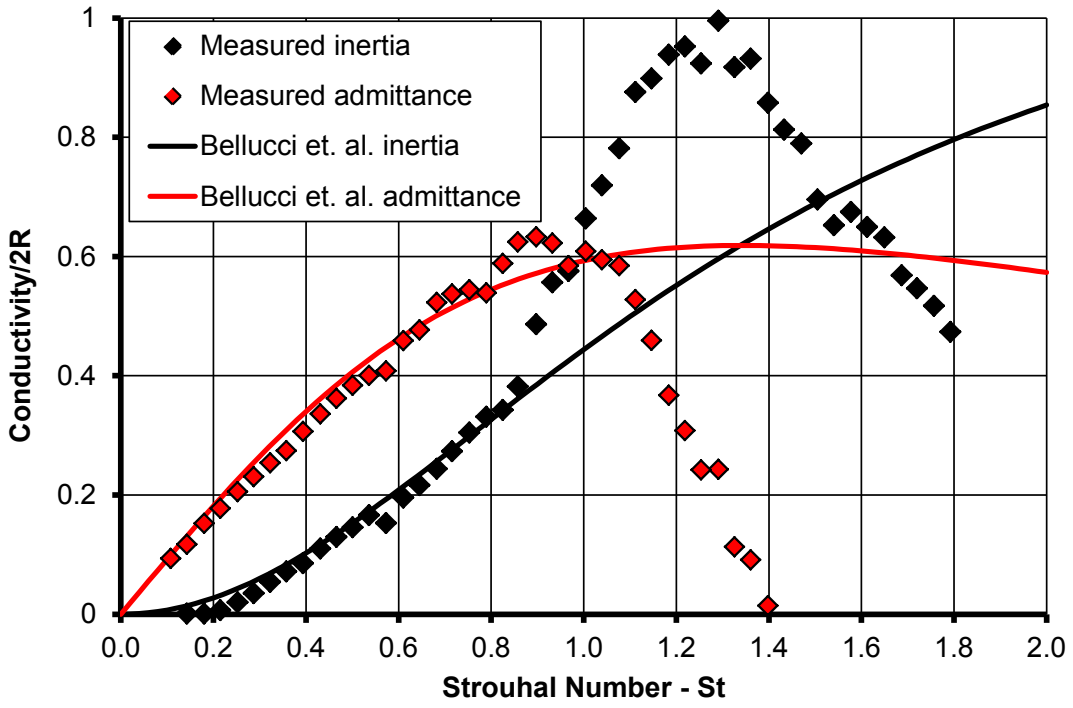

Figure 5.44: Comparison of Bellucci et. al. model using calculated discharge coefficient and length correction with experimental data. Plate number 20, *L/D* = 0.5

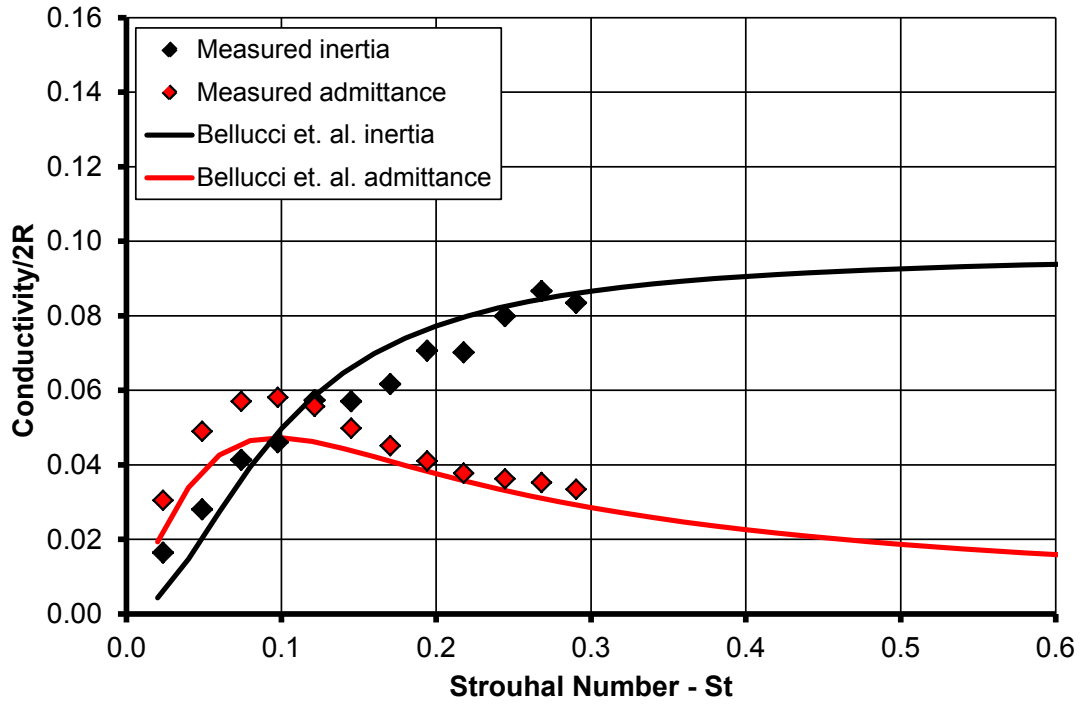

Figure 5.45: Comparison of Bellucci et. al. model using mean flow discharge coefficient and length correction with experimental data. Plate number 28, L/D = 6.8.

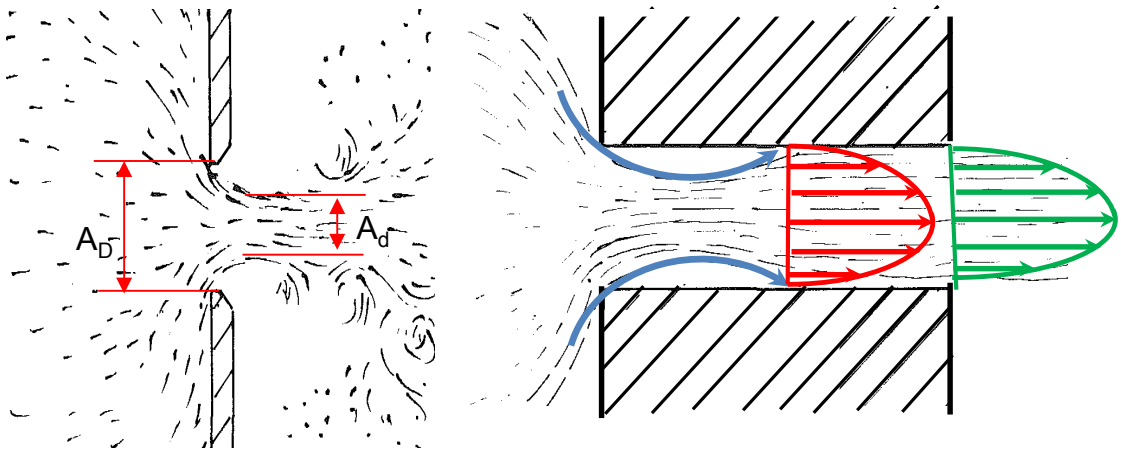

Short orifice with L/D < 2 Long orifice with L/D > 2

Figure 5.46: Short and long orifice mean flow profiles, underlying pictures from Hay and Spencer (1992)

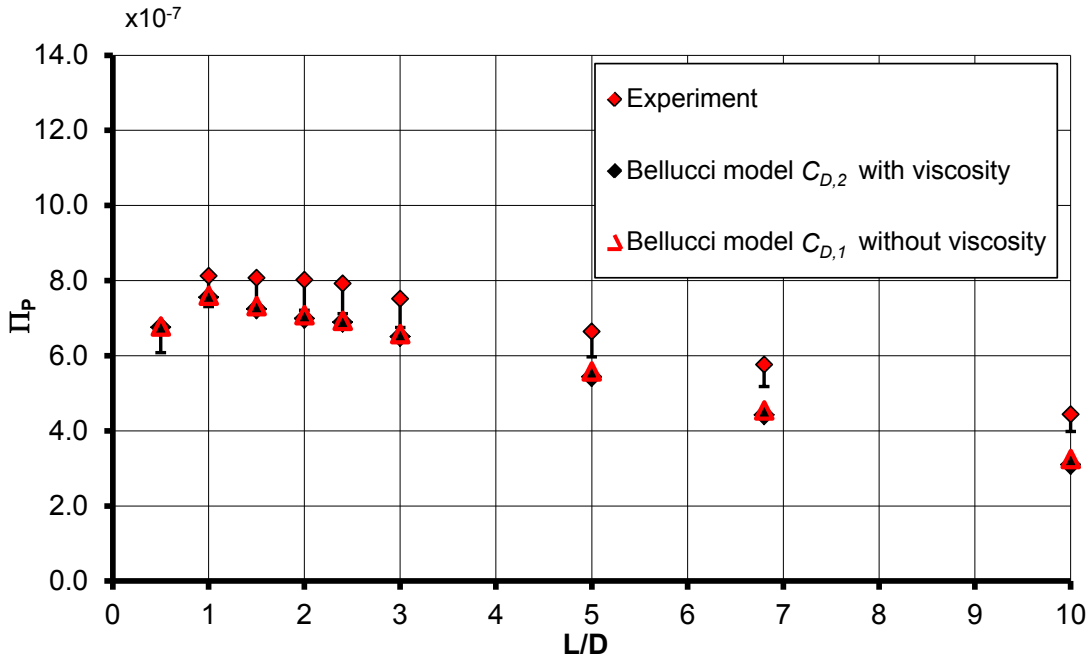

Figure 5.47: Comparison of Bellucci et. al. model using discharge coefficient and length correction from Table 5.1 with experimental absorption data, *dp/p* = 0.5% Plate numbers 3-11.

6 Acoustic Absorption Results – Non-Linear Acoustic Absorption

Experiments to investigate the non-linear absorption characteristic of a generic orifice were initially conducted without mean flow. The non-linear acoustic absorption is likely to be observed if the unsteady velocity oscillation amplitude is of the order, or larger than, the mean flow velocity. At these conditions the amount of absorption is dependent on the excitation amplitude. Note the acoustic pressure amplitudes remained within the linear acoustic regime (i.e. $\hat{p} << \overline{p}$) throughout the non-linear absorption experiments.

6.1 Optimum Non-Linear Acoustic Absorption

The experiments without mean flow have been conducted on the absorption coefficient test facility described in section 3.2.1. Figure 6.1 shows some example data from an acoustic absorption measurement for a test case without mean flow (orifice plate number 1). The absorption coefficient is shown with respect to the magnitude of the complex pressure amplitude travelling from the loudspeakers towards the orifice.

The results, as also shown and described in Rupp et. al. (2010), indicate that the absorption coefficient is a function of the incident acoustic energy (and hence absorption is non-linear). It can be seen that the absorption coefficient increases between 117dB and 135dB where the absorption coefficient reaches a value of 0.49. However, further increases in the incident energy results in a decrease in absorption. It could be argued that in excess of 135 dB the absolute amount of energy that can be absorbed by the flow field is constant, and so the absorption coefficient decreases due to the increasing incident energy. To investigate this behaviour further the acoustic energy loss is compared to the incident acoustic energy flux in Figure 6.2. The acoustic energy loss was estimated from the difference of incidental and reflected acoustic energy flux in the duct (equation (5.3)). At excitation amplitudes higher than 135 dB the acoustic energy absorbed still increases but at a rate which is less than the incident acoustic energy flux. It is the decreasing rate at which the energy is lost with increasing pressure

amplitude that is responsible for the observed decrease in absorption coefficient at high excitation levels (Figure 6.1).

This behaviour can be further expressed in terms of the measured impedance of the orifice and comparing it to the normalised acoustic energy loss in Figure 6.3. In this case the impedance is defined as the incident pressure amplitude onto the orifice divided by the orifice velocity amplitude (i.e. $Z = \hat{p}/\hat{u}_D$). Moreover a theoretical reactance as defined by Ingard and Ising (1967)

$$\mathrm{Im}(Z) = X_Z = \rho\omega\left(L + 1.7R\right) \tag{6.1}$$

is also included in Figure 6.3. It can be seen for small velocity amplitude (or incident pressure amplitudes) the measured reactance agrees with the theoretical prediction proposed by Ingard and Ising (1967). Furthermore it is shown that the reactance reduces with increasing velocity amplitude. On the contrary the resistance of the aperture is small at low pressure amplitudes and increases with increasing velocity amplitudes. In general this characteristic is the same as shown in Ingard and Ising (1967). The acoustic energy loss maximum occurs at a velocity amplitude of approximately 15 m/s. This optimum is also located in the vicinity where the resistance and reactance are equal (approximately at 12 m/s). Hence at velocity amplitudes below 12 m/s the aperture flow field is reactive (dominated by the inertia forces due to the acceleration of the fluid in the aperture) and for larger velocities (above 12 m/s) the flow field is dominated by the resistance effects (viscous effects in any shear layer of the aperture flow field). The resistance rapidly rises for larger velocity amplitudes whilst the reactance seems to reduce to an asymptotic value. The acoustic absorption increases for velocity amplitudes below 15 m/s. In this case the reactance reduces and thus the phase angle between pressure and velocity amplitude reduces. However as the resistance becomes significantly larger than the reactance the velocity amplitudes, relative to the incident pressure amplitude, reduce. Therefore the acoustic loss relative to the acoustic pressure amplitude decreases. This behaviour is confirmed in Figure 6.4 where the aperture velocity amplitude is shown relative to the incident pressure amplitude. Initially, at low amplitudes below 200 Pa, the velocity amplitude is increasing with a constant gradient to approximately 15 m/s ($p' \sim u'$). At this point the gradient changes and the velocity amplitude increases at a lower rate than the increase in pressure amplitude ($p' \sim u'^2$).

When the orifice behaviour is described in terms of impedance it can be seen that there are regions where (i) the reactance dominates, and (ii) the resistance dominates.

i) In reactance dominated regions the acoustic absorption increases with increasing pressure amplitudes and is associated with a reduced effective length of the orifice.

ii) In the resistance dominated region the acoustic absorption decreases with increasing pressure amplitude and is associated with an orifice resistance. This means the rate of increase in velocity amplitude relative to the incident pressure amplitude is reduced.

6.2 Influence of Orifice Length upon Non-Linear Acoustic Absorption

In a conventional combustion system various orifice geometries can be found with hole length-to-diameter ratios ranging from *L/D* of 0.5 to 10. Figure 6.5 shows the non-linear acoustic absorption characteristic for such orifice geometries. It can be seen that the acoustic absorption increases with decreasing orifice length. Moreover the optimum absorption occurs at smaller incident wave amplitudes as the *L/D* ratio decreases. If the length of the orifice increases the inertial forces, due to the acceleration of a larger fluid mass inside the orifice, must also increase and a reduction in velocity amplitude is therefore expected. In terms of impedance this indicates an increased reactance associated with the orifice flow field. This can be seen for the example of two orifice plates with *L/D* of 0.5 and 1.98 in Figure 6.6. Note this data has been measured with 125 Hz forcing frequency. Nevertheless the basic principles explained with this data do also apply for the data shown in Figure 6.5. As expected the measured impedance shows an increased reactance for the longer aperture. Ultimately this leads to reduced velocity amplitudes for the longer aperture as shown in Figure 6.7. Moreover the occurrence of the optimum acoustic absorption coefficient appears at larger excitation pressure as the cross-over point from the reactive regime to the resistive regime appears at higher pressure amplitudes (Figure 6.6).

As already mentioned non-linear acoustic absorption is governed by vortex ring structures shed from the rim of the orifice. With this in mind it is interesting to note the

observations of several authors whose investigations were not directly linked to that of acoustic absorption as highlighted and discussed in Rupp et. al. (2010). For example Gharib et. al. (1998), Linden and Turner (2001) or Jabbal et. al. (2006) have studied the formation of vortex rings and the optimum conditions whereby the circulation in the vortex core obtains a maximum value. It was not possible to increase the maximum circulation of the vortex ring, and hence the kinetic energy associated with the vortex ring, despite increasing the fluctuating velocity in the orifice used to form the rings. Instead secondary flow features, e.g. wakes, start to absorb the energy and become visible in the flow field. More details of the fluid dynamic properties of vortex rings can be found in section 2.3. A formation number has been proposed which is a measure of the velocity amplitude for a vortex ring which is based on the orifice diameter D and the fluid slug length during half of the excitation cycle (see also equation 2.12):

$$\frac{L_0}{D} = \frac{\int_0^{T/2} u_D'(t)\,dt}{D} \tag{6.2}$$

Using the measured velocity amplitude in the aperture of the orifice and assuming a sinusoidal time variation of this amplitude based on the fundamental forcing frequency leads to the definition of the vortex ring formation number:

$$\frac{L_0}{D} = \frac{\int_0^{T/2} |\hat{u}_D| \sin(\omega t)\,dt}{D} = \frac{2|\hat{u}_D|}{\omega D} = \frac{|\hat{u}_D|}{\omega R} = \frac{1}{St'}. \tag{6.3}$$

This approach is equivalent to assuming a top hat velocity profile issuing from the aperture. To first order, the higher order harmonics can be ignored, as the amplitude of the harmonic frequencies are greatly reduced compared to the fundamental mode (Ingard (1970)). It can be seen that the formation number is inversely proportional to a Strouhal number based on the unsteady velocity amplitude. Authors investigating optimum vortex ring formation, e.g. Gharib et. al. (1998) or Jabbal et. al. (2006) state $L_0/D = 4$ or $St' = 0.25$ for optimum vortex ring formation. The data presented in Figure 6.5 is now shown in Figure 6.8 relative to the vortex ring formation number L_0/D. It can be seen the optimum acoustic absorption does not coincide with one vortex ring

formation number. This becomes clearer in Figure 6.9 which shows the vortex ring formation number at the maximum acoustic absorption. It can be seen that the location of the optimum acoustic absorption does not collapse on the optimum vortex ring formation number of four. The literature concerned with optimum vortex ring formation (e.g. Gharib et. al. (1998), Aydemir et. al. (2012)) uses a pulsatile nozzle flow which is characterised by a top hat velocity exit profile from the nozzle which generates the vortex ring and unsteady jet flow. Moreover the influence of the flow field reactance was not of interest for the mentioned experiments. The apparatus used in Jabbal et. al. (2006), where a loudspeaker is exciting the flow field of an orifice with $L/D = 1$, is the closest to the application in this work. Jabbal et. al. (2006) showed the optimum vortex ring formation of L_0/D of four which is close to the estimated formation number in this work which shows a vortex ring formation number of five in Figure 6.9. The data suggests that the formation number with changing L/D is showing two regimes as the formation number at optimum acoustic absorption linearly varies with L/D. The slope of the linear behaviour changes around an L/D ratio of one. This could be influenced by the flow behaviour of the aperture. For example for short apertures the assumption of a top hat velocity profile might not be valid. Hence this could change the slope of the shown characteristic in Figure 6.9. As the flow reattaches within the longer L/D apertures the generated exit profile could look more like a fully developed flow profile. Furthermore the increased viscosity for long L/D ratios (larger than one) might also effect the vortex ring formation. However, as already mentioned the optimum absorption occurs in the region where the acoustic resistance and reactance are of equal value. Due to the increased reactance for longer orifice plates (e.g. as shown in Figure 6.6) the occurrence of the optimum absorption occurs at larger velocity amplitudes and therefore larger formation numbers. In the synthetic jet experiments of Gharib et. al. (1998) or Jabbal et. al. (2006) it was important to maximise the amount of energy transferred into the vortex core. For the purpose of the work in this thesis it is important to maximise the kinetic energy flux of the aperture flow field at a given incident pressure amplitude. The unsteady kinetic energy of the aperture flow field in the acoustic measurements is described with the acoustic resistance and reactance where both parameters in the non-linear absorption regime are a function of incident pressure amplitude. Ultimately the changes in the described acoustic properties are caused by the

fluid dynamic properties of the vortex ring and the potential secondary flow structures. Hence this is further investigated in the unsteady flow fields in chapter 7.

6.3 Comparison with Non-Linear Acoustic Absorption Models

The model used to predict the non-linear acoustic absorption was developed by Bellucci et. al. (2004). This model has been assessed in terms of its ability to predict the experimental data. Moreover, the model was also used to derive the effective length and the loss coefficients for the best match with the experimental data. The model is based on a momentum balance across the orifice and has been introduced in detail in section 2.5.3. In this case the downstream pressure amplitude is set to zero as measured in the experiment. Thus the momentum balance for the calculations shown in this section was defined as:

$$i\omega\rho\, l_{eff}\hat{u}_D + \rho\varsigma_{vis}\hat{u}_D - \hat{p}_{us} + \rho\frac{1}{C_D^2}g\left(\frac{\overline{U}_D}{|\hat{u}_D|}\right)\hat{u}_D|\hat{u}_D| = 0\,. \tag{6.4}$$

Note the model is valid for the linear and non-linear acoustic absorption regime. This characteristic of the model is controlled by the function $g\left(\overline{U}_D/|\hat{u}_D|\right)$ in equation (6.4). If the velocity amplitude is much smaller than the mean velocity the relationship between incident pressure amplitude and velocity amplitude is linear. In the non-linear regime the velocity amplitude is in the order of the mean velocity through the aperture or larger. The experiments have been conducted in the absence of mean flow through the orifice. Hence equation (6.4) with $\overline{U}_D = 0$ reduces to

$$i\omega\rho\, l_{eff}\hat{u}_D + \rho\varsigma_{vis}\hat{u}_D - \hat{p}_u + \rho\frac{1}{C_D^2}\frac{4}{3\pi}\hat{u}_D|\hat{u}_D| = 0\,, \tag{6.5}$$

according to equation (2.55).

The non-linear equation (6.5) is solved using a non-linear numerical solver within MATLAB. In this case the pressure amplitude was an input variable and the velocity amplitude was the solution provided by the numerical solver. As the acoustic length of the orifice and its discharge coefficient were not known a priori the length correction and discharge coefficient were matched to reproduce the measured acoustic impedance.

Figure 6.10 shows a comparison of the measured impedance and the acoustic energy loss without mean flow for two orifice plates: Plate number 19 with L/D = 0.25 and Plate number 22 with L/D = 1. Note the acoustic loss is calculated from the measured data as described in section 5.1 and normalised with the square of the incident pressure amplitude. The non-linear model can be used to calculate the admittance of the aperture which enables the loss calculation as described in equation (5.4) which leads to the same result as in equation (2.62). Finally the calculated energy loss is also normalised with the incident pressure amplitude. In general it can be seen, as also shown in the previous section, that both the resistance and reactance are a function of excitation pressure amplitude. However it seems as if the model agrees with the impedance of the longer orifice (L/D = 1) much better than for the shorter orifice (L/D = 0.25). The reactance of the longer orifice remains constant over a wider excitation amplitude (i.e. up to L_0/D of 2 instead of L_0/D of 0.7 for the aperture with L/D = 0.25). Moreover the resistance follows a linear trend to higher excitation amplitudes than for the shorter orifice. The reason for the differences in measured reactance for the two apertures is caused by the distribution of internal and external reactance. The aperture internal reactance is governed by inertial forces accelerating the mass of the fluid within the aperture. Whereas the external reactance of the aperture flow field is simulated with the length correction. The external length correction is affected by the vortex ring aerodynamic behaviour. For a thin aperture (L/D = 0.25) the external flow reactance dominates. As the amplitudes increase so changes the unsteady flow field controlled by the large scale structures and thus the aperture reactance is changing. For the long aperture the internal reactance seems to have the larger influence upon the overall reactance and hence the effect of the external flow field seems to have a reduced influence upon the acoustic behaviour of the aperture.

The assumption of constant loss coefficient and length correction in the model is not sufficient for the prediction of the impedance for the short orifice. Hence it cannot be accurately reproduced which leads to discrepancies in the acoustic loss predictions. And the model does only agree with the points where resistance and reactance are matched with the experiment. The longer orifice however shows better agreement with modelled

impedance on the basis of constant loss coefficient and length correction and therefore the acoustic loss is reproduced more accurately.

In general the modelling of the non-linear acoustic absorption behaviour is a challenge with simple one dimensional calculation tools. The flow field in the non-linear regime is complex due to large scale structures, such as vortex rings, which influence the unsteady flow field. Moreover the nature of these structures is also dependent on the excitation amplitude itself. This is simplified in a one dimensional model by using acoustic length corrections and discharge coefficient. It is therefore not surprising that the length correction or the loss coefficient is dependent on the excitation amplitude. Furthermore this dependency needs to be estimated using empirical data as, for example, conducted in Cummings (1986), Hersh et. al. (1999), Betts (2000) and Bellucci et .al. (2004b). For the purpose of this work an investigation was conducted into the flow field during non-linear absorption to understand the fluid dynamic nature of the changes in length correction and loss coefficient. This will be discussed in the following chapter.

6.4 Transition from Linear to Non-Linear Acoustic Absorption

The transition from linear to non-linear absorption behaviour is of great importance for the design of acoustic dampers within gas turbine combustion systems. Moreover it is of importance in terms of the unsteady characteristic of the cooling flow through effusion holes. In general acoustic damping devices connected to the combustion chamber require a mean flow through the apertures for cooling purposes. If combustion instabilities occur, at some point during the gas turbine operating envelope, and these cannot be adequately controlled by the damping device the pressure amplitudes within the combustion chamber rises. At this point transition from linear to non-linear absorption can occur. Thus linear absorption models cannot predict the orifice velocity amplitudes associated with the non-linear acoustic absorption and vice versa. Investigating which parameters influence the transition and the point at which the transition from linear to non-linear absorption occurs are important for several reasons. The non-linear absorption characteristic will influence the limit cycle pressure amplitude of the combustion instability. Thus accurate non-linear absorption models

will be necessary for thermo-acoustic pressure amplitude predictions. Moreover the transition from linear to non-linear absorption changes the relationship between unsteady velocity and acoustic pressure amplitude. With rising pressure amplitudes relative to the mean aperture the risk of hot gas ingestion into the damper geometry or cooling geometry increases. This will reduce the cooling effectiveness of the combustor wall and, ultimately, could lead to overheating of the combustor wall. To be able to predict the occurrence of hot gas ingestion is of great importance to understand the velocity amplitude relative to the mean velocity through the apertures. Hence the transition from linear to non-linear absorption needs to be understood and adequately described.

6.4.1 Acoustic Absorption Coefficient Measurements during the Transition from Linear to Non-linear Absorption

Figure 6.11 shows a summary of measured acoustic absorption coefficients for single orifice geometries. In this case the absorption coefficient Δ is shown with respect to the incident wave amplitude. The figure shows an example of four orifice geometries with length-to-diameter ratios of 0.5, 1.98, 3 and 6.8. For each of the geometries the measured absorption coefficient at four test conditions is shown: *dp/p* of 0-0.5% mean pressure drop resulting in a Strouhal number range from 0.08 to 0.19. In this case the solid symbols represent the linear absorption regime (i.e. the acoustic absorption coefficient is constant with pressure amplitudes) and the hollow symbols signify the non-linear absorption regime (i.e. the acoustic absorption coefficient varies with pressure amplitudes). For the geometry with *L/D* of 0.5 (Figure 6.11 a)) it can be seen that for finite levels of pressure drop the non-linear absorption coefficients increase to a maximum. This maximum value coincides with the non-linear absorption coefficient without mean flow through the aperture. After reaching the maximum value, for the cases with mean flow, all coefficients (with and without mean flow) converge onto the same absorption coefficient for further increases in excitation pressure amplitude. However this is not the same for all the shown examples. As Figure 6.11 b) shows the absorption coefficient reduces in the non-linear acoustic absorption regime compared to the linear acoustic absorption coefficient for *dp/p* = 0.1%. It can also be seen, e.g. Figure 6.11 c) *dp/p* = 0.1%, that the linear absorption regime generates larger absorption

coefficients than the non-linear optimum absorption for the case with no mean flow. In general all the data shows that the non-linear absorption behaviour with mean flow is converging on the absorption coefficient characteristic of the non-linear regime without mean flow. Hence the absorption coefficient increases or decreases during transition from linear to non-linear absorption dependent on the level of the non-linear absorption coefficient without mean flow. In other words, if the linear absorption is larger than the non-linear absorption without mean flow the absorption coefficient reduces during transition from the linear to the non-linear regime and vice versa. At high velocity amplitude to mean velocity ratios the influence of the mean flow becomes insignificant. Hence the convergence of the data with and without mean flow at large amplitudes in the non-linear regime. In this case the flow field is governed by the same phenomena as for the non-linear absorption regime without mean flow, i.e. pulsatile jet flows and the presence of large scale vortex rings.

Figure 6.11 also shows that for the cases with mean flow the transition from linear to non-linear absorption occurs at lower excitation amplitudes with reducing pressure drops. Thus it is not the actual pressure amplitude which controls the point of transition, it is the pressure amplitude relative to the mean pressure drop. Hence the transition can occur at relative small pressure amplitudes if the mean pressure drop is sufficiently low.

As discussed in section 1.3.1.3 within the non-linear acoustic absorption regime the pressure amplitude is proportional to the square of the velocity amplitude within the aperture. Hence non-linear absorption occurs at the point where the velocity amplitude and the incidental pressure amplitude are no longer proportional. Figure 6.12 shows the measured velocity amplitudes in the plane of the aperture relative to its mean flow with respect to the pressure amplitude incident on the orifice relative to the mean pressure drop. Moreover the calculated velocity ratio using the linear model introduced in section 5.9 is shown as a reference. It can be seen that the linear model and the measured velocity amplitudes compare very well up to $\left|\hat{p}_d\right|/d\overline{p} \approx 0.75$. At this point the measured velocity amplitudes deviate from the linear model and the transition to the non-linear absorption regime occurs. Hence at this point the velocity amplitude is no longer linearly related to the incident pressure amplitude. Thus the unsteady velocity ratio at which non-linear absorption occurs is approximately $\left|\hat{u}_D\right|/\overline{U}_D \approx 0.4$.

It is expected that the velocity ratio, at which non-linear absorption occurs, should remain constant. The measured velocity amplitude and pressure amplitude ratios for *L/D* of 0.25 and 1.98 is shown in Figure 6.13. Again the measured data is compared to the linear acoustic model. It can be seen that the transition occurs for velocity amplitude ratios larger than 0.4 in both cases. Moreover the transition of non-linear absorption occurs at larger pressure amplitudes relative to the mean pressure drop for the longer orifice geometry (*L/D* = 1.98) compared with the orifice geometry at *L/D* of 0.5. Due to the increased reactance of the orifice the velocity amplitude is smaller for a given pressure amplitude. Hence the ratio of unsteady to mean velocity through the aperture of 0.4 occurs at larger pressure amplitudes for a longer aperture.

Based on the conducted experiments it can be concluded that the transition from linear to non-linear acoustic absorption occurs for velocity amplitude ratios of approximately 0.4. Hence the application of linear acoustic absorption models is also only valid up to velocity amplitude ratios of 0.4.

6.4.2 Characteristics of Acoustic Parameters during Transition from Linear to Non-Linear Acoustic Absorption

The absorption coefficients with and without mean flow across the aperture presented in Figure 6.11 showed that the absorption coefficients with mean flow converged onto the absorption coefficients without mean flow at high amplitudes. This behaviour will be further investigated in this section using the measured acoustic impedance. Figure 6.14 shows the measured acoustic impedance for an orifice with *L/D* = 0.25. In this case the impedance was measured with mean flow (mean pressure drop of 0.1%) and without mean flow. It can be seen that the acoustic resistance with mean flow is larger at low velocity amplitudes (< 5 m/s) than for the case without mean flow. Moreover the acoustic reactance is smaller for the case with mean flow compared to the cases without mean flow. As the velocity amplitudes increase the impedance for the case with and without mean flow converges. The same can be seen for the example with *L/D* of 1.98 in Figure 6.15. This behaviour is caused by the fundamentally different flow fields. For the cases with mean flow the flow field is expected to be not influenced by any flow structure. As the velocity amplitudes increase and the absorption becomes non-linear flow structures such as vortex rings occur. In this case the fluid dynamic behaviour of

the aperture flow field is the same as for the cases without flow and so the measured acoustic impedance with and without flow converges as it is governed by the same fluid dynamic behaviour and large oscillating velocity amplitudes.

6.4.3 Modelling Aspects of the Transition from Linear to Non-Linear Acoustic Absorption

As already discussed in section 2.5.3 the modelling methodology is based on the introduced momentum balance for the calculation of the acoustic velocity amplitudes due to the incident pressure amplitude:

$$Z = \frac{\hat{p}_{us}}{\hat{u}_D} = \rho \frac{1}{C_D^2} g\left(\frac{\overline{U}_D}{|\hat{u}_D|}\right)|\hat{u}_D| + \rho \varsigma_{vis} \hat{u}_D + i\omega\rho\, l_{eff}\,. \tag{6.6}$$

However the difference to the previous approach is that there is mean flow influencing the non-linear absorption part. Hence the *g*-function within the resistance term has to be included in the solution. The definition of the g-function can be found in equation (2.55). In general the change from linear to non-linear behaviour is controlled by this function using the ratio of mean velocity to unsteady velocity amplitude:

- If $\frac{\overline{U}_D}{|\hat{u}_D|} < 1$ the velocity amplitude is solved in the non-linear regime.
- If $\frac{\overline{U}_D}{|\hat{u}_D|} \geq 1$ the velocity amplitude is solved in the linear regime.

As it was shown in the previous section the transition from linear to non-linear behaviour occurs at $|\hat{u}_D|/\overline{U}_D \approx 0.4$. Hence the transition in the above described model should take place at $\overline{U}_D/|\hat{u}_D| \approx 2.5$. Therefore the transition to non-linear absorption starts for velocity amplitude ratios larger than 1. This means the solver remains within the linear regime even if the transition to non-linear absorption has already happened. Therefore, as it is the case for the non-linear regime, the accurate prediction of the transition to non-linear acoustic absorption is only possible using semi-empirical correlations and curve fits for one-dimensional models as for example in Bellucci et. al. (2004b). Otherwise much more sophisticated methods modelling the actual fluid

dynamic phenomena are needed to be able to capture the relevant processes in the unsteady flow field.

6.5 Closure

In this chapter the fundamental characteristics of the non-linear acoustic absorption have been discussed. In general the amount of acoustic absorption in the non-linear absorption regime is dependent on the pressure amplitude being in the reactive range (region where the acoustic reactance is much larger than the resistance) or in the resistive range (region where the acoustic resistance is much larger than the reactance). Within the region of dominating reactance the effective length reduces with increasing pressure amplitude. Therefore the absorption increases with increasing pressure amplitude in this regime. In the resistive regime the resistance increases with increasing pressure amplitudes and so the acoustic absorption coefficient reduces. The optimum acoustic absorption occurs in the region where the acoustic resistance and the acoustic reactance are equal. It is believed that this behaviour is governed by the interaction of the pulsatile orifice flow field and the generated vortex rings within the flow.

The influence of the orifice length upon the non-linear absorption has been shown. It could be seen that the absorption coefficient reduces with increasing orifice length due to the increasing reactance of the orifice. Thus velocity amplitudes decrease and ultimately the absorption coefficient decreases.

It has been shown that the non-linear acoustic modelling is challenging and depends heavily on pressure amplitude dependent empirical loss coefficients and length corrections. It is expected that the generated vortex rings within the pulsatile flow field are the reason for the changing loss coefficients and length corrections. Thus an investigation of the fluid dynamic behaviour would provide further insight into the measured acoustic behaviour.

Finally the transition from linear to non-linear absorption was presented. It was shown that transition from linear to non-linear absorption occurs at a velocity amplitude of $\hat{u}_D / \overline{U}_D \approx 0.4$ which is much earlier as anticipated by the used modelling technique.

Figures

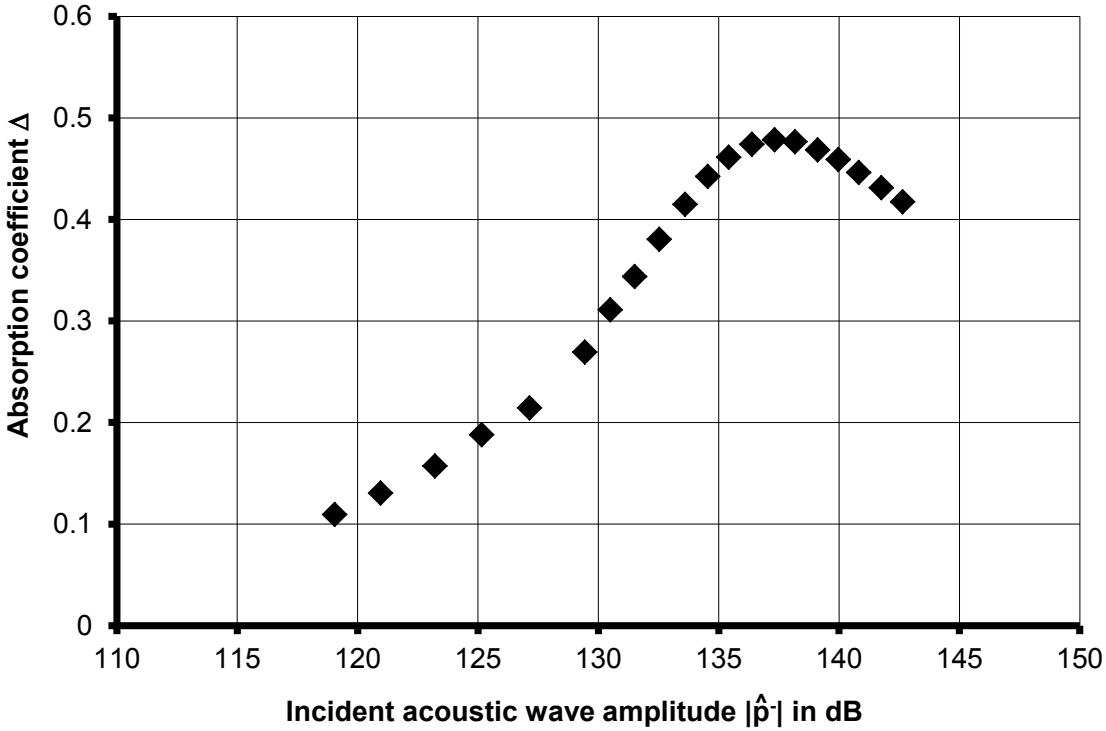

Figure 6.1: Acoustic absorption without mean flow. Plate number 1, *L/D* = 0.47

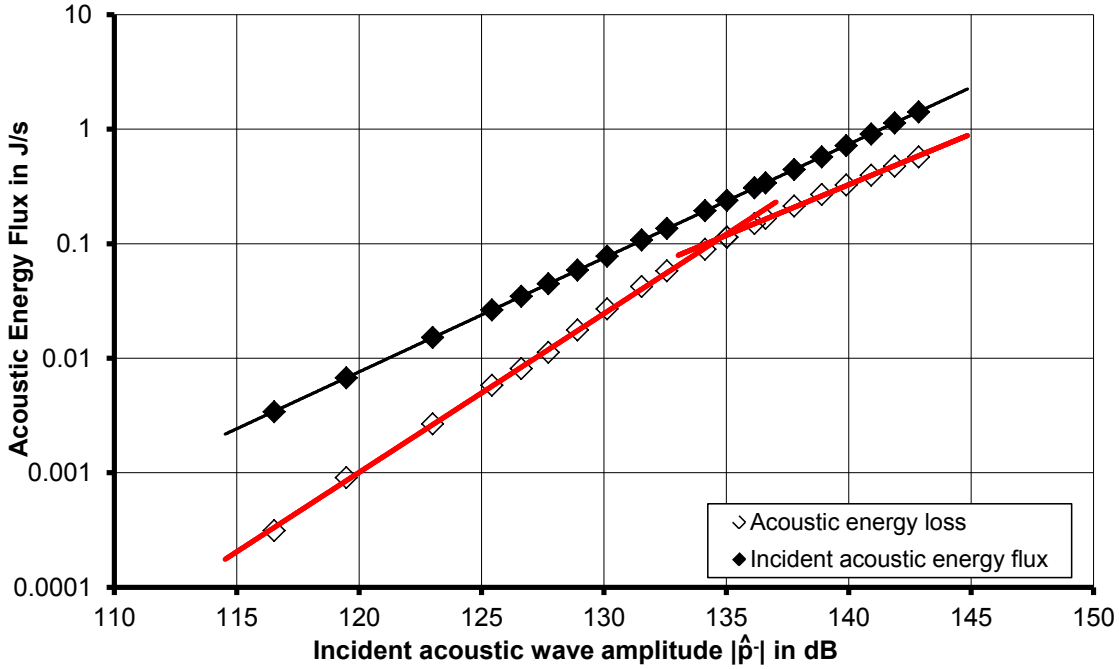

Figure 6.2: Acoustic energy loss. Plate number 1, *L/D* = 0.47

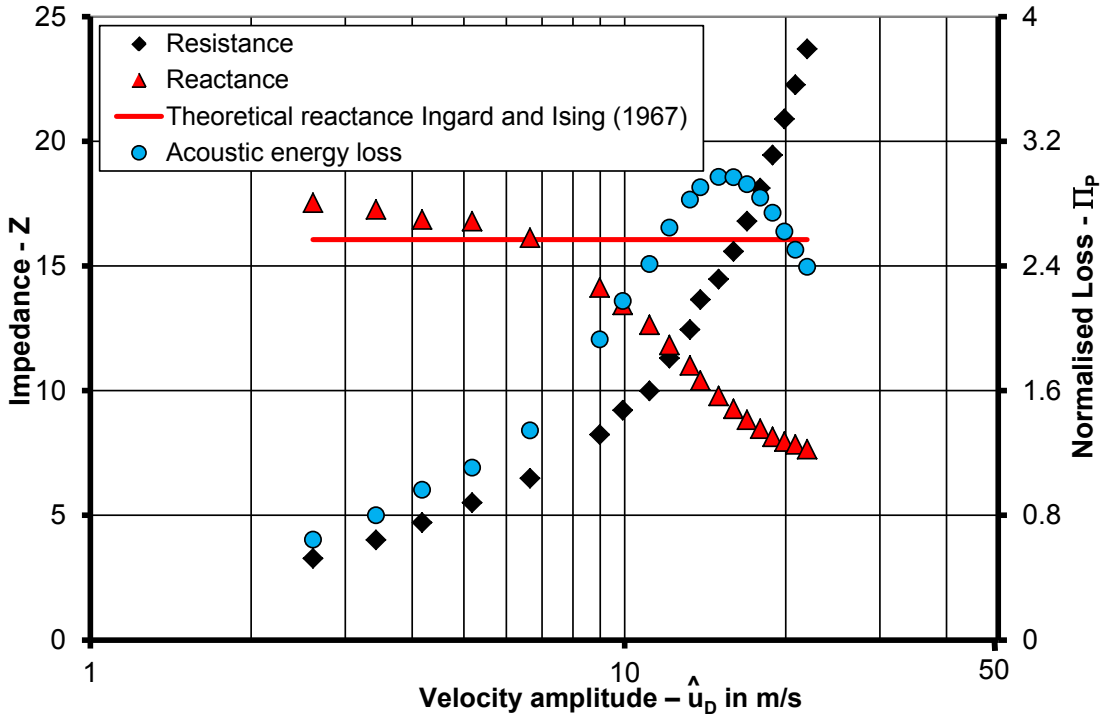

Figure 6.3: Impedance and normalised acoustic energy loss for the non-linear absorption test case. Plate number 1, *L/D* = 0.47

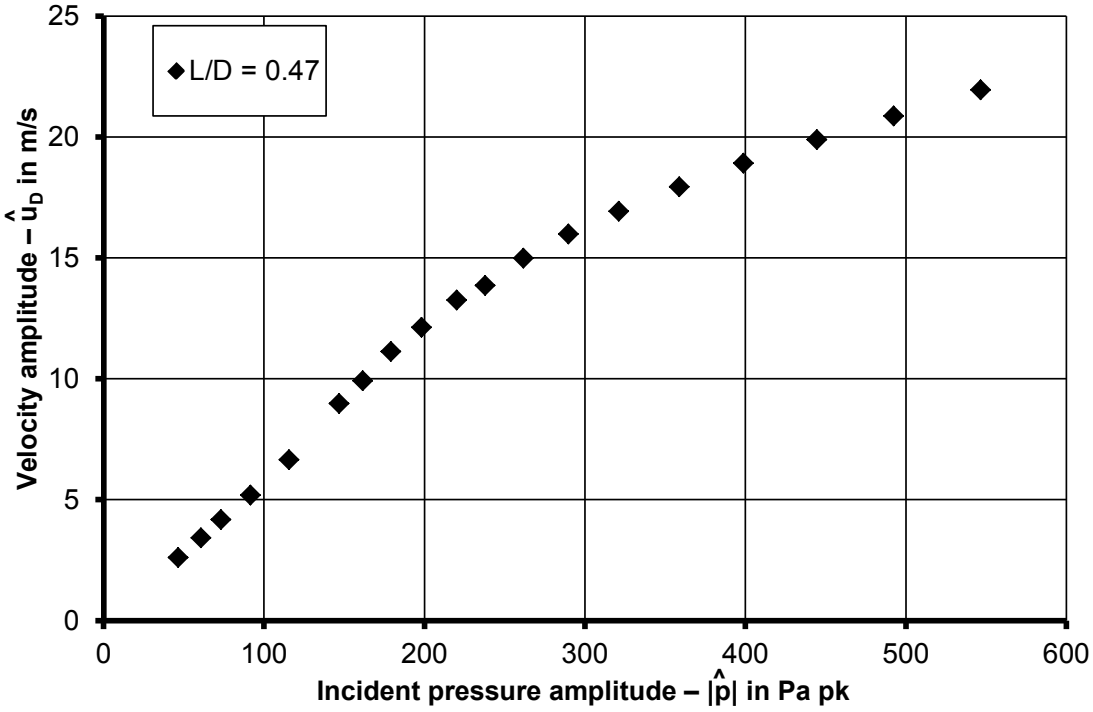

Figure 6.4: Orifice velocity amplitude relative to incident pressure amplitude for the non-linear absorption test case. Plate number 1, *L/D* = 0.47

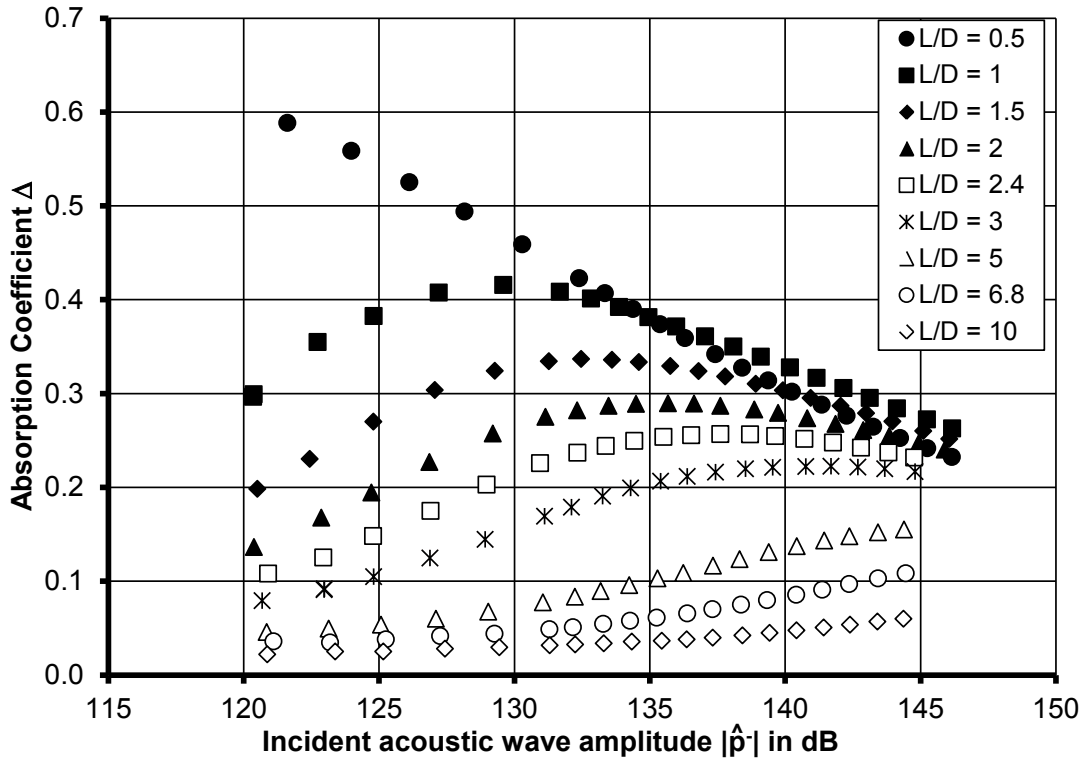

Figure 6.5: Non-linear absorption coefficient for *D* = 9.1mm orifice at various *L/D*. Plate number 3 – 11, forcing frequency 62.5 Hz.

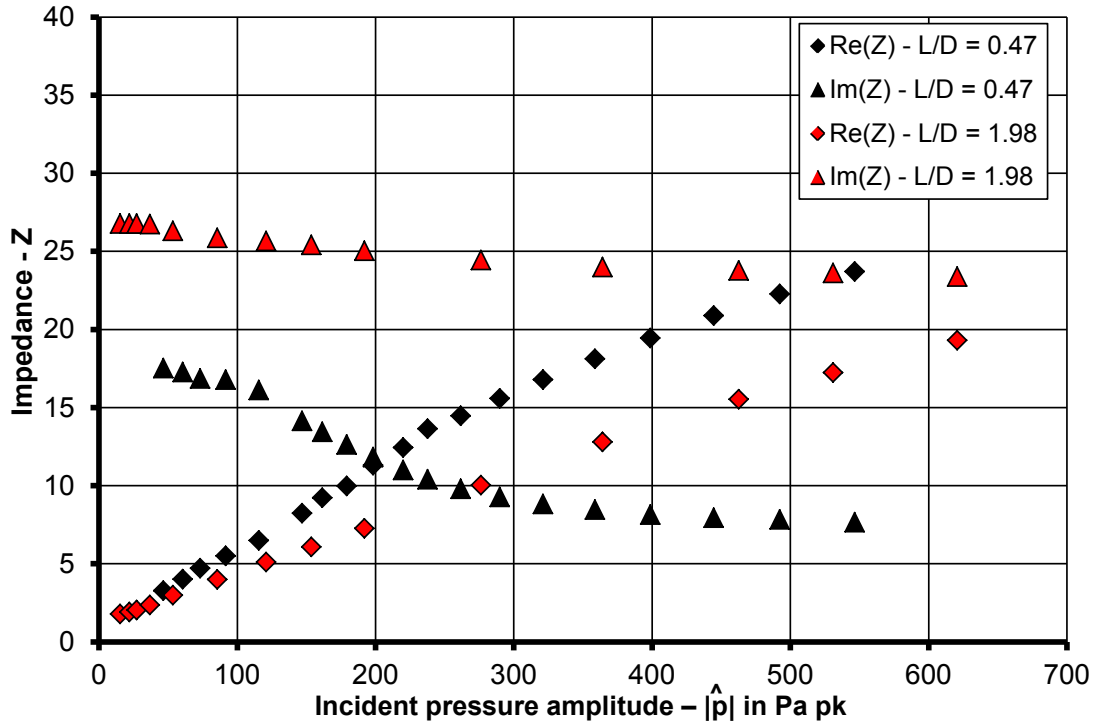

Figure 6.6: Impedance comparison for *L/D* of 0.47 and *L/D* of 1.98. Forcing frequency of 125 Hz. Plate number 1 and 13.

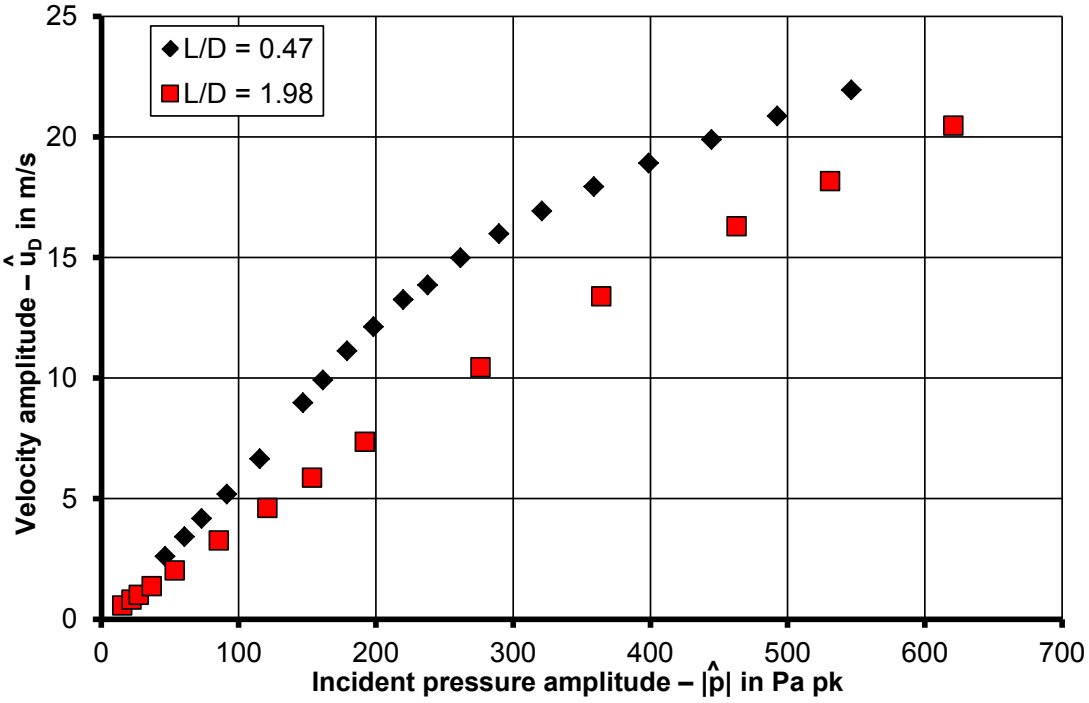

Figure 6.7: Non-linear absorption coefficient for various *L/D*. Plate number 1 and 13, forcing frequency 125 Hz.

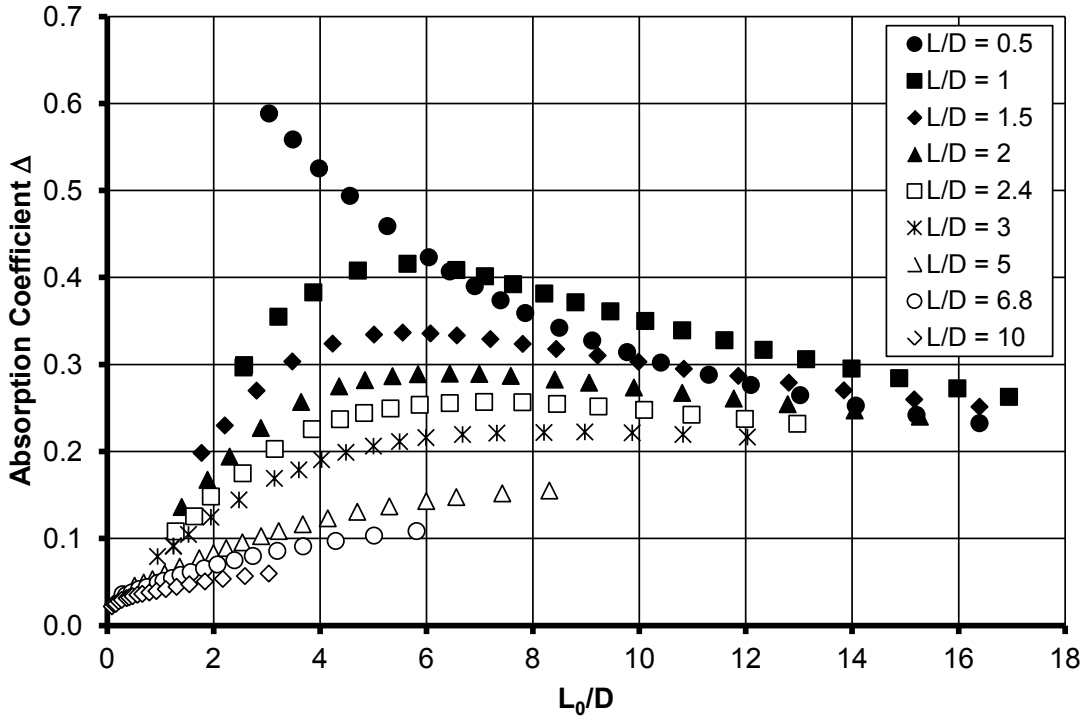

Figure 6.8: Non-linear admittance dependent on vortex ring formation number for orifice length-to-diameter range of 0.5< *L/D* < 10. Plate number 3 – 11.

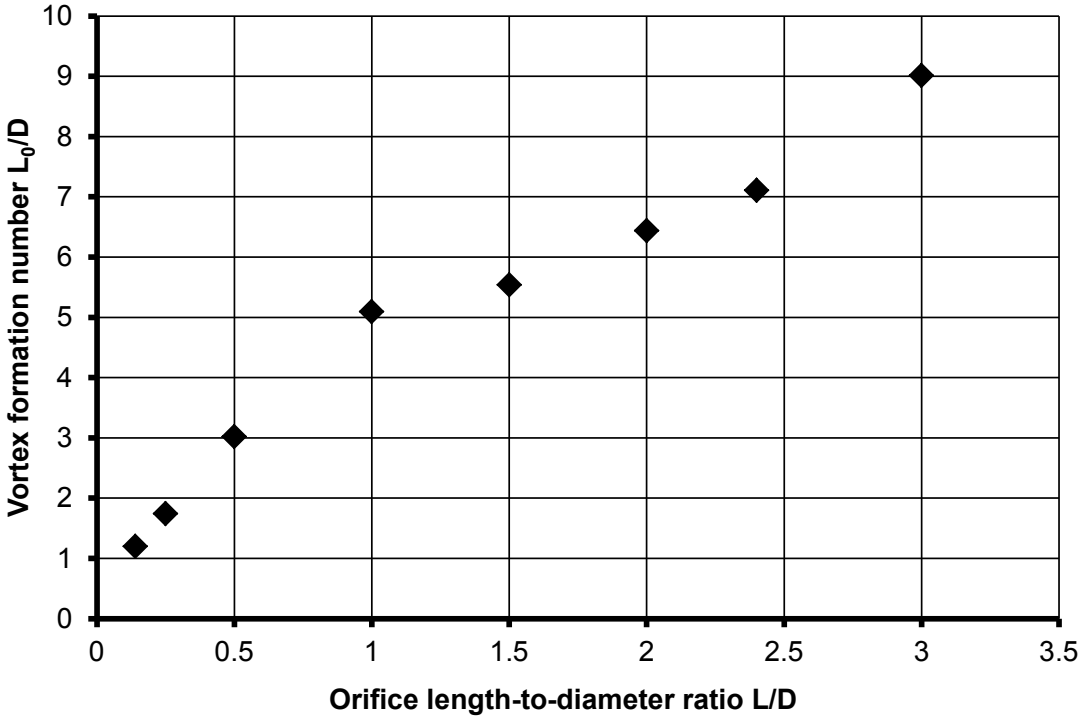

Figure 6.9: Vortex ring formation numbers at maximum absorption for a range of orifice length-to-diameter ratios. Plate numbers 3 – 8, 18 and 19.

Impedance	Acoustic energy Loss
Plate number 19, L/D = 0.25	Plate number 19, L/D = 0.25
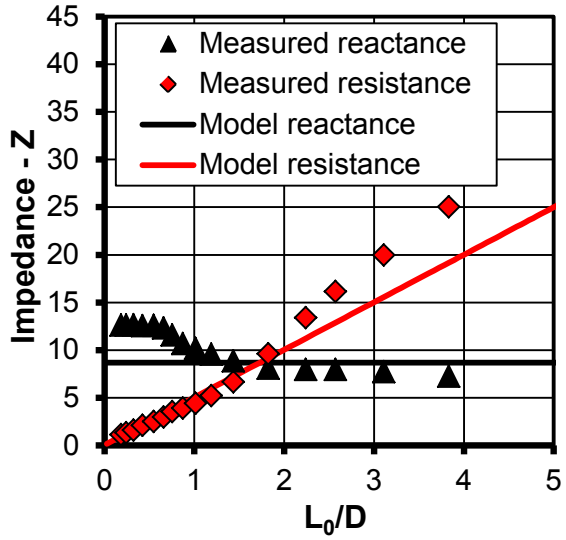	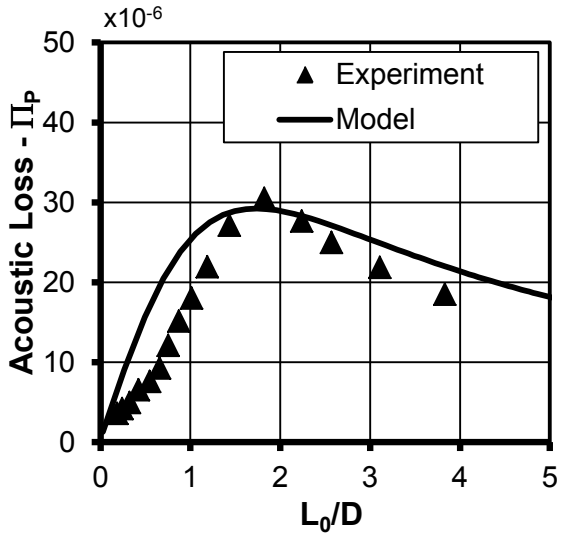
Plate number 22, L/D = 1	Plate number 22, L/D = 1
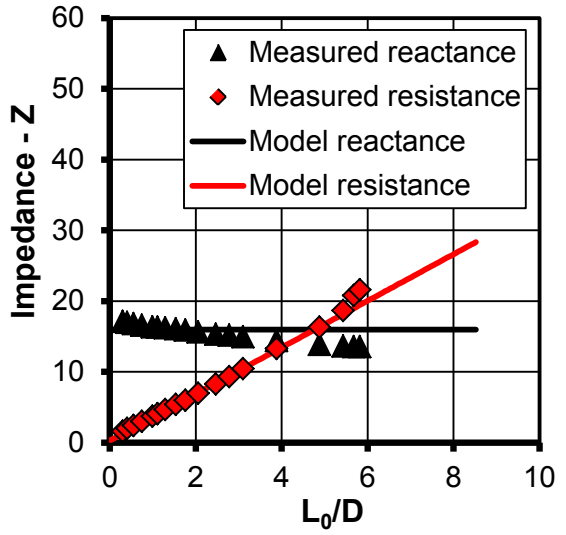	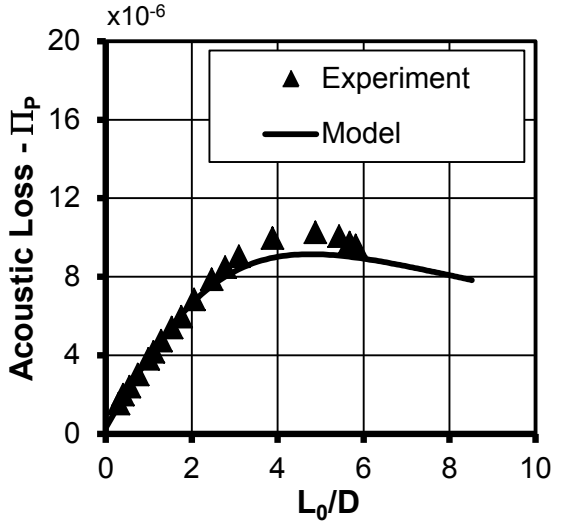

Figure 6.10: Comparison between non-linear acoustic experiment and non-linear acoustic absorption model

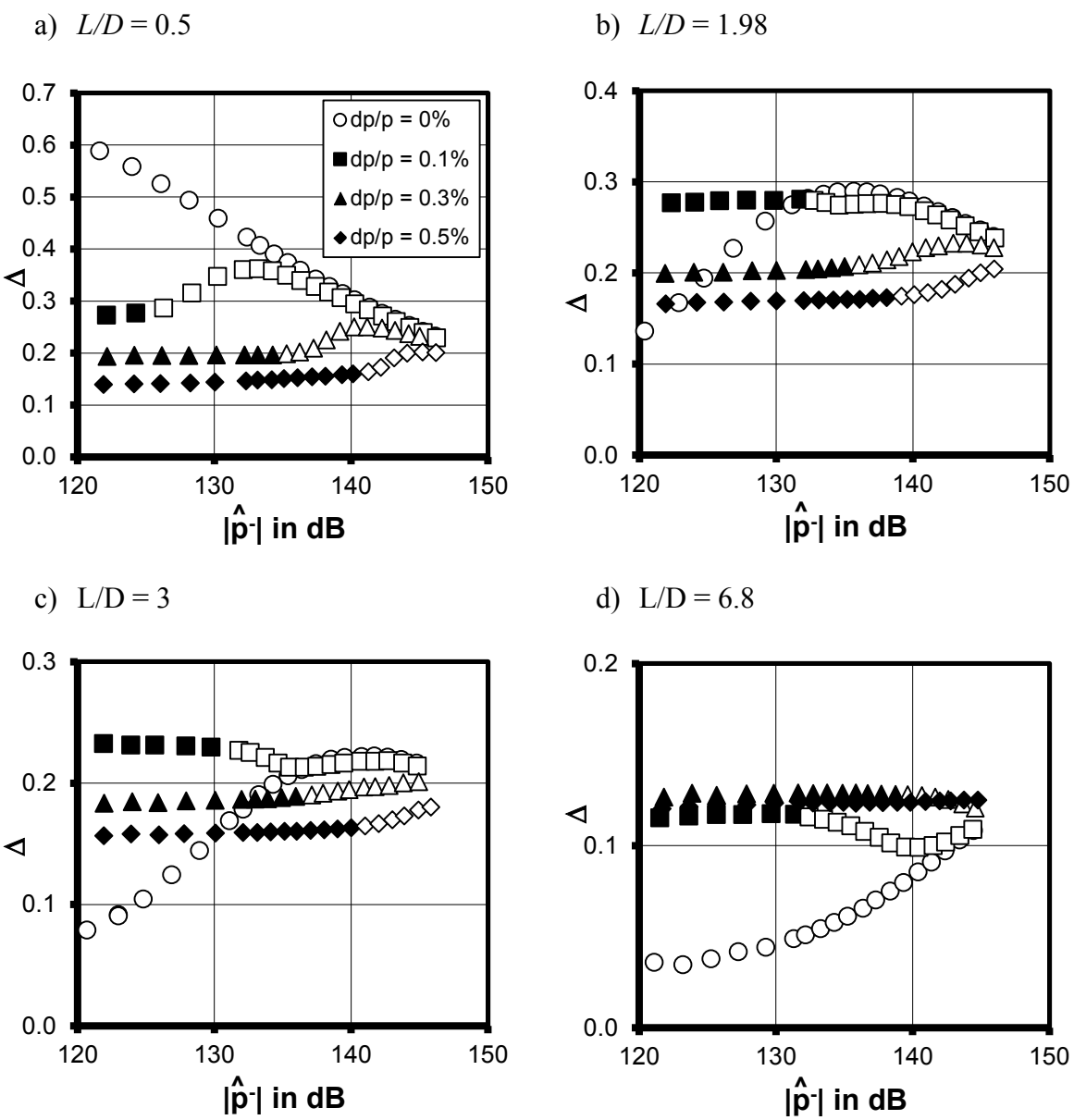

Figure 6.11: Transition from linear to non-linear acoustic absorption, acoustic absorption experiment, forcing frequency of 62.5 Hz. Plate numbers 3, 6, 8, 10.

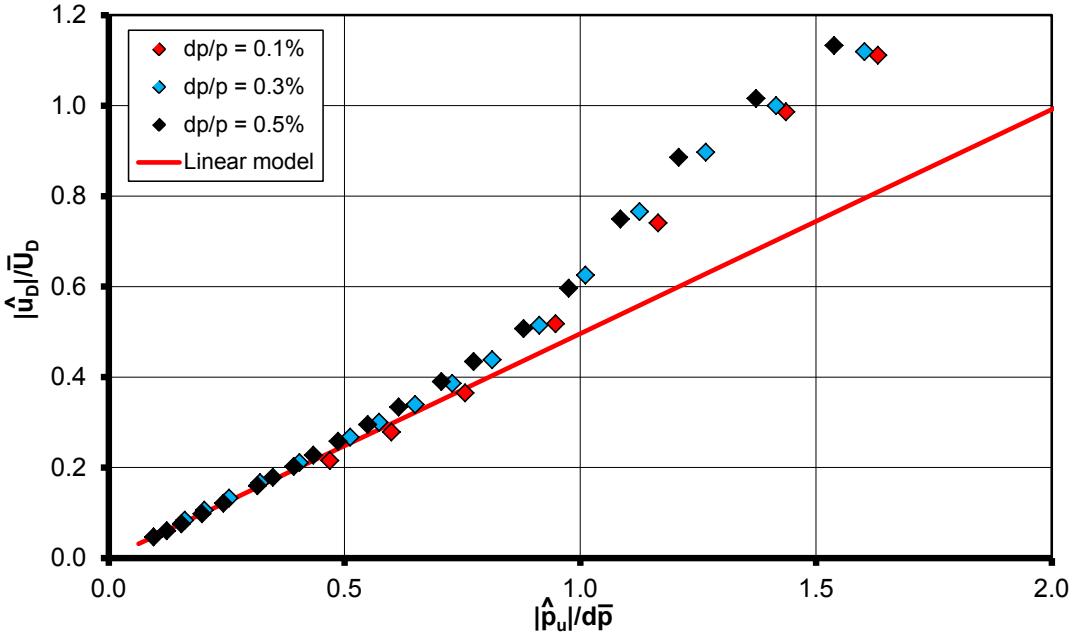

Figure 6.12: Transition from linear to non-linear acoustic absorption, acoustic absorption experiments, forcing frequency 62.5 Hz. Plate number 3, *L/D* = 0.5

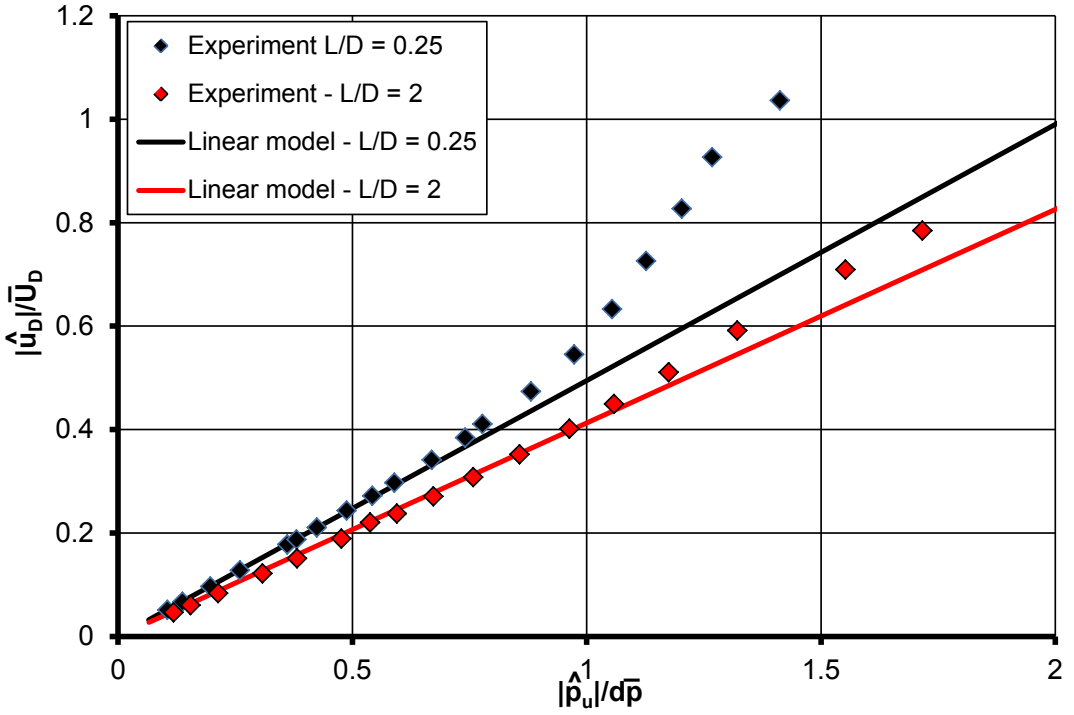

Figure 6.13: Transition from linear to non-linear acoustic absorption, Rayleigh Conductivity experiments, *dp/p* = 0.3%. Plate numbers: 19 and 24.

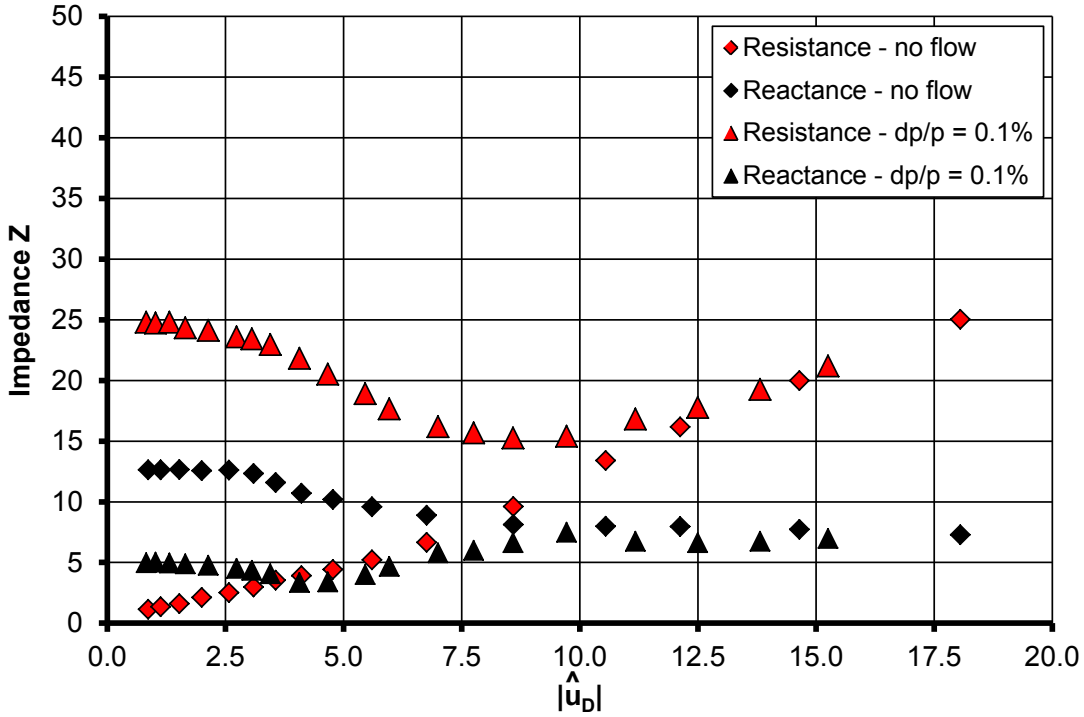

Figure 6.14: Impedance comparison during transition from linear to non-linear acoustic absorption with and without flow, forcing frequency 125 Hz. Plate number 19, *L/D* = 0.25.

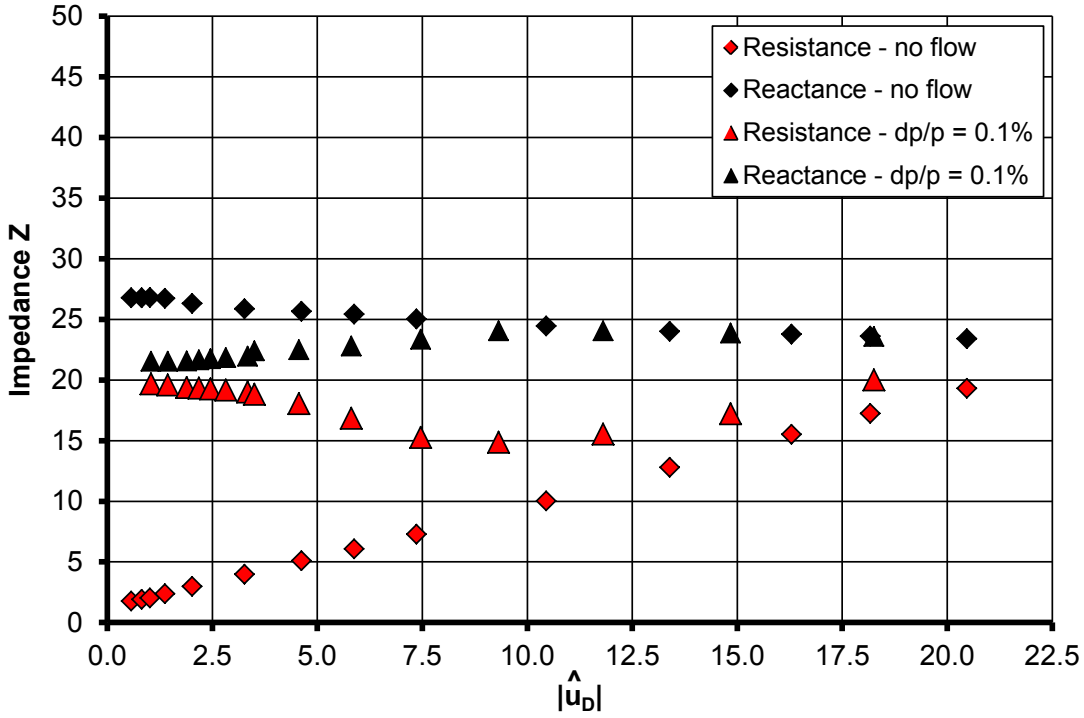

Figure 6.15: Impedance comparison during transition from linear to non-linear acoustic absorption with and without flow, forcing frequency 125 Hz. Plate number 24, *L/D* = 1.98.

7 Methodology to Identify Unsteady Flow Structures Associated with Acoustic Absorption

The amount of energy absorbed from the acoustic field is directly linked to various features within the unsteady flow field in the vicinity of an orifice. Investigation of this unsteady flow field will therefore provide a greater understanding of the relevant flow field characteristics associated with the acoustic absorption process. An experimental technique has been developed to enable interrogation of this region using Particle Image Velocimetry (PIV) with adequate spatial and temporal velocity field information. However, the mean pressure drop across the orifice will generate a mean flow field and turbulence even in the absence of an acoustic pressure perturbation. Hence a data analysis technique has been developed that identifies the unsteady features caused by the incident acoustic pressure waves from other flow field features. This method is based on the application of Proper Orthogonal Decomposition (POD). Initially an introduction to the POD analysis will be given. Thereafter the developed methodology is explained. This method will then be validated against the acoustic measurements using the two-microphone method based on the acoustic absorption results shown in the previous chapter. Finally the methodology is used to highlight fluid dynamic phenomena leading to the absorption of acoustic energy within the linear and non-linear acoustic absorption regime.

7.1 Introduction to the Proper Orthogonal Decomposition

The Proper Orthogonal Decomposition, (POD) is a well-established method used for structure identification within turbulent flow research, e.g. Adrian et. al. (2000), Bernero and Fiedler (2000), Graftieaux et. al. (2001), Patte-Rouland et. al. (2001), Kostas et. al. (2005), Midgley (2005), Robinson (2009),etc. In general the method is used to calculate time averaged instantaneous velocity field data. The description of the used POD analysis can also be found in Rupp et. al. (2010) and Rupp et. al. (2010b). In this work before the Proper Orthogonal Decomposition is applied the time averaged flow field

$$\bar{u}(x) = \langle \vec{u}(x,t) \rangle = \frac{1}{T} \sum_{i=1}^{N} \vec{u}(x,t) \tag{7.1}$$

is subtracted from the data set. The symbol $\langle\ \rangle$ represents an ensemble average and N denotes the amount of samples. Some authors do not subtract the mean flow field and perform the POD method over the complete data set. In this case the first POD mode is associated with the mean flow field However for this study the resulting data set investigated in the Proper Orthogonal Decomposition is then defined by the instantaneous fluctuating velocity vectors where the time average is

$$\bar{u}'(x) = \langle u'(x,t_i) \rangle = \frac{1}{N} \sum_{i=1}^{N} u'(x,t_i) = 0 \tag{7.2}$$

and the time index is defined as $i = 1,\ldots,N$, where N is the maximum amount of samples, i.e. 3072.

The overall objective of the method is to extract time-independent orthonormal basis functions (structural modes) $\varphi_k(x)$ and time dependent orthonormal coefficients (temporal coefficients) $a_k(t_i)$ such that their reconstruction of the instantaneous velocity field

$$u'(x,t_i) = \sum_{k=1}^{N} a_k(t_i) \cdot \varphi_k(x) \tag{7.3}$$

is optimal. In this case the parameter k defines the POD mode number. This reconstruction is optimal in the sense that it reconstructs the original data most accurately from the first $m < N$ sequential POD modes. The structural modes contain information on the shape of the coherent structures within the fluctuating velocity field. Each structural mode has a temporal coefficient which describes how the coherent structure changes in time. A simple analogy is that the structural mode represents the amplitude of a fluctuating velocity field associated with that mode, and the change of this amplitude over time is represented by the temporal coefficient. Therefore the temporal coefficient gives an indication of any coherent structures (or other features) in the associated mode that are either periodic or of a random nature.

Mathematical optimality is ensured by the maximisation of the averaged projection of u' onto φ (Holmes et. al. (1998)). Therefore, to satisfy the maximisation problem, φ must be an eigenfunction of the two-point correlation tensor as discussed in Berkooz et. al. (1993):

$$\int_D R(x,x')\varphi(x')dx' = \lambda\varphi(x). \tag{7.4}$$

Thus the maximum is achieved for the largest eigenvalue λ. The integral is applied over a spatial domain D. Moreover the spatial correlation tensor is represented by $R(x,x')$. This spatial correlation tensor is a measure of the size of the structures within the flow field and can also be used in calculating the integral length scales of the structures within the flow field (e.g. Midgley (2005), Robinson (2009), Dunham (2011), etc).

To calculate the spatial correlation tensor the matrix A can be constructed containing the fluctuating velocity components of the sampled planar PIV velocity field. In this case the coordinate x resembles a pair of x and y coordinates, i.e. $(x,y)_i$ and m represents the number of vectors within the flow field ($m = 64 \times 64 = 4096$). It can be seen that the spatial variation of the oscillating velocity vector is contained in the rows of the matrix and its temporal variation within the columns of matrix A (e.g. Midgley(2005)):

$$A = \begin{bmatrix} u'(x_1,t_1) & \cdots & u'(x_1,t_N) \\ \vdots & \ddots & \vdots \\ u'(x_m,t_m) & \cdots & u'(x_m,t_N) \end{bmatrix}. \tag{7.5}$$

Thereafter the spatial correlation function can be calculated $R(x,x')$:

$$R(x,x') = \frac{1}{N}\left(AA^T\right). \tag{7.6}$$

As described in Sirovich (1987) the spatial POD modes can be calculated from the eigenvectors of the spatial correlation matrix. Chatterjee (2000) showed that the spatial modes can be inferred by using a Singular Value Decomposition (SVD):

$$R(x,x') = U\Sigma\Phi^T . \tag{7.7}$$

In this case the large spatial correlation matrix is decomposed into three matrices: the $N \times N$ matrix U, the $m \times m$ matrix Φ and the $N \times m$ matrix Σ. The matrix Σ consist of zero elements except for the singular values along the diagonal elements of the matrix. Furthermore the singular values are also ordered so that the first diagonal element is the largest value. Moreover the columns of matrix Φ contain the eigenvectors. Therefore the k^{th} spatial POD mode can be extracted by using the k^{th} column of the matrix Φ.

Calculating the spatial POD modes using the described method is computationally expensive, as it is considering the $m \times m$ spatial correlation matrix $R(x,x')$. Thus, a method proposed by Sirovich (1987), known as the Snapshot-POD method, was used. In this case the SVD was conducted on the matrix C

$$C = \frac{1}{N}\left(AA^T\right) \tag{7.8}$$

instead of the spatial correlation matrix R. Thus the elements in C are reduced to $N \times N$ which reduces the computational effort as less time steps N are used than vectors in the flow field m. However the Snapshot-method does not calculate the eigenvectors for the spatial POD modes directly. In this case the eigenvectors κ_κ of the SVD need to be multiplied with the matrix A containing the fluctuating velocity components:

$$\varphi_k(x) = \sum_{i=1}^{N_s} \kappa_k(t_i) A(x,t_i) \tag{7.9}$$

An important characteristic of the POD analysis is that the eigenvalue λ_i, which is the square-root of the diagonal elements of matrix Σ, associated with a particular POD mode divided by the sum of all eigenvalues of all POD modes is representative of the kinetic energy contained in each mode relative to the total fluctuating kinetic energy.

$$E_k = \frac{\sum_{i=1}^{k} \lambda_i}{\sum_{i=1}^{N} \lambda_i} . \tag{7.10}$$

Therefore the POD modes are ordered in terms of their kinetic energy. The first POD mode contains the most energy averaged over the field of view. An example of the cumulative kinetic energy distribution is shown in Figure 7.1. This data is based on a acoustic flow field with 62.5 Hz excitation with 0.1% and 0.8% mean pressure drop. It can be seen that the flow field at the smaller pressure drop contains an increased amount of kinetic energy in the first POD modes.

The temporal variation of the spatial POD mode can be inferred from the unsteady velocity field and the calculated spatial POD mode:

$$a_k = u' {\varphi_k}^T \left(\varphi_k \varphi_k^T \right). \tag{7.11}$$

Thus the unsteady velocity field as defined in equation (7.3*)* can be reconstructed using the temporal coefficient a_k and the spatial modes φ_k.

The described POD method was implemented in the MATLAB routine Xact developed by Robinson (2006). Velocity vectors calculated by the LaVision Davis 7.2 software were used as an input into the Xact analysis routine, which performed the Snapshot-POD method on the unsteady velocity vectors.

The maximum amount of samples per test point for the represented test cases specified by the high speed camera was 3072. At a sampling frequency of 1100 Hz this results in 8 to 9 data points (i.e. velocity fields) per cycle for the excitation frequency of 125 Hz and 16 to 18 data points per cycle for the excitation frequency of 62.5 Hz. The POD analysis was conducted on all 3072 data points. Due to the periodic signal this resulted in 349 statistical independent samples for 125 Hz excitation and 174 independent samples for the 62.5 Hz excitation. Patte-Rouland et. al. (2001) mentions that 400 statistical independent samples are sufficient for a good statistical representation of the lower POD modes. Moreover it is shown that the cumulative energy within the lower POD modes converge for a normalised mode number of k/N = 0.585, where k represents the mode number and N is the total number of snapshots. Figure 7.2 shows the cumulative energy within the POD modes for examples of the linear and non-linear acoustic absorption cases. It can be seen that the modes converge around the same value of 0.585 with more than 99.9% of the cumulative kinetic energy.

Hence the used amount of independent samples for this work seems sufficient for the convergence of the amount of energy within the lower POD modes.

7.2 Methodology to Identify Unsteady Flow Structures Associated with Acoustic Absorption

The experimental investigation of the unsteady flow field was conducted using particle image velocimetry (PIV). Various PIV velocity measurements have been undertaken for the linear and non-linear absorption regime. The non-linear velocity fields have been measured for plate number 1 (Table A.1) with 12.7 mm diameter and L/D = 0.47. A small pressure drop across the orifice plate of 8 Pa has been applied to drag the necessary seeding particles through the test section. The excited flow fields have been measured at three different excitation pressure amplitudes (130 dB, 137 dB and 142 dB) for the 125 Hz forcing cases. However to illustrate the developed methodology the test point at 137 dB will be described in more detail. The absorption measurement relative to the PIV test condition is also shown Figure 7.3 and suggests the absorption is non-linear. Hence the reversing flow field is likely to generate vortex ring type structures either side of the aperture, i.e. a significant amount of acoustic energy is dissipated upstream of the orifice as well as downstream of the orifice. Thus two flow field measurements at the same forcing amplitude have been conducted either side of the orifice so that the vortex ring structures upstream and downstream of the orifice, due to the reverse flow within the acoustic cycle, could be captured. The following description of the methodology to identify the unsteady flow structures is taken from Rupp et. al. (2010b).

The flow field chosen for the linear absorption regime was measured at 137 dB as indicated in Figure 7.4. In this case the orifice diameter was 9.1 mm with a length-to-diameter ratio (*L/D)* of 0.5 (plate number 3 in Table A.1) and an excitation frequency of 62.5 Hz. In the linear regime it is assumed that all the energy dissipation occurs within the downstream flow field, hence no PIV measurements upstream of the aperture have been captured. It should be noted that some of the energy could be dissipated within the boundary layer internal to the orifice. However, due to the length of the investigated

orifice plate the loss of acoustic energy, due to the boundary layer inside the orifice, could be neglected (see chapter 5.9.1).

Figure 7.5 and Figure 7.6 show examples of the measured instantaneous flow fields during non-linear and linear acoustic absorption. The total velocity is indicated in the contour of both figures and stream traces have been added to show the characteristic of the measured flow fields. Furthermore the Cartesian coordinates x and y have been normalised using the orifice diameter. In Figure 7.5 two sequential instantaneous flow fields within one acoustic cycle are shown for the flow field downstream of the orifice. Figure 7.6 shows two sequential flow fields during linear absorption. At first glance obvious differences within the flow fields are visible. It can be seen that the flow field within the non-linear acoustic absorption regime shows large vortex ring structures whereas the linear acoustic absorption regime is characterised by a pulsatile turbulent jet. However, both flow fields are influenced by:

(i) the acoustic pressure oscillation producing the *unsteady* orifice pressure drop

(ii) the mean flow field which is caused by the centrifugal fan producing the *mean* orifice pressure drop

(iii)almost random turbulent oscillations within the flow.

Thus a quantitative assessment of the coherent structures relevant to the acoustic absorption may be possible if the fluctuating velocity could be decomposed into a velocity field containing coherent, periodic structures (that correlate in some form with the acoustic field and the incident acoustic pressure waves) and fluctuations that are more random and turbulent in nature, (and which exhibit no correlation with the acoustic field), i.e.

$$\vec{u}(x,t) = \underbrace{\overline{u}(x)}_{\text{Mean flow field}} + \underbrace{\tilde{u}(x,t)}_{\text{Coherent structures generated by the periodic velocity field}} + \underbrace{u'(x,t)}_{\text{Random turbulent fluctuations}} \quad (7.12)$$

Having decomposed the measured velocity field into these components an instantaneous flow field can be reconstructed. For example, the reconstructed flow field could include the mean flow field and periodic structures that exhibit coherence with the

incident acoustic pressure waves (i.e. so that the random turbulent fluctuations are ignored). In this way the reconstructed flow field and its subsequent analysis offers the potential for identifying features generated by the incident pressure waves which are responsible for absorbing energy from the acoustic field. However, careful consideration is required as to how this analysis should be undertaken. This is because as the flow field develops energy can, and will, be transferred between components. For example, as the coherent structures in the flow field decay and mix out energy will be transferred from these coherent structures into random turbulent fluctuations, whilst the random turbulent fluctuations lose energy due to dissipation. In this work an attempt was undertaken to decompose the unsteady velocity field using the Proper Orthogonal Decomposition. This procedure is described in the following section which is based on the data and methods described in Rupp et. al. (2010) and Rupp et. al. (2010b).

7.2.1 Flow Field Decomposition

In general the methodology to identify the velocity field related to the acoustic forcing relies on the analysis of the calculated POD modes based on the measured unsteady velocity fields. All the POD modes have been calculated using the in-house MATLAB routine Xact.

Figure 7.7 shows an example of three spatial POD modes calculated in the downstream field within the non-linear absorption regime. Moreover the corresponding temporal coefficients related to the spatial POD modes are shown in Figure 7.8. The method to identify the acoustically related POD modes relies on an analysis of these temporal coefficient. Thus, a Fourier transformation of the temporal coefficient was conducted and is shown for the corresponding POD modes in Figure 7.9.

It can be seen that a large vortex structure is featured within POD mode 2 (Figure 7.7). Furthermore the temporal coefficient for this mode shows responses at the excitation frequency of 125 Hz and its harmonics (Figure 7.9). In other words this structure, and its associated energy, is strongly correlated with the incident pressure wave. Similar behaviour can be seen from mode 4, which also shows vortex structures within the spatial modes (Figure 7.7) and a frequency response in the temporal coefficient at the excitation frequency (Figure 7.9). However in this case the 2nd and 3rd

(250 and 375 Hz) harmonics seem to show a larger amount of energy than the fundamental forcing frequency. Since the pressure spectrum does not show excitation frequencies up to the third harmonic, the harmonics shown for mode 4 and mode 2 have been generated in the flow field as a response to the 125 Hz excitation. This is expected as it was also observed in the hotwire velocity measurements from Ingard (1960). A mode representing random turbulent fluctuations is also presented (mode 100 in Figure 7.7 and Figure 7.9). It can be seen that no coherent structures are visible in the structural mode and the temporal coefficients exhibit no significant response at the excitation frequency (or its harmonics).

Moreover as another example the spatial modes, temporal coefficients and the Fourier transforms of the temporal coefficients are shown in Figure 7.10 - Figure 7.12 for the flow field within the linear absorption regime. In this case the shown POD modes are representative of the pulsatile jet flow (e.g. mode 1 in Figure 7.10). Moreover no structures seem to be visible in the vicinity of the aperture, i.e. $y/D > -1$, for mode 1 and mode 3 (Figure 7.10). However the Fourier transformed coefficients (Figure 7.12) do show evidence of the acoustic forcing frequency within their associated temporal coefficients (in particular for modes 1 and 3). In this case almost no harmonic frequencies at multiples of 62.5 Hz are visible. Finally random turbulent modes are also shown, as for example for mode 100.

The periodic flow field related to the acoustic absorption can now be reconstructed using only the modes which show a dominant frequency component in the temporal coefficient which is either equal to the forcing frequency or a harmonic of that frequency. This reconstruction of the flow field is detailed in the following section.

7.2.2 Flow Field Reconstruction

In conventional flows the turbulent flow field is characterised by a range of turbulent structures in which energy typically cascades from the large, energy containing, eddies into smaller structures from which turbulent energy is dissipated into heat. Hence the turbulent energy is distributed over a broad range of frequencies and gives rise to classic spectra (e.g. Pope (2000)) in which the various sub-ranges can be identified (i.e. energy containing range, non-viscous sub range, etc). Such a process would result in modes

whose temporal coefficients exhibit no preferred frequencies (e.g. mode 100 in Figure 7.9 and Figure 7.12). However, as already shown some modes exhibit temporal coefficients which suggest the velocity field, associated with that mode, has a preferred frequency of fluctuation that corresponds to the acoustic excitation frequency (or its harmonic). Hence this suggests that the velocity field associated with this mode, and its associated flow field features, has been generated by the incident acoustic pressure waves. In other words the energy associated with this mode has, potentially, originated from the acoustic field and therefore represents the mechanism by which energy is being absorbed from the incident acoustic waves.

A filter routine was developed which identifies modes whose temporal coefficients exhibit preferred frequencies at the excitation frequencies, or its harmonics, such as that indicated by modes 2 and 4 (Figure 7.9) or modes 1 and 3 (Figure 7.12). The function of the filtering is illustrated in Figure 7.13 with the spectrum of the temporal coefficient of mode 2 in the non-linear absorption example. The routine is averaging all the amplitudes within the spectrum. Furthermore the maximum amplitude and its frequency are also identified. The frequency at which the maximum amplitude occurs must lie within a frequency band Δf of $\pm$ 1% of the excitation frequency or its harmonics so that the mode is considered as an acoustically related mode. Finally the amplitude within the frequency band has to be at least two times larger than the averaged amplitude of the spectrum.

Applying the filter to the data set resulted in approximately 140 modes, out of the possible 3072 modes, being identified within the flow field of the non-linear absorption regime. Furthermore 720 modes have been identified within the flow field in the linear absorption regime. Figure 7.14 shows the cumulative energy distribution for the POD modes in the non-linear regime. The diamonds which coincide with the cumulative energy curve symbolise the filtered POD modes used by the reconstruction of the flow field. The diamonds which coincide with 0% cumulative energy indicate that these modes were not used. The same can be seen from Figure 7.15 for the measurement in the linear acoustic absorption regime. It can be seen that 9 out of the 10 first POD modes were used in the non-linear regime (Figure 7.14). Moreover these modes equate to 90% of the total kinetic energy of the oscillating flow field. For the linear regime

only 5 of the first 10 POD modes are used (Figure 7.15). Moreover comparing both cumulative energy curves it can be seen that more oscillating kinetic energy is contained within the first 10 modes relative to the total kinetic energy within the non-linear absorption regime. This is implying that the linear absorption regime case is dominated by smaller scale structures containing less of the total energy within the flow field compared to the non-linear absorption case.

The filtered POD modes are referred to as the 'acoustically related' modes and the flow field was then reconstructed using only these modes. This reconstructed velocity field is thought to represent the unsteady flow field generated by the acoustic pressure fluctuations. The remaining modes can also be reconstructed and this, of course, represents the random turbulent field. This flow field is associated with, for example, the mean flow and the turbulence generated as it passes through the orifice. In this way the instantaneous velocity field components defined in equation (7.12) could be identified and the associated flow fields reconstructed.

The power spectral density for the v-velocity component has been used to initially assess the velocity field of the acoustically related modes with respect to the total velocity field and the turbulent field. The turbulent field was reconstructed from the modes which were rejected by the filter function. Two points within the non-linear acoustic flow field, as indicated in Figure 7.16, were used for this analysis. In this case the total velocity was shown as a contour within the flow field and the orifice is located at $y/D = 0$. Point 1 was located on the centreline of the unsteady jet flow ($x/D = 0$ and $y/D = -0.4$) and point 2 was located within the shear layer of the pulsatile flow field ($x/D = 0.4$ and $y/D = -0.6$). The power spectral density for point 1 is shown in Figure 7.17. Spectra are presented for the total velocity field and the velocity fields reconstructed from the 'acoustically related' and 'turbulent related' POD modes identified by the filter. It can be seen that all the energy contained in the spectra at 125 Hz and its harmonics has been captured in the filtered flow field reconstructed from the 'acoustic related' modes. Alternatively the reconstructed velocity field from the 'turbulent related' modes has its energy distributed over a broad frequency range (as required). Similar behaviour can be seen for different regions of the flow field, such as in the shear layer region at the edge of the unsteady jet (point 2) as shown in Figure 7.18. These results suggest the

methodology has been successful in identifying the coherent structures and other features that are generated by the incident acoustic pressure waves.

The same filter has been applied to the POD modes of the flow fields within the linear absorption regime, e.g. Figure 7.10 - Figure 7.12. Again two points within the unsteady flow field are chosen (Figure 7.19) to assess the effectiveness of the filter routine. The power spectral densities of point 1, on the centreline of the jet, and point 2, within the shear layer of the jet, are shown in Figure 7.20 and Figure 7.21. It can be seen that all the periodic components within the power spectral densities has been filtered out of the total velocity flow field for both cases. Moreover the turbulent fluctuations within the flow field have been minimised within the periodic acoustically related flow field. Hence the filter function was capable of filtering the relevant periodic coherent POD modes.

Comparison of Raw and Reconstructed Flow Field – Non-Linear Absorption Regime

The flow field reconstructed on the downstream side of the orifice, using the 'acoustic related' modes, is shown for various phases of the acoustic cycle in comparison to the raw velocity field (Figure 7.22) for the non-linear absorption regime. Moreover the phase angle of the acoustic oscillation, streamtraces to highlight the vortex rings within the flow field as well as the contour of the unsteady velocity magnitude are included in the figures. It can be seen that the incident acoustic waves generate an unsteady pressure drop across the orifice which leads to the pulsation of flow through the orifice. As fluid issues from the orifice it rolls up to form a vortex ring structure. The vortex ring structure then induces a flow field through the centre of the ring propelling the structure away from the aperture. It can be seen that most of the random turbulent velocity oscillations have been suppressed in the reconstructed acoustically related velocity field compared to the raw velocity field which is further encouragement that the filter method for the acoustically related modes is working in the non-linear absorption regime.

Comparison of Raw and Reconstructed Flow Field – Linear Absorption Regime

Figure 7.23 shows the reconstructed acoustically related flow field in comparison to the raw velocity field for the example in the linear regime. Note that the mean flow field is included in the acoustically related field as well as in the raw velocity field for

comparison. The contours of the velocity magnitude together with streamtraces to highlight the flow field characteristic are shown in the figures. In this case two instantaneous flow fields near the maximum velocity within the acoustic cycle are shown. A pulsatile jet flow is visible which develops a shear layer at the edge of the orifice. Again comparing the raw velocity field with the acoustically related flow field shows that the majority of the random turbulent velocity oscillations have been filtered out just leaving the oscillating jet flow. Hence the filter routine is operating as intended within the linear absorption regime.

7.2.3 Validation of the Unsteady Flow Field Methodology

A further validation of the method has been conducted comparing the acoustic energy loss (derived from the pressure measurement) to the kinetic energy captured within the acoustically related flow field. For the described method to be valid the calculated energy loss for both cases has to agree. The validation within the linear and non-linear regime is described in detail in appendix C or in Rupp et. al. (2010b). However a brief overview of the energy loss calculation and the validation results is shown in this section.

The loss of acoustic energy derived from the pressure measurements can be calculated based on the acoustic energy fluxes as shown in equations (5.1) to (5.3). Moreover the unsteady energy flux measured from the filtered acoustically related unsteady velocity field can be derived using the unsteady energy flux of the jet flow:

$$\dot{E} = \frac{1}{2}\dot{m}\bar{v}^2 . \tag{7.13}$$

The detailed energy flux calculation performed on the acoustically related flow field is described in appendix C.

Figure 7.24 shows the comparison between the acoustic energy loss and the kinetic energy flux derived from the unsteady flow field for an example in the non-linear and the linear acoustic absorption regime. It can be seen that the kinetic energy flux derived from the acoustically related flow field agrees very well with the measured acoustic energy loss for both the linear and non-linear regime. As it can be seen in the non-linear absorption regime only a small amount of the kinetic energy originates from the mean

flow field. Hence the total velocity field and the acoustically related flow field show very similar kinetic energy fluxes. However, as is shown for the linear case, the mean flow field and the associated random turbulent portion show a much larger acoustic energy flux compared with the acoustic measurement and the filtered acoustically related velocity field. This shows the importance of the method for the cases where the influence of energy sources other than the acoustic energy sources are large. In general the method agrees very well with the acoustic absorption measurement. Therefore the data suggests that the relevant acoustic flow field has been captured and the method is valid.

7.3 Characteristics of the Unsteady Velocity Field Related to Acoustic Absorption

As the flow field analysis technique has been validated using the data measured from the acoustic experiments it is now possible to investigate the flow field features associated with the acoustic absorption behaviour in more detail.

7.3.1 Non-Linear Absorption Regime

As discussed in the previous sections the non-linear acoustic absorption regime is characterised by large scale vortex rings. The interaction of the large scale structures with the unsteady jet flow is thought to be the main influence on the acoustic absorption characteristics described in chapter 6. For example Figure 7.25 shows a comparison of the mean velocity field between the unforced flow field (no acoustic excitation) and the forced flow field (137 dB excitation). In the unforced case a steady jet flow entering and exiting the aperture is visible. This is very different in the case with acoustic excitation. The generated vortex ring structures upstream and downstream of the orifice induce a velocity field through the centre of the vortex ring which is directed away from the aperture. In this way the vortex rings are propelled further downstream from the aperture. The induced flow field generated by the vortex rings produces a mean flow field which is significantly different to the mean flow field without acoustic excitation. Hence the unsteady flow field and the influence of the vortex ring structures have been investigated further in this section.

Prior to discussing the unsteady flow field in more detail some important parameters are introduced. The velocities shown in this section have been non-dimensionalised using the mean blowing velocity (e.g. Jabbal et. al. (2006))

$$\overline{U}_{blow} = \frac{1}{T}\int_0^{T/2} U_{bulk}(t)dt \,. \tag{7.14}$$

In this case the blowing velocity represents the outflow velocity into the downstream or upstream flow field integrated over half an acoustic cycle. Moreover the bulk velocity U_{bulk} is defined as the area averaged *v*-velocity component at the downstream exit of the aperture (e.g. Jabbal et. al. (2006))

$$U_{bulk}(t) = \frac{\dot{m}(t)}{A_D \rho} = \frac{2\pi}{A_D}\int_0^R v(r,t)\, r\, dr \,. \tag{7.15}$$

Another important parameter is the generated vorticity of the unsteady jet flows. The measured planar flow fields consist of *u* and *v*-velocity components; hence the vorticity in the z-direction can be considered (equation 2.7)

$$\omega_z = \frac{\partial v}{\partial x} - \frac{\partial u}{\partial y} \,. \tag{7.16}$$

The measured flow field is *i* and *j* ordered for the *x* and *y* coordinate directions. Thus the first order differential operators in the vorticity equation (7.16*)* have been defined using the least squares method as defined in Raffel et. al. (1998):

$$\frac{\partial u(i,j)}{\partial y(i,j)} \approx \frac{2u(i,j+2)+u(i,j+1)-u(i,j-1)-2u(i,j-2)}{10\Delta y} \,. \tag{7.17}$$

The same differential operator was used on the *v*-velocity derivative. Furthermore at the edges of the flow field less accurate forward and backward differences are applied. In this case the vorticity has been non-dimensionalised using the mean blowing velocity of the unsteady jet case

$$\omega_N = \frac{\omega_z\, \overline{U}_{blow}}{D} \,. \tag{7.18}$$

Similar vorticity normalisations have been defined by other authors, e.g. Krueger et. al. (2006) and Aydemir et. al. (2012).

As shown in the previous section the measured acoustic energy loss agrees very well with the kinetic energy present in the unsteady flow field. The method by which the kinetic energy of the unsteady flow field was calculated provides an insight into the energy transfer that occurs within the flow field. In the non-linear regime two methods can be used to estimate the energy within the flow field upstream and downstream of the orifice.

i) An integration was used over a cylindrical volume (see Figure 7.26 (a)) to estimate the kinetic energy within the flow field. The calculation of the kinetic energy in the unsteady flow field was based on the method proposed by Tam and Kurbatskii (2000). This method captures the kinetic energy contained within the vortex ring structure and the pulsatile jet flow.

ii) The kinetic energy flux of the upstream flow field was calculated in the plane immediately upstream and downstream of the orifice (example of downstream surface is shown in Figure 7.26 (b)). In this case only the kinetic energy flux of the pulsatile jet flow is represented.

Figure 7.27 shows a comparison between (i) the two kinetic energy calculation methods derived from the acoustically related flow field and (ii) the measured acoustic energy loss from the acoustic experiment The detailed definition for both methods can be found in appendix C. As can be seen both methods agree very well within the accuracy of the experiments. To investigate the energy transfer further the measured velocity fields have been phase averaged as described in appendix D. The phase averaged data was then used to calculate the kinetic energy of the pulsatile flow and the vortex ring in the flow field at various time steps throughout the acoustic cycle.

Figure 7.28 shows the calculated kinetic energy in the downstream field of view as well as the v-velocity component on the centreline immediately downstream of the aperture. The kinetic energy in Figure 7.28 has been normalised using the maximum kinetic energy calculated within one acoustic cycle. Furthermore the velocity has been normalised using the mean blowing velocity as described in (7.14) It can be seen that

the kinetic energy of the pulsatile flow field is increasing up to a maximum at t/T = 0.34. Thereafter the kinetic energy is reducing. The presented data can be used to estimate the transfer of kinetic energy from the pulsatile jet into the kinetic energy of the vortex ring. During the outflow of fluid into the downstream control volume the sign of the velocity is negative. During the inflow phase (i.e. change of flow direction from downstream to upstream) where the velocity changes sign no further kinetic energy flux will be transferred into the downstream flow field. As Figure 7.29 shows the vorticity field for the 131 dB forcing at the time step t/T = 0.57 does only show the vortex ring and the induced flow field through the centre of the ring vortex. Hence the kinetic energy at time step t/T = 0.57 can be used to estimate the kinetic energy of the vortex ring structure (identified with a red line in Figure 7.28). In this case approximately 73% of the maximum kinetic energy within the flow field has been transferred to the vortex ring structure. The same approach was used for the 137 dB excitation case and approximately 86% of the maximum kinetic energy in the flow field was transferred to the vortex ring. For the 142 dB excitation case the vortex ring energy could not be estimated as parts of the ring vortex travelled already outside the field of view (Figure 7.29). This shows that the acoustic excitation generates an unsteady jet flow across the aperture. Parts of the kinetic energy of this pulsatile jet flow is converted into the kinetic energy of large scale vortex rings and parts of the energy being dissipated in the shear layers of the pulsatile jet.

The non-linear acoustic absorption coefficient for the investigated flow fields was shown in Figure 7.3. The changes in acoustic reactance and resistance have been discussed in the previous section. However it is apparent that the phase angle between the pressure amplitude incident onto the aperture and the velocity amplitude within the aperture is reducing with increasing excitation pressure amplitude due to the discussed reduction in acoustic reactance with increasing pressure amplitude (section 6.1). This is indicated in the acoustic experiment as shown in Figure 7.30. The phase averaged centreline velocities of the acoustically related flow field downstream of the aperture is also shown in Figure 7.31 for the three forcing cases. Unfortunately the velocity measurements have not been synchronised with the pressure measurement. However, as the PIV measurement has been triggered off the function generator for the loudspeaker

signal it can be expected that the PIV measurement was taken at the same phase location of the acoustic cycle. Hence the relative phase of the oscillating velocity field with increasing incident pressure amplitude can be assessed. The example in Figure 7.31 shows that the maximum downstream centreline velocity for three different acoustic pressure amplitudes occurs at an earlier time within the acoustic cycle for increasing excitation pressure amplitudes. This is indicative of a reduction in phase angle between the pressure amplitudes and velocity amplitudes and agrees with the measured acoustic data.

The explanation for this shift in frequency can be found by investigating the location of the vortex ring relative to the aperture. This has been conducted for the example of the downstream velocity field in Figure 7.32. The total velocity contours as well as stream traces are shown for the three excitation cases. Note for convenience the total velocity contour has been normalised with the mean blowing velocity. The three forcing cases are shown at the point where the flow direction changes from the downstream flow field into the upstream flow field. It can be seen that the direction of the centreline velocities at the orifice exit ($x/D = 0$ and $y/D = 0$) are still pointing into the downstream flow filed. However at the aperture edges ($-0.5 < x/D < -0.3$ and $0.3 < x/D < 0.5$ at $y/D = 0$) inflow into the aperture occurs with stream traces pointing into the upstream flow field. It can be seen that for the small forcing amplitude of 131 dB the vortex ring remains in the direct vicinity of the aperture (i.e. $y/D \sim 0.6$). The cases with larger excitation amplitude show the location of the vortex ring further downstream (i.e. $y/D \sim 1.4$ for 137 dB excitation and $y/D \sim$ 142 dB excitation). In these cases the larger kinetic energy of the vortex ring together with the higher unsteady jet velocity has propelled the structure further away from the orifice. As the ring remains in the vicinity of the aperture for the small excitation cases it is acting as an additional blockage for the flow to pass through the aperture during the change in flow direction. In this case the inflow to the aperture needs to flow around the structure and therefore more time is needed for the fluid to get through the aperture. The further the ring vortex structure is away from the orifice the smaller is the interaction with the incoming fluid to the aperture and therefore the phase between the pressure oscillation and the velocity oscillation reduces.

This phenomenon explains the reduction in the measured acoustic reactance for the aperture.

Overall it can be concluded that the change in the acoustic impedance, i.e. the decrease in reactance with increasing pressure amplitude, as described in the previous chapter, is caused by the characteristics of the generated vortex ring structure within the non-linear acoustic absorption regime. The changes in the acoustic quantities are controlled by the interaction between the unsteady jet flow and the vortex ring structures. The pulsatile jet seems to supply the energy for the vortex ring structures as indicated by kinetic energy within the flow field and the energy flux across the aperture. Moreover the vortex ring interacts with the fluid flowing in and out of the aperture during the change of sign in the acoustic forcing cycle. Therefore the changes in the measured acoustic impedance and ultimately the acoustic absorption are directly related to the interaction between vortex rings and the pulsatile jet flow and thus to the location of the ring relative to the orifice. Hence a better understanding of this behaviour would improve the non-linear modelling techniques. Therefore the developed methodology could aid in further detailed unsteady flow investigations in the non-linear acoustic absorption regime.

7.3.2 Linear Absorption Regime

In this section the acoustically related flow field during linear acoustic absorption is investigated. Figure 7.33 shows the phase averaged v-velocity contour on the centreline (x/D = 0 and y/D = -0.07) of the orifice within the downstream flow field for an orifice with L/D = 0.5 at dp/p = 0.8% as well as L/D = 1 at dp/p = 0.3%. Three components of the acoustically related velocity field are shown in both graphs: the acoustically related flow fields including mean flow and all relevant POD modes, POD mode 1 including the mean flow field and POD mode 1 only. It can be seen that the velocity oscillation on the centreline can be reproduced using POD mode 1 including the mean flow only. Moreover the first POD mode also contains 77% of the kinetic energy flux, which also accounts for 77% of the total acoustic energy loss. Hence this could be seen as the most dominant mode in the flow field. Hence the linear flow field and in particular the first POD mode will be investigated in this section.

Figure 7.34 shows the phase averaged acoustically related flow field including mean flow for four instances during the acoustic cycle. In this case the flow fields for an orifice of L/D = 0.5 at dp/p = 0.8% pressure drop was investigated. However, this flow field is representative of the characteristics for all the investigated flow fields within the linear regime for Strouhal numbers below 0.2. The orifice location is also indicated at the top of the downstream flow field at $-0.5 < x/D < 0.5$ and $y/D = 0$. The flow field is indicating a pulsatile jet flow with no visible significant flow structures such as eddies or vortex rings. This is expected for a flow field associated with the linear acoustic absorption as described in chapter 5.

However the flow field and its pulsatile nature can be further investigated showing POD mode 1, which is seen as the dominant mode within the linear acoustic absorption. Figure 7.35 shows the total velocity contours of POD mode 1 for L/D = 0.5 and dp/p = 0.8% during linear acoustic absorption. Four instances along the acoustic cycle are shown together with the velocity vectors. The length of each vector is scaled relative to the velocity contour. No mean flow is present within the POD mode and hence the velocity contour is changing sign from negative maximum velocity at t/T = 0.02 to 0 at t/T = 0.2 and maximum positive velocity at t/T = 0.5. As could have been expected from the quasi-steady investigation in chapter 5.5, the linear acoustic absorption is dominated by a pulsatile flow field. This flow field subsequently decays into smaller scale structures as for example shown in Figure 7.36 which ultimately decay within the turbulent field of the jet. The structures indicated in Figure 7.36 do not seem to influence the pulsatile jet flow field as they are not visible within the acoustically related field of Figure 7.34. It can be assumed that these structures are part of the energy dissipation process in the flow field (following the cascade processes as described for example in Pope (2000)). Moreover an example of a forced and unforced mean jet flow within the linear absorption regime is shown in Figure 7.37. There is no significant difference between the forced and unforced jet visible. Therefore it can be concluded that the unsteady flow field characteristics do not influence the mean flow field.

The measurements indicate that linear acoustic absorption at gas turbine combustion system Strouhal numbers is associated with pulsatile, quasi-steady flow. In these cases the acoustic length correction and the steady state discharge coefficient remain constant,

i.e. chapter 5.9.1, which seems to be indicative that the unsteady flow structures produced are not large enough to influence the pulsatile flow field of the orifice. Hence simple one-dimensional models with representative steady state discharge coefficient and constant length correction simulating the oscillating mass of the aperture flow field are adequate. The flow field studies seem to be only required in areas where the linear acoustic absorption is affected by unsteady flow structures within the flow field. However a useful application of the described method would be the investigation of the unsteady flow field within an aperture with large *L/D* ratio. As chapter 5 has shown this is still a challenging area for a linear absorption model. Hence the application of the method to CFD simulations or more sophisticated measurements within the aperture would have the potential to improve the accuracy of the analytical modelling technique.

7.3.3 Transition from Linear to Non-Linear Absorption

Another purpose for the developed methodology is the transition from linear to non-linear absorption. As described in chapter 6.4 this is an important part for acoustic dampers designed for gas turbine combustors. As amplitudes increase and the absorption transitions from linear to non-linear acoustic absorption the relationship between pressure and velocity oscillation changes from linear to non-linear. The accurate prediction of the velocity amplitude is not only important for an accurate absorption prediction but also the assessment of hot gas ingestion into the damper geometry. The modelling aspects of the transition was described in Chapter 6.4.3 and it was highlighted that this is a challenging task and heavily reliant on empirical data. Unfortunately only limited data has been recorded for the unsteady flow field investigation within the transition region. Nevertheless the developed methodology was used to show some of the relevant unsteady flow features.

Figure 7.38 shows the acoustic absorption measurements for two orifice plates at two mean pressure drops. Moreover for each orifice plate two PIV measurements have been conducted. It can be seen that the PIV flow field measurement for the cylindrical orifice with $L/D = 0.5$ and the conical orifice at a mean pressure drop of $dp/p = 0.3\%$ is within the linear acoustic absorption regime as indicated by constant absorption coefficients for increasing excitation pressure amplitudes. Moreover the PIV measurement for both orifice plates at reduced pressure drop of 0.1% is within the transition region to non-

linear acoustic absorption. Thereby the cylindrical orifice is located closer to the onset of non-linear absorption whereas the test condition for the conical orifice plate is further within the transition region of non-linear absorption.

The phase averaged normalised total velocity contours for the cylindrical orifice are shown in Figure 7.39 together with the spectrum of the *v*-velocity component for the two mean pressure drops at $x/D = 0$ and $y/D = -0.26$. It can be seen that the phase averaged velocity for the $dp/p = 0.3\%$ case is looking more like a sine-wave whereas the phase averaged normalised velocity trace is distorted indicating the occurrence of harmonics. This is confirmed by the Fourier transformation of the *v*-velocity component on the centreline of the orifice from the acoustically related flow field. In both cases the first harmonic of 125 Hz is visible. However in the non-linear absorption case the harmonic is larger. Moreover higher order harmonics are also visible. The velocity amplitude ratio calculated using the *v*-velocity amplitude on the centreline of the orifice and the time averaged *v*-velocity component at the same location is measured as 0.19 for the linear absorption case and 0.39 for the transition to non-linear acoustic absorption case (which is in agreement with the velocity amplitude ratio shown in chapter 6.4.1). The same behaviour can be seen for the conical orifice plate with 45° cone angle as shown in Figure 7.40. Again the phase averaged normalised velocity is shown for the linear and non-linear case as well as a Fourier spectrum of the centreline velocity. Again the velocity amplitude for the linear case is measured as 0.27 and 0.6 for the non-linear case. However in this case the onset of higher order harmonics (3^{rd} and 4^{th}) is already shown in the velocity spectrum for the $dp/p = 0.3\%$ case. This is due to the increased velocity amplitude and the vicinity to the onset of non-linear absorption which is also shown in Figure 7.38 for the $dp/p = 0.3\%$ case.

The acoustically related normalised total velocity field for cylindrical orifice of $L/D = 0.5$ and $dp/p = 03\%$ is shown in Figure 7.41. In general this pulsatile jet flow is very similar to the one shown earlier for the linear regime, e.g. Figure 7.34. Moreover the streamtraces of the velocity fields are shown to highlight any occurring flow structures. It can be seen that there are no significant unsteady flow structures visible affecting the unsteady flow field.

Figure 7.42 shows the phase averaged normalised total velocity contours for the acoustically related flow field associated with the onset to non-linear acoustic absorption. In this case the mean pressure drop was 0.1% and the cylindrical orifice with L/D = 0.5 was investigated. The three flow fields represent phases within the acoustic cycle which clearly show the development of a vortex structure within the flow field during the pulsatile outflow cycle for $t/T > 0.5$.

The influence of the vortex ring structure is also clearly visible in Figure 7.43 where the acoustic forcing is much further into the non-linear absorption regime. This flow field is looking very similar to the flow field shown in the non-linear absorption cases, e.g. Figure 7.22.

The captured data suggests that the occurrence of vortex rings is related to the transition to non-linear acoustic absorption. No significant large scale flow structure is visible within the data captured during the linear acoustic absorption. However at the onset of non-linear acoustic absorption the occurrence of higher order harmonics in the velocity field become visible. The harmonics in the spectrum are most likely produced by the occurrence of large scale flow structures which are interacting with the unsteady flow field. Thus the transition from a linear relationship between pressure and velocity to a non-linear relationship is caused by the change from a pulsatile flow field without flow structures to the pulsatile flow field influenced by large scale vortex ring structures.

7.4 Closure

In this chapter an analysis technique has been developed which enables the identification of the unsteady flow field associated with the acoustic absorption. This method was based on POD analysis and an adequate filter function for the identification of the acoustically related POD modes. In this case the method has been applied to PIV measurement data. Nevertheless the methodology could also be applied to any velocity field prediction or measurements with adequate temporal or spatial resolution. The method has been successfully validated against the measured acoustic energy loss based on the data described in chapter 5 and 6. For all the investigated flow fields the kinetic energy flux of the acoustically related flow field was in very good agreement with the

measured acoustic energy loss from the two-microphone measurements. Moreover the method has shown its potential in identifying relevant mechanism to describe the acoustic absorption behaviour of the investigated orifice plates in the linear and non-linear absorption regime as well as in the transition region from linear to non-linear acoustic absorption.

For example the investigation into the flow field during non-linear acoustic absorption has shown that observed changes in acoustic absorption and acoustic impedance reflect the fluid dynamic characteristics of the generated large scale vortex ring structures. It was found that the unsteady kinetic energy flux across the aperture agree with the amount of acoustic energy absorbed. Furthermore it was shown that a significant amount of this energy flux is transferred into the kinetic energy of vortex ring structures. These vortex rings interact with the mean flow field as well as with the unsteady pulsatile flow field. It was shown that the reduction in acoustic reactance is due to the increasing distance between the vortex ring and the orifice for increasing pressure amplitudes. At small amplitudes the large scale structure remains in the vicinity of the aperture and acts as an additional blockage for the flow into the aperture. As the amplitudes are increased the ring vortex is propelled further away from the aperture. Hence the additional blockage is reduced enabling the fluid to pass through the orifice without having to flow around the ring structure. Thus the ring vortex interacts less with the inflow into the aperture and the phase between pressure and velocity amplitudes reduces. Furthermore the measured flow fields also show that large scale ring vortices occur at the onset of non-linear acoustic absorption.

The flow field for the linear acoustic absorption regime has shown no significant unsteady flow structures within the flow field. In this case the unsteady flow field is dominated by a pulsatile jet flow for the operating conditions investigated. Hence the acoustic absorption mechanism is an energy transfer from the acoustic field into the kinetic energy of the unsteady jet. Ultimately kinetic energy of the flow field is dissipated by turbulence. It seems as if a flow field investigation is less important for the linear flow field within the considered Strouhal number range of relevance to this investigation. However for technical applications with higher Strouhal numbers this method could be used to identify the unsteady flow phenomena.

The developed method could be applied to CFD simulations or experimental measurements of the unsteady flow. In this way the influence of the optimum vortex ring formation upon the optimum acoustic absorption with changing length-to-diameter ratios could be further assessed. Moreover the method could also be used to investigate the linear absorption regime and the unsteady flow within long apertures with *L/D* larger two. In this way the unsteady flow analysis could be used to improve the current analytical modelling assumptions.

Figures

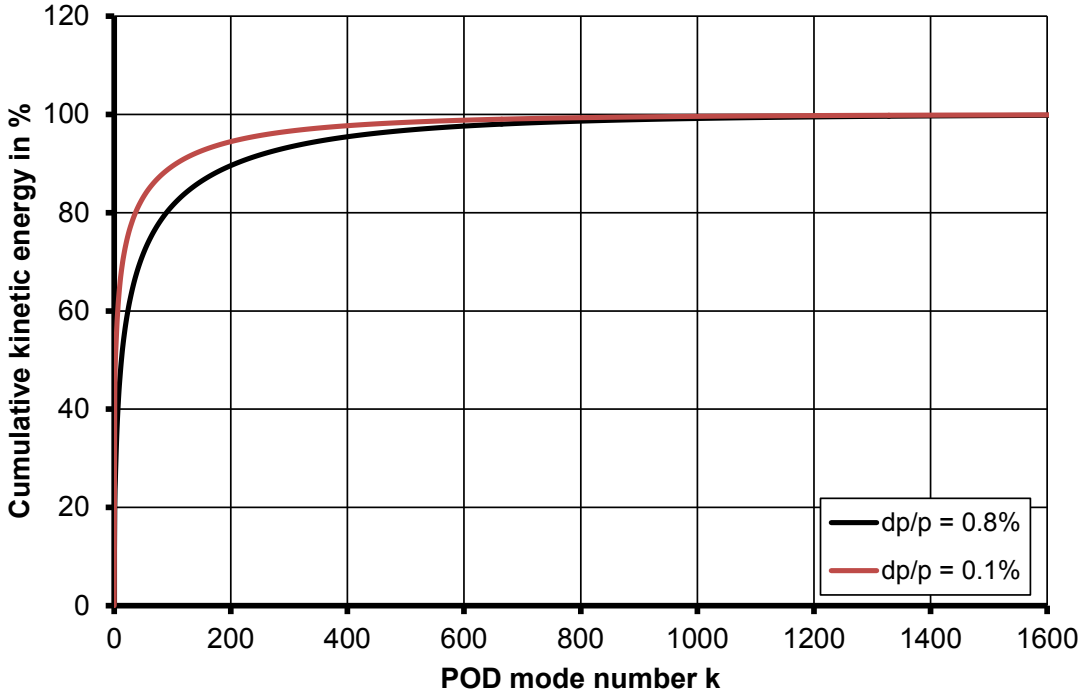

Figure 7.1: Example of cumulative kinetic energy within POD modes for the data set at 0.8% *dp/p* and 135 dB excitation amplitude, plate number 3.

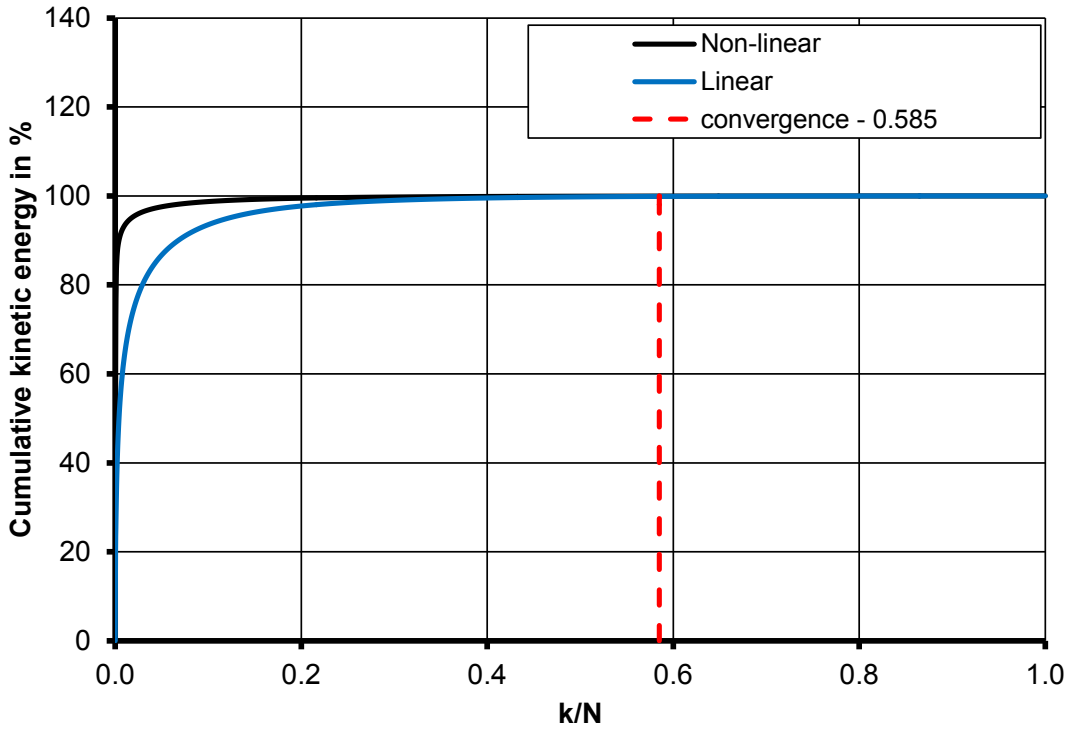

Figure 7.2: Example of convergence of cumulative energy for example POD modes

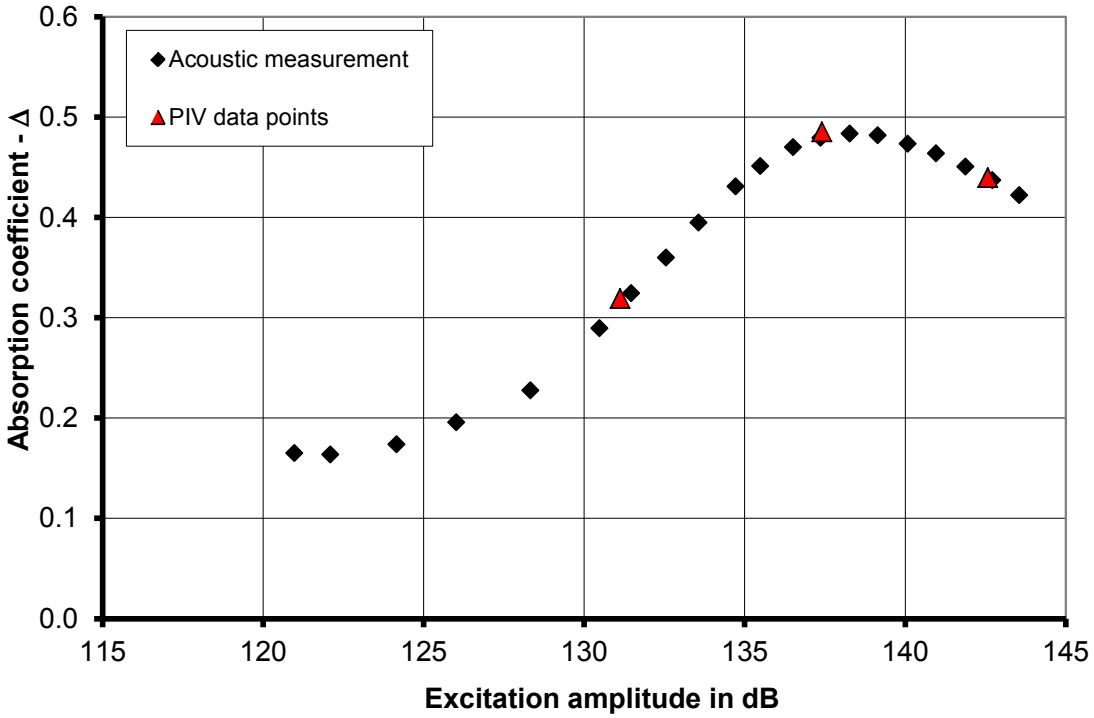

Figure 7.3: PIV data points relative to measured absorption coefficient curves, non-linear acoustic absorption, *L/D* = 0.47, *f* = 125 Hz, plate number 1.

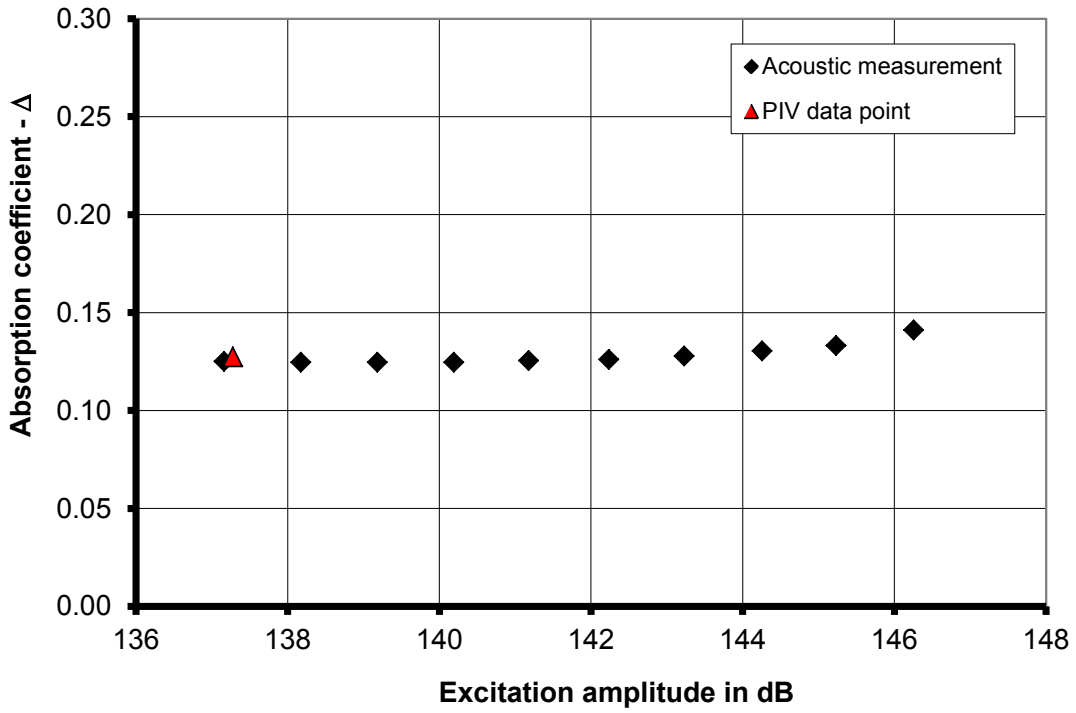

Figure 7.4: PIV data points relative to measured absorption coefficient curve, linear acoustic absorption, *L/D* = 0.5, *f* = 62.5 Hz, 0.8% *dp/p,* plate number 3.

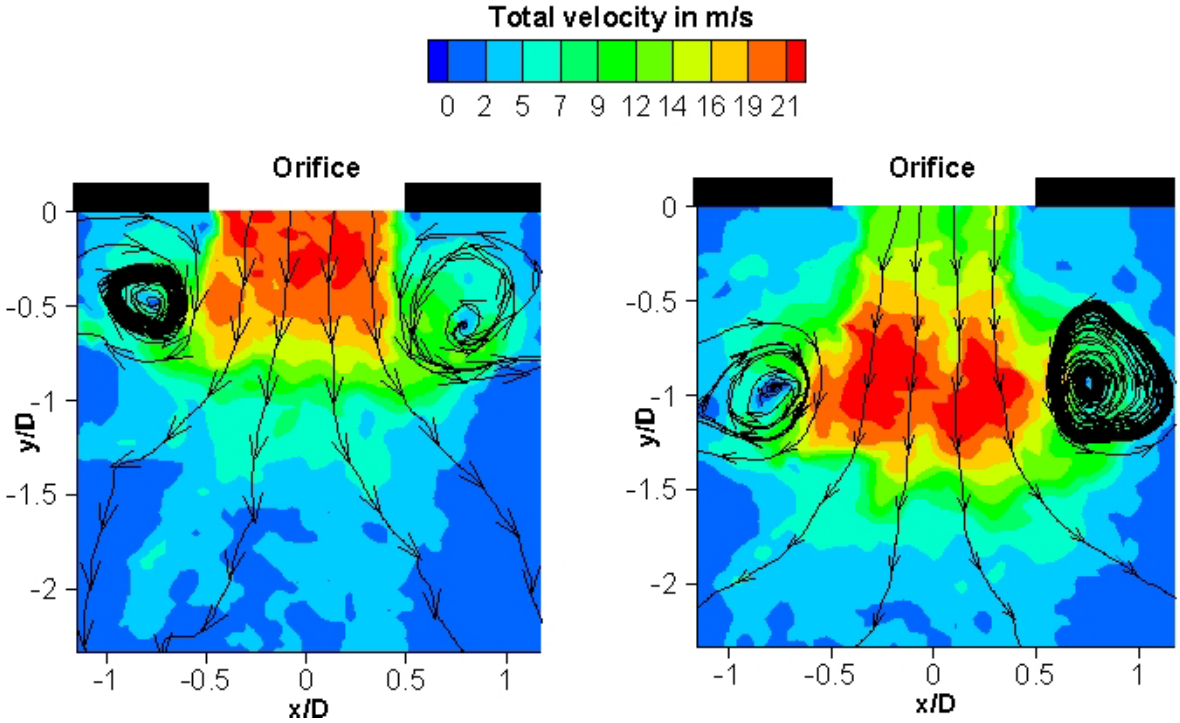

Figure 7.5: Example of instantaneous velocity field, non-linear acoustic absorption, *L/D* = 0.47, *f* = 125 Hz, plate number 1.

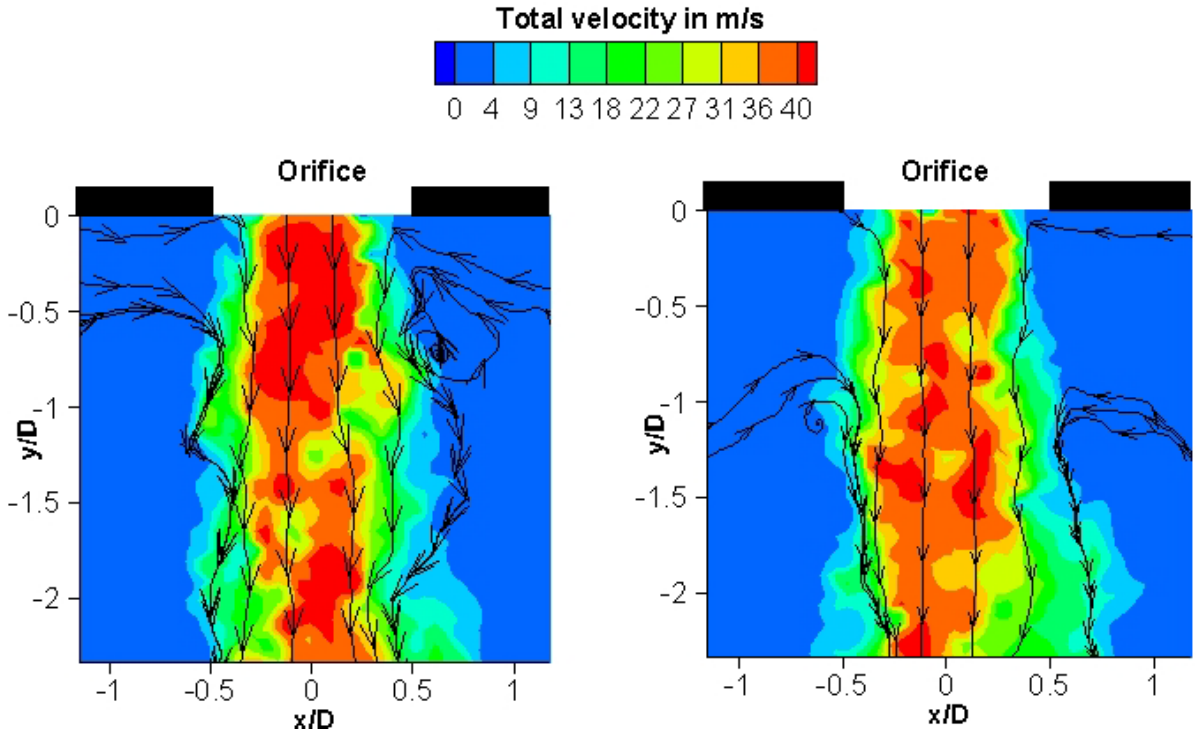

Figure 7.6: Example of instantaneous velocity field, linear acoustic absorption, *L/D* = 0.5, *f* = 62.5 Hz, 0.8% *dp/p,* plate number 3.

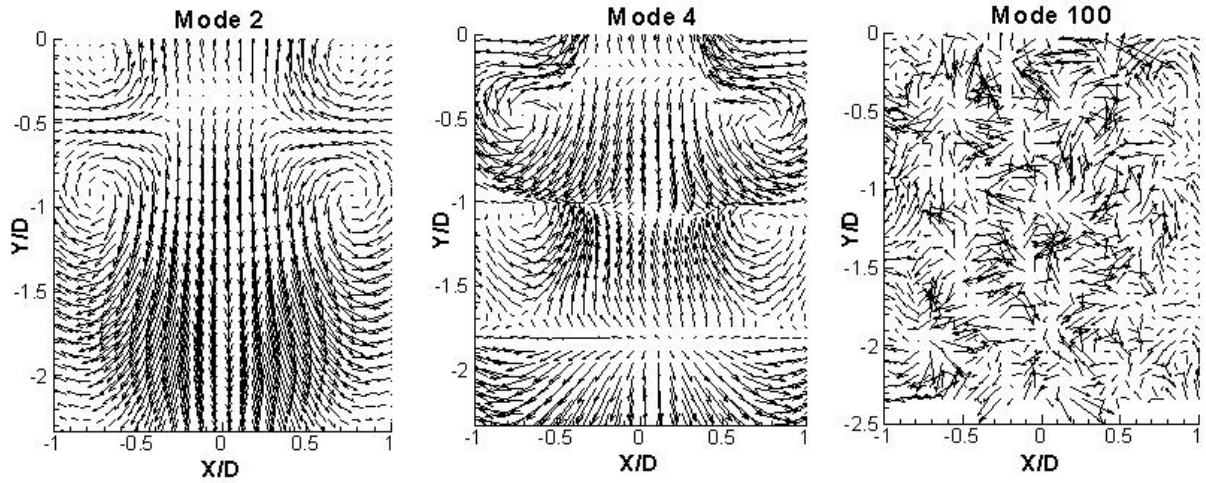

Figure 7.7: Example of structural modes (vectors not to scale), non-linear absorption, 137 dB and 125 Hz, plate number 1.

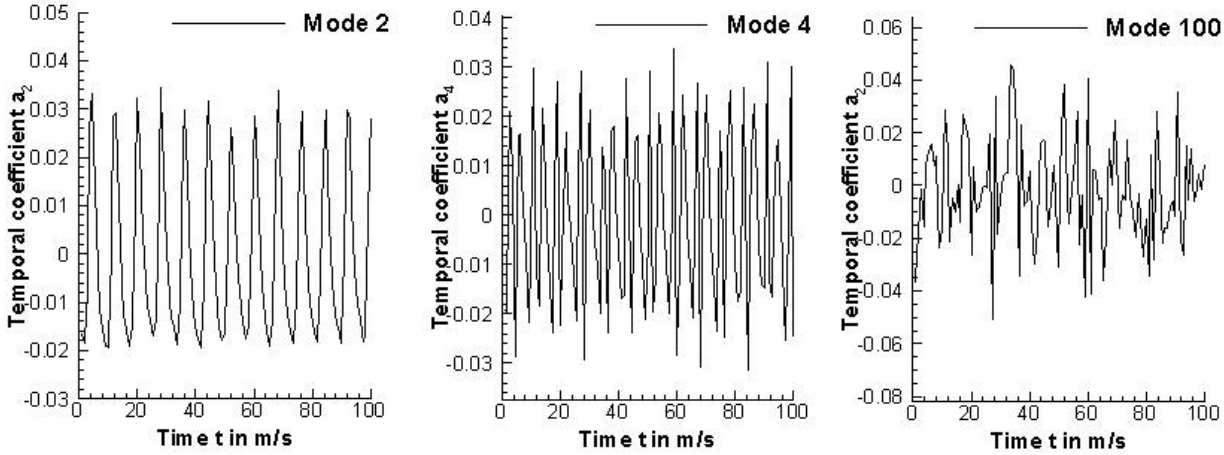

Figure 7.8: Example of temporal coefficient, non-linear absorption, 137 dB and 125 Hz, plate number 1.

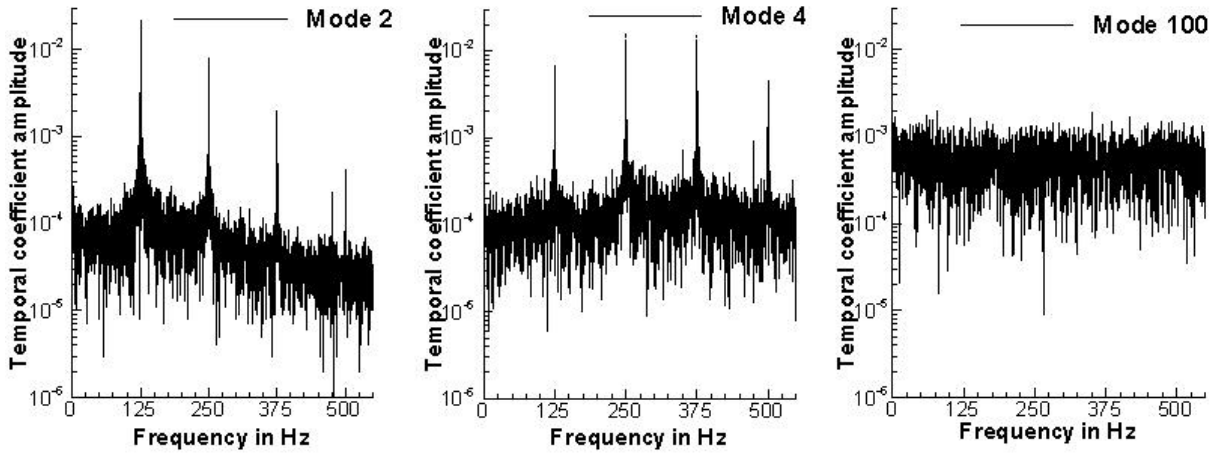

Figure 7.9: Example of Fourier transformed temporal coefficient, non-linear absorption, 137 dB and 125 Hz, plate number 1.

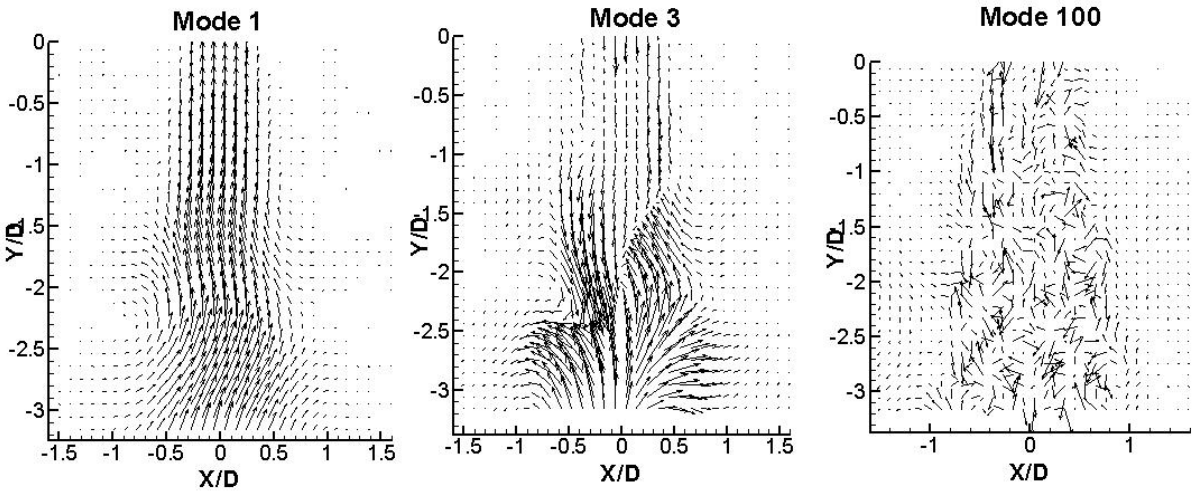

Figure 7.10: Example of spatial modes (vectors not to scale), linear absorption, 135 dB, 62.5 Hz, 0.8% *dp/p,* , plate number 3.

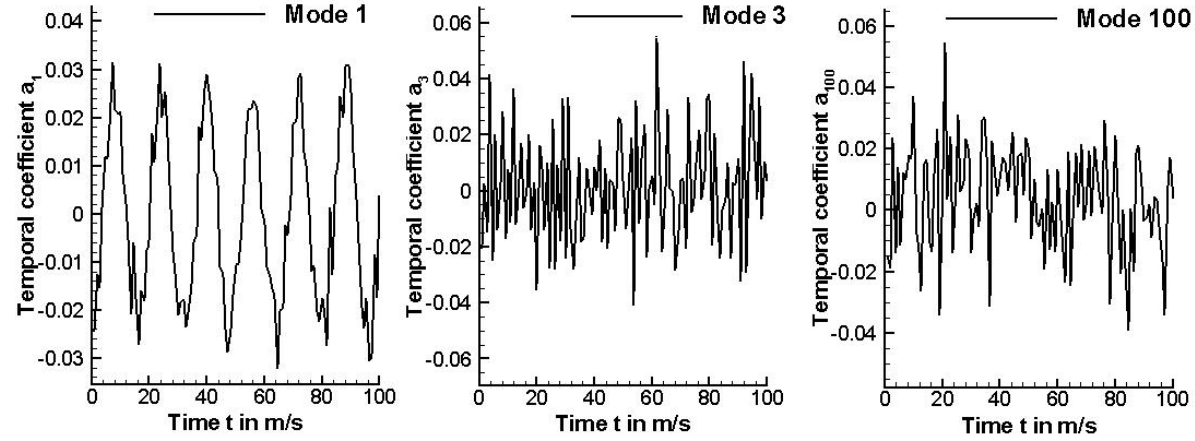

Figure 7.11: Example of temporal coefficient, linear absorption, 135 dB, 62.5 Hz, 0.8% *dp/p,* , plate number 3.

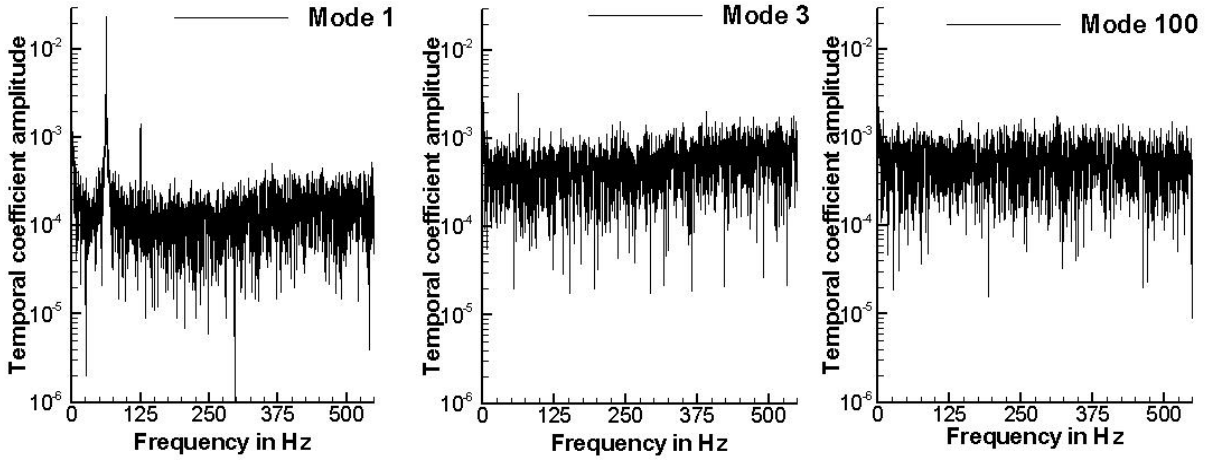

Figure 7.12: Example of Fourier transformed temporal coefficient, linear absorption, 135dB, 62.5 Hz 0.8% *dp/*, plate number 3.

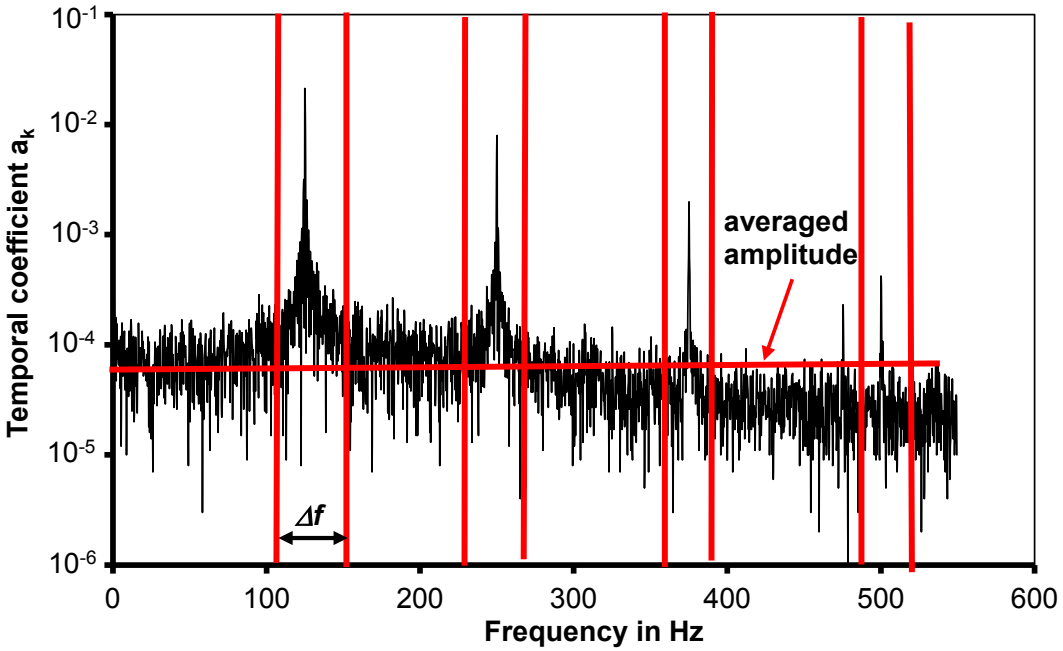

Figure 7.13: Example of developed filter for temporal coefficient, Mode 2, 137 dB, 125 Hz, non-linear absorption regime, plate number 1.

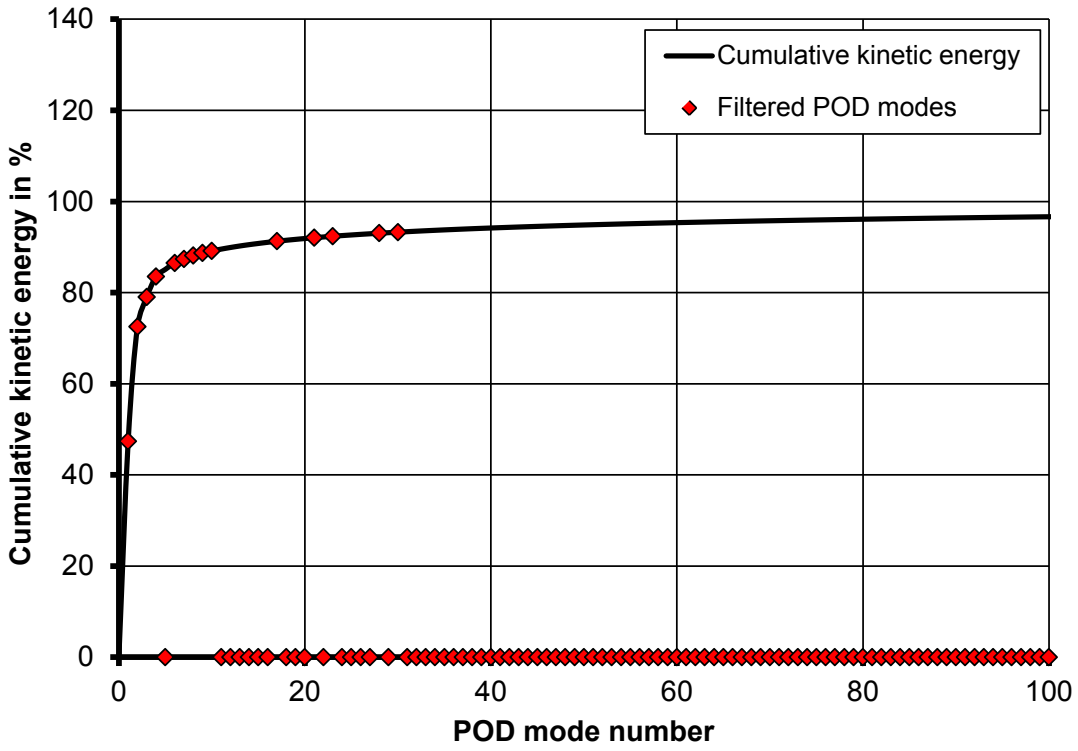

Figure 7.14: Example of filtered POD modes in the non-linear absorption regime

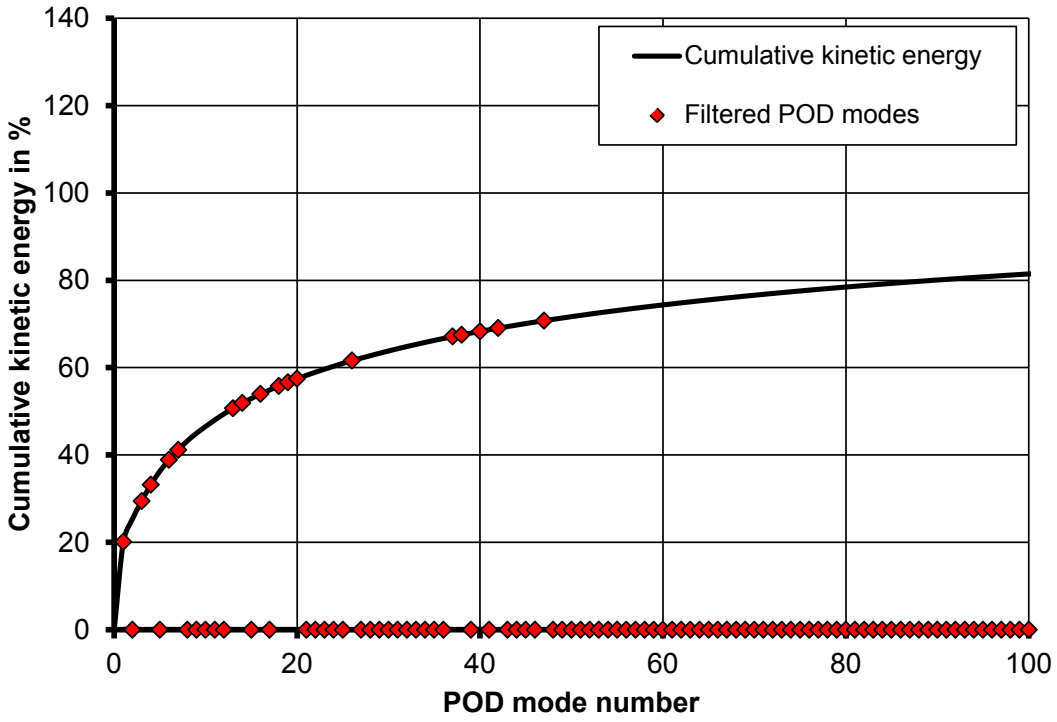

Figure 7.15: Example of filtered POD modes in the linear absorption regime

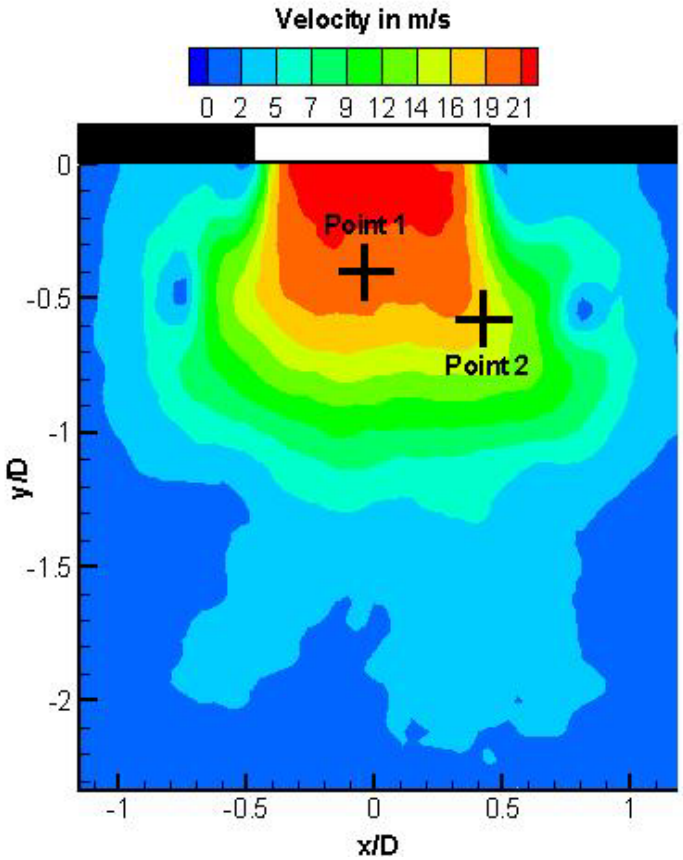

Figure 7.16: Position of calculated power spectral density, non-linear absorption.

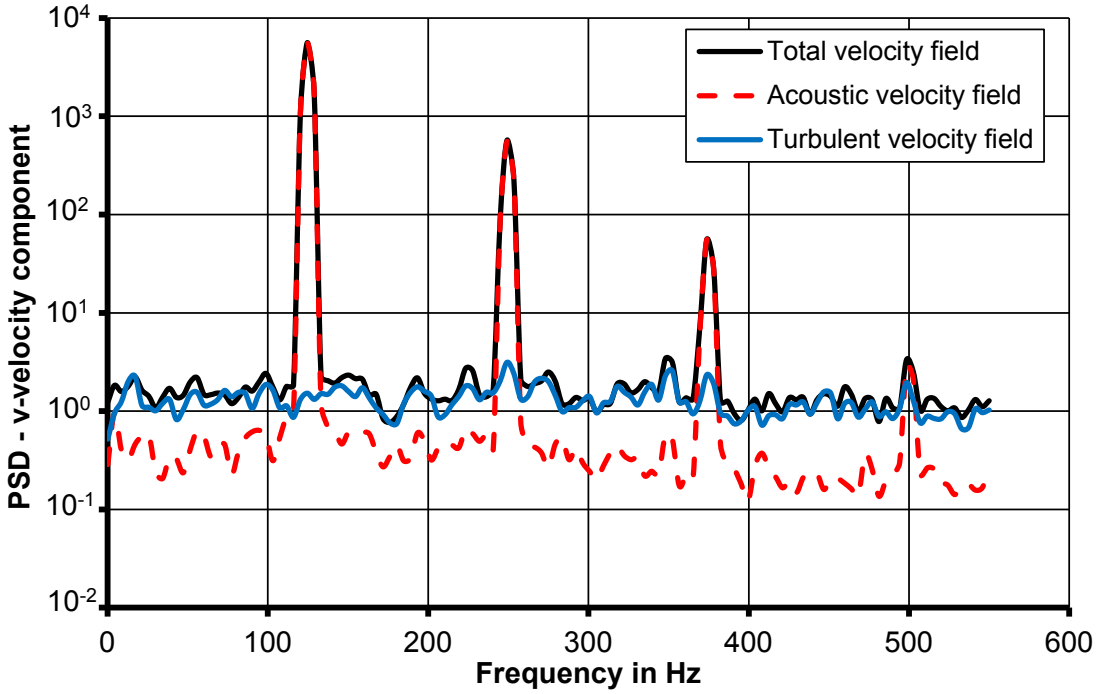

Figure 7.17: Power spectral density of the v-velocity component on the jet centre-line, $x/D = 0$ and $y/D = -0.4$

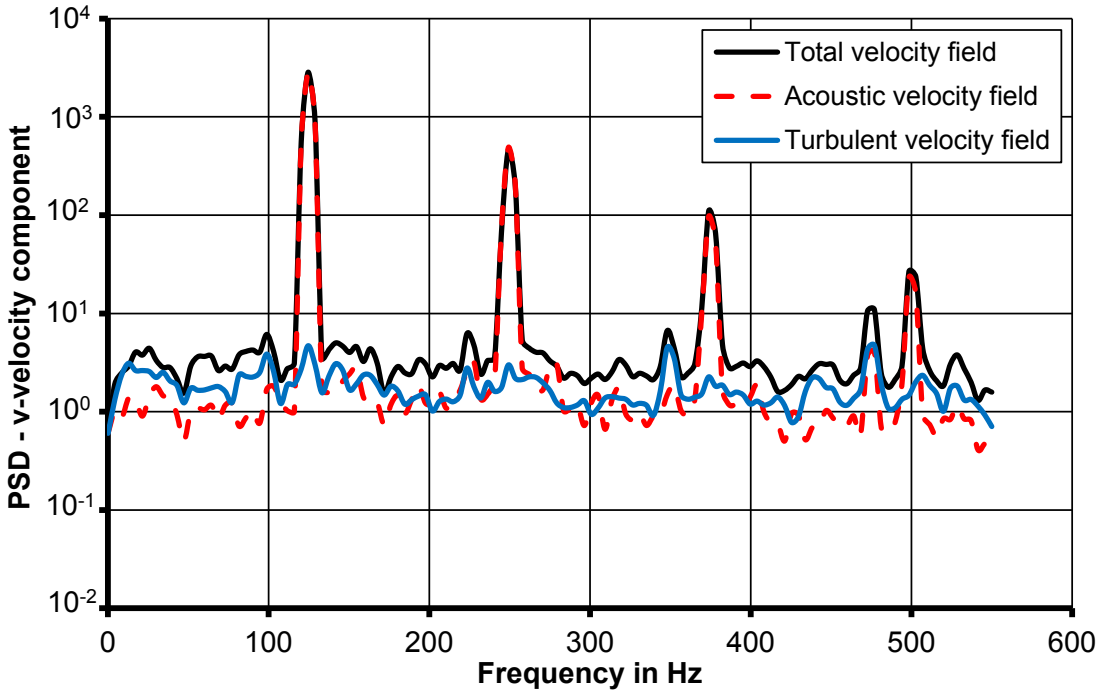

Figure 7.18: Power spectral density of the v-velocity component in the shear layer at $x/D = 0.4$ and $y/D = -0.6$

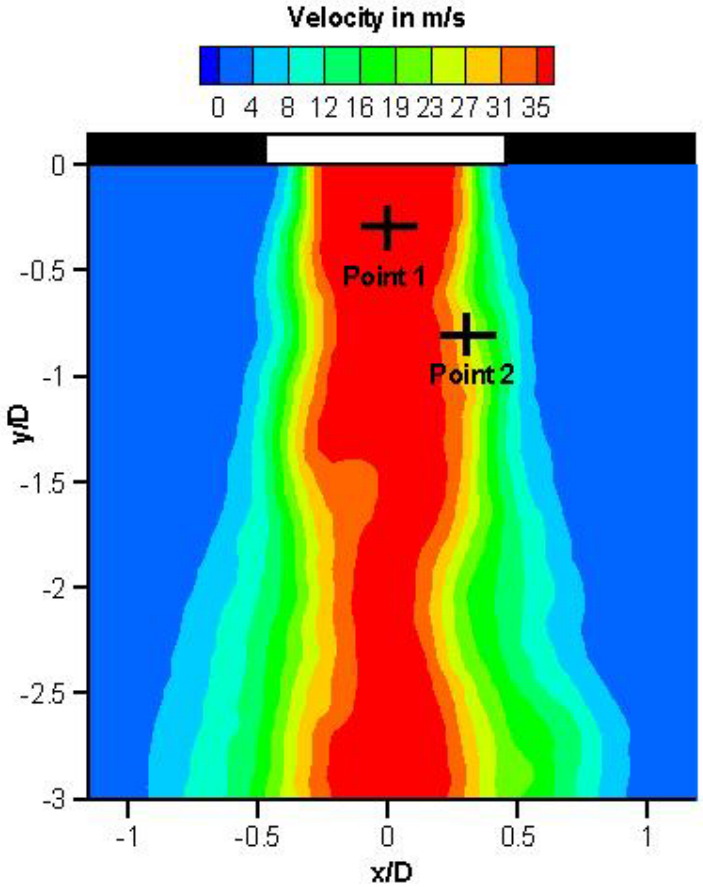

Figure 7.19: Position of calculated power spectral density, linear absorption.

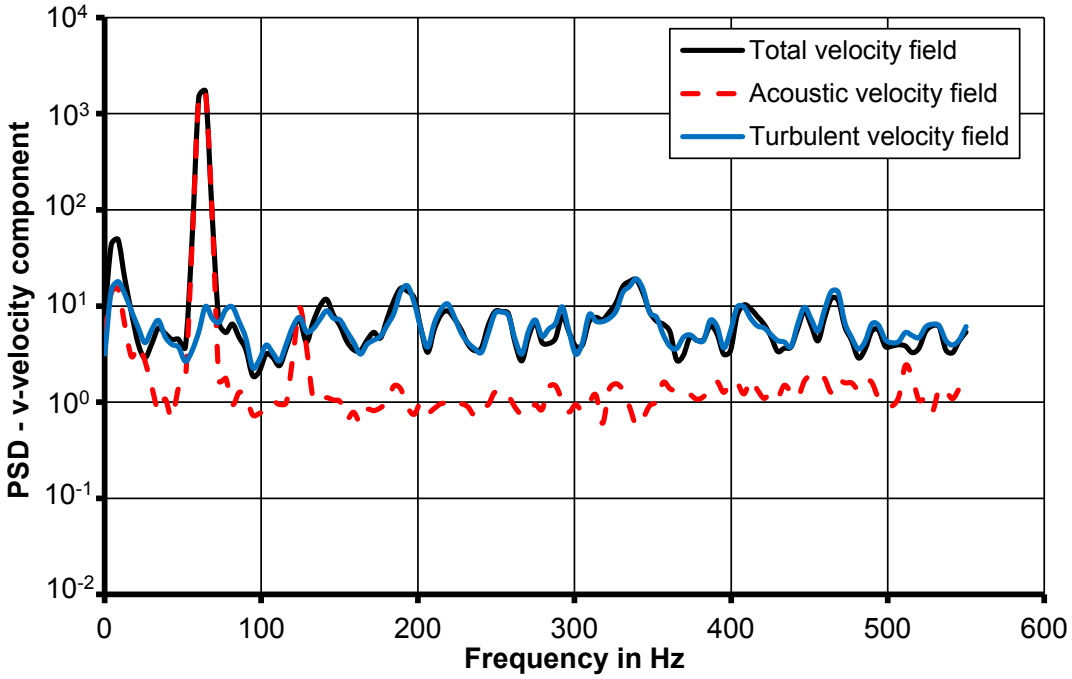

Figure 7.20: Power spectral density of the v-velocity component on the jet centre-line, linear absorption regime, *x/D* = 0 and *y/D* = -0.3

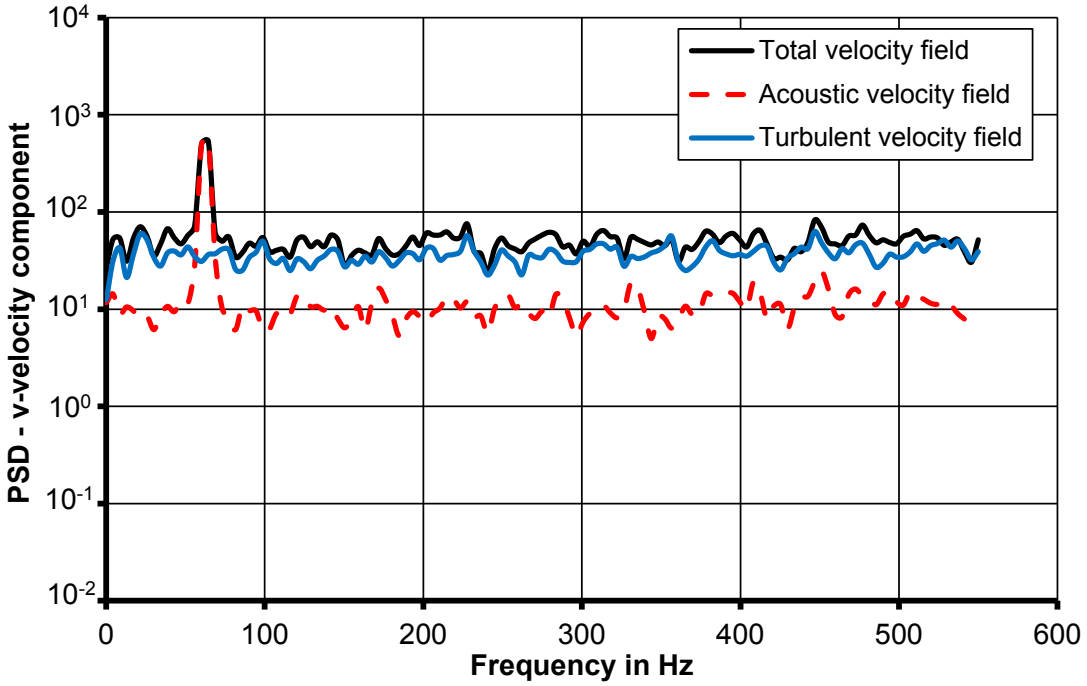

Figure 7.21: Power spectral density of the v-velocity component in the jet shear layer, linear absorption regime, *x/D* = 0.3 and *y/D* = -0.8

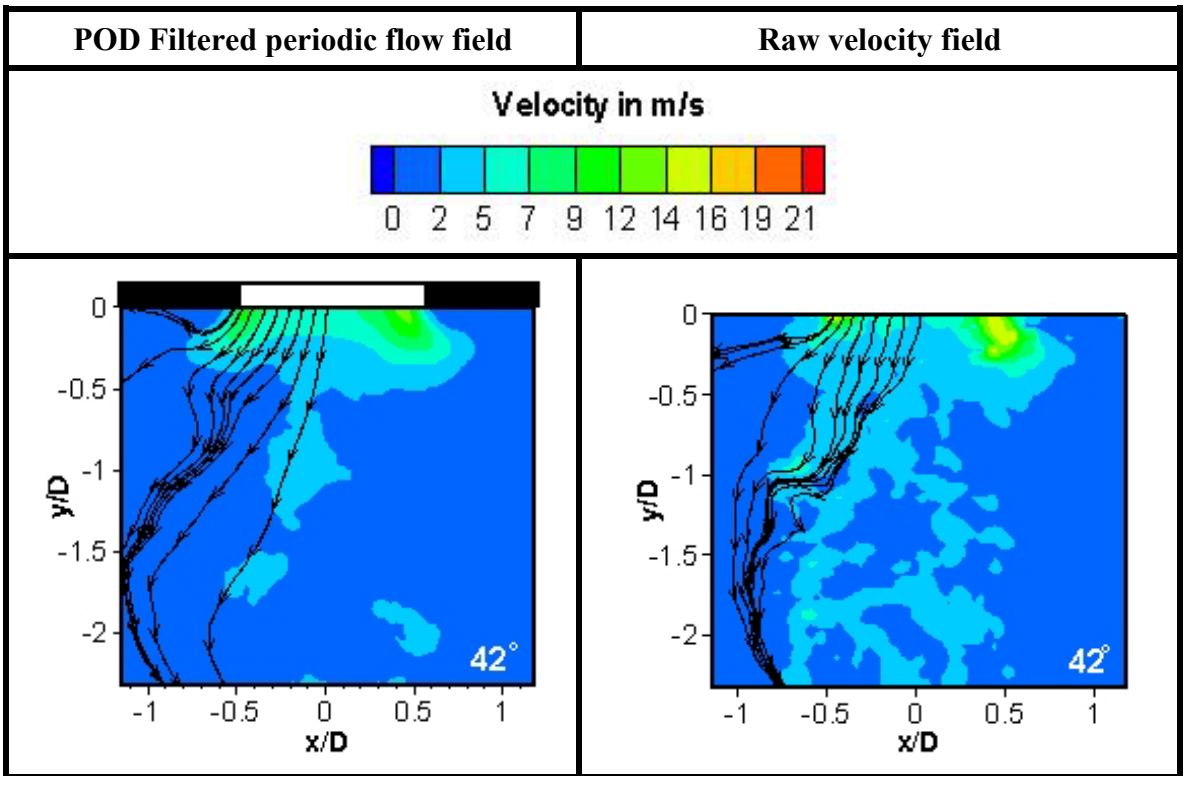

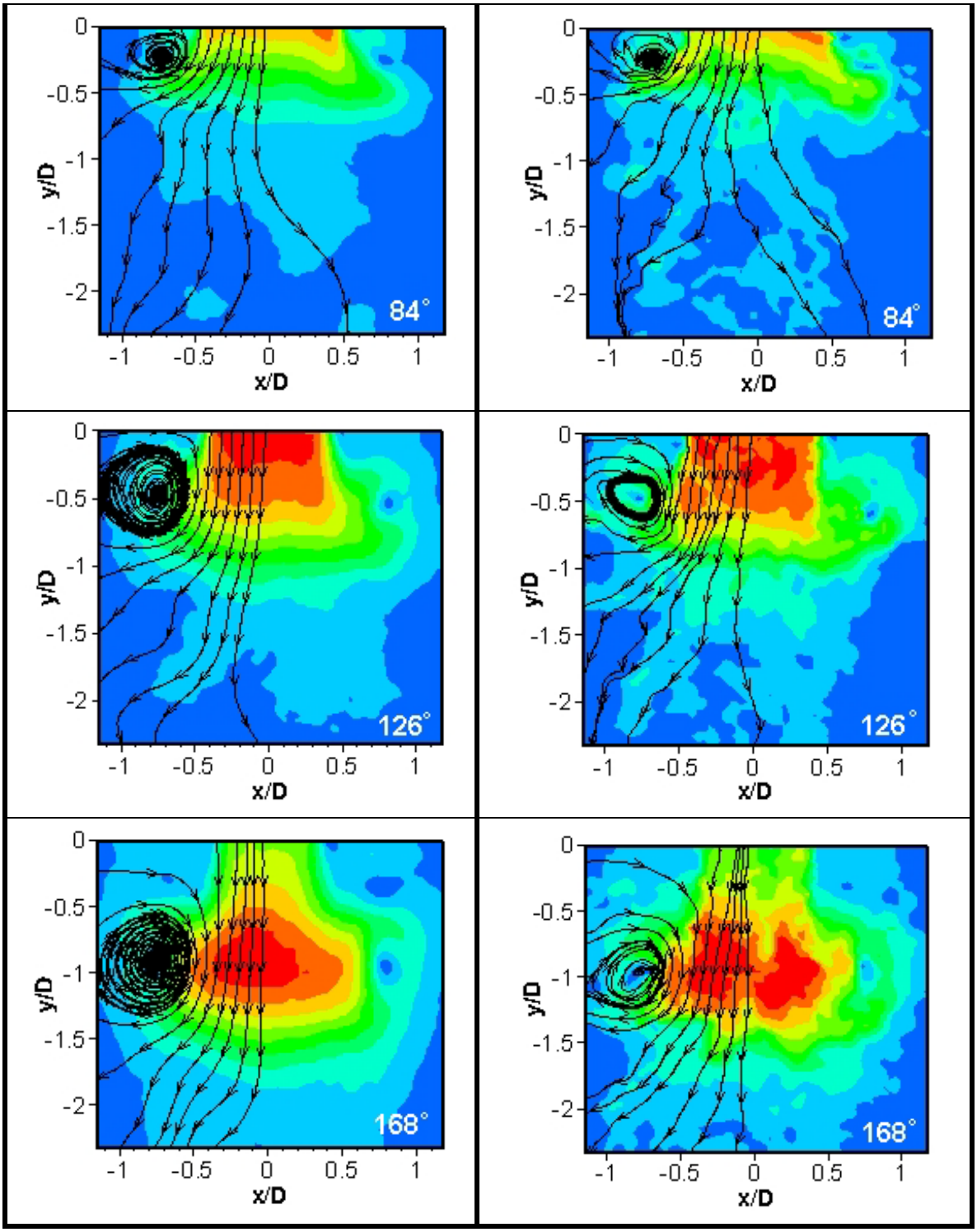

Figure 7.22: Comparison of POD filtered and raw velocity field for four phases within one acoustic cycle, non-linear absorption, 137 dB, 125 Hz, *L/D* = 0.47, plate number 1

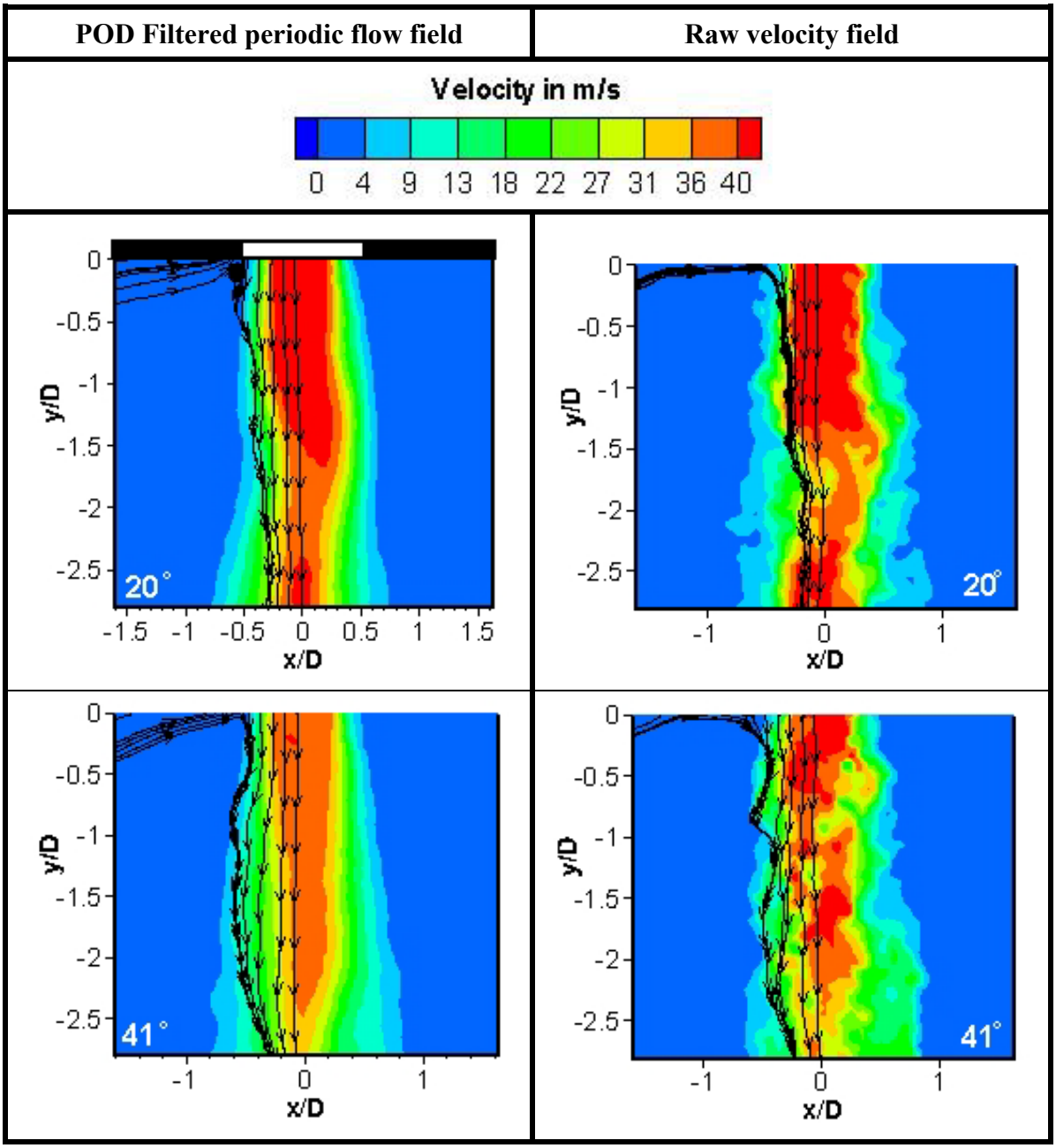

Figure 7.23: Comparison of POD filtered and raw velocity field for four different instantaneous flow fields within one acoustic cycle, linear absorption, 137 dB, 62.5 Hz, *L/D* = 0.5, plate number 3.

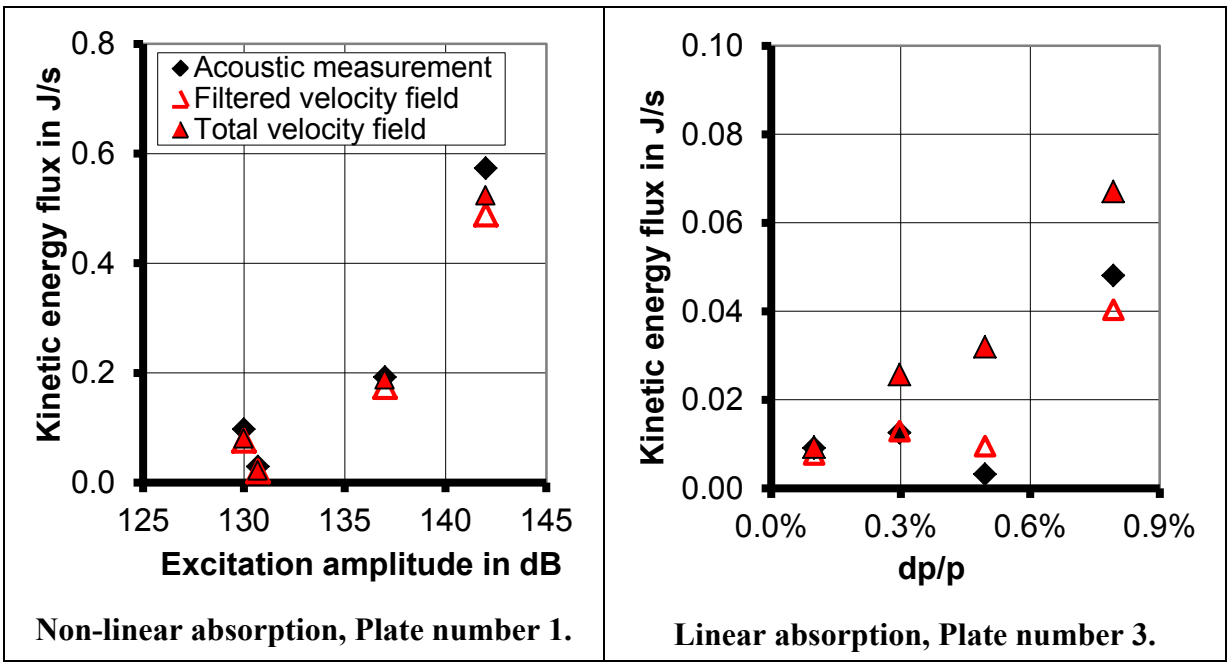

Non-linear absorption, Plate number 1. **Linear absorption, Plate number 3.**

Figure 7.24: Averaged kinetic energy flux per acoustic cycle compared to acoustic energy loss

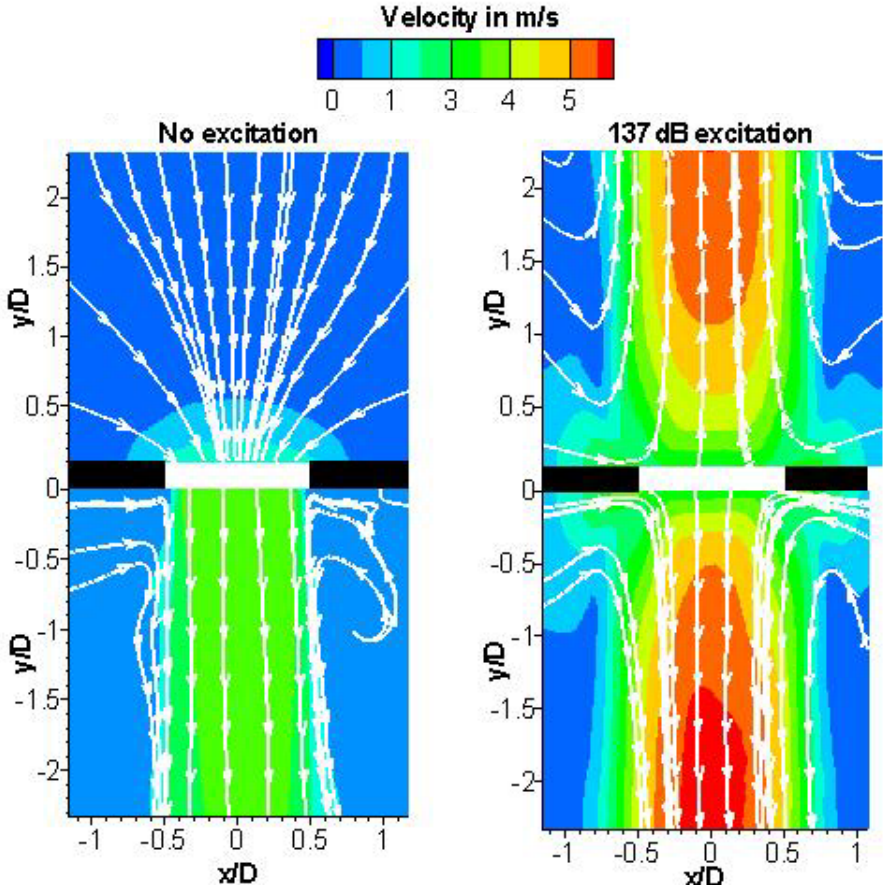

Figure 7.25: Example of forced and unforced mean flow field, non-linear acoustic absorption, $L/D = 0.47$, $f = 125$ Hz, plate number 1.

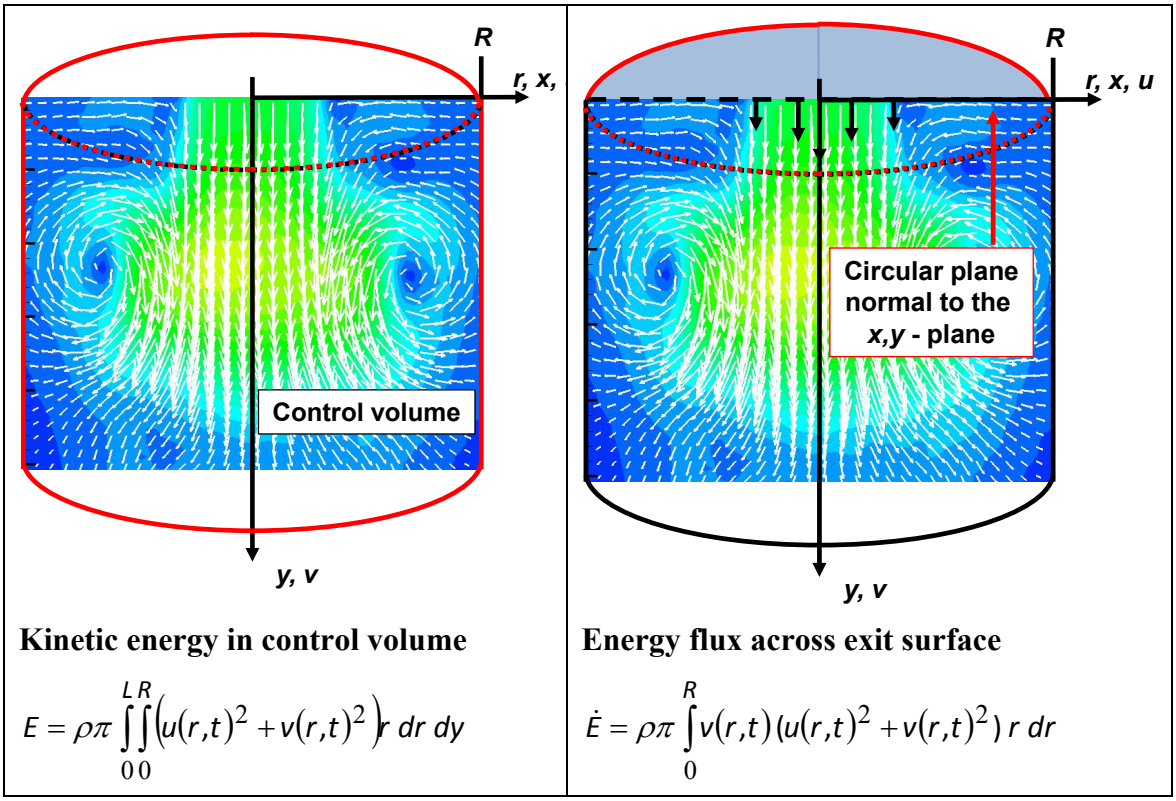

Figure 7.26: Schematic of control volume of kinetic energy calculation and control surface of kinetic energy flux calculation

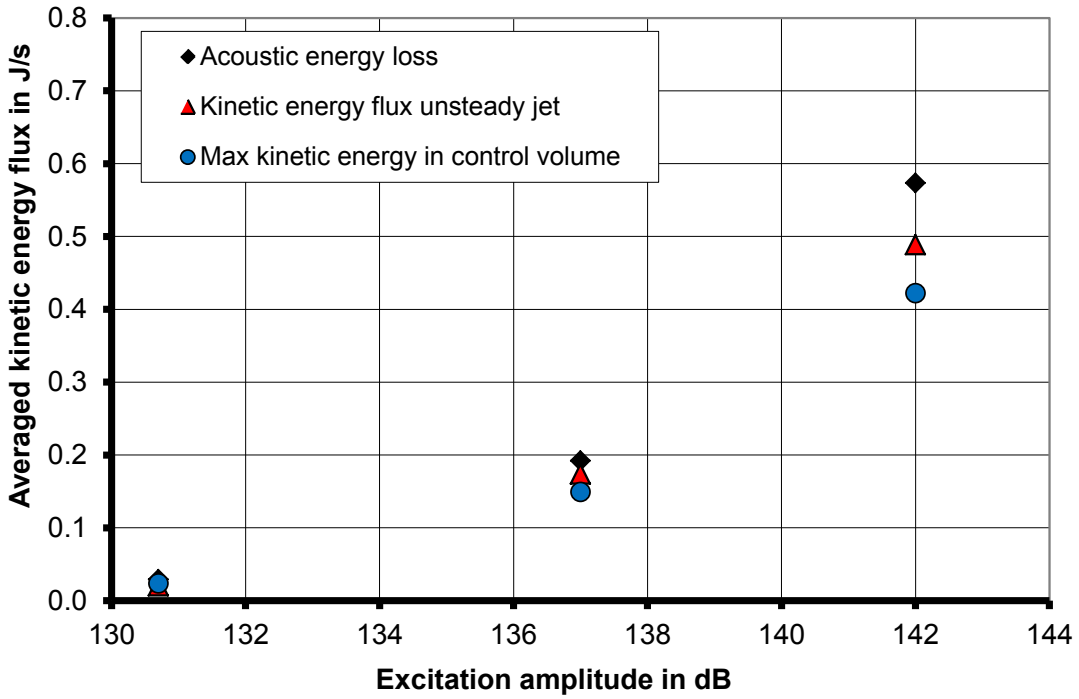

Figure 7.27: Comparison between acoustic energy loss and kinetic energy contained in the unsteady flow field

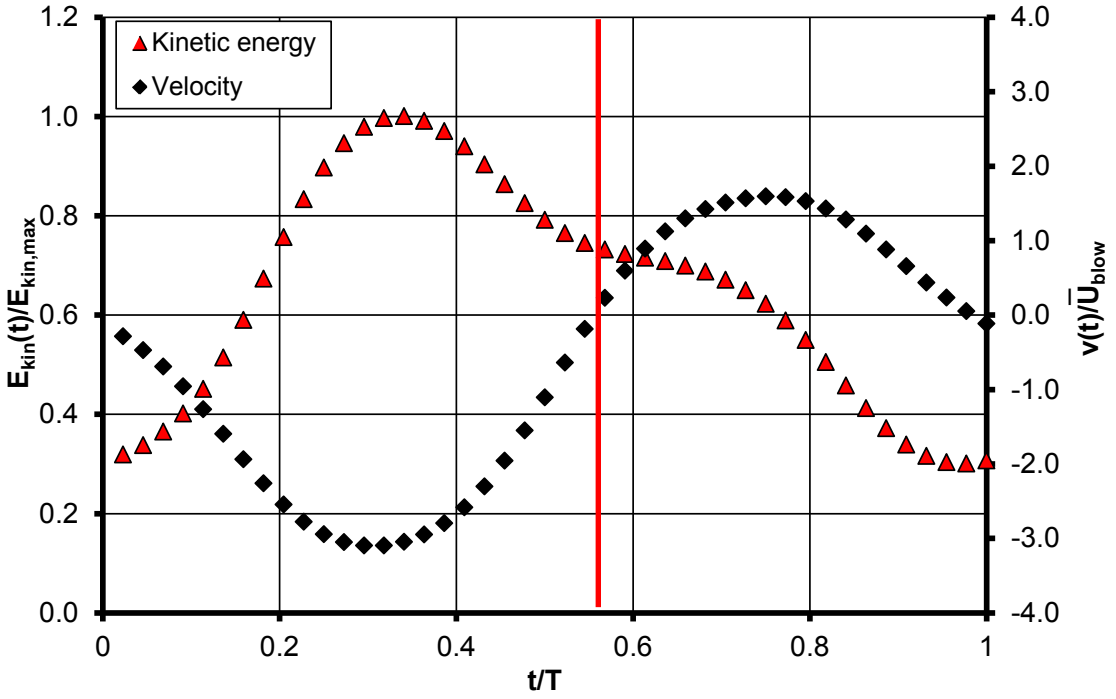

Figure 7.28: Comparison between acoustic energy loss and kinetic energy contained in the unsteady flow field, 131 dB excitation

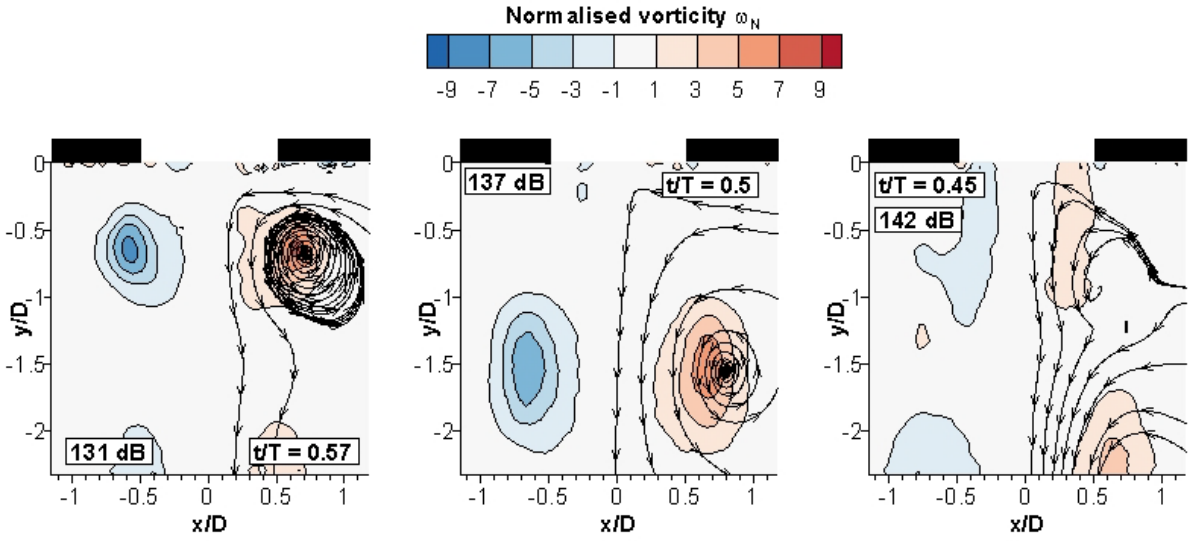

Figure 7.29: Vorticity contours at various time steps during change from in – to outflow, downstream flow field.

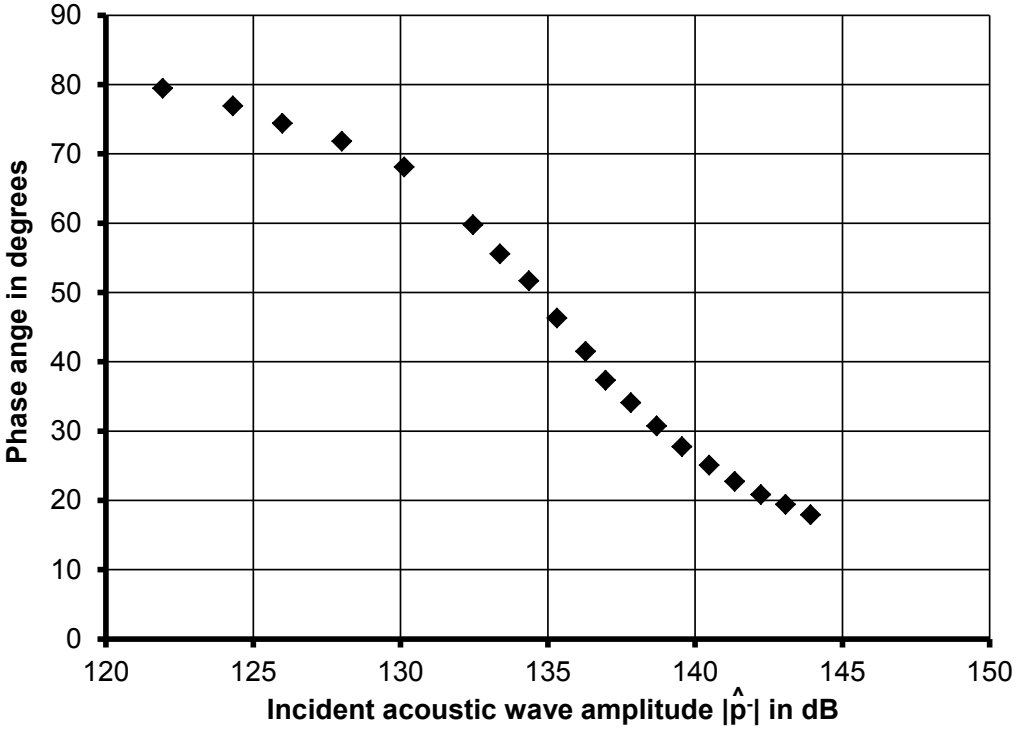

Figure 7.30: Phase between pressure and velocity amplitude (acoustic impedance) for non-linear absorption measurement. Plate number 1, *L/D* =0.47.

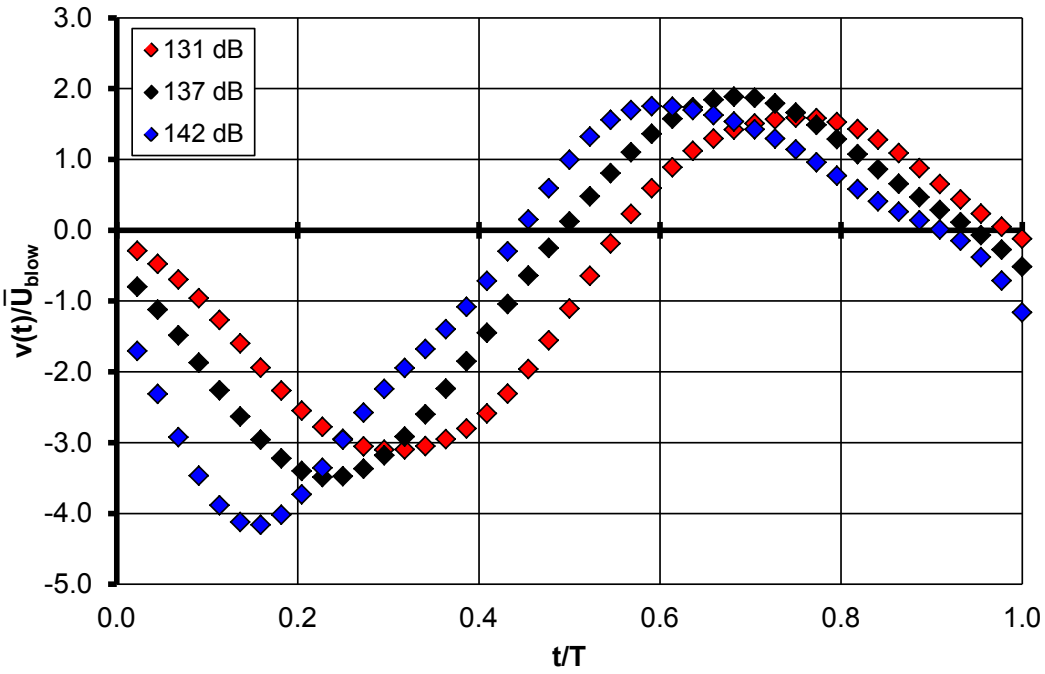

Figure 7.31: Centreline velocity oscillation for phase averaged downstream flow field, *x/D* = 0.0, *y/D* = -0.07, *L/D* = 0.5, plate number 1.

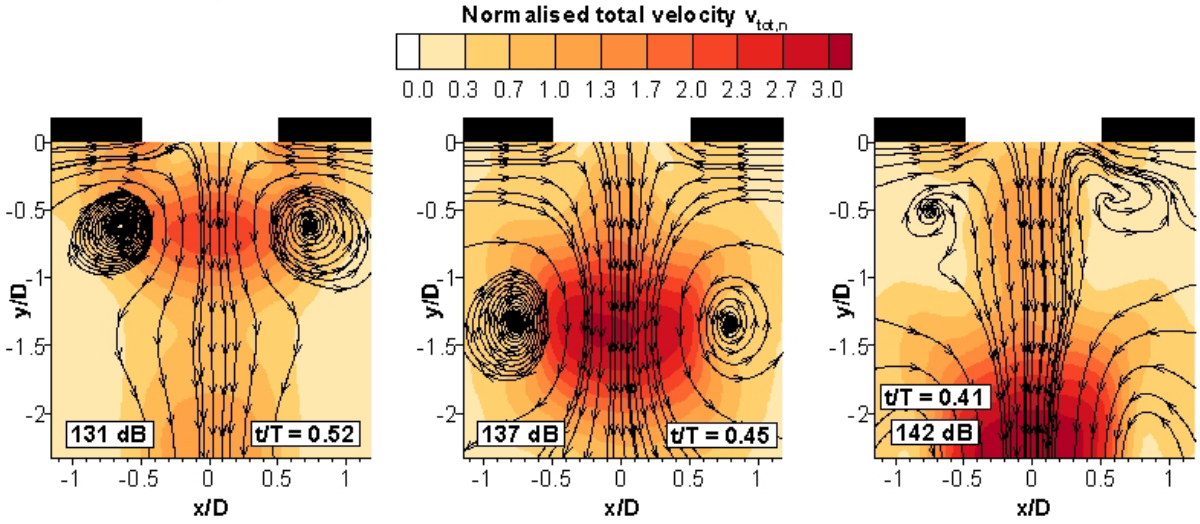

Figure 7.32: Downstream velocity contour during flow direction sign change from downstream to upstream flow direction. Non-linear forcing, *L/D* = 0.47, plate number 1.

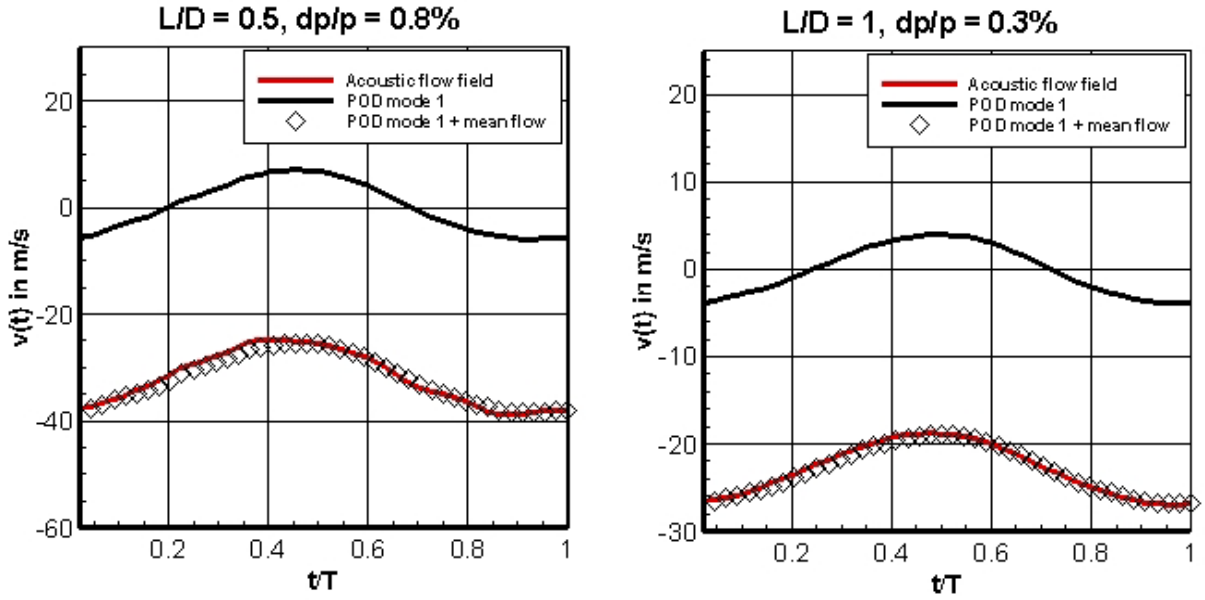

Figure 7.33: Example of phase averaged centreline v-velocity oscillations at *x/D* = 0 and *y/D* = -0.07 for the acoustic related flow field, POD mode 1 and POD mode 1 without mean flow. *L/D* = 0.5 and *L/D* = 1, plate number 3 and 4, 62.5 Hz forcing.

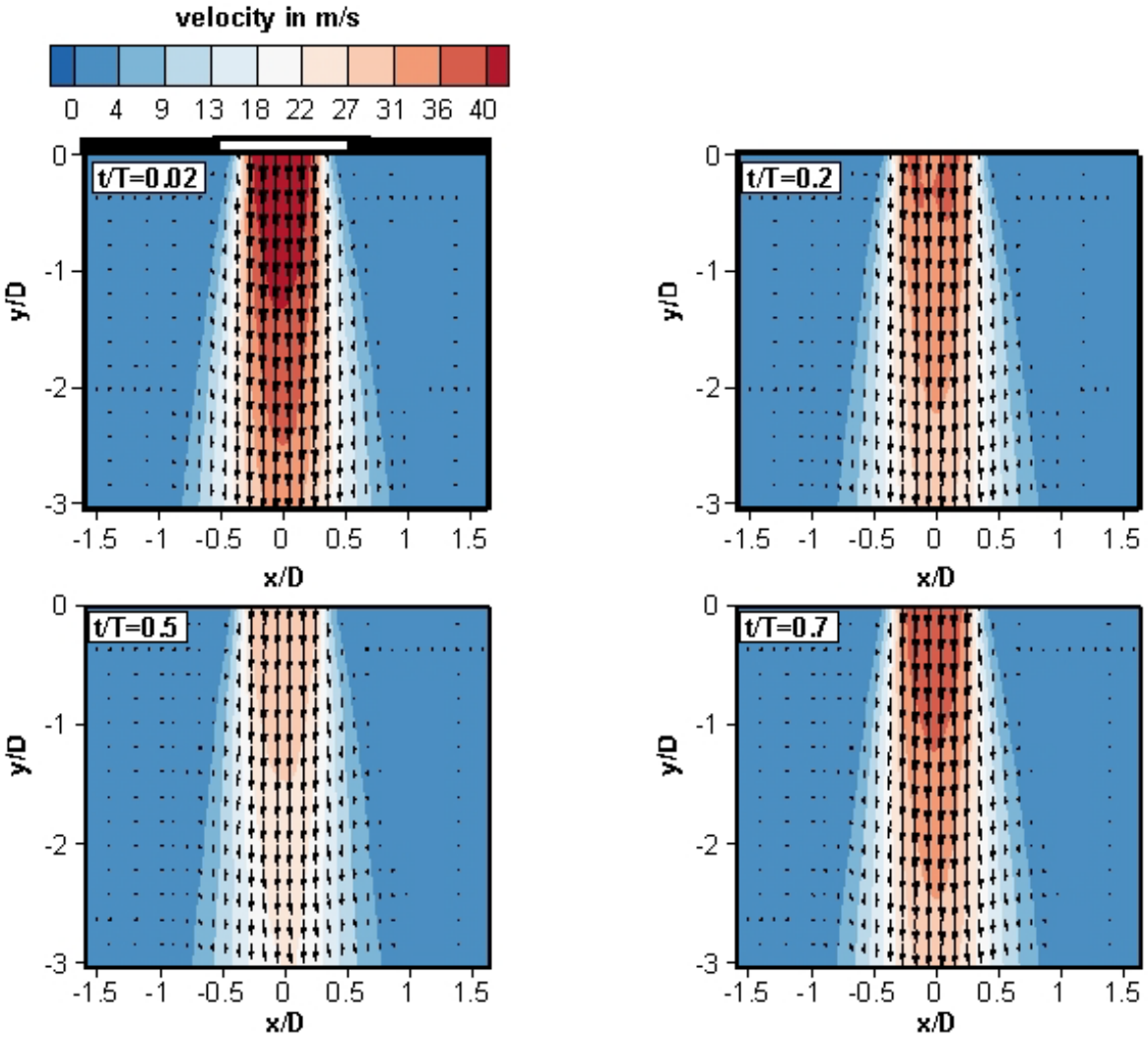

Figure 7.34: Example of phase averaged total velocity contours for the acoustic related flow field. *L/D* = 0.5, plate number 3, 62.5 Hz forcing

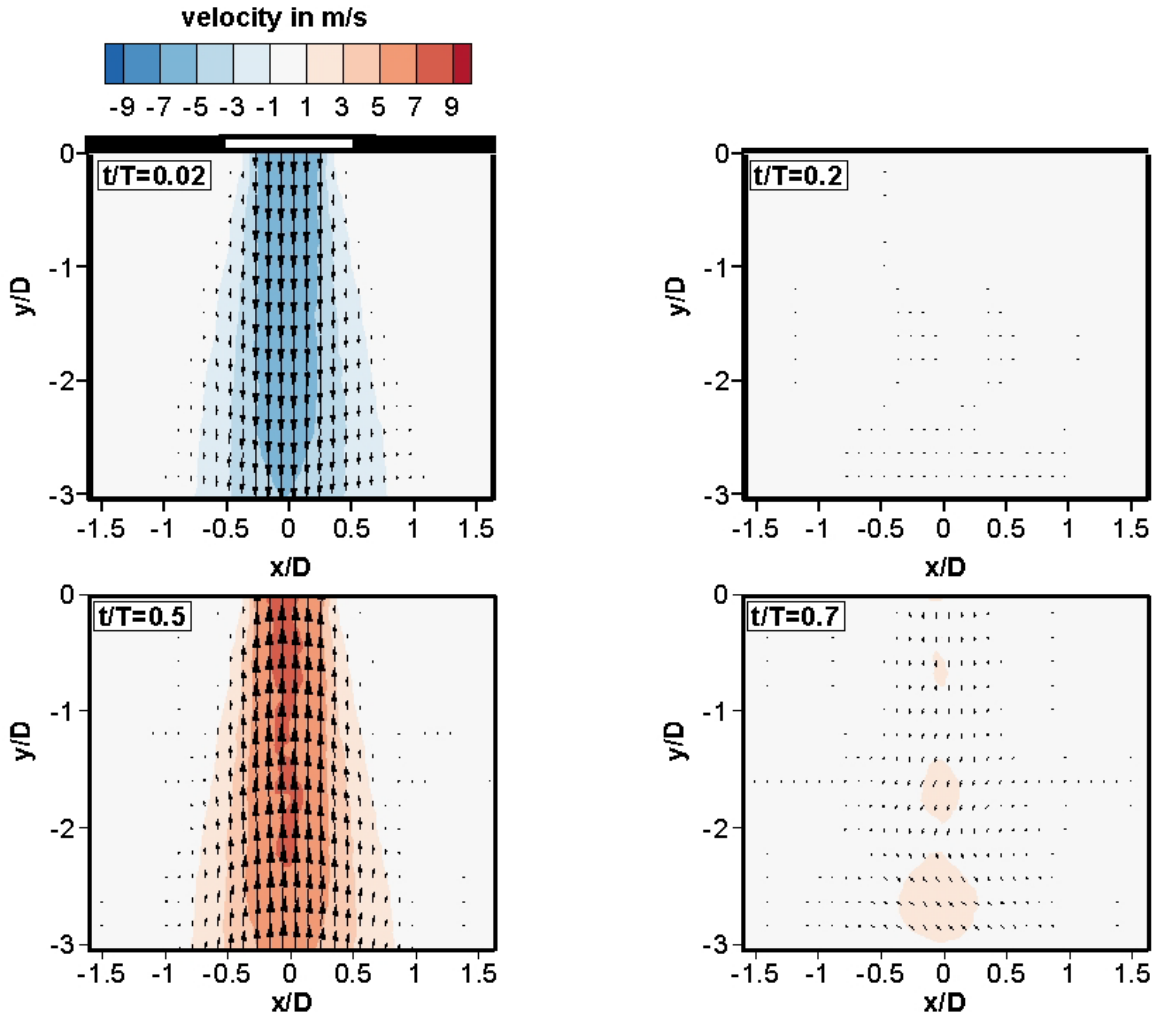

Figure 7.35: Example of phase averaged total velocity contours for the flow field of POD mode 1 only. *L/D* = 0.5, plate number 3, 62.5 Hz forcing.

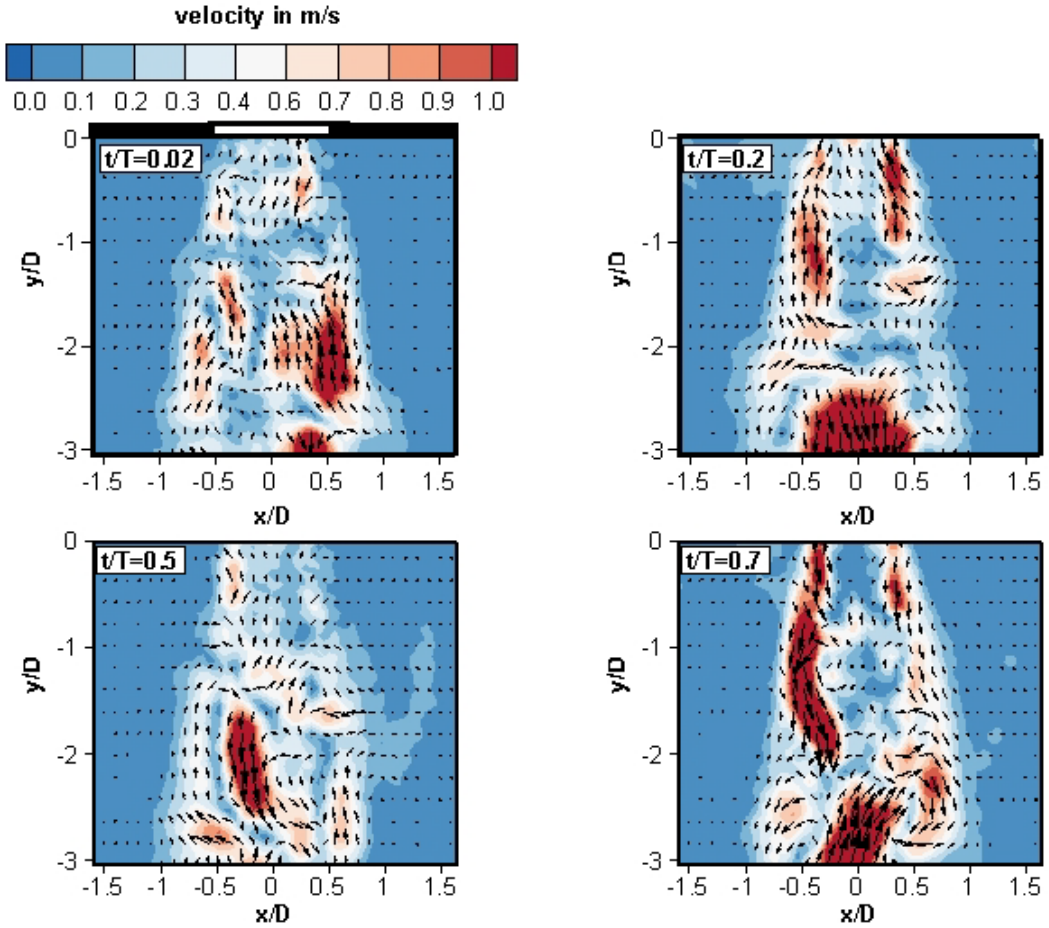

Figure 7.36: Example of phase averaged total velocity contours for POD mode 2 onwards of the acoustically related flow field. Plate number 3, 62.5 Hz forcing.

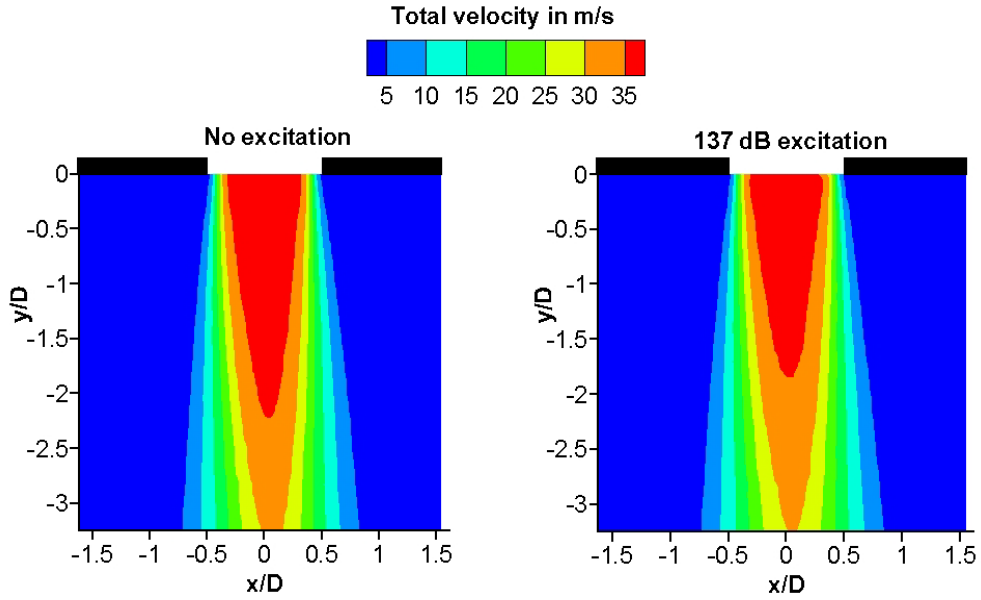

Figure 7.37: Example of forced and unforced mean flow field, linear acoustic absorption, $L/D = 1$, $f = 62.5$ Hz, 0.8% *dp/p*, plate number 4.

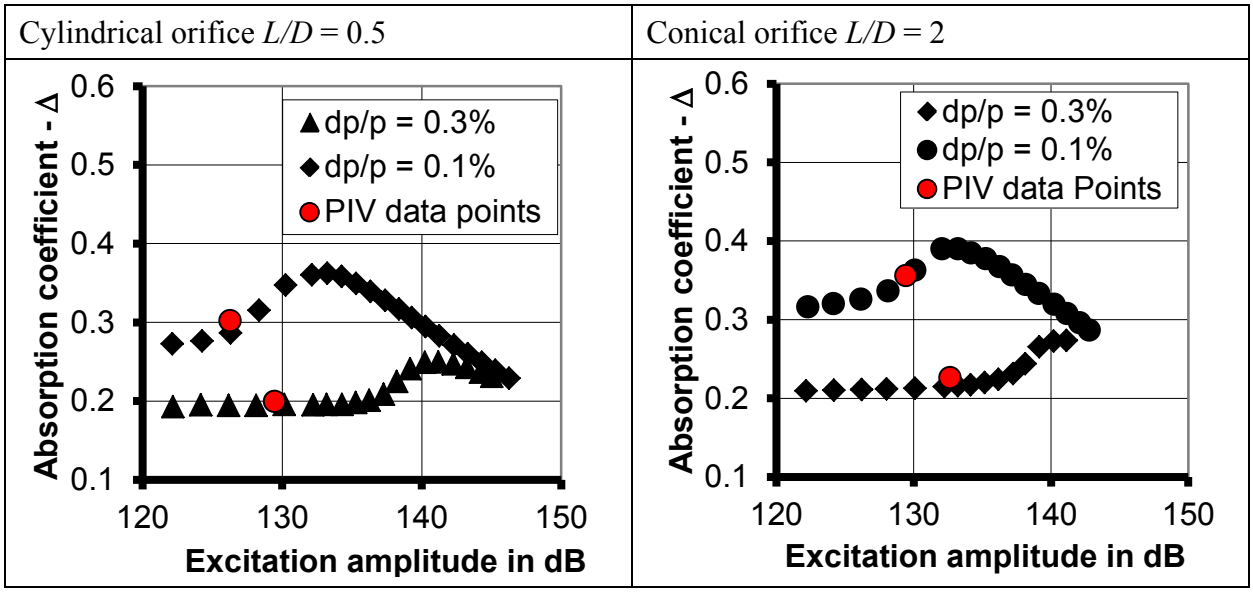

Figure 7.38: Example of acoustic absorption coefficient and PIV data points for transition from linear to non-linear acoustic absorption, plate number 3 and 13.

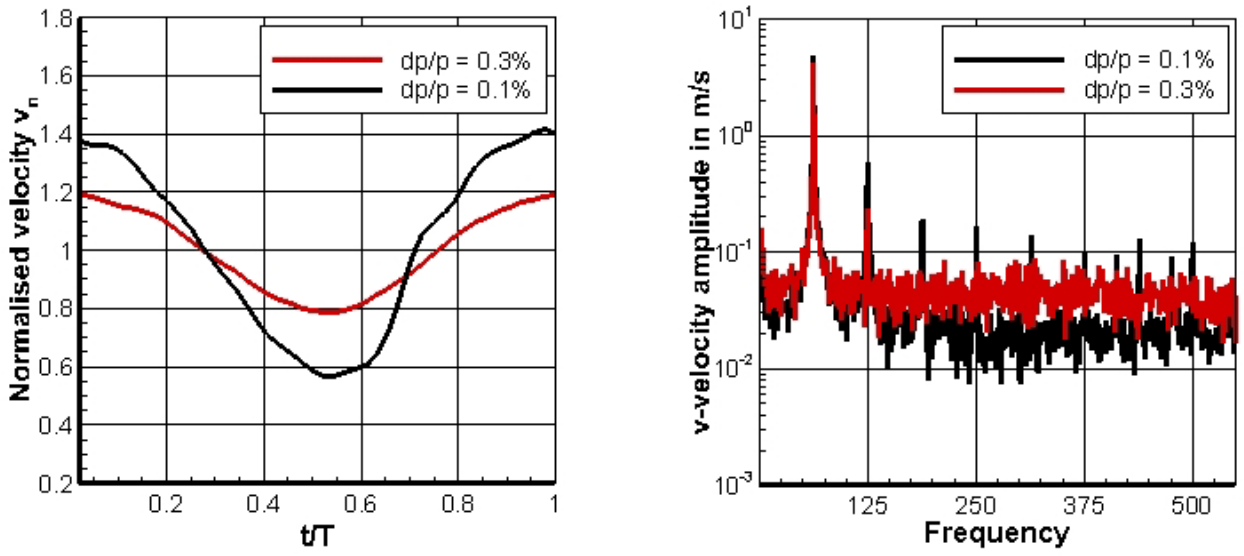

Figure 7.39: Example of phase averaged normalised v-velocity and v-velocity spectrum of the acoustically related flow fields at *x/D* = 0 and *y/D* = -0.26. *L/D* = 0.5, *dp/p* = 0.1 and 0.3%, plate number 3, 62.5 Hz forcing.

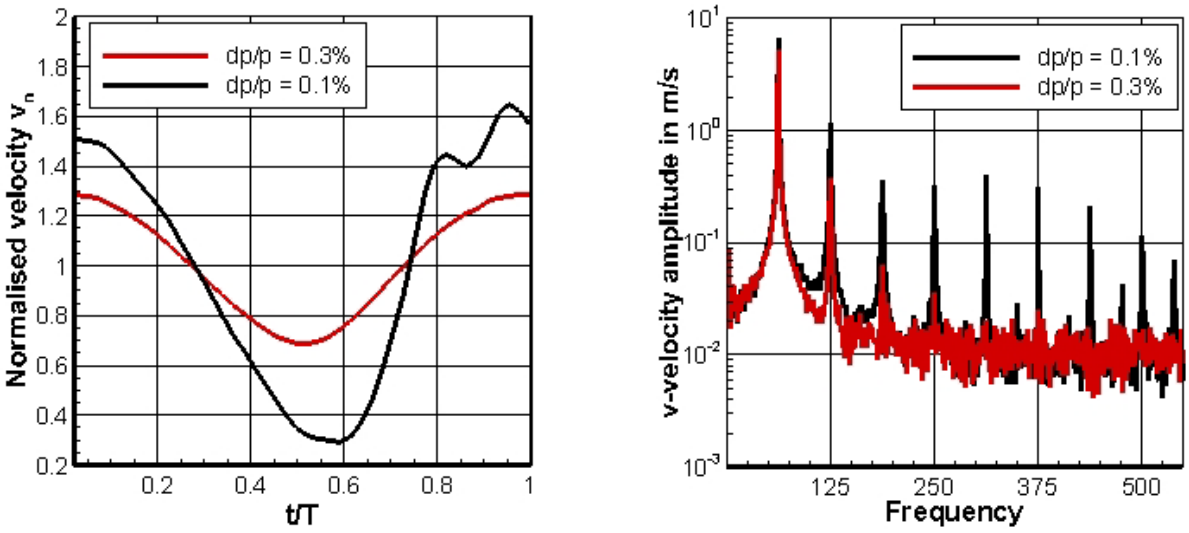

Figure 7.40: Example of phase averaged normalised v-velocity and v-velocity spectrum of the acoustically related flow fields at *x/D* = 0 and *y/D* = -0.26. Conical aperture, *dp/p* = 0.1 and 0.3%, plate number 13, 62.5 Hz forcing.

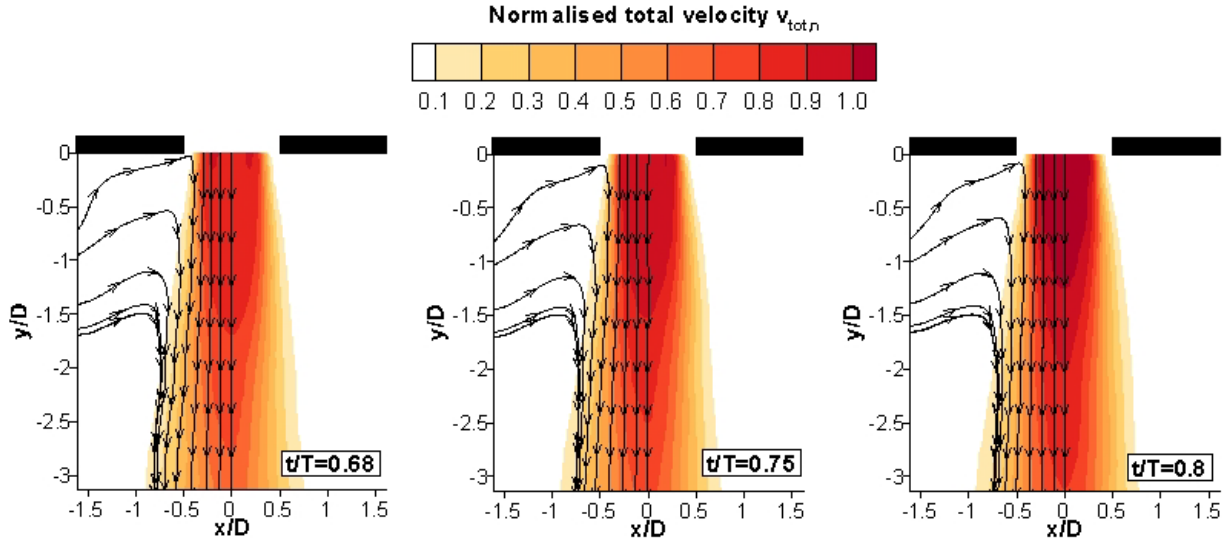

Figure 7.41: Example of phase averaged normalised total velocity contours acoustically related flow field during linear acoustic absorption. *L/D* = 0.5, *dp/p* = 0.3%, plate number 3.

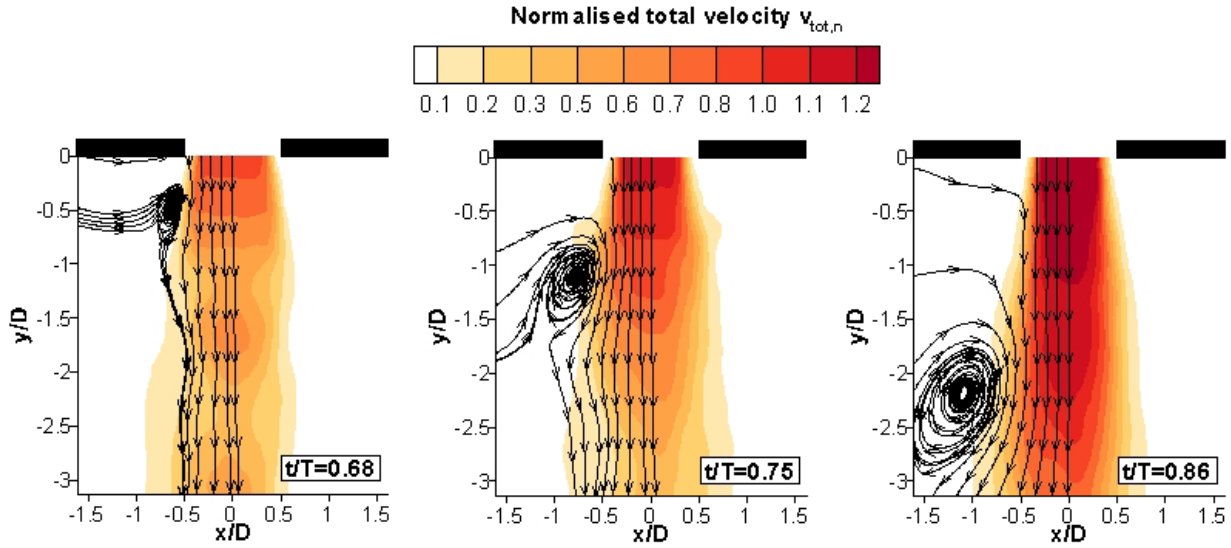

Figure 7.42: Example of phase averaged normalised total velocity contours acoustically related flow field during transition to non-linear acoustic absorption. *L/D* = 0.5, *dp/p* = 0.1%, plate number 3.

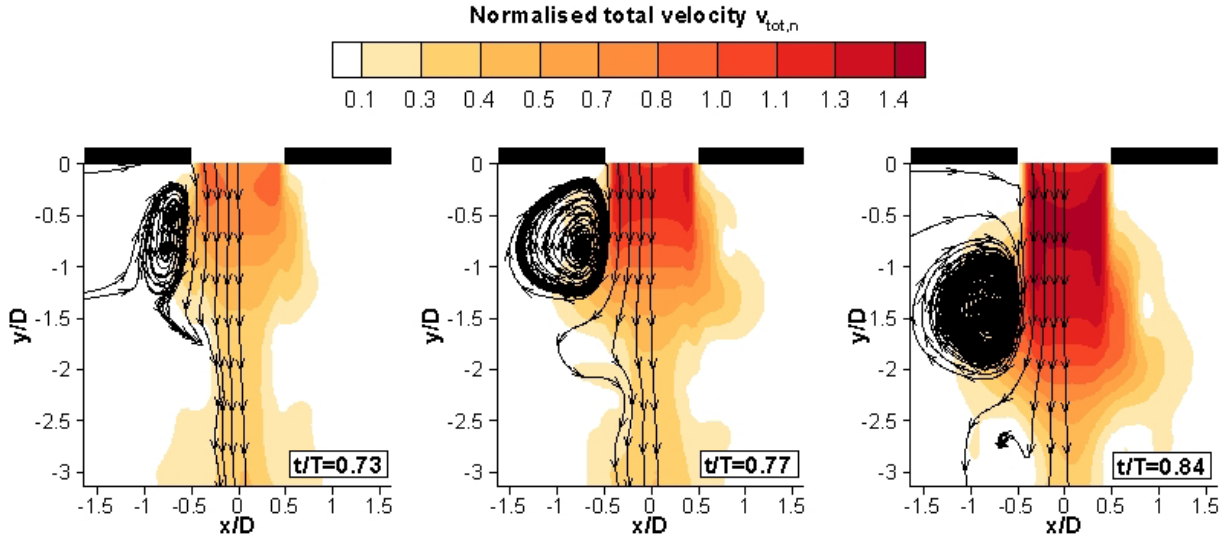

Figure 7.43: Example of phase averaged normalised total velocity contours of acoustically related flow field during transition to non-linear acoustic absorption. *L/D* = 2, *dp/p* = 0.1%, plate number 13.

8 Combustion System Passive Damper Design Considerations

Designing an efficient acoustic damper system to operate within a real engineering environment such as a gas turbine engine is challenging. This is even more so if the acoustic damper has to be located within the combustion chamber, when typically it is directly coupled with the heat release region. This means that various other design constraints must be considered such as (Rupp et. al. (2012)):

- The damper inner surface will be exposed to a relatively complex flow field. For example, this could include an impinging swirling fuel injector flow or the passage of a coolant film across the surface. The interaction of the swirling and cross flow phenomena with the pulsatile flow field of the damper apertures could potentially generate large scale structures within the unsteady jet shear layers (e.g. Lim et al (2001)). As discussed in the previous sections (chapter 5 and 6), the current analytical models within the linear and non-linear regime are not capturing well the influences of large scale flow structures such as vortex rings. Thus, there could be large discrepancies in the prediction of the acoustic damping performance due to the complex interaction between the combustor flow field and the flow associated with acoustic damping.

- The perforated liner can form part of the combustion chamber wall. However, the pressure drop across the flame tube is dictated by the fuel injector and the need to generate sufficient turbulent mixing of the air and fuel passing through it. A perforated liner exposed to this same pressure drop would result in a very high mean (bias) velocity through the orifice which leads to reduced acoustic energy loss as discussed in chapter 5 (see equation (5.26)). As a consequence an additional metering skin is required to reduce the pressure drop and control the amount of bias flow through the damper.

- The double skin damping system must be incorporated within a limited space envelope. This is because the combustion system casing, defining the volume available in the annulus surrounding the combustion chamber, has to be kept to a minimum

diameter to reduce the weight impact on the combustion system design for aero-engine applications.

- The flame tube liner cooling requirements dictate a certain level of cooling flow, per unit surface area, to maintain the structural integrity of the liner material. This means the number and size of the orifices, within the perforated liner, must consider both cooling and acoustic absorption requirements.

- The cooling design of such a damping system must also consider the potential for hot gas ingestion into the passive damper geometry. Hence the mean pressure drop over the final hot skin has to be carefully chosen. This is because the unsteady velocity amplitudes, relative to the mean velocity, must be considered so as to avoid large pressure amplitudes driving hot gas into the passive damper.

This chapter is concerned with the design of dampers for an aero-engine gas turbine combustion system. Initially isothermal experiments in which a single sector of a gas turbine aero-engine style combustor is simulated are described. A non-resonant liner was incorporated in the test rig and its acoustic absorption characteristic has been assessed experimentally. A simplified analytical model was developed based on the findings described in Chapter 5 and validated against the experimental measurements. In this way the observed acoustic performance can be related to the fundamental processes generated by the incident acoustic waves. Furthermore the validated acoustic model enables a prediction of the performance of a wide range of acoustic geometry, at a variety of operating conditions, to be investigated. Moreover the model has also been validated against acoustic absorption experiments using resonant acoustic liner concepts to demonstrate the advantages of such damper technologies in the confined design space of a gas turbine combustion chamber.

8.1 Analytical Model Development

A simple one-dimensional analytical model was developed enabling the interpretation of the experimental results as also introduced in Rupp et. al. (2012). The model is also intended to be used as a rapid passive damping design tool to optimise acoustic absorbers for gas turbine combustors. Moreover the performance of the Rayleigh Conductivity modelling methods as described in chapter 5 can be further investigated

on representative multi-aperture acoustic damping systems. Figure 8.1 shows a schematic of the underlying geometry simulated by the developed analytical model. The model assumes that the acoustic wavelength is much greater than the liner length (i.e. a 'long wavelength' assumption) so that a uniform fluctuating pressure ($p'_0(y) = \text{const}$) is imposed on the face of the damper.

This fluctuating pressure generates velocity perturbations leading to fluctuations in (i) the mass flow entering ($\dot{m}_{in}$) and leaving ($\dot{m}_{out}$) the volume between the damping skins and (ii) fluctuations in pressure inside the cavity (p'_1). Hence the time dependent mass flow variation inside the volume (V) between the skins is

$$\frac{dm}{dt} = V\frac{d\rho}{dt} = \dot{m}'_{in} - \dot{m}'_{out}. \tag{8.1}$$

Assuming isentropic fluctuations ($p'/\bar{p} = \gamma\, \rho'/\bar{\rho}$) then

$$(i\omega)V\bar{\rho}_1\frac{p'_1}{\gamma\bar{p}_1} = \dot{m}'_{in} - \dot{m}'_{out}\ . \tag{8.2}$$

where $p' = \hat{p}\exp(i\omega t)$, $\dot{m} = \hat{m}\exp(i\omega t)$ etc. Note that it is assumed the gap between the skins is not of sufficient size to result in the generation of mode shapes within the damper cavity (i.e. uniform properties within the cavity). Hence it can be shown that:

$$\hat{p}_1 = \frac{\bar{p}_1}{\bar{\rho}}\gamma\frac{1}{V}\frac{1}{i\omega}\left[\dot{m}'_{in} - \dot{m}'_{out}\right] = \frac{\bar{p}_1}{\bar{\rho}}\gamma\frac{1}{V}\frac{1}{i\omega}\left[\bar{\rho}A_2\hat{u}_{D2} - \bar{\rho}A_1\hat{u}_{D1}\right]. \tag{8.3}$$

The area A is defined as the damper geometric hole area which is the sum of the geometric area of each aperture, e.g. $A_1 = N_1\pi R^2$ where N_1 represents the amount of apertures in the liner. Furthermore the parameters $\hat{u}_{D1}$ and $\hat{u}_{D2}$ are the unsteady velocities associated with the 1st (damping) and 2nd (metering) skins. In the initial work described in Rupp et. al. (2012) the model used to describe the velocity amplitudes across the liner was based on the modified Howe model (as described in section 5.8) using the compliance expression as defined in Eldredge and Dowling (2003). In this work the modified Howe model was calibrated using the single aperture measurements as, for example, shown in chapter 5 leading to good agreement with the experiments

shown in Rupp et. al. (2012). However, the dampers investigated in this study operate at low Strouhal number (i.e. Strouhal numbers smaller than the Strouhal number of maximum admittance). Section 5.8 highlighted the discrepancies of the Howe models in this Strouhal number regime. In this region the change in aperture length-to-diameter ratio and the associated change in the unsteady flow field were not reproduced by the modified Howe model which can lead to significant errors in the prediction of absorbed acoustic energy. As shown in section 5.9, the unsteady flow field, within the Strouhal number regime considered here, is much more reliably represented by the momentum balance introduced by Bellucci et. al. (2004). Therefore this approach has been implemented in the current analytical model. Thus the velocity amplitudes in the plane of the apertures can be calculated using the following two equations, one for each damping skin, based on the described linear model in section 5.9:

$$i\omega\rho L_1\hat{u}_1 + \hat{p}_0 - \hat{p}_1 + \rho\varsigma_{vis,1}\hat{u}_{D1} + \rho\varsigma_1\overline{U}_{D1}\hat{u}_{D1} = 0 \text{ and} \tag{8.4}$$

$$i\omega\rho L_2\hat{u}_2 + \hat{p}_1 + \rho\varsigma_{vis,2}\hat{u}_{D2} + \rho\varsigma_2\overline{U}_2\hat{u}_{D2} = 0\,. \tag{8.5}$$

Hence the unsteady velocities are defined as:

$$\hat{u}_{D1} = \frac{\hat{p}_1 - \hat{p}_0}{\rho\varsigma_1\overline{U}_{D1} + \rho\varsigma_{vis,1} + i\omega\rho L_1} \text{ and} \tag{8.6}$$

$$\hat{u}_{D2} = \frac{-\hat{p}_1}{\rho\varsigma_2\overline{U}_{D2} + \rho\varsigma_{vis,2} + i\omega\rho L_2}\,. \tag{8.7}$$

It can be seen that the unsteady velocity across the apertures in the damping skin is affected by four components:

(i) the unsteady pressure difference between the incident amplitude ($\hat{p}_0$) and the pressure amplitude inside the cavity ($\hat{p}_1$).

(ii) the resistance of the aperture which is a function of the mean jet flow and its loss coefficient $\rho\zeta_1\overline{U}_{D1}$

(iii) the reactance due to the acceleration forces onto the mass of the fluid within the aperture $\rho\omega L_1$

(iv) the viscosity due to the boundary layer within the aperture $\rho\zeta_{vis,1}$ (as described in equation (5.34)), which is an additional contribution to the aperture resistance as well as the reactance.

The same applies to the metering skin aperture with the exception that the upstream pressure amplitude is assumed to be negligible as the liner is plenum fed. As described in chapter 5.9 the loss coefficients ζ_1 and ζ_2 can be approximated using the mean flow discharge coefficient of the damping and metering skins. The discharge coefficients for the perforated liner geometries have been measured on the facility described in appendix B and used in the model to calculate the acoustic absorption at the relevant liner pressure drop and Reynolds number representative of the operating conditions during the acoustic experiments. The measured discharge coefficients were used as in equation (5.35) to calculate the loss coefficient for the resistance of the perforated plates. Moreover the length correction for the effective length of each perforated plate was estimated using the single orifice geometries defined in Table 5.1.

Equations (8.3), (8.6) and (8.7) form a linear equation system which can be solved analytically. According to Bellucci et. al. (2004) the absorbed acoustic energy can be calculated as:

$$\Pi_L = \frac{1}{2}\,\mathrm{Re}\left(\hat{u}_1^{*}\hat{p}_0\right)A_1\,, \tag{8.8}$$

or in accordance with Howe (1979b) or Luong et. al. (2005):

$$\Pi_L = \left|\hat{p}_u - \hat{p}_d\right|^2 \frac{R_1\delta_1}{\rho\omega}N_1 + \left|\hat{p}_u\right|^2 \frac{R_2\delta_2}{\rho\omega}N_2\,. \tag{8.9}$$

Both acoustic energy expressions have been used in this work and lead to the same result and therefore include the acoustic energy being absorbed by the damping and metering skins. It can be seen that the acoustic energy loss calculated from equation (8.8) is a function of the unsteady velocity amplitude which is expressed in equation (8.9) by the unsteady pressure difference and the admittance for each liner. Hence the acoustic absorption can be increased by increasing the unsteady velocity amplitudes across the apertures.

Finally the acoustic energy loss is normalised with the excitation pressure amplitude ($\hat{p}_0$) as proposed in Rupp et. al. (2010):

$$\Pi_P = \frac{\Pi_L}{\left|\hat{p}_0\right|^2} . \tag{8.10}$$

This normalisation makes the results independent of the applied pressure amplitude within the linear acoustic absorption regime. Moreover the incident pressure amplitude is used as an inlet condition into the model.

8.2 Non-Resonant Passive Damper

As described in Rupp et. al. (2012) most experimental and theoretical investigations have considered the performance of perforated liners within a simple 1D duct type flow or impedance tube, e.g. Eldredge and Dowling (2003), Hughes and Dowling (1990), Lahiri et. al. (2011). However, considered here is the application of a perforated liner to aero style gas turbine combustion systems. This study has been undertaken on the experimental facility described in chapter 3.3.2. In this case a passive damper which consists of a porous liner and metering skin can be incorporated into the flame tube liner. Plane axial acoustic waves are generated by loudspeakers and pass into the combustor test section. Based on the magnitude of the incident and reflected waves an assessment can be made of the acoustic energy being absorbed in this relatively complex environment.

8.2.1 Experimental Results

The experimental results and discussions in this section can also be found in Rupp et. al. (2012). As already discussed the flow field in the vicinity of the perforated liner in the test section will be affected by the swirling flow field of a fuel spray nozzle which was also incorporated on the test rig. The fuel injector geometry was representative of a lean burn combustion technology fuel spray nozzle. However in this case the injector was only used to provide a representative swirling flow field impinging onto the perforated liner. The burner was provided by the industrial partner in this project and its geometry remains confidential but is representative of the geometry likely to be used with future low emissions aero-engines. The mean pressure drop across the passive

damper, as well as the fuel injector, was set to 3% which is also thought typical of gas turbine combustion system pressure drops.

The mean static pressure distribution measured on the face of the damping skin is presented (Figure 8.2). The contours show the static pressure difference between the actual static pressure and the reference pressure in the centre of the perforated liner, i.e. $x/W_D = 0.5$ and $y/L_D = 0.6$. This was non-dimensionalised using the spatially averaged mean pressure difference across the damping skin. Note the highly non-uniform distribution being measured on the face of the damper. A high static pressure is observed where the efflux from the injector impinges onto the passive damper (and $y/L_D < 0.4$), this pressure being greater than the design pressure drop across the damping skin. In other words at this location the pressure on the damper face, inside the flame tube, is greater than the pressure within the cavity between the porous liners. This must give rise to some concern regarding the ingestion of hot gas into the cavity between the damping and metering skins. As fluid accelerates away from the impingement point the static pressure reduces so increasing the pressure drop across the damping skin. On a spatially averaged basis the damping skin is designed to operate in a linear absorption regime such that any fluctuations in velocity associated with the acoustic pressure oscillations is less than the mean velocity through the orifices. However, on a local basis the measurements suggest that, potentially, this may not be the case.

With the loudspeakers activated a typical mode shape is presented (Figure 8.3), this being normalised by the maximum pressure amplitude. As to be expected in all cases a pressure anti-node is located close to the downstream face of the injector. Thus the proximity of the damper to the fuel injector means that the damper is also exposed to a region of high pressure fluctuations, although these fluctuations will reduce towards the damper trailing edge. This variation is a function of the acoustic wavelength relative to the damper length. From data such as this the magnitude of the acoustic waves travelling towards, and away from, the test section can be calculated. In terms of an energy budget the acoustic energy travelling towards the test section can either (i) pass through the fuel injector, (ii) be absorbed by the damper, or (iii) be reflected back down the duct. Usually the reflection coefficient is defined as the ratio of the reflected and incident pressure amplitude. However, for convenience, in this case the reflection

coefficient was defined as the ratio between the incidence and reflected acoustic energy i.e.

$$\left|R_C\right|^2 = \frac{\left|\hat{B}_r\right|^2}{\left|\hat{B}_i\right|^2}. \tag{8.11}$$

Initially the reflection coefficient was measured over a range of frequencies for the case where the damper was replaced by a solid surface (Figure 8.4). In this case the difference between the incident and reflected acoustic energy reflects that portion of the acoustic energy that is being transmitted through the fuel injector. For example, at 300 Hz the results indicate approximately 35% of the incident energy is reflected back down the duct, with the remaining energy (65%) exiting the test section through the fuel injector. In addition, results are also presented with the passive damper present in which the gap between the two skins was set to its datum value ($S/H = 0.125$). Note that other tests performed at smaller gaps also indicated a similar reflection coefficient. The reduction in reflected energy is associated with the inclusion of the passive damper assembly and the absorption of acoustic energy by the damper. However, additional tests were also performed in which the damping skin was removed and only the metering skin was present (placed flush with the inside surface of the duct). Note the similarity in the reflection coefficient over the range of frequencies tested. This suggests that for this datum configuration the acoustic energy absorption was associated with the metering skin, with no acoustic energy being absorbed by the damping skin. However, further measurements were undertaken with the passive damper in place but where the gap between the two liners was increased, in various increments, from $0.125 \leq S/H \leq 1.46$ (Figure 8.5). It can be seen that with an increasing gap the amount of reflected energy decreases until, at the larger separations, virtually no acoustic energy is being reflected back from the test section. In other words for these configurations the results suggest a relatively large amount of acoustic energy is being absorbed. This behaviour is clearly an important aspect relating to the design of an efficient passive damping system within a gas turbine space envelope. Therefore the aforementioned acoustic absorption model (section 8.1) was used to investigate the observed characteristic

relating to the reduction of increasing acoustic absorption with increasing damper volume.

8.2.2 Analytical Model Validation

Initially the model introduced in the previous section can be validated against the experimental results in a similar way as described in Rupp et. al. (2012). Due to the transmission of acoustic energy introduced by the fuel injector it is not possible to directly compare the loss of acoustic energy between the experiment and the model previously presented (i.e. the model only captures the loss associated with the passive damping system and not the acoustic energy transmitted through the fuel injector). Therefore the validation of the model is split into two sections. Initially the acoustic energy loss calculated by the model will be compared to absorption measurements conducted without the presence of the fuel injector. Afterwards the model is compared to the pressure amplitude measurements in the presence of the fuel injector flow field. The discharge coefficients used within the acoustic model for the damping skin and metering skin as well as the length corrections are defined in Table 8.1. In this case the mean flow discharge coefficients were measured using the test specimen and the plenum fed arrangement described in appendix B. Moreover the length corrections were estimated from the geometry used in Table 5.1.

	L/D	C_D	**Length correction (Table 5.1)**
Damping skin	2.86	0.88	1.35 *(L/D* = 3)
Metering skin	2	0.87	1.06 (*L/D* = 1.98)

Table 8.1 Measured discharge coefficient and used loss coefficient in analytical model

8.2.2.1 Acoustic Energy Absorption

In this case the fuel injector is removed and replaced by a blanking plate. As the upstream boundary condition in the test rig is now a closed end it can be assumed that the difference between incident and reflected energy is only associated with the energy absorbed by the passive damping system. All the experimental data compared to the

modelling data in this section (Figure 8.7) has been conducted with a closed wall termination instead of the fuel injector.

For this configuration three test cases have been used (S/H = 0.125, 0.33 and 1.56 at a $\Delta p/p$ of 3% across the two perforated skins). The acoustic energy loss has been calculated from the experiments using the difference in acoustic energy flux travelling towards and away from the test section (as defined in equations (5.1) to (5.3)). As already discussed the analytical model relies on the long wavelength assumption. At relatively low frequencies the assumption of a constant pressure fluctuation across the face of the damper will be valid but this may not be the case at higher frequencies. Moreover the amplitude on the face of the damper, which is used to normalise the acoustic loss, could be overestimated due to the appearance of the acoustic mode shape along the face of the damper. With this in mind Figure 8.6 shows the measured mode shapes for 250, 300 and 350 Hz (note that the amplitudes have been normalised with the maximum pressure amplitude).

To reduce the source of error, due to the changing pressure amplitude along the damper surface, the measured mode shapes were used as an input to the model. The associated velocity fluctuations described in equation (8.6) for the metering and damping skins have been divided into n sections with a damper length of $dL = L/n$. In this way the input excitation amplitude $\hat{p}_0(y)$ has been set according to the mode shape amplitudes along the y-axis, i. e.:

$$\hat{u}_{D11} = \frac{\hat{p}_1 - \hat{p}_0(y_1)}{\rho\varsigma_1\overline{U}_{D1} + \rho\varsigma_{vis,1} + i\omega\rho L_1}$$

$$\hat{u}_{D12} = \frac{\hat{p}_1 - \hat{p}_0(y_2)}{\rho\varsigma_1\overline{U}_{D1} + \rho\varsigma_{vis,1} + i\omega\rho L_1}$$

$$\vdots$$

$$\hat{u}_{D1n} = \frac{\hat{p}_1 - \hat{p}_0(y_n)}{\rho\varsigma_1\overline{U}_{D1} + \rho\varsigma_{vis,1} + i\omega\rho L_1}.$$

The linear equation system was then solved and the energy loss of each section along the damping skin surface was accumulated to give the total energy loss. Thus acoustic energy loss has been normalised according to equation (8.10) using the spatially averaged pressure amplitude on the face of the damper inside the main duct.

Figure 8.7 shows the comparison of the experimental data to the mode shape corrected analytical absorption model. It can be seen that the model shows very good agreement throughout the frequency range. However to reduce any ambiguity due to the normalisation of the acoustic loss Figure 8.8 compares the actual measured acoustic loss with the loss calculated by the model using the mode shape pressure amplitude as an input. It can be seen that there is excellent agreement between the model and the measurement. It should be noted that when using the model for predicting damper performance the measured mode shape is not known a priori. However this is deemed acceptable within a preliminary design assessment (i) enabling the relative performance of different damping configurations to be assessed and (ii) identifying the main factors controlling the amount of acoustic absorption.

Another interesting aspect is the application of such an analytical model to annular gas turbine combustor geometries. In this case the pressure excitation can be caused by a circumferential wave travelling through the combustor annulus geometry. The developed analytical model would be valid for a circumferential moving pressure wave where the wavelength in the circumferential direction is much larger than the width of the damper in circumferential direction. However, for more accurate calculations the tool should be incorporated in acoustic network models simulating the actual pressure mode shapes. In this way the effect of the acoustic damper on the combustor stability can be assessed.

8.2.2.2 Damper Cavity Pressure Amplitude Assessment

For the experimental data in this section the fuel injector was installed onto the test rig. Hence no direct comparison of the acoustic energy loss due to the damper is possible. However, as suggested by equations (8.6), (8.7) and (8.9) the unsteady pressure drop across the damping and metering skins has a significant effect on the amount of acoustic energy being absorbed. Hence some further validation of the model was conducted comparing the ratio of pressure amplitudes inside the cavity, $\hat{p}_1$ (i.e. between the damping and metering skins), with those within the test section, $\hat{p}_o$ (i.e. incident onto the damping skin). Again in this case the pressure mode shape along the face of the damper has been averaged over the axial length of the damper to estimate the

incident pressure amplitude $\hat{p}_o$. Space constraints meant that experimentally the cavity pressure amplitude could only be measured for liner separations greater than 0.33. However some example results are presented (Figure 8.9) for which measurements were available.

It can be seen that the model is able to capture the pressure ratio indicated by the experimental data. This includes the reduction in the oscillating cavity pressure amplitude, relative to the pressure incident onto the damping surface, with increasing liner separation. Moreover Figure 8.10 shows the phase difference between the cavity pressure oscillation and the incidental pressure oscillation as a comparison between the measured data and the prediction by the model. In this case the phase of the incidental pressure wave was averaged along the damper surface. As the cavity measurement is a point measurement it was assumed that there is no significant phase change within the cavity between the damping and the metering skin. It can be seen that the model is agreeing very well with measured phase difference across the damping skin. Moreover the trend of increasing phase difference with increasing cavity volume is also captured well by the model. Overall it can be seen that the model is capable of predicting the acoustic characteristics of the double liner system despite the complex mean flow condition the damping skin is operating in. As already described in section 5.9 the model takes no account of the complexity of the flow field and simulates a pulsatile flow field based on a constant loss coefficient and length correction. Hence the good agreement between the experiment and the model suggests that the swirling flows and cross-flows along the damper surface have no significant effect on the overall damper performance. Moreover this data indicates that overall the absorption is linear on the face of the damper (although locally this may not be the case due to the pressure drop distribution for the cases with fuel injector). Due to the very good agreement between the model and the experimental results the model can now be used to further understand the absorption behaviour of the investigated passive damper geometry.

8.2.3 Damper Performance Assessment

As described in Rupp et. al. (2012) both the experimental measurements and analytical model have been used to relate the observed absorption characteristics with

the unsteady flow field generated by the incident acoustic waves. The previous section has shown the model is most accurate if a representative input mode shape profile is used into the model. Hence the experimental mode shape measurement from the S/H = 1.56 test case has been used as input to the model. However in this case only the profile of the mode shape along the y-axis is important, not the actual amplitude of the mode shape. Hence calculations from other test cases do generate identical results for equivalent frequencies.

For aero-type applications there is a desire to minimise the space occupied by the damping system so resulting in a relatively small separation, or volume (V), between the metering and damping skins. However, this small volume means that the pressure inside the cavity is sensitive to any changes in mass flow. The incident acoustic pressure fluctuation will therefore cause a change in mass flow, through the damping skin, which quickly leads to a change in the cavity pressure (i.e. due to the small volume). In reality this means that at small volumes the unsteady cavity pressure approximately equals the unsteady incident pressure. Thus the unsteady pressure drop across the damping skin is minimal. This is suggested both by the experiment data already presented (Figure 8.4 and Figure 8.5), and also the cavity pressures generated by the analytical model that have been plotted for an excitation frequency of 250 Hz (Figure 8.11). The experimental data measured in the presence of the fuel injector flow field was also added into Figure 8.11 for comparison. Moreover the phase between the cavity pressure and the excitation pressure in Figure 8.12 shows that the fluctuations for small volumes occur in phase i.e. as the incident pressure increases so does the cavity pressure at virtually the same instant in time. Furthermore it can be seen that the analytical model is agreeing very well with the measured phase even when the fuel injector flow field is present in the experiment.

As a consequence at small cavity gaps nearly the entire unsteady pressure drop occurs across the metering skin. This explains why there was little difference in the reflection coefficient between tests undertaken with the single (metering) skin and with the damper present when the cavity gap was less than S/H = 0.125. The metering skin is designed with a high mean pressure drop and therefore the acoustic absorption generated by the metering liner is relatively small. As the gap between the skins within

the passive damper increases, however, so the volume will tend towards a plenum. In this case fluctuations in mass flow through the damping skin, due to the incident unsteady pressure, will have a limited effect on the pressure within the damper cavity (Figure 8.11). Consequently large unsteady pressure fluctuations and mass flow variations are generated across the damping skin enabling a significant amount of acoustic energy to be absorbed (Figure 8.5). This behaviour is also illustrated in Figure 8.13 where the predicted unsteady velocities (normalised with the mean velocities across the damping and metering skins) are shown for a perturbation at 250 Hz. The significant increase in the unsteady damping skin velocity with increasing liner separation can be seen. In contrast at small volumes the unsteady damping skin velocity is small and of the order of the metering skin velocity amplitudes. However in this case the unsteady pressure drop across the damping skin is reduced which leads to a much reduced acoustic energy loss as described in equation (8.9) and the majority of the damping is caused by the metering skin. Even though the *unsteady* pressure drop across the metering skin is increased for the small cavity volumes the large *mean* pressure drop results in much smaller Strouhal numbers. Hence the admittance, which is also a measure of the acoustic energy loss as indicated in equation (8.9), is much smaller for the metering skin than for the damping skin (Figure 8.14). Thus the acoustic energy loss is reduced for the metering skin despite the increased unsteady pressure difference.

8.2.4 Damper Optimisation

In addition to understanding the unsteady flow field and the absorption characteristics the simplified model can be used to explore the impact and trade-off between various changes to the damper geometry in the same way as described in Rupp et. al. (2012). In equations (8.8) and (8.9) it was shown that the pressure amplitude is proportional to the unsteady velocity amplitude and the unsteady pressure drop. Previously section 5.7 showed that the maximum acoustic energy loss within the quasi-steady regime (low Strouhal number) is proportional to the unsteady pressure difference and the ratio of mean mass flow through the porosity and the mean pressure drop (equation 5.25)

$$\Pi_L^{QS} \sim \left|\hat{p}_{ds} - \hat{p}_{us}\right|^2 \frac{\overline{\dot{m}}}{\Delta\overline{p}}. \tag{8.12}$$

The damper within the gas turbine combustion system has to operate within a given air mass flow budget. Hence one way of optimising a damper is to reduce the mean pressure drop for a given mean air mass flow by using a second liner (i.e. metering skin). However as shown in the previous section reducing the mean pressure drop across the damping skin might not be beneficial for the given space envelope and the associated unsteady pressure difference which is also affecting the acoustic energy loss (equation (8.9) and (8.12)). Hence the model is used to understand the optimum mean pressure drop for a given cavity volume size. For example the amount of energy absorbed, as indicated by the model, is presented for three different cavity separations and for various combinations of metering skin and damping skin porosity. These changes in porosity were achieved by varying the number of orifices within each skin. The total pressure drop across the passive damper system was kept constant as well as the mass flow through the damper.

Figure 8.15 presents the normalised acoustic loss with respect to a change in the mean pressure drop across the damping skin. The occurrence of the acoustic loss maxima can be explained by considering the acoustic loss defined by equation (8.9) as well as the velocity amplitude equations (8.6) and (8.7). The acoustic energy loss is a function of the unsteady pressure difference across the aperture and the admittance of the apertures. Moreover equations (8.6) and (8.7) show that the velocity amplitudes are calculated using the loss coefficients, mean velocity, length corrections and the unsteady pressure drop. Hence changes in mean pressure drop will also result in changes in mean velocity. If the length-to-diameter ratio is constant it can be assumed that the discharge coefficient and thus the loss coefficient remain constant. Hence one strategy to increase the absorption of a passive damper is to reduce the mean velocity, by reducing the mean pressure drop. This will lead to an increase in velocity amplitude and therefore to an increase in admittance for the apertures as explained in section 5.3. However as Figure 8.16 shows the cavity unsteady pressure ratio, for a given volume, increases with decreasing mean pressure drop i.e. the cavity becomes more sensitive to mass flow fluctuations and so the *unsteady* pressure drop across the damping skin decreases with a decreasing *mean* pressure drop. Hence the possible increase in velocity amplitude, and therefore the acoustic absorption, is also accompanied by a reduction in the *unsteady*

pressure drop. Consequently there is an optimum *mean* pressure drop across the damping skin i.e. where the acoustic absorption is at its maximum for a given cavity volume.

It can be seen from Figure 8.15 that the volume effect is much larger than the pressure drop reduction. Hence the design of non-resonant acoustic dampers should aim at maximising the available volume. As equations (8.8) and (8.9) show the actual area of the damper (or amount of apertures within the damper) also affects the acoustic absorption performance. However this parameter is set by the available air mass flow budget. Hence the optimisation of a non-resonating damper can only aim on optimisation of the porosities between the metering and damping skin such that the unsteady pressure difference across the damping skin apertures is maximised. This needs to be in conjunction with the necessary cooling requirements of the combustor wall.

8.2.5 Impedance Methodology

As already discussed in the previous section it is not straightforward to compare the analytical modelling data to the measured data if the fuel injector is also present in the experiment. In this case some of the energy is also transmitted through the fuel injector or even dissipated by the fuel injector. Hence the measured reflection coefficient is representative of the total system, i.e. fuel injector and acoustic damper. Therefore the model also needs to consider the superposition of the acoustic characteristic of the fuel injector (this being more representative of an engine configuration). Hence an approach as described by Kinsler et. al. (1999) was implemented which enables the superposition of impedances of the considered acoustic elements. This process is shown schematically in Figure 8.17, and as previously discussed, assumes that the acoustic wavelength is much longer compared to the length of the damper or size of the fuel injector. In this case the test section is split into an acoustic system of three impedances: the damper impedance Z_D, the fuel injector impedance Z_{inj} and the total impedance of the system Z_{tot}. In accordance with Kinsler et. al. (1999) this system of impedances has been split into three acoustic branches joined together at the plane $y/L_D = 0$. The plane at $y/L_D = 0$ was chosen just downstream of the fuel injector. Hence as a first approximation the assumption was made that the change in pressure amplitude along the damper is

negligible, i.e. $\partial\hat{p}/\partial(y/L_D)=0$. However this approach can be included within a network model in the future which should take the mode shape along the damper surface into account.

Mathematically the acoustic system can be described using impedances considering the volume velocity (e.g. Kinsler et. al. (1999) or Lucas et. al. (1997))

$$Z_{tot}(x=0)=\frac{\hat{p}(x=0)}{\hat{u}_{tot}(x=0)A_{tot}}, \tag{8.13}$$

where A_{tot} represents the cross-sectional area of the duct to which the fuel injector and damper are connected. Applying continuity of mass across the boundaries of the acoustic branches and assuming that all acoustic elements are exposed to the same pressure amplitudes the total acoustic impedance can be described as

$$\frac{\hat{p}}{\hat{u}_{tot}A_{tot}}=\frac{\hat{p}}{\hat{u}_{D}A_{D}}+\frac{\hat{p}}{\hat{u}_{inj}A_{inj}}. \tag{8.14}$$

Hence the total impedance can be calculated as the sum of the reciprocal of the acoustic component impedances

$$\frac{1}{Z_{tot}}=\frac{1}{Z_{D}}+\frac{1}{Z_{inj}}. \tag{8.15}$$

The acoustic impedance of the non-resonant acoustic damper is calculated using the described analytical model. A representative pressure mode shape is used as input to the model and the impedance is averaged along the face of the damper. This averaged impedance is then used as the damper impedance in equation (8.15).

The remaining unknown is the fuel injector impedance. In this case the fuel injector impedance was measured by blanking the damper section off with a rigid wall, with the fuel injector upstream side being open to atmosphere (i.e. plenum fed). For this configuration the acoustic impedance could be measured using the two microphone method and a mean pressure drop across the fuel injector of 3%. The setup was not optimised for an impedance measurement as for example explained in section 5.4. Hence reference data was also used relating to the same injector in a similar plenum fed arrangement forced by plane axial pressure waves (but over a wider frequency

bandwidth) conducted by Peacock (2011). The measured resistance and reactance of the fuel injector is shown in Figure 8.18. Note that the impedances shown in this figure do show the impedance based on the velocity amplitude, i.e. $Z = \hat{p}/\hat{u}$. For the purpose of this work the measured fuel injector impedance could be matched using the momentum balance as used in section 5.9 to calculate the impedance of the investigated orifice geometry. In this case the assumption was made that the resistance of the injector remains constant across the investigated frequencies with no viscosity effects being considered. The fit to the experimental data obtained by changing the loss coefficient and the acoustic length of the fuel injector is also shown in Figure 8.18. It should be noted this is not suggested that this is the correct model to use, but for the purpose of this work it was sufficient to get a reasonable representation of the fuel injector boundary condition. The increase in resistance from 250 Hz and 350 Hz could be partly due to real behaviour of the fuel injector or due to experimental inaccuracies. The only frequency dependent change to the resistance on the basis of the used model from section 5.9 would be the influence of viscosity. However this increase is too sharp to be reproduced by the model. Nevertheless the fuel injector swirling flow field is complex and flow instabilities in the swirling shear layers could also cause changes to the resistance of the fuel injector. Similar behaviour was found for jet flow instabilities for circular orifice plates in section 5.9. The fuel injector acoustic behaviour was not part of this work and it is suggested that future projects could provide a better representation of the acoustic characteristic of the injector. Ultimately this would increase the accuracy of acoustic network models for combustion instabilities. Nevertheless the estimated resistance and reactance was used to represent the fuel injector impedance in equation (8.14) to a first approximation.

The calculated total impedance from equation (8.14) was then used to estimate the reflection coefficient as defined for example by Bellucci et. al. (2004):

$$R_C = \frac{Z_{tot} + \rho c}{Z_{tot} - \rho c}. \tag{8.16}$$

Hence the total system reflection coefficient estimated by the model with the help of equations (8.14) and (8.15) has been compared with the measured reflection coefficient for the total system of fuel injector and acoustic damper (Figure 8.19). It can be seen

that the calculated reflection coefficient agrees reasonably well with the measured reflection coefficient. The previous two sections have shown the analytical damper model agrees well with the measured acoustic losses and so any discrepancies in the total system loss are most likely due to inaccuracies of the fuel injector impedance measurements. To emphasise this source of error in the method a variation on the fuel injector resistance and reactance is also presented. Figure 8.20 shows the measured fuel injector impedance in comparison to a modelling match with increased resistance and reactance. This has then been used to predict the total system reflection coefficient for the example test case of S/H = 0.74 (Figure 8.21). It can be seen that the calculated reflection coefficient is much increased compared to the previous solution with a reduced resistance. This supports the suggestion that the fuel injector impedance is the greatest source of error within the prediction and has also the largest effect upon the total system reflection coefficient.

However the used method of reproducing rather complex multi-impedance system experiments seems to be valid due to the generally good agreement between the model and experiment. This can be used to validate elements of the acoustic network models for multi-acoustic element experiments. As long as the system impedances, i.e. fuel injector, tiles, dampers, are known the experimental data can be either split into single element impedances or models of total systems can be reproduced. This enables the acoustic assessment of complex acoustic systems (such as gas turbine combustion systems).

8.3 Resonating Linear Acoustic Dampers

One of the outcomes of the previous section was that the complex fuel injector flow field has no significant effect upon the performance of the acoustic damper. Therefore the acoustic damper geometries can be optimised on a simple test rig without the influence of a fuel injector. Hence the experimental facility described in section 3.3.1 has been used to assess various acoustic damper designs as described in appendix A.3. The previous section introduced a perforated liner system aimed at absorbing acoustic energy within a gas turbine combustion system environment. In this case the cavity between the damping skin and the metering skin was not resonating and it was shown

that the damper absorbs more energy if the cavity is operating as a plenum, i.e. no pressure amplitudes within the cavity. However, the volume size required to generate acoustic plenum conditions would be typically too large to fit into the design space envelope for an aero-engine gas turbine combustion system. The advantage of having a plenum between the damping and metering skin is the increased unsteady pressure drop across the damping skin. Hence the velocity amplitudes within the apertures of the damping liner are maximised and thus the acoustic absorption is greatly enhanced. Therefore alternative ways of increasing the unsteady pressure drop across the damping skin of a two liner system were investigated.

In this section damper designs were investigated with a resonant cavity volume. This is equivalent to an array of Helmholtz resonators tuned to the same frequency (as for example described in Figure 1.12 in section 1.3.1.4).Therefore the cavity between the damping and metering skin can be tuned using the length of the apertures, the area of the apertures as well as the available volume. Hence a number of resonating cavities have been designed using cavity volumes which are available within the gas turbine combustion design envelope as well as liner porosities representative of gas turbine cooling geometries and mean pressure drops. The theory used to tune the investigated damper designs was based on the Helmholtz resonator frequency as described in equation (1.14) in chapter 1 extended to two resonator necks as in Keller and Zauner (1995) using the geometric area and length of the used apertures

$$f_{res} = \frac{c}{2\pi}\sqrt{\frac{1}{V}\left(\frac{A_1}{L_1}+\frac{A_2}{L_2}\right)}. \tag{8.17}$$

If the damper is operated at its resonance frequency the pressure amplitude inside the cavity is increased. Furthermore the phase difference between the pressure oscillation upstream and downstream of the damping skin is 90°. This therefore results in large unsteady velocities and the potential for enhanced damping.

All the acoustic absorption results shown in this section were measured within the linear acoustic absorption regime despite the acoustic resonance within the damper volume. In the following sections the experimental results will be discussed followed by

a further comparison between the developed analytical acoustic absorption model (section 8.1) applied to the resonant liner geometries.

8.3.1 Experimental Results

This section describes the experimental results measured for the five resonant liner configurations (Table A.5) in an impedance tube arrangement as shown in Figure 3.6. The acoustic energy loss was calculated from the incident and reflected acoustic energy flux. In this case it was assumed that no acoustic energy is transmitted through the damper system. Thus the reflected and incident acoustic energy flux was used in equation (5.3) to calculate the acoustic energy loss. Furthermore this loss was then normalised using the incident acoustic pressure amplitude at the exit plane of the acoustic damper ($x = 0$) as defined in equation (8.10).

As already discussed the aim of this study was to increase the acoustic loss by enhancing the unsteady pressure amplitude across the damping skin. Hence a similar volume size ($V = 0.3$ l) was used for the resonant liner as for the datum non-resonating damper configuration ($S/H = 0.125$, $V = 0.24$ l). Moreover to maximise the acoustic absorption behaviour the pressure drop across the damping skin was nominally set to 0.2% for a 2.5% total pressure drop across the metering skin and damping skin which is a typical value for gas turbine combustion system wall pressure drops. The non-resonating damping system in the previous section extended itself across the outer combustion chamber wall. However for cooling purposes this might not be possible for a gas turbine application. For example the static pressure profile along the outer combustor wall is shown in Figure 8.2. It can be seen that the fuel injector flow field is impinging onto the first part of the acoustic damper, i.e. $y/L_D < 0.4$. In this region an adequate wall pressure drop is needed to avoid hot gas ingestion and cool the liner wall. Hence it might not be possible to use this region for the application of an acoustic damper. However the damper could be applied to other areas within the combustion system including, for example the downstream end of the outer wall or the combustor head. In this case the damper will have less effective area and ultimately take less air mass flow. Hence in this section the damping skin effective flow area is reduced by a factor four compared to the non-resonating damper.

The aim for this study was to keep the resonance frequency of the damping system below 1000 Hz at full engine operating conditions scaled on combustor inlet temperatures. Therefore the resonance frequencies at ambient conditions were targeted to be at a maximum of 500 Hz at isothermal ambient conditions (if the combustor inlet temperature were 900 K).

Ideally the backing wall should consist of a rigid wall without perforations, as for example in Hughes and Dowling (1990) or Bellucci et. al. (2004b). However due to cooling requirements in this application it is likely that cooling air is introduced through the backing plate into the damper cavity. Hence in this work a porous backing plate was incorporated (i.e. a metering skin) similar to that presented in the previous section for non-resonating liners. The metering skin apertures were chosen to have large *L/D* ratios (~16.7) to increase the inertia for the metering plate and minimise the unsteady mass flow across the metering skin. Thus the effect on resonance within the volume due to the metering skin is reduced.

The measured acoustic energy loss for the datum resonant damper configuration (configuration 1) is shown in Figure 8.22. Moreover for comparison the acoustic energy loss (measured without the presence of the fuel injector flow field) for a non-resonating damper with $S/H = 0.125$ is also shown as a comparison. It can be seen that the resonant liner configuration shows a maximum acoustic loss at 500 Hz which corresponds to the resonance frequency of the liner. The resonant liner generates a similar amount of acoustic energy absorption compared with the non-resonating liner at a frequency range around 300 Hz. However this is achieved with four times less effective area which highlights the advantages of a resonating design. The resonating damper therefore offers an opportunity to maximise the acoustic absorption within a small design space compared to non-resonating dampers. It can also be seen that absorption is greatly enhanced if the damper is excited on its actual resonance frequency of 500 Hz.

Figure 8.23 shows the pressure amplitude ratio between the cavity pressure amplitude, measured inside the damper cavity, and the excitation pressure amplitude immediately downstream of the damping skin along with the phase difference between the two pressure amplitudes. Initially (300 – 500 Hz) the pressure amplitude ratio is similar to the measured pressure amplitude ratio of the non-resonant liner for $S/H = 0.33$

(unfortunately it was not possible to measure pressure amplitudes in the cavity for non-resonating liners at smaller *S/H* due to space constraints). It can also be seen that the pressure amplitude ratio reduces for increasing excitation frequency larger 350 Hz. However, the phase difference in Figure 8.23 also shows a varying phase shift, with a 90 phase difference between the cavity pressure amplitude and the excitation amplitude occurring at 500 Hz. This is evidence that the system is in resonance with a vanishing system reactance (Figure 8.24) occurring at the resonance frequency as described for Helmholtz resonators in equation (1.13) and (1.14). This 90 phase shift coincides with the maximum acoustic energy loss for the resonant damper in Figure 8.22. Due to the reducing pressure amplitude ratio and the increasing phase shift from 300 to 500 Hz the unsteady pressure difference is increasing (Figure 8.25) leading to more acoustic energy being absorbed (equation (8.9)). The unsteady pressure drop remains high for frequencies higher than 500 Hz. However, the reactance increases at larger frequency and hence the acoustic velocity amplitudes in the liner reduce (as does the acoustic energy absorption).

The sensitivity of the acoustic absorption to varying total pressure drop was also tested for the resonant damper configuration 1. Mean damping skin pressure drops of 0.1, 0.16 and 0.2% were investigated. The results for this mean pressure drop variation are shown in Figure 8.26 for the measured normalised acoustic energy loss. It can be seen that the maximum acoustic energy loss reduces with increasing mean pressure drop. Moreover away from the resonance frequency, i.e. at frequencies much smaller or much larger than 500 Hz, the increase in mean pressure drop from 0.1 to 0.2% has negligible influence on the acoustic energy loss. This demonstrates that whilst the mean pressure drop does not influence the resonance frequency, it does affect the actual acoustic energy loss. Hence the mean pressure drop across the damping skin will need to be designed to a minimum while maintaining sufficient pressure loss for cooling requirements and the avoidance of hot gas ingestion.

As can be seen from Figure 8.22 and Figure 8.26 the resonance frequency for the acoustic damper system is measured as 500 Hz at ambient temperature. Assuming a gas turbine engine with 900 K combustion chamber inlet temperature this would equate to a frequency of 880 Hz. For medium to large civil aero-engines combustion instabilities

relating to the first order circumferential mode in the full annular combustor occur, dependent on the combustor size, in a range of 400 to 1000 Hz at full engine conditions. Hence it might be necessary to tune the resonant liner to lower and higher resonance frequencies. There are several options for tuning the liner. Initially the size of the volume has been increased by factor 1.6. As expected and shown by Figure 8.27 this reduces the damper resonance frequencies to 390 Hz for the damper with the enlarged volume. In this case the metering skin and the damping skin remained identical (i.e. only the volume was increased). Moreover the damping skin pressure drop for both test cases was set to 0.2%. As can be seen the reduction in resonance frequency due to the large volume was achieved with a negligible reduction in acoustic energy loss. However, enlarging the volume of the resonating damper within a gas turbine combustion chamber is not always feasible due to the restricted design space envelope. Hence another option of reducing the acoustic damper resonance frequency is by increasing the length of the apertures. This has been achieved by increasing the aperture length from 6 mm to 8 mm in configuration 2 and 12 mm in configuration 3. The aperture diameter was kept constant leading to *L/D* ratios of 5.45, 7.2 and 10.91. The measured acoustic energy loss for the three damper configurations with varying aperture length is shown in Figure 8.28. It can be seen that the resonance frequency reduces with increasing aperture length (from 500 Hz to 421 Hz for configuration 2 and 500 Hz to 390 Hz for configuration 3). The drop in the maximum absorption for configuration 2 and 3 is due to the slightly reduced amount of damping skin apertures, e.g. 184 compared to 192 for configuration 1 and 3. Hence the generated acoustic energy loss is slightly less.

To compare the change in damper performance in more detail the excitation frequency has been normalised with the damper resonance frequency. Hence Figure 8.29 shows the comparison for configurations 1, 2 and 3 relative to the normalised frequency. It can be seen that the increase in aperture length had no significant effect upon the acoustic energy loss at the resonance frequency of the damper. The only slight difference is that the damping bandwidth of the acoustic liner is reduced for the configuration with the longest aperture (configuration 3) compared to configuration 1 with the shortest aperture. This behaviour can be explained with the increasing

reactance for the longer apertures. The gradient for the damping system reactance as shown for the three configurations in Figure 8.30 is steeper for the configurations with longer apertures. Hence the bandwidth of the resonant damper is reduced at lower frequencies.

The experimental results show that a resonating passive damper system can operate more efficiently, in terms of acoustic energy loss compared with a non-resonant liner system within the restricted space envelope of a gas turbine combustion system. Various examples of tuning the resonant liner have been shown and analysed. However a further objective of acquiring this data was to provide additional validation data for the analytical models and derive some simple geometrical parameters for the tuning, design and optimisation of a resonating damping system. This will be discussed in the following sections.

8.3.2 Analytical Model Validation

The developed analytical model described in section 8.1 will be compared to the experimental results. In this case the prediction of the damper is more challenging due to (i) the increased length of the aperture which was shown to be more challenging in section 5.9 and (ii) the increased Strouhal numbers for some of the investigated geometries. To be able to assess the mean flow loss coefficient accurately the discharge coefficients were measured for the described liner configurations. In this case the total damping system, metering skin and damping skin, was placed in a plenum and the total effective area for the given damper configuration was measured. Simultaneously the metering skin and damping skin pressure drop was also measured. Hence it was possible to derive the effective area of the metering and damping skins and hence derive their respective discharge coefficients. The measured discharge coefficients for each resonating damper geometry are presented in Table 8.2. Moreover the length corrections for the apertures in the damping skin were approximated from the length corrections presented in Table 5.1 for the aperture length to diameter ratios of 3, 5, 6.8 and 10. In addition the length correction defined for the aperture with $L/D = 10$ was also used for the metering skin impedance model with $L/D = 16.67$.

Damper configuration	Damping skin *L/D*	Damping skin *dp/p* in %	Damping skin C_D	Metering skin C_D
1	5.45	0.1%	0.69	0.58
1	5.45	0.16%	0.7	0.6
1	5.45	0.2%	0.72	0.6
2	7.27	0.14%	0.64	0.58
3	10.91	0.15%	0.58	0.58
4	5.45	0.1%	0.69	0.58
4	5.45	0.22%	0.72	0.6
5	3.75	0.03%	0.83	0.59

Table 8.2: Measured discharge coefficients for metering skin and damping skin for the five investigated resonant damper configurations

It was mentioned in section 5.9.1 that the measured mean flow discharge coefficient deviated from the discharge coefficient derived from the acoustic model for apertures with *L/D* longer than two. Moreover section 5.9.2 discussed additional sources of error in the model due to the change of the aperture flow field and the development of orifice internal boundary layers for the apertures longer than *L/D* of two. The previous section showed good agreement between the developed analytical model for apertures of *L/D* ~ 3. However to gain a better estimate of the accuracy of the prediction for even larger *L/D* the measured discharge coefficient (as in Table 8.2) has been used and the model described in section 8.1 was compared to the measured data in the previous section.

The resonant liner experiments were conducted in an impedance tube arrangement with the damper perpendicular to the axial acoustic waves. Hence the measured results are not affected by acoustic mode shapes as the pressure amplitude and phase along the damper surface is constant. Therefore the measured pressure amplitude immediately downstream of the damping skin at $x = 0$ was used as an input excitation amplitude into the acoustic model and for the normalisation of the acoustic energy loss.

Figure 8.31 shows a comparison of the calculated and measured normalised acoustic energy loss for the resonant damper configuration 1. It can be seen that the model predicts the maximum acoustic loss at the same frequency as the experiment. In general the predicted acoustic loss is showing the same trend as the experimental data. However the maximum acoustic loss is estimated to be approximately 13% smaller than in the

experiment. Moreover the pressure amplitude ratio is showing the same characteristic as the experimental data (Figure 8.32). In this case the predicted maximum amplitude ratio is shifted to higher frequencies compared to the measurement and the maximum value is approximately 8% smaller for the prediction. Finally the phase difference between the cavity amplitude and the excitation amplitude is shown in Figure 8.33. It can be seen that the trend of the phase difference predicted by the model is in agreement with the experiment. Hence the frequency for the maximum calculated normalised acoustic loss compared to the experimental data is in agreement in Figure 8.31. The reason for the mismatch in pressure amplitude ratio and acoustic energy loss is caused by the calculated impedance of the damping skin and the metering skin used in the model. Hence the measured system impedance has been compared to the calculated impedance. Note in this case the impedance was defined as the ratio between incident pressure amplitude and the velocity amplitudes within the apertures of the damping skin

$$Z = \frac{\hat{p}_0}{\hat{u}_{D1}}. \tag{8.18}$$

The calculated and measured acoustic resistance is compared in Figure 8.34. The predicted resistance is on average 20 % larger than the measured resistance. This overestimate of the liner resistance is therefore causing a reduction in the acoustic energy loss relative to the measured data (Figure 8.31.)

Figure 8.35 shows the comparison between the measured and predicted acoustic reactance. It can be seen that the predicted reactance is in excellent agreement with the measured reactance. This shows that the length correction estimates for the aperture geometry in the liner was approximated correctly based on the aperture measurements presented in section 5.9. The accurate prediction of the length correction for the liner apertures is important for resonant liners and the calculation of the liner resonance frequency. Currently an estimate on the length correction can be undertaken based on measurements of similar orifice geometries or with semi-empirical length correction estimates as they are shown in Bellucci et. al. (2004b). However, experimental validation for the used geometry is still necessary. In this case the error in the acoustic energy loss prediction is caused by the discrepancies in the resistance prediction which

is based on a viscosity model for the boundary layer within the aperture as well as on the loss coefficient estimated from the mean flow discharge coefficient.

As Figure 8.36 shows the model captures the trend in acoustic energy loss with varying pressure drop across the damping skin. In this case the measured discharge coefficients for each pressure drop have been used in the analytical model to predict the acoustic energy loss. The model shows a reduction in acoustic loss with increasing mean pressure drop (from 0.1 to 0.2%). However it can be seen that the maximum acoustic energy loss calculated by the analytical model is consistently underestimated. Nevertheless the relative change in predicted energy loss for the three cases seems to agree very well with the relative change in acoustic energy loss measured in the experiment. Moreover the resonance frequencies are predicted at the correct frequency.

Figure 8.37 shows a comparison between the modelling and the experimental data with a variation in damper volume with a damping skin mean pressure drop of 0.2%. It can be seen that the modelling technique again captures the acoustic energy loss characteristics. The change in resonance frequency due to the increased damper volume is also captured very well. This also provides further evidence that the measured length corrections in section 5.9 can be used for an initial estimate of the length correction and resonance frequency prediction. Again the relative change in acoustic energy loss is reproduced very well by the model, but the maximum energy loss is predicted to be smaller than the experiment.

For the data presented the maximum loss is consistently under estimated by the developed model due to the over prediction of the damping skin resistance. To investigate this issue further the model has been used to compare acoustic damper configurations 2 and 3. In this case the hole length of the damping skin apertures has been increased. The comparison between the acoustic model and the measurement is shown in Figure 8.38. This indicates that the acoustic loss prediction deviates further away from the experimental data with increasing aperture length. For example the deviation in the maximum acoustic loss is approximately 13%, 18% and 30% for *L/D* ratios of 5.45, 7.27 and 10.91 respectively.

Figure 8.39 shows that the reactance prediction agrees very well with the measured data apart for the geometry with *L/D* of 10.91. In this case the length correction is

overestimated for this geometry. However the discrepancies in acoustic energy loss is caused by an over prediction of the acoustic resistance of the damping skin as it is shown in Figure 8.40. It can be seen that the discrepancy between the measured and the calculated resistance is increasing with increasing length-to-diameter ratio.

In general the model reproduces the acoustic energy loss characteristics for the investigated damper experiments very well. This is encouraging and therefore the model can be used to maximise acoustic dampers with larger aperture length-to-diameter ratio. However the maximum acoustic energy loss is consistently underestimated by the modelling method. The data suggests that this is caused by an overestimation for the acoustic resistance and will be further investigated in the following section.

8.3.3 Sources of Errors in the Analytical Modelling for Apertures with Large Length-to-Diameter Ratios

As already discussed in section 5.9.2 the increased inaccuracies for large *L/D* ratio apertures is caused by the complex interaction of the losses surrounding an aperture with *L/D* ratios larger than two. The results in section 8.2.2 suggest that the model is sufficient for apertures with *L/D* of 3 as the viscosity effects seem to be small. However this is not the case for the resonating liner configurations with apertures longer than *L/D* of 3.

Section 5.9.2 suggested two options to estimate the inflow and outflow losses as well as the viscous losses within the aperture, as they are assessed against the experimental data in this section. Initially the measured mean flow discharge coefficient is used without including any viscosity term within the model for the resistance estimation. In this case the reactance is still dependent on the unsteady viscosity model, i.e. only the imaginary part in equation (5.34) is used. This approach is shown in Figure 8.41 for damper configurations 1, 2 and 3 indicated as ‘Model 2’. In general predicted acoustic absorption has increased and the difference between measurement and prediction has reduced compared to the data presented in Figure 8.38. However significant deviations remain for apertures with *L/D* of 10.91. It can be concluded that the inclusion of the viscosity term in the resistance of the model increases the discrepancy to the experimental data.

The second option as proposed in section 5.9.2 was also used to calculate the acoustic energy loss for the three damper configurations as shown in Figure 8.42 indicated by 'Model 3'. In this case it was assumed that the inflow and outflow losses were best represented by the mean flow discharge coefficient of an aperture where the mean flow is just attaching to the inside of the orifice, i.e. *L/D* of two. Hence the discharge coefficient of 0.81 was used in this calculation. The effects of viscosity have been included in the acoustic resistance and reactance calculation. It can be seen that this approach significantly improved the accuracy of the acoustic energy loss prediction. The calculated energy loss agrees well with damper configurations 1 and 2, and much reduced discrepancies can also be seen for configuration 3. This seems to indicate that this approach is the more representative method for the calculation of the acoustic loss of long apertures. However as already mentioned in section 5.9.2 further research is needed to understand the fundamental physics of the unsteady flow field for long apertures to generate more reliable modelling techniques. This has technical relevance as the application of long aperture length-to-diameter ratios is important to tune resonant liners to aero-engine gas turbine combustion system representative frequencies. In chapter 7 a method was presented capable of identifying unsteady flow behaviour relevant to the acoustic absorption process. Hence this could be applied onto CFD methods or sophisticated experimental setups resolving the relevant unsteady flow characteristics of long *L/D* ratio apertures to develop a more reliable modelling technique.

8.3.4 Resonance Parameter for Preliminary Damper Design

During the initial design stages it would be useful to develop a simple relationship of all the relevant geometric parameters of a resonant liner to establish the resonance frequency of the damping device. Therefore a simple optimisation within the design space envelope can be conducted to tune the passive damper onto the desired frequency. In this work the method described by Hughes and Dowling (1990) was initially used to assess the resonance frequency of the linear passive damping device. In their study they have used the classic Helmholtz resonator equation as defined by Rayleigh (1899):

$$k_{res} = \sqrt{\frac{K_D}{V}} . \tag{8.19}$$

Hence the wave number at the resonance frequency is defined by the square root of the Rayleigh Conductivity divided by the resonator volume. Thus the resonance frequency is defined as

$$f_{res} = \frac{c}{2\pi}\sqrt{\frac{K_D}{V}} . \tag{8.20}$$

Comparing equation (8.20) with equation (1.13) shows that the Rayleigh Conductivity for the Helmholtz resonator can be expressed as:

$$K_D = \frac{A}{L_{eff}} = \frac{\pi R^2}{L + 0.85R} . \tag{8.21}$$

In the study by Hughes and Dowling (1990) a perforated liner backed by a resonating volume was studied. Moreover the aim was to damp high frequency combustion instabilities in afterburners (also known as screech). As the frequencies are large the length of the apertures need to be short and in this case, can be neglected. Therefore the Conductivity of a circular aperture with negligible aperture length and the absence of mean flow can be expressed as (Rayleigh (1896), Hughes and Dowling (1990))

$$K_D = 2R . \tag{8.22}$$

This is also valid as a first approximation for the resonance frequency of a resonant linear damper (initially ignoring the effect of the mean flow upon the Conductivity of the aperture). Finally the cavity volume of the resonating liner needs to be defined. In this case the passive damper is divided into multiple Helmholtz resonators. Hence each aperture and its portion of the backing volume is regarded as a Helmholtz resonator. Therefore the relevant volume can be estimated by using the cavity depth S and the pitch between the apertures P_a:

$$V = P_a^2 S . \tag{8.23}$$

Substituting equations (8.22) and (8.23) into equation (8.19) leads to the wave number at the resonance frequency for a perforated liner backed by a resonating cavity:

$$k_{res} = \sqrt{\frac{2R}{P_a^2 S}}. \tag{8.24}$$

Hughes and Dowling (1990) used this expression to define the resonance parameter

$$Q = \frac{k_{res}^2 P_a^2 S}{2R}. \tag{8.25}$$

If this parameter is equal to one than the damper is tuned to the resonance frequency. In the work of Hughes and Dowling (1990) equation (8.25) successfully enabled the prediction of the resonance frequency and non-dimensionalised the frequency axis for the conducted experiments. However, this work is aimed at frequencies that are significantly lower than those associated with afterburner screech. Thus an elegant way of reducing the resonance frequency, for a given damper porosity and limited volume, is to increase the aperture length. This was the approach taken in this work to reduce the resonance frequency of the acoustic damper. As Figure 8.43 shows the maximum acoustic energy loss for each of the investigated geometries does not coincide with a Q-parameter of one (based on the definition in Hughes and Dowling (1990)). Moreover the phase between the incident and the cavity pressure amplitude, which is 90° at resonance, is also not coinciding with a Q-parameter of one at 90° (Figure 8.44). This mismatch is due to the additional aperture length, which was negligible in the work of Hughes and Dowling (1990) but needs to be included in this work. Hence the resonance parameter has been modified using a length correction as defined in Stow and Dowling (2003):

$$K_D = \frac{K_D}{1 + K_D \frac{L_{eff}}{\pi R^2}} = \frac{2R}{1 + 2R \frac{L_{eff}}{\pi R^2}} = \frac{2R^2 \pi}{\pi R + 2 L_{eff}}. \tag{8.26}$$

Therefore the aperture length corrected Q-parameter can be defined by substituting equation (6.17) into equation (6.10):

$$Q_L = \frac{k_{res}^2 P_a^2 S}{K_D} = k_{res}^2 P_a^2 S \frac{\pi R + 2 L_{eff}}{2\pi R^2}. \tag{8.27}$$

This parameter was successfully used with resonant acoustic damper data presented in Rupp and Carrotte (2011). However, this parameter is only valid for perforated liners backed by a rigid wall, e.g. Hughes and Dowling (1990). Hence equation (8.27) needs to be extended to a double liner system, i.e. the damping liner is backed by a metering skin instead of a rigid wall. This extension can be conducted using the formula to calculate the resonance frequency of a Helmholtz resonator with two apertures connected to the resonator volume as, for example, defined by Keller and Zauner (1995)

$$f_{res} = \frac{c}{2\pi}\sqrt{\frac{1}{V}\left(\frac{A_1}{L_1}+\frac{A_2}{L_2}\right)}\,. \tag{8.28}$$

In this case the resonance frequency is a function of both areas (damping skin and metering skin) and the effective length of their apertures. Hence using equations (8.20) and (8.23) the wave number at resonance can be defined based on two aperture Conductivities

$$k_{res}^2 = \frac{1}{P_{a,1}^2 S}K_{D1} + \frac{1}{P_{a,2}^2 S}K_{D2}\,, \tag{8.29}$$

where 1 denotes the damping skin and 2 denotes the metering skin. The pitch between the apertures can be defined using the porosity of the damping and metering skin assuming a square pattern orifice array in the liner

$$P_{a,j} = \sqrt{\frac{\pi R_j^2}{\sigma_l}} \quad \text{for } j = 1, 2\,. \tag{8.30}$$

Note the hole pattern in this work was not an exact square pattern thus the pitch calculated by equation (8.30) is an effective pitch sufficient for the calculation of the resonance parameter. Hence the modified resonance parameter for resonant acoustic dampers with two perforated liners relevant to combustion system liners can be defined as

$$Q_{2L} = \frac{k_{res}^2}{\frac{1}{P_{a,1}^2 S}K_{D1} + \frac{1}{P_{a,2}^2 S}K_{D2}}\,. \tag{8.31}$$

Figure 8.45 shows the measured normalised acoustic energy loss for the five investigated damper configurations. In this case the modified resonance parameter was calculated using the same effective aperture length assumptions as for the analytical model in the previous section. It can be seen that the maximum acoustic energy loss occurs at a modified resonance parameter equal to one for all geometries. Moreover the measured phase difference between cavity and excitation pressure amplitude, shown in Figure 8.46, is also showing 90° phase difference for the modified resonance parameter. This is further proof that the resonance condition is predicted correctly by the modified version of the parameter.

Hence the simple relationship of geometric parameters and damper operating conditions, as defined in equation (8.31) for the modified resonance parameter, can be used to define a resonating acoustic damper geometry tuned to the relevant combustion instability frequency.

8.4 Hot Gas Ingestion

As described in Rupp et. al. (2012) the ingestion of hot gases from the combustor into the damper volume is of concern during the design of passive dampers. This ingestion of hot gas can arise both from the time averaged and time dependent flow field characteristics. The following description of the phenomena can also be found in Rupp et. al. (2012).

The mean pressure drop across the damping skin means that on a spatially averaged basis the pressure within the damper cavity is greater than the flame tube pressure i.e. so relatively cool gas flows through the damping skin and into the combustor and no hot gas ingestion occurs. However, locally the mean pressure distribution will vary across the damper surface, as shown in Figure 8.2, resulting in the potential for hot gas to *locally* flow into the damper cavity. Hence as the mean pressure drop across the damping skin is reduced so the likelihood for local hot gas ingestion increases. However this process can be predicted by time averaged numerical (CFD) prediction of the flow field. Also of concern, though, and of primary interest here is the time dependent ingestion of hot gas into the damper cavity due to the unsteady flow field.

As the magnitude of the unsteady pressure amplitudes inside the combustor increases so there is the potential for flow to reverse through the damping skin orifices on a time dependent basis i.e. so that hot gas is ingested at certain phases of the acoustic cycle. However, this can be investigated using the developed 1D analytical model in terms of

- assessing the robustness of different damper designs to gas ingestion and

- at what level of pressure oscillations within the combustor will hot gas ingestion commence.

As the velocity perturbation in the damping holes tends to the mean velocity hot gas ingestion will occur (i.e. $\left|\hat{u}_{D1}\right|/\overline{U}_{D1}$~1). However, this also corresponds to the operating condition where the acoustic absorption transitions into the non-linear regime. It was shown in the analysis of the acoustic absorption experiments in section 6.4.1 that non-linear absorption occurs for unsteady to mean velocity ratios of approximately 0.4 and greater. Therefore the model can be used to identify at which excitation pressure amplitudes non-linear absorption occurs. This not only indicates the operating condition where the analytical model becomes invalid (i.e. since the linear absorption model is no longer valid), but this can also be used to provide a design margin against hot gas ingestion.

Figure 8.47 shows the unsteady velocity amplitude normalised with the mean velocity across the damping skin for three different liner separations for the non-resonant liner geometry described in section 8.2. Note that the magnitude of the excitation pressure $\left|\hat{p}_0\right|$ is normalised with the absolute mean pressure inside the main duct $\overline{p}_0$. For the largest cavity depth (*S/H* = 0.67) it can be seen that the orifice perturbation $\left(\hat{u}_1\right)$ is reaching the onset of non-linear absorption for an excitation amplitude of approximately 0.5% of the combustion chamber pressure. For example, at 40 bar this would equate to an excitation amplitude of 177 dB. However as the cavity depth decreases so less acoustic energy is absorbed and the velocity perturbation $\left(\hat{u}_1\right)$, for a given excitation amplitude, decreases. Hence with decreasing cavity depth the damper becomes more robust to time dependant hot gas ingestion but absorbs less energy. In this way both the relative sensitivity of different configurations to hot gas ingestion can be assessed along with the unsteady pressure amplitudes at which this will occur.

As expected a resonant liner is more prone to hot gas ingestion due to the high unsteady velocity amplitudes. This can be seen, for example, in Figure 8.48 for the resonant damper configuration 1. In this case the transition from linear to non-linear absorption occurs at an equivalent sound pressure of 168 dB at 40 bar combustor inlet pressure. This highlights the importance of accurate non-linear acoustic modelling as the resonant dampers are operating close to the transition range within gas turbine combustors.

As already discussed the current modelling for the transition from linear to non-linear acoustic absorption is assuming a velocity amplitude ratio of one for the onset to non-linear absorption. Hence for a given geometry a curve fit to the measured velocity amplitude should enable a more accurate assessment of the onset to hot gas ingestion which occurs at velocity amplitude ratios of approximately one. Hence the current design tool is giving a pessimistic assessment of the onset of hot gas ingestion into the damper cavity.

8.5 Closure

This chapter has discussed a set of design tools developed during this work:

- a simple parameter which enables the preliminary design and tuning for the geometric parameters of a multi-liner resonating damping system,
- an analytical model to estimate the acoustic energy loss of acoustic dampers with a high accuracy for apertures up to a length-to-diameter ratio of 3 (larger *L/D* ratios are possible with reduced accuracy),
- an impedance methodology to investigate the interaction and optimisation of isolated acoustic components such as fuel injectors or acoustic dampers,
- a prediction and scaling method to investigate the risk of hot gas ingestion due to the unsteady velocity amplitudes within the damping skin.

The developed tool set enables a comprehensive preliminary design of non-resonant and resonant acoustic absorbers with multiple perforated liners within a gas turbine combustion system. Moreover the model has been extended to assess the impact of

circumferential waves (appendix E). Finally the analytical model can also be used as a development platform for aperture Rayleigh Conductivity models.

It has been shown that the bulk acoustic modelling is independent of complex flow characteristics downstream of the apertures. Hence cross-flow influence and complex swirling flow fields across the downstream end of the damping skins had no significant effect. This can be concluded from the excellent agreement of the experimental non-resonating damper data compared to the linear acoustic model which does not include any cross flow effects upon the damping skins. Using the methods for the hot gas ingestion analysis it has been shown that the liners with increased unsteady pressure drop, such as large volume non-resonant liners and resonating dampers, are more prone to hot gas ingestion due to the larger unsteady velocity amplitudes for a given pressure amplitude. The analytical modelling of long *L/D* apertures has shown discrepancies with the measured data. It has been discussed that this is caused by the rather complex flow field through the longer apertures with unsteady inflow profiles, boundary layer and outflow effects. Some short term solutions have been shown to improve the accuracy. However it is recommended to investigate the unsteady flow physics of larger *L/D* apertures in the future to improve the modelling accuracy for this technically relevant application.

Experimental investigations into non-resonant liner systems have shown that the design of efficient liners would necessitate large cavity volumes between the metering and damping skins. Hence the absorption was maximised for plenum conditions in the said cavity. Unfortunately this would not fit in the design space envelope for an aero-engine gas turbine combustion system without unacceptable increases in weight of the engine. Hence other damping options such as resonating acoustic dampers have been investigated experimentally. It was demonstrated that the resonance effect can greatly enhance the absorption of the applied acoustic dampers. Thus the application of such a device shows a better acoustic damping performance within the given space envelope. However the device needs tuning which can only be accurately done if the length corrections of the apertures in the metering and damping skin are known. Moreover the relevant frequencies occurring in aero gas turbine combustion systems make it necessary to use rather large *L/D* ratio apertures in the damping skin.

Figures

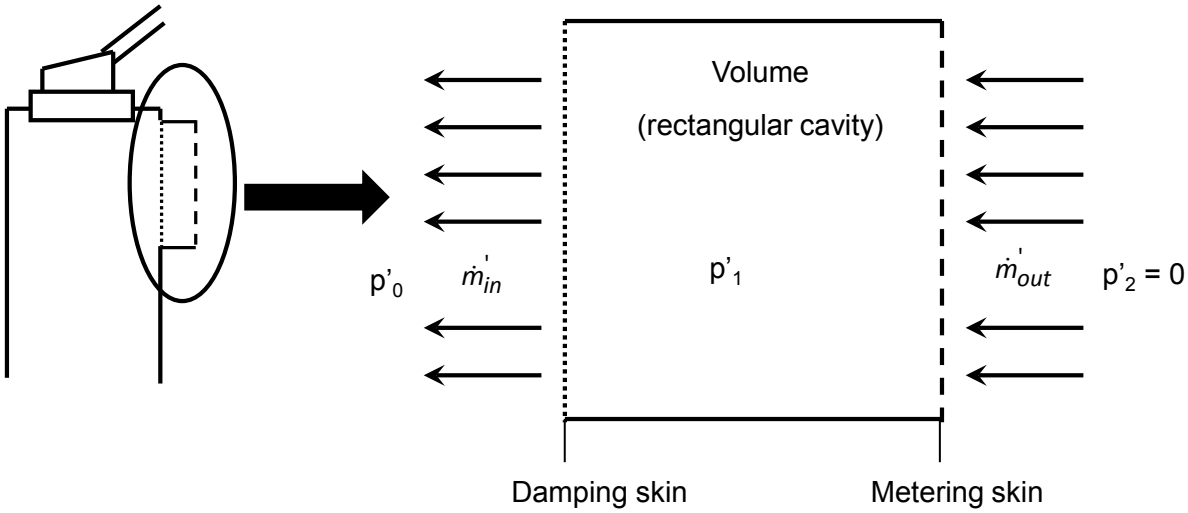

Figure 8.1: Schematic of control volume for analytical linear absorption model.

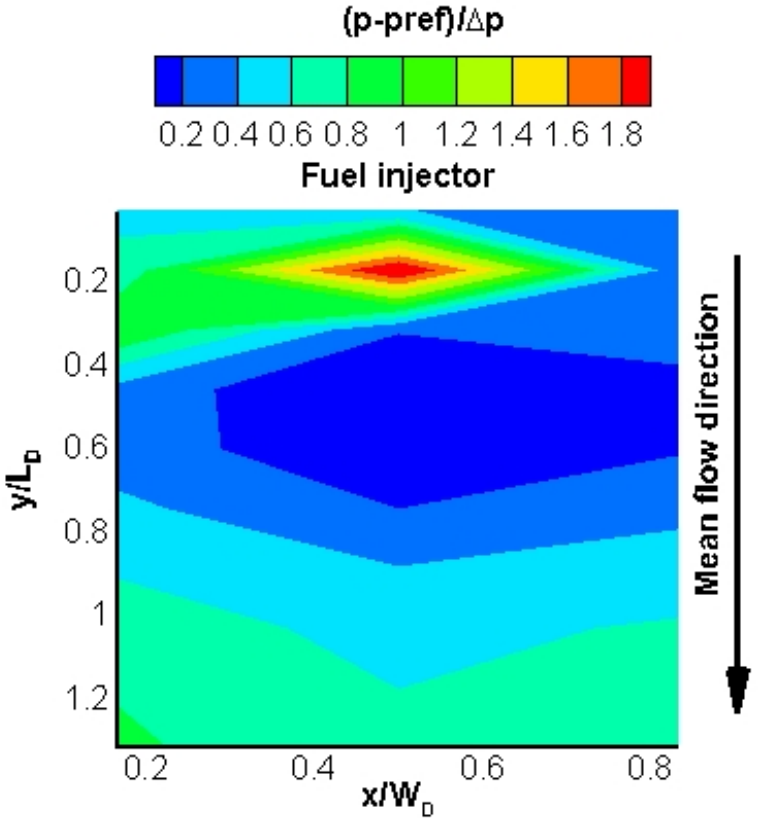

Figure 8.2: Mean pressure distribution along damper surface

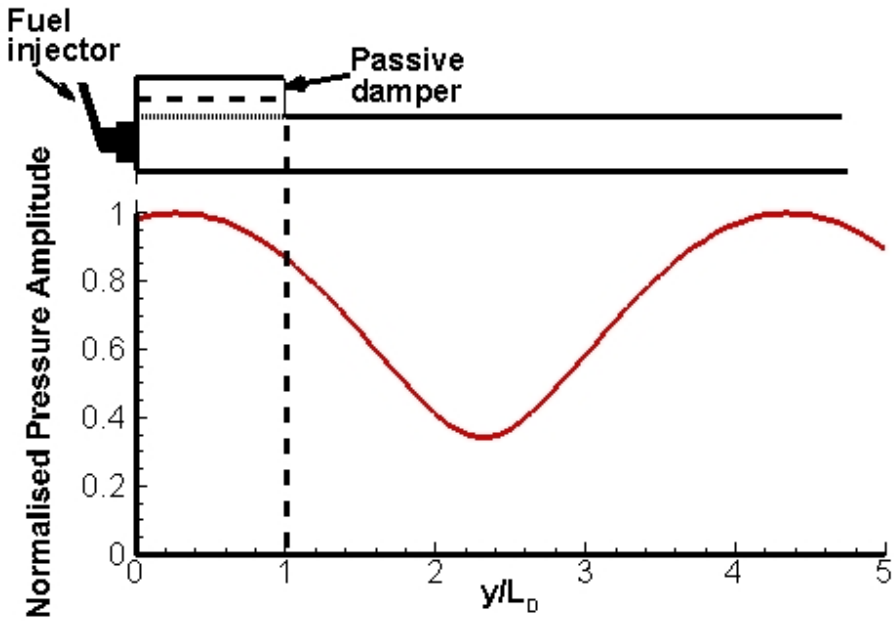

Figure 8.3: Pressure amplitude mode shape example

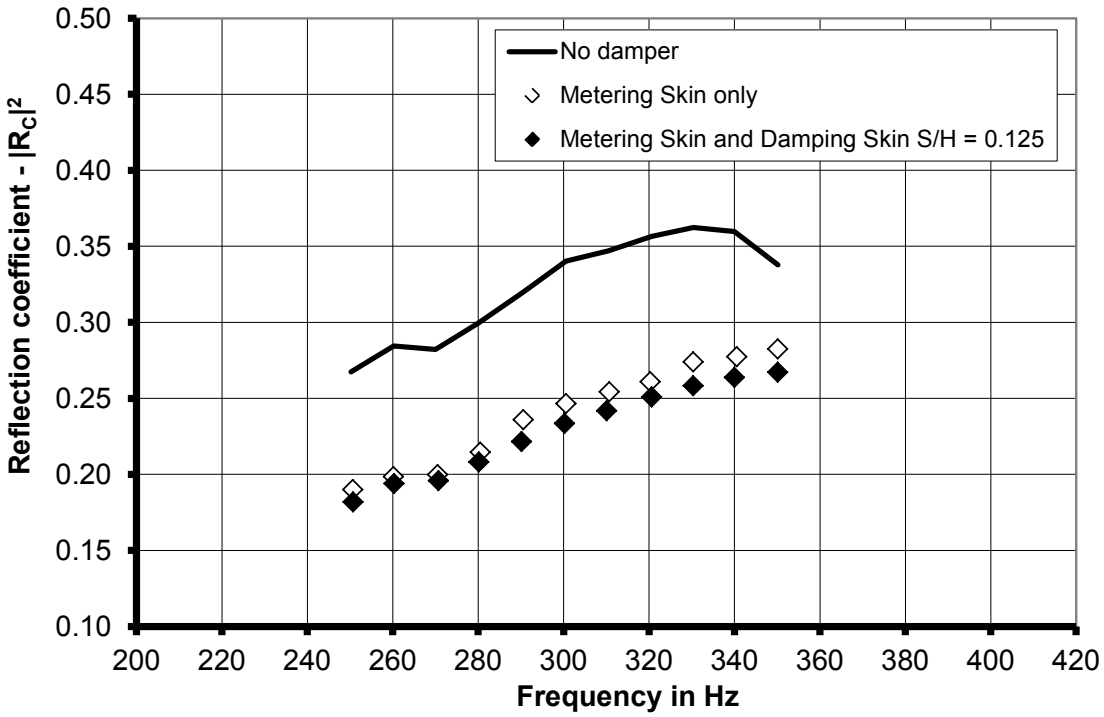

Figure 8.4: Comparison of measured reflection coefficients

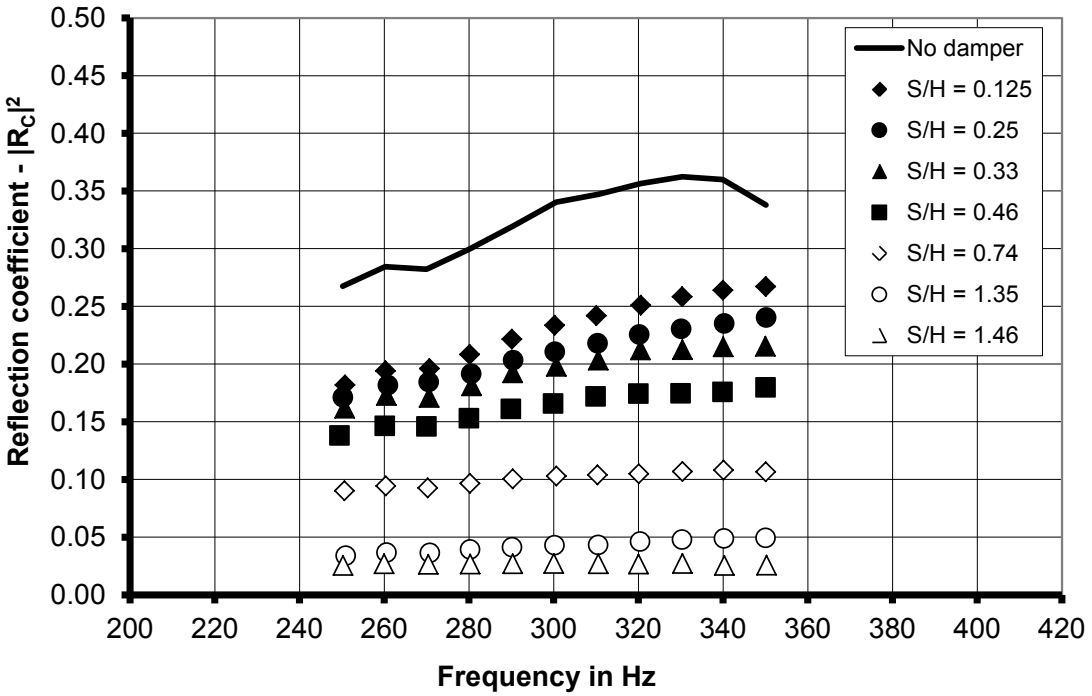

Figure 8.5: Reflection coefficients of various liner separations

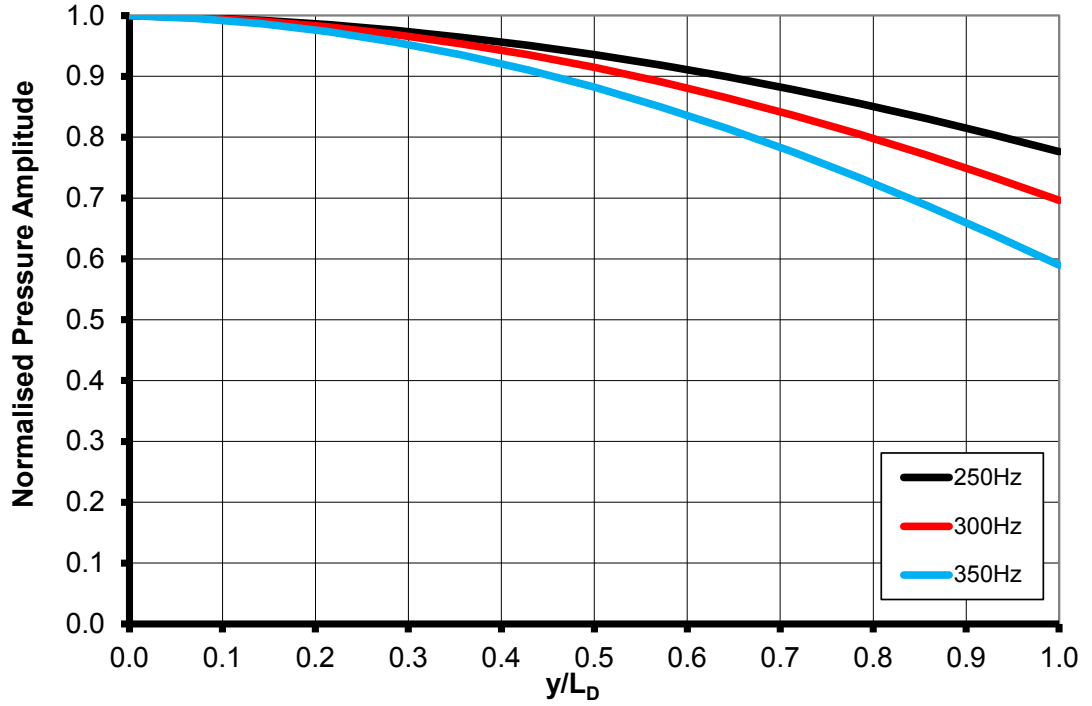

Figure 8.6: Normalised mode shape pressure amplitudes at various frequencies

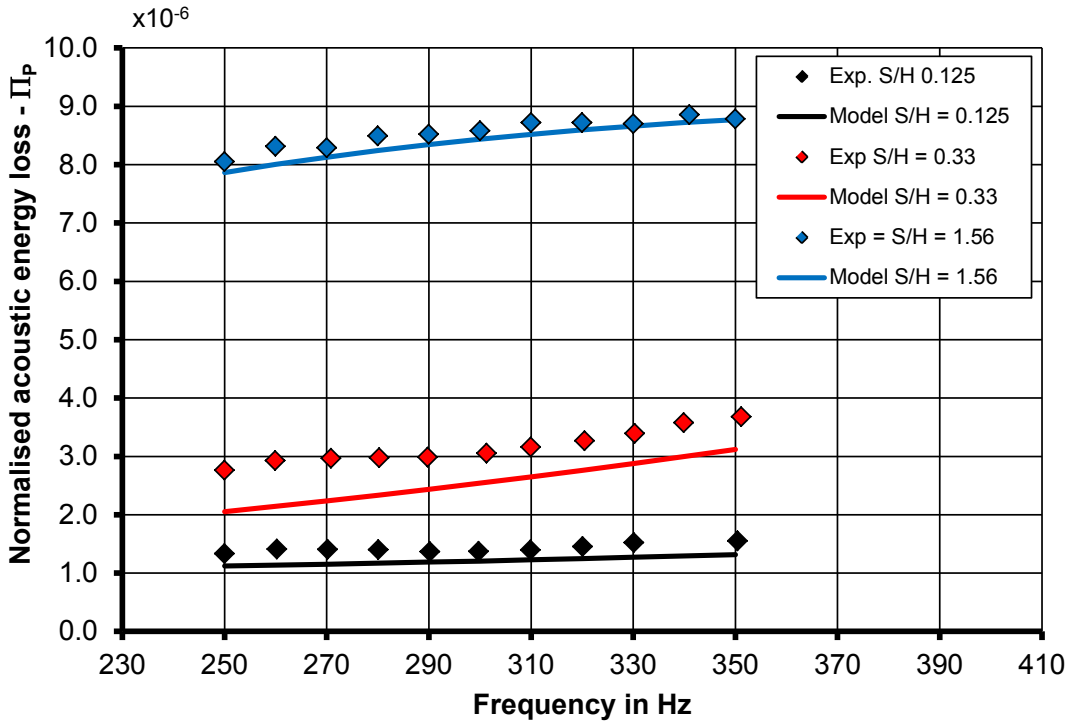

Figure 8.7: Normalised acoustic loss comparison between experiment and analytical model with pressure mode shape input function

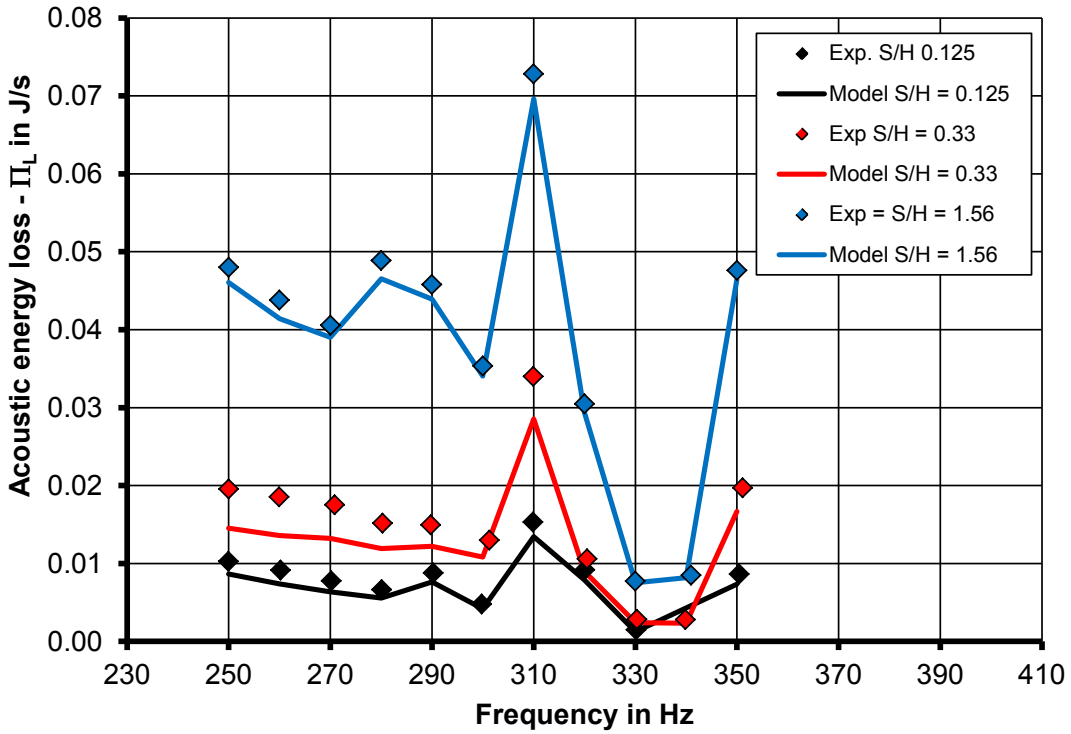

Figure 8.8: Acoustic energy loss comparison between experiment and modified model with pressure mode shape input function

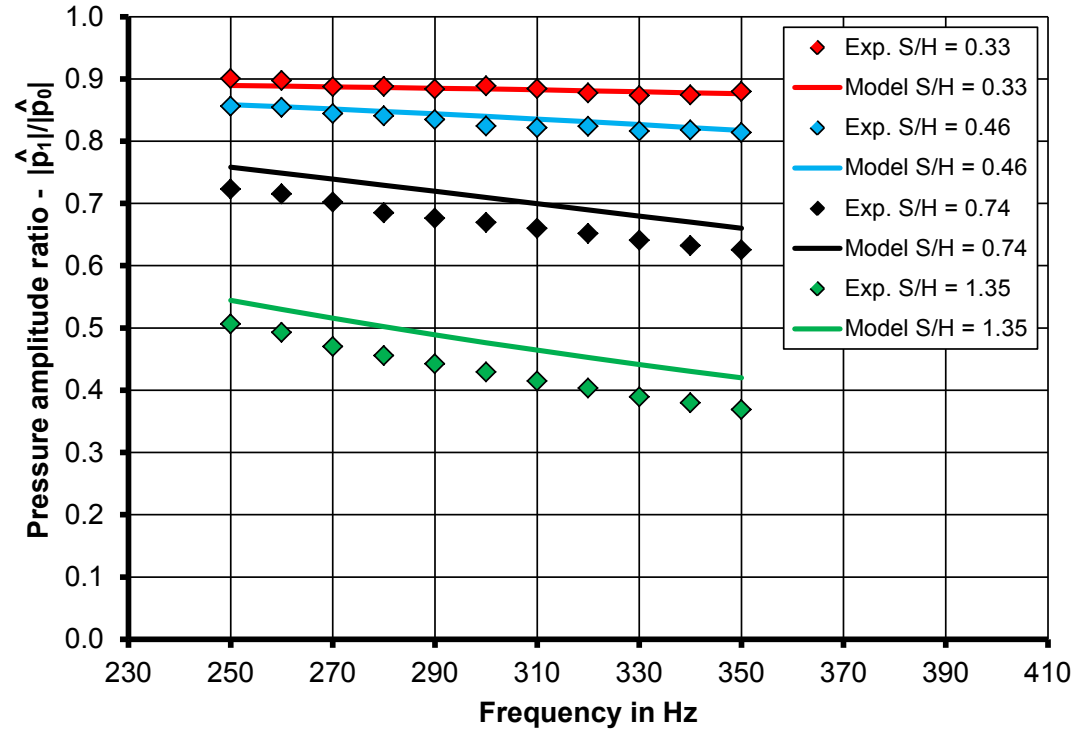

Figure 8.9: Cavity pressure ratio comparison between the experiment (Exp.) and the model

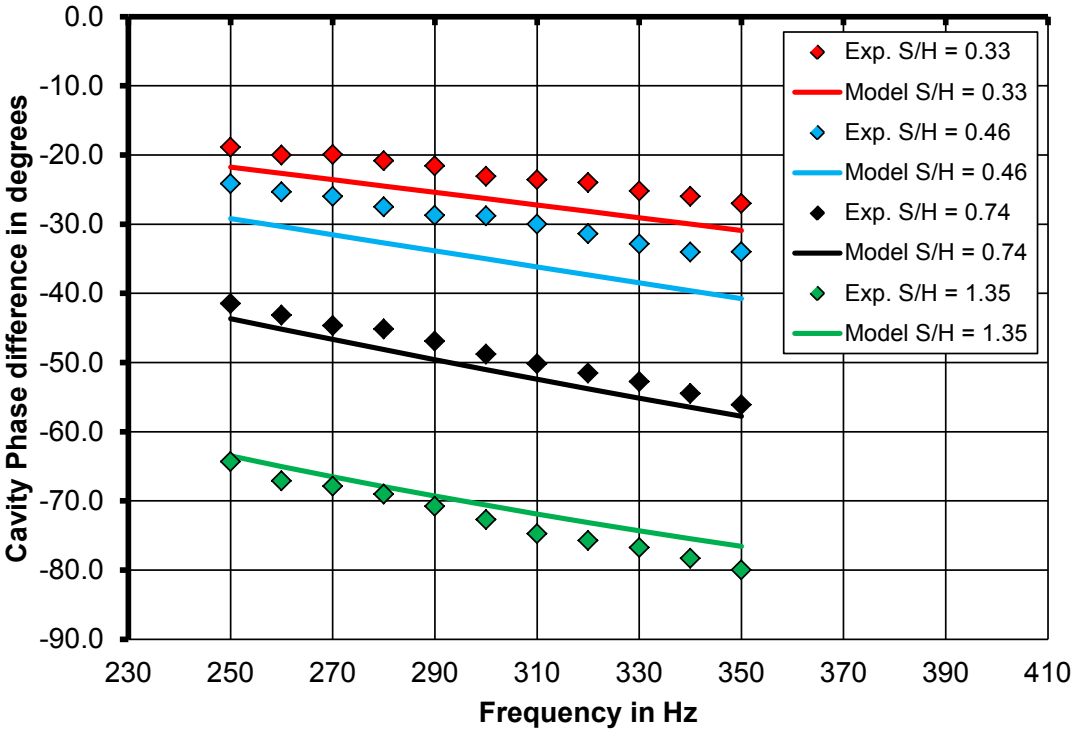

Figure 8.10: Phase difference between cavity pressure amplitude and incident pressure amplitude

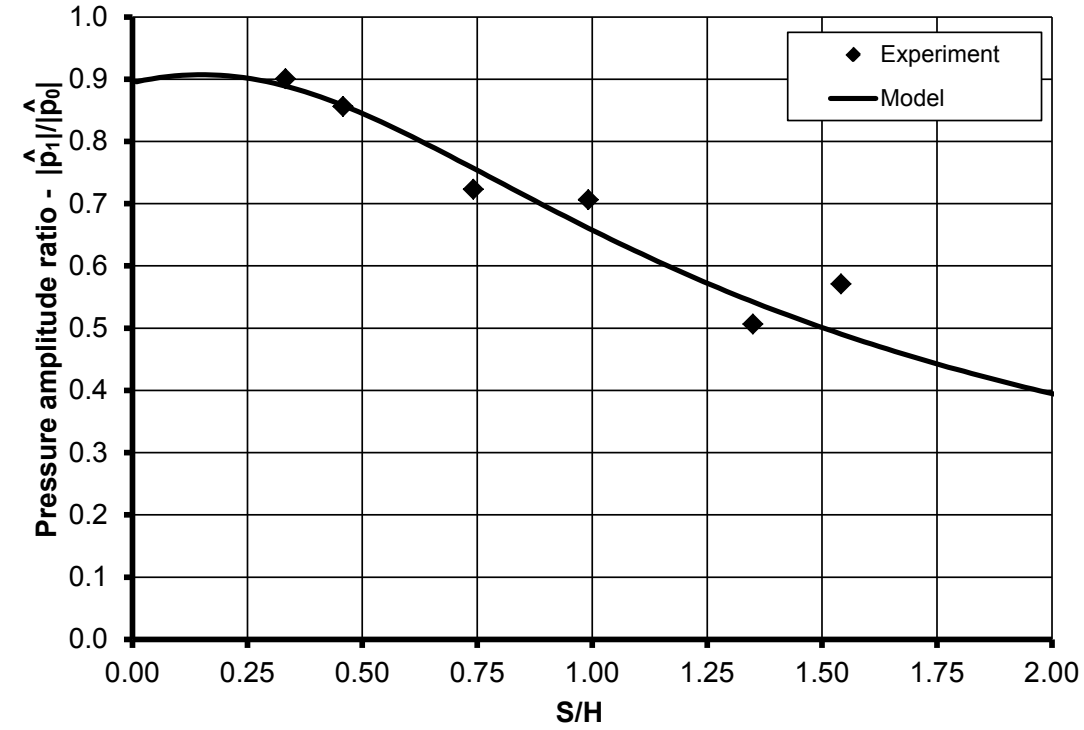

Figure 8.11: Cavity pressure ratio variation with liner separation, experiment with fuel injector

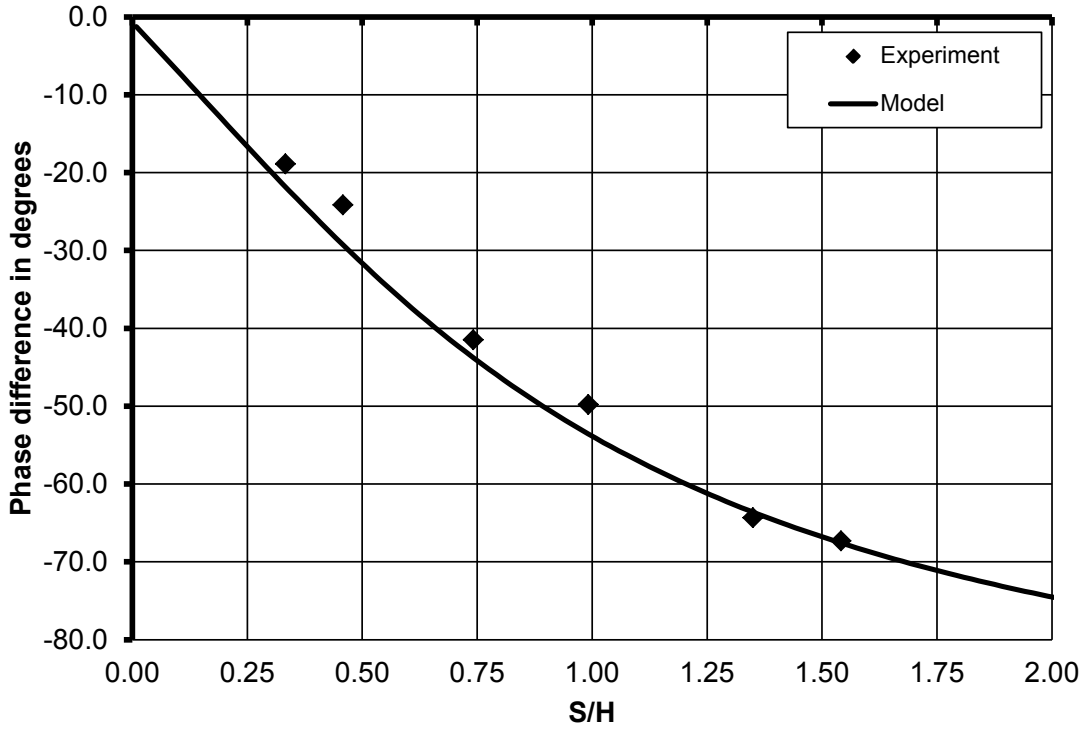

Figure 8.12: Phase angle between cavity pressure amplitude and excitation pressure amplitude, experiment with fuel injector

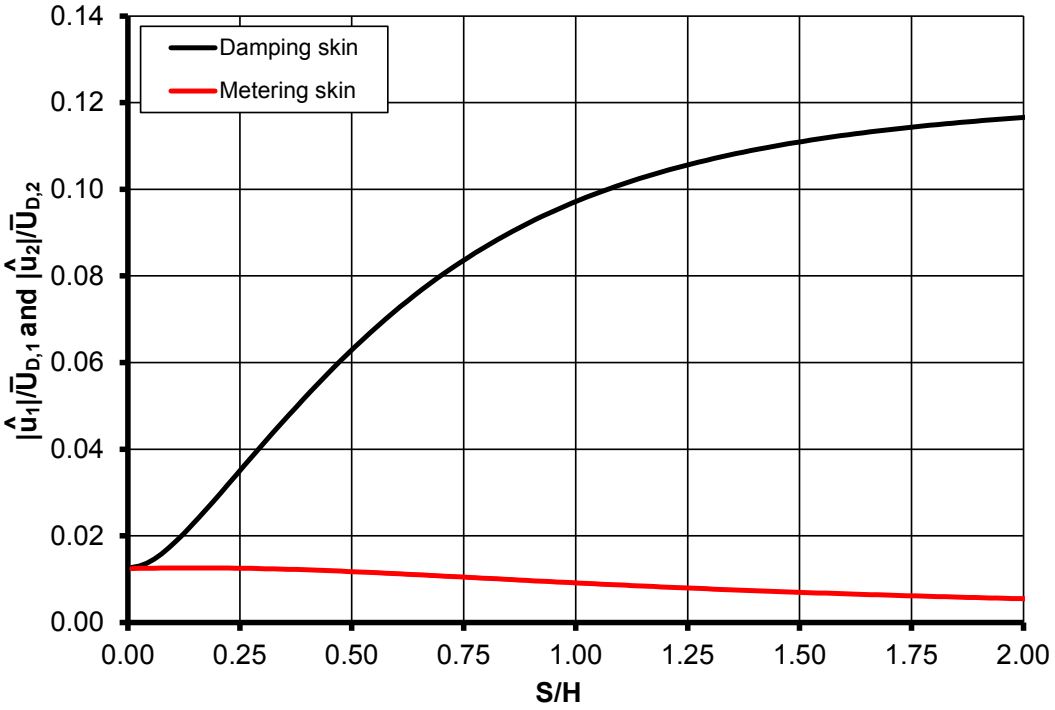

Figure 8.13: Unsteady velocity amplitudes with varying liner separation

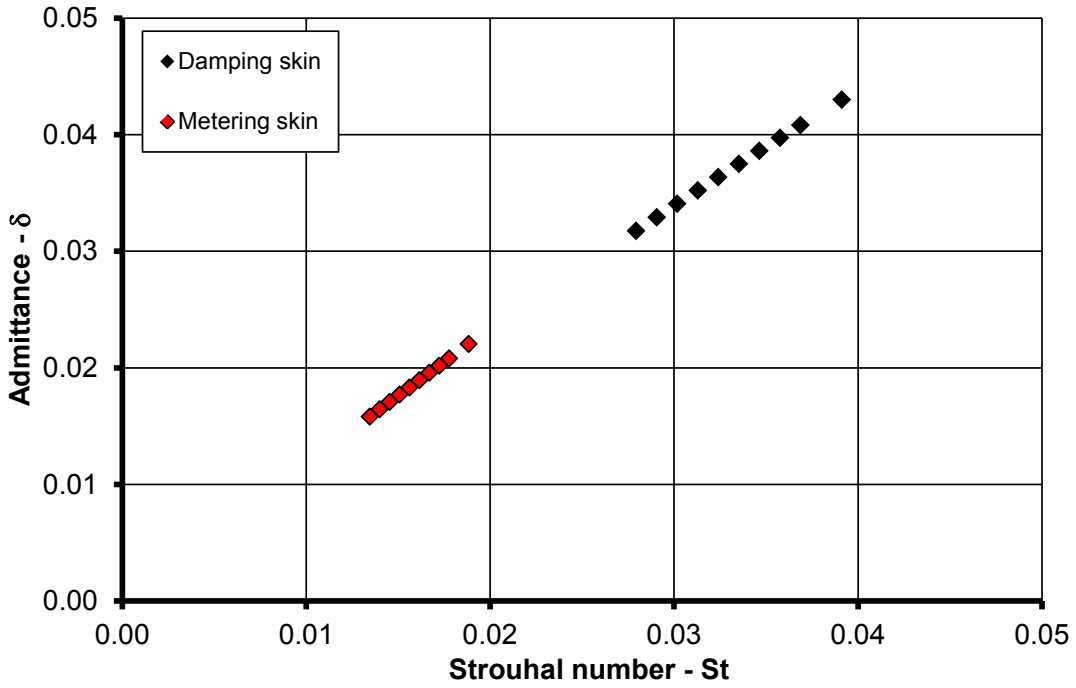

Figure 8.14: Calculated damping and metering skin admittance for *S/H* = 0.125

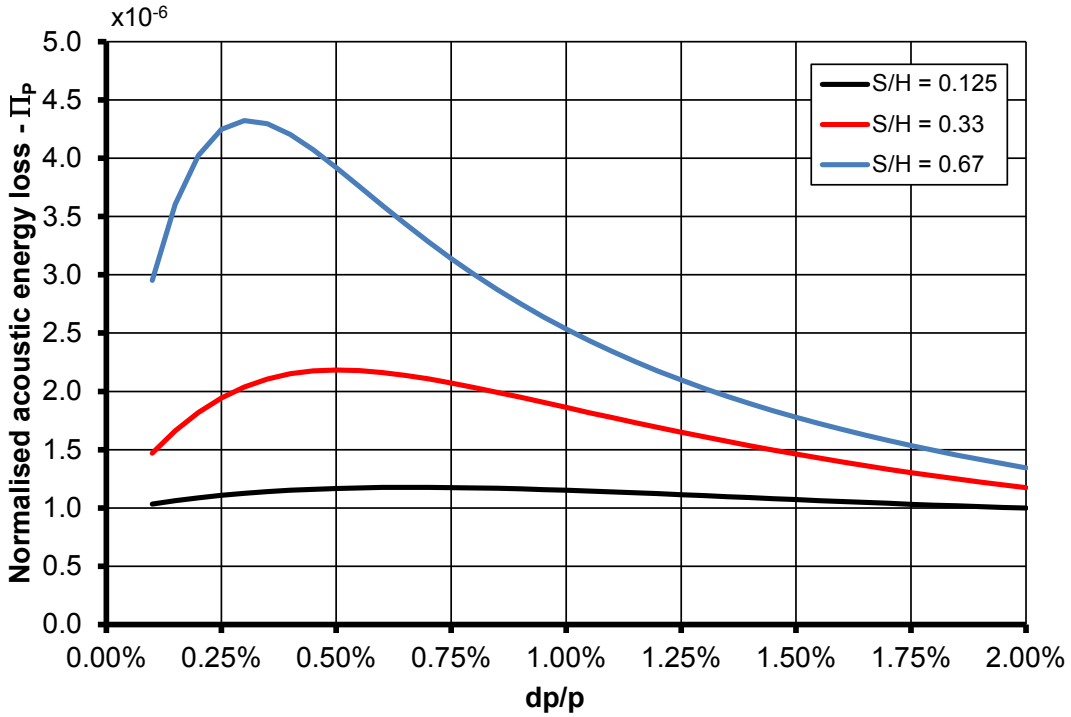

Figure 8.15: Normalised loss for varying damping skin mean pressure drop

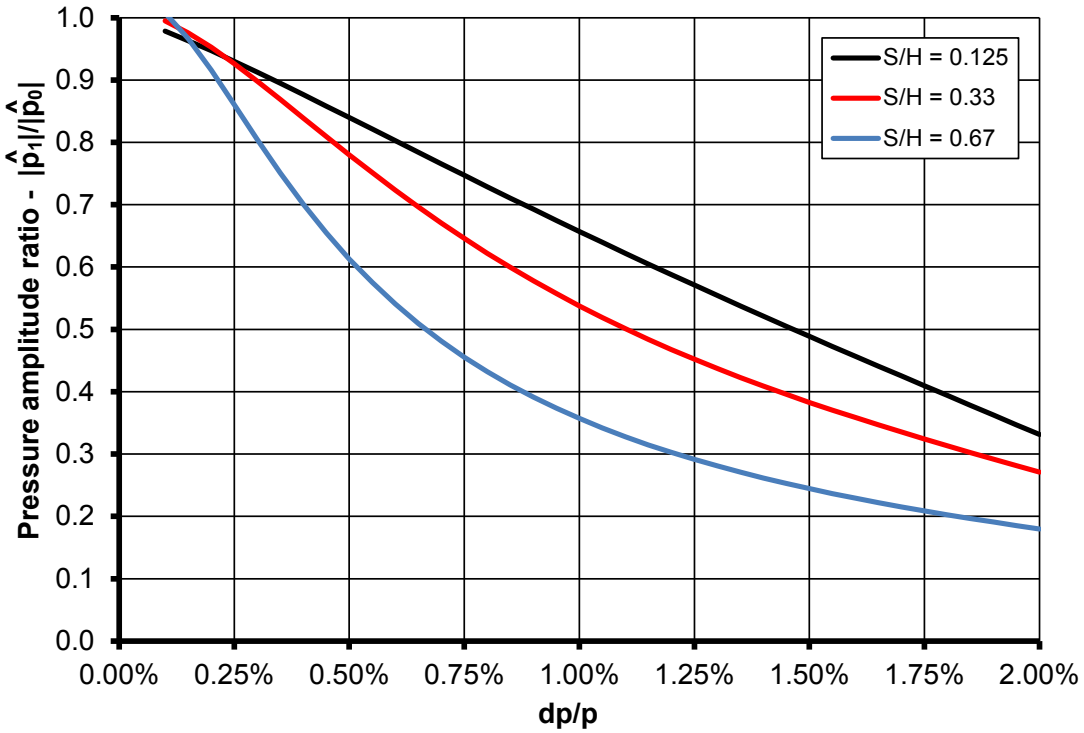

Figure 8.16: Cavity pressure ratio with varying damping skin mean pressure drop

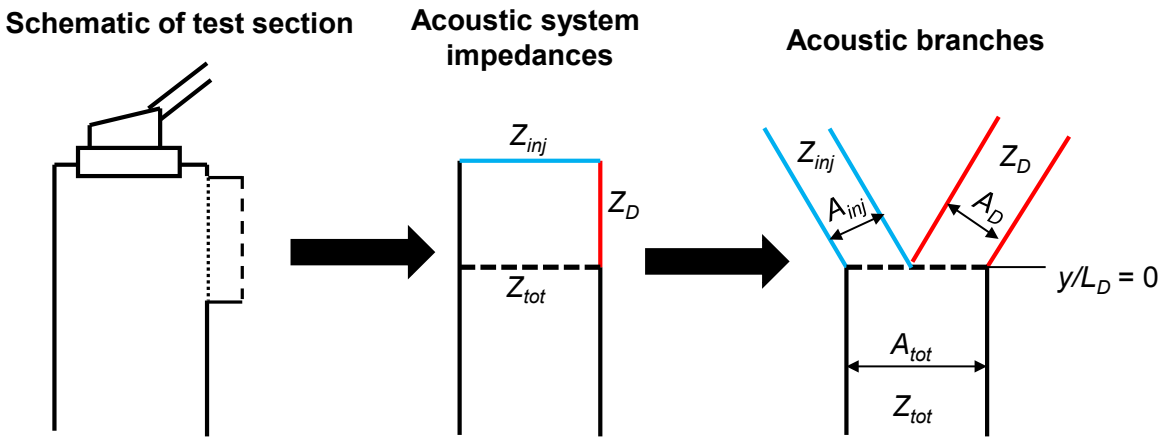

Figure 8.17: Schematic of non-resonant damper test section as a system of acoustic branches.

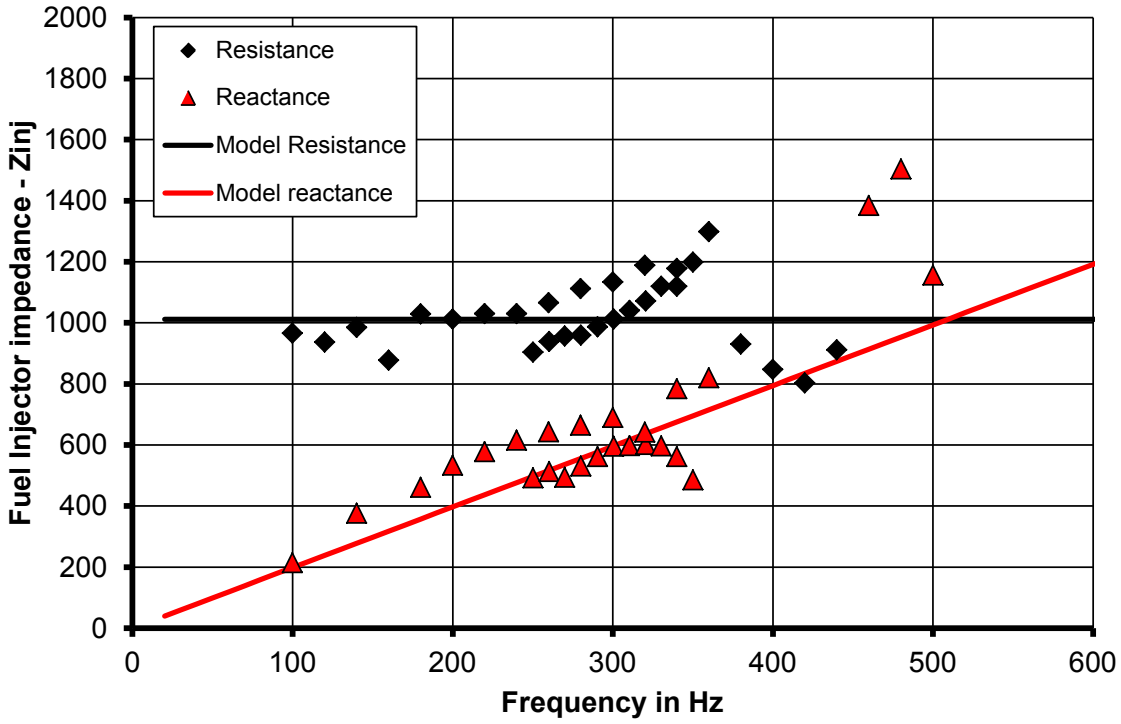

Figure 8.18: Fuel injector impedance.

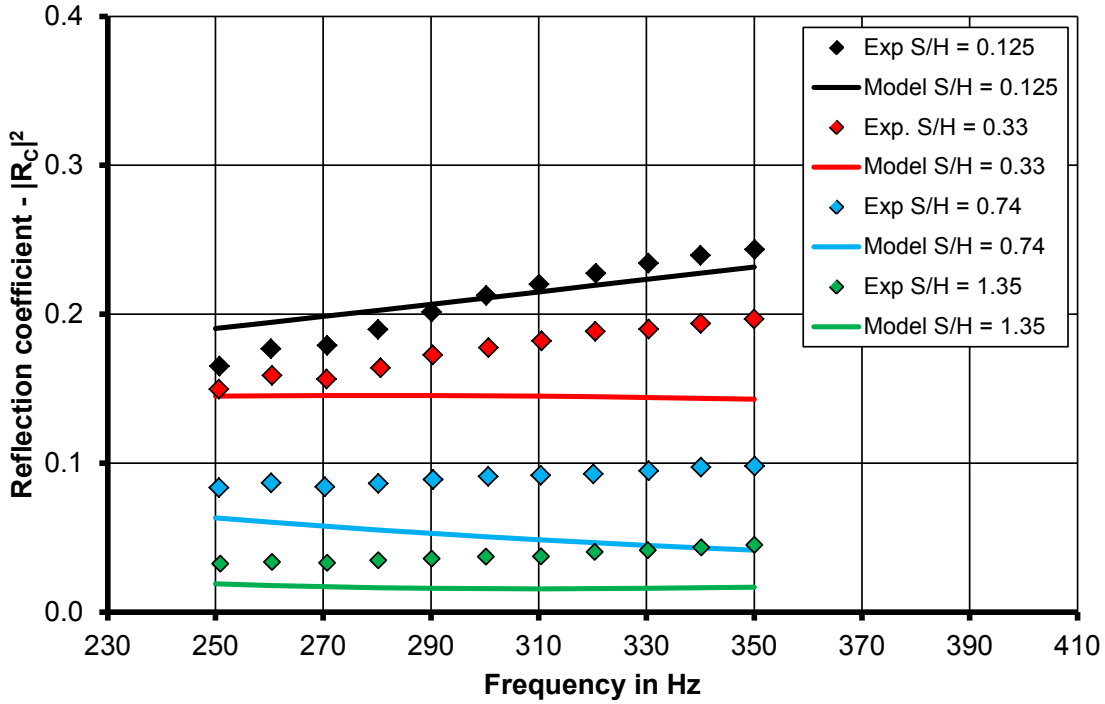

Figure 8.19: Magnitude of reflection coefficient for experiments with non-resonant liner and fuel injector compared to model using the total impedance of fuel injector and acoustic damper.

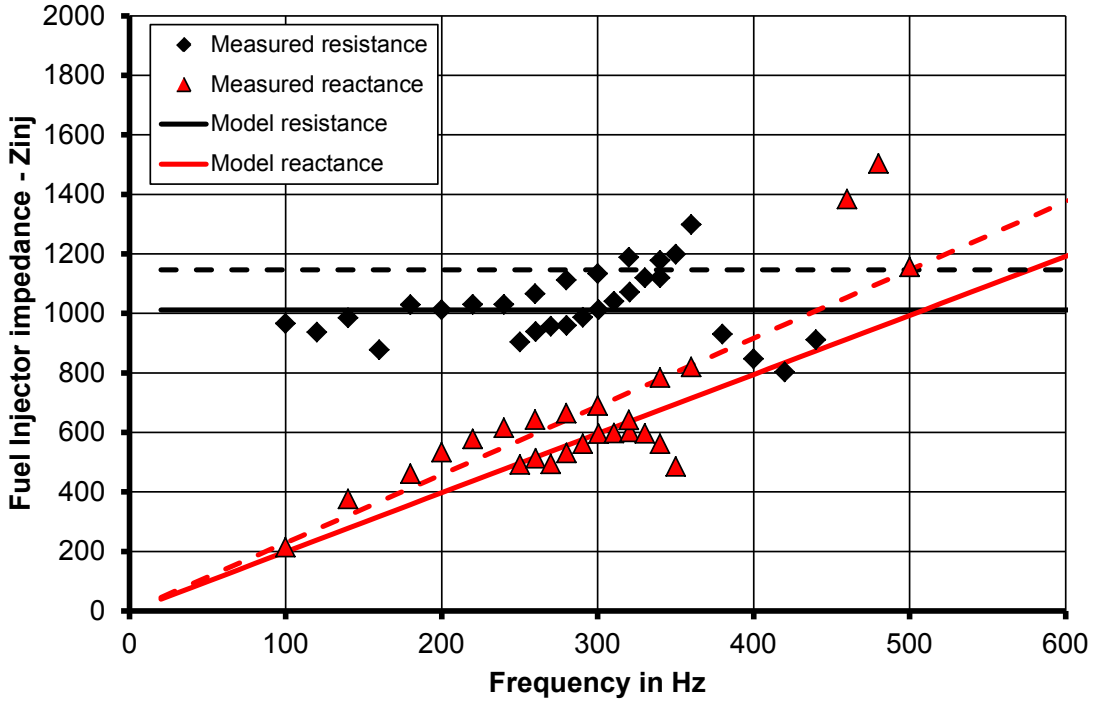

Figure 8.20: Sensitivity on fuel injector impedance.

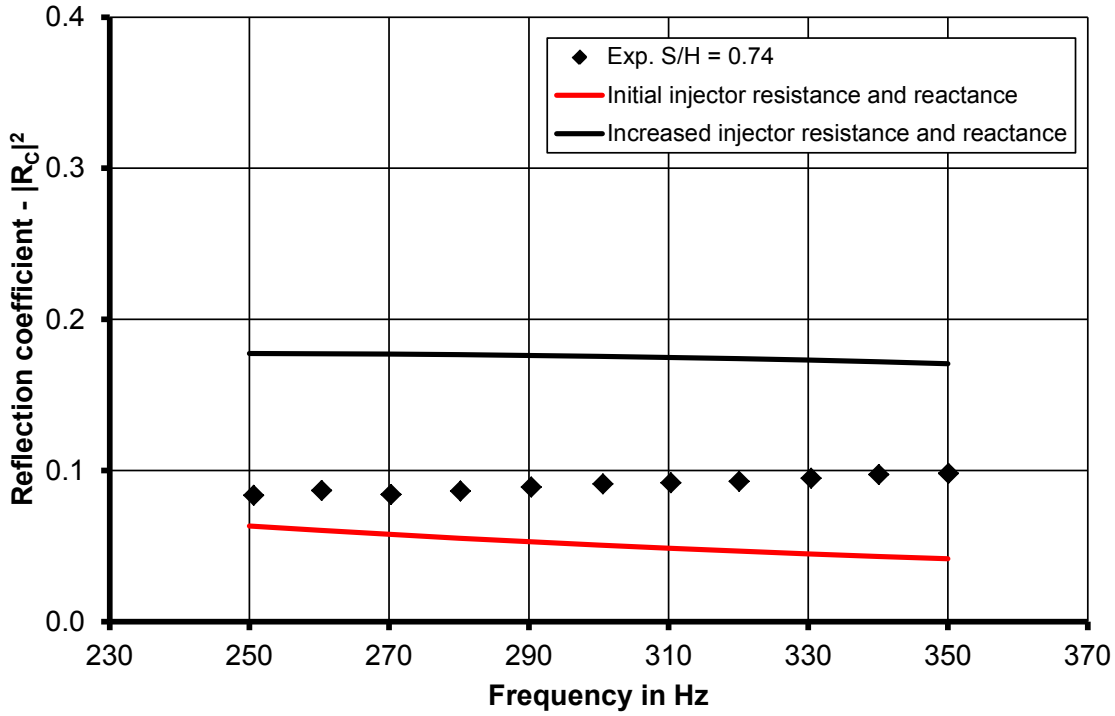

Figure 8.21: Impact on fuel injector impedance on total system reflection coefficient.

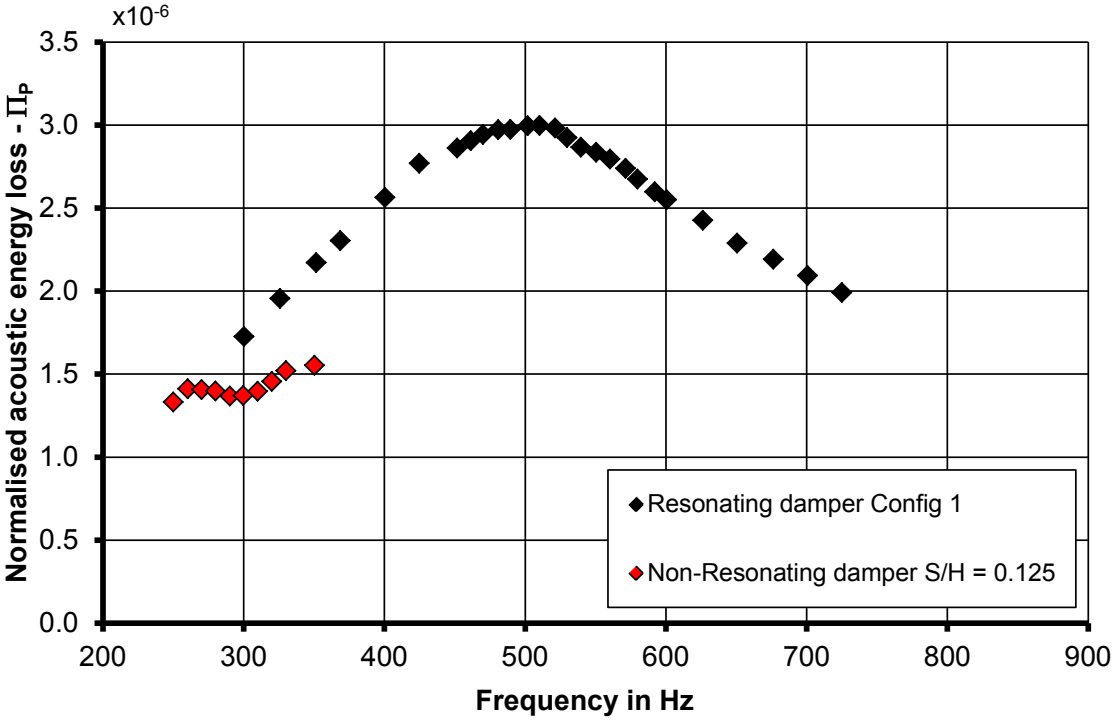

Figure 8.22: Comparison between resonating damper configuration 1 and datum non-resonating damper with *S/H* = 0.125.

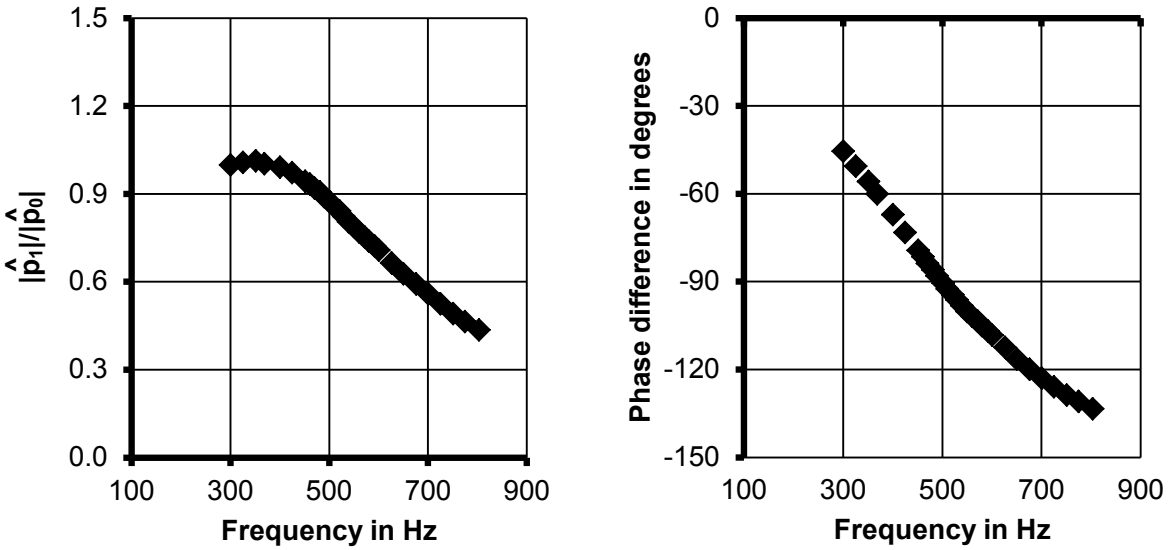

Figure 8.23: Pressure amplitude ratio and phase difference between damper cavity and excitation pressure amplitude for damper configuration 1.

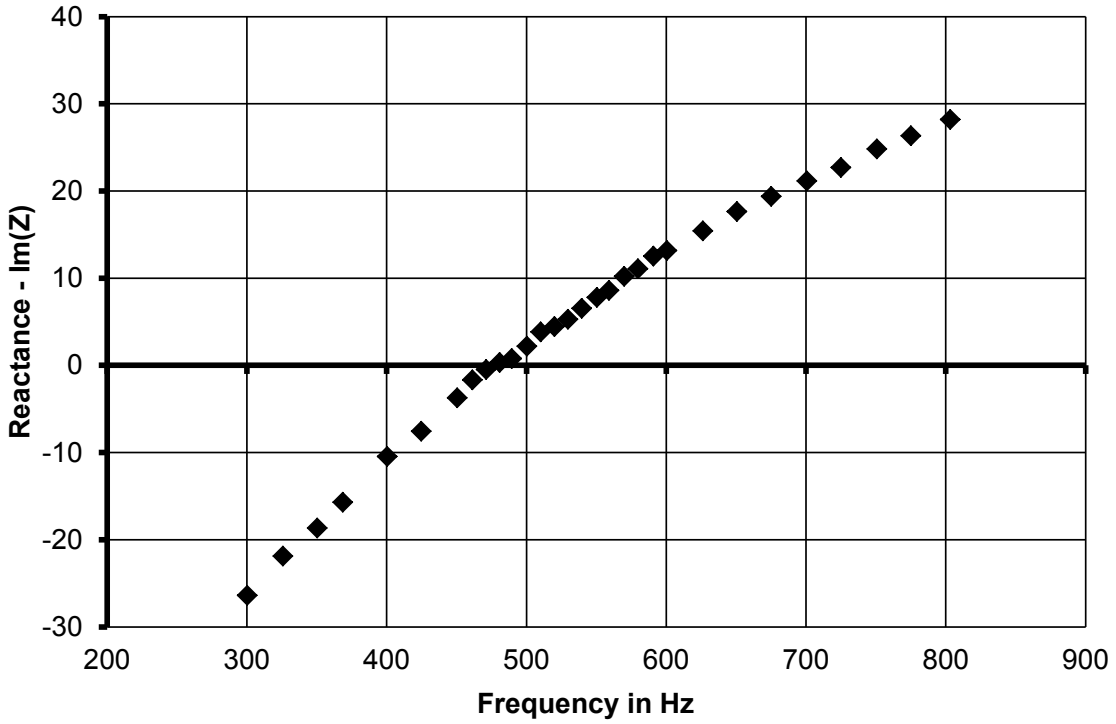

Figure 8.24: Acoustic reactance of damper configuration 1.

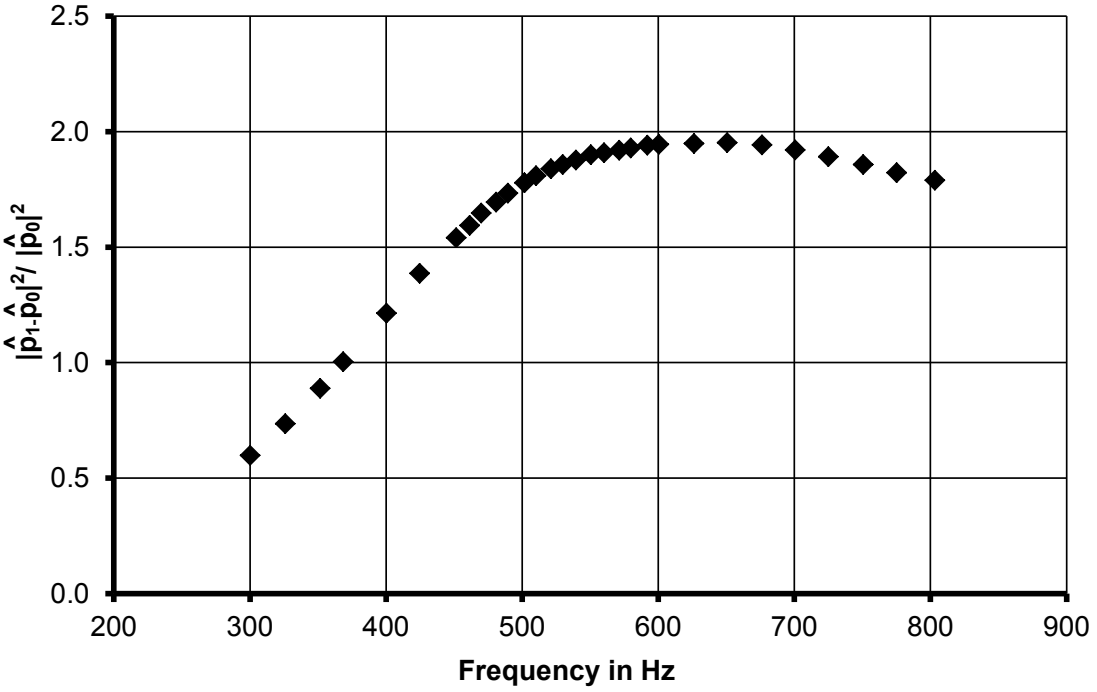

Figure 8.25: Unsteady pressure difference across damping skin for damper configuration 1.

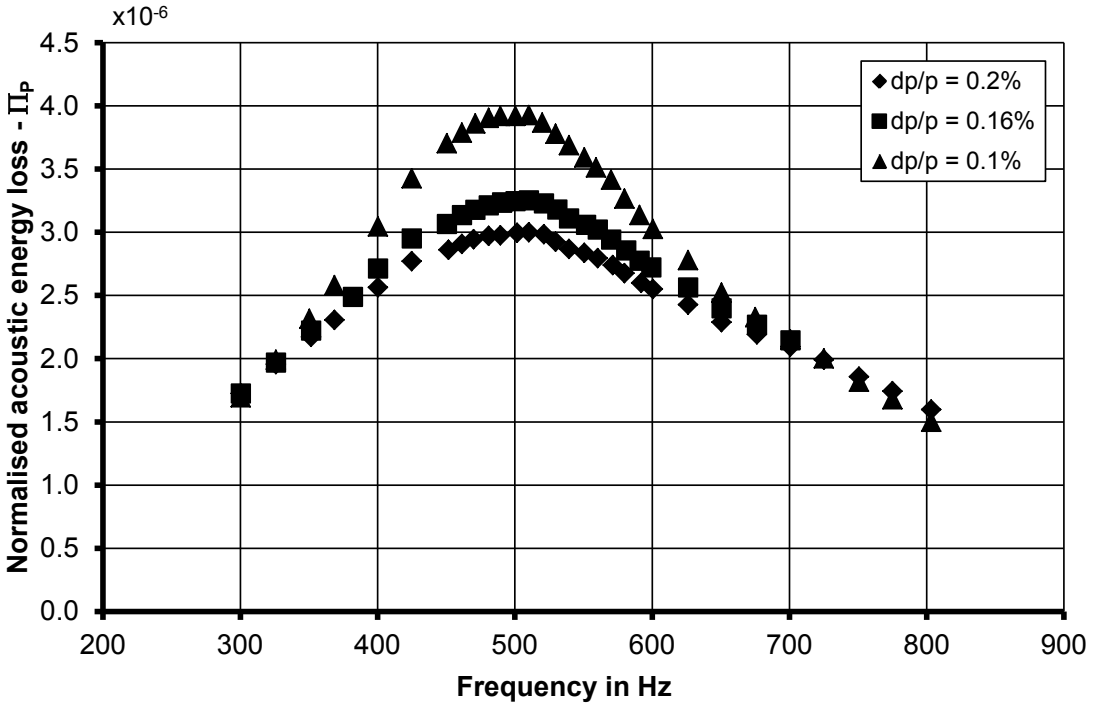

Figure 8.26: Variation of mean pressure drop across the damping skin for resonating damper configuration 1.

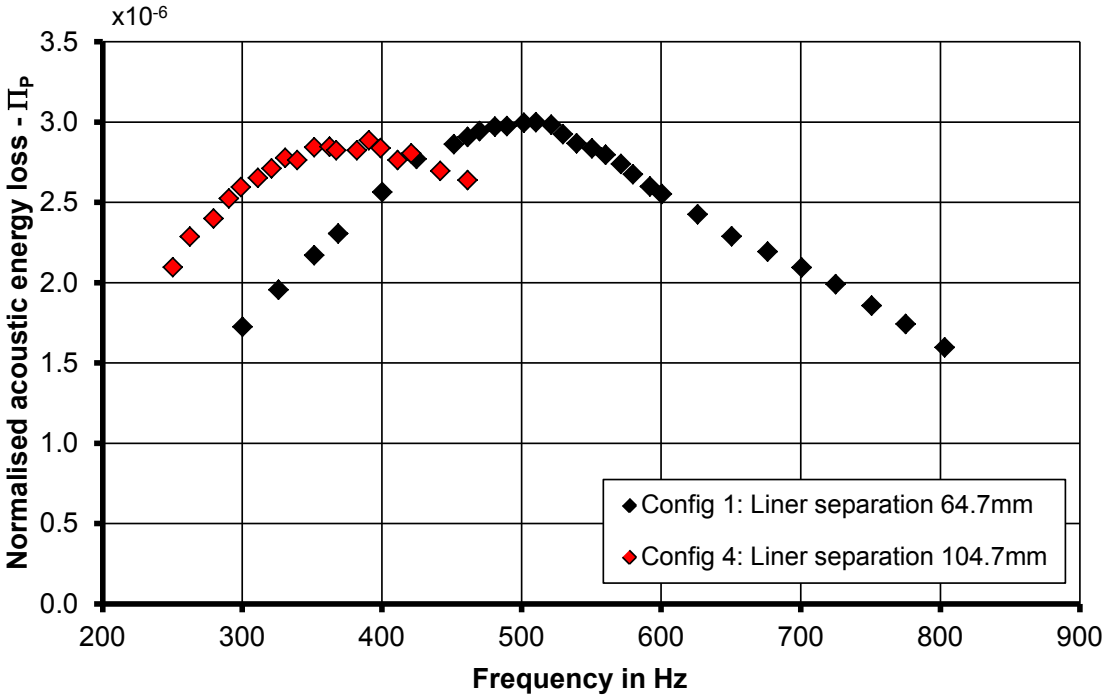

Figure 8.27: Comparison for two resonating dampers with enlarged cavity volume.

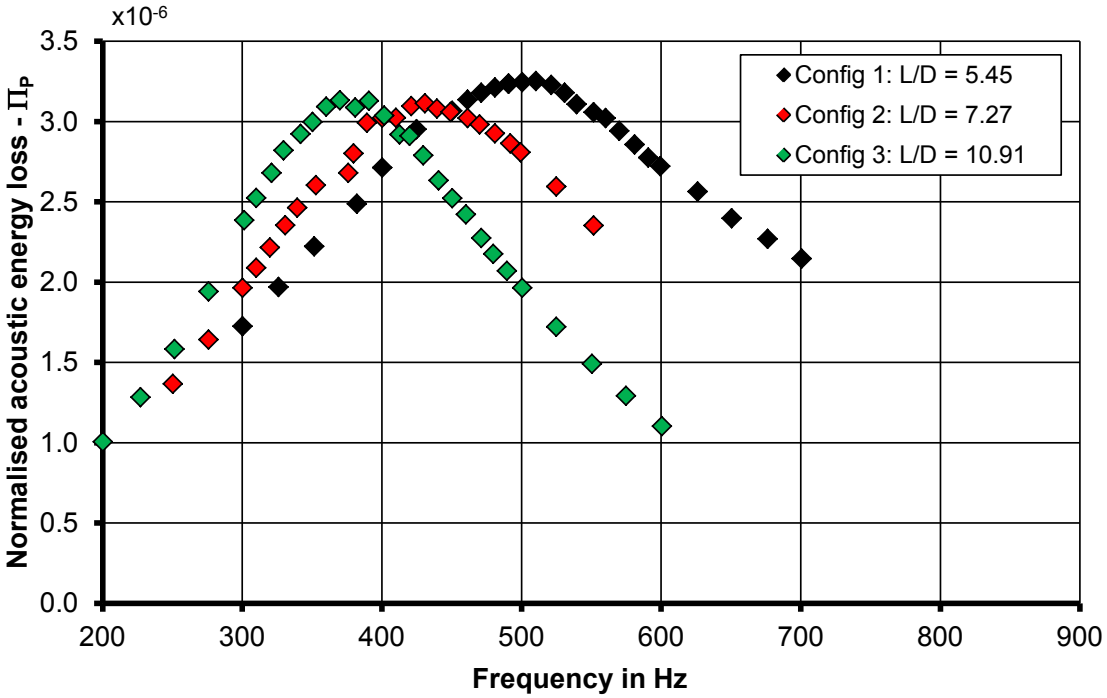

Figure 8.28: Normalised acoustic energy loss comparison of damper configuration 1, 2 and 3 with effective length variation for damping skin pressure drop of *dp/p* = 0.15%.

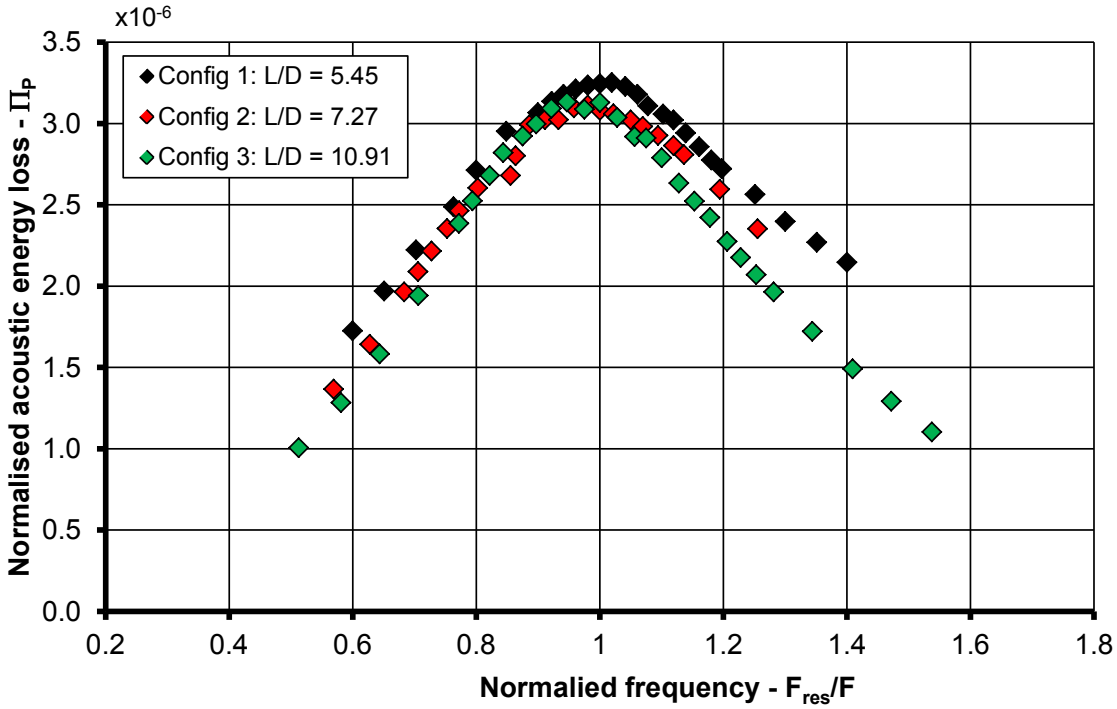

Figure 8.29: Normalised acoustic energy loss comparison of damper configuration 1, 2 and 3 relative to the normalised frequency, damping skin pressure drop of *dp/p* = 0.15%.

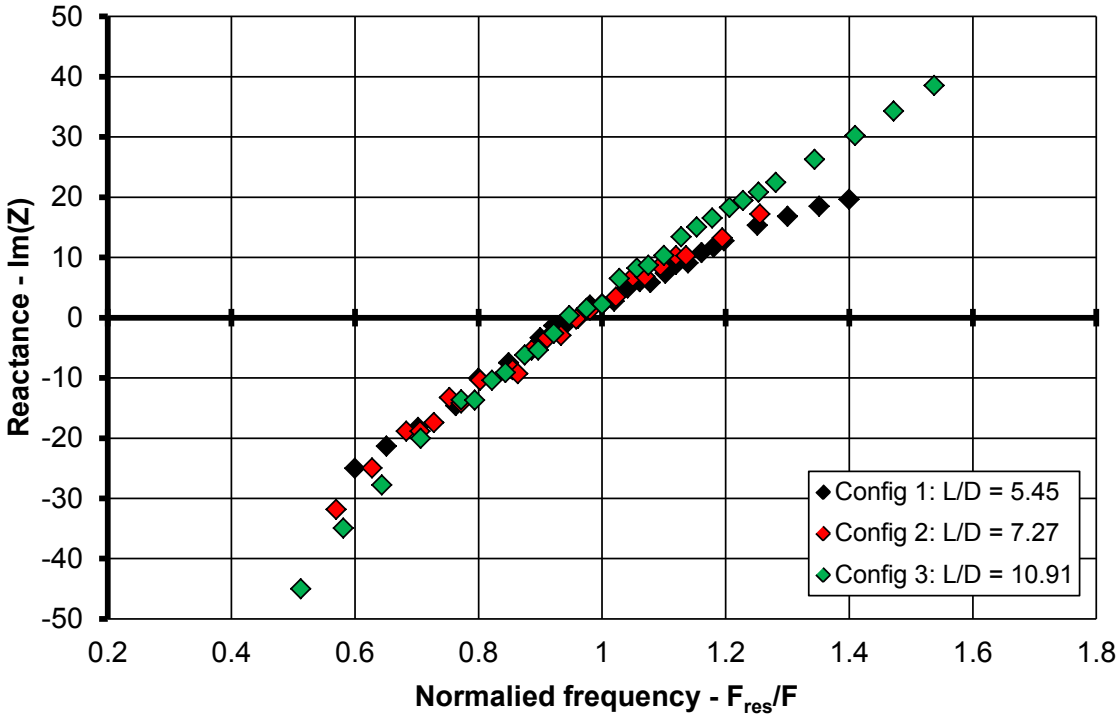

Figure 8.30: Measured acoustic reactance for configuration 1, 2 and 3 relative to the normalised frequency, damping skin pressure drop of *dp/p* = 0.15%.

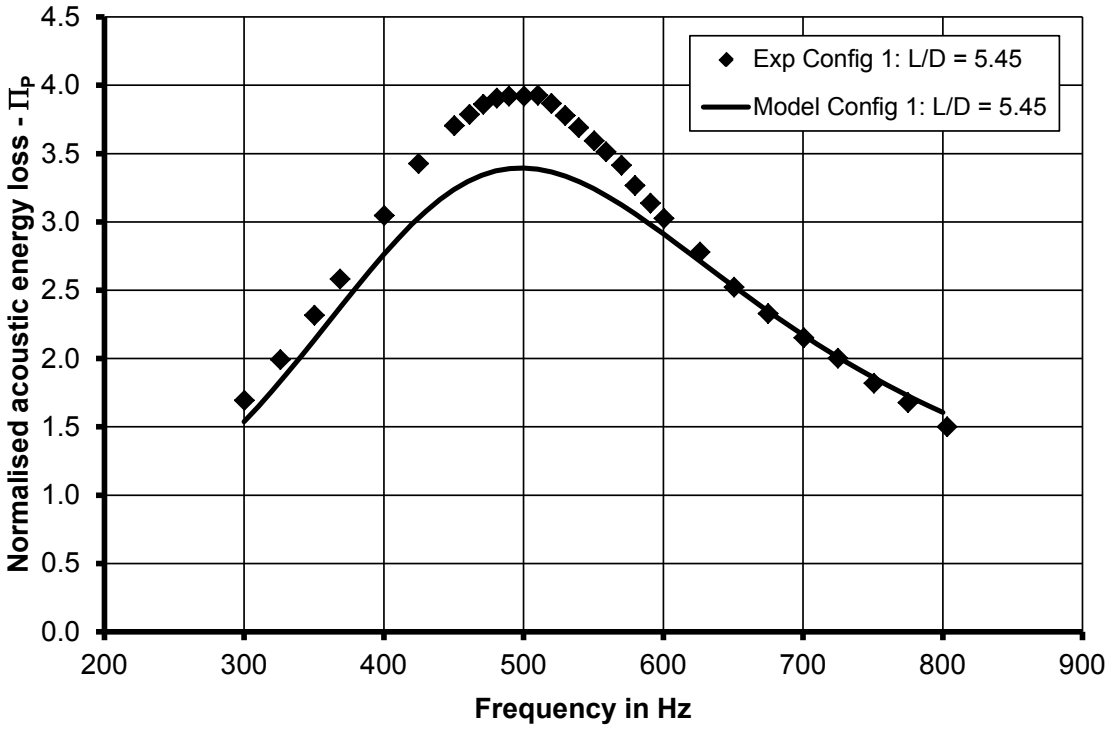

Figure 8.31: Normalised acoustic loss comparison for analytical model and experiment with damper configuration 1, damping skin pressure drop *dp/p* = 0.1%.

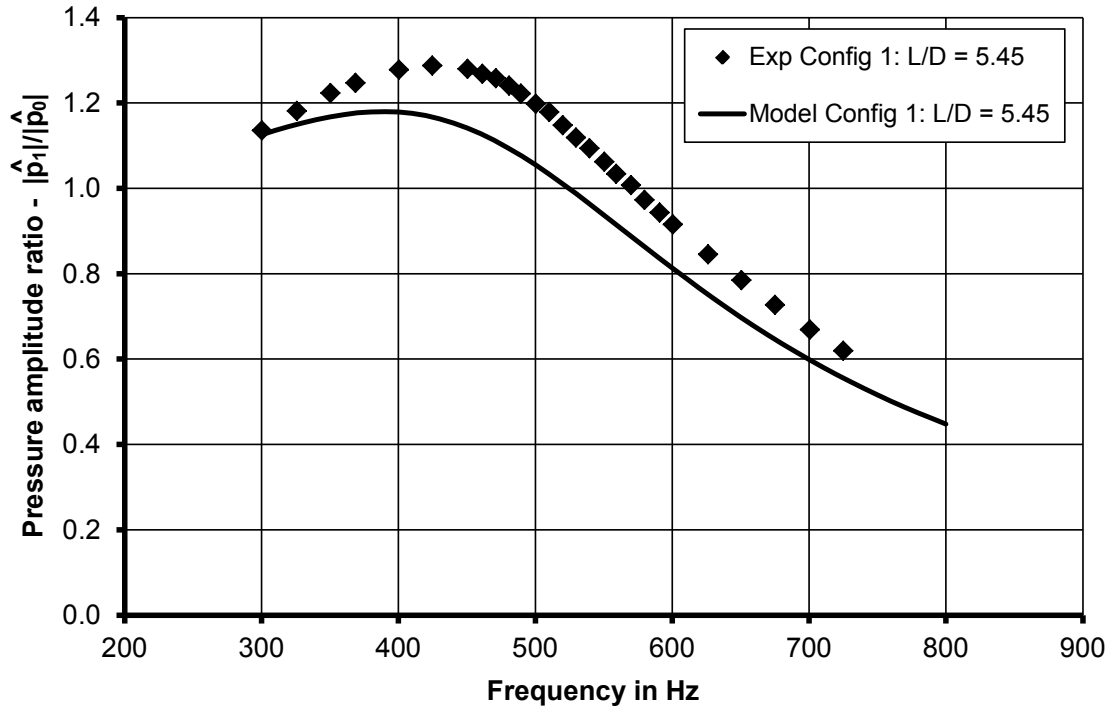

Figure 8.32: Pressure amplitude ratio comparison for analytical model and experiment with damper configuration 1, damping skin pressure drop *dp/p* = 0.1%.

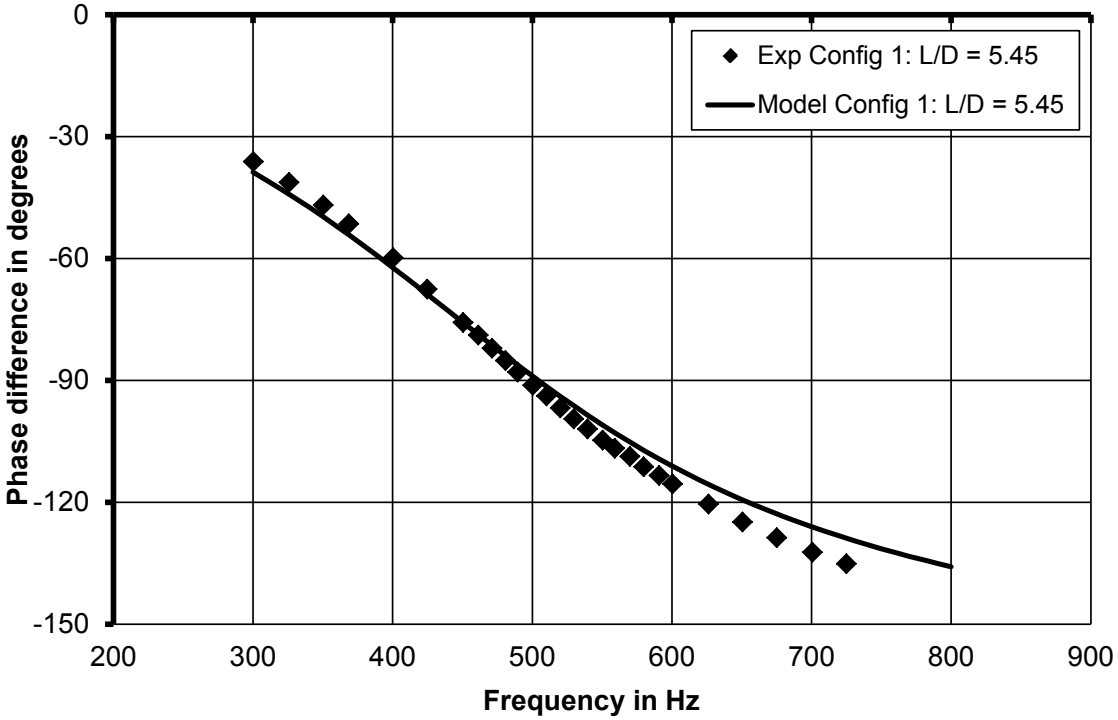

Figure 8.33: Phase difference between cavity pressure amplitude and excitation amplitude calculated by the analytical model and compared to the experiment with damper configuration 1, damping skin pressure drop *dp/p* = 0.1%.

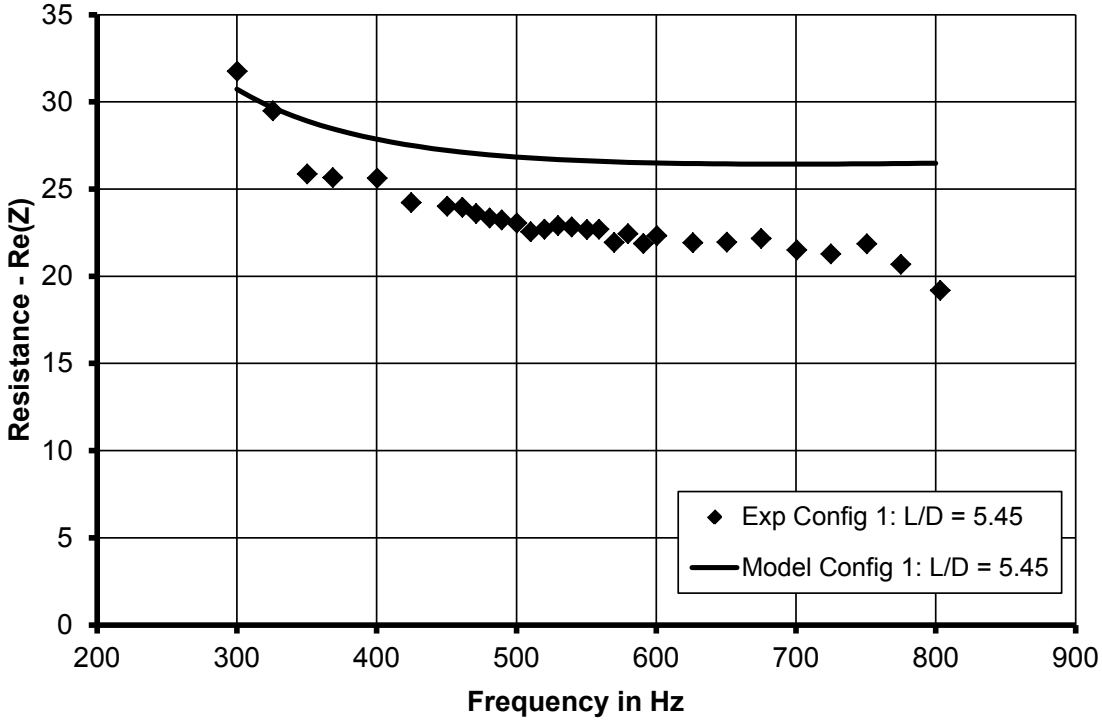

Figure 8.34: Comparison of measured and calculated acoustic resistance for acoustic damper configuration 1, damping skin pressure drop *dp/p* = 0.1%.

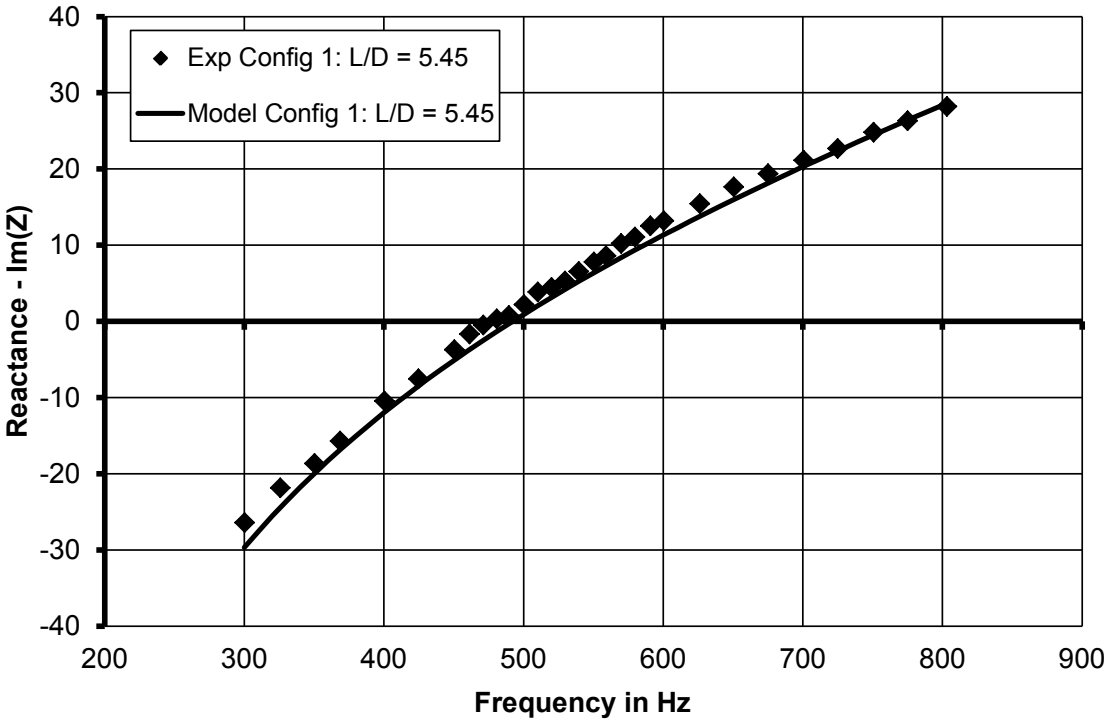

Figure 8.35: Comparison of measured and calculated acoustic reactance for acoustic damper configuration 1, damping skin pressure drop *dp/p* = 0.1%.

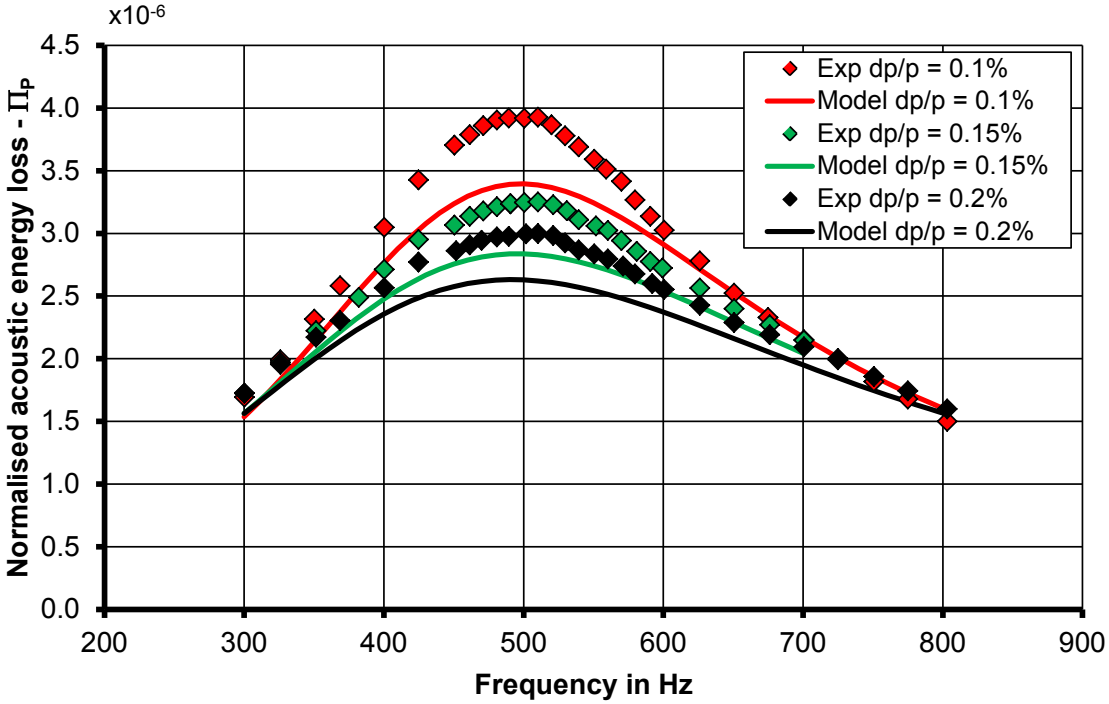

Figure 8.36: Comparison of measured and calculated acoustic energy loss with changing mean pressure drop across the damping skin for damper configuration 1.

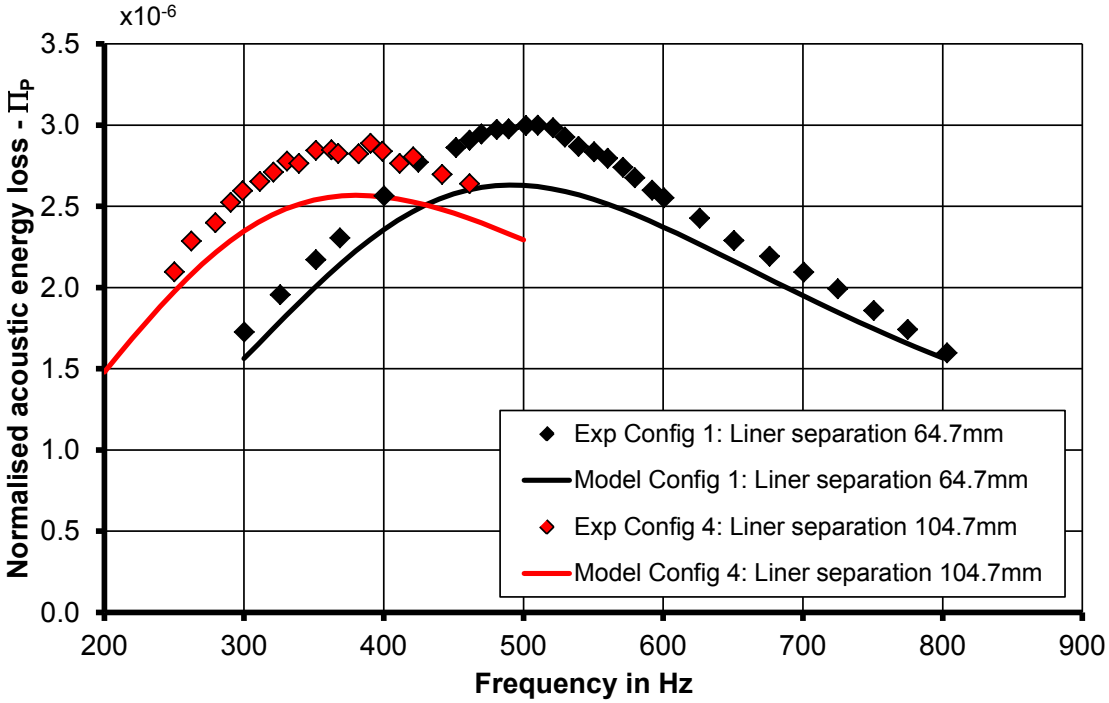

Figure 8.37: Comparison of measured and calculated acoustic energy loss for damper configuration 1 and 4. Damping skin pressure drop *dp/p* = 0.2%.

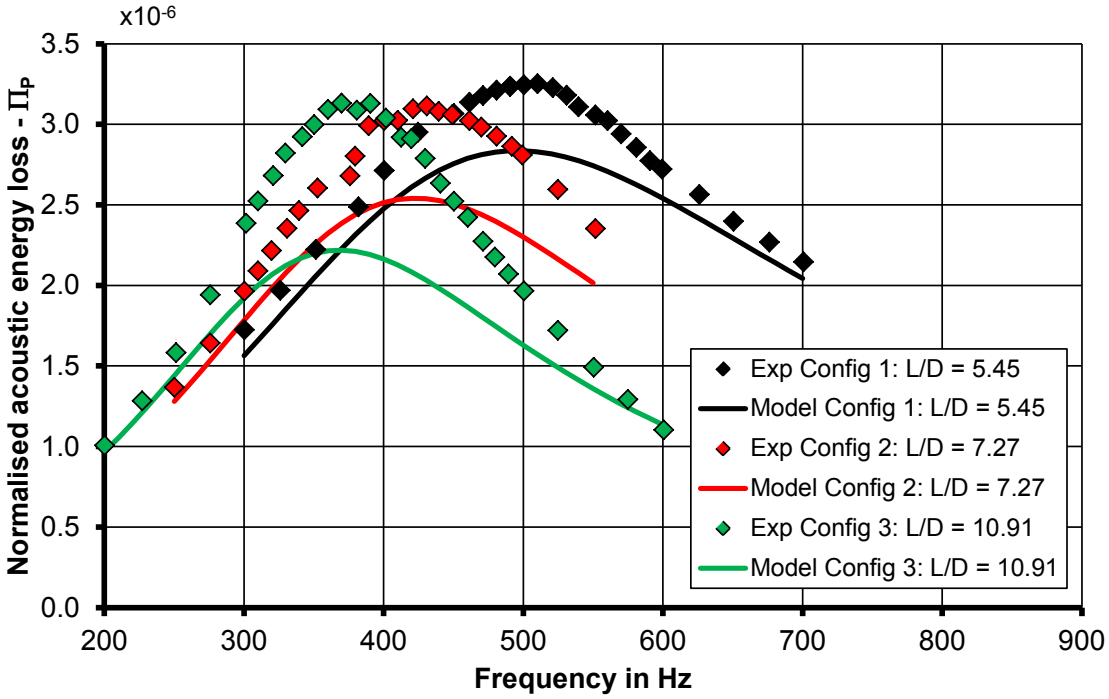

Figure 8.38: Comparison of measured and calculated acoustic energy loss for damper configuration 1, 2 and 3. Damping skin pressure drop *dp/p* = 0.15%.

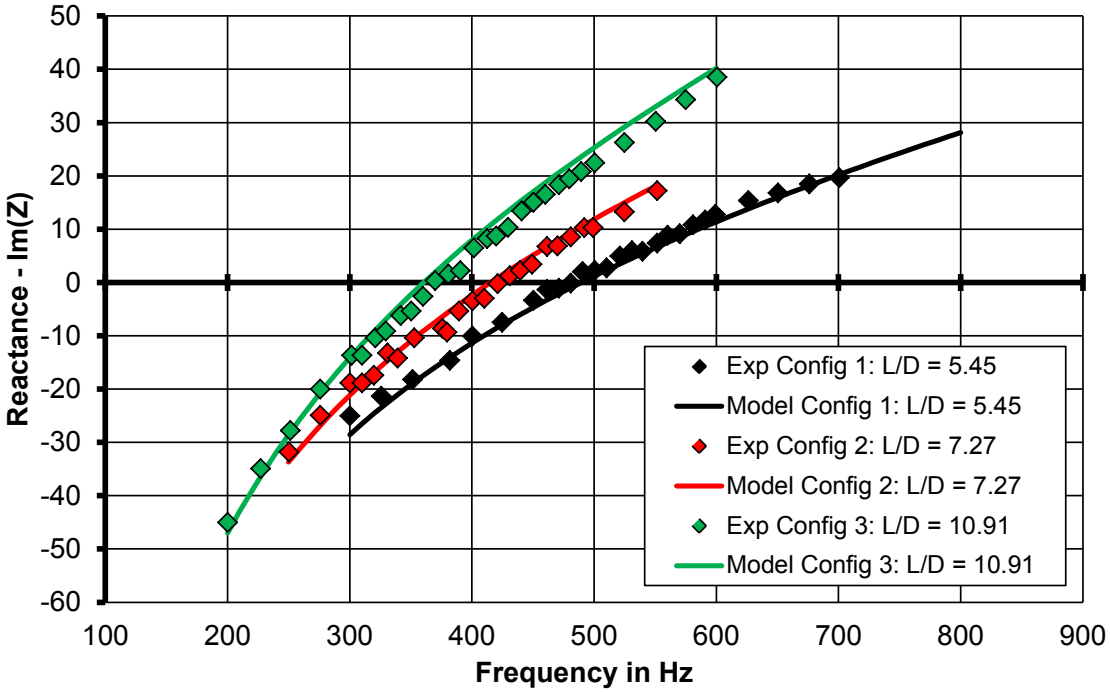

Figure 8.39: Comparison of measured and calculated acoustic reactance for damper configuration 1, 2 and 3. Damping skin pressure drop *dp/p* = 0.15%.

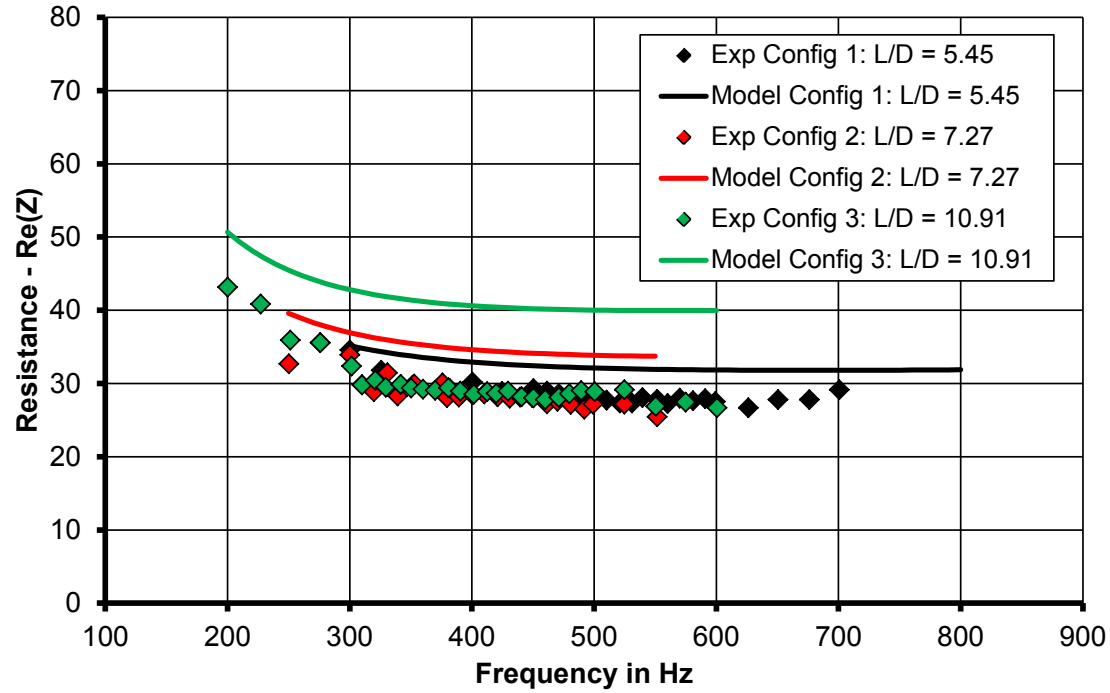

Figure 8.40: Comparison of measured and calculated acoustic resistance for damper configuration 1, 2 and 3. Damping skin pressure drop *dp/p* = 0.15%.

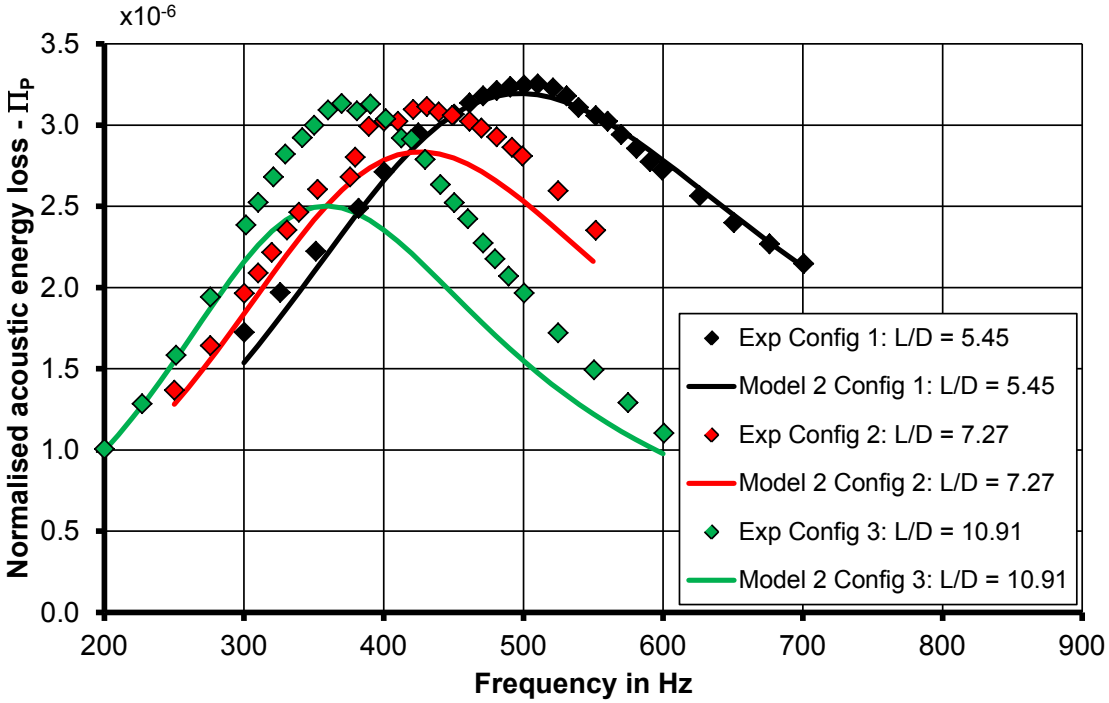

Figure 8.41: Comparison of measured and calculated normalised acoustic energy loss damper configuration 1 to 3 using modelling option 2.

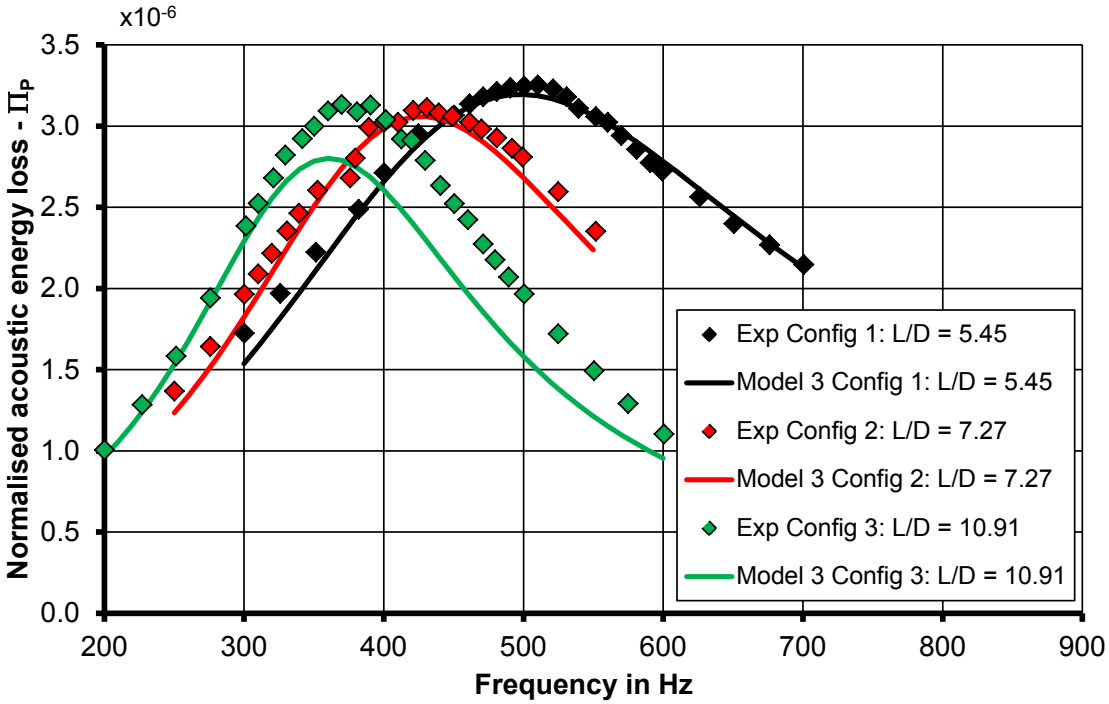

Figure 8.42: Comparison of measured and calculated normalised acoustic energy loss damper configuration 1 to 3 using modelling option 3.

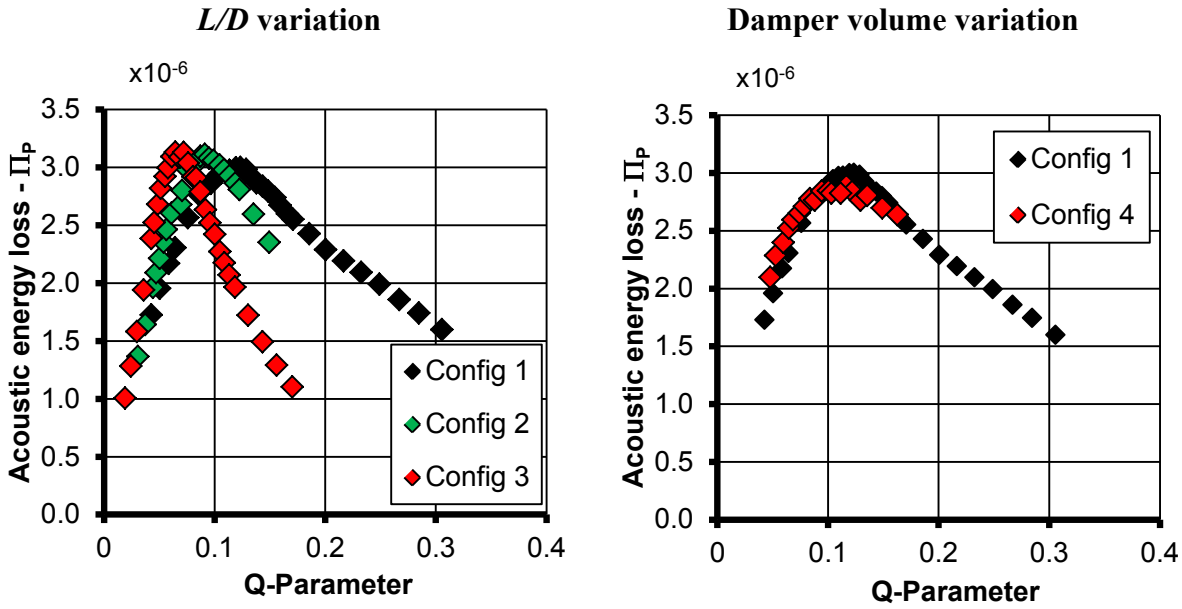

Figure 8.43: Measured normalised acoustic energy loss resonating liner experiments compared to resonance parameter assessment.

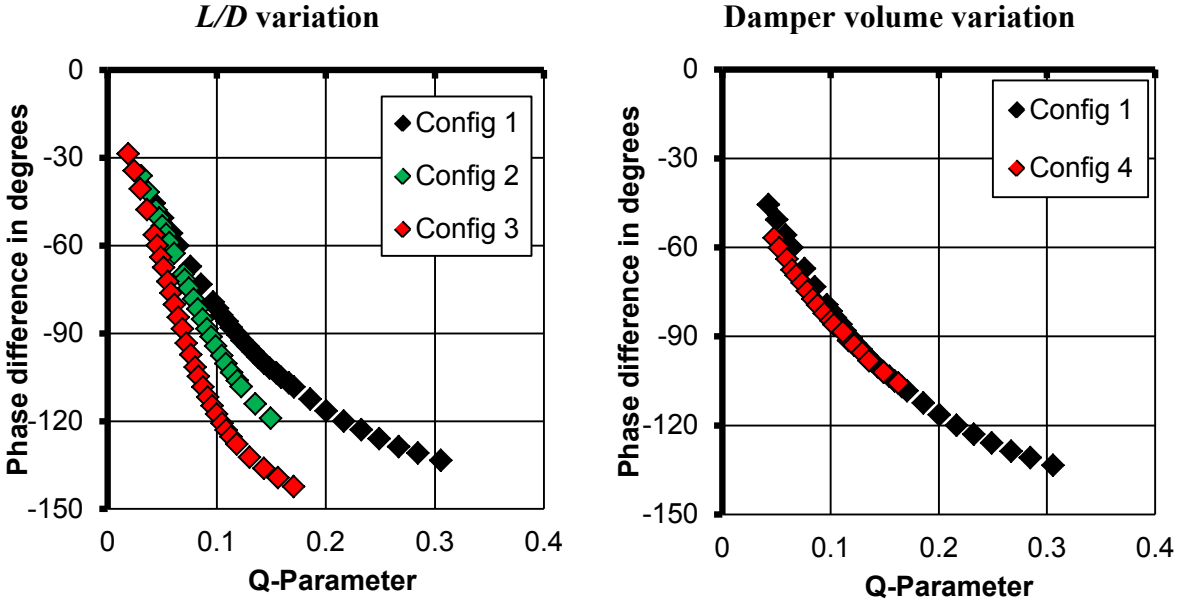

Figure 8.44: Phase of resonating liner experiments compared to resonance parameter assessment.

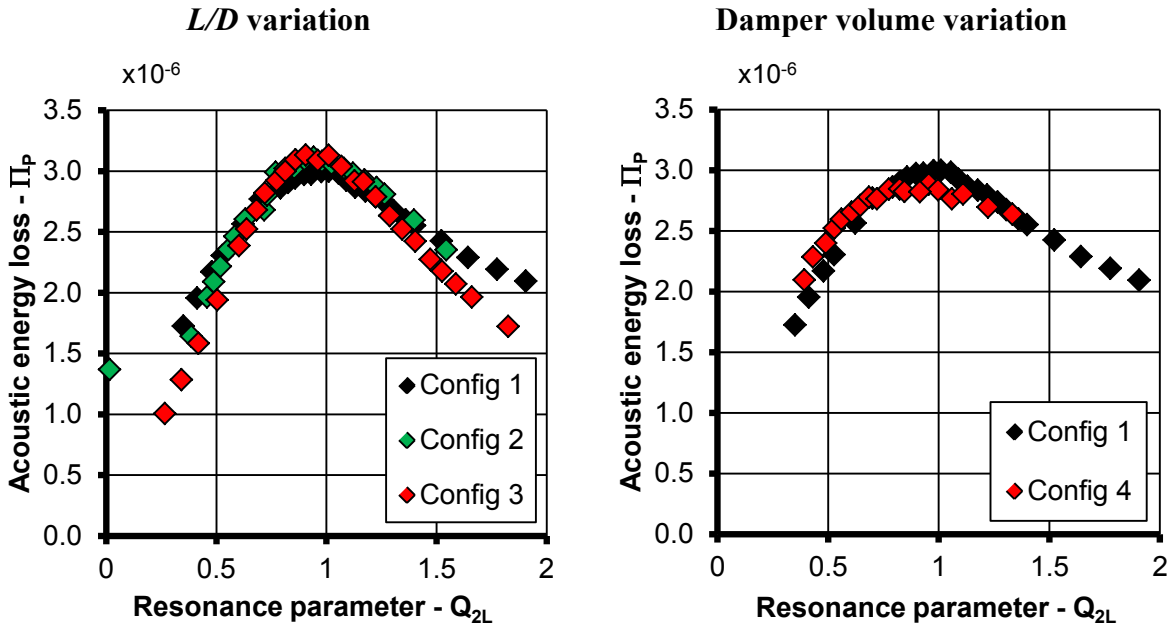

Figure 8.45: Measured normalised acoustic energy loss resonating liner experiments compared to modified resonance parameter assessment.

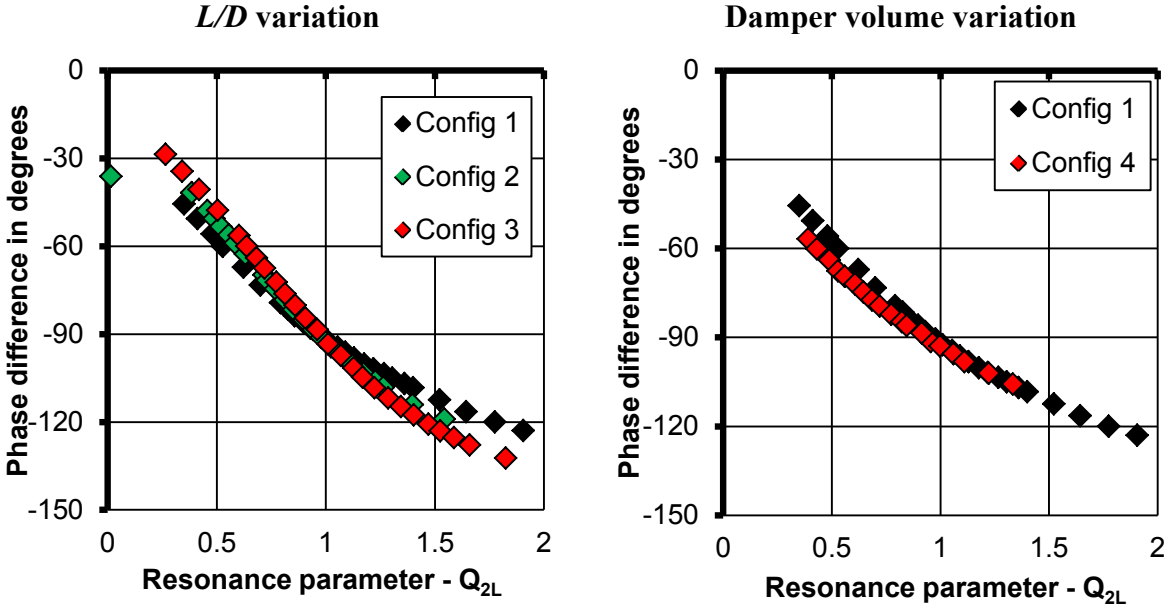

Figure 8.46: Phase of resonating liner experiments compared to modified resonance parameter assessment.

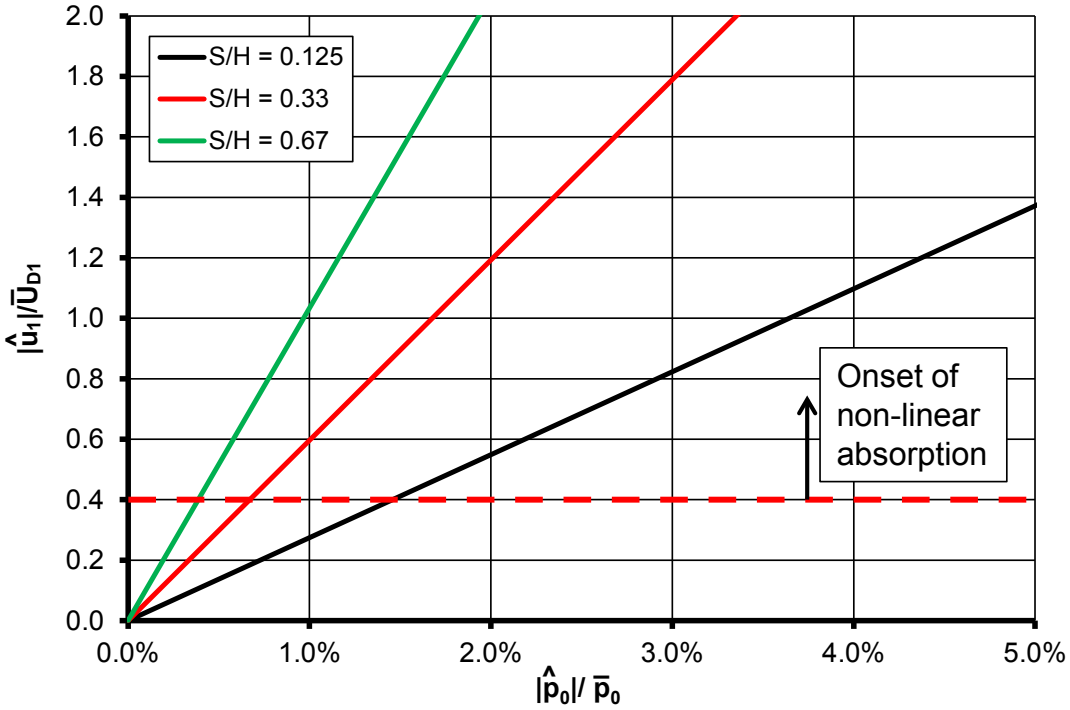

Figure 8.47: Estimate of pressure amplitude for hot gas ingestion non-resonant liner geometry.

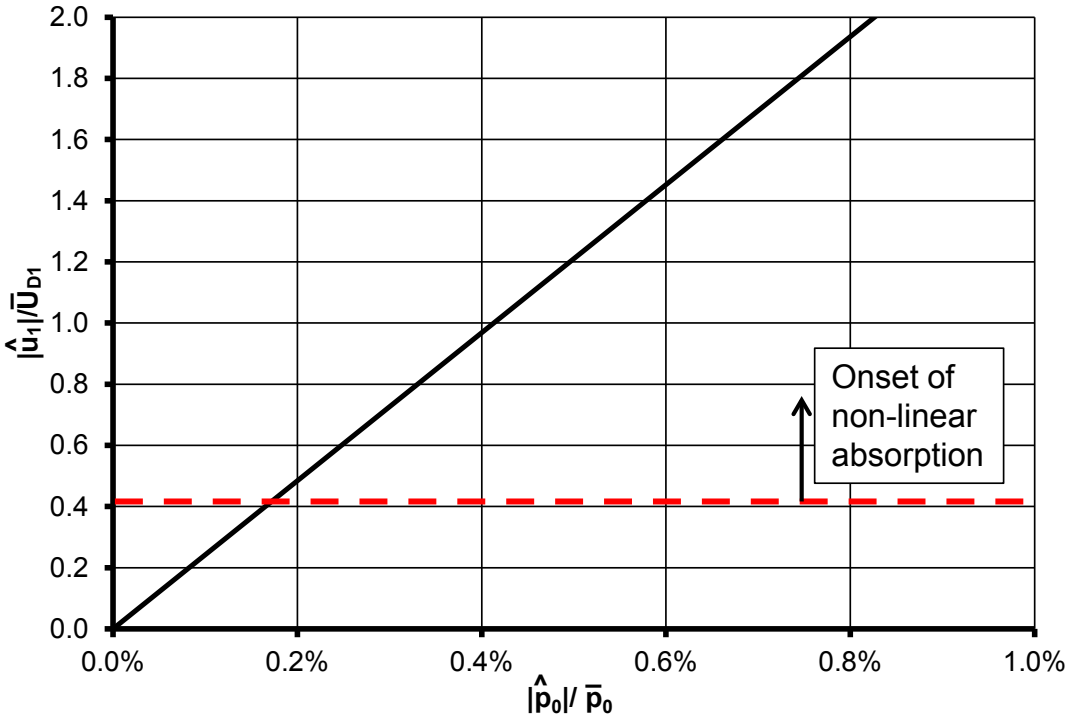

Figure 8.48: Estimate of pressure amplitude for hot gas ingestion resonant liner configuration 1, damping skin *dp/p* = 0.2%.

9 Conclusions and Recommendations

The overall objective of this thesis was to establish the amount of acoustic energy absorption associated with apertures that can be applied within a practical engineering environment. In this work in particular the acoustic absorption characteristics of orifice geometries typically found in a gas turbine combustion system have been investigated. Initially single aperture isothermal experiments have been conducted to investigate the acoustic energy loss for various orifices in the linear and non-linear acoustic absorption regimes. These experiments have been used to assess the performance of current acoustic absorption modelling methods and further the understanding of linear and non-linear acoustic absorption. Particle image velocimetry measurements have been conducted to capture the unsteady flow field generated in the presence of acoustic waves to aid the investigation into the fundamental characteristics associated with the acoustic absorption process. A methodology has been developed to identify the relevant flow field features associated with the acoustic energy loss. The method has been validated by comparing the kinetic energy flux of the acoustically related flow field to the measured acoustic energy loss.

9.1 Experimental Measurements

In general the acoustic absorption of an aperture is a function of the unsteady velocity amplitude within the aperture (i.e. the larger the velocity amplitude the larger the acoustic absorption for a given incident pressure amplitude). For the linear acoustic absorption regime, within the Strouhal number range relevant to aero-engine combustion systems, it has been shown that the acoustic energy loss varies with aperture length-to-diameter ratio and this also reflects changes in the mean flow discharge coefficient. In other words if the discharge coefficient for the relevant geometry is high so is the acoustic absorption. It was shown that this behaviour is due to the pulsatile flow field within the quasi-steady Strouhal number regime as typically present within the combustion system environment. The increase in mean flow discharge coefficient leads to an increase in in the unsteady kinetic energy within the aperture. This energy

subsequently dissipates through turbulent processes as shown in the unsteady velocity field measurements. This is a characteristic of a purely pulsatile flow field which can be modelled using a linearised unsteady momentum equation neglecting the inertial forces within the quasi-steady regime. The measured acoustically related flow field indicated that there were no coherent flow structures interacting with the pulsatile jet flow. The main energy carrying modes represented the characteristics of a pulsatile jet flow which subsequently dissipates into smaller structures due to the turbulent dissipation processes. The maximum unsteady velocity amplitude, for a given incident pressure amplitude, is achieved within the quasi-steady regime. Hence the maximum acoustic energy of an aperture geometry, for a given unsteady pressure difference across the aperture, is achieved within the quasi-steady Strouhal number regime. Outside the quasi-steady regime inertial forces, due to the mass within the aperture, reduce the velocity amplitudes relative to the incident pressure amplitude. Hence the acoustic absorption is reduced. It is therefore not surprising that increasing the length of the aperture leads to reductions in linear acoustic absorption outside the quasi-steady regime.

The linear absorption regime is characterised by a nominally linear relationship between pressure amplitude and velocity amplitude within the aperture, i.e. $\hat{p} \sim \hat{u}$. However the non-linear acoustic absorption regime is characterised by a non-linear relationship between pressure and velocity amplitude, i.e. $\hat{p} \sim \hat{u}^2$. Based on the data shown in this work, the non-linear acoustic absorption regime occurs if the unsteady velocity amplitude is larger than 40% of the mean flow velocity through the aperture. In general the non-linear acoustic absorption is characterised by large scale vortex ring structures within the unsteady flow field. Hence it is thought that the change from a linear relationship, between pressure and velocity amplitude, to a non-linear relationship is caused by the occurrence of the vortex rings in the flow field and their interaction with the pulsatile jet flow. After the transition into the non-linear acoustic absorption regime the velocity field is dominated by the vortex rings and hence the effects of the mean flow upon the acoustic absorption are negligible. The amount of acoustic absorption is then dependent on the incident pressure amplitude. It was shown that the absorption coefficient shows an optimum after which the absorption reduces with

increasing pressure amplitude. It was shown that the acoustic absorption is increasing with increasing pressure amplitude in the region where the acoustic reactance is larger than the resistance. In this case inertial forces due to the acceleration of the fluid within the aperture are dominant. Moreover the non-linear acoustic absorption coefficient is reaching a maximum in the region where reactance and resistance are of similar size. Further increases in pressure amplitude lead to the resistance dominated regime and to reducing absorption coefficients. In this region the viscous effects due to the aperture surrounding shear layers are dominating the pulsatile flow field. As the unsteady fluid dynamic measurements have shown the non-linear acoustic absorption regime is characterised by large vortex ring structures. A large amount of the kinetic energy flux at the exit of the orifice is transferred into the kinetic energy of the vortex rings. The generated vortex rings induce a flow field which significantly influences the mean flow field. It is thought that the distance between the aperture and the vortex ring influences the unsteady flow field due to the interaction of the ring structure with the inflow and outflow behaviour surrounding the aperture. Therefore this interaction leads to changes in the measured acoustic quantities, i.e. decreasing acoustic reactance with increasing pressure amplitude.

9.2 Analytical Model Development

The experiments conducted in the linear acoustic absorption regime have been used to assess the performance of the linear acoustic absorption model. It has been shown that the Howe model (e.g. Howe (1979b)) and the length modified Howe model (e.g. Jing and Sun (2000)) are not able to reproduce the acoustic absorption characteristic with varying orifice *L/D* ratio. Strictly speaking the Howe model seems only valid for an aperture with a mean flow discharge coefficient of 0.7 and an inertia equivalent to the *L/D* of 0.5 orifice geometry. This is as expected as the model introduced by Howe (1979b) was originally developed for infinitesimal thin apertures in the presence of a thin cylindrical shear layer. The predicted absorption with changing *L/D* has shown the opposite trends to the measured absorption data, i.e. increasing acoustic absorption with decreasing orifice C_D. Hence the Howe and modified Howe model require calibration against experiments of the same geometry if attempts are being made to apply these models to practical engineering configurations.

A better model to use is the linear solution to the unsteady momentum equation as proposed by Bellucci et. al. (2004). It was shown that it is sufficient to use the mean discharge coefficients in the linear regime to predict the absorption characteristic with changing *L/D* ratio. Nevertheless the model still needs empirical length correction terms for an accurate prediction of the acoustic absorption over a wide Strouhal number range. It has been shown that the use of constant loss coefficients and length corrections in the linear acoustic absorption model is valid as long as there are no large scale structures developing (as is the case for self-excited jet instabilities). The Bellucci et. al. linear acoustic absorption model showed excellent agreement with all experimental validation data for *L/D* ratios up to five. For increasing hole length the modelling techniques showed increasing discrepancies with the experimental data.

The model proposed by Bellucci et. al. (2004) can also be used in the non-linear absorption regime. A function based on the ratio of unsteady velocity amplitude to mean velocity controls the transition from linear to non-linear acoustic absorption. However as the experimental results have shown the transition to non-linear acoustic absorption occurs at a smaller ratio of velocity amplitude to mean velocity through the aperture than assumed by the current model. In the non-linear regime the mentioned interactions between large scale vortex rings and the pulsatile flow field cause changes in loss coefficients and length corrections which are required as an input to the model. Thus the input parameters to the model are no longer constant but functions of pressure amplitude and frequencies. Currently empirical curve fits could be used to estimate the change in length correction and loss coefficients with varying pressure and frequency.

9.3 Engine Representative Damper Configurations

The analytical model proposed by Bellucci et. al. has been incorporated into a set of design tools for acoustic dampers applied to gas turbine combustion systems. Using this approach it is possible to define the geometric parameters of a damper, tune it to the relevant frequencies within the gas turbine combustion system design envelope and assess the generated acoustic absorption as well as the risk of hot gas ingestion for increased pressure amplitude. The acoustic damper performance has also been assessed in a more representative geometry. In this way a test section representative of a single

sector of a full annular combustion system has been studied. This includes exposure of an acoustic damper to the complex swirling flow field generated by a modern lean burn fuel injector has been investigated. The developed acoustic modelling method based on Bellucci et. al. (2004) was used to predict the acoustic absorption of the damper. It was shown that the model and the experiment were in good agreement. The model does not take any swirling or cross-flow influences into account. Hence the influence of the complex swirling flow field and cross flow field had no significant effect upon the bulk absorption characteristic of the damper. The acoustic energy loss is not only a function of the aperture geometry but also a function of the unsteady pressure drop across the damping skin. Hence maximising the unsteady pressure drop for a given aperture geometry increases the acoustic losses. Therefore the loss of the investigated broadband liner could be increased if the cavity volume between the perforated liners acts as a plenum (i.e. pressure amplitude equal to zero). However in this case the size of the cavity volume would be too large to fit into the design envelope of an aero-engine gas turbine. Hence a more efficient way to increase the absorption of double skin acoustic dampers is to tune the cavity such that it is in resonance (e.g. as it is found with Helmholtz resonators). In this case the unsteady pressure difference across the damping skin can be maximised in the vicinity of the resonance frequency.

As already mentioned the main objective was to understand how much acoustic absorption is available within a conventional combustion system. Within the linear acoustic absorption regime this can be answered using the developed modelling techniques. Most of the combustor wall cooling apertures operate within the quasi-steady regime. In this case the developed quasi-steady acoustic loss assumption based on the mean mass flow and mean pressure drop quantities can be used. Finally the developed impedance methodology can be utilised to superimpose the cooling geometries, damping geometries and fuel injector impedances to estimate the total acoustic loss of a combustion system. Ultimately the linear acoustic absorption model should be used within acoustic network models to improve the accuracy of the full annular combustion system stability predictions.

9.4 Recommendations

The used linear acoustic model has shown increasing discrepancies with the experimental data for aperture geometries longer than *L/D* of five. For long apertures with orifice length larger *L/D* of two the flow field reattaches within the orifice leading to the formation of a boundary layer inside the orifice. Hence the associated loss coefficients are a representation of inflow losses, viscous losses due to the boundary layer and outflow losses. Two possible short term solutions have been shown within the work: (i) only use the measured mean flow discharge coefficient without the unsteady viscosity model or (ii) use the mean flow discharge coefficient for an *L/D* of two orifice together with the unsteady viscosity model. The latter option showed the better agreement with the experiment. However, this behaviour should be further investigated by utilising flow field simulations (e.g. Mendez and Eldredge (2009) or Gunasekaran and McGuirk (2011)) or measurements inside a long *L/D* aperture to develop representative unsteady viscosity models as well as getting a better understanding of the inflow and outflow loss coefficient. The developed unsteady flow field methodology could be used to identify the relevant flow field phenomena.

In this study all the apertures where investigated during inflow conditions without the influence of cross flow. It is known that the mean flow discharge coefficient is significantly affected by cross flow conditions on the inflow side to the aperture. In gas turbine combustors this has technical relevance as many apertures are fed from the surrounding annulus with cross-flow streams across the aperture on the inflow side. Hence the linear analytical modelling technique and its validity should be assessed against experiments with cross flow on the upstream side of the orifice.

The non-linear modelling technique as well as the transition from linear to non-linear acoustic absorption remains challenging. In this case vortex ring structures interact with the unsteady flow field which therefore affect the acoustic absorption characteristic. More detailed unsteady flow simulations using CFD or measurements in conjunction with the developed unsteady flow field methodology should be utilised to improve the simplified analytical non-linear modelling techniques.

Similar analytical modelling techniques applied to circular orifices should also be applied to fuel injector geometries. Accurate impedance models of the fuel injectors are

important for an accurate application of acoustic network models for the stability prediction of a gas turbine combustion system. Moreover the acoustic impedance of the fuel injector could also be studied with the aim of reducing the unsteady velocity field through the fuel injector relative to an incident pressure amplitude. This may help to reduce the onset of thermo-acoustic instabilities at source.

References

Åbom, M. & Bodén, H. 1988, "Error analysis of two-microphone measurements in ducts with flow", *The Journal of the Acoustical Society of America,* vol. 83, pp. 2429-2438.

ACARE 2011, “Flightpath 2050 Europe's vision for aviation”.

ACARE 2001, “European aeronautics: A vision for 2020”.

Adrian, R.J. 2005, "Twenty years of particle image velocimetry", *Experiments in Fluids,* vol. 39, no. 2, pp. 159-169.

Adrian, R.J. 1991, "Particle-imaging techniques for experimental fluid mechanics", *Annual Review of Fluid Mechanics,* vol. 23, no. 1, pp. 261-304.

Adrian, R.J., Christensen, K.T. & Liu, Z.C. 2000, "Analysis and interpretation of instantaneous turbulent velocity fields", *Experiments in Fluids,* vol. 29, no. 3, pp. 275-290.

Andreini, A., Bianchini, C., Facchini, B., Simonetti, F. & Peschiulli, A. 2011, "Assessment of numerical tools for the evaluation of the acoustic impedance of multi-perforated plates", *ASME Turbo Expo, GT2011-46303*, June 6-10, Vancouver, Canada.

Atig, M., Dalmont, J.P. & Gilbert, J. 2004, "Termination impedance of open-ended cylindrical tubes at high sound pressure level", *Comptes Rendus Mécanique,* vol. 332, no. 4, pp. 299-304.

Aydemir, E., Worth, N.A. & Dawson, J.R. 2012, "The formation of vortex rings in a strongly forced round jet", *Experiments in Fluids,* vol. 52, pp. 729-742.

Barker, A., Carrotte, J. & Denman, P. 2005, "Analysis of hot-wire anemometry data in an acoustically excited turbulent flow field", *Experiments in Fluids,* vol. 39, no. 6, pp. 1061-1070.

Barker, A. & Carrotte, J.F. 2006, “Factors limiting the performance of Helmholtz resonators in gas turbine combustors”, *TT06R04, Loughborough University*.

Batchelor, G.K. 2000, “An introduction to fluid dynamics”, Cambridge University Press.

Bechert, D., Michel, U. & Pfizenmaier, E. 1977, "Experiments on the transmission of sound through jets", *American Institute of Aeronautics and Astronautics, 4th Aeroacoustics Conference, Atlanta, Georgia*.

Bechert, D. 1980, "Sound absorption caused by vorticity shedding, demonstrated with a jet flow", *Journal of Sound and Vibration,* vol. 70, no. 3, pp. 389-405.

Bellucci, V., Flohr, P. & Paschereit, C.O. 2004b, "Numerical and experimental study of acoustic damping generated by perforated screens", *AIAA Journal,* vol. 42, no. 8, pp. 1543-1549.

Bellucci, V., Flohr, P., Paschereit, C.O. & Magni, F. 2004, "On the use of Helmholtz resonators for damping acoustic pulsations in industrial gas turbines", *Journal of engineering for gas turbines and power,* vol. 126, pp. 271-275.

Bellucci, V., Schuermans, B., Nowak, D., Flohr, P. & Paschereit, C.O. 2005, "Thermoacoustic modeling of a gas turbine combustor equipped with acoustic dampers", *Journal of turbomachinery,* vol. 127, pp. 372-379.

Beranek, L.L. 1954, "Acoustics", McGraw-Hill.

Berkooz, G., Holmes, P. & Lumley, J.L. 1993, "The proper orthogonal decomposition in the analysis of turbulent flows", *Annual Review of Fluid Mechanics,* vol. 25, no. 1, pp. 539-575.

Bernero, S. & Fiedler, H.E. 2000, "Application of particle image velocimetry and proper orthogonal decomposition to the study of a jet in a counterflow", *Experiments in Fluids,* vol. 29, pp. 274-281.

Betts, J.F. 2000, "Experiments and impedance modeling of liners Including the effect of bias flow", Virginia Polytechnic Institute and State University.

Blokhintsev, D. 1956, "Acoustics of a Nonhomogeneous Moving Medium", *NACA, Technical Memorandum 1399*.

Bodén, H. & Åbom, M. 1986, "Influence of errors on the two-microphone method for measuring acoustic properties in ducts", *The Journal of the Acoustical Society of America,* vol. 79, pp. 541-549.

Bonnell, J.M., Marshall, R.L. & Riecke, G.T. 1971, "Combustion instability in turbojet and turbofan augmentors", *AIAA/SAE 7th Propulsion Joint Specialist Conference*, June 14-18.

Bothien, M.R., Noiray, N. & Schuermans, B. 2012, "A Novel Damping Device for Broadband Attenuation of Low-Frequency Combustion Pulsations in Gas Turbines", *ASME Turbo Expo, GT2012-68873*, June 11-15, Copenhagen, Denmark.

Brown, G.B. 1935, "On vortex motion in gaseous jets and the origin of their sensitivity to sound", *Proceedings of the Physical Society,* vol. 47, pp. 703-732.

Candel, S. 2002, "Combustion dynamics and control: progress and challenges", *Proceedings of the combustion institute,* vol. 29, no. 1, pp. 1-28.

Chanaud, R. 1994, "Effects of geometry on the resonance frequency of Helmholtz resonators", *Journal of Sound and Vibration,* vol. 178, no. 3, pp. 337-348.

Chatterjee, A. 2000, "An introduction to the proper orthogonal decomposition", *Current science,* vol. 78, no. 7, pp. 808-817.

Chu, B.T. 1965, "On the energy transfer to small disturbances in fluid flow (Part I)", *Acta Mechanica,* vol. 1, no. 3, pp. 215-234.

Coats, C. 1996, "Coherent structures in combustion", *Progress in Energy and Combustion Science,* vol. 22, no. 5, pp. 427-509.

Cole-Parmer 2009, “Precision Gas Flow Controller Operating Manual”.

Crow, S.C. & Champagne, F.H. 1971, "Orderly structure in jet turbulence", *Journal of Fluid Mechanics,* vol. 48, no. 3, pp. 547-591.

Culick, F. 2006, “Unsteady motions in combustion chambers for propulsion systems”, AGARD, RTO-AG-AVT-039.

Cummings, A. 1987, "The response of a resonator under a turbulent boundary layer to a high amplitude non-harmonic sound field", *Journal of Sound and Vibration,* vol. 115, no. 2, pp. 321-328.

Cummings, A. 1986, "Transient and multiple frequency sound transmission through perforated plates at high amplitude", *The Journal of the Acoustical Society of America,* vol. 79, pp. 942.

Cummings, A. & Eversman, W. 1983, "High amplitude acoustic transmission through duct terminations: theory", *Journal of Sound and Vibration,* vol. 91, no. 4, pp. 503-518.

de Bedout, J., Franchek, M., Bernhard, R. & Mongeau, L. 1997, "Adaptive passive noise control with self-tuning Helmholtz resonators", *Journal of Sound and Vibration,* vol. 202, no. 1, pp. 109-123.

Dean, P. & Tester, B. 1975, "Duct wall impedance control as an advanced concept for acoustic suppression", NASA Contractor Report CR-134998.

Didden, N. 1979, "On the formation of vortex rings: rolling-up and production of circulation", *Zeitschrift für Angewandte Mathematik und Physik (ZAMP),* vol. 30, no. 1, pp. 101-116.

Disselhorst, J. & Wijngaarden, L.V. 1980, "Flow in the exit of open pipes during acoustic resonance", *Journal of Fluid Mechanics,* vol. 99, no. 02, pp. 293-319.

Dodds, W. 2005, "Twin annular premixing swirler (TAPS) combustor", *The Roaring 20th Aviation Noise & Air Quality Symposium*.

Dodds, W. 2002, "Engine and aircraft technologies to reduce emissions", *UC Technology Transfer Symposium—Dreams of Flight*.

Douglas, J.F., Gasiorek, J.M., Swaffield, J.A. & Jack, L.B. 2005, “Fluid Mechanics”, 5th edition, Pearson Prentice Hall.

Dowling, A.P. 2003, "The challenges of lean premixed combustion", *Proceedings of the International Gas Turbine Congress, Tokyo*, November 2-7.

Dowling, A.P. & Morgans, A.S. 2005, "Feedback control of combustion oscillations", *Annual Review of Fluid Mechanics,* vol. 37, pp. 151-182.

Dowling, A.P. & Stow, S.R. 2003, "Acoustic analysis of gas turbine combustors", *Journal of Propulsion and Power,* vol. 19, no. 5, pp. 751-764.

Dowling, A. & Hubbard, S. 2000, "Instability in lean premixed combustors", *Proceedings of the Institution of Mechanical Engineers, Part A: Journal of Power and Energy,* vol. 214, no. 4, pp. 317-332.

Dowling, A. & Hughes, I. 1992, "Sound absorption by a screen with a regular array of slits", *Journal of Sound and Vibration,* vol. 156, no. 3, pp. 387-405.

Dunham, D. 2011, “Unsteady fluid mechanics of annular swirling shear layers”, Loughborough University.

Eckstein, J. 2004, “On the mechanisms of combustion driven low-frequency oscillations in aero-engines”, *Technische Universität München.*

Eckstein, J., Freitag, E., Hirsch, C. & Sattelmayer, T. 2004, "Experimental study on the role of entropy waves in low-frequency oscillations for a diffusion burner", *ASME Turbo Expo, GT2004-54163*, June 14-17, Vienna, Austria.

Eldredge, J.D. 2004, "On the interaction of higher duct modes with a perforated liner system with bias flow", *Journal of Fluid Mechanics,* vol. 510, no. 1, pp. 303-331.

Eldredge, J.D., Bodony, D.J. & Shoeybi, M. 2007, "Numerical investigation of the acoustic behavior of a multi-perforated liner", *Proceedings of the 13th AIAA/CEAS Aeroacoustics Conference, AIAA Paper 2007-3683*, 21-23 May.

Eldredge, J.D. & Dowling, A.P. 2003, "The absorption of axial acoustic waves by a perforated liner with bias flow", *Journal of Fluid Mechanics,* vol. 485, no. 25, pp. 307-335.

Forster, S. & Michel, U. 2003, "Experimental investigation of the dissipation of acoustic energy in perforated walls with bias flow", *Combustion and Noise Control* Cranfield University Press.

Freymuth, P. 1966, "On transition in a separated laminar boundary layer", *Journal of Fluid Mechanics,* vol. 25, no. 4, pp. 683-704.

Garrison, G.D., Russel, P.L. & Stettler, J. 1972, “Investigation of damping methods for augmentor combustion instability”, *DTIC Document, AFAPL-TR-7284*.

Gharib, M., Rambod, E. & Shariff, K. 1998, "A universal time scale for vortex ring formation", *Journal of Fluid Mechanics,* vol. 360, no. 1, pp. 121-140.

Glezer, A. 1988, "The formation of vortex rings", *Physics of Fluids,* vol. 31, no. 12, pp. 3532-3542.

Graftieaux, L., Michard, M. & Grosjean, N. 2001, "Combining PIV, POD and vortex identification algorithms for the study of unsteady turbulent swirling flows", *Measurement Science and technology,* vol. 12, pp. 1422-1429.

Gritsch, M., Schulz, A. & Wittig, S. 1998, "Discharge coefficient measurements of film-cooling holes with expanded exits", *Journal of Turbomachinery,* vol. 120, pp. 557-563.

Gunasekaran, B. & McGuirk, J.J. 2011, "Mildly-Compressible Pressure-Based CFD Methodology for Acoustic Propagation and Absorption Prediction", *ASME Turbo Expo, GT2011-45316*, June 6-10, Vancouver, Canada.

Gysling, D.L., Copeland, G.S., McCormick, D.C. & Proscia, W.M. 2000, "Combustion system damping augmentation with Helmholtz resonators", *Journal of Engineering for Gas Turbines and Power,* vol. 122, pp. 269-274.

Hafsteinsson, H., Burak, M., Eriksson, L.E. & Billson, M. 2010, "Experimental and numerical investigation of a novel acoustic liner concept", *16th AIAA/CEAS Aeroacoustics Conference, AIAA 2010-3847*, 7-9 June.

Hart, R. & McClure, F. 1965, "Theory of acoustic instability in solid-propellant rocket combustion", *Symposium (International) on Combustion ,* vol. 10, no. 1, pp. 1047-1065.

Hay, N., Henshall, S.E. & Manning, A. 1994, "Discharge coefficients of holes angled to the flow direction", *Journal of Turbomachinery,* vol. 116, pp. 92-96.

Hay, N. & Spencer, A. 1992, "Discharge coefficients of cooling holes with radiused and chamfered inlets", *Journal of Turbomachinery,* vol. 114, pp. 701-706.

Heavens, S.N. 1980, "Visualization of the acoustic excitation of a subsonic jet", *Journal of Fluid Mechanics,* vol. 100, pp. 185-192.

Hersh, A.S. & Rogers, T. 1976, “Fluid mechanical model of the acoustic impedance of small orifices”*,* NASA Contractor Report, CR-2682.

Hersh, A.S., Walker, B.E. & Celano, J.W. 1999, "Semi-empirical Helmholtz resonator impedance model", *AIAA/CEAS Aeroacoustics Conference and Exhibit, AIAA-99-1825*.

Heuwinkel, C., Enghardt, L. & Röhle, I. 2007, "Experimental investigation of the acoustic damping of perforated liners with bias flow", *AIAA 13th Aeroacoustics Conference, AIAA 2007-3525*, 21-23 May.

Higgins, B. 1802, "On the sound produced by a current of hydrogen gas passing through a tube", *Journal of Natural Philosophy Chemistry and the Arts,* vol. 1, p. 129.

Hollis, D. 2004, “Particle image velocimetry in gas turbine combustor flow fields”, Loughborough University.

Holmes, P., Lumley, J.L. & Berkooz, G. 1998, “Turbulence, coherent structures, dynamical systems and symmetry”, *Cambridge University Press*.

Howe, M.S. 1979a, "Attenuation of sound in a low Mach number nozzle flow", *Journal of Fluid Mechanics,* vol. 91, no. 2, pp. 209-229.

Howe, M. 1979b, "On the theory of unsteady high Reynolds number flow through a circular aperture", *Proceedings of the Royal Society of London A. Mathematical and Physical Sciences,* vol. 366, pp. 205-223.

Huang, Y. & Yang, V. 2009, "Dynamics and stability of lean-premixed swirl-stabilized combustion", *Progress in energy and combustion science,* vol. 35, no. 4, pp. 293-364.

Hughes, I. & Dowling, A. 1990, "The absorption of sound by perforated linings", *Journal of Fluid Mechanics,* vol. 218, pp. 299-335.

Hussain, A.K.M.F. & Zaman, K.B.M.Q. 1981, "The ‘preferred mode’of the axisymmetric jet", *Journal of Fluid Mechanics,* vol. 110, no. 1, pp. 39-71.

ICAO 2010, “Environmental Report”.

Illingworth, S.J. & Morgans, A.S. 2010, "Adaptive feedback control of combustion instability in annular combustors", *Combustion Science and Technology,* vol. 182, no. 2, pp. 143-164.

Ingard, U. 1970, "Nonlinear distortion of sound transmitted through an orifice", *The Journal of the Acoustical Society of America,* vol. 48, no. 1, pp. 32-33.

Ingard, U. 1968, "Absorption characteristics of nonlinear acoustic resonators", *The Journal of the Acoustical Society of America,* vol. 44, no. 4, pp. 1155-1156.

Ingard, U. 1953, "On the theory and design of acoustic resonators", *The Journal of the Acoustical Society of America,* vol. 25, no. 6, pp. 1037-1061.

Ingard, U. & Ising, H. 1967, "Acoustic nonlineartry of an orifice", *The Journal of the Acoustical Society of America,* vol. 42, no. 1, pp. 6-17.

Ingard, U. & Labate, S. 1950, "Acoustic circulation effects and the nonlinear impedance of orifices", *The Journal of the Acoustical Society of America,* vol. 22, pp. 211-218.

Jabbal, M., Wu, J. & Zhong, S. 2006, "The performance of round synthetic jets in quiescent flow", *Aeronautical Journal,* vol. 110, no. 1108, pp. 385-393.

Jeong, J. & Hussain, F. 1995, "On the identification of a vortex", *Journal of Fluid Mechanics,* vol. 285, no. 1, pp. 69-94.

Jing, X. & Sun, X. 2002, "Sound-excited flow and acoustic nonlinearity at an orifice", *Physics of Fluids,* vol. 14, no. 1, pp. 268-276.

Jing, X. & Sun, X. 2000, "Effect of plate thickness on impedance of perforated plates with bias flow", *AIAA Journal,* vol. 38, no. 9, pp. 1573-1578.

Jing, X. & Sun, X. 1999, "Experimental investigations of perforated liners with bias flow", *The Journal of the Acoustical Society of America,* vol. 106, no. 5, pp. 2436-2441.

Johnston, J.P. & Schmidt, W.E. 1978, "Measurement of acoustic reflection from an obstruction in a pipe with flow", *The Journal of the Acoustical Society of America,* vol. 63, pp. 1455-1460.

Kato, S., Fujimori, T., Dowling, A. & Kobayashi, H. 2005, "Effect of heat release distribution on combustion oscillation", *Proceedings of the Combustion Institute,* vol. 30, no. 2, pp. 1799-1806.

Kaufmann, P., Krebs, W., Valdes, R. & Wever, U. 2008, "3D thermoacoustic properties of single can and multi can combustor configurations", *ASME Turbo Expo, GT2008-50755*, June 9-13, Berlin, Germany.

Keane, R.D. & Adrian, R.J. 1990, "Optimization of particle image velocimeters. I. Double pulsed systems", *Measurement Science and Technology,* vol. 1, pp. 1202-1215.

Keller, J.J. & Zauner, E. 1995, "On the use of Helmholtz resonators as sound attenuators", *Zeitschrift für Angewandte Mathematik und Physik (ZAMP),* vol. 46, no. 3, pp. 297-327.

Kinsler, L.E., Frey, A.R., Coppens, A.B. & Sanders, J.V. 1999, "Fundamentals of acoustics", 4th edition, Wiley-VCH.

Klinger, H., Lazik, W. & Wunderlich, T. 2008, "The engine 3E core engine", *ASME Turbo EXPO, GT2008-50679*, June 9-13, Berlin, Germany.

Ko, S.H. 1972, "Sound attenuation in acoustically lined circular ducts in the presence of uniform flow and shear flow", *Journal of Sound and Vibration,* vol. 22, no. 2, pp. 193-210.

Kolár, V. 2007, "Vortex identification: New requirements and limitations", *International Journal of Heat and Fluid Flow,* vol. 28, no. 4, pp. 638-652.

Kostas, J., Soria, J. & Chong, M.S. 2005, "A comparison between snapshot POD analysis of PIV velocity and vorticity data", *Experiments in Fluids,* vol. 38, no. 2, pp. 146-160.

Krebs, W., Bethke, S., Lepers, J., Flohr, P., Prade, B., Johnson, C. & Sattinger, S. 2005, "Thermoacoustic design tools and passive control: Siemens power generation approaches", *Combustion Instabilities in Gas Turbine Engines Operational Experience, Fundamental Mechanisms and Modeling*, editors T.C. Lieuwen & V. Yang, AIAA.

Krueger, P.S., Dabiri, J.O. & Gharib, M. 2006, "The formation number of vortex rings formed in uniform background co-flow", *Journal of Fluid Mechanics,* vol. 556, no. 1, pp. 147-166.

Lahiri, C., Enghardt, L., Bake, F., Sadig, S. & Gerendas, M. 2011, "Establishment of a high quality database for the acoustic modeling of perforated liners", *Journal of Engineering for Gas Turbines and Power,* vol. 133, pp. 091503.

Langhorne, P. 1988, "Reheat buzz: an acoustically coupled combustion instability. Part 1. Experiment", *Journal of Fluid Mechanics,* vol. 193, no. 1, pp. 417-443.

Laudien, E., Pongratz, R., Pierro, R. & Preclik, D. 1995, "Experimental procedures aiding the design of acoustic cavities", *Liquid Rocket Engine Combustion Instability*, editors V. Yang & W.E. Anderson, AIAA.

LaVision 2011, “Product Manual Darwin Duo”, LaVision.

LaVision 2007, “Flow master product manual”, La Vision.

Lawn, C. 2000, "The thermo-acoustic response of a premixed swirl burner", *Proceedings of the Institution of Mechanical Engineers, Part A: Journal of Power and Energy,* vol. 214, no. 4, pp. 333-354.

Lazik, W., Doerr, T., Bake, S., von der Bank, R. & Rackwitz, L. 2008, "Development of lean-burn Low-NOx Combustion Technology at Rolls-Royce Deutschland", *ASME Turbo EXPO, GT2008-51115*, June 9-13, Berlin, Germany.

Lebedeva, I.V., Grushin, A.E. & Kravtsov, Y.U. 2005, "Experimental study of aeroacoustic characteristics of screens with an orifice", *International Journal of Aeroacoustics,* vol. 4, no. 3, pp. 345-352.

Lee, D.S., Fahey, D.W., Forster, P.M., Newton, P.J., Wit, R.C.N., Lim, L.L., Owen, B. & Sausen, R. 2009, "Aviation and global climate change in the 21st century", *Atmospheric Environment,* vol. 43, no. 22-23, pp. 3520-3537.

Lee, S.H., Ih, J.G. & Peat, K.S. 2007, "A model of acoustic impedance of perforated plates with bias flow considering the interaction effect", *Journal of Sound and Vibration,* vol. 303, no. 3, pp. 741-752.

Lefebvre, A.H. & Ballal, D.R. 2010, “Gas turbine combustion alternative fuels and emissions”, 3rd edition, CRC Press.

Lewis, J.S. & Niedzwiecki, R.W. 1999, "Aircraft technology and its relation to emissions", *Avaiation and the Global Atmosphere, Intergovernmental Panel on Climate Change*, editors J.E. Penner, D.H. Lister, D.J. Griggs, D.J. Dokken & M. MacFarland, Cambridge University Press, Oxford.

Lichtarowicz, A., Duggins, R.K. & Markland, E. 1965, "Discharge coefficients for incompressible non-cavitating flow through long orifices", *Journal of Mechanical Engineering Science,* vol. 7, no. 2, pp. 210-219.

Lieuwen, T.C. 1999, “Investigation of combustion instability mechanisms in premixed gas turbines”, Georgia Institute of Technology.

Lieuwen, T.C. & Zinn, B.T. 1998, "The role of equivalence ratio oscillations in driving combustion instabilities in low NO_X gas turbines", *Symposium (International) on Combustion*, vol. 27 , no. 2, pp. 1809-1816.

Lim, T.T., New, T.H. & Luo, S.C. 2001, "On the development of large-scale structures of a jet normal to a cross flow", *Physics of Fluids,* vol. 13, pp. 770-775.

Lörstad, D., Pettersson, J. & Lindholm, A. 2009, "Emission reduction and cooling improvements due to the introduction of passive acoustic damping in an existing SGT-800 combustor", *ASME Turbo Expo, GT2009-59313*, June 8-12, Orlando, Florida.

Lucas, M.J., Noreen, R., Sutherland, L.C., Coleman, J.E. & Junger, M.C. 1997, "Handbook of the acoustic characteristics of turbomachinery cavities"*, ASME Press*.

Luong, T., Howe, M.S. & McGowan, R.S. 2005, "On the Rayleigh conductivity of a bias-flow aperture", *Journal of Fluids and Structures,* vol. 21, no. 8, pp. 769-778.

Lynn, P.A. 1989, "Introduction to the Analysis and Processing of Signals"*,* Hemisphere Publishing Corporation.

Macquisten, M.A., Holt, A., Whiteman, M., Moran, A.J. & Rupp, J. 2006, "Passive damper LP tests for controlling combustion instability", *ASME Turbo Expo, GT2006-90874*, May 8-11, Barcelona, Spain.

Maxworthy, T. 1977, "Some experimental studies of vortex rings", *Journal of Fluid Mechanics,* vol. 81, no. 3, pp. 465-495.

Melling, T.H. 1973, "The acoustic impedance of perforates at medium and high sound pressure levels", *Journal of Sound and Vibration,* vol. 29, no. 1, pp. 1-65.

Mendez, S. & Eldredge, J. 2009, "Acoustic modeling of perforated plates with bias flow for Large-Eddy Simulations", *Journal of Computational Physics,* vol. 228, no. 13, pp. 4757-4772.

Michalke, A. 1972, "The instability of free shear layers", *Progress in Aerospace Sciences,* vol. 12, pp. 213-216.

Midgley, K. 2005, "An isothermal experimental study of the unsteady fluid mechanics of gas turbine fuel injector flow fields", Loughborough University.

Moler, C.B. 2004, "Numerical computing with MATLAB"*,* Society for Industrial Mathematics.

Mongia, H.C., Held, T.J., Hsiao, G.C. & Pandalai, R.P. 2003, "Challenges and progress in controlling dynamics in gas turbine combustors", *Journal of Propulsion and Power,* vol. 19, no. 5, pp. 822-829.

Montgomery, D.C. & Runger, G.C. 1994, "Applied statistics and probability for engineers"*,* Wiley.

Moran, A.J., Steele, D. & Dowling, A.P. 2001, “Active control of combustion and its applications”, DTIC Document, ADP011145.

Morfey, C.L. 1971, "Acoustic energy in non-uniform flows", *Journal of Sound and Vibration,* vol. 14, no. 2, pp. 159-170.

Morris, A.S. 2001, “Measurement and instrumentation principles”*,* Butterworth-Heinemann.

Oertel, H. & Böhle, M. 2002, “Strömungsmechanik: Grundlagen-Grundgleichungen-Lösungsmethoden-Softwarebeispiele”*,* Vieweg Verlag.

Paschereit, C.O., Gutmark, E. & Weisenstein, W. 1999, "Control of combustion driven oscillations by equivalence ratio modulations", *ASME Turbo Expo, 99-GT-118*, June 7-10, Indianapolis, IN.

Paschereit, C.O., Schuermans, B., Polifke, W. & Mattson, O. 2002, "Measurement of transfer matrices and source terms of premixed flames", *Journal of Engineering for Gas Turbines and Power,* vol. 124, pp. 239-247.

Patte-Rouland, B., Lalizel, G., Moreau, J. & Rouland, E. 2001, "Flow analysis of an annular jet by particle image velocimetry and proper orthogonal decomposition", *Measurement Science and Technology,* vol. 12, pp. 1404-1412.

Peacock, G. 2011, “Fuel injector impedance measurements”.

Poinsot, T., Le Chatelier, C., Candel, S. & Esposito, E. 1986, "Experimental determination of the reflection coefficient of a premixed flame in a duct", *Journal of Sound and Vibration,* vol. 107, no. 2, pp. 265-278.

Poinsot, T.J., Trouve, A.C., Veynante, D.P., Candel, S.M. & Esposito, E.J. 1987, "Vortex-driven acoustically coupled combustion instabilities", *Journal of Fluid Mechanics,* vol. 177, no. 1, pp. 265-292.

Pope, S.B. 2000, “Turbulent flows”*,* Cambridge University Press.

Prather, M., Sausen, R., Grossman, A.S., Haywood, J.M., Rind, D. & Subbaraya, B.H. 1999, "Potential climate change from aviation", *Aviation and the Global Atmosphere, Intergovernmental Panel on Climate Change*, editors J.E. Penner, D.H. Lister, D.J. Griggs, D.J. Dokken & M. McFarland, Cambridge University Press.

Putnam, A.A. 1971, “Combustion-driven oscillations in industry”*,* Elsevier New York.

Raffel, M., Willert, C.E., Wereley, S. & Kompenhans, J. 2007, “Particle image velocimetry: a practical guide”*,* 2nd edition, Springer Verlag.

Rayleigh, J.W.S. 1896, “The Theory of Sound, Vol. 2”*,* 2nd edition, 1945, Dover, New York.

Richards, G.A., Straub, D.L. & Robey, E.H. 2003, "Passive control of combustion dynamics in stationary gas turbines", *Journal of Propulsion and Power,* vol. 19, no. 5, pp. 795-810.

Rijke, P.L. 1859, "LXXI. Notice of a new method of causing a vibration of the air contained in a tube open at both ends", *The London, Edinburgh, and Dublin Philosophical Magazine and Journal of Science,* vol. 17, no. 116, pp. 419-422.

Riley, A.J., Park, S., Dowling, A.P., Evesque, S. & Annaswamy, A.M. 2003, "Adaptive closed-loop control on an atmospheric gaseous lean-premixed combustor", *ASME Turbo Expo, GT2003-38418*, June 16–19, Atlanta, Georgia.

Robinson, M.D. 2009, "Unsteady inlet condition generation for large eddy simulation CFD using particle image velocimetry", Loughborough University.

Robinson, M.D. 2006, "Xact - User's guide", Loughborough University.

Rogers, D.E. & Marble, F.E. 1956, "A mechanism for high-frequency oscillation in ramjet combustors and afterburners", *Jet Propulsion,* vol. 26, no. 6, pp. 456-462.

Rolls-Royce 2010, "Powering a better world Health, safety and environment report".

Rolls-Royce 2005, "The jet engine".

Rouse, H. & Abul-Fetouh, A. 1950, "Characteristics of irrotational flow through axially symmetric orifices", *Journal of Applied Mechanics,* vol. 17, no. 12, pp. 421-426.

Rowbury, D.A., Oldfield, M.L.G. & Lock, G.D. 2001, "Large-scale testing to validate the influence of external crossflow on the discharge coefficients of film cooling holes", *Journal of Turbomachinery,* vol. 123, pp. 593-600.

Rupp, J. & Carrotte, J.F. 2011, "Acoustic energy/velocity field interactions for circular holes", *Annual Review*, Loughborough University.

Rupp, J., Carrotte, J.F. & Macquisten, M.A. 2012, "The use of perforated damping liners in aero gas turbine combustion systems", *Journal of engineering for gas turbines and power,* vol. 134, no. 7, pp. 071502.

Rupp, J., Carrotte, J.F. & Spencer, A. 2010b, "Methodology to identify the unsteady flow field associated with the loss of acoustic energy in the vicinity of circular holes", *ASME Turbo Expo, GT 2010-22178*, June 14-18, Glasgow, UK.

Rupp, J., Carrotte, J.F. & Spencer, A. 2010, "Interaction between the acoustic pressure fluctuations and the unsteady flow field through circular holes", *Journal of Engineering for Gas Turbines and Power,* vol. 132, no. 6, pp. 061501.

Saffman, P.G. 1992, "Vortex dynamics", Cambridge University Press.

Saffman, P.G. 1970, "The velocity of viscous vortex rings", *Studies in Applied Mathematics,* vol. 49, no. 4, pp. 371-380.

Salikuddin, M. & Brown, W. 1990, "Non-linear effects in finite amplitude wave propagation through orifice plate and perforated plate terminations", *Journal of Sound and Vibration,* vol. 139, no. 3, pp. 383-405.

Salikuddin, M., Syed, A. & Mungur, P. 1994, "Acoustic characteristics of perforated sheets with throughflow in a high intensity noise environment", *Journal of Sound and Vibration,* vol. 169, no. 2, pp. 145-177.

Sattelmayer, T. 2003, "Influence of the combustor aerodynamics on combustion instabilities from equivalence ratio fluctuations", *Journal of Engineering for Gas Turbines and Power,* vol. 125, pp. 11-19.

Scarano, F. & Riethmuller, M. 2000, "Advances in iterative multigrid PIV image processing", *Experiments in Fluids,* vol. 29, pp. 51-60.

Scarinci, T. 2005, "Combustion instability and its passive control: Rolls-Royce aeroderivative engine experience", *Combustion Instabilities in Gas Turbine Engines Operational Experience, Fundamental Mechanisms and Modeling*, editors T.C. Lieuwen & V. Yang, AIAA.

Scarinci, T. & Halpin, J.L. 2000, "Industrial trent combustor - combustion noise characteristics", *Journal of Engineering for Gas Turbines and Power,* vol. 122, pp. 280-286.

Schoeneborn, P.R. 1975, "The interaction between a single particle and an oscillating fluid", *International Journal of Multiphase Flow,* vol. 2, pp. 307-317.

Schram, C. & Riethmuller, M.L. 2002, "Measurement of vortex ring characteristics during pairing in a forced subsonic air jet", *Experiments in Fluids,* vol. 33, no. 6, pp. 879-888.

Schram, C. & Riethmuller, M. 2001, "Vortex ring evolution in an impulsively started jet using digital particle image velocimetry and continuous wavelet analysis", *Measurement Science and Technology,* vol. 12, pp. 1413-1421.

Schuermans, B. 2003, “Modeling and control of thermoacoustic instabilities”, École Polytechnique Fédérale de Lausanne.

Schuermans, B., Guethe, F., Pennell, D., Guyot, D. & Paschereit, C.O. 2010, "Thermoacoustic modeling of a gas turbine using transfer functions measured under full engine pressure", *Journal of Engineering for Gas Turbines and Power,* vol. 132, pp. 111503.

Selamet, A. & Lee, I. 2003, "Helmholtz resonator with extended neck", *The Journal of the Acoustical Society of America,* vol. 113, pp. 1975-1985.

Seo, S.H. & Kim, Y.H. 2005, "Silencer design by using array resonators for low-frequency band noise reduction", *The Journal of the Acoustical Society of America,* vol. 118, pp. 2332-2338.

Seybert, A. & Ross, D. 1977, "Experimental determination of acoustic properties using a two-microphone random-excitation technique", *The Journal of the Acoustical Society of America,* vol. 61, no. 5, pp. 1362-1370.

Seybert, A. & Soenarko, B. 1981, "Error analysis of spectral estimates with application to the measurement of acoustic parameters using random sound fields in ducts", *The Journal of the Acoustical Society of America,* vol. 69, pp. 1190-1199.

Siegel, D. & Plueddemann, A. 1991, "The motion of a solid sphere in an oscillating flow- An evaluation of remotely sensed Doppler velocity estimates in the sea", *Journal of Atmospheric and Oceanic Technology,* vol. 8, pp. 296-304.

Sirovich, L. 1987, "Turbulence and the dynamics of coherent structures. Part I: Coherent structures", *Quarterly of Applied Mathematics,* vol. 45, no. 3, pp. 561-571.

Steele, R.C., Cowell, L.H., Cannon, S.M. & Smith, C.E. 2000, "Passive control of combustion instability in lean premixed combustors", *Journal of Engineering for Gas Turbines and Power,* vol. 122, pp. 412-419.

Stow, S.R. & Dowling, A.P. 2003, "Modelling of circumferential modal coupling due to Helmholtz resonators", *ASME Turbo Expo, GT 2003-38168*, June 16-19, Atlanta, Georgia.

Sullivan, I.S., Niemela, J.J., Hershberger, R.E., Bolster, D. & Donnelly, R.J. 2008, "Dynamics of thin vortex rings", *Journal of Fluid Mechanics,* vol. 609, no. 1, pp. 319-347.

Sun, X., Jing, X., Zhang, H. & Shi, Y. 2002, "Effect of grazing–bias flow interaction on acoustic impedance of perforated plates", *Journal of Sound and Vibration,* vol. 254, no. 3, pp. 557-573.

Tam, C.K.W., Ju, H., Jones, M., Watson, W. & Parrott, T. 2010, "A computational and experimental study of resonators in three dimensions", *Journal of Sound and Vibration,* vol. 329, no. 24, pp. 5164-5193.

Tam, C.K.W. & Kurbatskii, K.A. 2000, "Microfluid dynamics and acoustics of resonant liners", *AIAA Journal,* vol. 38, no. 8, pp. 1331-1339.

Tam, C.K.W., Kurbatskii, K.A., Ahuja, K. & Gaeta, R. 2001, "A numerical and experimental investigation of the dissipation mechanisms of resonant acoustic liners", *Journal of Sound and Vibration,* vol. 245, no. 3, pp. 545-557.

Tang, S. 2005, "On Helmholtz resonators with tapered necks", *Journal of Sound and Vibration,* vol. 279, no. 3-5, pp. 1085-1096.

Testud, P., Aurégan, Y., Moussou, P. & Hirschberg, A. 2009, "The whistling potentiality of an orifice in a confined flow using an energetic criterion", *Journal of Sound and Vibration,* vol. 325, no. 4, pp. 769-780.

Tondast-Navaei, A. 2005, “Acoustic particle image velocimetry - Development and applications”, The Open University.

Tran, N., Ducruix, S. & Schuller, T. 2008, "Passive control of the inlet acoustic boundary of a swirled turbulent burner", *ASME Turbo Expo, GT2008-50425*, June 9-13, Berlin, Germany.

Umeh, C.O., Kammer, L.C. & Barbu, C. 2007, "Active combustion control by fuel forcing at non-coherent frequencies", *ASME Turbo Expo, GT2007-27637*, May 14-17, Montreal, Canada.

Wendoloski, J.C. 1998, "Sound absorption by an orifice plate in a flow duct", *The Journal of the Acoustical Society of America,* vol. 104, no. 1, pp. 122-132.

Westerweel, J. 1997, "Fundamentals of digital particle image velocimetry", *Measurement Science and Technology,* vol. 8, pp. 1379-1392.

Westerweel, J. 1994, "Efficient detection of spurious vectors in particle image velocimetry data", *Experiments in Fluids,* vol. 16, no. 3, pp. 236-247.

Whiffen, M.C. & Ahuja, K.K. 1983, "An improved schlieren system and some new results on acoustically excited jets", *Journal of Sound and Vibration,* vol. 86, no. 1, pp. 99-105.

Wigley, G. 2008, “SAFEX fog generator particle size measurement”, Loughborough University.

Xu, M., Selamet, A. & Kim, H. 2010, "Dual Helmholtz resonator", *Applied Acoustics,* vol. 71, no. 9, pp. 822-829.

Yang, V. & Anderson, W.E. 1995, “Liquid rocket engine combustion instability”*,* AIAA.

Yule, A.J. 1978, "Large-scale structure in the mixing layer of a round jet", *Journal of Fluid Mechanics,* vol. 89, no. 3, pp. 413-432.

Zhao, D., A'BARROW, C., Morgans, A.S. & Carrotte, J. 2009, "Acoustic Damping of a Helmholtz Resonator with an Oscillating Volume", *AIAA journal,* vol. 47, no. 7, pp. 1672-1679.

Zhao, D. & Morgans, A.S. 2009, "Tuned passive control of combustion instabilities using multiple Helmholtz resonators", *Journal of Sound and Vibration,* vol. 320, no. 4-5, pp. 744-757.

Zinn, B.T. 1970, "A theoretical study of non-linear damping by Helmholtz resonators", *Journal of Sound and Vibration,* vol. 13, no. 3, pp. 347-356.

Appendix

A. Orifice Geometry Definition

A.1 Orifice Geometries for Absorption Measurements

The orifice plates investigated for the absorption experiments described in section 3.2.1 are specified in Table A.1. In the majority of cases the plates contain only one aperture. However the plate with 3.3 mm orifice diameter contains multiple apertures to increase the absorption of the orifice geometry which improved the measurement accuracy. The diameters of the orifice were scaled to the relevant gas turbine engine conditions (section 3.1). Where applicable the porosity and pitch-to-diameter ratio was chosen to similar arrangements of gas turbine cooling geometries. For these values it is assumed that the apertures within the gas turbine combustor cooling geometry are not interacting (i.e. so allowing their absorption characteristic to be investigated in isolation).

In total 17 orifice geometries have been investigated and their linear and non-linear absorption has been measured. The length-to-diameter ratios L/D ranged from 0.5-10, this range being relevant for the geometries found within gas turbine combustors. In addition to cylindrical orifice plates various alternative orifice geometries where investigated to enable an assessment on the effect of aperture geometry on linear and non-linear absorption. Table A.2 shows schematics of the orifice shapes investigated in this work. In general the shapes have been designed with the aim of showing significant differences to cylindrical apertures. The conical shapes where used to investigate the effect of sharp edged geometries on the linear and non-linear absorption as some beneficial effects in the non-linear regime have been noted within tapered necks on Helmholtz resonators (Tang (2005)). A stepped geometry was designed to utilise multiple edges over which vorticity can be shed and the effect of this geometry upon its acoustic absorption can be investigated. As a comparison a shallow angled effusion hole was also investigated. However, this was done without the effects of cross-flow upon

the orifice flow field. Finally a Bellmouth geometry was investigated. The Bellmouth geometries were included based on the observations from Keller and Zauner (1995) who noted improvements in acoustic absorption if the aerodynamic loss coefficients associated with the resonator neck were small.

Plate No	**Aperture diameter *D* in mm**	**Aperture length *L* in mm**	***L/D***	**Amount of holes**	**Porosity σ in %**	***P_a/D***	**Shape**
1	12.7	6	0.47	1	0.88	4.7	cylindrical
2	3.3	4.95	1.5	5	0.3	10	cylindrical
3	9.1	4.55	0.5	1	0.45	6.6	cylindrical
4	9.1	9.1	1	1	0.45	6.6	cylindrical
5	9.1	13.65	1.5	1	0.45	6.6	cylindrical
6	9.1	18	1.98	1	0.45	6.6	cylindrical
7	9.1	21.84	2.4	1	0.45	6.6	cylindrical
8	9.1	27.3	3	1	0.45	6.6	cylindrical
9	9.1	45.5	5	1	0.45	6.6	cylindrical
10	9.1	61.88	6.8	1	0.45	6.6	cylindrical
11	9.1	91	10	1	0.45	6.6	cylindrical
12	9.1	18	1.98	1	0.45	6.6	Conical, α=30°
13	9.1	18	1.98	1	0.45	6.6	Conical, α=45°
14	9.1	18	1.98	1	0.45	6.6	Conical, α=60°
15	9.1	18	1.98	1	0.45	6.6	Sharp edged, α=45°
16	9.1	18	1.98	1	0.45	6.6	Stepped S_x = 1mm S_y = 4.5mm
17	9.1	18	1.98	1	0.45	6.6	Bellmouth r_B=18mm

Table A.1: Orifice plate specification for absorption measurements

Orifice shape	**Schematic, not to scale**
Cylindrical	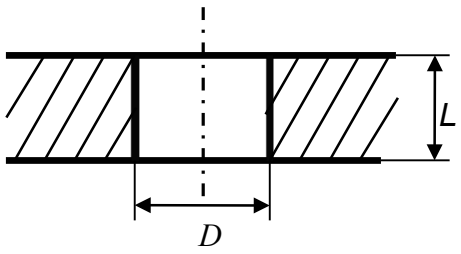
Conical	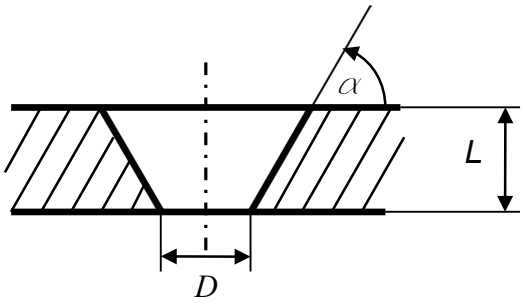
Sharp edged	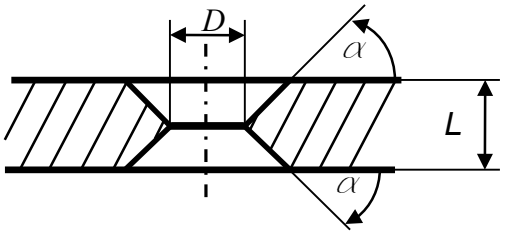
Stepped	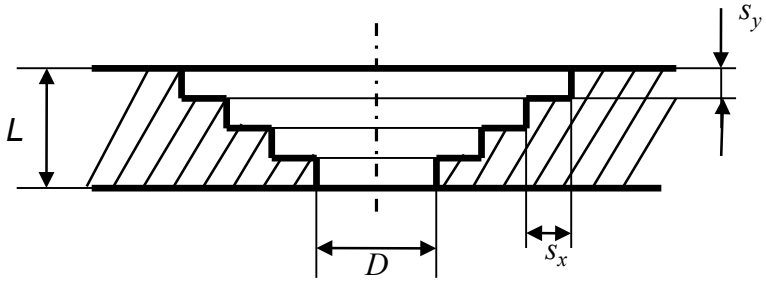
Bellmouth	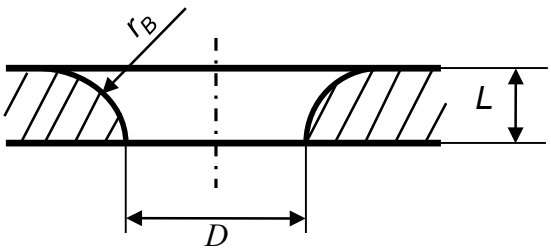

Table A.2: Definition of orifice shapes

A.2 Orifice Geometries for Rayleigh Conductivity measurement

The orifice geometries investigated for Rayleigh Conductivity measurements are shown in Table A.3. The orifice length-to-diameter ratio was ranging from $0.14 < L/D < 10$. In this case additional thinner orifice plates were investigated to simulate orifice plates with negligible thickness as it is assumed in the analytical model described in Howe (1979b). However, some thickness was needed to avoid structural vibration affecting the measurement. Moreover to improve the accuracy of the measurement over the large frequency range the porosity of the orifice plates has been increased.

Plate No	Aperture diameter *D* in mm	Aperture length *L* in mm	*L/D*	Amount of holes	Porosity σ in %	P_d/D	Shape
18	9.1	1.3	0.14	9	4.1	4.4	Cylindrical
19	12	3	0.25	9	7.1	3.33	Cylindrical
20	12	6	0.5	9	7.1	3.33	Cylindrical
21	10.5	8	0.76	9	5.4	3.8	Cylindrical
22	9.1	9.1	1	9	4.1	4.4	Cylindrical
23	9.1	13.65	1.5	9	4.1	4.4	Cylindrical
24	9.1	18	1.98	9	4.1	4.4	Cylindrical
25	9.1	21.84	2.4	9	4.1	4.4	Cylindrical
26	9.1	27.3	3	9	4.1	4.4	Cylindrical
27	9.1	45.5	5	9	4.1	4.4	Cylindrical
28	9.1	61.88	6.8	9	4.1	4.4	Cylindrical
29	9.1	91	10	9	4.1	4.4	Cylindrical
30	6.5	3.3	0.51	9	2.1	6.15	Cylindrical
31	12	6	0.5	9	7.1	3.33	Bellmouth $r_B = 3$ mm
32	10.5	8	0.76	9	5.4	3.8	Bellmouth $r_B = 3$ mm
33	9.1	18	1.98	9	4.1	4.4	Bellmouth $r_B = 9$mm

Table A.3: Orifice plate definition for Rayleigh Conductivity measurements

A.3 Test Specimen for Combustion System Representative Acoustic Liners Without The Influence of the Fuel Injector Flow Field

The investigated damper geometries are specified in Table A.4. In this case the damping skin consisted of a multi aperture perforated liner. The metering skin (Plate 37) was designed to have a high inertia. Hence the long holes with a large length-to-diameter ratio. Thus it is assumed that the aperture acts as a solid wall which transmits negligible noise out of the cavity into the surrounding test cell. This assumption has also been investigated within the results section for the experiments undertaken on this test facility.

Plate	Aperture diameter *D* in mm	Aperture length *L* in mm	*L*/*D*	Amount of holes	Porosity σ in %	P_a/D	Liner function
34	1.1	6	5.45	192	3.9	4.5	Damping
35	1.1	8	7.27	184	3.7	4.5	Damping
36	1.1	12	10.9	192	3.9	4.5	Damping
37	1.2	20	16.67	59	1	10	Metering

Table A.4: Definition of passive damper with resonant cavity

The described combinations of damper liners and metering liners are then combined with each other to form a resonating cavity tuned to the relevant frequencies. Table A.5 shows the various combinations. Most of the combinations were undertaken at constant volume with liner separation S_D = 64.7 mm. However as a further variation the distance has been increased to 104.7 mm for configuration 4.

Configuration	Damper plate	Metering plate	Spacing *S* in mm
1	34	37	64.7
2	35	37	64.7
3	36	37	64.7
4	34	37	104.7

Table A.5: Resonating damper configuration

A.4 Damper Test Geometry for Acoustic Dampers Exposed to Fuel Injector Flow Field

The damper geometries exposed to a representative fuel injector flow field are discussed in this section; the fuel injector geometry will not be presented as its geometry is confidential. Table A.6 specifies the geometric definition for the investigated passive damping system. All the orifices within the damping skin and metering skin were cylindrical and drilled normal to the liner surface. The damping skin was optimised so that a high porosity for a minimised pressure drop could be achieved. However a minimum pressure drop is required so there is no steady inflow of hot gases from the combustor into the damper cavity. Moreover, the amount of air for such a system is specified by the wall cooling budget of the gas turbine combustor. Hence the maximum porosity available cannot exceed the wall cooling budget of the system.

The damping skin and the metering skin were separated to form a rectangular cavity. This cavity was not tuned to resonate at the frequencies investigated. A sensitivity of the distance between the damping skin and metering skin was conducted. Therefore the separation was varied throughout the experiments from $0.125 \le S/H \le 1.46$, where H is the height of the duct as shown in Figure 3.9.

Liner	Aperture diameter *D* in mm	Aperture length *L* in mm	*L/D*	Amount of holes	Porosity σ in %	P_a/D	Shape
Damping liner	0.7	2	2.86	1490	3.56	4.3	Cylindrical
Metering liner	1	2	2	252	1.23	7.2	Cylindrical

Table A.6: Definition of passive damper for non-resonant cavity experiments

B. Effective Flow Area Experiments

A variation of orifice plates are investigated in terms of their acoustic absorption characteristic. As already discussed in the previous chapters the acoustic absorption of an aperture is dependent on the mean flow Strouhal number across the orifice equation (1.16). This Strouhal number definition uses the velocity in the plane of the aperture. Thus the discharge coefficient of the orifice geometry has to be known for the calculation of the mean velocity in the plane of the aperture based on the measured mean velocity at the end of the vena contracta:

$$\overline{U}_D = C_D \overline{U}_d \,. \tag{A.1}$$

The discharge coefficient can be calculated from a known mass flow and pressure difference across the orifice as defined in equation (2.5). Thus a test rig has been used to measure the discharge coefficient for steady state flow conditions. The test rig consisted of a plenum chamber of 3763 mm^3. All the investigated orifice plates (Table A.1 - A.3) were connected to this volume. A Cole Parmer 0-250 SLPM (standard liters per minute) air mass flow meter was used to accurately measure the air flow rate into the plenum chamber. Moreover the static pressure inside the plenum was measured using a tapping connected to Furnace FC0510 Micro-Manometer. And finally the air temperature was measured using a K-Type thermo-couple within the plenum chamber connected to a TME Model 6000 Thermocouple thermometer. The accuracy of the mass flow meter was $\pm 0.8\%$ of reading +0.2% of full scale (Cole-Parmer (2009)). Moreover the accuracy of the Micro-Manometer was $\pm 0.1\%$ and the temperature measurement is of the order of ± 0.6 C as indicated on the TME data sheet. This can therefore lead to an accuracy of the discharge coefficient measurement of $\pm 1\%$.

The steady state discharge coefficients have been measured for mean pressure drops across the orifice of dp/p = 0.1%-1.0%. This results in Reynolds numbers larger than 7000 which is sufficient for the measured discharge coefficients to remain constant with changing pressure drop as indicated in Lichtarowicz et. al. (1965).

C. Validation of the Methodology to Identify the Acoustically Related Flow Field

In this section the validation of the developed methodology to identify the acoustically related flow field will be described as in Rupp et. al. (2010b). Initially the acoustically related flow field relevant to the non-linear acoustic absorption will be validated and subsequently the linear acoustic absorption regime. The validation will be based on the acoustic absorption measurements discussed in chapter 5 and 6.

C.1 Kinetic Energy Balance - Non-Linear Absorption Regime

To validate the methodology, and its ability to identify the flow structures associated with acoustic absorption, the energy content of the flow field can be considered. Energy to drive the total velocity field can originate either from (i) the centrifugal fan used to draw air through the test section or (ii) or the loudspeakers generating a pressure wave which controls the unsteady pressure drop across the aperture. The energy derived from the centrifugal fan can be determined by the mean pressure drop across the orifice and the volume flow rate i.e.

$$\Pi = \Delta p \dot{V} . \tag{C.1}$$

The acoustic energy loss was calculated from the difference in the flux of acoustic energy going towards (in), and away from (out) the orifice for each side of the orifice. The acoustic energy flux was calculated as

$$\Pi^{\pm} = \frac{A}{2\rho c}(1 \pm M)^2 \left|\hat{p}^{\pm}\right|^2 \tag{C.2}$$

and hence the loss of acoustic energy is defined as

$$\Pi = \Pi_{in}^{\pm} - \Pi_{out}^{\pm} . \tag{C.3}$$

For non-linear absorption only a small amount of air was drawn through the test section. Hence for the total velocity field typically 5% of the energy originated from the centrifugal fan with 95% being absorbed from the acoustic field. The kinetic energy in

the flow field was calculated using a similar method as described in Tam and Kurbatskii (2000). The flow field was assumed to be axis-symmetric as indicated in the schematic in Figure C.1. The kinetic energy is defined as:

$$E_{kin} = \frac{1}{2} m \vec{u}^2 . \tag{C.4}$$

In this case the mass is defined as:

$$m = \rho V . \tag{C.5}$$

Thus the kinetic energy within the flow field has to be integrated over the total cylindrical volume:

$$E_{kin} = \rho\pi \int_0^L \int_0^R \left(u(r,t)^2 + v(r,t)^2 \right) r \, dr \, dy . \tag{C.6}$$

The radius is then replaced by the coordinate x and the integrals is replaced by a numerical summation:

$$E_{kin} = \rho\pi \sum_0^{Y\max} \sum_0^{X\max} \left(u^2 + v^2 \right) x \, dx \, dy. . \tag{C.7}$$

This, of course, is calculated from the acoustically related reconstructed flow field for every recorded time step.

A further point that needs to be considered is, for the non-linear absorption case, whether the mean flow should be included in the reconstructed flow field from which the kinetic energy is calculated. Intuitively one might suspect that the mean flow field should not be included. However, as already indicated the acoustic field is responsible for generating vortex ring type structures which induces a mean velocity field. This mean flow field is responsible for the convection of each ring structure away from the orifice. This is further suggested by the change in the mean velocity field that was observed for the case with and without excitation (Figure C.2). Hence some of the energy absorbed from the acoustic field must be present in the mean flow field. Thus the reconstructed flow field consists of the mean flow field (with excitation) together with all the ‘acoustic related’ modes. The kinetic energy loss associated with the centrifugal

fan (equation (C.1)) must then be subtracted from the kinetic energy of the reconstructed 'acoustically related' flow field.

An example of the total kinetic energy calculated from the upstream and downstream reconstructed flow fields can be seen in Figure C.3 at various time steps during the acoustic cycle. Note that the frequency at which the PIV measurements were obtained (1100 Hz) was not a multiple of the acoustic excitation frequency (125 Hz). This was done to ensure data was obtained at all phases of the excitation cycle during the period of data capture and accounts for the slight variations in the kinetic energy maxima observed between acoustic cycles. It can be seen that the energy shows a maximum in the upstream and downstream field exactly once per cycle. In reality the fluctuating pressure drop across the orifice caused by the acoustic waves generates a pulsatile flow within the orifice and, as flow is discharged from the orifice, a ring vortex structure is generated. As this structure grows so the kinetic energy associated with this structure increases. Eventually the structure is swept away from the orifice and the kinetic energy within the field of view decreases. This phenomenon happens once per cycle either side of the orifice and is reflected in the observed variations in kinetic energy (Figure C.3). Note that the small mean flow through the orifice is responsible for the greater energy observed within the downstream vortex structures. The maxima of the kinetic energy have been averaged and divided by the time period of one acoustic cycle:

$$\Pi = \frac{E_{kin}}{T}. \tag{C.8}$$

The maximum energy loss as well as the averaged energy loss was then compared to the acoustic loss as shown in Figure C.4. The maximum acoustic energy loss was calculated using the maximum measured energy in the upstream and downstream flow field (e.g. $6.5\text{x}10^{-4}$ J downstream and $4.1\text{x}10^{-4}$ J upstream in Figure C.3). The mean energy loss was calculated by ensemble averaging the energy maxima in the upstream and downstream flow field. It can be seen that the energy calculated using the reconstructed flow fields agree with the energy that is being absorbed from the acoustic field. The discrepancies are caused if the maximum kinetic energy within the vortex ring structure is not captured within the measured flow fields. Hence the maximum kinetic energy shows the better agreement with the method. Moreover some of the

kinetic energy might have already been lost due to viscous dissipation. This is already a very good indication that the reconstructed acoustically related flow field is representative of the flow field associated with the acoustic absorption. More evidence for this conclusion can be found in the following section where the energy flux balance is used within the non-linear and linear regime.

C.2 Energy Flux Balance – Non-Linear and Linear absorption Regime

The fluid dynamics of the linear absorption process makes it difficult to apply the same method used previously for validating the methodology. This is due to the continuous shedding of coherent structures which gives rise to issues associated with identifying which structures are related to a given acoustic cycle, are all the structures captured in the field of view etc. In addition, the scale of these structures means that the transfer of energy into the random turbulent flow field will occur relatively quickly i.e. so some of the absorbed energy will be present in the random turbulent POD modes rather than the 'acoustic related' modes. Hence an alternative method has to be adopted, which can be used within the linear and non-linear absorption regime.

The kinetic energy flux of the flow, normal to the *x*-*z*-plane (Figure C.5), was calculated for various downstream locations and instances in time. This was done using the flow field reconstructed from the 'acoustic related' modes. The acoustic energy flux is defined as

$$\dot{E} = \frac{1}{2}\dot{m}\vec{v}^{\,2}. \tag{C.9}$$

Moreover the mass flow through the aperture can be defined using the *v*-velocity component and an integration across the circular aperture area. Hence the kinetic energy flux at a given radius r and time t can be defined as:

$$d\dot{E} = \frac{1}{2}\rho v(r,t)\,\vec{v}(r,t)^2\,dA. \tag{C.10}$$

Using a circular area just downstream the orifice and integrating over the radial coordinate results in (e.g. Pope (2000))

$$\dot{E} = \rho\pi \int_0^R v(r,t)\,(u(r,t)^2 + v(r,t)^2)\, r\, dr\,. \tag{C.11}$$

Thus the kinetic energy flux of the flow field through the aperture was expressed using the *x*-coordinate in radial direction:

$$\dot{E} = \rho\pi \sum_0^{X\max} v(x,t)\,(u(x,t)^2 + v(x,t)^2)\, x\, \Delta x\,. \tag{C.12}$$

C.2.1 Non-Linear Absorption Regime

The kinetic energy flux, as defined in equation (C.12), was applied immediately upstream and downstream of the orifice as indicated in Figure C.6. The actual coordinate in the upstream and downstream flow field for the integration of the kinetic energy flux is defined in Table C.1.

	y/D	
	Upstream	**Downstream**
131 dB	0.03	-0.07
137 dB	0.03	-0.07
142 dB	0.06	-0.07

Table C.1: Coordinates for energy flux calculation for flow field associated with the non-linear acoustic absorption regime

The result of this integration for some instances in time is shown in Figure C.7. The change in sign is due to the change in flow direction. The PIV measurement was triggered and thus synchronised with the function generator input to the loudspeakers. Therefore the phase relationship between the velocities in the upstream and downstream flow fields remained constant. Hence the maximum energy flux in the upstream and downstream flow field is 180° out of phase. During the low pressure part of the acoustic cycle the fluid is accelerated to the downstream side of the orifice and the maximum kinetic energy flux occurs on the downstream side, i.e. time step ~3 in Figure C.7. During the maximum pressure part of the acoustic cycle, the fluid is accelerated upstream and the maximum kinetic energy flux occurs in the upstream side of the aperture, i.e. time step 8 in Figure C.7. Moreover increases caused by the acceleration of the fluid into the aperture can also be seen, e.g. time step 3 in the upstream field and 8

in the downstream field. Hence the total kinetic energy flux averaged over the acoustic cycle can be calculated by investigating the kinetic energy flux of equal sign on each side of the aperture as indicated in Figure C.8. In this case the absolute of the kinetic energy flux in the downstream field was used. The averaged kinetic energy flux per acoustic cycle was then calculated by integrating both curves upstream and downstream of the aperture relative to the total sampling time of the velocity measurements:

$$\left\langle \dot{E}' \right\rangle = \frac{1}{T}\left(A_1 + A_2\right) = \frac{1}{T}\int_0^T \left(\dot{E}'_u + \dot{E}'_d\right) dt \,. \tag{C.13}$$

As already discussed both sides of the apertures are important during non-linear absorption as reverse flow is occuring. Hence the acoustic loss per cycle is split between the upstream and downstream flow fields. Furthermore as already discussed, the kinetic energy introduced by the centrifugal fan has to be deducted. In this case the kinetic energy flux of the mean flow field without excitation was calculated as shown in Figure C.9. Therefore the mean kinetic energy flux at y/D = -0.07 has been deducted from the unsteady kinetic energy flux of the forced case:

$$\Pi = \left\langle \dot{E}' \right\rangle - \left\langle \dot{E}_{unforced} \right\rangle . \tag{C.14}$$

The comparison between the calculated kinetic energy flux and the measured acoustic loss is shown in Figure C.10. The agreement between the acoustic energy loss and the kinetic energy flux within the acoustically related flow field is very good. Hence it can be concluded that the developed methodology is capturing the relevant fluid dynamic characteristics important to the non-linear acoustic absorption very well.

C.2.2 Linear Absorption Regime

Within the linear absorption regime, both the kinetic energy flux for the mean flow and the instantaneous flow are important and need to be calculated. The kinetic energy flux of the mean flow field $\left\langle \dot{E} \right\rangle$ is presented in Figure C.11 for an unsteady jet flow of 0.8% and 0.3% *dp/p* within the linear absorption regime where, as expected, the maximum energy flux occurs close to the orifice. The decreasing nature of the energy flux further downstream reflects the transfer of energy into random turbulence.

The instantaneous kinetic energy flux $\dot{E}'$ of the filtered flow, including the mean flow field, is shown in Figure C.12 at a location close to the orifice exit plane (i.e. so that only a small amount of energy has been dissipated into random turbulence). The data is presented for several acoustic cycles. The variation in kinetic energy reflects the pulsatile nature of the flow through the orifice due to the effect of the oscillating pressure drop on the jet flow. The peaks and troughs represent the points where the pulsatile flow reaches its maximum and minimum velocities. Note also that the case of 0.8% *dp/p* shows a larger modulation, relative to 0.3% *dp/p*, due to the larger excitation amplitude (137dB and 128dB respectively). For the current experimental configurations the acoustic energy transmitted through the orifice is several orders of magnitude less than the acoustic energy absorbed by the orifice. In other words all the energy associated with this pulsatile flow is being absorbed from the acoustic field. This pulsatile flow then generates the turbulent structures observed in the reconstructed flow field and which eventually decay into random turbulence.

This can be confirmed by comparing the acoustic energy being absorbed with the kinetic energy flux of the pulsatile flow. The instantaneous energy flux is therefore integrated over a complete cycle from which the mean energy flux has to be subtracted i.e.

$$\Pi = \left\langle \dot{E}' \right\rangle - \left\langle \dot{E} \right\rangle . \tag{C.15}$$

As already mentioned the mean energy flux is generated by the mean pressure drop due to the work input by the centrifugal fan. Figure C.13 shows, in contrast with the non-linear absorption the mean flow field with and without excitation is nearly identical. Hence it can be assumed that all the kinetic energy contained in the mean flow field is related to the work of the centrifugal fan. Thus the mean kinetic energy flux has to be deducted from the acoustically related kinetic energy flux (equation (C.15)).

The resulting energy flux is then compared to the acoustic energy loss. The loss of acoustic energy and the acoustic absorption coefficient has been measured simultaneously while measuring the velocity field using PIV. PIV experiments for the 9.1 mm diameter orifice plate with length-to-diameter ratios of 0.5, 1, 2, 3 and 5 have been conducted with excitation amplitudes as indicated in Figure C.14 and 62.5 Hz

excitation frequency. All of this data has then been compared to the measured acoustic energy loss in Figure C.15. It can be seen that the agreement between the acoustic energy loss and the measured acoustic energy flux is excellent for all the considered test cases. Moreover the filtering of the acoustically related modes is necessary to be able to identify the relevant flow properties carrying the relevant kinetic energy flux. As it can be seen the kinetic energy calculated by the total velocity field, i.e. the raw velocity field, would show far more energy than the measured acoustic energy loss. The PIV methodology of the acoustically related flow field was within 20% of the acoustic loss measurement, which is most likely the resolution of this challenging PIV application.

Figures

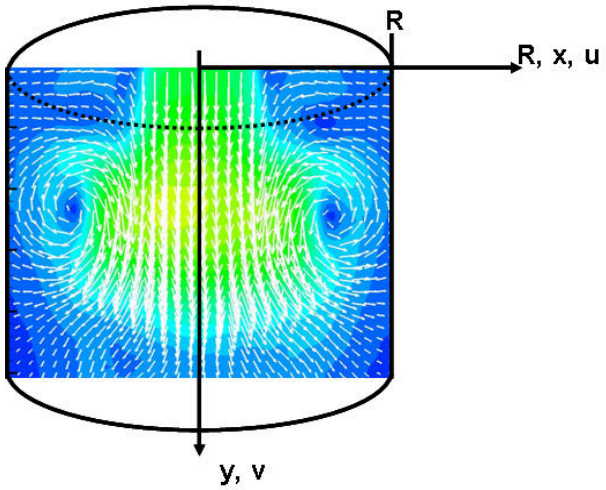

Figure C.1: Schematic of control volume of kinetic energy calculation in the non-linear absorption regime

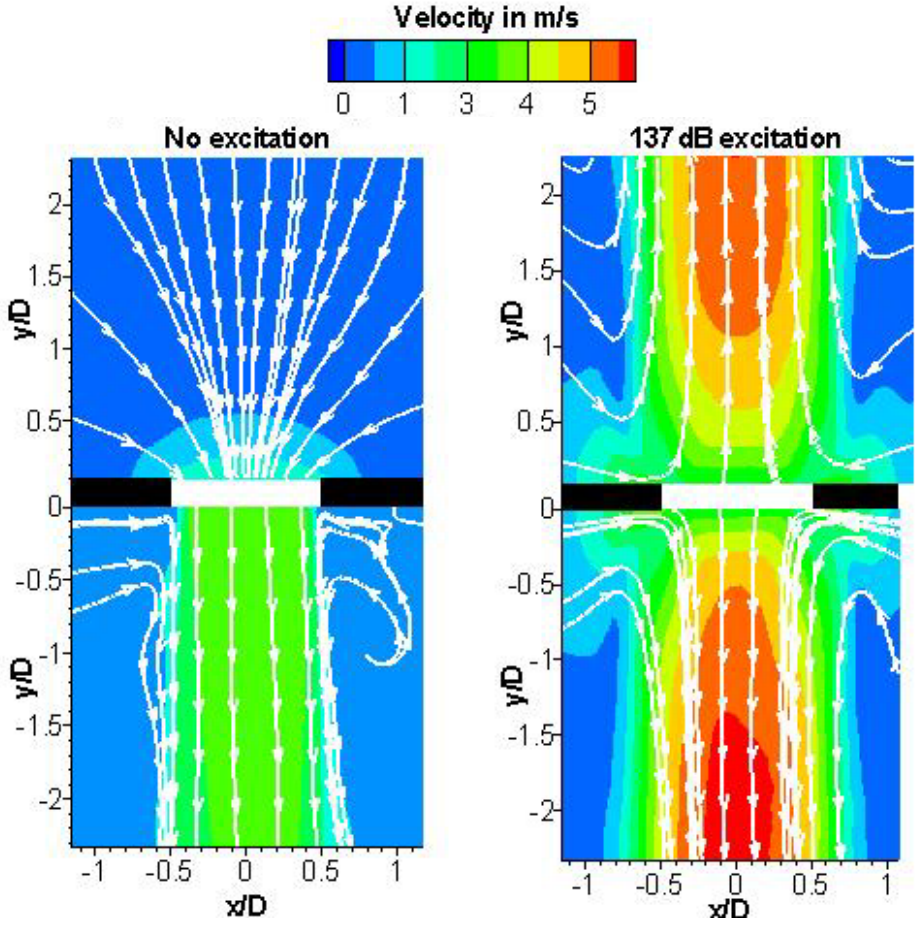

Figure C.2: Example of forced and unforced mean flow field, non-linear acoustic absorption, L/D = 0.47, f = 125 Hz, plate number 1.

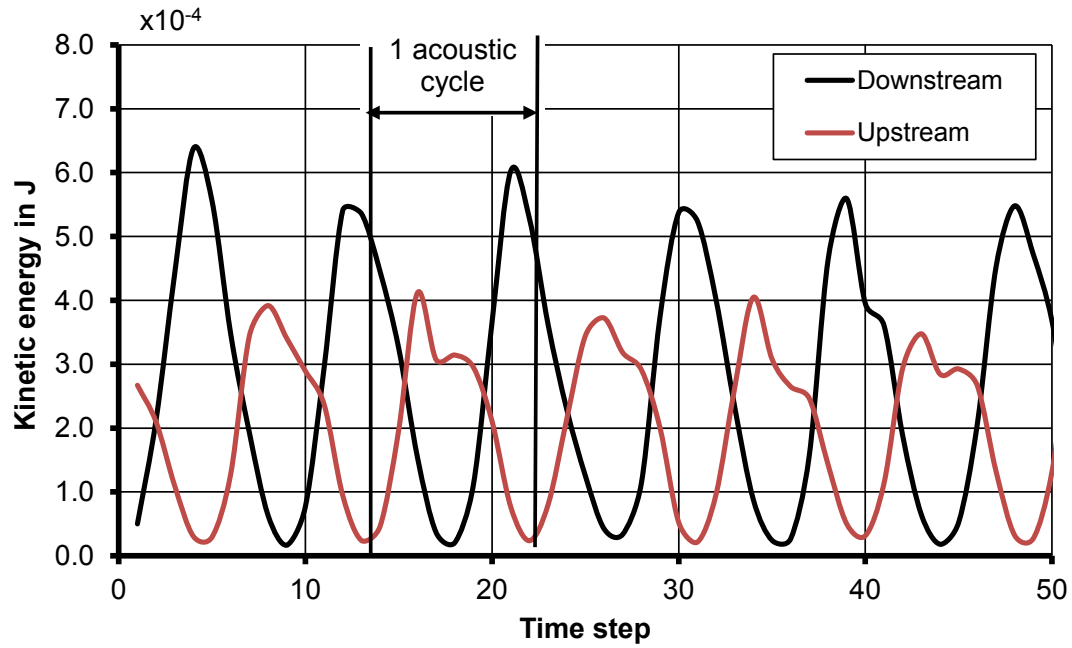

Figure C.3: Kinetic energy contained in the upstream and downstream flow field, non-linear acoustic absorption, plate number 1.

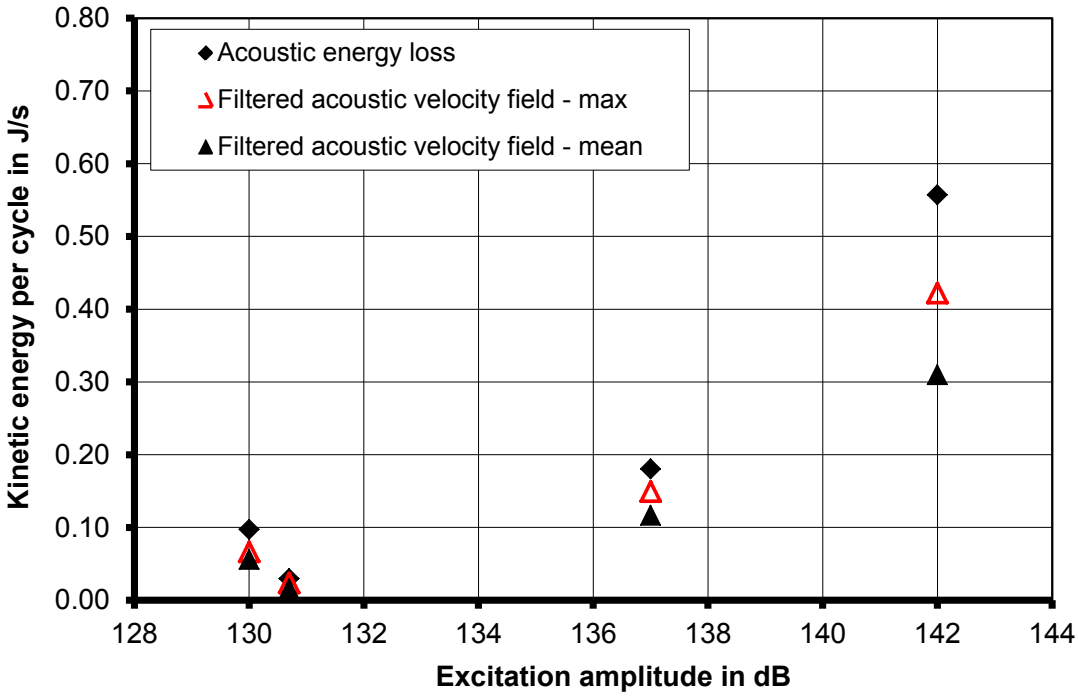

Figure C.4: Energy loss comparison (non-linear absorption), plate number 1.

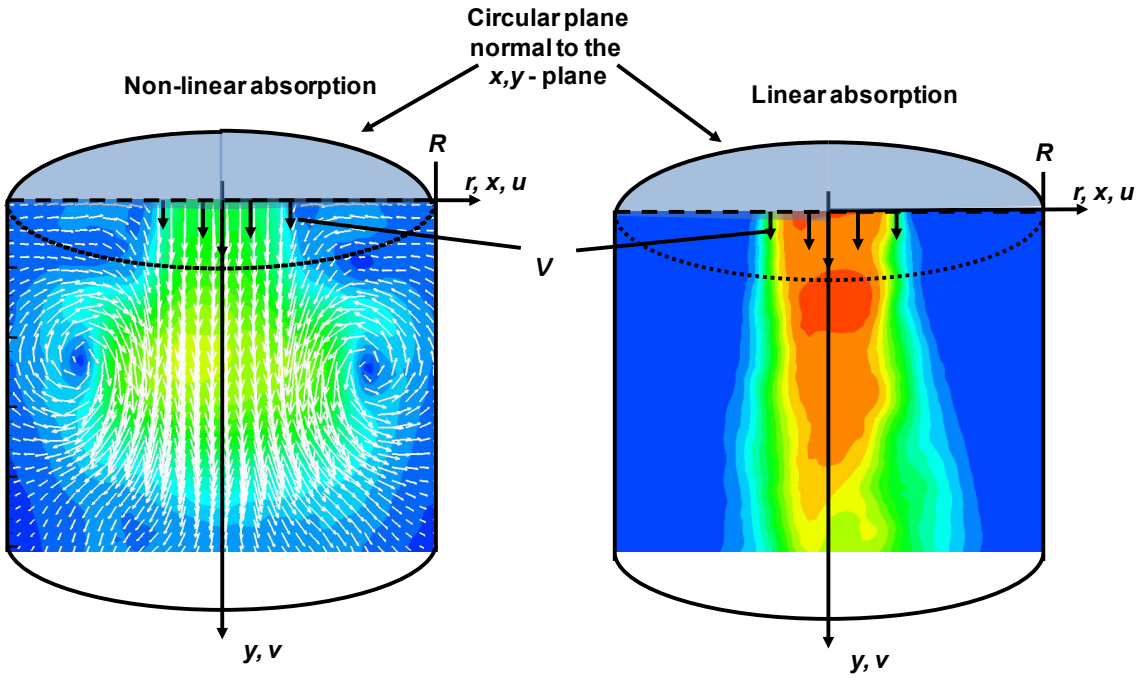

Figure C.5: Schematic of control surface for energy flux calculation

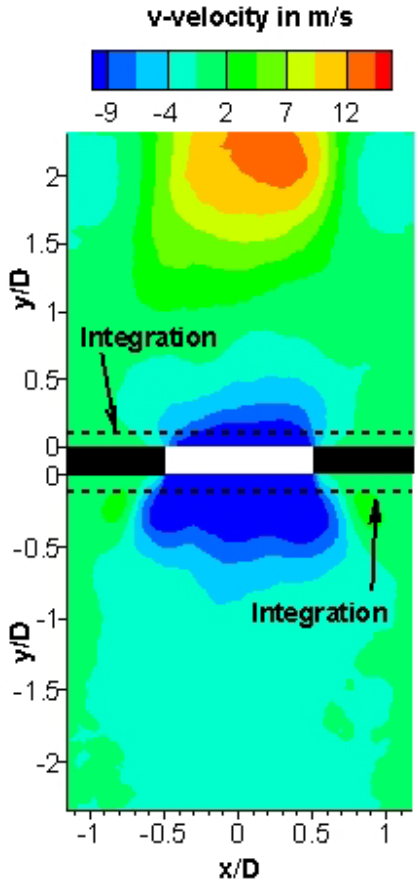

Figure C.6: Schematic of integral location upstream and downstream of the aperture, non-linear absorption regime, *L/D* = 0.47, 137 dB, 125 Hz, plate number 1

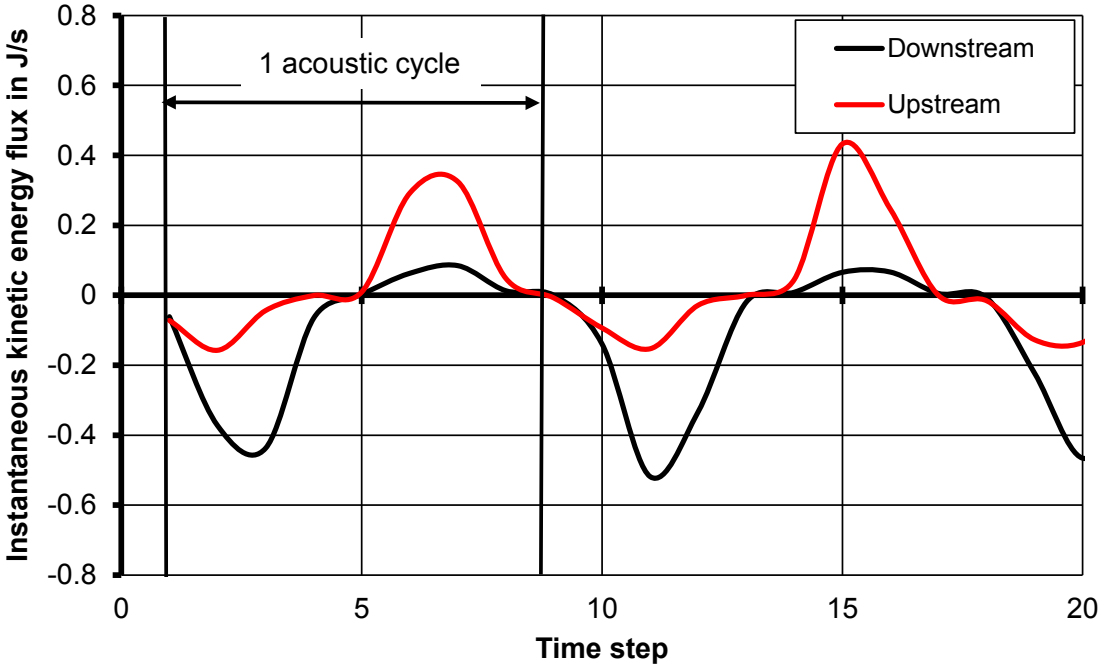

Figure C.7: Instantaneous kinetic energy flux of the aperture, non-linear absorption regime, *L/D* = 0.47, 137 dB, 125 Hz, plate number 1.

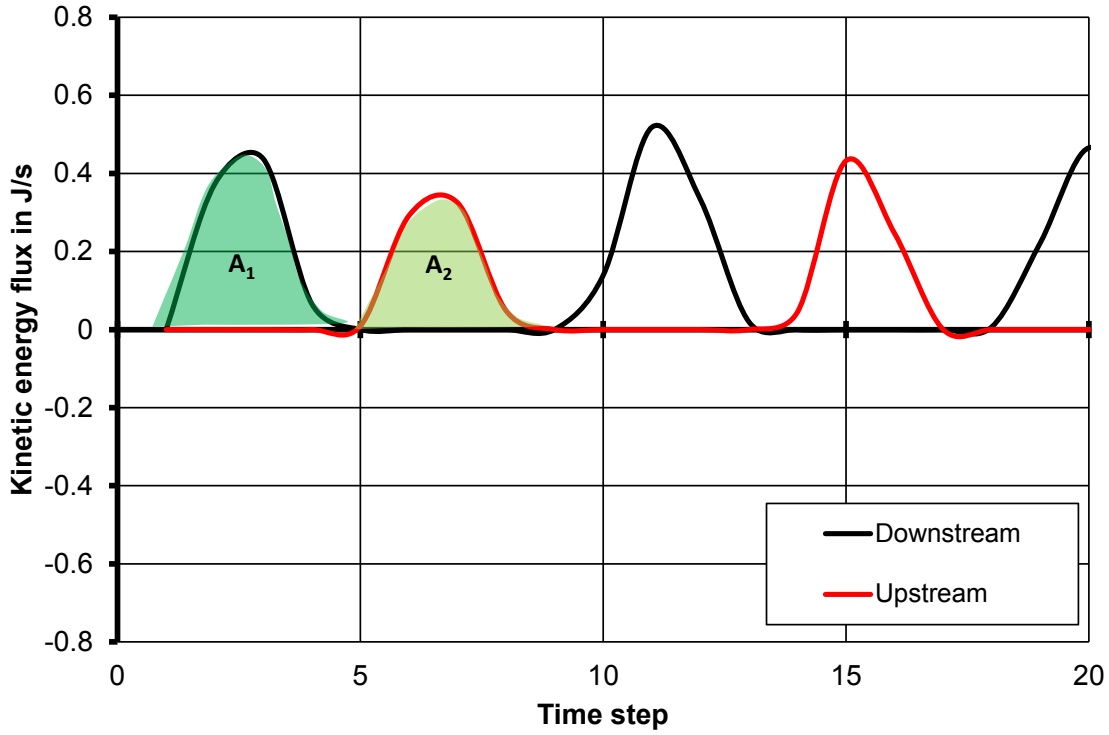

Figure C.8: Absolute instantaneous kinetic energy flux upstream and downstream of the aperture, non-linear absorption regime, *L/D* = 0.47, 137 dB, 125 Hz, plate number 1.

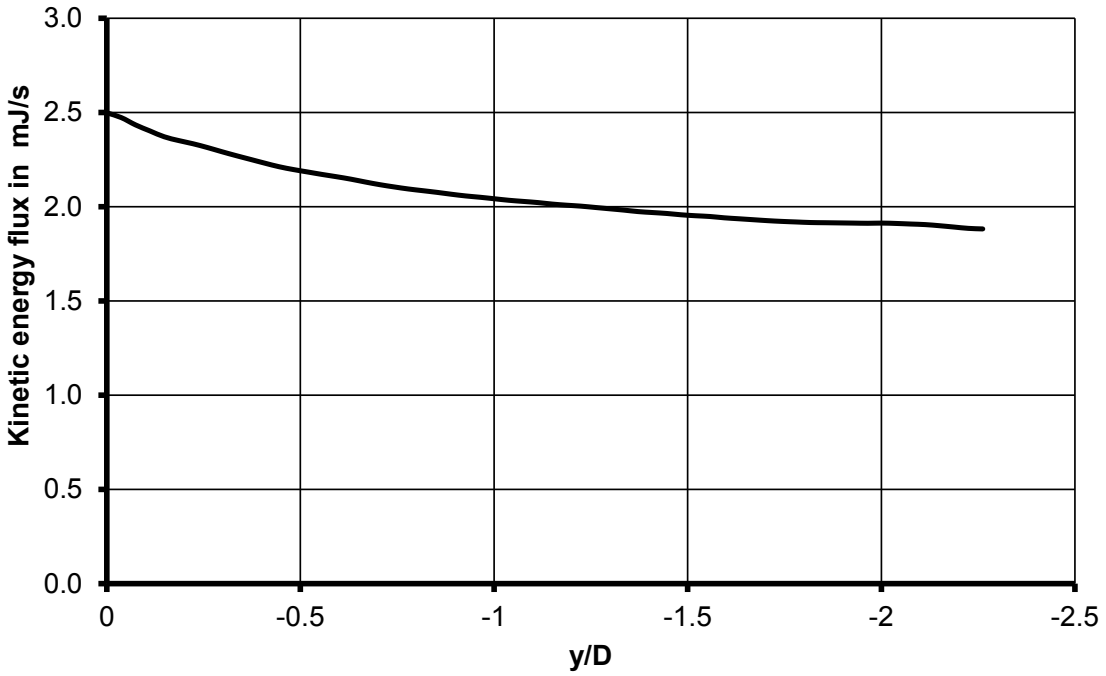

Figure C.9: Schematic of mean energy flux, no excitation, *L/D* = 0.47, *dp* = 8 Pa, plate number 1

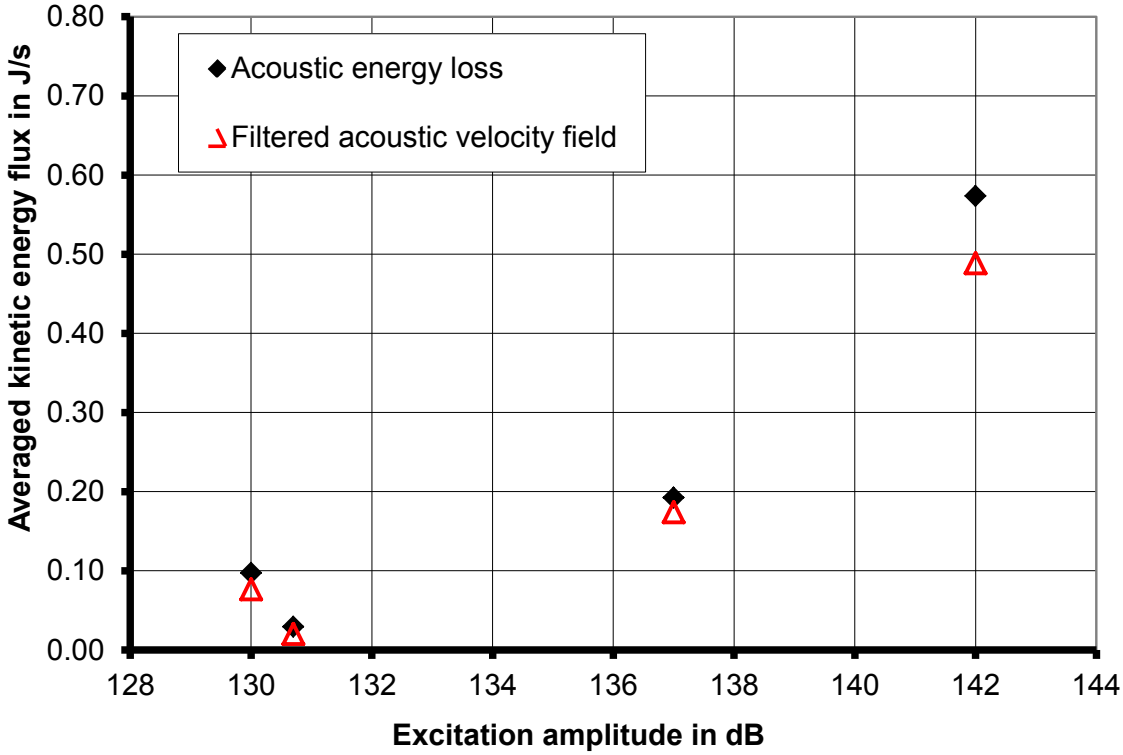

Figure C.10: Averaged kinetic energy flux per acoustic cycle compared to acoustic energy loss, non-linear absorption regime, *L/D* = 0.47, plate number 1.

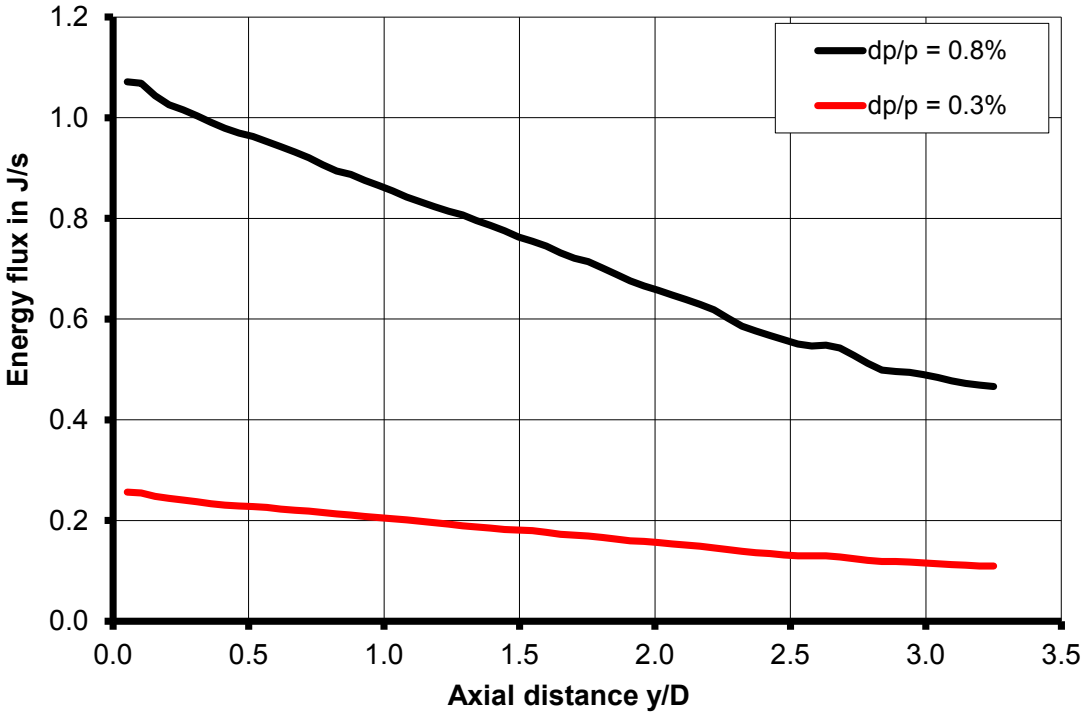

Figure C.11: Kinetic energy flux of the mean flow field for 0.8 and 0.3% *dp/p*, *L/D* = 0.5, plate number 2.

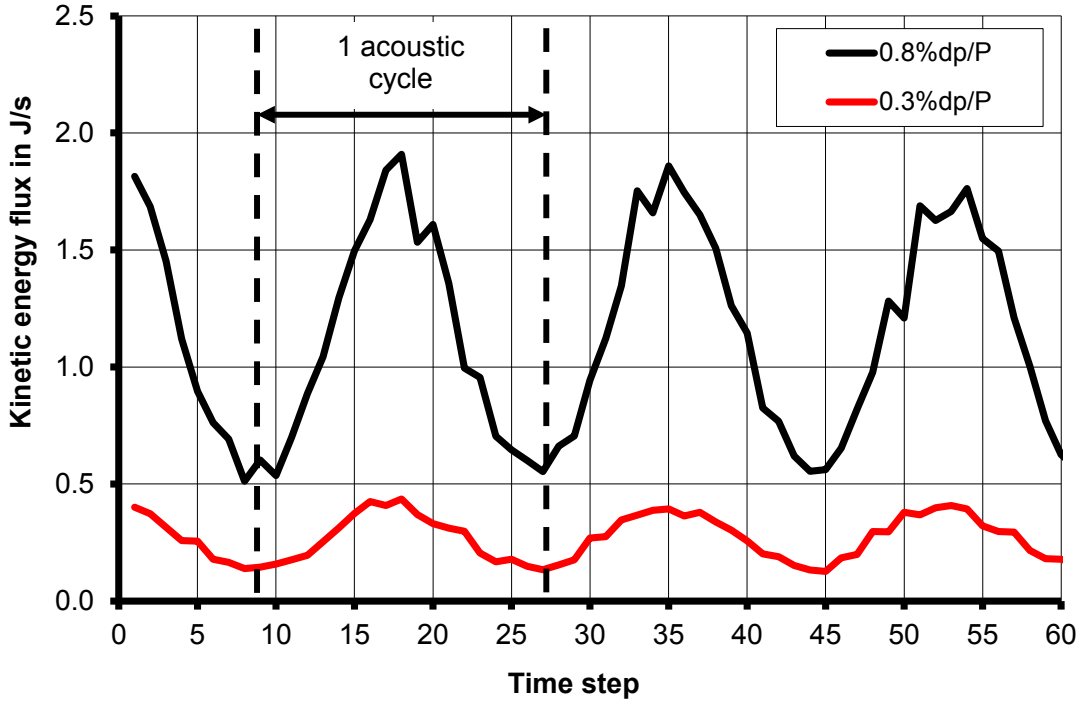

Figure C.12: Instantaneous kinetic energy flux at the orifice exit

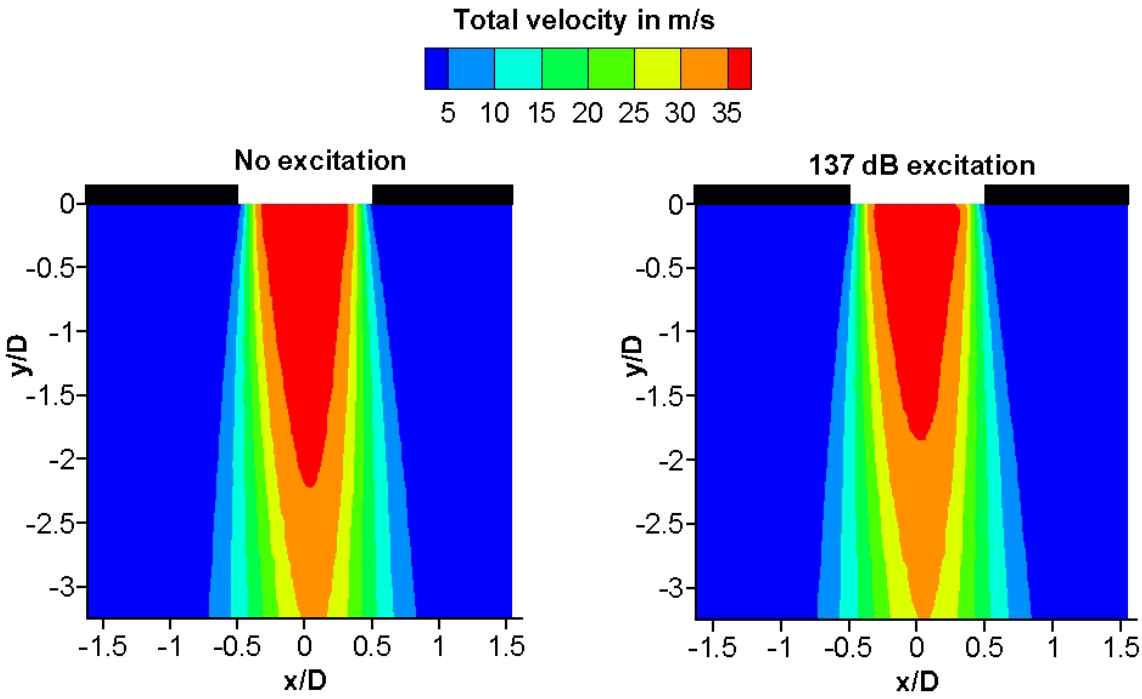

Figure C.13: Example of forced and unforced mean flow field, linear acoustic absorption, *L/D* = 1, *f* = 62.5 Hz, 0.8% *dp/p*, plate number 3.

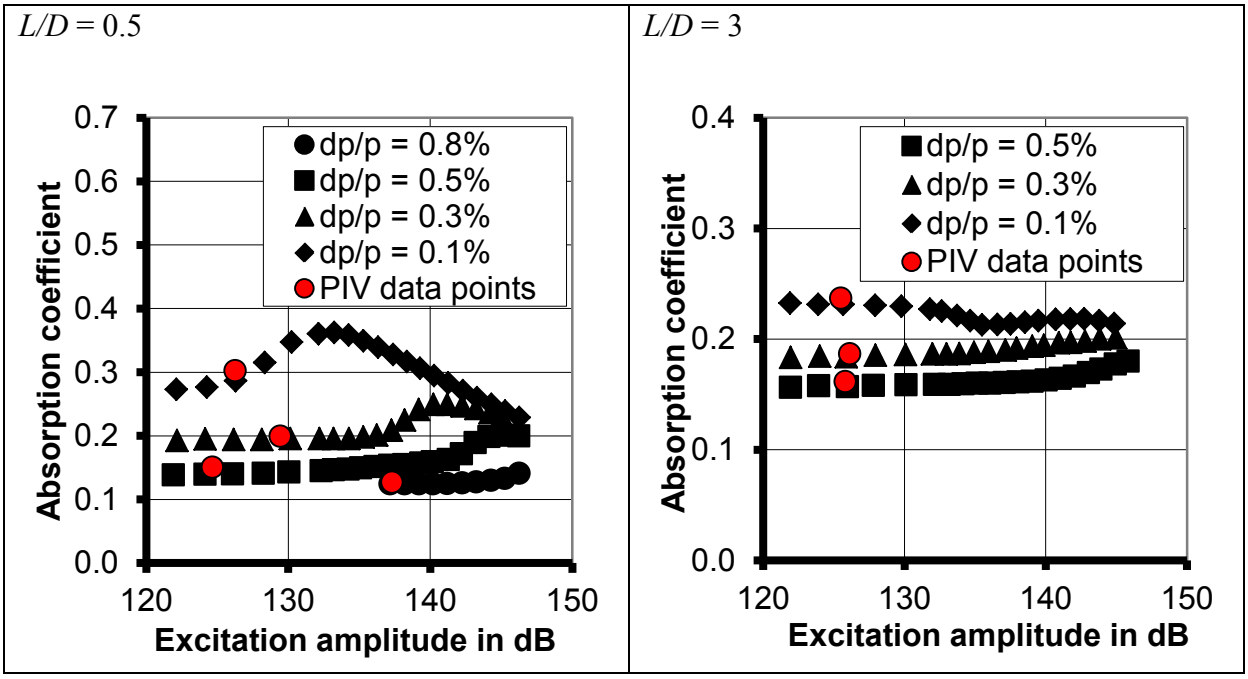

Figure C.14: PIV data points relative to measured absorption coefficients

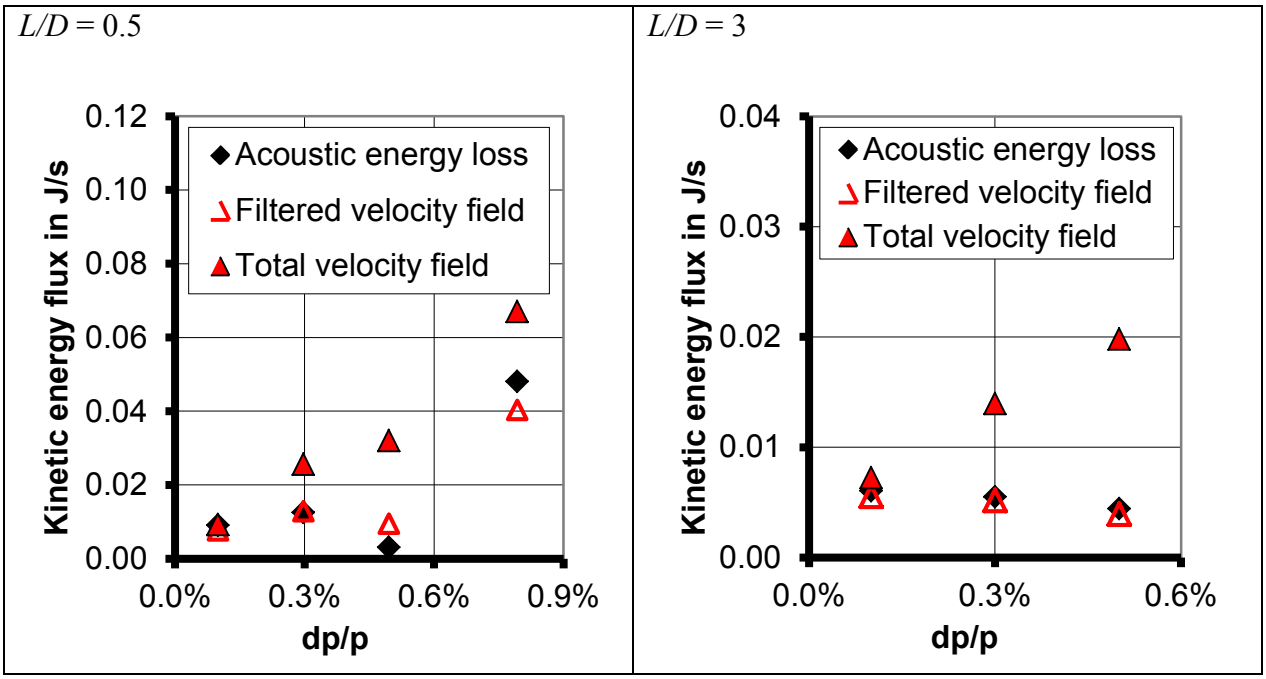

Figure C.15: PIV flow field kinetic energy comparison with acoustic loss

D. Phase Averaging of Acoustically Related Velocity Field

To get a more meaningful characterisation of the velocity field the filtered acoustically related flow field has been phase averaged. However, as the excitation frequency is 125 Hz and the PIV sampling frequency is 1100 Hz this is not straightforward. Hence the temporal coefficient of each acoustically related POD mode has been interpolated using the Fast Fourier interpolation technique in MATLAB. Therefore the sampling frequency has been increased by factor 5 leading to 44 phases for one acoustic cycle at 125 Hz forcing frequency. Moreover 70 instances for each phase along the acoustic cycle have then been averaged. An example of the statistical accuracy of this data can be found in Figure D.1 for the best case and Figure D.2 for the worst case. The data shows a deviation of the true mean (at 0%) to the actual mean velocity calculated by the amount of samples. This deviation, and the standard error, has been normalised relative to the mean velocity over half an acoustic cycle:

$$U = \frac{2}{T}\int_0^{T/2} U_{bulk}(t)dt\,. \tag{D.1}$$

The standard errors have been calculated as in Montgomery and Runger (1994):

$$\varepsilon_u = z\sigma\sqrt{\frac{1}{N}}\,, \tag{D.2}$$

where z represents the confidence band, which is defined as 2.576 for a 99% band and 1.96 for a 95% band. Moreover the parameter σ represents the standard deviation of the sample and N denotes the amount of samples. In the worst case scenario of $t/T = 0.45$ where the velocity at $x/D = 0$ and $y/D = -0.07$ is close to zero the error estimated for the statistical accuracy of the phase average velocity is no worse than 4% for a 95% confidence band. Hence the estimate for the phase averaged acoustically related flow field was seen as sufficient in terms of its statistical accuracy.

Furthermore the acoustically related flow field during linear acoustic absorption was also phase averaged. The only difference to the non-linear acoustic absorption flow field

is that in the linear regime the forcing frequency was set to 62.5 Hz. Hence the data was interpolated using the MATLAB Fourier spectrum interpolation based on 7680 samples and an interpolated sampling frequency of 2750 Hz. This has also led to 70 samples per phase average. Figure D.3 shows the statistical accuracy of the phase average at t/T = 0.5 which is the velocity minimum for the considered orifice geometry. In this case the deviation from the true mean has been normalised relative to the mean v-velocity component at the exit of the aperture for the test case. As it can be seen the statistical accuracy is within 3% for a 99% confidence band.

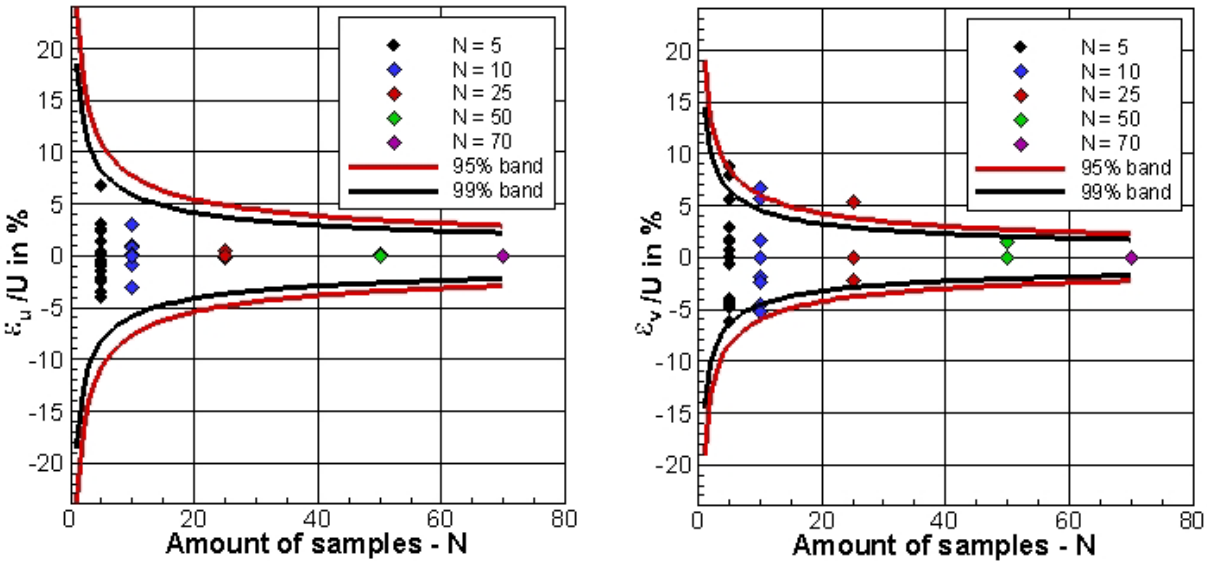

Figure D.1: Example of best case statistical analysis of phase average data, 137 dB excitation amplitude, t/T = 0.3, L/D = 0.47, plate number 1.

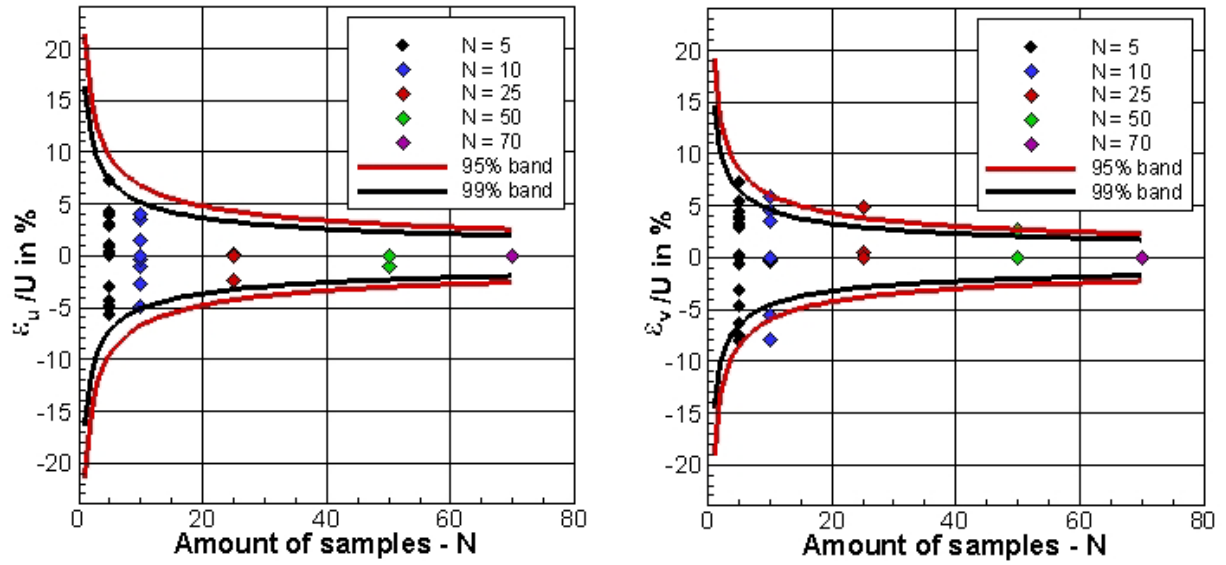

Figure D.2: Example of worst case statistical analysis of phase average data, 137 dB excitation amplitude, *t/T* = 0.45, *L/D* = 0.47, plate number 1.

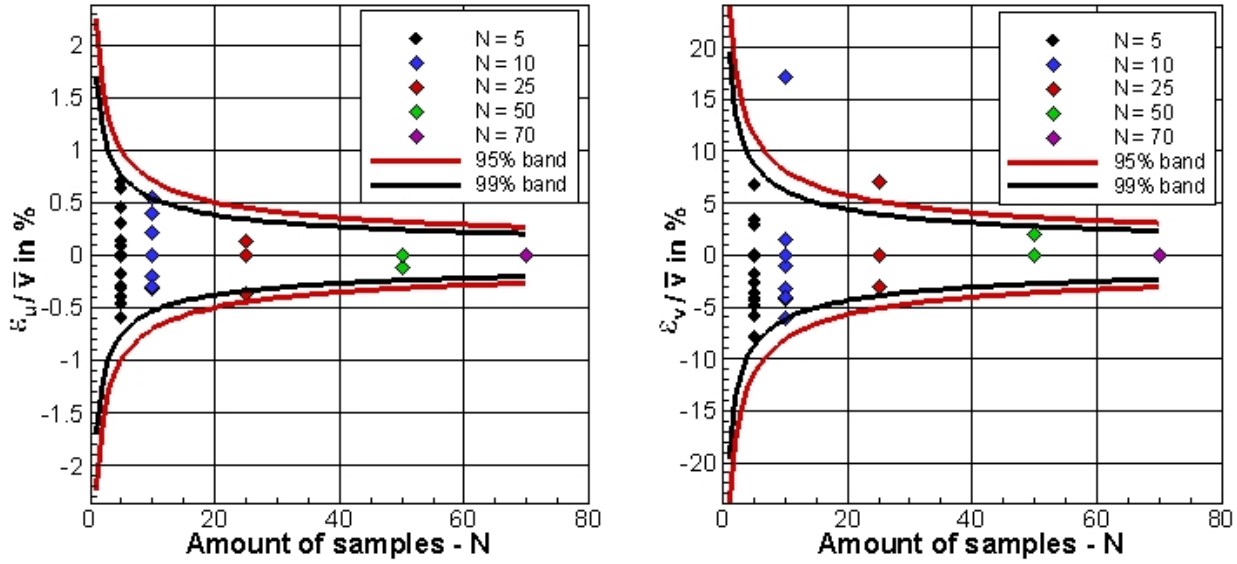

Figure D.3: Example of worst case statistical analysis of phase average data, *dp/p* = 0.8%, *t/T* = 0.5, *L/D* = 0.5, plate number 3.

E. Circumferential wave considerations

As already discussed the damper test facility, described in chapter 3.3.2, used for the non-resonant acoustic damper investigation (section 8.2) was simulating one sector of a full annular combustor. Plane axial acoustic waves were used to measure the acoustic performance of the damper system exposed to a realistic flow field generated by a fuel injector. This resulted in an axial acoustic standing wave with its anti-node being at the fuel injector exit extending over the face of the damping skin. Figure E.1 shows a schematic of an axial cut through a full annular combustor rotated around the centreline (C_L). Moreover a front view along the line (*A-A'*) of a schematic full annular combustor is shown on the right hand side of Figure E.1. In this case a passive damping system is applied to the outer combustor wall. In practice full annular combustion systems are prone to combustion instabilities coupling with circumferential pressure waves travelling in the azimuthal direction. For the experiments and modelling conducted in the previous section it was assumed that the azimuthal change in pressure amplitude was small. Hence the pressure amplitude would remain constant along the circumferential coordinate as long as the damper length in circumferential direction is much smaller than the wave length, i.e. long wave length assumption in circumferential direction. However the designer of an acoustic damping system might want to extend the damper volume over more than one sector or ultimately would like to assess if the total annulus between the metering skin and damping skin can be used for the passive damper. If no separating walls between the damper cavity is used, i.e. full annular cavity between metering and damping skin, the azimuthal modelling developed by Eldredge (2004) can be applied. However very little is known using separated cavities within the annulus between the damping and metering skin. Hence a design tool is proposed for the acoustic absorption assessment of the circumferential length of the damper cavity.

E.1 Definition of Circumferential Wave Model

A model was developed to simulate a travelling wave along the surface of the damper with the emphasis of the assessment of the cavity acoustics between damping and

metering skin. This model is described in this section. Therefore the circumferential combustor as shown in Figure E.1 was modelled as an axial duct where the axial length is representing the circumferential length of the damper segments as indicated in Figure E.2. Hence the circumferential coordinate in the full annular system was replaced by the axial coordinate x. Moreover the circumferential length of the damping segments is represented by the parameter L_D. In this case waves perpendicular to the axial coordinate x, i.e. axial waves and radial waves within the full annular combustion system are neglected, as they are below the cut-off frequency for the considered frequency range (below 1000 Hz at full engine operating conditions). Another simplification has been incorporated by assuming the metring skin of the damping system is fed by a plenum, i.e. the pressure amplitude upstream of the metering skin is set to zero. In reality the metering panel will be fed by a thin annulus between the metering skin and the engine casing. However, the model is used as a preliminary design tool for the damper geometry and so this detail is initially neglected. Nevertheless this should be incorporated in more detailed network representations for the linear stability analysis of a fully representative combustion system.

The input to the developed model is an axial travelling wave with a given amplitude $\hat{p}_0$ which is introduced to simulate a travelling wave within the combustion system. Therefore the travelling wave is defined as

$$\hat{p}_0(x) = \hat{p}_{exc} \exp(-ikx). \tag{E.1}$$

In the previously developed model the long wave length assumption was used assuming there is no change in pressure amplitude along the coordinate x. However in this case this needs to be incorporated to assess the acoustic mode shapes within the cavity between damping and metering skin. According to Eldredge and Dowling (2003) the change in stagnation enthalpy relative to the axial coordinate can be described in non-dimensional form as

$$\frac{d\hat{B}_C}{dx} = -ikL\hat{u}_C . \tag{E.2}$$

Moreover the change in acoustic velocity amplitude within the cavity with respect to the axial coordinate was defined as

$$\frac{d\hat{u}_C}{dx} = -ikL\hat{B}_C - \frac{C_1 L_D}{A_C}\hat{v}_1 + \frac{C_2 L_D}{A_C}\hat{v}_2 \quad . \tag{E.3}$$

For the purpose of this work mean velocity is only present across the metering and damping skin. Within the duct representing the combustion chamber there will be no mean flow in the axial direction, i.e. no mean flow component in circumferential direction for the full annular combustion system. Moreover the damping skin and metering skin forms a rectangular cavity of length L_D, width W_D and height S. Hence reintroducing the dimensions into equations (E.2) and (E.3) and changing the geometric parameters for the circumference (C_1 and C_2) and cross-sectional area (A_C) of the tubular damper cavity into a rectangular cavity leads to the change in cavity pressure amplitude in axial direction

$$\frac{d\hat{p}_1(x)}{dx} = -i\rho\omega\hat{u}_C(x) \tag{E.4}$$

and change in axial acoustic velocity amplitude in axial direction

$$\frac{d\hat{u}_{C(x)}}{dx} = -i\omega\frac{1}{\gamma\bar{p}_1}\hat{p}_1(x) - \frac{1}{S}\hat{v}_1(x) + \frac{1}{S}\hat{v}_2(x) \tag{E.5}$$

with respect to time and space. In this case the velocity amplitude over the damping skin can be defined as in Eldredge and Dowling (2003) or Rupp et. al. (2012):

$$\hat{v}_1(x) = \frac{\eta_1}{j\omega}\frac{\bar{c}^2}{L}\left[\frac{\hat{p}_1(x)}{\gamma\bar{p}_1} - \frac{\hat{p}_0(x)}{\gamma\bar{p}_0}\right]. \tag{E.6}$$

Moreover the metering skin velocity amplitude is defined in the same way

$$\hat{v}_2 = \frac{\eta_2}{j\omega}\frac{\bar{c}^2}{L}\left[-\frac{\hat{p}_1(x)}{\gamma\bar{p}_1}\right]. \tag{E.7}$$

The parameter η represents the compliance of the perforated liner. According to Eldredge and Dowling (2003) the compliance is defined as

$$\frac{1}{\eta} = \frac{\pi R^2}{\sigma L_D}\frac{1}{K_D} + \frac{L}{\sigma L_D}. \tag{E.8}$$

In this case the compliance is representing the modified Howe model as discussed in section 2.5.2 or 5.8 with the Rayleigh Conductivity defined as in Howe (1979b)

$$K_D = \frac{-i\omega\rho\pi R}{2}\frac{\hat{v}}{\hat{p}} = \Gamma(St) + i\delta(St). \tag{E.9}$$

As discussed in section 5.9 the model utilising the linear solution of the unsteady momentum balance is a more intuitive and accurate representation of the linear acoustic absorption characteristics for acoustic dampers within gas turbine combustors. Hence the Conductivity terms used by Eldredge and Dowling (2003) have been modified so that they are calculated form the liner impedance of the damping and metering skin

$$\Gamma(St) + i\delta(St) = \frac{-i\omega\rho\pi R}{2}\frac{1}{Z}. \tag{E.10}$$

The liner impedance Z was defined as in chapter 5.9:

$$Z_1 = \frac{\hat{p}_1 - \hat{p}_0}{\hat{v}_{D1}} = \frac{1}{C_{D1}^2}\rho\,\overline{U}_{D1} + \rho\zeta_{vis,1} + i\rho\omega L_1, \tag{E.11}$$

$$Z_2 = \frac{-\hat{p}_1}{\hat{v}_{D2}} = \frac{1}{C_{D2}^2}\rho\,\overline{U}_{D2} + \rho\zeta_{vis,2} + i\rho\omega L_2. \tag{E.12}$$

Thus the compliance used in travelling wave model in this section is then based on the Conductivities of the damping and metering skin using the impedance of the liners derived from the unsteady momentum balance as defined in equations (E.11) and (E.12):

$$\eta = \frac{\sigma L_D 2(\Gamma + i\delta)}{\pi R}. \tag{E.13}$$

The compliance is then used in equations (E.6) and (E.7) to define the unsteady velocity amplitudes across the damping skin and metering skin. Thereafter the velocities are substituted into equation (E.5)

$$\frac{d\hat{u}_C(x)}{dx} = \left(-i\omega - \frac{1}{S}\frac{\eta_1}{i\omega}\frac{c^2}{L_D} - \frac{1}{S}\frac{\eta_2}{i\omega}\frac{c^2}{L_D}\right)\frac{\hat{p}_1(x)}{\gamma\overline{p}_1} + \frac{1}{S}\frac{\eta_1}{i\omega}\frac{c^2}{L_D}\frac{\hat{p}_0(x)}{\gamma\overline{p}_0}. \tag{E.14}$$

This equation can then be differentiated with respect to the axial coordinate and equation (E.4) can be substituted for the differential of pressure amplitude in the cavity with respect to the axial coordinate. Hence an inhomogeneous ordinary differential equation of second order can be derived

$$\frac{d^2\hat{u}_C(x)}{dx^2} - \alpha\hat{u}_C(x) = \beta\exp(-ikx)\ . \tag{E.15}$$

The time and space independent constant α is therefore defined as

$$\alpha = \left(-i\omega\frac{1}{\gamma\bar{p}_1} - \frac{1}{S}\frac{\eta_1}{i\omega}\frac{c^2}{L_D}\frac{1}{\gamma\bar{p}_1} - \frac{1}{S}\frac{\eta_2}{i\omega}\frac{c^2}{L_D}\frac{1}{\gamma\bar{p}_1}\right)(i\rho\omega). \tag{E.16}$$

and the constant β is defined as

$$\beta = -ik\frac{1}{S}\frac{\eta_1}{i\omega}\frac{c^2}{L_D}\frac{1}{\gamma\bar{p}_0}\hat{p}_{exc}\,. \tag{E.17}$$

This differential equation can be solved analytically as a superposition of the general solution for a homogenous differential equation and the particular solution of the inhomogeneous equation. The particular solution was derived based on the right hand solution of the differential equation (E.15). Hence the acoustic velocity amplitude in the damper cavity with respect to time and axial coordinate *x* can be defined as

$$\hat{u}_C(x,t) = Const_1\exp\left(\sqrt{\alpha}x\right) + Const_2\exp\left(-\sqrt{\alpha}x\right) + \frac{\beta}{(-ik)^2-\alpha}\exp(-ikx). \tag{E.18}$$

The time dependent constant $Const_1$ and $Const_2$ can be derived using the boundary conditions for the systems. As the volume is enclosed by rigid walls the boundary conditions can be defined so that the acoustic velocity amplitude vanishes at the walls of the cavity volume, i.e.

$$\hat{u}_C(x=0) = \hat{u}_C(x=L_D) = 0\,. \tag{E.19}$$

Thus the time dependent constants can be defined as

$$Const_1 = -\frac{\beta}{(-ik)^2-\alpha} - Const_2 \tag{E.20}$$

and

$$Const_2 = \frac{\beta}{(-ik)^2 - \alpha} \; \frac{-\exp(-ikL_D) + \exp\left(\sqrt{\alpha}L_D\right)}{\exp\left(-\sqrt{\alpha}L_D\right) - \exp\left(\sqrt{\alpha}L_D\right)} \; . \tag{E.21}$$

The cavity pressure amplitude mode shape can then be calculated by differentiating the cavity velocity amplitude (equation (E.18)) with respect to the axial coordinate x and substituting it into equation (E.14). Thereafter the velocity amplitudes can be calculated using the incident pressure amplitude and the cavity pressure amplitudes in equations (E.6) and (E.7).

Finally the acoustic energy loss is derived as proposed by Eldredge and Dowling (2003) in non-dimensionalised form for tubular damping and metering skin with circumference C_1 and C_2

$$\Pi_L = \int_0^1 \left\langle B'(x) v_1'(x) \right\rangle dx = \frac{kL_D}{2} \left(\left(\frac{1}{\eta_1} \right) \int_0^1 \left| \hat{v}_1(x) \right|^2 dx + \frac{C_2}{C_1} \mathrm{Im}\left(\frac{1}{\eta_2} \right) \int_0^1 \left| \hat{v}_2(x) \right|^2 dx \right) . \tag{E.22}$$

This equation was dimensionalised and the velocity amplitudes have been numerically integrated along the axial coordinate of the damper surface:

$$\Pi_L = \frac{1}{2} \rho \, \omega L_D W_D \left[\mathrm{Im}\left(\frac{1}{\eta_1} \right) \int_0^{L_D} \left| \hat{v}_1(x) \right|^2 dx + \mathrm{Im}\left(\frac{1}{\eta_2} \right) \int_0^{L_D} \left| \hat{v}_2(x) \right|^2 dx \right] . \tag{E.23}$$

Finally the calculated energy loss along the acoustic damper was normalised with the incident pressure amplitude

$$\Pi_P = \frac{\Pi_L}{\left| \hat{p}_{exc} \right|^2} . \tag{E.24}$$

E.2 Circumferential Modelling Results for the Example of a Resonating Liner

The developed circumferential acoustic absorption model was used to assess the acoustic characteristics of resonant liners exposed to travelling waves. One aspect of this investigation is to assess at which point the resonance behaviour in the cavity between metering and damping skin is breaking down and thus reduces the generated

acoustic energy loss. During the design process it is cost effective to validate and optimise acoustic damper designs exposed to axial acoustic waves in impedance test facilities. Nevertheless if the damper is applied to full annular gas turbine combustors suffering from circumferential travelling waves it is important to analyse if the damper cavity is able to resonate and the long wave length assumption within the damper cavity is still valid. Hence the circumferential model has been applied to the resonant damper configuration 1 (details of the test specimen can be found in section A.3). In this case the resonant liner is mounted as shown in Figure E.1 and Figure E.2 (unlike the experimental results shown in section 8.3.1 where the damper was mounted perpendicular to the axial wave). The initial analytical model describing the cavity pressure amplitude with a single point (i.e. incident pressure amplitude if the damper is mounted perpendicular to an incident axial wave), assuming the long wave length assumption as used in chapter 8. Hence for an initial validation of the circumferential modelling behaviour the resonant liner configuration using the "single point model" was compared to the circumferential travelling wave model. The length of the damper L_D was set to the circumferential width of one sector of a reference full annular test facility.

Figure E.3 shows a comparison between the calculated acoustic energy loss by the single point model and the travelling wave model for the resonant damper configuration 1. In general the two models are nearly identical for the chosen sector length. Both models show the same amount of acoustic absorption and predict the resonance frequency to 500 Hz. In general the effects of a travelling wave upon the absorption of the investigated single sector damper configuration seem to be negligible within the investigated frequency band. Discrepancies between the two models occur for frequencies larger than 600 Hz and this deviation seems to increase with frequency. Hence it is expected that the long wave length assumption used in the single point method is starting to break down at higher frequencies than 600 Hz for the considered damper.

This can be confirmed by considering the ratio of cavity pressure amplitude with excitation pressure amplitude along the face of the damper as shown in Figure E.4. In this case it can be seen that the pressure amplitude ratios are virtually constant along the axial coordinate up to 600 Hz. As expected, small deviations away from the constant

pressure amplitude ratio occur for increasing frequencies, as indicated by the pressure amplitude ratio along the axial coordinate for 800 Hz excitation frequency. Figure E.5 shows the phase difference between the cavity amplitude and the excitation pressure amplitude. The gradient in phase difference is caused by the travelling wave along the damper surface. Within the cavity the phase remains constant up to the resonance frequency of 600 Hz as Figure E.6 shows.

An important design task, where this model can be used, is the assessment of the trade-offs between the amount of dampers and the size of the volume. For example using multiple small volume dampers compared to a small amount of large volume dampers. Hence an acoustic energy loss study was undertaken using the travelling wave model to assess the damper cavity volume size. In this case the size of the cavity volume has been doubled by doubling the length of the damper. Moreover the amount of holes has been doubled to keep the porosity of the acoustic damper constant (and ultimately the resonance frequency). In other words this would simulate a resonant liner stretching over the width of two sectors of a full annular combustor. The outcome of this simulation can be compared to two single sector dampers by doubling the acoustic energy loss of the single sector calculation. This comparison is shown in Figure E.7. Initially and not surprisingly, at 300 Hz, the acoustic energy loss is identical to the acoustic loss generated by two separated volumes. However the loss for the larger volume damper is less with increasing frequency compared to the two separated dampers. Moreover the discrepancy between the two test cases is increasing with increasing frequency. Furthermore the maximum acoustic energy loss is occurring at lower excitation frequency for the resonant liner with a volume covering two sectors of a full annular combustor. There should not be a shift in resonance frequency as the porosity, has been increased by the same amount as the volume with constant effective length of the apertures (equation (8.28)). Hence this change in frequency for the maximum acoustic energy loss must be caused by the behaviour of the cavity amplitude mode shape.

Furthermore the damper performance deteriorates further for a damper with a cavity volume equivalent to three sectors of a full annular test rig (compared to three acoustic dampers utilising a volume the size of one sector of a full annular combustor). In this

case two maxima appear at 370 and 700 Hz occur. Moreover the resonance frequency of the single sector dampers, i.e. 500 Hz, is now a minimum of acoustic energy loss for the three sector volume. Again the porosity for the damper using the three sector volume has been tripled and the orifice geometries have been kept constant to ensure a constant resonance parameter or cavity resonance frequency. However the multi-sector damper behaviour does not show the maximum in energy loss at the cavity pressure amplitude. This shows that the unsteady pressure amplitude is largest for the single sector volumes. Hence multiples single sectors will generate a larger acoustic energy loss than a small amount of dampers with larger volumes.

Another interesting aspect of the cavity volume size is indicated by an acoustic energy loss maximum at an excitation frequency of 700 Hz for a cavity volume size equivalent to three full annular combustor sectors shown in Figure E.7. This maximum is caused by a half wave resonance mode within the cavity volume as the pressure mode shape and the phase angle of the cavity pressure wave show for this frequency in Figure E.8 and Figure E.9. Hence the cavity acoustics can be also utilised to form standing waves insight the volume generating larger unsteady pressure drops for the relevant standing wave frequencies. This could be utilised for off design conditions away from the resonant liner frequencies. However the performance of such a damping device needs to be assessed against multiple resonating damping devices at various frequencies to investigate the benefits. Thus the reasons for the change in absorption characteristic with varying volume size (shown in Figure E.7) is caused by the changes in the cavity acoustics. In this case the long wavelength assumption within the damper cavity is no longer valid and the pressure amplitude and phase inside the damper cavity is no longer constant along the length of the damper. This destroys the resonance effect of the damper cavity and axial mode shapes within the cavity occur which influence the acoustic absorption of the damper.

The developed analytical model simulating a circumferential travelling wave along the damper showed advantageous for assessing acoustic damping geometries for full annular combustion systems. Moreover it highlighted opportunities for the damping performance enhancement as well as damper performance shortfalls due to occurring circumferential mode shapes within the damper cavity. Hence the model can be used as

a preliminary design tool for the acoustic damper optimisation prior to the damper geometry application in a more detailed acoustic network model.

Figures

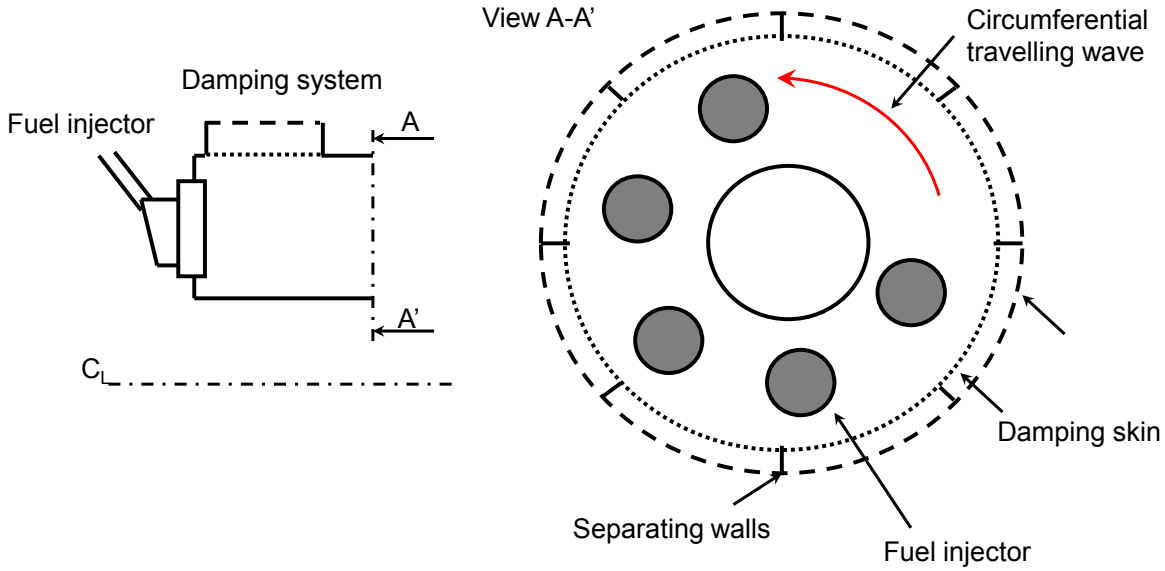

Figure E.1: Schematic of full annular combustion system and circumferential acoustic wave.

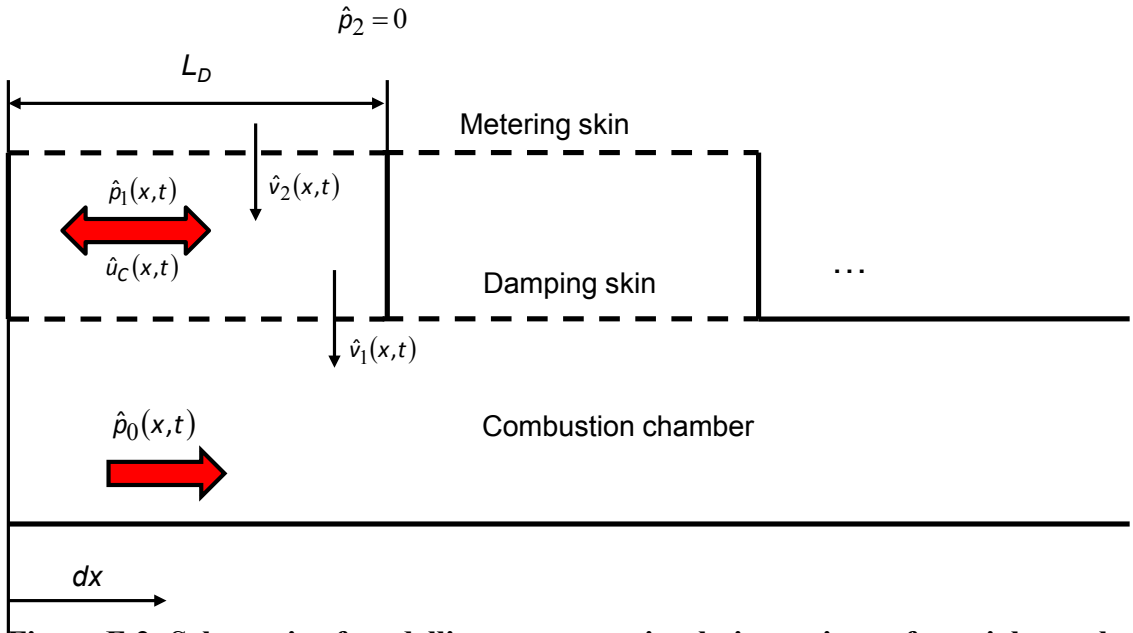

Figure E.2: Schematic of modelling geometry simulating a circumferential travelling wave.

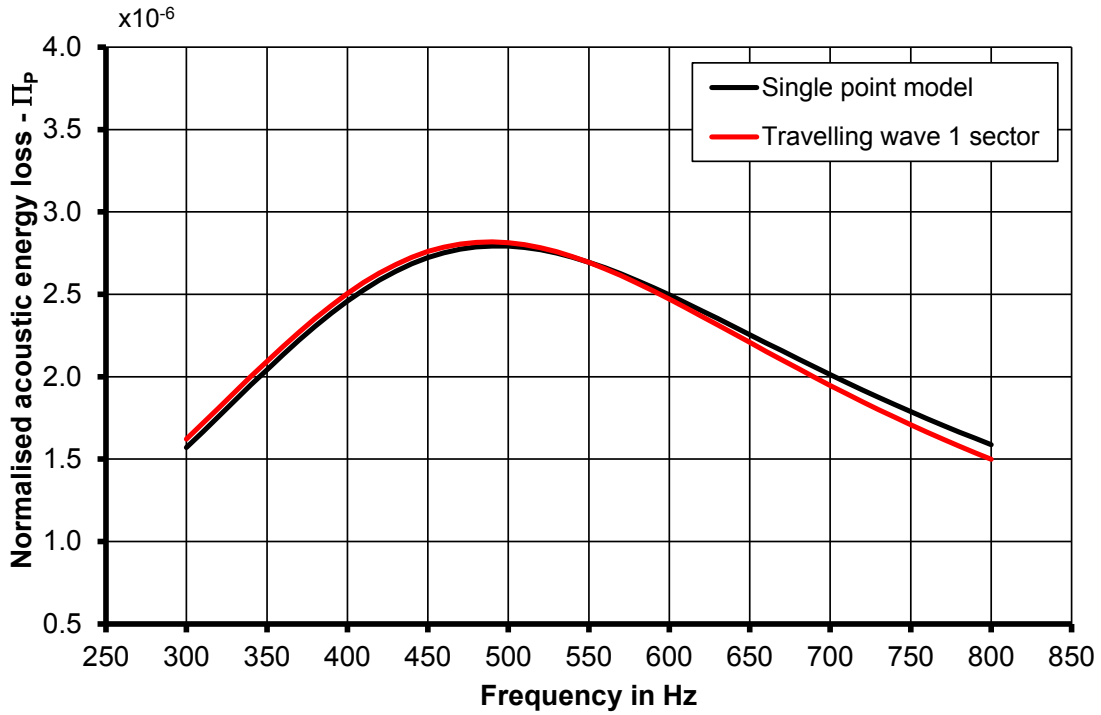

Figure E.3: Comparison of normalised acoustic energy loss using single point and travelling wave model calculating resonating damper configuration 1.

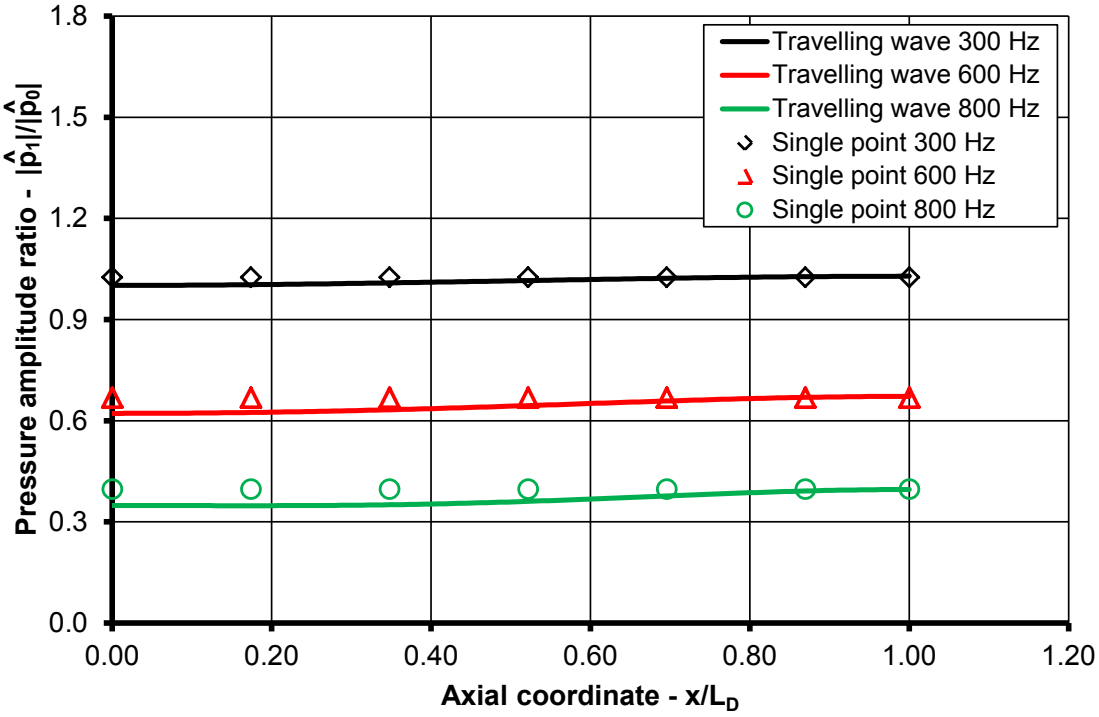

Figure E.4: Comparison of amplitude ratios for single point and travelling wave model for resonating damper configuration 1.

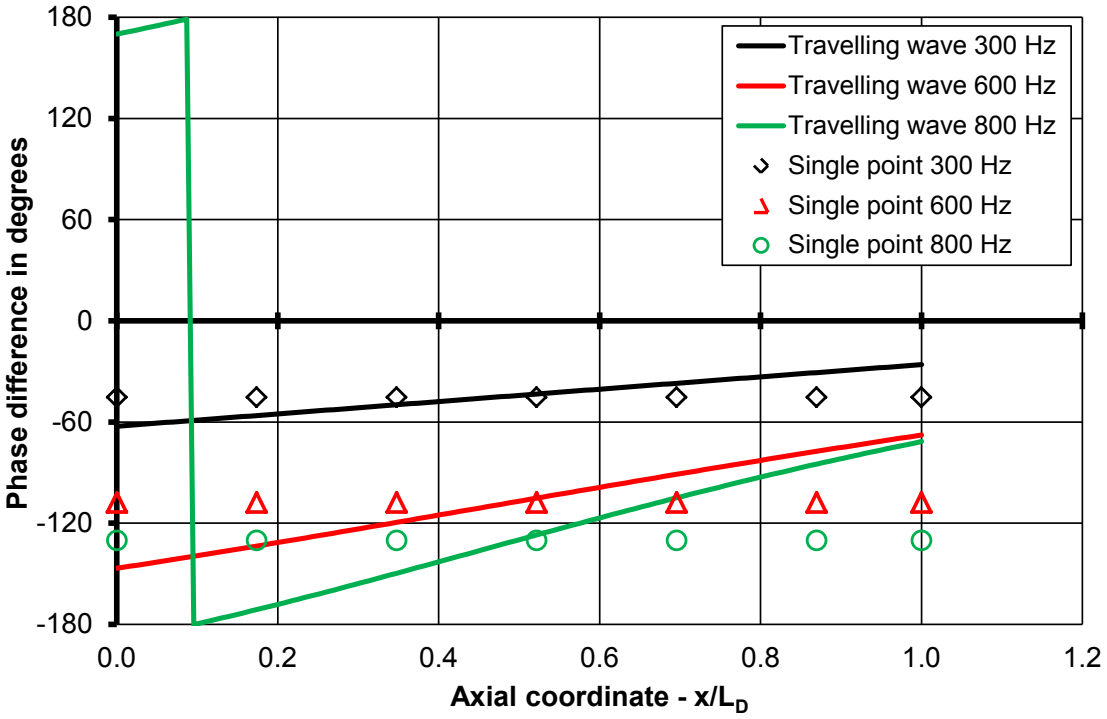

Figure E.5: Comparison of phase difference between excitation amplitude and cavity amplitude for single point and travelling wave model calculating resonating damper configuration 1.

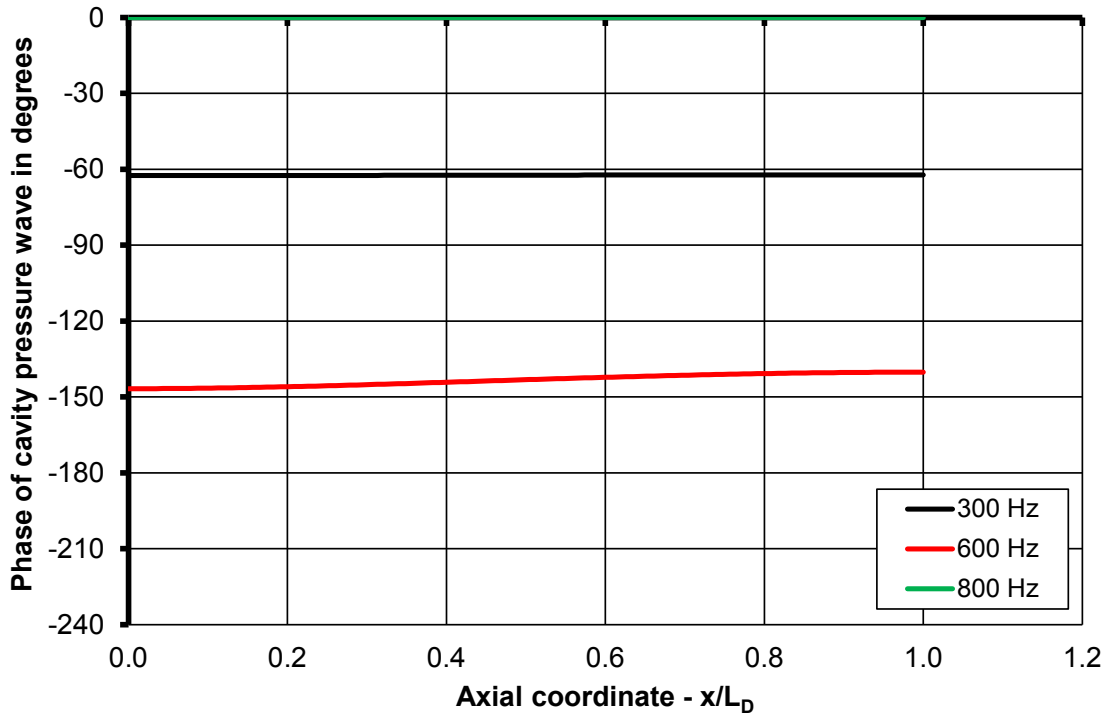

Figure E.6: Comparison of phase angle of cavity pressure wave calculated by travelling wave model for resonating damper configuration 1.

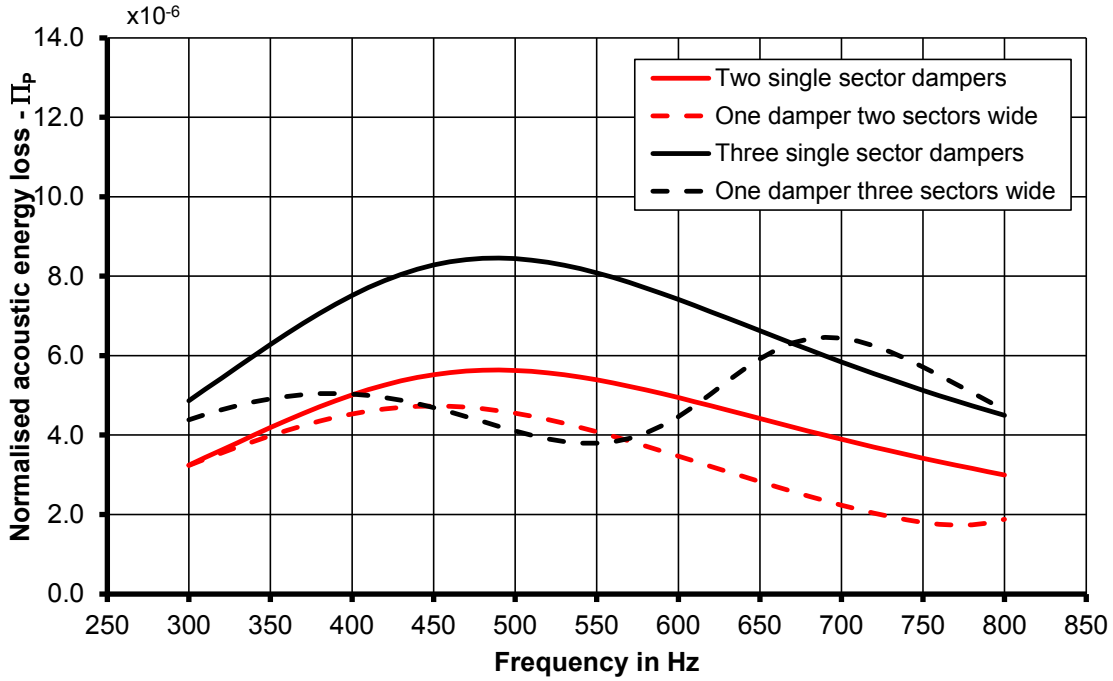

Figure E.7: Variation of damper length compared to multiple single sector damper configurations.

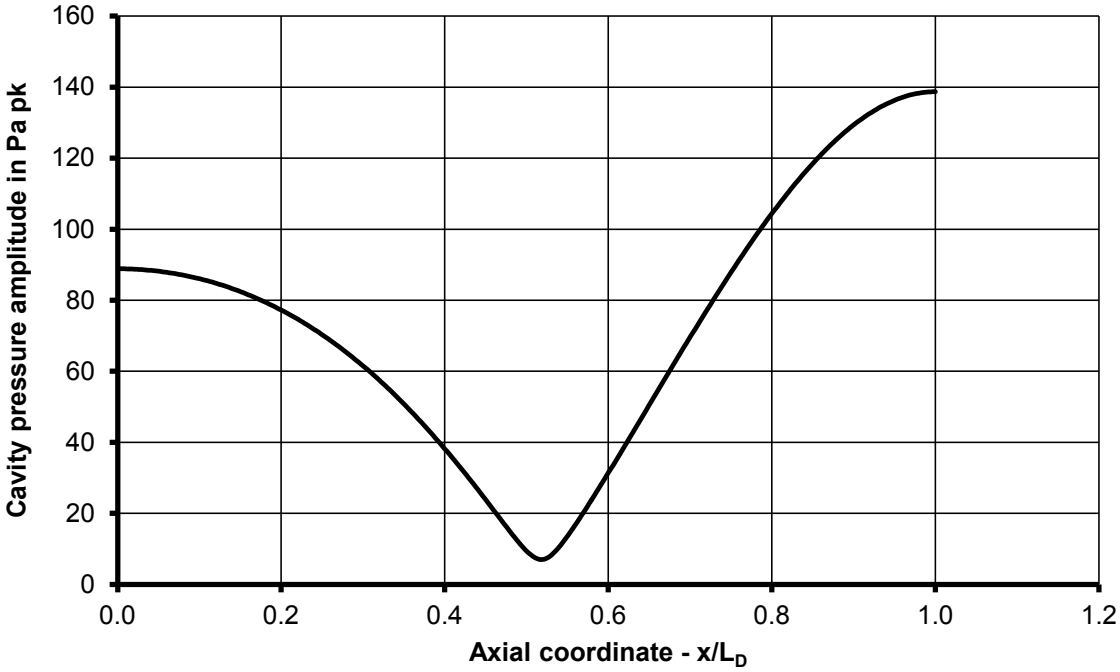

Figure E.8: Half wave mode shape in damper cavity volume at 720 Hz for three sector calculation.

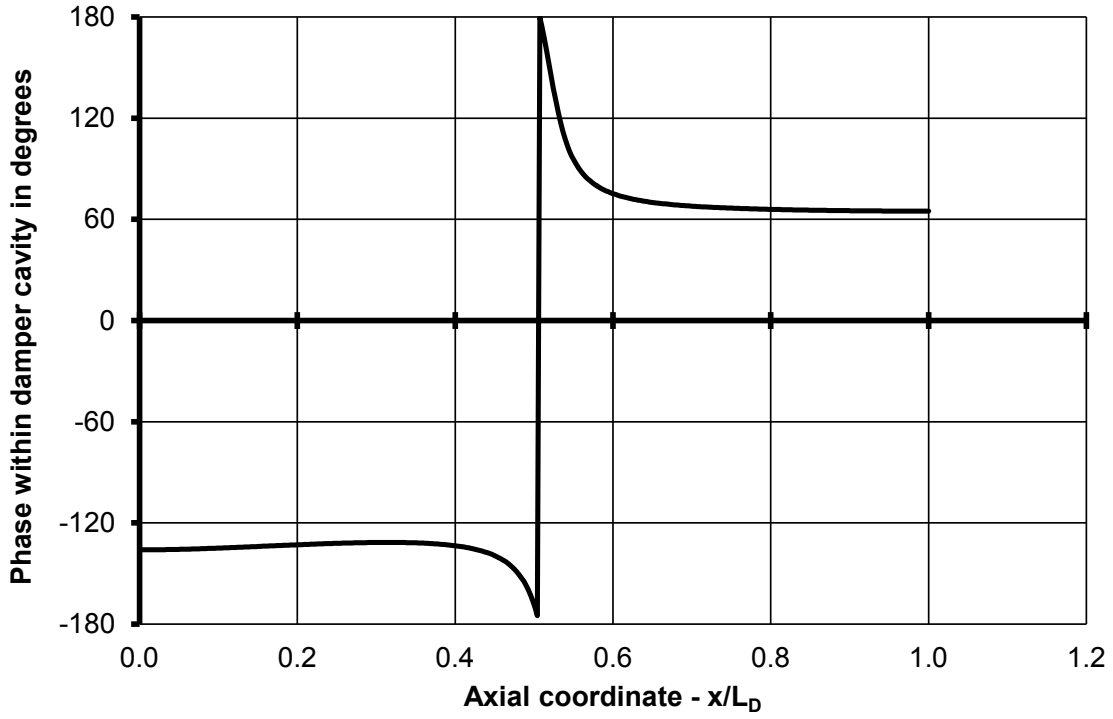

Figure E.9: Phase of half wave mode shape in damper cavity volume at 720 Hz for three sector calculation.